

Development of a Steel Bridge System - Simple for Dead Load and Continuous for Live Load

Volume 1 - Analysis and Recommendations

Dr. Atorod Azizinamini
Aaron Yakel
Mohammadreza Farimani

National Bridge Research Organization (NaBRO)
(<http://www.NaBRO.unl.edu>)
Department of Civil Engineering
College of Engineering and Technology

W150 Nebraska Hall
Lincoln, Nebraska 68588-0531
Telephone (402) 472-5106
FAX (402) 472-6658

Sponsored By

Nebraska Department of Roads



July, 2005

UNIVERSITY OF
Nebraska
Lincoln

Table of Contents

Table of Contents	ii
List of Figures	vi
List of Tables	xii
Acknowledgement	xiii
Abstract	xiv
Executive Summary	1
CHAPTER 1	
Introduction	3
1.1 PROBLEM STATEMENT	3
1.2 BACKGROUND	7
1.3 RESEARCH OBJECTIVE	9
1.4 REPORT SCOPE AND LAYOUT	9
CHAPTER 2	
Market Analysis	12
2.1 GENERAL DESCRIPTION	12
2.2 DATA REDUCTION	13
2.3 ANALYSIS RESULTS	14
2.3.1 NEBRASKA	14
2.3.2 KANSAS	15
2.3.3 OKLAHOMA	16
2.3.4 IOWA	18
2.3.5 COLORADO	19
2.3.6 SOUTH DAKOTA	19
2.3.7 WYOMING	21
2.4 CONCLUSIONS	24
CHAPTER 3	
Vision of the System	25
3.1 INTRODUCTION	25
3.2 BRIDGE MATERIALS MARKET ANALYSIS	26
3.3 CONVENTIONAL VERSUS NEW METHOD	27

3.4	CASE STUDIES	30
3.4.1	SPRAGUE STREET BRIDGE.	30
3.4.2	N-2 OVER I-80 BRIDGE	31
3.5	DESIGN PROCEDURE AND RESULTS	31
3.6	COST-BENEFIT ANALYSIS	33
3.7	NEW CONCEPT IN PRACTICE	35

CHAPTER 4

Experimental Program	38
4.1 INTRODUCTION	38
4.2 DESIGN OF SPECIMENS	39
4.3 SPECIMENS DETAILS.	39
4.3.1 CONCRETE DIAPHRAGM	40
4.3.2 REINFORCED CONCRETE SLAB.	40
4.3.3 SPECIMEN ONE	43
4.3.4 SPECIMEN TWO	44
4.3.5 SPECIMEN THREE	45
4.4 CONSTRUCTION AND ERECTION	45
4.5 INSTRUMENTATION	47
4.5.1 PERFORMANCE OF GAGES DURING TESTS.	50
4.6 MATERIAL PROPERTIES	51
4.6.1 CONCRETE.	52
4.6.2 REINFORCEMENT STEEL.	53
4.6.3 STEEL GIRDER.	55
4.6.4 NEOPRENE PAD	56
4.7 FATIGUE TESTING	57
4.7.1 BACKGROUND.	58
4.7.2 SHEAR CONNECTORS	61
4.7.3 TEST PROCEDURES.	61
4.7.4 TEST RESULTS	63
4.7.5 FATIGUE FORMULAS VALIDATION	76
4.8 ULTIMATE TESTS	81
4.8.1 TEST FAULTS	82
4.8.2 TEST RESULTS	84
4.8.3 RESISTANCE MECHANISM.	112
4.9 SUMMARY	117

CHAPTER 5

Finite Element Model Development & Verification	118
5.1 INTRODUCTION	118

5.2	FINITE ELEMENT MODEL DEVELOPMENT	119
5.2.1	GEOMETRY OF MODELS.	119
5.2.2	MATERIAL PROPERTIES	123
5.2.3	ELEMENT TYPE	132
5.2.4	MESHING.	135
5.2.5	ELEMENT CONNECTIVITY	139
5.2.6	BOUNDARY CONDITIONS AND LOADING	141
5.2.7	SOLUTION STRATEGY	142
5.2.8	LOAD STEPS	144
5.3	EXPERIMENTAL VERIFICATION	145
5.3.1	FAILURE MECHANISM	145
5.3.2	CRACKING BEHAVIOR	150
5.3.3	YIELDING.	153
5.3.4	CRUSHING OF CONCRETE	158
5.3.5	STRAIN DISTRIBUTION.	161
5.4	CONCLUSION	177

CHAPTER 6

Mathematical Modeling of the Structural Behavior 179

6.1	INTRODUCTION	179
6.2	MODES OF FAILURE	180
6.3	FORCES AND STRESSES IN THE SPECIMENS.	181
6.3.1	THE FIRST SPECIMEN	181
6.3.2	THE THIRD SPECIMEN.	183
6.4	STRAIN AND STRESS DISTRIBUTIONS	185
6.4.1	VERTICAL DIRECTION	187
6.4.2	STRESS DISTRIBUTION IN SLAB REBAR.	190
6.5	CONCRETE BEHAVIOR	202
6.5.1	CONCRETE FAILURE STRAIN	202
6.5.2	CONCRETE STRENGTH	205
6.6	OUTSIDE THE CORE CONCRETE PARTICIPATION	213
6.6.1	WEB SHEAR BARS BEHAVIOR	214
6.6.2	STRAIN GRADIENT	217
6.7	FLEXURAL CAPACITY OF THE CONNECTIONS AT THE CENTERLINE OF THE PIER228	
6.7.1	STRESS AND STRAIN DISTRIBUTIONS.	228
6.7.2	CONCRETE STRENGTH	231
6.7.3	REINFORCEMENT STRENGTH.	233
6.7.4	CONNECTING PLATE STRENGTH	234

CHAPTER 7

Conclusions and Recommendations 235

7.1	SUMMARY	235
-----	-------------------	-----

7.2	CONCLUSIONS	237
7.2.1	COST-BENEFIT ANALYSIS	237
7.2.2	EXPERIMENTAL INVESTIGATION	237
7.2.3	NUMERICAL INVESTIGATION	239
7.2.4	MATHEMATICAL MODELING	241
7.3	RECOMMENDATIONS FOR FURTHER RESEARCH	242
	References	244

Appendix A

Failure of a Concrete Core Based on a Three Parameter Model 245

A.1	CONCRETE COMPRESSIVE STRENGTH	245
A.2	NUMERICAL EXAMPLE.	247

Appendix B

Foundation Analogy 250

B.1	INTRODUCTION.	250
B.2	STRESS DISTRIBUTION	251
B.3	FINITE ELEMENT MODEL	252
B.4	TIE-STRUT MODEL	252

List of Figures

CHAPTER 1	
Introduction	3
Figure 1-1: Construction sequence for a two span bridge made continuous for live load: a) girders placed on substructure, b) cast-in-place diaphragm and slab rebar, c) cast-in-place deck	6
CHAPTER 2	
Market Analysis	12
Figure 2-1: Steel and Prestressed Concrete Bridges in Nebraska	16
Figure 2-2: Steel and Prestressed Concrete Bridges in Kansas	17
Figure 2-3: Steel and Prestressed Concrete Bridges in Oklahoma	18
Figure 2-4: Steel and Prestressed Concrete Bridges in Iowa	20
Figure 2-5: Steel and Prestressed Concrete Bridges in Colorado	21
Figure 2-6: Steel and Prestressed Concrete Bridges in South Dakota	22
Figure 2-7: Steel and Prestressed Concrete Bridges in Wyoming	23
CHAPTER 3	
Vision of the System	25
Figure 3-1: The number of bridges in the U.S. by construction material.....	27
Figure 3-2: The conventional erection method of steel girders.....	28
Figure 3-3: The conventional erection method of steel girders.....	30
Figure 3-4: I-girder field splice details.	35
Figure 3-5: Erection of first span of Sprague Street Bridge over Interstate 680. .	37
Figure 3-6: Erection of Box Girder Bridge over Interstate 80.	37
CHAPTER 4	
Experimental Program	38
Figure 4-1: Conceptual Test Specimen	40
Figure 4-2: Typical Specimen Longitudinal View (Dimensions in inches)	42
Figure 4-3: Typical Specimen Side View (Dimensions in inches)	42
Figure 4-4: Concrete Slab Section A-A	43
Figure 4-5: Concrete Diaphragm Detail, Section B-B	43
Figure 4-6: Concrete Diaphragm Detail, Section C-C.....	44
Figure 4-7: Specimen 1 Detail Inside of Diaphragm.....	44
Figure 4-8: Specimen 2 Detail Inside of Diaphragm.....	45
Figure 4-9: Specimen 3 Detail Inside the Diaphragm.....	46
Figure 4-10: Spot weldable gages on the steel girder of the first specimen	48
Figure 4-11: Strain gages attached to the web of steel girder in second test	49
Figure 4-12: Embedment gages in the second specimen.....	49
Figure 4-13: Deformation of an Embedment Gauge After Ultimate Test 2	52
Figure 4-14: Stress-Strain Curve From Rebar Tensile Test	54
Figure 4-15: Stress-Strain Diagram for the Steel Girder	56
Figure 4-16: First Specimen Cycling Setup and Fixtures	64
Figure 4-17: Cracks Mapped From the First Test Specimen After 1.5 Million Cycles	65

Figure 4-18:	Deck Cracking Over Pier From Second Cycling Test	66
Figure 4-19:	Load-Deflection Graph for the First Specimen's Fatigue Testing	68
Figure 4-20:	Load-Deflection Graph for the Second Specimen's Fatigue Testing	68
Figure 4-21:	Load-Deflection Graph for the Third Specimen's Fatigue Testing ...	69
Figure 4-22:	Stiffness Variation During Cycling Tests	69
Figure 4-23:	Strain Distribution Across the Depth of the Girder at the Pier Centerline During Cycling Loading	71
Figure 4-24:	Strain Distribution Across the Steel Girder Depth Outside the Diaphragm	71
Figure 4-25:	Vertical Strain Profile Inside the Concrete Diaphragm.....	72
Figure 4-26:	Strain Profile in the Bottom of the Diaphragm Concrete	74
Figure 4-27:	Strain in Top Rebar During Cycling Tests Near the Center of the Deck 74	
Figure 4-28:	Horizontal Strain Distribution From the First Cycling Test	77
Figure 4-29:	Horizontal Strain Profile in the Second Cycling Test.....	77
Figure 4-30:	Horizontal Strain Distribution in the Third Cycling Test.....	78
Figure 4-31:	Ultimate Test Setup for the Second Specimen.....	82
Figure 4-32:	Schematic of the Loading Setup	84
Figure 4-33:	Moment-Drift Plots of the Three Experiments	86
Figure 4-34:	The First Test Cracking After the Ultimate Test.....	88
Figure 4-35:	Cracks After Ultimate Test Two	89
Figure 4-36:	Concrete Cracking After the Third Specimen Test.....	89
Figure 4-37:	Moment at Which Yield Started in Top Layer Rebar at Pier Centerline 91	
Figure 4-38:	Strain in Concrete Diaphragm Between Two Girders in Test 1 at Three Elevations from Bottom Flange	93
Figure 4-39:	Penetration of the Bottom Flange of Specimen 2 into the Diaphragm	94
Figure 4-40:	Relative Displacement of Bottom Flange After Ultimate Test Two and Deformation of an Embedment Gauge	94
Figure 4-41:	Concrete Strain at the Pier Centerline From the Third Ultimate Test	97
Figure 4-42:	Penetration of Bottom Flanges into the Diaphragm Versus Applied Load (3rd Test).....	97
Figure 4-43:	Strain Distribution at Pier Centerline Inside Concrete Diaphragm Along the Width of the Diaphragm	98
Figure 4-44:	Vertical Strain Distribution of Test 1 Near Ultimate Load.....	100
Figure 4-45:	Strain Profile Inside the Concrete Diaphragm at the Ultimate Condition of the First Test	100
Figure 4-46:	Strain Distribution Outside the Diaphragm at Near Ultimaded Load	101
Figure 4-47:	Exaggerated Deformed Shape of the Girders at the Pier Location.	101
Figure 4-48:	Strain Profile in the Bottom Flange Along the Longitudinal Axis of the Steel Girder	102
Figure 4-49:	Strain Distribution on the Top Flange.....	103
Figure 4-50:	Strain Profile for (a) a Non-composite Section and (b), a Semi- Composite Section.....	105
Figure 4-51:	The Strain in the Slab During Ultimate Test One at a Load of 340 kips 107	
Figure 4-52:	A Concrete Specimen Under Uniaxial Tension	107
Figure 4-53:	Cracking of Concrete Diaphragm Around Bottom Flange of Specimen 2	109
Figure 4-54:	Separation of Steel Web and Concrete Diaphragm During Test 2..	109
Figure 4-55:	Large Deformation of Shear Bars Inside Diaphragm After Test 2..	110

Figure 4-56:	Shear Failure of Diaphragm Shear Bar After Specimen 2 Ultimate Test	110
Figure 4-57:	Strain of Three Points Around the Web Shear Rods.....	111
Figure 4-58:	Cracking of the Diaphragm During the Third Test	111
Figure 4-59:	Load Resistance Stages for the First Test.....	113
Figure 4-60:	Structural Behavior During the Second Ultimate Test	115
Figure 4-61:	Failure of the Concrete in the Second Specimen Slab.....	115
Figure 4-62:	The Load-Deflection Response of the Third Specimen.....	117

CHAPTER 5

Finite Element Model Development & Verification 118

Figure 5-1:	Plan View of Finite Element Model Component.....	121
Figure 5-2:	Longitudinal Section View (Sec B-B) of Finite Element Model Components	122
Figure 5-3:	Transverse Section View (Sec A-A) of Finite Element Model Components	122
Figure 5-4:	Multilinear Approximation of Steel Girder Stress-Strain Response .	124
Figure 5-5:	Bilinear Stress-Strain Model for Steel Girder Elements	125
Figure 5-6:	Average of rebar sample tests for the three specimens	125
Figure 5-7:	Pre-Peak Stress-Strain Plots for Concrete Material.....	130
Figure 5-8:	Part of Neoprene Stress-Strain Curve	132
Figure 5-9:	A Portion of a Finite Element Model of Specimens and Employed Element Types	133
Figure 5-10:	Modeling of Rebar and Stirrups with Link Elements.....	134
Figure 5-11:	The Concrete Slab and Diaphragm Modeled by Solid Elements.	136
Figure 5-12:	Typical Meshing of Symmetric Model.....	137
Figure 5-13:	Analysis of the First Specimen with Two Mesh Sizes	138
Figure 5-14:	Analysis of the Third Specimen with Two Mesh Sizes	139
Figure 5-15:	Effect of Slippage on Load-Deflection Response for Second Specimen	141
Figure 5-16:	Analysis of the First Specimen with Two Time Step Sizes.....	145
Figure 5-17:	Load vs. Deflection for the First Test	149
Figure 5-18:	Load vs. Deflection for the Second Test	149
Figure 5-19:	Load vs. Deflection for the Third Test	150
Figure 5-20:	Longitudinal View of the Cracks in the First Specimen.....	151
Figure 5-21:	Half-Symmetric View of Diaphragm and Slab of the Second Specimen	152
Figure 5-22:	Longitudinal View of Cracks in Diaphragm and Slab of Third Specimen	153
Figure 5-23:	Yielding of the Slab Rebar in the First Simulation (in/in)	155
Figure 5-24:	Initiation of Yielding in the Bottom Flange in the First Specimen .	155
Figure 5-25:	Strain Distribution in Top Layer of Rebar at First Yield at the Pier for the First Specimen.....	156
Figure 5-26:	Strain Distribution in Top Layer of Rebar at First Yield at the Pier for the Second Specimen	156
Figure 5-27:	Strain Distribution in Top Layer of Rebar at First Yield at the Pier for the Third Specimen.....	157
Figure 5-28:	Yield Moment of Each Top-Layer Rebar in the Slab	157
Figure 5-29:	Stress (ksi) in x-dir in Concrete Diaphragm and Part of the Slab at Crushing in the First Specimen	159

Figure 5-30:	Stress (ksi) in x-dir in Concrete Diaphragm and Part of the Slab at Crushing in the Second Specimen.....	160
Figure 5-31:	Stress (ksi) in x-dir in Concrete Diaphragm and Part of the Slab at Crushing in the Third Specimen(t=4.00, 184)	160
Figure 5-32:	Stress-Strain Relation in Bottom of Concrete Diaphragm for the First Specimen	161
Figure 5-33:	Stress-Strain Relation in Bottom of Concrete Diaphragm for the Third Specimen	162
Figure 5-34:	Stress Distribution in the Concrete Core for the Test one Ultimate Condition.....	162
Figure 5-35:	Stress Distribution in the Core Concrete in the Third Test at the Ultimate Condition.....	163
Figure 5-36:	Strain History of One of the Top Layer Rebar in the First Specimen	164
Figure 5-37:	Strain History of One of the Top Layer Rebar in the Second Specimen	164
Figure 5-38:	Strain Distribution in Concrete Diaphragm, Test 1 at 360 kip	165
Figure 5-39:	FEA Model Strain Distribution at the Pier Centerline at 360 kip, Test 1	166
Figure 5-40:	FEA Model Strain Distribution at Pier Centerline Before Crushing, Third Specimen, 346 kip	166
Figure 5-41:	Strain Distribution of the First Specimen at the Pier Centerline 410 kip	167
Figure 5-42:	Strain Distribution of First Specimen at Pier Centerline, 500 kip ..	168
Figure 5-43:	Vertical Distribution of Strain at Pier Centerline Before Concrete Crushing, Third Specimen	168
Figure 5-44:	Vertical Profile of Strain Outside Diaphragm Before Collapse, First Test.....	169
Figure 5-45:	Vertical Profile of Strain Outside Diaphragm Before Collapse, Third Test.....	170
Figure 5-46:	Strain Along Bottom Flange at the Ultimate Condition, First Test.	170
Figure 5-47:	Strain Along Bottom Flange at the Ultimate Condition, Third Test	171
Figure 5-48:	Strain Along Top Flange at the Ultimate Condition, First Test.....	172
Figure 5-49:	Strain Along Top Flange at the Ultimate Condition, Third Test.....	172
Figure 5-50:	Strain Distribution in Bottom of Concrete Diaphragm at Pier Centerline, at First Yield, First Test.....	173
Figure 5-51:	Strain Distribution at Bottom of Concrete Diaphragm at Pier Centerline, First Test at 500 kip.....	173
Figure 5-52:	Strain Distribution at the Bottom of the Concrete Diaphragm at Pier Centerline at Ultimate Condition, Second Test.....	174
Figure 5-53:	Strain Distribution at Bottom of Diaphragm at Pier Centerline, Third Test.....	175
Figure 5-54:	Strain Distribution in Top Layer Rebar at Ultimate Condition, First Test.....	175
Figure 5-55:	Strain Distribution in Top Layer Rebar at Ultimate Condition, Second Test.....	176
Figure 5-56:	Strain Distribution in Top Layer Rebar at Ultimate Condition, Third Test.....	176
Figure 5-57:	Movement of Bottom Flange into Concrete Diaphragm	177

CHAPTER 6
Mathematical Modeling of the Structural Behavior 179

Figure 6-1:	Strain distribution at the three lines at the pier centerline	186
Figure 6-2:	Strain surface at the pier centerline.....	186
Figure 6-3:	Deflection profiles (in longitudinal direction) of the first specimen at ultimate condition.....	188
Figure 6-4:	Deflection profiles (in longitudinal direction) of the third specimen at the ultimate condition.....	188
Figure 6-5:	Strain profile at the pier centerline of the third specimen at a load of 350 kip	189
Figure 6-6:	Strain profile at the pier centerline of the first specimen at different location along the width of diaphragm for load of 500 kip.....	189
Figure 6-7:	Strain profile at the pier centerline of the third specimen at different location along the width of diaphragm for load of 350 kip.....	190
Figure 6-8:	Free body diagram for a slice of the diaphragm	199
Figure 6-9:	Plan view of concrete slab and parallel cracks	199
Figure 6-10:	A strip of the concrete slab with the reinforcements and the applied loads.....	200
Figure 6-11:	Beam-spring model for the concrete slab and the rebar.....	200
Figure 6-12:	Winkler model for half of the concrete slab and the rebar	200
Figure 6-13:	Comparison of Winkler method and FEA results for the first test at a load of 500 kips	201
Figure 6-14:	Comparison of Winkler method and FEA results for the third test at a load of 382 kips	201
Figure 6-15:	The developed concrete model in compression.....	204
Figure 6-16:	Multi-axial state of stress in the core concrete	211
Figure 6-17:	Concrete response under triaxial compression (Paulay, 1974).....	212
Figure 6-18:	Failure surface for concrete (ANSYS).....	212
Figure 6-19:	End bearing plate resting on the core concrete.....	213
Figure 6-20:	Load transfer mechanism of the web plate to the concrete through shear bars (plan view).....	217
Figure 6-21:	The slab concrete and the diaphragm under the rebar loads.....	225
Figure 6-22:	Free body diagram of a slice of the concrete diaphragm.....	226
Figure 6-23:	The strain and stress distribution of a slice of the diaphragm under the load transferred from the reinforcement.....	226
Figure 6-24:	Linear stress and strain distribution inside the concrete diaphragm ..	227
Figure 6-25:	Variation of compressive force in the diaphragm along the diaphragm width	227
Figure 6-26:	Stress and strain distribution across the width of slab in reinforcements.....	229
Figure 6-27:	Strain, stress and force diagrams in the vertical direction at the girder axis.....	230
Figure 6-28:	Stress distribution of the compressive concrete across the width of diaphragm.....	230

CHAPTER 7

Conclusions and Recommendations235

Failure of a Concrete Core Based on a Three Parameter Model 245

Figure A-1: r Failure surface for the biaxial stress state of the concrete 249

Foundation Analogy 250

Figure B-1:	A linear elastic plate under symmetrical loading and induced normal stress across the length of the plate	254
Figure B-2:	Stress in the x-dir in the core concrete and diaphragm centerline for the third test under 6 ksi pressure.....	254
Figure B-3:	Stress in the y-dir in the core concrete and diaphragm centerline for the third test under 6 ksi pressure.....	255
Figure B-4:	Finite element model of the core concrete being pressed by two plates	255
Figure B-5:	Lateral stress (y-dir) contours in a deformed shape.....	256
Figure B-6:	Cracks formed at the edges of the plate.....	256
Figure B-7:	A simple tie-strut model for the core concrete under compression	257
Figure B-8:	An approximate estimate for the lateral pressure on the core concrete	257
Figure B-9:	The variation of stress ratio versus size ratios	258

List of Tables

CHAPTER 1	
Introduction	3
CHAPTER 2	
Market Analysis	12
CHAPTER 3	
Vision of the System	25
Table 3-1: Properties of the Girders	32
Table 3-2: Costs of the Girders	33
CHAPTER 4	
Experimental Program	38
Table 4-1: Specifications of Gauges	51
Table 4-2: Average Concrete Strength	53
Table 4-3: Reinforcement Tensile Test Results for the First Specimen	54
Table 4-4: Reinforcement Tensile Test Results for the Second Specimen	55
Table 4-5: Reinforcement Tensile Test Results for the Third Specimen	55
Table 4-6: Fatigue Testing Results	63
Table 4-7: The Maximum Fatigue Stress in the Concrete	81
Table 4-8: Location of the Application of the Load with Respect to Pier Centerline	82
Table 4-9: Ultimate Displacement, Load, and Moment of Specimens	86
Table 4-10: Cracking Strain and Corresponding Load for the Tested Specimens	88
Table 4-11: Yield Load, Displacements, and Ductility Ratios of the Three Specimens	92
CHAPTER 5	
Finite Element Model Development & Verification	118
Table 5-1: Material Properties Input in Analyses	128
Table 5-2: Experimental and FEA Results at the Ultimate Condition	146
Table 5-3: Concrete Stress Before Crushing from FEA with Uniaxial Strength ..	159
CHAPTER 6	
Mathematical Modeling of the Structural Behavior	179
Table 6-1: The force and stress in the resisting components of the first test at the pier centerline at the ultimate condition	183
Table 6-2: The force and stress in the resisting components of the third test at the pier centerline at the ultimate condition	184
Table 6-3: The contribution of each resisting element in test one and three	185
Table 6-4: Comparing Hawkins' test results with predictions of Equation (6-36) ..	210
CHAPTER 7	
Conclusions and Recommendations	235

Failure of a Concrete Core Based on a Three Parameter Model 245
Foundation Analogy 250

Acknowledgement

Funding for this investigation was provided primarily by the Nebraska Department of Roads, The U.S. Department of Transportation, and The Federal Highway Administration (FHWA). The authors would like to express their thanks to Mr. Lyman Freeman and Mr. Sam Fallaha of the Bridge Division at the Nebraska Department of Roads (NDOR).

The opinions expressed in this report are those of the authors and do not necessarily represent the opinions of the sponsors.

Abstract

A market analysis of bridge materials was completed, which indicated a declining trend in the use of steel girders over the last two decades. A new construction technique for steel girder bridges was developed to enhance their competitiveness in the short to medium span length range. In the new method, girders are placed on the supports as simple spans under construction loads. The continuity of the girders is obtained for traffic loads after hardening of the slab and diaphragm concrete through steel reinforcements. A cost-benefit analysis of two bridges constructed using the new method was completed. The study revealed that the cost and time of construction of the superstructure in each case was reduced by employing the new technique. Three possible connection details were proposed to complete the design of the new concept. In order to investigate the structural behavior of the proposed connections, a full-scale specimen of each type was designed, constructed and tested. In the first phase of testing, a cyclic load was applied to study the fatigue behavior. In the second phase, an ultimate load test was conducted to investigate the failure mechanism. To further study the structural behavior of the system, a series of finite element analyses was carried out and verified by the experimental testing results. Through these methods, the failure mode of each test specimen was identified. To explore the design capabilities of the new method, the mechanical behavior of the first and third specimens was described with a mathematical model. Design equations were then extracted from the simplified model and verified through finite element analyses.

Executive Summary

The market analysis of bridge material in the range of short to medium span length indicates a declining trend for steel girders during the last two decades. A new construction technique was developed to enhance the competitiveness of steel girder bridges in the short to medium span length ranges. In the new method the beams are erected as simple supports under the construction loads. The continuity of girders is provided by reinforcements in deck and diaphragm after hardening of the concrete for the traffic loads. In this case the field splices are eliminated and there is no need for temporary shoring. The cost-benefit study of two bridges revealed that the cost and time of construction of superstructures decreases by employing the new technique.

In order to investigate the strength of the proposed connections, three full scale tests were planned. The design and construction of each specimen was done according to the AASHTO-LRFD provisions and practical considerations. In the first test, the bottom flanges of two adjacent girders were welded at the pier centerline and end bearing plates were welded to the ends of the girders. In the second test, the girders simply were embedded in the concrete diaphragm. The third specimen was similar to the first specimen without connection of the bottom flanges. Extensive instrumentation was planned for each test. To consider the performance of each system under repeated loadings and fatigue phenomenon, first a cycling load test was conducted on each specimen. The ultimate load test was carried out after the cycling test for each specimen to investigate the failure mechanism of each specimen. The test results and observations indicate that the cracking of the concrete slab around the pier region is the first damage in the specimens. The next failure can be yielding in slab rebar,

crushing of concrete, or debonding of steel and concrete. The order of these events depends on the strength of the materials, steel and aspect ratios.

To obtain more information about the behavior of the system, a series of finite element analyses was carried out to complement the experimental studies. A detailed numerical model for the finite element analyses was developed. The geometry and material properties of the constructed models were based on the actual data obtained from the laboratory. Material and geometrical nonlinearities were included in the numerical simulations. The load-deflection response of specimens, the yielding pattern, cracking behavior, and strain distributions were compared with those obtained from experimentation to verify the numerical model. The force transfer mechanism of each test was described using the finite element simulation results. The failure modes observed in the test results were similar to what was seen from the numerical simulations.

The mechanical behaviors of the connection type one and three are described in the form of mathematical models. The mathematical explanation is based on the equilibrium of the forces and moments, and a deformation field which satisfies the boundary conditions.

The flexural strengths of the proposed connection types one, two and three are computed using a simplified approach. The framework of the simplified design formula is similar to the approach currently used to design reinforced concrete beams. The developed design equations are verified by several finite element parametric studies in the range of short to medium span bridges.

Introduction

1

1.1 PROBLEM STATEMENT

The four principal bridge materials, which according to the Federal Highway Administration (FHWA, 2003) represent 99 percent of the bridges built in the United States since 1982, are prestressed concrete, steel, timber, and reinforced concrete. Based on the study done by Smith et. al. (1995) the initial cost and long term maintenance costs of each alternative are the most influential criteria in choosing bridge materials. Another issue that is important for the engineers in selection of material is the duration of the project. A shorter construction time allows the bridge to be opened sooner and returns more profit for the public or private owner. In the latter half of the twentieth century, the use of concrete bridges, especially prestressed concrete, has become popular for economical and durability rea-

sons. The increase in the use of concrete for bridges has caused a decline in steel usage in short to medium span bridges.

The major factors for the diminishing competitiveness of steel bridges in the bridge market can be attributed to steel material price, labor and equipment. Traditionally, the cost of material was more important in estimation of total cost of the projects; but now the least labor generally results in least cost. Cost of labor can be substantially reduced by using simpler methods of construction. To reduce the construction costs of steel bridges, several innovative methods have been studied in the National Bridge Research Organization. Based on interviews with the steel bridge professionals, it was concluded that one of the bottlenecks of the construction of multi-span steel bridges is the installation of the girders as continuous beams.

The current design methodology for multi-span steel bridges is to build bridge girders continuous to distribute applied dead loads more evenly between the spans. The multi-span steel bridges are connected together at the site to make the continuous beams. The construction sequence consists of placing the middle segment and connecting the two end sections using a bolted or welded field splice. When using bolted splices, the cost of material, installation and inspection makes this type of connection expensive. In addition, this type of construction usually requires extra cranes or temporary shoring which makes the total time of project longer. In a series of discussions with designers, fabricators, and contractors, two factors were identified to be essential in improving the system: the elimination of expensive conventional details in the design of bridge girders and the erection costs by simplifying the construction method. It was concluded that designing and constructing steel girders as simple spans would cut costs considerably. This modification also leads to shorter project duration.

As show in Figure 1, in the proposed method, the girders of each span are designed as simply supported to resist the construction loads such as the weight of the concrete slab and girders. However, the girders are connected through a concrete diaphragm on the pier location to be continuous after hardening of the concrete for applied live loads such as traffic weight. In this case, the connection over the pier shall be simple during the slab pour and continuous during the service life of the bridge. This requires designing a pseudo-continuous connection over the pier which connects two adjacent girders.

The connection of two girders at the pier location by a concrete diaphragm is different than the current method in practice. In the current approach, the steel girders are continuous before casting the concrete deck; therefore the negative moment is induced at the pier location in the steel girders under the weight of the concrete slab and the beam's self weight. However, in the new system, girders are separated during the construction period and thus there is no negative moment at the pier region. After the pouring of the concrete slab and the hardening of concrete, the continuity of the girders is established through the slab reinforcement and concrete diaphragm. The transfer of negative moment induced from live loading such as truck weights and superimposed loads shall be provided by the girder connection at the pier. The transformation of live load negative moment, especially at the interface of the steel girder and concrete diaphragm, is structurally challenging.

Based on a parametric study done in the National Bridge Research Organization by using 3-D linear finite element analysis, three types of connections were proposed for further investigation. For the first type, the bottom flanges of the two girders are connected together by a plate before pouring the concrete diaphragm. This type of connection can be used in situations in which there is a possibility of tension in the bottom flange like three span bridges. The second type of connection was aimed at being as simple

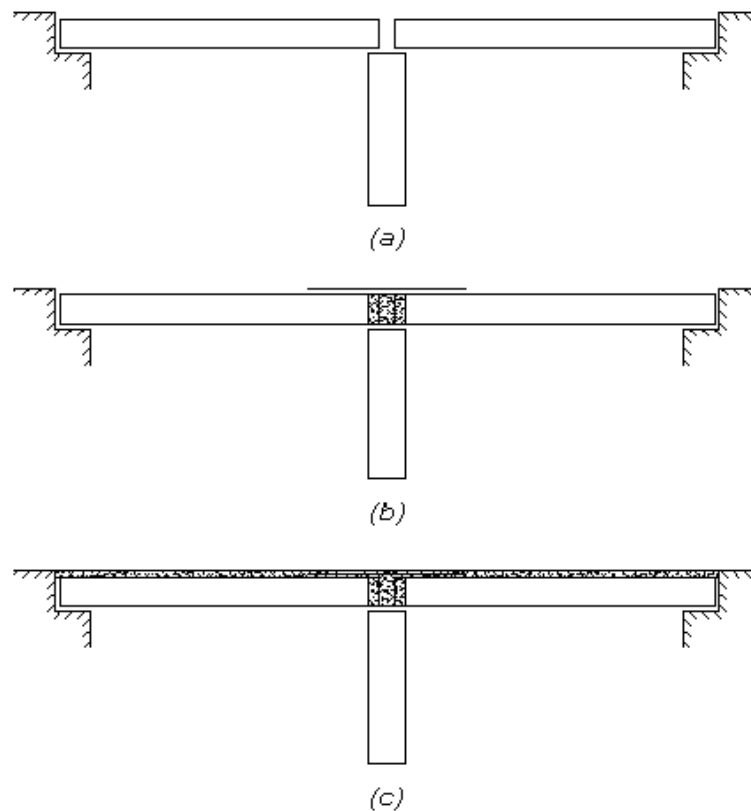


Figure 1-1: Construction sequence for a two span bridge made continuous for live load: a) girders placed on substructure, b) cast-in-place diaphragm and slab rebar, c) cast-in-place deck

as possible. The steel girders simply sit on the pier and the concrete diaphragm connects them. This case is similar to the method currently employed to strengthen some old bridges. In the third connection type, end bearing plates were welded at the girders ends to provide a better load transfer at the concrete-steel interface. However, the compressive force is transferred through the concrete diaphragm.

The three proposed connection details were constructed and tested in the structural lab at the University of Nebraska-Lincoln. The tested specimens were modeled by nonlinear finite element analysis and the results were compared with the experimentation. The force-resistance mechanism of each connection was derived from the experimental and simulation data. The formula for designing the similar connection was developed based on

the structural behavior. The accuracy of the developed formulas was verified with a finite element analysis parametric study.

Figure 1 Construction sequence for a two span bridge made continuous for live load: a) girders placed on substructure, b) cast-in-place diaphragm and slab rebar, c) cast-in-place deck

1.2 BACKGROUND

The idea of a simple span for dead load and continuous for live load was developed originally in the 1960's for precast, prestressed concrete girders to prevent leakage through the deck joints in simple beam spans (Walton, 2001). Although several steel girder bridges have been built based on this method, the author has not found any documented research on this topic in the field of steel construction. However, there has been research carried out on precast concrete girder construction implementing the proposed method. An extensive research program (Freyermuth, 1969) was conducted on this type of bridge by the Portland Cement Association during 1960-61. The use of continuity for live load in precast prestressed bridge girders permits a reduction of 5 to 15 percent in the required prestress force when compared to simple-span design. In the calculation of negative moment resistance over the pier, this study recommends the use of the ultimate design method. The negative moment reinforcement is instructed to be determined by assuming the beam to be a rectangular section with a width equal to the bottom flange width of the girder. The findings of this research states that, due to the lateral restraint of the diaphragm concrete, ultimate negative compression failure in the conducted tests always occurred in the concrete girders, even though the diaphragm concrete strength was about 2 ksi less than that of the girder concrete.

Walton and Bradberry (2003) studied the application of live load continuity in precast concrete bridges in Texas. Their evaluation of a concrete bridge shows that the live load continuity of a span can reduce the total moment by 11 percent. On the other hand, the continuity of girders needs more detailing at the beam ends. Also, it increases the amount of longitudinal reinforcement required in the slab to handle the negative moments above the bents. One of the flaws of the new system, as stated in this research, is the cracking of the negative moment region of the slab. However, this flaw is not applicable in the case of a steel girder since the negative moment cracking is more severe in the conventional method than in the proposed technique.

The idea of simple connections was pursued by researches in the National Bridge Research Organization in the late 1990's. Following interviews with steel bridge professionals, it was concluded that the application of a pseudo-connection over the pier could be beneficial in the design of steel bridges too. A preliminary cost benefit analysis revealed that the implementation of the same idea as prestressed concrete could lead to a cheaper and faster construction method. Further studies were done by linear finite element analysis to select the most proper detailing for the connections. Based on the conducted studies, three tests were carried out at the Structural Laboratory of the University of Nebraska-Lincoln.

The first test which demonstrated the first type of connection was implemented by Nick Lampe (2001). The second test, according to the detailing of the second type of the connection, as described earlier, was carried out by Nazanin Mosahebbi (2004). Finally, the last type of connection was conducted by staff of the National Bridge Research Organization in 2004. The results and behavior of the three conducted full-scale tests are presented and compared in this report.

1.3 RESEARCH OBJECTIVE

The idea of simple-for-dead and continuous-for-live or pseudo-connectivity of the girders over the pier was shown to be practical and feasible. The experimental tests and finite element simulations were conducted to reveal the structural characteristics of the different types of connections. However, to design the connection for different loadings and geometry, the load resistance mechanism of the system should first be understood. Understanding the mechanical behavior of the system will help to evaluate the strength, ductility, and deformation of the connections in a wider range. The simpler design provisions can be developed based on the load resistance mechanism to provide the bridge engineers with information necessary for designing steel bridges. The main objectives of this research are summarized as follows:

1. Comprehend the force transfer mechanism for the type of connection that could be used for connecting the two girders over the support
2. Develop mechanistic model that could predict detailed behavior of the connection when subjected to traffic loads

Using the mechanistic model, a design provision is developed for the bridge system under the consideration that it could be adopted in a design office.

1.4 REPORT SCOPE AND LAYOUT

This report discusses details of a newly developed design method which enhances constructibility of steel bridges. The results from three tests and analyses completed on rolled I-shaped girders representing the interior pier (negative flexure) region of a two-span bridge are discussed. The goal of this study is to find a load-resistance mechanism to explain the structural behavior of the system. This report presents the mechanical behavior

of the tested system in the form of mathematical formulas. These formulas are presented to assist in the design of similar steel bridge systems.

Chapter 2 of this report summarizes a 10-year market analysis carried out to study the state of steel bridges among other materials. Identification of the new bridge system in comparison with the conventional method is outlined in this chapter. The cost-benefit analysis of two recently-built bridges, designed based on the new concepts, is presented the Chapter 2.

Chapter 3 contains a summary of the test results of the three full-scale tests representing three different types of connections which fulfill the new concept requirement. This chapter documents the details of the connection, test setup, laboratory testing, and test results. This description includes loading and support geometry, instrumentation types and locations, material testing and properties, and specimen construction and erection. Test results for the cycling and ultimate testing are presented and failure mechanism for each case is discussed based on the acquired data.

Chapter 4 describes the nonlinear finite element analysis of the tested specimens. Several numerical models were developed which considered the nonlinearity of the specimens during the tests, such as cracking, crushing and yielding. Then the actual properties of the specimen based on the lab information were employed in the analyses. The analyses were verified using the experimental data. The structural behaviors of the systems are described using the detailed finite element results.

The mathematical descriptions of the specimen behaviors observed in the experimentation and simulations are presented in Chapter 5. The solid mechanics concepts and finite element parametric studies are used to generalize the structural behavior of specimens. The proposed mathematical models were checked by the finite element findings.

A simple design approach is introduced in Chapter 6. The flexural capacity of the connections similar to type one and type three at the pier centerline is identified using the proposed design method. The bending strengths of the tested specimens are compared with those predicted with the developed design formulas. Several more bridges in the range of short to medium span are designed based on the new concept, and their ultimate capacities are computed using nonlinear finite element analysis. Finally, the flexural capacities of trial bridges are checked with the proposed formulas.

A summary of the research findings and conclusions is provided in Chapter 7, along with suggestions for future research.

The support information leading to the mathematical modeling is contained in the appendices. These include the employed concrete failure model and the foundation analogy of the concrete core.

Market Analysis

2

A detailed market analysis was carried out to investigate trends in bridge construction in the mid-west region of the country. This chapter presents an overview of the analysis of National Bridge Inventory (NBI) data obtained from the Federal Highway Administration (FHWA) for seven mid-western states. The data was separated into categories based on the material of construction. The objective of this analysis was to identify trends in the use of bridge materials in Nebraska and the surrounding region.

2.1 GENERAL DESCRIPTION

Bridge inventory data is included from the following states: Colorado, Iowa, Kansas, Nebraska, Oklahoma, South Dakota, and Wyoming. The inclusion of several states was intended to reduce the overall effect of one state's tendency to favor the use of one particular material over another. The National Bridge Inspection Standards (NBIS) [3] mandate an inspection of

each bridge at regular intervals and not to exceed two years unless a Federal Highway Administrator approves a proposal stating otherwise. Data from the inspection reports are sent in a standard format from the states to the Federal Highway Administration.

2.2 DATA REDUCTION

Bridges were categorized based on their construction material (NBI Item 43A). Only bridges built of reinforced concrete, prestressed concrete, steel and timber were included in the analysis. The material of the superstructure for the main span determined the classification. For each state, the different construction material categories were compared to each other on the basis of total numbers by the year built and by the maximum span length. Particular attention was given to the comparison between prestressed concrete and steel bridges in each of the states.

The time period examined (NBI Item 027) was the 88-year span from 1911 through 1998, with particular attention paid to bridges built during the last two decades. The overall time period was divided into eight groups of ten years each, with the exception of the oldest group, 1911-1930, and the most recent time period, 1991-1998. The maximum span lengths (NBI Item 048) were divided into thirty-three groups. The first set includes bridges with maximum span lengths less than 25 ft. The next twenty-seven groups have 5-ft span increments, including bridges from 26 ft through 160 ft. The next four groups have 10-ft span increments, with the final set including bridges from 201 ft through 550 ft.

The performance of the bridges in Nebraska was based on the condition ratings submitted to the FHWA (NBI Items 058 and 059). The ratings of existing physical conditions of the deck and superstructure elements determined the overall deterioration measurement. Bridges classified as "structurally deficient" are those with ratings in the poor, serious, critical

or failure categories, corresponding to a four or less on the condition ratings scale. A condition rating of four is described as "poor condition - advanced section loss, deterioration, spalling or scour." A rating equal or less than the limit given above for one or more components indicates a potentially critical structural problem.

2.3 ANALYSIS RESULTS

Based on the data from the inspection reports compiled in the NBI, the characteristics by state can be generalized in the following manner.

2.3.1 NEBRASKA

Timber bridges were not considered in the evaluation and comparison of the Nebraska data. Reinforced concrete (RC) has been used as a dominant material for bridge construction in the 60 ft or less span ranges over the historical period studied (68% RC, 15% Prestressed Concrete (PC), 17% steel). Over the last two decades, in the 60 ft - 100 ft maximum span group, PC had a marginally higher percentage of bridges over steel (RC 3%, PC 52%, steel 45%). Considering all span lengths during 1980-1998, distribution of bridge materials was fairly even with RC at 29%, PC at 37% and steel at 34%. From 1991-1998, however, the shift has been toward more concrete with RC at 34%, PC at 40%, and steel at only 26%. As a trend, PC had peaks over steel in the number of bridges reported in the early 1990's. In comparing materials across the span lengths, RC was dominant in the 60 ft and under lengths, PC showed solid numbers in the 100 ft and under lengths with a definitive peak in the 66 ft - 70 ft group, and steel was distributed throughout the span lengths. The comparison of PC with steel over the last two decades indicates an increase in length and number of PC bridges, particularly for span lengths of 130 ft and less.

The measure of performance of the bridges in Nebraska comes from the condition ratings of the existing deck and superstructure elements. If the

bridge is having or has the potential to have serious structural problems, it is classified as structurally deficient. The number of bridges classified as deficient compared to the number of bridges in service gives the percent deficiency. As could be predicted, there were no deficient bridges in either reinforced concrete, prestressed concrete or steel from 1981-1998. Concentrating on the time period from 1961 to 1980, each material has a representative number of bridges built (259 RC, 292 Steel, 243 PC). Considering all three materials, the total number of structurally deficient bridges is low with only 34 out of 794 bridges receiving that classification. This equates to only 4.282% of the total number of bridges built during that 20-year time period. The percentage of structurally deficient bridges does not vary significantly by material as RC contributes 3.5%, steel 4.8% and PC 4.5%. Maximum span length also appears to have little effect on the performance level of the materials. As expected, there is an increase in the deficiency percentage with age for all three materials. Figure 2-1 illustrates the trends in the number of bridges vs. span length vs. year built for steel and prestressed concrete.

2.3.2 KANSAS

Approximately 87% of all the timber bridges in Kansas have been constructed for span lengths of 25 ft or less, with only 4% of the timber bridges being built in the last three decades. PC bridges constitute only 5% of the total number of bridges, with their peak span length in the 36 ft - 40 ft group. From 1991-1998, RC and steel almost equally have controlled the span lengths of 65 ft - 70 ft and less (RC 46%, PC 5%, steel 47%, timber 2%). Over all time periods, more bridges have been built of steel than RC in all span lengths except the 35 ft - 65 ft. Figure 2-2 illustrates the trends in the number of bridges vs. span length vs. year built for both steel and prestressed concrete bridges.

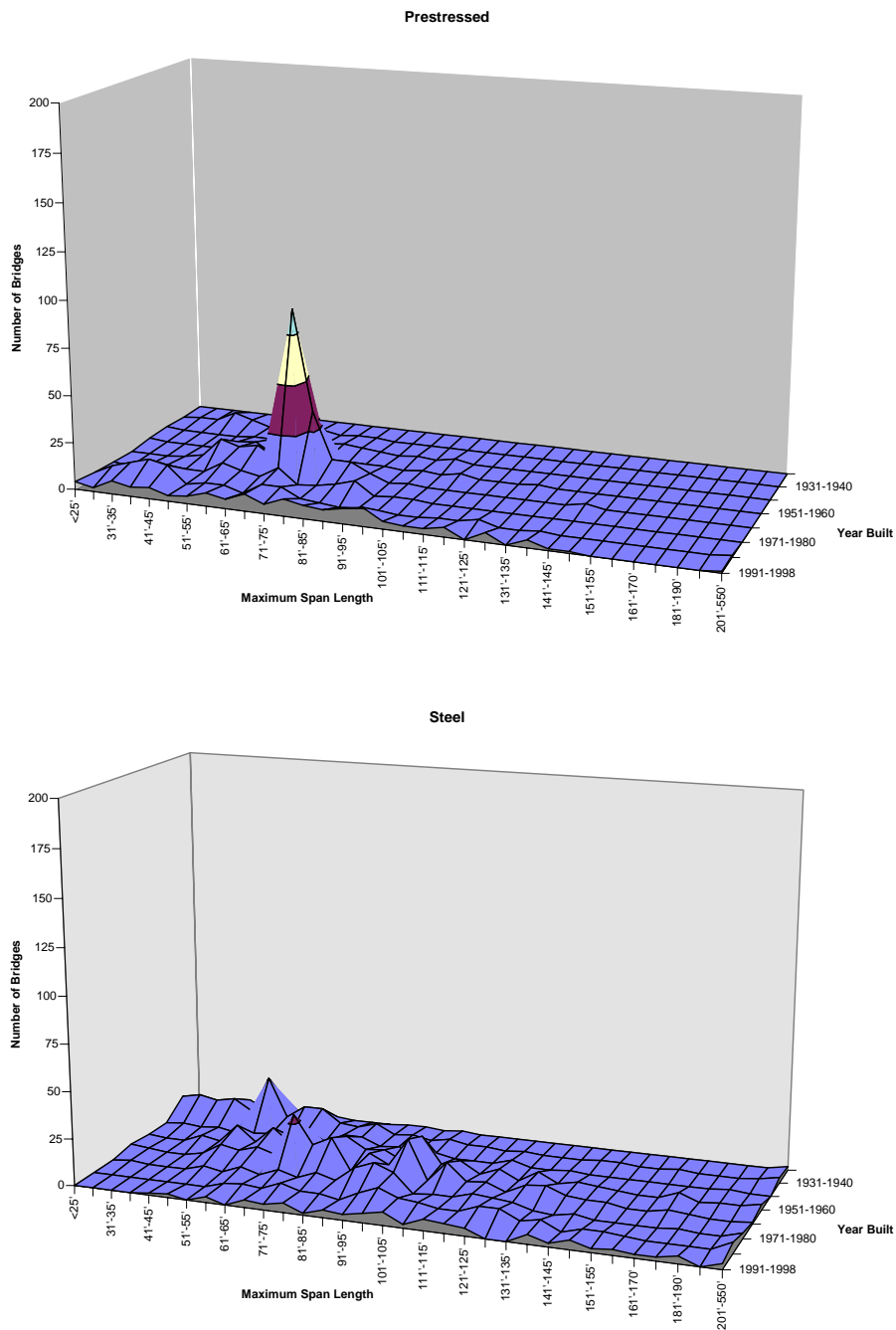


Figure 2-1: Steel and Prestressed Concrete Bridges in Nebraska

2.3.3 OKLAHOMA

There has been very little bridge construction activity in Oklahoma over the last three decades. Of the bridges constructed, a significant number have been PC in the 45 ft - 100 ft span lengths. In the 71 ft - 100 ft range, PC has 85% of the bridges while steel represents 15% (49 PC to 9 steel). Steel has a

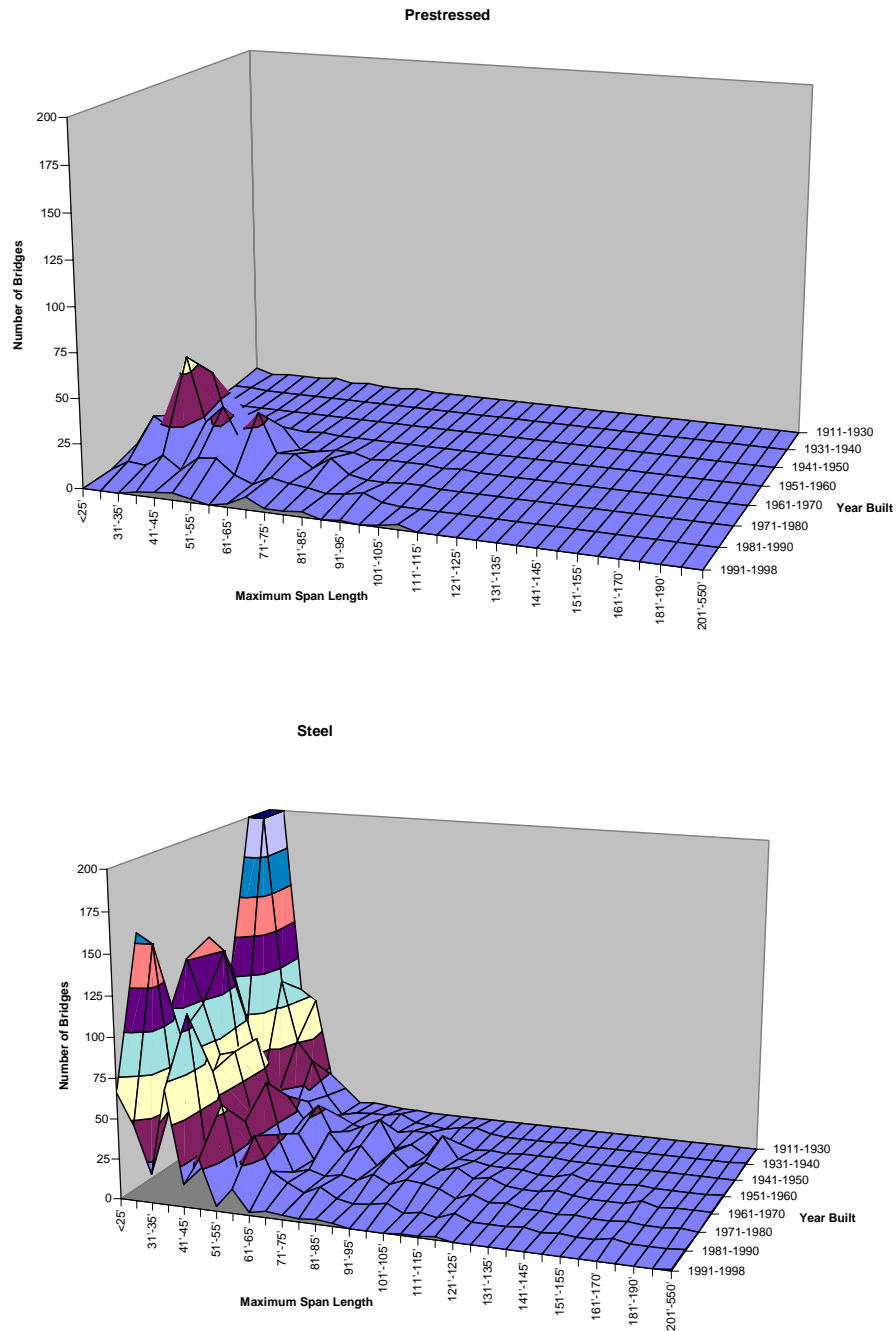


Figure 2-2: Steel and Prestressed Concrete Bridges in Kansas

significantly higher percentage than PC in the span lengths 60 ft and below. Figure 2-3 illustrates the trends in the number of bridges vs. span length vs. year built for both steel and prestressed concrete bridges.

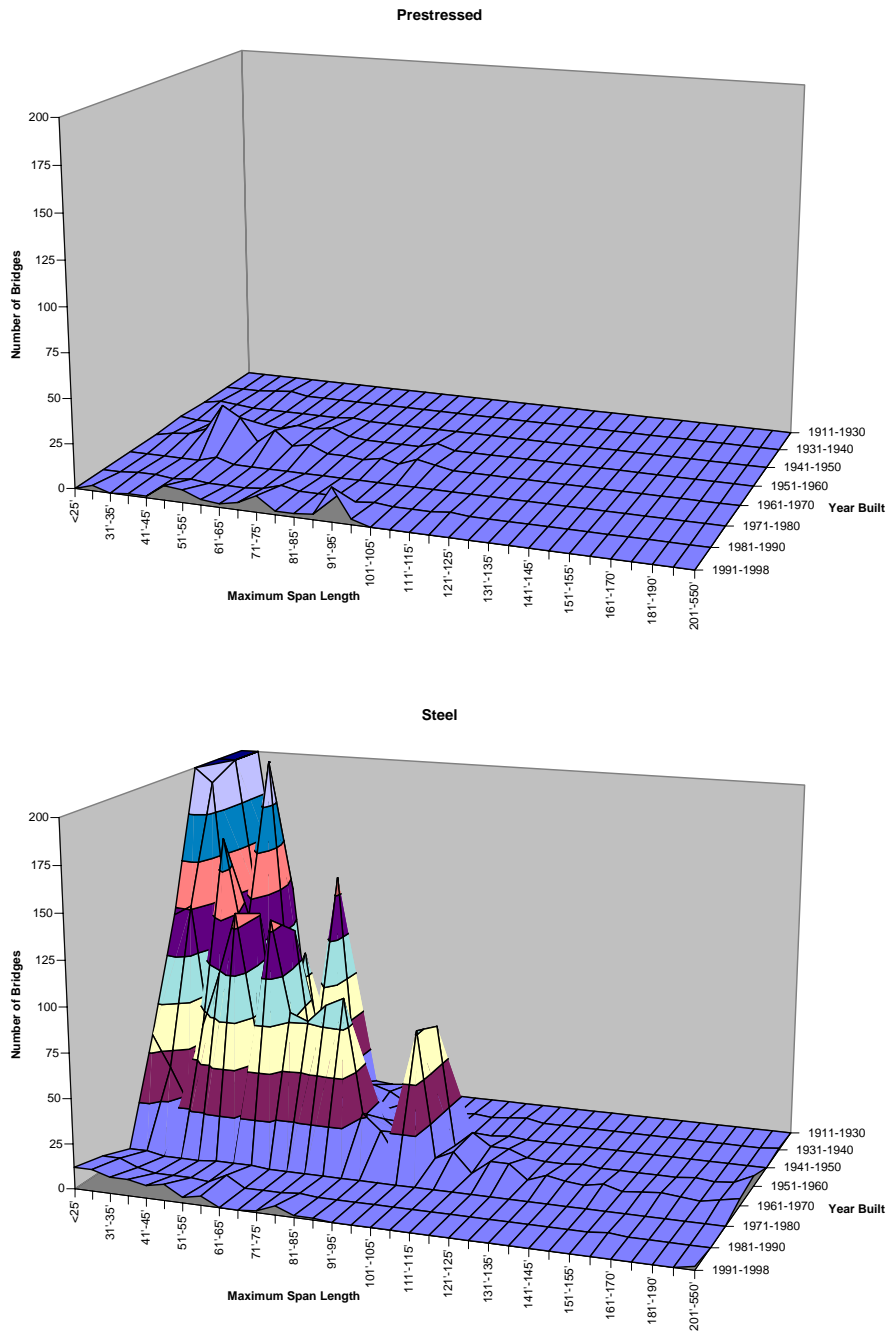


Figure 2-3: Steel and Prestressed Concrete Bridges in Oklahoma

2.3.4 IOWA

Timber bridges in Iowa have basically been limited to maximum span lengths of 35 ft or less. Approximately 51% of the RC bridges have been built in the last three decades, 26% in the last two decades, and the majority of the RC bridges, 96%, have been constructed at span lengths of 55 ft or

less. Over the last two decades, steel bridges have had maximum span lengths primarily in the 70 ft or less groups. From 1991-1998, 73% of the bridges have been constructed of concrete, both reinforced and prestressed (RC 34%, PC 39%, steel 16%, timber 11%). PC has had a prominent impact at almost all span lengths up to 115 ft, dominating specifically at the longer length spans from 50 ft - 115 ft. Figure 2-4 illustrates the trends in the number of bridges vs. span length vs. year built for both steel and prestressed concrete bridges.

2.3.5 COLORADO

The majority of the timber bridges (81%) were built between 1930-1960, with over half of those in the 1930's alone. Approximately 66% had maximum span lengths between 50 ft and 70 ft. Very few timber bridges have been constructed in Colorado in the last three decades. Reinforced concrete also has not generally been selected as a bridge construction material for most span ranges over that time period. More recently, PC and steel have both been selected as construction materials in basically all span lengths. In the 90 ft - 115 ft range, PC has claimed more than three times as many bridges as steel (66 PC compared to 19 steel). In the 90 ft - 150 ft range, PC has almost doubled the number of bridges made of steel (117 PC to 64 steel). Steel dominates the numbers in the span ranges up to 90 ft. Figure 2-5 illustrates the trends in the number of bridges vs. span length vs. year built for both steel and prestressed concrete bridges.

2.3.6 SOUTH DAKOTA

Data from South Dakota reflects the impact the state-owned cement plants have on the choice of bridge material. From 1991-1998, PC accounts for 59% of the bridges, with RC next at 26%, steel with 13% and timber with only 2%. Only 5% of all the timber bridges have been built in the last three decades. The majority (93%) of the timber bridges have maximum span lengths of 30 ft or less. Although in the past, steel has been chosen for the longer span ranges, 90 ft - 150 ft, the last two decades show an increased

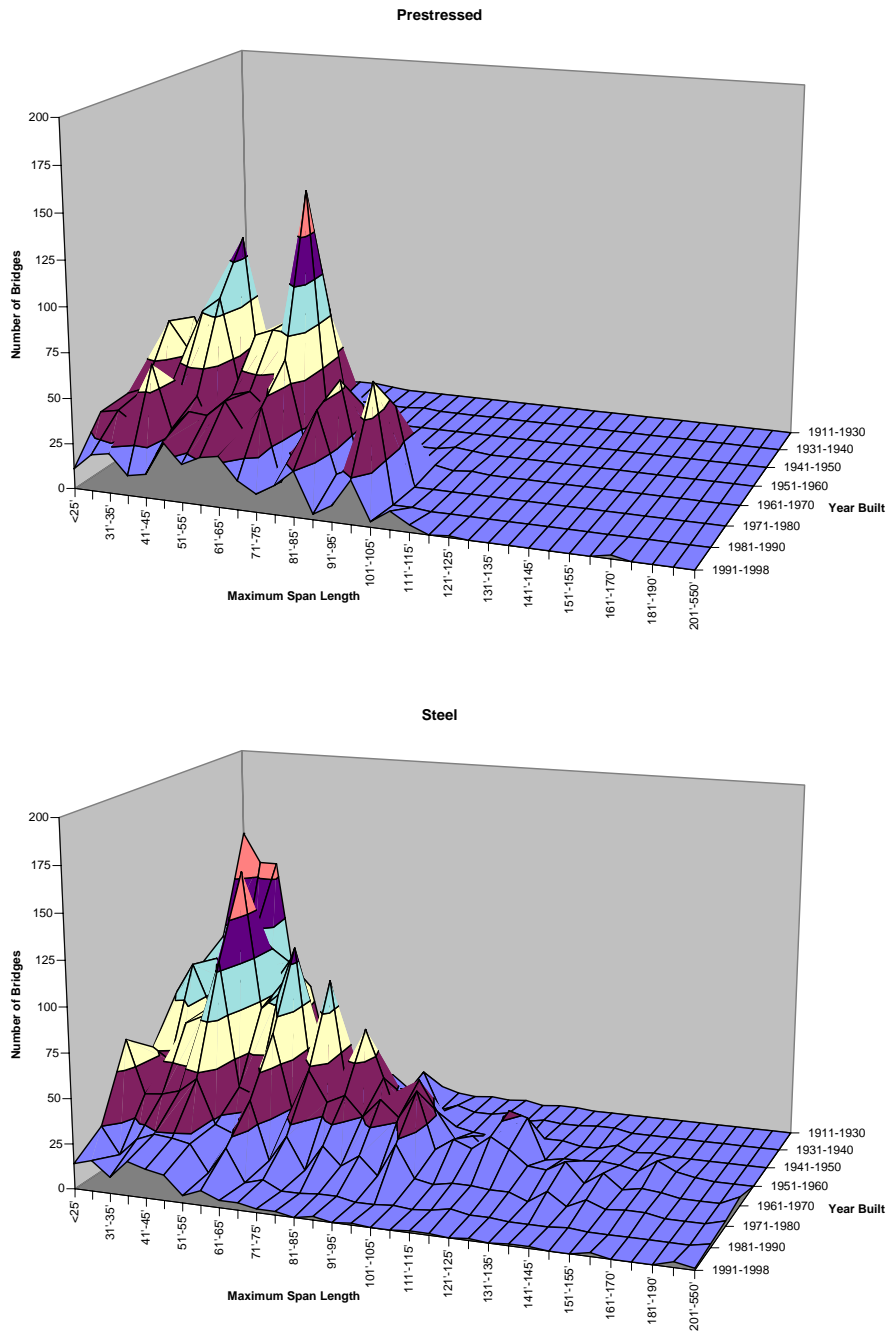


Figure 2-4: Steel and Prestressed Concrete Bridges in Iowa

usage of PC in these span lengths. RC has concentrated in the 50 ft or less span range, but PC has fairly steady numbers across all span ranges up to 135 ft, with peaks in the 35 ft - 65 ft ranges. Figure 2-6 illustrates the trends in the number of bridges vs. span length vs. year built for both steel and prestressed concrete bridges.

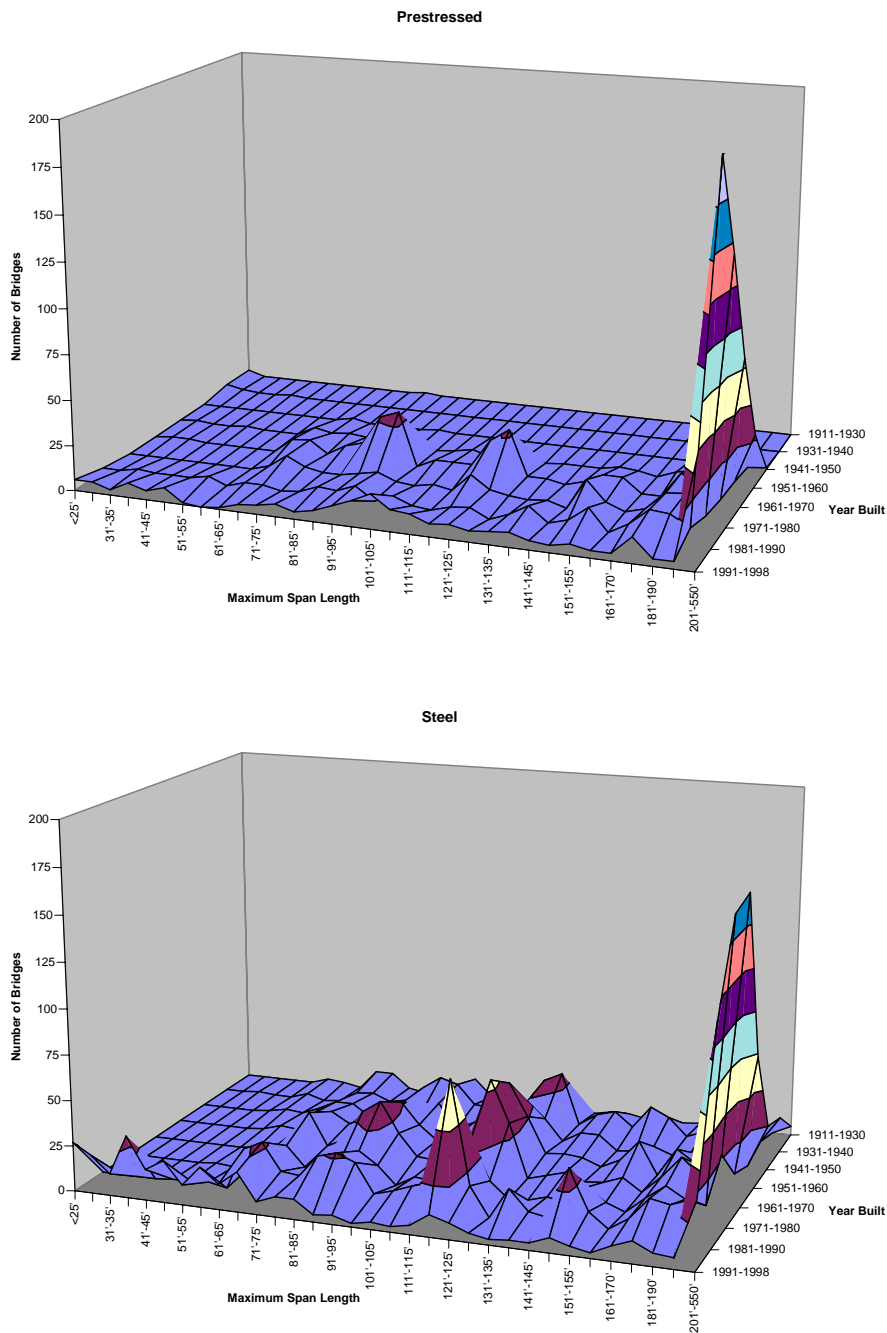


Figure 2-5: Steel and Prestressed Concrete Bridges in Colorado

2.3.7 WYOMING

Over the last two decades, steel has dominated all span ranges, with 72% of the total number of bridges (RC 12%, PC 13%, timber 3%). Steel had high concentrations of numbers in the 100 ft or less span lengths and was the material of choice in most span lengths over 100 ft. PC was used rather

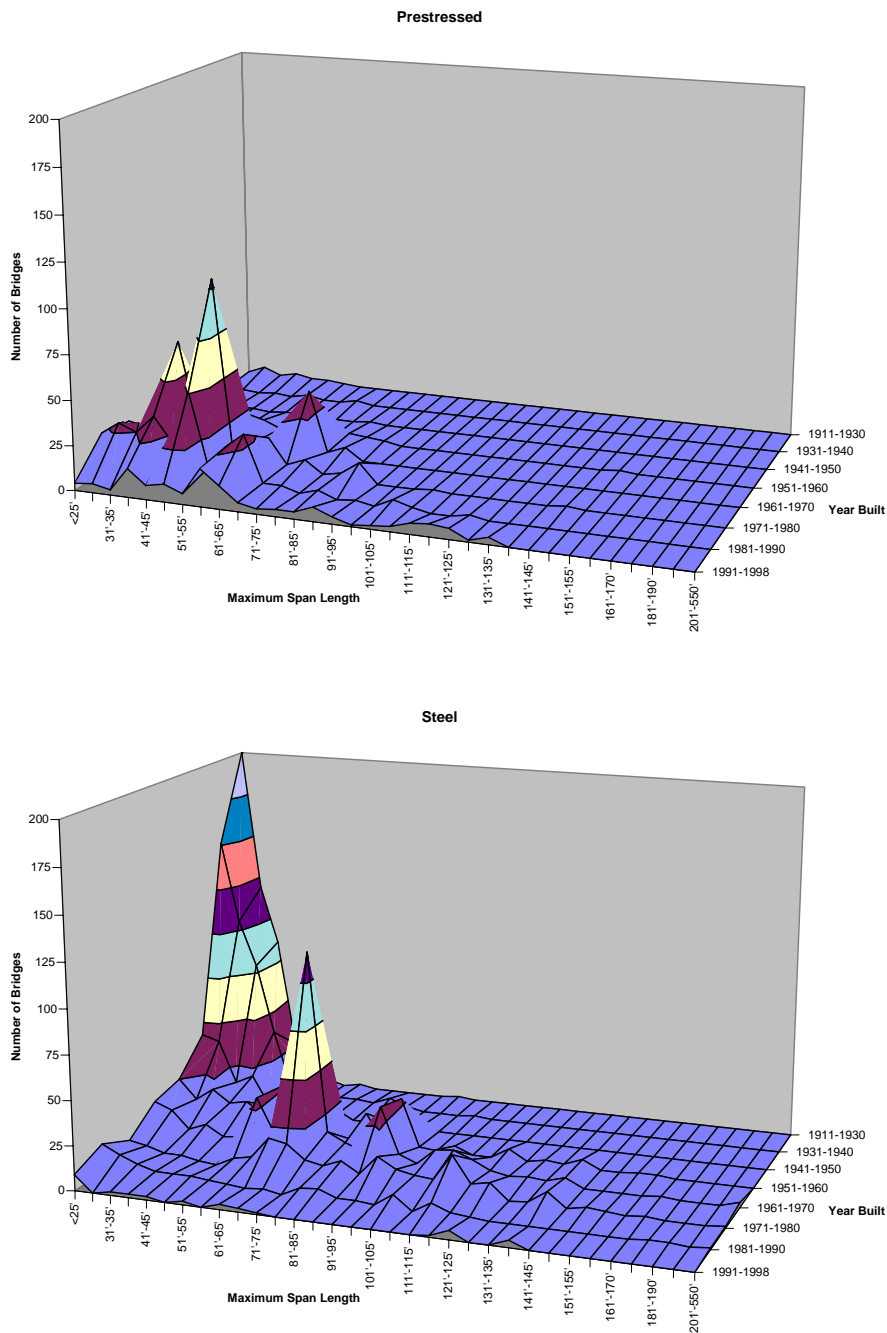


Figure 2-6: Steel and Prestressed Concrete Bridges in South Dakota

evenly in the 115 ft and below range, with particular usage in the 40 ft - 80 ft range from 1991-1998, the 110 ft or less range from 1981-1990, and the 75 ft or less group from 1971-1980. Only 6% (18/288) of the timber bridges have been built during the last 20 years. Figure 2-7 illustrates the trends in

the number of bridges vs. span length vs. year built for steel and prestressed concrete bridges.

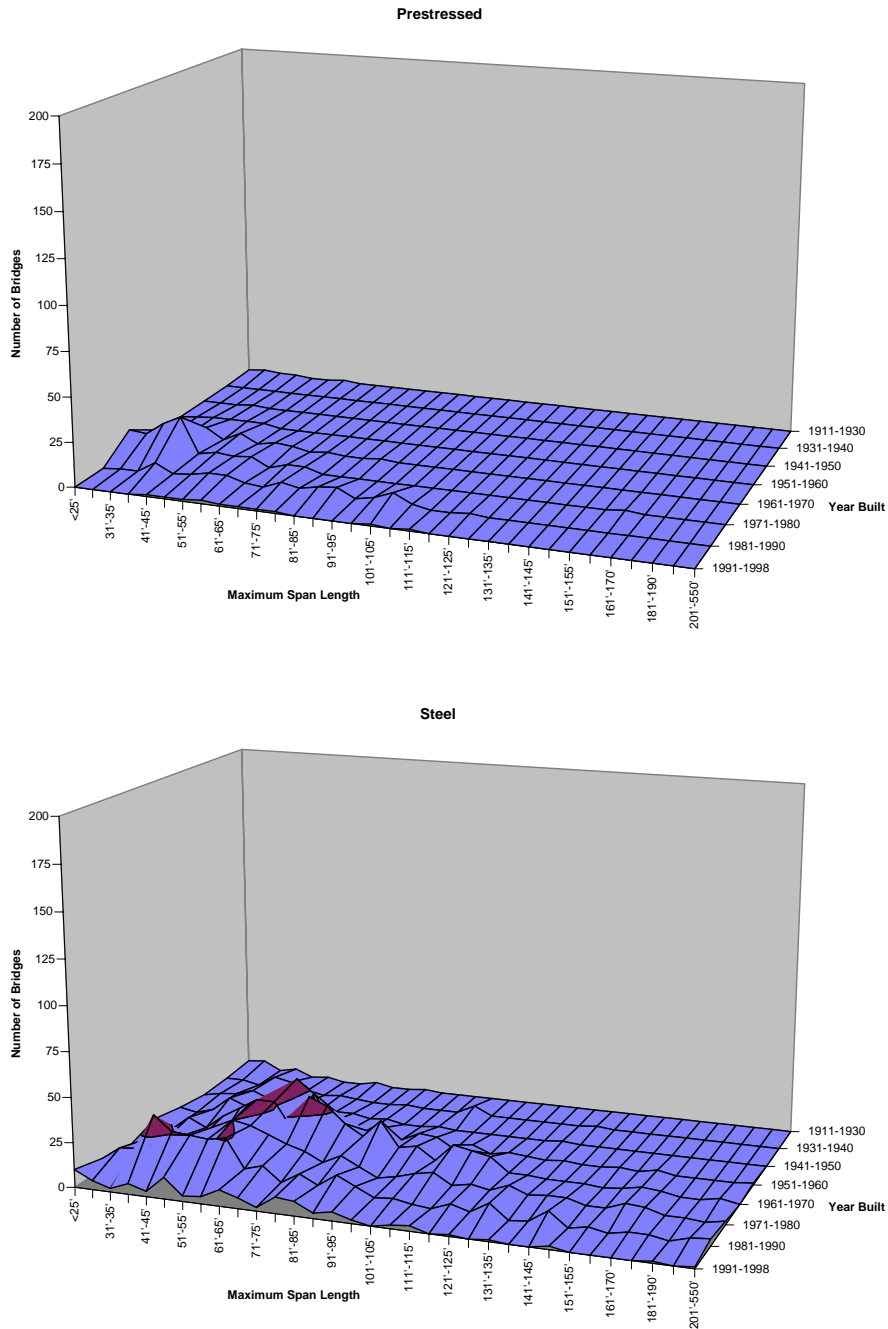


Figure 2-7: Steel and Prestressed Concrete Bridges in Wyoming

2.4 CONCLUSIONS

Based on the trends identified through the market analysis, the primary conclusions are as follows:

1. The use of timber as a bridge construction material, although basically limited to lower span lengths, has significantly decreased over the time period examined.
2. In most states studied, reinforced concrete has remained a fairly consistent choice for span lengths of 50 ft or less.
3. Prestressed concrete construction captured a large share of the market in the 60 ft - 100 ft span ranges in the 1960's and 1970's. The current trends indicate that prestressed concrete has extended its presence as a construction material choice across all span lengths. In the last two decades, steel bridge construction in all span lengths has remained steady or decreased in number. However, there has been an increase in the number of prestressed concrete bridges built in the longer span lengths.
4. In the short span ranges (80 - 110 ft), prestressed concrete girder bridges have become the dominant bridge type.

Vision of the System

3.1 INTRODUCTION

The need for innovative steel bridge construction techniques is driven by the market demands. The competition between various bridge materials in the current markets demands the bridge professionals and researchers to find cheaper and faster construction methods. To respond this issue, a new design and construction concept was developed to enhance the competitiveness of the short to medium span steel bridges. The details of the new proposed method and its difference with the current method in practice are discussed. The benefits of the new system in regard to cost and time of the projects are shown by two case studies.

3.2 BRIDGE MATERIALS MARKET ANALYSIS

An 11-year overview of National Bridge Inventory (FHWA, 2003) data obtained from the Federal Highway Administration (FHWA) for fifty states is shown in Figure 1. The data was separated into categories based on the material of bridge construction. It is seen that the number of steel and timber bridges constructed in this period are declining while the number of concrete and prestressed bridges are increasing. To identify trends in the use of bridge materials, a detailed market analysis was carried out by Lampe (2001) in the mid-west region of the United States. Based on these trends identified through the market analysis for a time period from 1911 through 1998, the primary conclusions were as follows:

1. The use of timber as a bridge construction material, although basically limited to lower span lengths, has significantly decreased over the time period examined.
2. In most states studied, reinforced concrete has remained a fairly consistent choice for span lengths of 50 ft or less.
3. Prestressed concrete construction captured a large share of the market in the 60 ft - 100 ft span ranges in the 1960's and 1970's. The current trends indicate that prestressed concrete has extended its presence as a construction material choice across all span lengths. In the last two decades, steel bridge construction in all span lengths has either remained steady or decreased in number.
4. In the short span ranges (80 - 110 ft), prestressed concrete girder bridges have become the dominant bridge type.

The market analysis showed the steel girder bridges to be less competitive in short to medium span bridges compared to the prestressed concrete types. The purpose of this research was to reduce the cost of steel bridges in the span length range of approximately 80-150 ft.

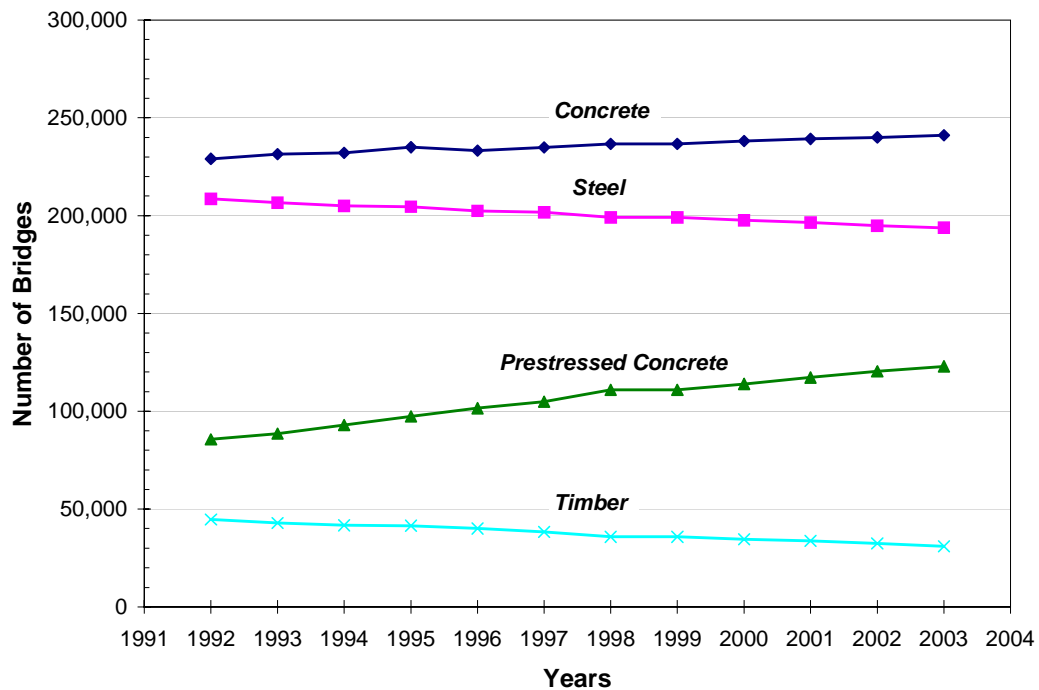


Figure 3-1: The number of bridges in the U.S. by construction material

3.3 CONVENTIONAL VERSUS NEW METHOD

The current design methodology for the multi span steel bridges is to build bridge girders continuous to distribute applied loads more evenly between the spans. The steel girders are usually fabricated in the shop in several pieces, due to handling limitations, and then transported to the site for assembly. The multi-span steel bridges are connected together at the site to make the continuous beams. The construction sequence consists of placing the middle segment and connecting the two end sections using a bolted or welded field splice. When using bolted splices, estimates for the average cost of material, installation and inspection of one bolt can be high. The location of field splices due to structural design considerations is pre-

ferred to be somewhere between piers rather than on the piers. This type of construction usually requires extra cranes or temporary shoring (see Figure 3-2) for erection with a possible interruption to traffic. .



Figure 3-2: The conventional erection method of steel girders.

The connection of two steel girders while hanging in the air can be hazardous for the steelworkers. Furthermore, the detailing and fabrication of splice holes requires extra inspection cost to avoid installation errors. In a series of discussions with designers, fabricators, and contractors, two factors were identified to be essential in improving the system:

- Elimination of field splices
- Simplification of the type of details at the pier location

Based on the newly developed concept, designers specify steel girders in simple span configuration as shown in Figure 3-a (girders sit simply on the abutments and piers). In the field, the contractor fixes them with a partial concrete diaphragm at the pier. This technique greatly simplifies the formation of continuous girders, which would otherwise be bolted or welded

together in the field by the contractor. After placing each girder on the bearing pads, the concrete slab and remaining portion of the diaphragm is poured. The concrete deck, diaphragm and longitudinal reinforcing provide the continuity of two adjacent steel girders for the traffic loads and superimposed dead loads (Figure 3-3-b). The advantages of this method of construction were investigated in a parametric study (Lampe, 2001) and are as follows:

- The need for expensive field splices is completely eliminated for spans of up to 150 ft (as controlled by transportation considerations).
- The contractor will need fewer cranes for installation. The need for less installation equipment allows smaller contractors to bid for jobs.
- A uniform cross section can be utilized for the entire span which reduces the fabrication effort.
- Girders can be placed over the support without significant interruption to the ongoing traffic.
- Improves safety of steel workers.
- The placement of girders directly on the pier and abutment reduces the erection time.
- Minimal detailing of the steel beams.
- No need for temporary shoring.

On the other hand, girders designed using the proposed concept increase the weight of steel material required because of the simple span action of each girder under the construction loads. However, implementations of simpler details enhance the overall economy of the bridge. Traditionally, the cost of materials was more important in the estimation of the total cost of a project, but now the least labor generally results in the least cost.

Labor costs can be substantially reduced by using simpler details in the new method. .

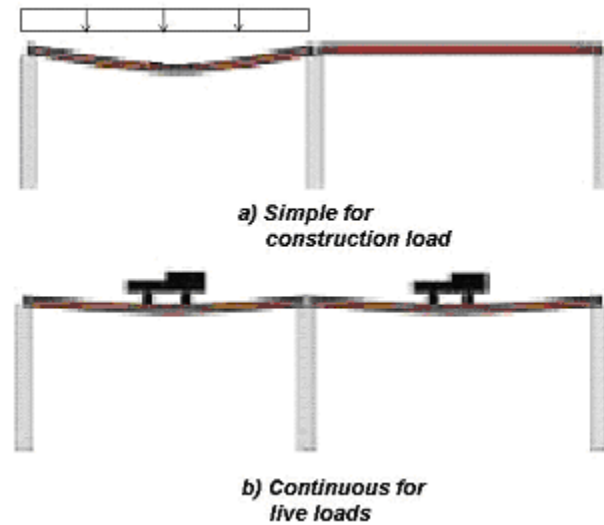


Figure 3-3: The conventional erection method of steel girders.

3.4 CASE STUDIES

To validate the economic advantages of the proposed concept, a parametric study was carried out. In this study, two steel bridges that had been recently constructed based on the new concept were selected. The design of the steel bridges, superstructure follows AASHTO-LRFD Bridge Design Specification (2001) provisions. Both bridges were designed based on the conventional method and the new concept for comparison purposes.

3.4.1 SPRAGUE STREET BRIDGE

The Sprague Street Bridge over Interstate 680 is located in Omaha, Nebraska and was opened to traffic in August 2004. The bridge has two spans, each 97 ft long with a four I-girder cross section. The clear roadway width is 32 ft, with a 7 ft pedestrian sidewalk on the south side of the bridge. Cast-in-place deck thickness is 7.5 in. with ½-in. integral wearing

surface. 50 ksi weathering steel was used for fabrication of the rolled I-girder. The Sprague Street project was selected for two reasons. First the 97-ft spans represent a common two-span bridge constructed in the US in the short span range. Second, the project was recently designed and erected and would provide current cost estimates for economical comparisons.

3.4.2 N-2 OVER I-80 BRIDGE

The N-2 Bridge was recently designed and constructed at Nebraska Highway 2 over Interstate 80. The Bridge structure consists of two 139-ft spans, and a three-box girder cross section. The spacing between centerlines of the boxes is 16'-1-in. and supports a 46'-4-in clear roadway and a pedestrian sidewalk. The cast-in-place deck thickness is 7.5 in. with ½-in. integral wearing surface. Exterior girder overhang is 4'-1-in from the center of the exterior girder to the edge of deck. 50 ksi weathering steel was used for fabrication of the box girders. The bridge was built using the proposed construction method. The reason in selecting this bridge was to examine the new concept on the different cross sections and its practicality in the medium span length range.

3.5 DESIGN PROCEDURE AND RESULTS

The designs for the preceding bridges were carried out using two methods; first, as a continuous beam for dead, live and superimposed loads (conventional method) and second as two simple beams for dead load and continuous for live loads according to the new proposed concept, which was described earlier. A summary of the design results is given in Table 3-1. The variation of flange thickness was limited to two thicknesses along the girder length to include the practical fabrication considerations. However, the obtained thickness is not market-standard size. The web depth and thickness remained constant in both methods to satisfy the deflection requirements. In weight calculations, the weights of stiffeners and cross

frames were ignored since they are similar in both alternatives. The values in the table are presented as ratios in the form of demand/resistance. The flange thickness was changed to obtain a demand to strength ratio of the section close to 1.00. Recall that the designs were optimized in terms of steel weight only. It is noticed that for each case the weight of the additional steel by using the new concept is about four percent for a box girder and approximately three percent for the I-girder.

	Box Girder		I-Girder	
	Conventional Method	New Method	Conventional Method	New Method
Top Flange Sizes (in)	(16x0.64) & (16x1.3)	(16x0.7) & (16x0.8)	(15.8x0.5) & (15.8x2.6)	(15.8x0.5) & (15.8x2.6)
Web Sizes (in)	(50x0.375)	(50x0.375)	(36.56x0.75)	(36.56x0.75)
Bottom Flange Sizes (in)	(72x0.64) & (72x1.3)	(72x0.7) & (72x0.8)	(15.8x0.5) & (15.8x2.6)	(15.8x0.5) & (15.8x2.6)
Demand/Strength Ratio	1.00	1.00	1.00	1.00
Weight of 1 Girder (kips)	52.47	54.63	21.46	22.07
Weight Increase Percentage	4.13%		2.82%	

Table 3-1: Properties of the Girders

3.6 COST-BENEFIT ANALYSIS

In the previous section it was noticed that the application of the new construction method could result in a slight increase in weight of the steel girder. In return, the field splices were eliminated in each girder. Although each of the design parameters somewhat affected the cost of bridge construction, the major factors remained the weight of the steel girders and the cost of the field splices

The cost of a steel girder consists of material, labor, and equipment costs. The average bid unit price of fabrication and erection of each steel girder is listed in Table 3-2. The unit price is based on the assumption that the girders have been fabricated using the conventional method. Since the weight of the girders designed following the new technique is greater than the conventional method, the total price of each steel girder is also greater. The increase in the cost of the materials by utilizing the new concept is \$923 for the I-girder and \$2380 for the box girder, as given in Table 3-2. This comparison is based on the unit price of a steel girder designed and constructed using the conventional method.

	Box Girder		I-girder	
	Conventional	New	Conventional	New
Weathering steel unit price (per lb)	\$1.1	\$1.1	\$0.75	\$0.75
Price of each steel girder	\$57,712	\$60,093	\$15,627	\$16,551
Difference between two methods	\$2,381		\$923	

Table 3-2: Costs of the Girders

The cost of fabrication and installation of each field splice needs to be estimated in order to determine the extra cost of each girder when designed using the conventional method as opposed to the new concept. The cost of fabrication and erection of one field splice for each girder consists of the

cost of bolts, holes, plates, an extra crane, steel workers for installation, and inspection. The unit price and required time for each item was obtained from RS Means Open Shop Building Construction Cost Data (2003). A 55 percent surplus was added to the total cost of material, equipment, and labor to consider the overhead, profit, and indirect costs of the contractor. The typical field splice designed for the I-girder bridge is shown in Figure 3-4. The fabrication and erection of each splice costs about \$2,000 for each I-girder. It is shown that the additional field splice adds approximately 13 percent to the total cost of each steel I-girder, while employing the new technique, increases the steel material cost only by six percent. Therefore, there is seven percent savings by using the new method of construction.

Another splice detail was designed for the box girder and the cost was estimated by the same method as described for the I-girder. The cost of each field splice is about \$6400, which is 11 percent of the total cost of a box girder. The increase in cost due to extra weight is about four percent. Therefore, by the elimination of each splice by using the new method, the contractor would save up to seven percent for each designed box girder.

The extra time for the fabrication and erection of each splice was evaluated based on a crew consisting of two steel workers for fabrication and installation and one crane operator and one inspector. The total estimated time for the field splice of the I-girder is about 10 hours. This will extend the project time for more than one day, since the fabrication and erection of a steel girder is usually on the critical path of the project schedule. The time estimation for the box girder indicates that employing field splices can extend the project time for more than four days.

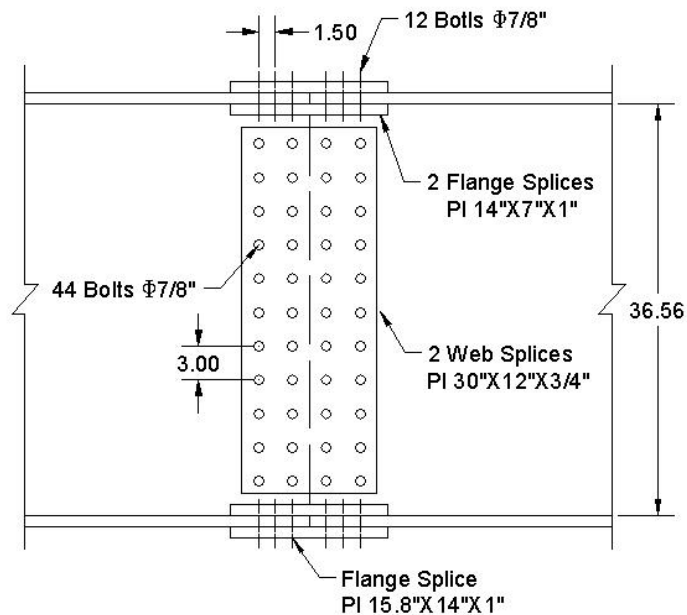


Figure 3-4: I-girder field splice details.

3.7 NEW CONCEPT IN PRACTICE

The Sprague Street over I-680 and the N-2 over I-80 Bridges were constructed based on the new technique in Nebraska in 2003 and 2004, respectively. The I-girder bridge was made of a rolled shape section with a uniform section across the length and thus did not need any change in cross section. The only additional detail added was the end bearing plates which were welded to both ends of the girder in the shop. The cross section of the box girder was also uniform across the span length; therefore the plate waste was minimized. The additional end bearing plates were welded to the ends to improve the stability of the box girder and continuity of the bridge system after pouring the concrete.

The girders of the first span of Sprague St. Bridge were set independently (see Figure 3-5) without erecting the second span girder, therefore the traffic under the second span did not need to be interrupted. The independency of the girders setting in two spans is not possible with the current method of practice, since the girders must be continuous over the pier

(Figure 3-2). The girders of the first span were erected at night in order to minimize disruption to traffic, as Interstate 680 below had to be closed during that time. The cost for in-place erected steel for the Sprague Street Bridge was approximately \$0.52/lb. This compares to rule-of-thumb value of engineering estimates of \$0.75/lb for erected rolled steel bridges having conventional bolted field splices (Azizinamini and Vander Veen, 2004). The duration of the project was about six calendar months. The elimination of field splices could have shortened the project schedule by about one day, which is approximately one percent of the total project duration.

The erection of the 139 ft box girder was carried out by two crawler cranes (Figure 3-6) without any temporary shoring. The placement of each girder from the semi-trailer on the abutment and pier took about 20 minutes. As it was pointed out earlier, the installation of a box girder with the traditional construction method could exceed four days considering the time needed for setting the temporary shoring and fastening of the field splices. The construction period for this bridge was also about six calendar months. The time savings estimated by eliminating the field splice based on the time calculation presented in the previous section, is about three days which is approximately three percent of the total project time...



Figure 3-5: Erection of first span of Sprague Street Bridge over Interstate 680.



Figure 3-6: Erection of Box Girder Bridge over Interstate 80.

Experimental Program

4.1 INTRODUCTION

In order to investigate the strength of the new proposed connections presented in the preceding chapter, three full-scale tests were planned. The design and construction of each specimen was done according to the AASHTO-LRFD (1998) provisions and practical considerations. The first test was intended to develop a connection detail that functioned sufficiently. The purpose of the second test was to develop a base data to compare the behavior of various details. The third test was a modification of the first test with a simpler detail. Extensive instrumentation was planned for each test. In order to represent the loads that the structure would encounter, two load stages were identified for each specimen:

1. Cyclic fatigue loading, which is based on the fatigue load from analysis and the fatigue category for the detail.
2. Ultimate moment capacity based on the governing strength limit state.

The results of the fatigue and ultimate tests are presented in this chapter.

4.2 DESIGN OF SPECIMENS

The design of test specimens was based on a two span continuous I-girder Bridge (Military Road Bridge, Nebraska). The bridge consists of two 95-ft spans with four girders. The trial design was completed in accordance with the American Association of State Highway and Transportation Officials (AASHTO) Load and Resistance Factor Design Specifications (LRFD, 1998). The design calculations can be found in a Master's Thesis by Nick Lampe (2001).

4.3 SPECIMENS DETAILS

The geometry of the test specimen was selected to represent an interior pier section of the two-span bridge subjected to construction and service loads described in previous section. The current AASHTO Bridge Design Specifications, 2004, do not recommend any design provisions for the proposed method; hence the preliminary design of the bridge at the pier location was done using reinforced concrete theory. In addition, testing of the entire bridge was not feasible in the lab; therefore only part of the bridge was designed and constructed to be tested. The double cantilever system provides an effective means of simulating loading of the structure in the field. This allows simulating the bridge behavior around the pier region without constructing the entire bridge. Figure 4-1 shows the conceptual test specimen. Figures 4-2 and 4-3 show the longitudinal and transverse views of the test specimens.

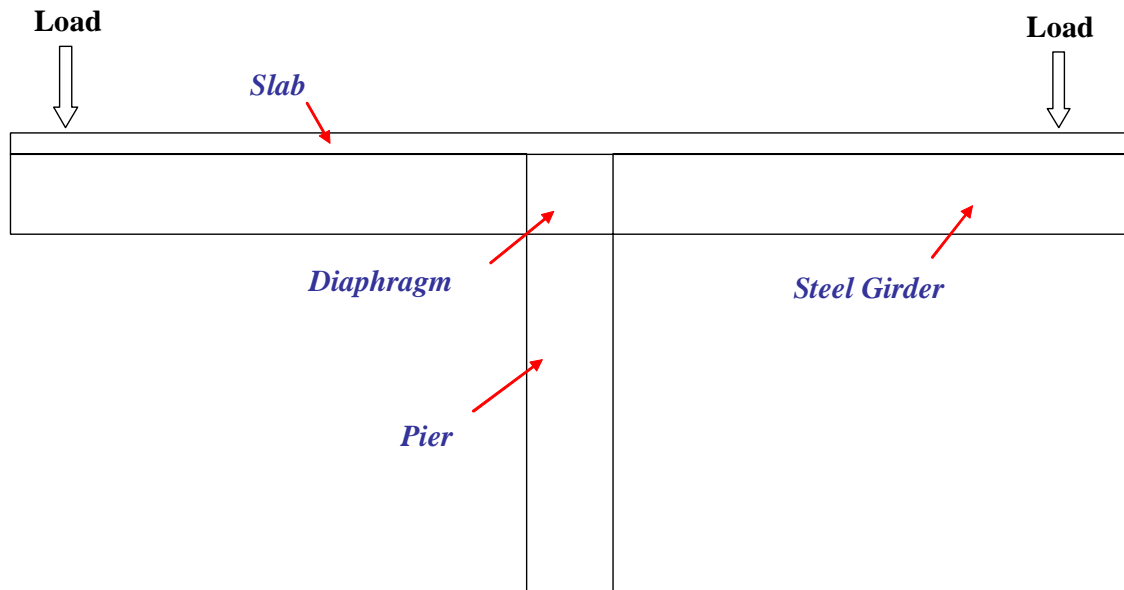


Figure 4-1: Conceptual Test Specimen

4.3.1 CONCRETE DIAPHRAGM

Details were similar to Nebraska Department of Road (NDOR) standards used in the design of prestressed concrete girder bridges. These included the transverse reinforcement in the diaphragm, for which holes were drilled or flame cut in the web. The stirrups were closed hoops with one spaced 6-in from the outer edge of the bottom flanges and 12-in on center within the remaining space between adjacent girders. The details of the diaphragm are shown in Figures 4-5 and 4-6.

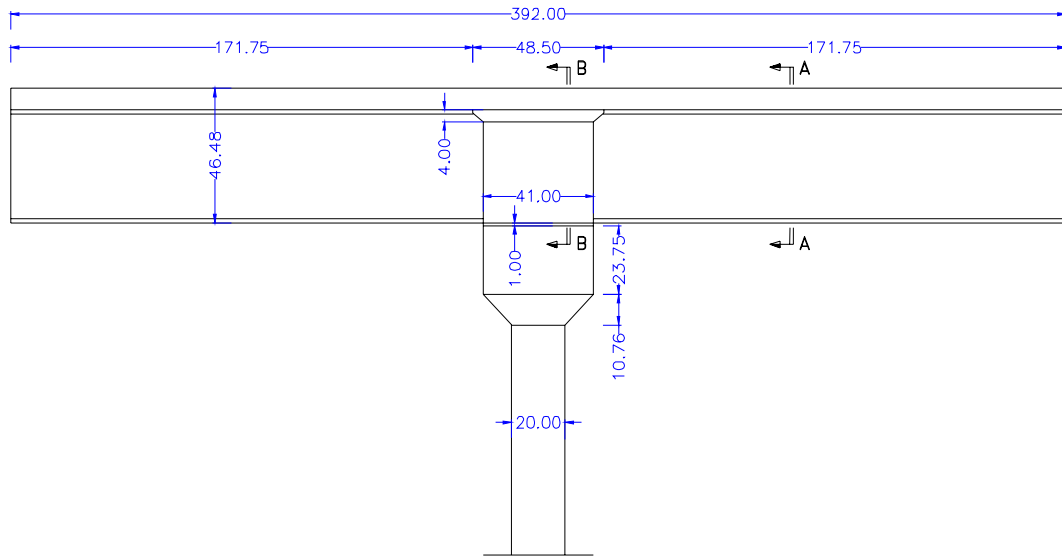
4.3.2 REINFORCED CONCRETE SLAB

In accordance with AASHTO-LRFD provisions, for the test specimens the effective flange width is calculated as 93-in with a thickness of 7.5-in. No haunch was included. Empirical deck design for longitudinal steel includes #4 bars at 12-in on centers in the top layer and #5 bars at 12-in on centers in the bottom layer. For transverse steel, reinforcement consists of #5 bars

at 12-in on centers in the bottom layer and #4 bars at 12-in on centers in the top layer.

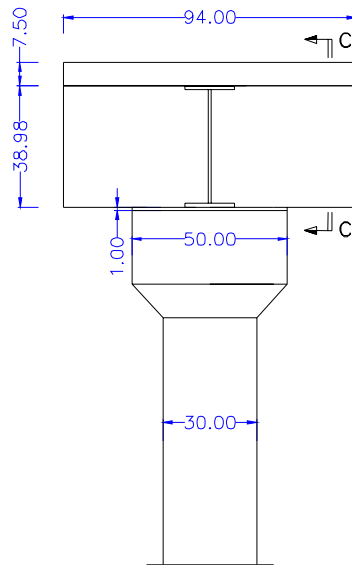
In the current proposed method of design, the negative moment induced from the live loads and superimposed dead loads shall be resisted by the slab rebar reinforcement at the pier location. Therefore, the amount of longitudinal rebar at the pier location cannot be checked only by empirical deck design which has been developed for the conventional systems. The purpose of this research is to determine the strength of the bridge at the pier location. However, for the preliminary design of longitudinal rebar at this point for the experimental program, the classical concrete theory was employed. The details of calculations can be found in the previously mentioned thesis (Lampe, 2001). Based on this method, the additional reinforcement required in the top layer is comprised of two #8 bars centered between adjacent #4 bars. Similarly, one #7 bar is centered between adjacent #5 bars in the bottom longitudinal layer. This follows the typical convention of $2/3$ of the reinforcing steel in the top layer and $1/3$ of the total area in the bottom layer. The details of the deck rebar can be seen in Figure 4-4.

Specimens Details



Longitudinal View

Figure 4-2: Typical Specimen Longitudinal View (Dimensions in inches)



Side View

Figure 4-3: Typical Specimen Side View (Dimensions in inches)

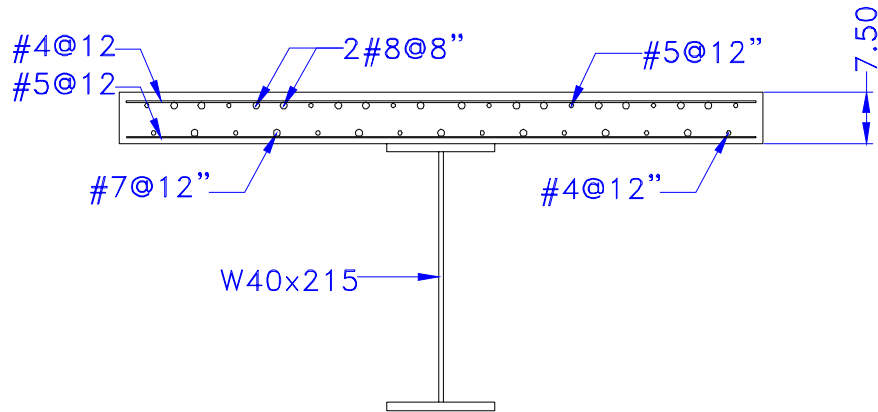


Figure 4-4: Concrete Slab Section A-A

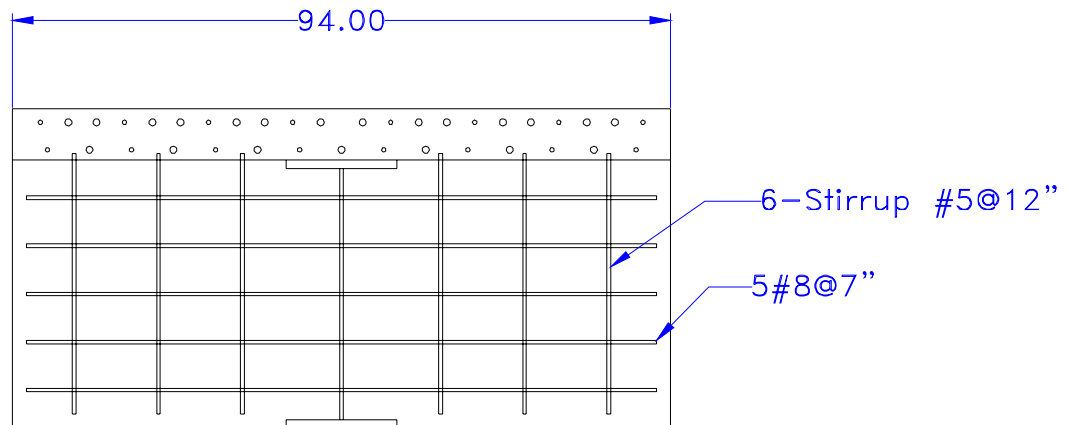


Figure 4-5: Concrete Diaphragm Detail, Section B-B

4.3.3 SPECIMEN ONE

In the first specimen, the length of cantilever, L , was 12-ft. A bearing plate was welded to the end of the girder (see Figure 4-7), and two triangular gusset plates were added to stiffen it above the bottom flange. The main characteristic of this specimen was continuity of the bottom flanges of two adjacent steel girders over the pier. This continuity ensured that the specimen was capable to transfer the compressive stress of the bottom flange without substantial crushing of the diaphragm concrete. The connection of the two girders was accomplished by extending the bottom plates and welding them together.

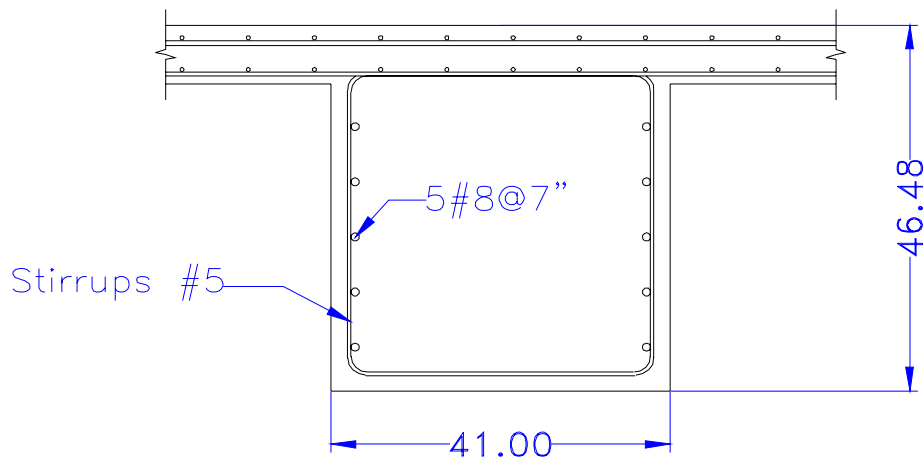


Figure 4-6: Concrete Diaphragm Detail, Section C-C

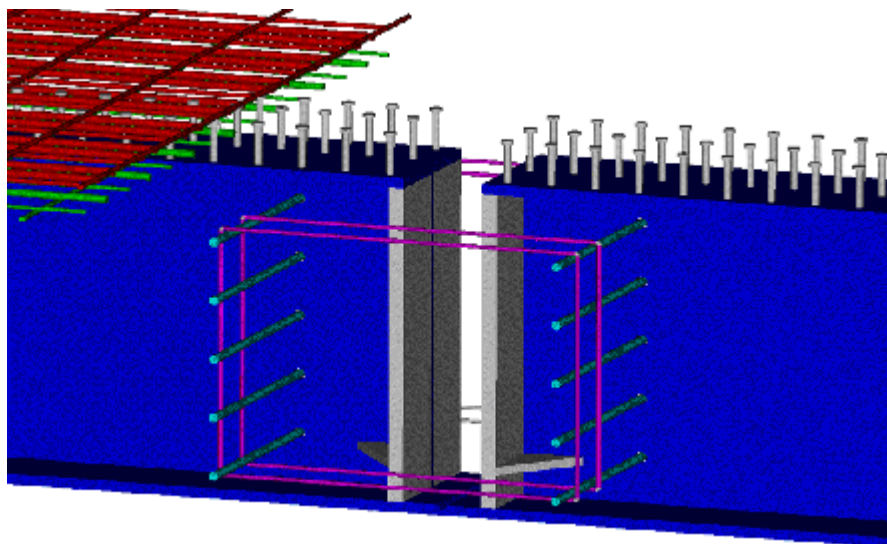


Figure 4-7: Specimen 1 Detail Inside of Diaphragm.

4.3.4 SPECIMEN TWO

In the second specimen, two girders simply sit on the pier and the concrete diaphragm confines them (see Figure 4-8). The two girders are totally separated and there is no connection between bottom flanges. The negative moment is transferred through the composite action of the concrete and steel in the diaphragm. This test aimed to investigate the simplest condition for the transferring the compressive stresses.

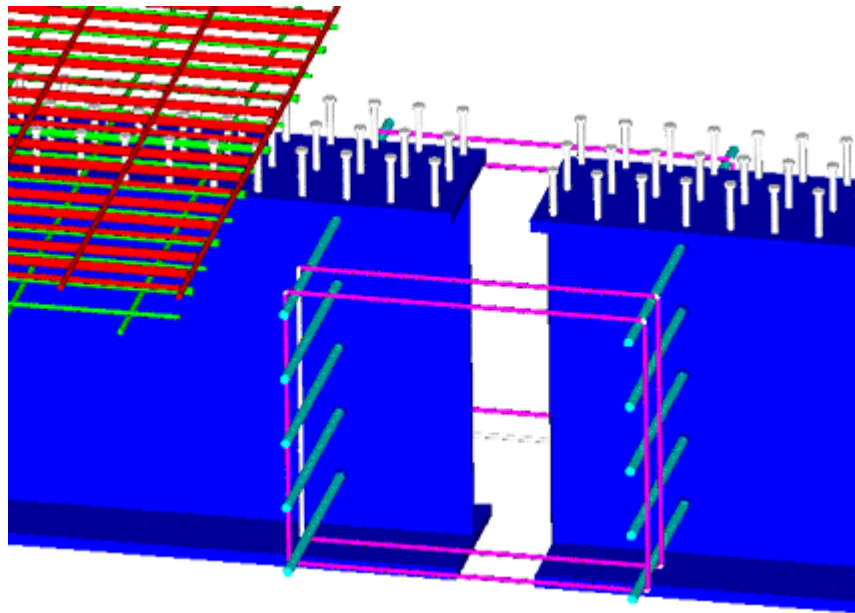


Figure 4-8: Specimen 2 Detail Inside of Diaphragm.

4.3.5 SPECIMEN THREE

In this case the end bearing plate was welded to the ends of steel girders, but the bottom flanges were not connected (see Figure 4-9). There was an 8 in. gap between the two girders. This specimen was designed to study the behavior of a connection with characteristics between specimens number one and two. The end bearing plate creates a more uniform distribution of the compressive stresses, yet it does not prevent the crushing of the concrete.

4.4 CONSTRUCTION AND ERECTION

Construction of the test specimen was completed in the structures laboratory at the University of Nebraska - Lincoln. A reinforced concrete pier was built to support the cantilever system for all three test specimen. The girders for the test specimens were cut from the same stock (W40 X 215 rolled I-girders). A 15.75 inch wide by 36 inch long by 1 inch thick elastomeric bearing pad was placed on the pier for the girders to bear on. One inch

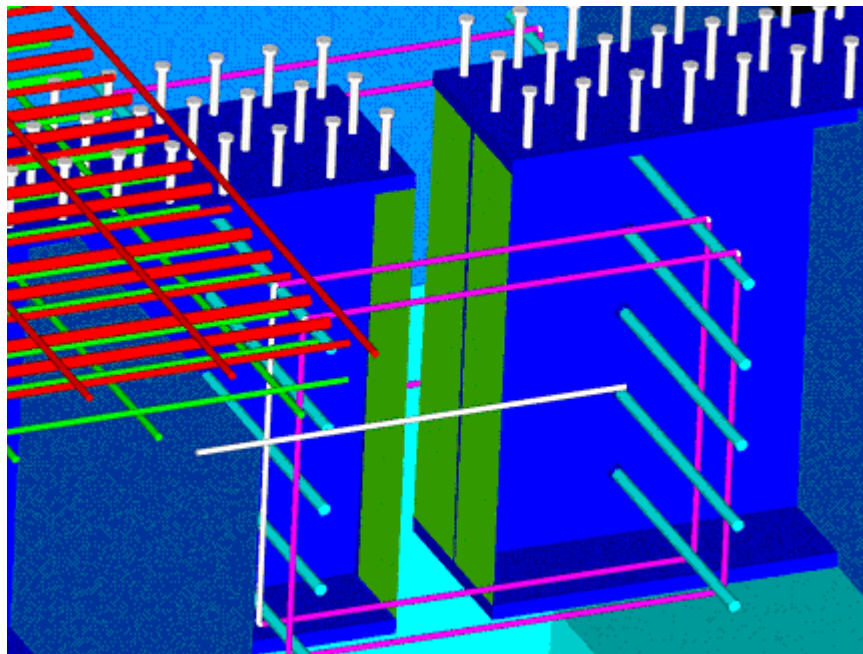


Figure 4-9: Specimen 3 Detail Inside the Diaphragm

thick polystyrene was placed at the base of the diaphragm in order to prevent bonding between the pier and concrete diaphragm.

After the girders were set, diaphragm reinforcing steel was placed and embedment gages were set. Formwork for the deck and diaphragm was added after the diaphragm reinforcing steel was placed. Once the deck formwork was completed, the diaphragm was partially cast in order to stabilize the specimen prior to casting of the deck. Once the diaphragm was poured, deck reinforcement was placed. Several days after the diaphragm was cast, the deck was cast. The construction sequence can be summarized as follows:

1. Reinforcing and pouring the concrete pier
2. Fabrication of the steel girders
3. Instrumentation of the steel girders
4. Installing steel girders on the pier and supporting them
5. Welding two girders together (only specimen number one)
6. Placing steel rebar for diaphragm
7. Instrumentation of the diaphragm
8. Formwork of the diaphragm and deck
9. Pouring partial depth of the diaphragm
10. Placing the deck rebar and instrumentation
11. Casting the deck and remaining diaphragm concrete
12. Curing of the concrete

4.5 INSTRUMENTATION

To obtain data from the two load stages, several types of instrumentation were used. The loading stages were cyclic and ultimate loading. Each stage had its own distinct load pattern, thus requiring slightly different instrumentation configurations. Instruments included electrical strain gages, vibrating wire embedment gages, and potentiometers. The strain gages were mounted on the steel girders and reinforcements. An application of this type of gages is seen in Figure 4-10 on the bottom flange and the web of the first specimen. Some of these type of gage glued on the web of the second specimen are shown in Figure 4-11. The embedment gages were placed inside the concrete diaphragm and deck. In the test specimens, a embedment strain gage was tied to the reinforcing cage as shown in

Figure 4-12. The potentiometers were used to measure the displacement of the end of the cantilevers. Also, the horizontal movement of the bottom flanges into the diaphragm was measured by a potentiometer in the third test. To apply load on the specimens, the displacement was applied at the end of the cantilevers by hydraulic rams. The pressure of hydraulic oil inside the rams was measured by pressuremeters built in the rams.

Each type of instrumentation was given a designation based on the type and location of the gages. The locations of strain gages for each test can be seen in the experimental report (Azizinamini, et al., 2005).



Figure 4-10: Spot weldable gages on the steel girder of the first specimen

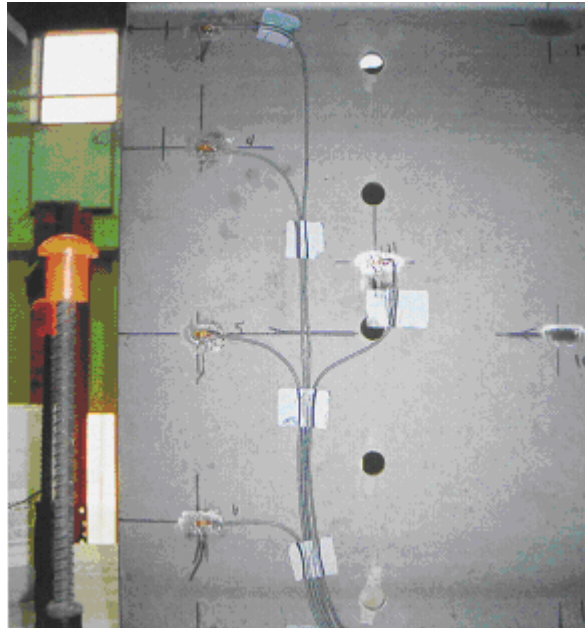


Figure 4-11: Strain gages attached to the web of steel girder in second test

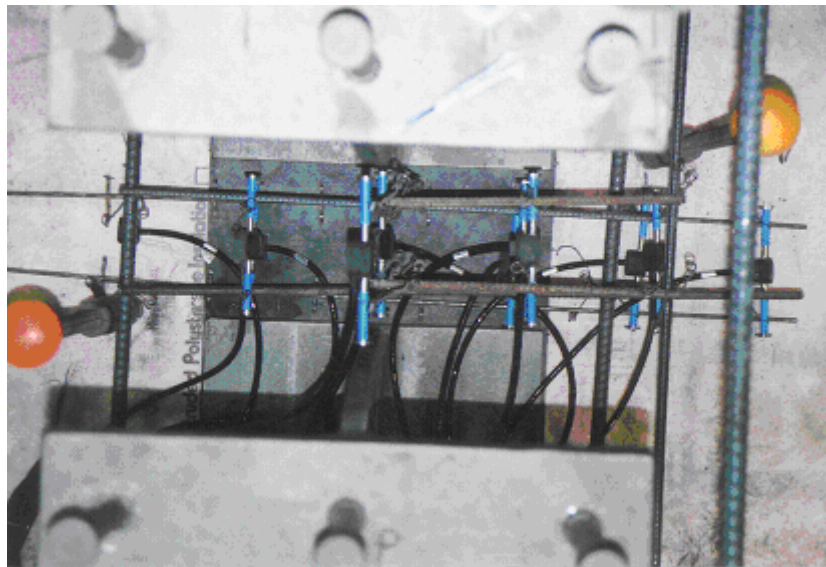


Figure 4-12: Embedment gages in the second specimen

4.5.1 PERFORMANCE OF GAGES DURING TESTS

One of the shortcomings of measurements during the cycling and ultimate tests was malfunctioning of gages. The reliability of test results directly depends on the accuracy of gages readings. Although the specified accuracy of the gages by manufacturers was adequate for the conducted tests, the performance of the gages inside the real test specimen was problematic.

One problem with gages was about their limitation in recording the strain. The range of reading of gages used is summarized in Table 4-1. According to embedment gage strain range, the gage cannot read strain after crushing of concrete which is around $3000 \mu\text{s}$. It seems malfunctioning of embedment gages located between the two bottom flanges in the second and the third test related to crushing of the concrete and exposing the gages to larger strains than their limits. It was observed that several embedment gages were deformed after the test. The location of these gages was inside the concrete diaphragm between the two bottom flanges. One deformed embedment gage after dissection of the second test is seen in Figure 4-13. The weldable strain gages were attached to the steel girders outside the diaphragm where there was unlikely to be large strain. As a result, their measured strain is below their limit. The uniaxial strain gage experienced very large strain after the yielding of the top rebar. The test data shows that the uniaxial strain gages were not able to measure the rebar strain after about $9000 \mu\text{s}$ in Test one and they did not work properly after $6000 \mu\text{s}$ in the second test.

The failure of embedment gages during the construction and test process was another issue in malfunctioning of the system. The embedment gages are prone to be damaged by pouring of concrete and by the vibrator. The uniaxial strain gages are vulnerable to water. The waterproofing of these gages might have been damaged during the construction. Another problem was the capacity of glue used to attach these gages to the steel surface. The

Gage Type	Range	Accuracy
Embedment	3000 ms	±0.1%
Spot-weldable	2500 ms	±0.1%
Uniaxial	30000 ms	NA
Potentiometer	4 in	±0.25%

Table 4-1: Specifications of Gauges

glue is not efficient for a long time and sometimes the test procedure took several months. Also, the movement of concrete over the strain gages attached on the steel surface might cause the separation of strain gages from the steel surface. This especially was a serious problem in the second test in which the steel girder web was moving inside the concrete during the cycling test. Most of the strain gages attached to the web failed. The induced high temperature (about 100 F) in this region due to friction during movement might have weakened the glue between the gages and web surface. In the third test, the malfunctioning of the string of one of the potentiometers caused the displacement of the cantilever at the beginning of the ultimate test not to be recorded correctly.

4.6 MATERIAL PROPERTIES

The laboratory test specimen was constructed using representative materials utilized in actual bridge construction. Several component tests were performed in order to ensure that the bridge components complied with published material specifications. The deck slab and diaphragm were cast with 47-BD concrete. Only grade 60 reinforcing steel was used in the construction of the test specimen. The bridge girders were fabricated from W40 X 215 rolled I-girders conforming to ASTM A709-50W specifications. The material testing procedure and results for each specimen are presented in the following sections.



Figure 4-13: Deformation of an Embedment Gauge After Ultimate Test 2

4.6.1 CONCRETE

For the concrete materials, several 6-inch diameter by 12-inch long concrete cylinder samples were taken during the casting of both the diaphragm and the deck. The average compressive strengths of the cylinder specimens is given in Table 4-2.

In the first test, two concrete cylinders were tested from both the deck and diaphragm samples after curing for ten days. Similarly, four were tested 28 days after the pouring of the concrete. Two from both pours were tested at 49 days; this day coincided with the ultimate strength test. The average compressive strength (f'_c) for this day is listed in Table 4-2. The 28-day compressive strength of the diaphragm concrete was 5190 psi. Similarly, the 28-day compressive strength of deck slab concrete was 4860 psi. The pier concrete compressive strength was tested after seven days only. The compressive strength at this time was approximately 4250 psi.

In the second test, similar to the first test, two concrete cylinders were tested from both the deck and diaphragm samples after curing for ten days. Similarly, four were tested 46 days after the pouring of the concrete.

The 46-day compressive strength of the diaphragm concrete was 7119 psi. Similarly, the 46-day compressive strength of deck slab concrete was 5299 psi. The second ultimate test was done 120 days after pouring the concrete. The average of the concrete compressive strength tests for this day is listed in Table 4-2.

In the third test, two concrete cylinders were tested from the deck and diaphragm components after curing for 28 days. The 28-day compressive strength of the diaphragm concrete was 5902 psi. Similarly, the 28-day compressive strength of deck slab concrete was 7242 psi. Results of the concrete compressive tests for the diaphragm concrete and deck slab for this day are given in Table 4-2.

Test	f'_c (ksi)	
	Slab	Diaphragm
1	4.98	6.26
2	5.45	7.14
3	7.24	5.89

Table 4-2: Average Concrete Strength

4.6.2 REINFORCEMENT STEEL

For the steel reinforcing materials, samples of each deck reinforcing bar size were tested. Each sample was tested as a full section according to ASTM A370 Specifications. A typical strain-stress plot is shown in Figure 4-14. The strain-stress data is based on engineering strain. Results of the tensile test are shown in Table 4-3, Table 4-4, and Table 4-5 for the first, second and third test, respectively. The average reinforcing bar yield stress was approximately 65 ksi for the first test, 73 ksi for the second test and 69 ksi for the last test. The average of all measured yield stresses is 69 ksi and their standard deviation is 4.5 ksi.

The ultimate strength of bars also was measured as given in Table 4-3, Table 4-4, and Table 4-5. The ratios of ultimate stress to the yield stress (overstrength ratio) of tested rebar also are listed in the tables. The average of overstrength ratio for all the rebar is 1.56. This means that the ultimate strength of rebar is 1.56 times of its yielding capacity.

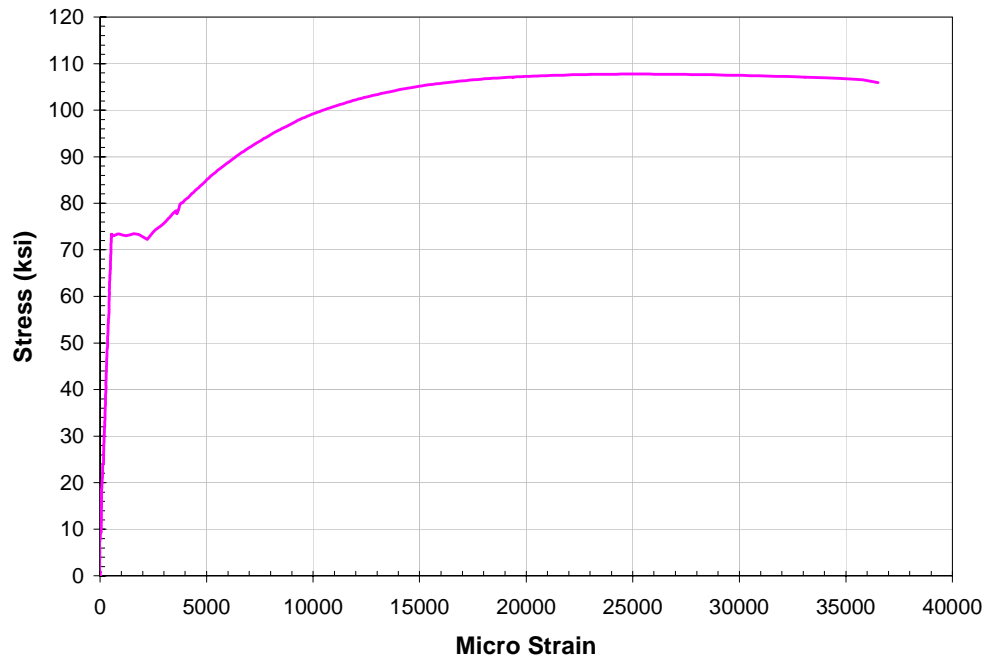


Figure 4-14: Stress-Strain Curve From Rebar Tensile Test

Bar Size	Area in ²	Yield Strength ksi	Ultimate Strength ksi	F_u/F_y
#4	0.2	64.2	101.0	1.57
#5	0.3	63.8	101.0	1.58
#7	0.6	68.2	101.0	1.48
#8	0.8	65.5	105.4	1.61

Table 4-3: Reinforcement Tensile Test Results for the First Specimen

Bar Size	Area	Yield Strength	Ultimate Strength	F_u/F_y
	in ²	ksi	ksi	
#4	0.2	71.5	114.2	1.59
#5	0.3	76.5	122.8	1.60
#7	0.6	67.5	109.5	1.62
#8	0.8	75.5	110.6	1.46

Table 4-4: Reinforcement Tensile Test Results for the Second Specimen

Bar Size	Area	Yield Strength	Ultimate Strength	F_u/F_y
	in ²	ksi	ksi	
#4	0.2	70.3	113.4	1.61
#5	0.3	68.9	108.7	1.57
#7	0.6	64.3	104.6	1.63
#8	0.8	73.2	107.8	1.47

Table 4-5: Reinforcement Tensile Test Results for the Third Specimen

4.6.3 STEEL GIRDER

In the first test, for the steel bridge girders, two samples were tested; one was from the girder web and the other from the tension flange. Both samples were taken from regions which were subjected to low flexural stresses during the testing sequence. Both of these samples were tested as full sections according to ASTM A370 Specifications. The 0.2% offset method was used to determine the yield strength of specimens. Figure 4-15 shows the results of the girder steel tensile test. The strain-stress data is based on engineering strain. The average yield strength of the girder steel was determined to be 57 ksi and the average ultimate stress was 72 ksi. The over-strength ratio is 1.26 for the steel girder. The steel girder material test was only carried out for the first test and since the second and the third test used a girder with the same specifications the results of the first specimen material test is used for them.

4.6.4 NEOPRENE PAD

The elastomeric bearing pad, Fiberlast, was made by Voss Engineering, Inc. Since all of the required mechanical properties of the employed bearing pad were not provided by the manufacturer manual, a compressive test was carried out in the Structural Lab for more information. Based on the strain-stress curve of the material, the modulus of elasticity is evaluated as 7207 psi by a linear fit. The Poisson's ratio is taken as 0.33 and material is assumed to be elastic linear in the analysis. The shear modulus is 230 ± 30 psi based on the manufacturer specifications. This test was carried out only for the first specimen bearing pad and its results were used for all three tests since the same type of bearing pad was used in the three tests.

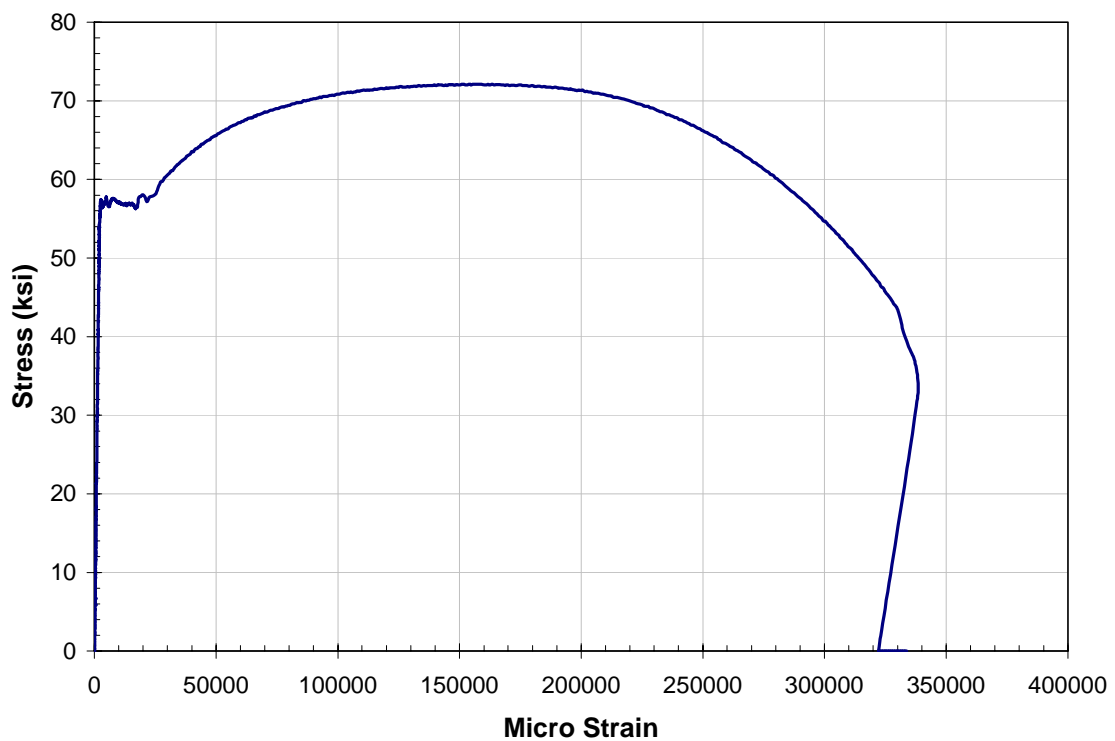


Figure 4-15: Stress-Strain Diagram for the Steel Girder

4.7 FATIGUE TESTING

The bridge structure is expected to directly resist millions of cycles of repeated axle loads from vehicles during its life. The available data shows that the number of trucks on a bridge can reach over 180 million vehicle load cycles during the life time of 100 years (Szarszen, Nowak, 2000). The proposed connection should be able to operate and survive when subjected to constantly changing loads such as cars and trucks passing over the bridge. Accumulated load cycles can cause cracking or even failure in the bridge components. The process that leads to fatigue failure is the initiation and growth of cracks in the material. Recent research suggests that fatigue cracking can be a precursor to severe spalling, reinforcement corrosion and shear punching failure of concrete in bridges.

The remaining life of a bridge superstructure is predicted based on a load model and a procedure to evaluate fatigue degradation of materials. The current connection consists of two materials: steel and concrete. The material degradation is often described using S-N curves based on fatigue test results. For steel girders, S-N curves are grouped in several categories of details. The fatigue strength of steel, which depends on the stress level and amplitude/frequency of loading, is usually established after 2 million cycles (Szarszen, Nowak, 2000). For reinforced concrete components, the fatigue-caused degradation applies to reinforcing bars, concrete and bond properties. The strength of concrete under cyclic loading can be drastically reduced. The process depends on amplitude and frequency of applied load and stress range. The degradation process is highly nonlinear approximately above 70% of the concrete ultimate strength (Szarszen, Nowak, 2000).

4.7.1 BACKGROUND

In the current experimental study, the fatigue degradation of materials can occur in the following parts:

1. Steel girder and its components
2. Concrete diaphragm in compression
3. Concrete diaphragm in tension
4. Bonding between steel girder and concrete
5. Steel reinforcement
6. Bonding between bars and concrete
7. Shear studs

The fatigue strength specifications are identified for the concrete material, steel girder, and steel reinforcement separately in the current design specifications such as AASHTO-LRFD (1998) and ACI-318 (2005). In this section the theoretical background of fatigue load-resistance equations is discussed based on the three mentioned design specifications.

4.7.1.1 STEEL GIRDER

The extensive experimental data have shown that the two most important factors governing the fatigue strength of steel girders are the stress range and the type of details (Taly, 1997). Besides these two factors, other parameters such as maximum stress, minimum stress, mean stress, and stress ratio which are less important on the fatigue life of a structure. The AASHTO fatigue nominal resistance is evaluated based on the following relationship (AASHTO, 1998)

$$(\Delta F)_n = \left(\frac{A}{N} \right)^{\frac{1}{3}} \geq \frac{1}{2} (\Delta F)_{TH} \quad (4-1)$$

where:

$$N = (365)(75)n(ADTT)_{SL} \quad (4-2)$$

A = constant

n = number of stress range cycles per truck passage

$(ADTT)_{SL}$ = single lane ADTT

$(\Delta F)_{TH}$ = constant-amplitude fatigue threshold

ADTT = average daily truck traffic

In this formula, the fatigue strength above the fatigue threshold is inversely proportioned to the cube of stress range. The constant-amplitude fatigue threshold is, in fact, the fatigue limit stress or endurance limit. If the maximum stress range experienced by a detail is less than the fatigue limit, then, according to AASHTO, it has theoretically infinite fatigue life. The constant A is a function of the fatigue behavior of a detail. In the current AASHTO specifications (2004) the maximum stress range is specified for eight categories for various kinds of details. In this formula the design life has been considered to be 75 years.

4.7.1.2 STEEL REBAR

A brief summary on the fatigue strength of reinforced concrete can be found in Taly (1997). Test results show that fatigue failure of concrete requires both cyclic loading generally in excess of 1 million load cycles and a change of reinforcement stress in each cycle of about 20 ksi (Taly, 1997).

The AASHTO (1998) has adopted the ACI-318 (2005) formula for the fatigue strength of the reinforcing bars in the form of the following equation:

$$f_f = 21 - 0.33f_{\min} + 8\left(\frac{r}{h}\right) \quad (4-3)$$

Where

f_f = safe stress range (ksi)

f_{\min} = minimum stress, positive in tension, negative in compression (ksi)

r/h = ratio of base radius to height of rolled-on transverse deformation, when unknown value 0.3 may be used

4.7.1.3 CONCRETE

In spite of steel, concrete can damage under both tensile and compressive stress fluctuations. The AASHTO Bridge Design Specifications (2004) does not address fatigue damage in the concrete members. The ACI Committee on Fatigue recommends an expression to design for a fatigue life of ten million cycles, but it does not give the S-N curves. The S-N relationship has been suggested by Aas-Jakobson and Lenschow (1973) in the following form:

$$\frac{f_{\max}}{f_c'} = 1 - \beta \left(1 - \frac{f_{\min}}{f_{\max}} \right) \log N \quad (4-4)$$

Where

f_{\max} = maximum stress

f_{\min} = minimum stress

f_c' = compressive strength of concrete

$\beta = 0.0685$ (Tepfers, 1979)

N = number of cycles

The fatigue behavior of concrete is similar in compression and tension. However, in the current test, the compression part is of interest since tensile strength of concrete usually is ignored for practical purposes. The maximum stress obtained from Equation (4-4) indicates that the concrete can not resist more than this value under the reversal compression loading after N cycles.

4.7.2 SHEAR CONNECTORS

The shear studs which connect the steel girders to the concrete are vulnerable to cyclic loads. The failure of shear bars which connect the steel girder web to the concrete diaphragm could be due to fatigue failure. The fatigue resistance of these elements is discussed in Chapter 6.

4.7.3 TEST PROCEDURES

For all tests, the Fatigue Limit States load combinations were used to calculate the shear and moment envelope according to AASHTO-LRFD Speci-

fications (1998). The fatigue resistance stress range was determined considering 75 years of service life for the bridge and using S-N curves recommended by AASHTO-LRFD. During this period, the bridge and consequently connection of two girders at the pier location will experience 135,000,000 cycles. The simulation of this number of cycles in the laboratory would take a long time. To conserve time, the number of cycles was reduced to fewer cycles. Instead, the applied force to the specimen was increased to compromise this reduction. The details of fatigue calculations and the reduction approach can be found in the previously mentioned thesis (Lampe, 2001). The test setup had the same configuration for all three tests. The cyclic load was applied using 220-kip MTS actuators placed at the ends of cantilever 14 feet from the centerline of the pier, as shown in Figure 4-16. Displacement control was used throughout the course of the fatigue investigation. The fatigue loading frequency was set at two cycles per second. At the beginning of the day, prior to the start of applying fatigue loads, the specimen was subjected to similar fatigue loads, however at a lower frequency. In this report these cycles are referred to as slow cycle tests. At the start of each day, the specimen was subjected to five slow cycle test (five cycles run at one cycle per 10 seconds). At the beginning of each of these five slow cycle tests, the specimen was held at the peak end load and data as collected from all instruments, including the embedment gages. During the application of the five slow cycles, data from all instruments except embedment gages were also collected and stored in the computer.

In the first test, the end load of 2 kip to 106 kip was applied successfully to the specimen in 2,000,000 cycles. In test 2 after applying a few cycles, it became apparent that the specimen could not resist the applied end loads of 104 kip. The maximum load achieved from the applied displacement had decreased to approximately 74 kips. As a result, the number of applied loading cycles had to be increased to 4,000,000 cycles. The maximum dis-

placement was adjusted three times during the cycling load test. The fatigue testing was terminated after applying approximately 2,780,000 cycles since the load continued to deteriorate. In test 3, based on the second specimen behavior during the fatigue test which dropped the load immediately after starting the test, it was decided to apply a smaller amount of load and observe the initial behavior of the specimen. Therefore, the end load was reduced to approximately 70 kip and 2,000,000 cycles were run with this configuration. However, because of the reduced end loads, the specimen had not yet fully experienced the effects of fatigue cycling. Therefore, it was decided to increase the end loads to about 85 kips and continue cycling. The 3,515,516 remaining cycles were run with this setup. The number of cycles and load range in each test are summarized in Table 4-6. .

Test	Cycles	Load Range
	#	kips
1	2,000,000	104
2	2,780,000	104 & 74
3	5,515,516	70 & 85

Table 4-6: Fatigue Testing Results

4.7.4 TEST RESULTS

4.7.4.1 CRACKING

For all the tests, the cracks on the surface of the deck slab were documented prior to application of fatigue cycles. In the first test, the majority of cracking occurred near the edge of the diaphragm. At this location, there is an abrupt change in rigidity. Mapping of deck cracking was done at 1 million, 1.5 million and 2 million cycles of load. From these maps, the largest crack widths occurred at the diaphragm edge, near the edge of the slab.

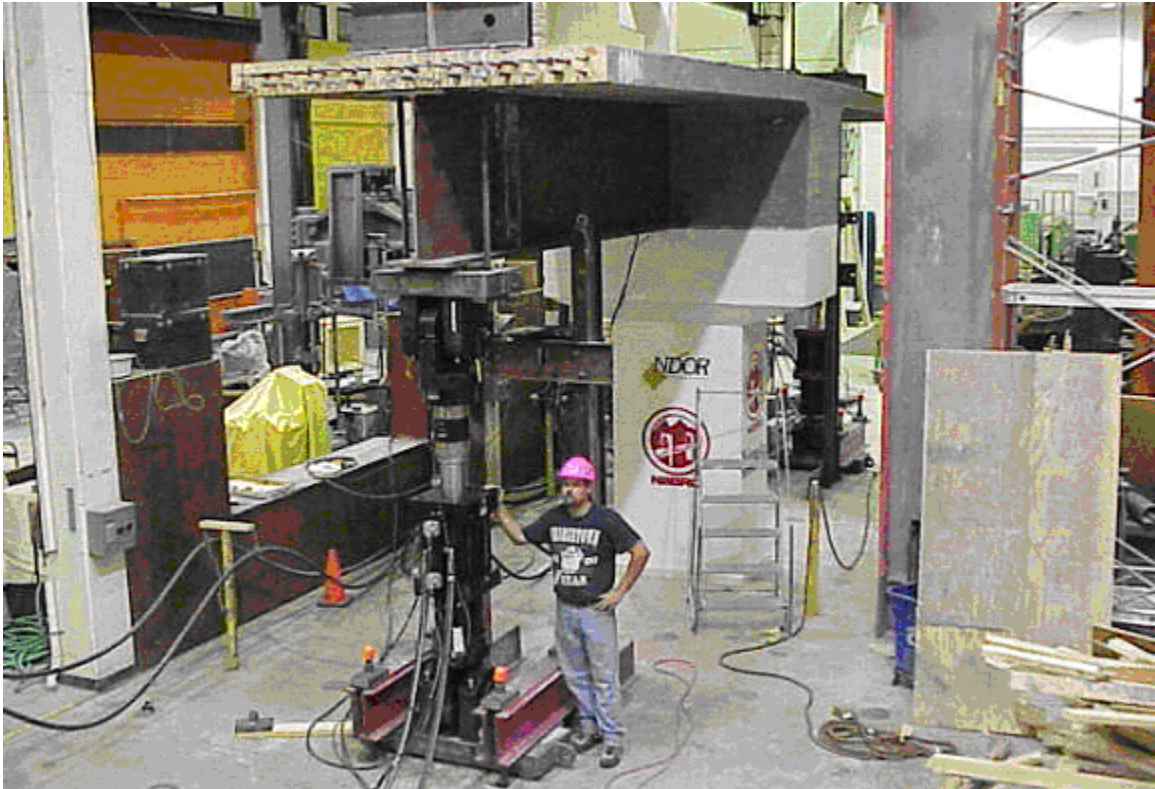


Figure 4-16: First Specimen Cycling Setup and Fixtures

Additional cracks had formed farther out from the diaphragm center-line. Crack maps for 1.5 million loading cycles are shown in Figure 4-18. A comparison of the crack widths from 1.5 million to 1 million load cycles shows that there was virtually no change in crack widths over this interval. There were a few additional short cracks propagating inward from the edge of the deck, but the measured widths of existing cracks were unchanged.

In test 2, as seen in Figure 4-18, cracks formed along the depth of the deck over the pier and close to the edge of the diaphragm during the fatigue test. The initial cracks were observed near the diaphragm edge. Also, several cracks were formed around the loading spreader at the end of the cantilever. As cycling progressed, the bottom flanges moved farther into the diaphragm. This movement could be seen during the fatigue test, but no cracking was observed. Before pouring the concrete diaphragm, polystyrene insulation foam was placed between the pier and diaphragm to allow

rotation of the girders over the pier. No gap formed between the pier and the foam around the edge of the pier during the cycling load test.

During test 3, cracking occurred through the depth of the deck over the pier. The initial cracks were observed near the location of the end of the girder inside the diaphragm. Unlike the second specimen the bottom flanges did not move further into the diaphragm.

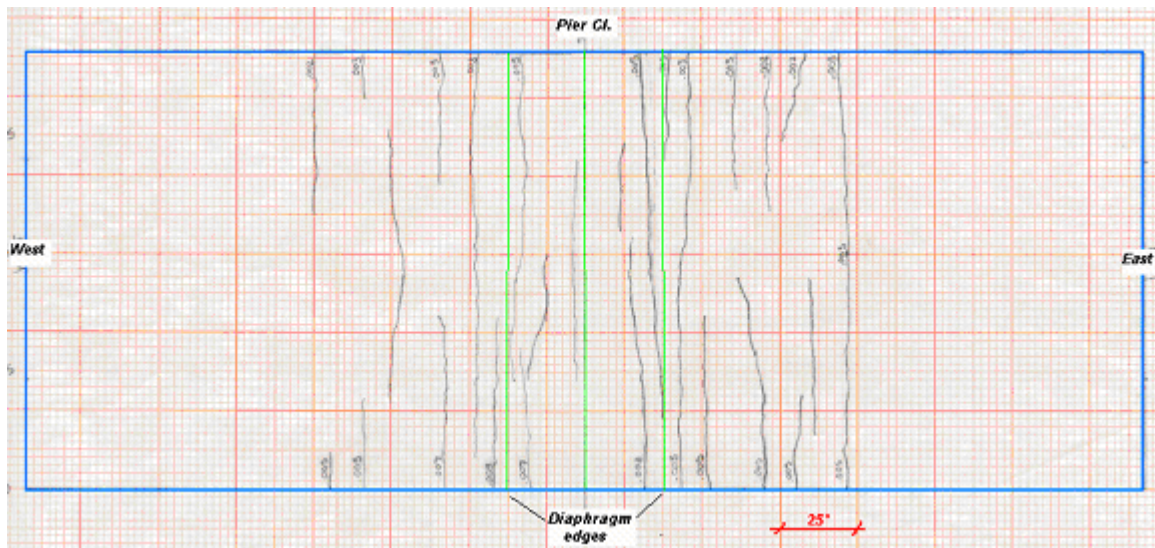


Figure 4-17: Cracks Mapped From the First Test Specimen After 1.5 Million Cycles

4.7.4.2 LOAD-DEFLECTION

The load deflection plots shown in Figures 4-19 through 4-21 were generated from data collected during the five cycles of loading. The first plot contains loops before starting the continuous cycling (except for the test 2) and the end of the cycling test as indicated on the plots. For the first specimen, little change in specimen stiffness is observed over the complete interval. In the second specimen, maximum load continued to diminish throughout the duration of the test. At certain points during cycling, the deflection was increased in order to bring the maximum end loads closer



Figure 4-18: Deck Cracking Over Pier From Second Cycling Test

to the target value. These adjustments can be seen in the load-deflection plots between the first cycles and the last cycles. In the third test, during the first 2,000,000 cycles, each day the maximum applied load would begin at approximately 70 kips, but diminish by nearly 10 kips by the end of the day's cycling. However, when cycling was started the next day, the maximum load had recovered to nearly the previous day's starting value.

4.7.4.3 STIFFNESS SOFTENING

In the first test, the experimental displacement required to attain the 106 kip load was 0.3083 in based on the finite element analysis of the specimen under this load. Only once the maximum deflection was adjusted to produce the 106 kip during the cycling test due to reduction in the stiffness of the connection. After 7400 cycles, the maximum displacement was increased from 0.3083 to 0.3115 in. to compensate for the stiffness reduction. The amount of adjustment was about 0.5 percent of the initial applied displacement. The stiffness softening in the load-deflection response of

the first specimen can be seen in Figure 4-19. The slope of the load-deflection curves at the zero cycle is about 437 kip/in. this slope decreased to 394 kip/in. after 2,000,000. Since the adjustment was only needed once at 7400 cycles and there was virtually no change in specimen response throughout the remaining fatigue cycles, it can be concluded that the slight stiffness change was due to initial concrete damage. This damage might be the tensile cracking of the concrete slab in the first cycles. The loss of stiffness in the first test was about 10 percent in the entire cycling test.

As seen in Figure 4-20, specimen two did experience some reduction in stiffness. However, the reduction of the stiffness is less than the first test. The specimen stiffness dropped sharply at the beginning of cycling such that applied load decreased. The stiffness given in Figure 4-22 for the first load cycle is after 8000 cycles, when the specimen already had been damaged. Based on an elastic approach the initial stiffness of the second specimen is predicted to be close to the third specimen. Assuming the response of the second test at the very beginning of loading is elastic, and then the initial stiffness could be at most equal to that of the third specimen. According to this approach, the loss of stiffness in the second test is about 13 percent. As was the case with the second specimen, the stiffness of the third specimen was initially very high, but dropped after fatigue load was increased. The stiffness of the third specimen was decreased by 12 percent throughout the test.

A slight increase in stiffness can be seen in Figure 4-22 during the early stages of cycling load. This increase of fatigue strength might be due to densification of concrete (Taly, 1997). Another reason for increase in the stiffness is error in readings by MTS system. A common trend was observed in three tests that the damage generation was more significant in the early cycles and diminishes upon cycling as seen in Figure 4-22.

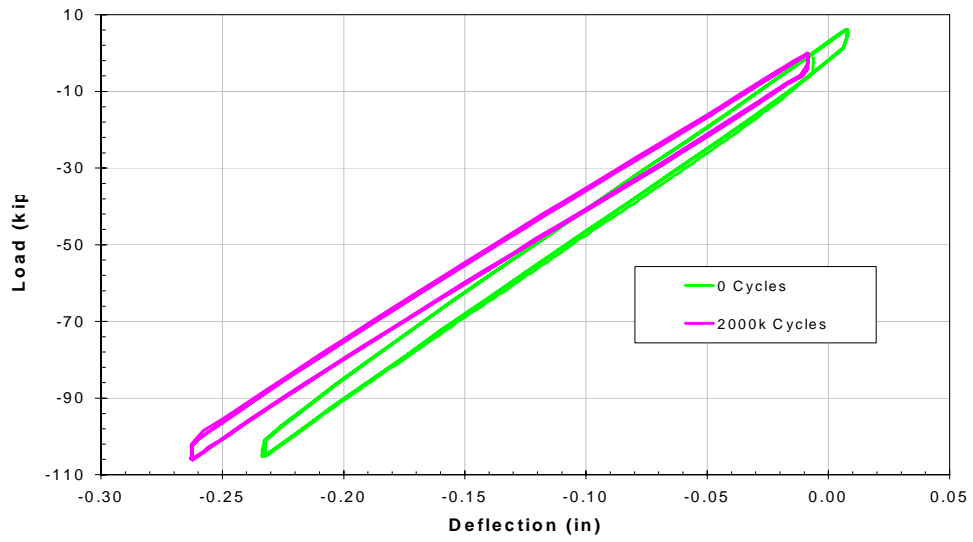


Figure 4-19: Load-Deflection Graph for the First Specimen's Fatigue Testing

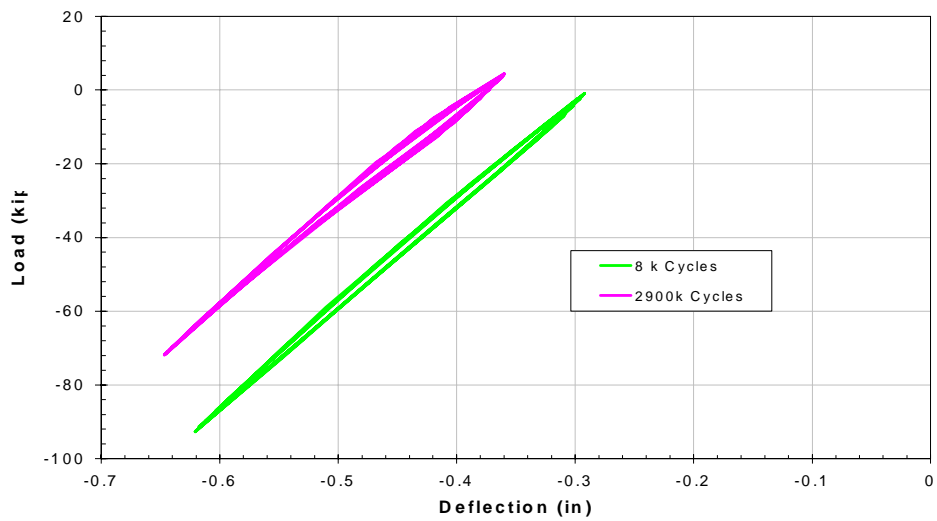


Figure 4-20: Load-Deflection Graph for the Second Specimen's Fatigue Testing

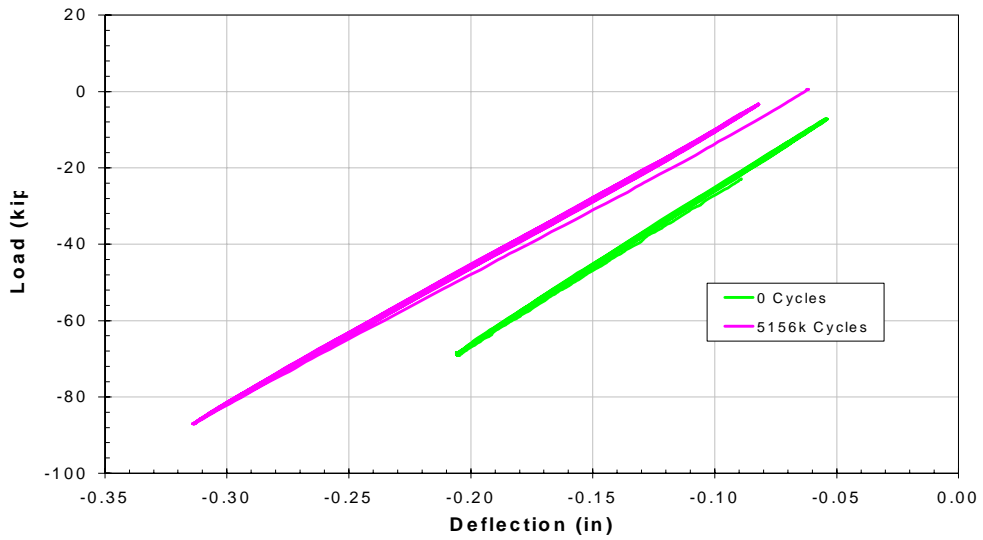


Figure 4-21: Load-Deflection Graph for the Third Specimen's Fatigue Testing

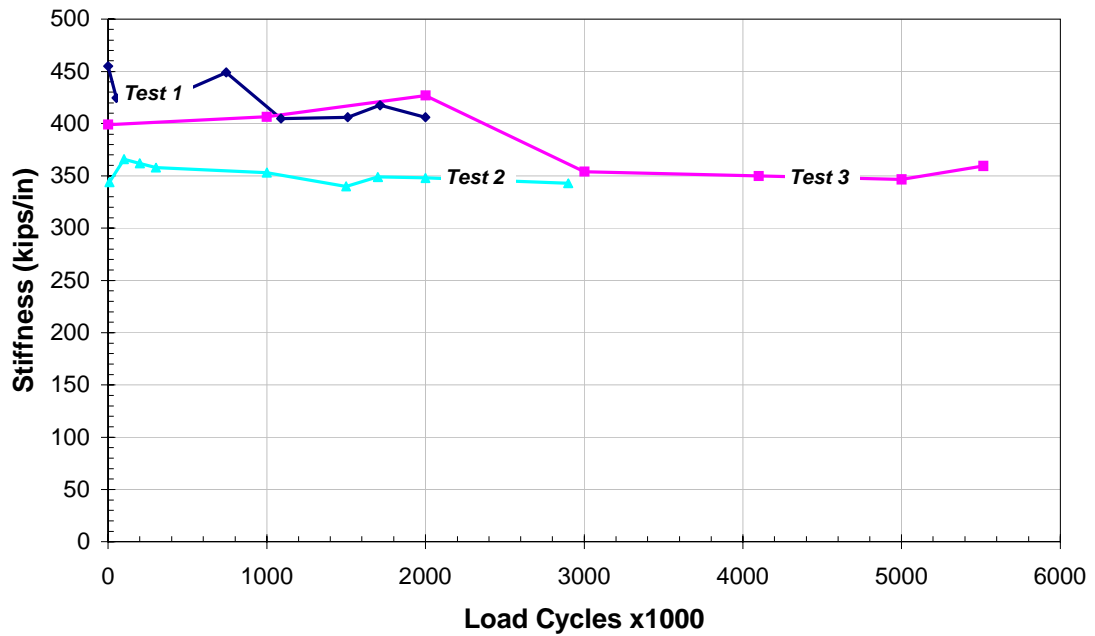


Figure 4-22: Stiffness Variation During Cycling Tests

4.7.4.4 VERTICAL STRAIN DISTRIBUTION

The longitudinal strain profiles (from embedment gages) across the depth of the diaphragm at the centerline of the pier are shown in Figure 4-23. These strains were measured by embedment gages inside the concrete diaphragm during the cycling test. In the first test, the strain distributions exhibited only slight variations over the 2 million cycle interval. The strain increase at five inches above the bottom plate inside the diaphragm is about 160 μs after application of 2 million cycles. This increase of strain is about 53 percent of the initial strain at zero cycles for the first test. The increase of strain at the bottom of the diaphragm is also seen in Figure 4-23 for the third test. Since concrete strain is well below the crushing strain of 3000 μs , the reason for the overall stiffness reduction of the specimen might be due to propagated micro cracks in the diaphragm concrete.

As seen in Figure 4-24, the first test strain profile changes slightly over the course of 2 million cycles. The variation of the stress at the bottom flange of the second specimen, as depicted in Figure 4-24, is about a 14 percent decrease. Recall that the third specimen had a load jump after 2 million cycles, so the increase of strain is less than what is illustrated in Figure 4-24. The increase in strain is also observed inside the concrete diaphragm as shown in Figure 3-23.

The vertical distribution of the strain across the depth of the girder is not linear inside the concrete diaphragm. This violates the assumption that the plane remains plane in the classical beam theory, even though the concrete strain is in the elastic limit in the compression zone. However, the trend of the strain distribution outside of diaphragm is close to a linear fit.

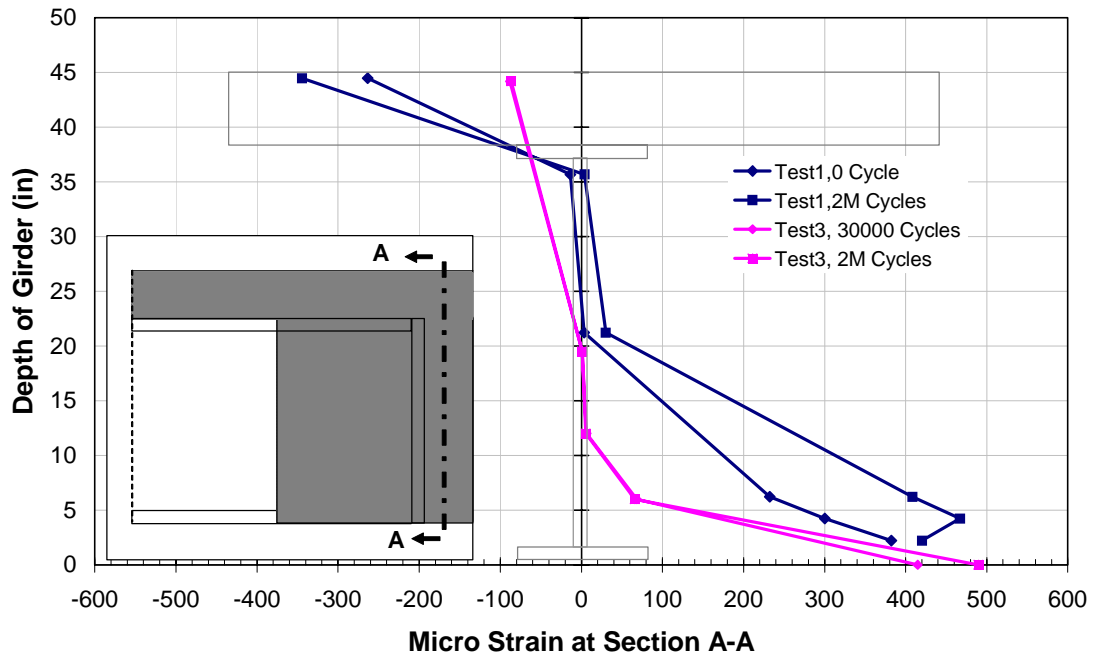


Figure 4-23: Strain Distribution Across the Depth of the Girder at the Pier Centerline During Cycling Loading

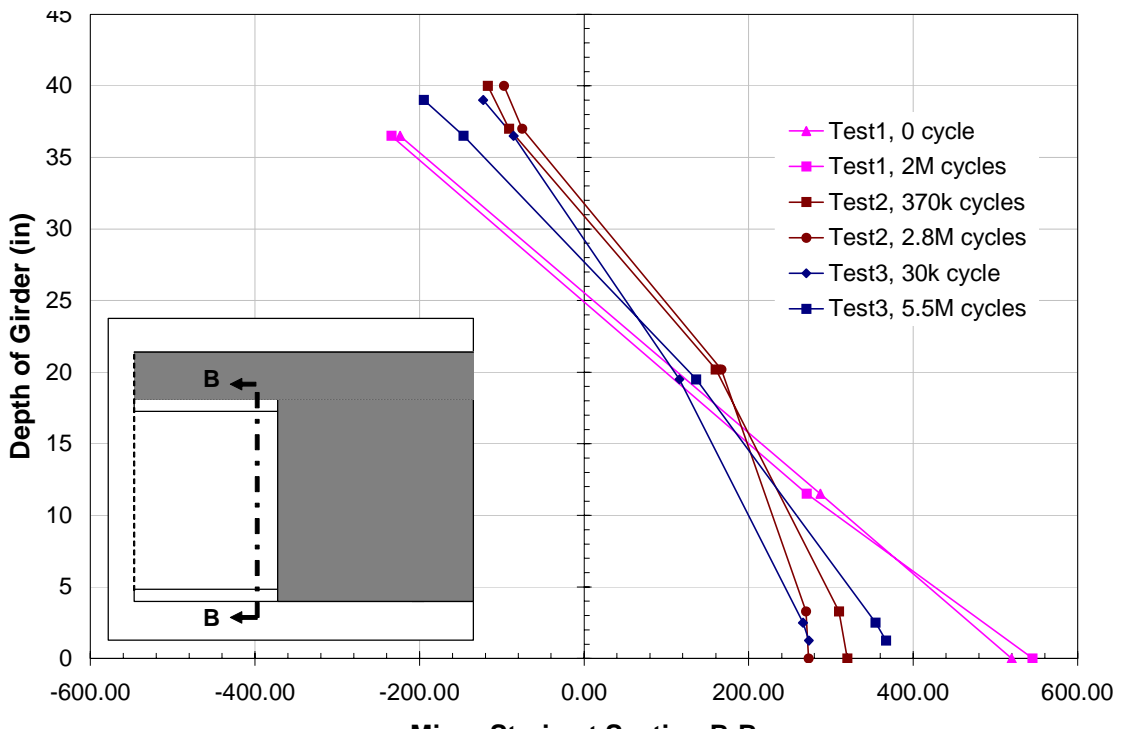


Figure 4-24: Strain Distribution Across the Steel Girder Depth Outside the Diaphragm

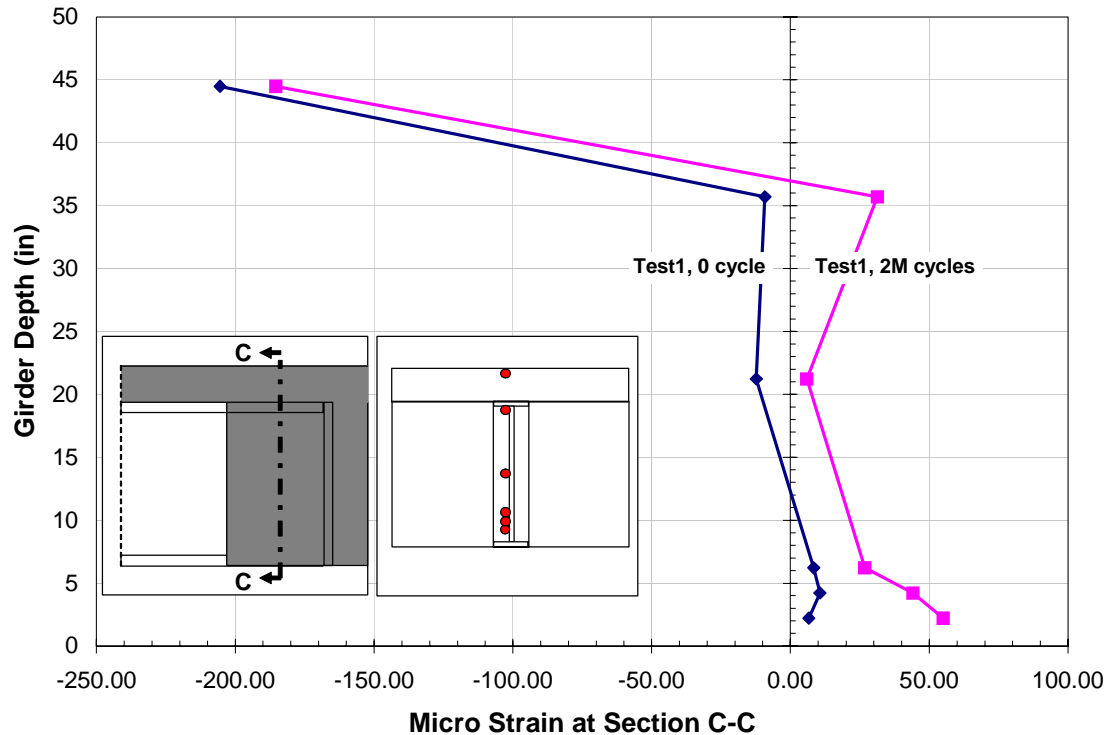


Figure 4-25: Vertical Strain Profile Inside the Concrete Diaphragm

4.7.4.5 HORIZONTAL STRAIN DISTRIBUTION

The strain distribution across the bottom of the concrete diaphragm is shown in Figure 4-26. Notice that in Test one, the strain in the concrete at the bottom of the diaphragm increases due to cycling loads. This increase is at most about 46 percent. In the second test, the embedment gages located inside the bottom flange width failed to measure strain since initial stage of loadings. However, the gages outside the flange width show increase in strain as it was observed in test number one. The strain measured from Test three indicates a decrease after 5 million cycles. It is not clear that this decrease is due to malfunctioning of the gages or because of mechanical characteristics of the system.

The shape of the strain distribution along the diaphragm width is similar to the normal distribution function or bell-shape. It is observed that the strain distribution is more concentrated in Test two and it is more uniform

in Test one. The compression force from the bottom flange of the steel girder is transferred to the concrete diaphragm through the interface of the two materials. In the first and the third tests, the end bearing plate and bottom plate transfer the compression force into a larger area of the concrete diaphragm. In the second test, the bottom flange and web plate have small contact areas with the concrete. As a result, the stress concentration is high in the concrete. This large stress causes local crushing of the concrete from the initial loading stage. This reasoning can be shown by the second specimen plots in Figure 4-26. In the second specimen, the concrete strain before the cyclic loading is about 800 μs for a load level of 22 kip. If a linear prediction is assumed, the strain at the load level of 102 kip is computed to be about 3700 μs . This strain is greater than the crushing strain of the concrete (0.003). It should be noted that the linear extrapolation of strain is not a very accurate method to evaluate the strain at the 102 kips load level since the stress-strain relationship for the concrete is not linear. However, the physical observation such as penetration of bottom flange into the concrete diaphragm and malfunctioning all of the embedment gages placed inside the flange width indicate the concrete at the bottom level of diaphragm crushed locally from the beginning of fatigue loading.

4.7.4.6 STRAIN IN DECK REINFORCEMENT

The strain in the deck reinforcement was also monitored over the cycle intervals for three tests. Figure 4-27 shows strain plots for the reinforcing bar located almost at the centerline of the deck in the top layer rebar. Besides, the longitudinal location of the gages was near the centerline of the pier. The trend of strain variations is increasing for all three tests. The tensile strain in the reinforcing steel varied only slightly over the 2 million cycles for the first test. In the second test, the increase of strain is more obvious. Notice that the strain reaches up to three times the initial value in the second test. In the third test, there is a jump in the strain plot which is

due to an increase in applied load from 70 kip to 85 kip after 2 million cycles.

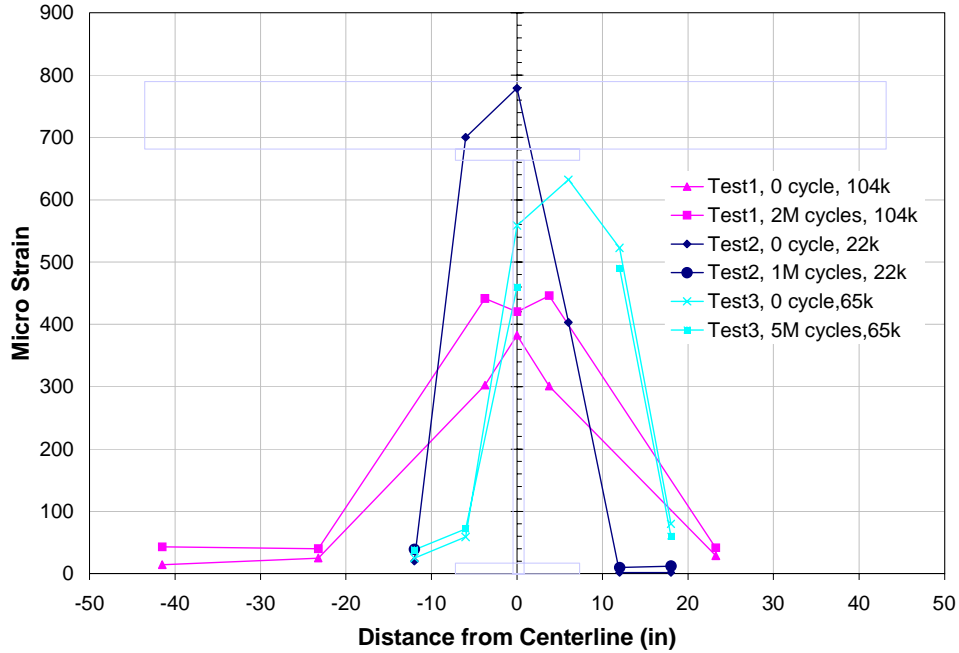


Figure 4-26: Strain Profile in the Bottom of the Diaphragm Concrete

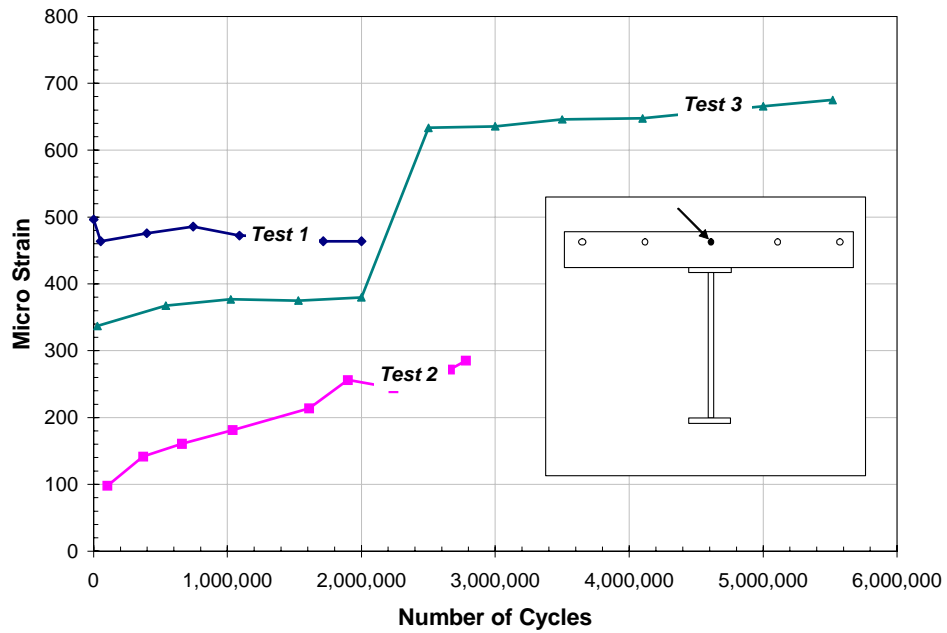


Figure 4-27: Strain in Top Rebar During Cycling Tests Near the Center of the Deck

4.7.4.7 BONDING OF STEEL GIRDER AND CONCRETE

The connection of the steel girder to the surrounding concrete at the diaphragm location has a great effect on the load transfer mechanism. The bonding between the steel components and the concrete can be investigated through some of the measurement and test observations during the fatigue tests.

The connectivity of the top flange and concrete deck was assured by providing adequate shear studs throughout the top flange. Besides, there was not any reported separation between the top flange and the slab during the cycling tests. In the first specimen, the connectivity of the steel girder and the concrete diaphragm can be shown by strain measured by the gages welded on the steel girder and the embedment gages inside the concrete. Figure 4-25 shows that the maximum concrete strain inside the concrete diaphragm behind the end bearing plate can pass 50 ms. This indirectly implies that there is bonding between steel girder web plate and the concrete diaphragm. However, the magnitude of this bonding is unknown. The other indication of bonding between the concrete diaphragm and the steel girder is the horizontal distribution of the strain on the I-girder and inside the diaphragm. The horizontal strain distribution of the steel girder obtained from the first test is shown in Figure 4-28. The strain at the location EG9,15 on the plot was computed based on the interpolation of values recorded at gage EG9 and EG15. It is seen that the strain is decreasing inside the concrete diaphragm i.e., from gage WG2 to gage SG34 which are attached on the web of steel girder. If there is no concrete diaphragm, one expects that the strain is increasing toward the pier centerline. The reason for the strain reduction in the steel girder web is the contribution of surrounding concrete in the transfer of the compressive forces. This contribution can be achieved by the direct bonding of steel and concrete or by the shear rebar passed through the web plate.

The slippage between the bottom flange and concrete diaphragm was observed during the second cycling test. This means that the bonding between the steel girder and concrete diaphragm failed under cycling loading. Figure 4-29 shows that in lower cycles (370,000) the horizontal strain profile trend is similar to the first test. In other word, the decrease in the measured strain from gage WG16 to WG5 is due to the composite action or bonding between concrete and steel. However, the strain profile at 2 million cycles does not show this trend. The strain profile at 2 million cycles (see Figure 4-29) is as if there is not any concrete resistance and the compressive forces are transferred by the steel girder alone.

The horizontal strain profile of the steel girder in the third specimen during the cycling test is depicted in Figure 4-30. The strain increases from WG20 to WG18 which are outside of the diaphragm. However, it increases toward the WG13 which is inside the concrete diaphragm. The reason for the reduction of the steel girder strain inside the concrete diaphragm is the contribution of the adjacent concrete in transferring the compressive forces.

4.7.5 FATIGUE FORMULAS VALIDATION

The formulas described in previous sections for fatigue assessment are verified by using the test results. In the steel structures, the fatigue only needs to be checked if the member is expected to undergo tensile stress. The sum of the dead load and applied live load usually produces the compression at the bottom flange at the pier location of a two-span bridge. Therefore, the bottom flange and bottom details do not need to be checked for the fatigue resistance. However, it is observed that the top flanges of the steel girders are in tension under the cyclic loads as seen in Figure 4-24.

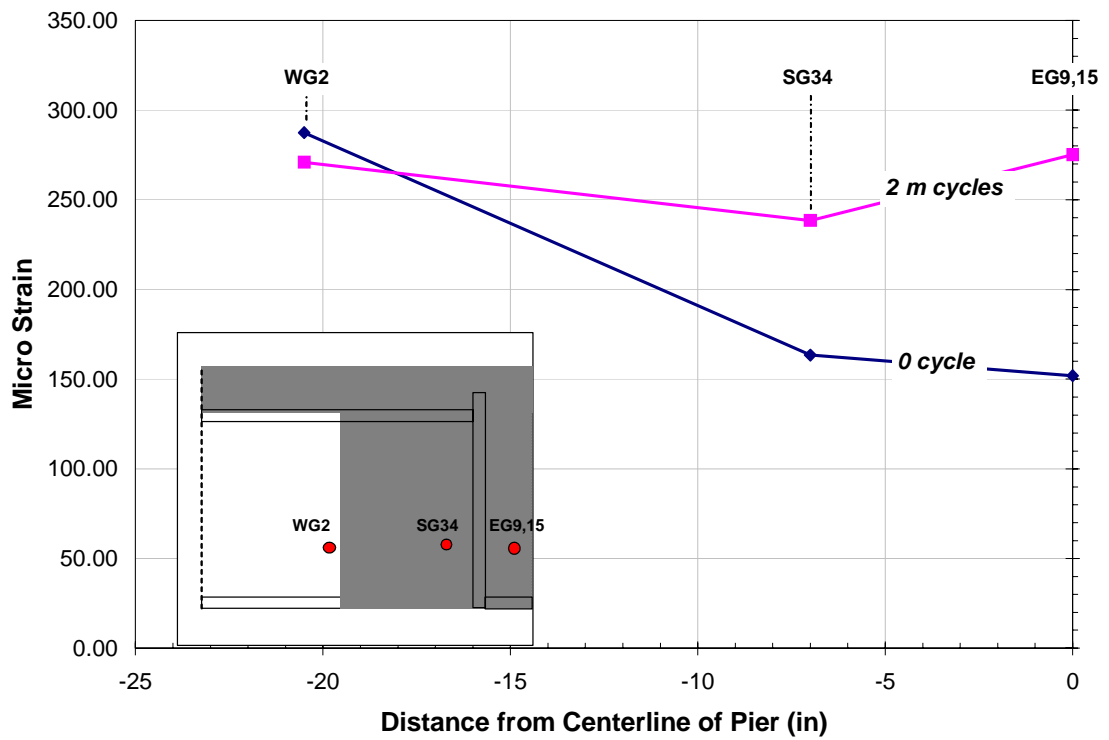


Figure 4-28: Horizontal Strain Distribution From the First Cycling Test

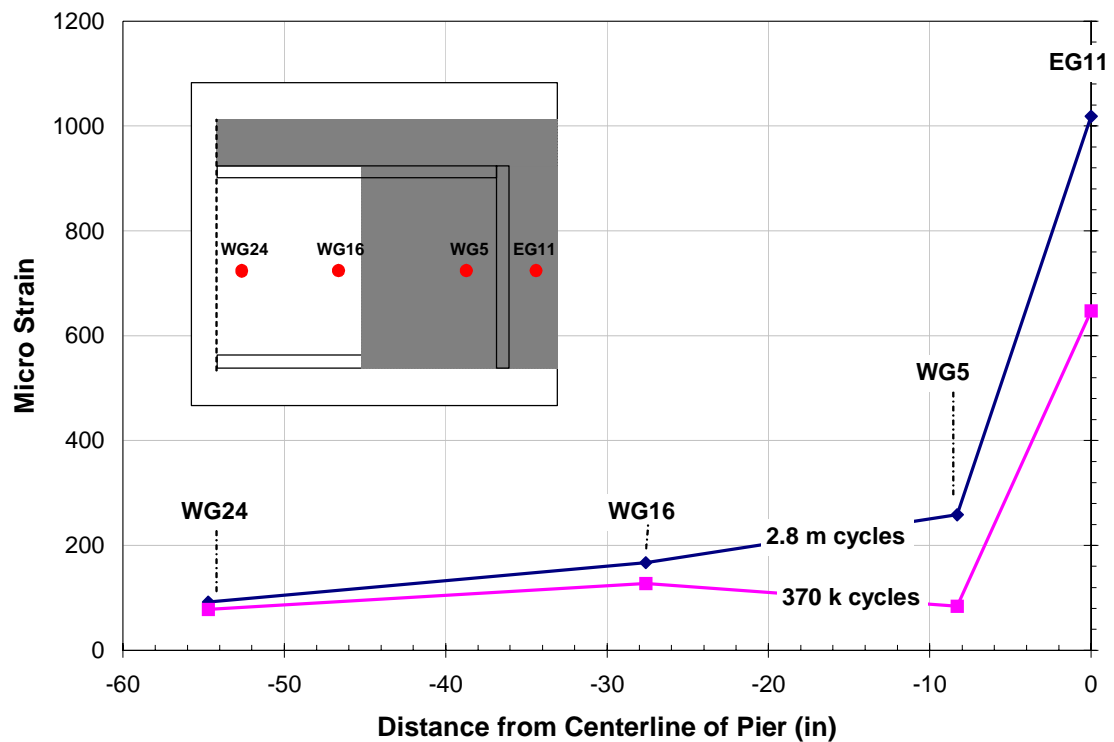


Figure 4-29: Horizontal Strain Profile in the Second Cycling Test

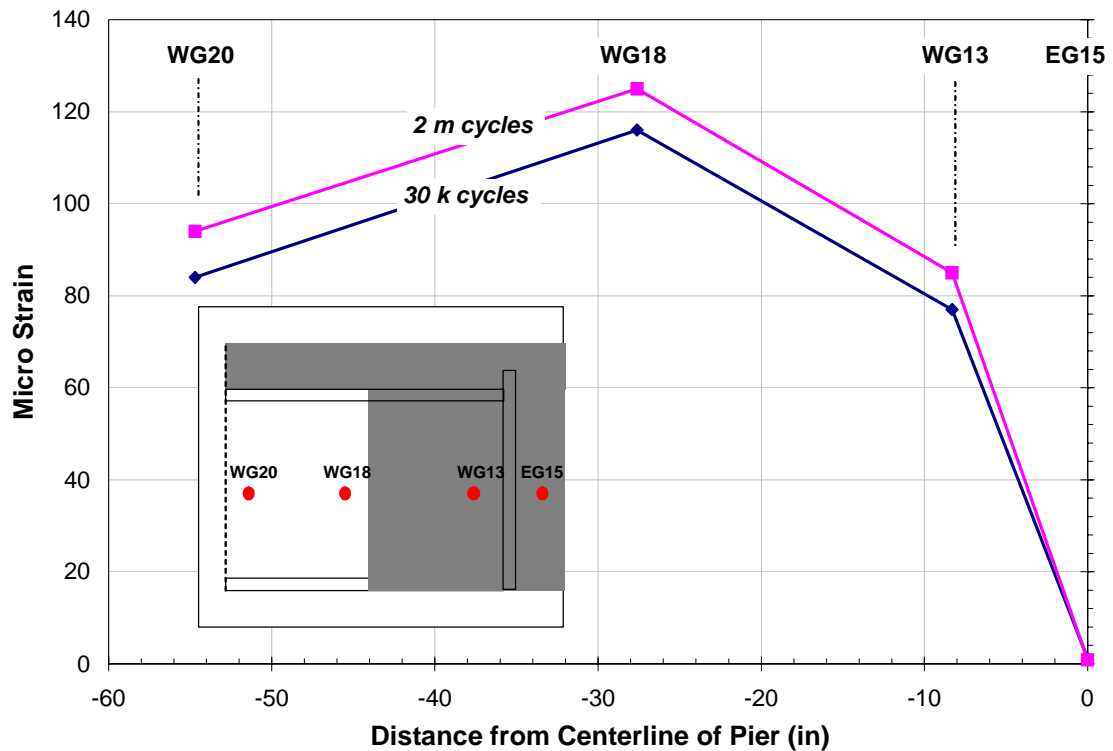


Figure 4-30: Horizontal Strain Distribution in the Third Cycling Test

As seen in Figure 4-24, the maximum strain at the top flange can reach about 250 microstrain. The stress, σ , equivalent to this strain, ε , can be obtained by multiplying the steel elasticity modulus, E_s , to the measured strain.

$$\sigma = E_s \varepsilon \tag{4-5}$$

$$\sigma = (29000)(250 \times 10^{-6}) = 7.25 \text{ksi}$$

An end bearing plate had been welded to the end of the steel girder in the first test. This detail can be identified as category C of AASHTO (1998). Based on this category, the other values in Equation (4-1) can be obtained from the AASHTO tables and test specifications described earlier as follows:

:

$$N = 2,000,000$$

$$A = 44 \times 10^8$$

$$(\Delta F)_n = \left(\frac{A}{N} \right)^{\frac{1}{3}} = \left(\frac{44 \times 10^8}{2,000,000} \right)^{\frac{1}{3}} = 13 \text{ksi}$$

According to AASHTO (1998), the threshold stress for the C category is 10 ksi. Therefore, the maximum stress range is greater than the half of the threshold stress and is governing the fatigue limit in Equation (4-1). Since the maximum measured tensile stress in the steel girder is less than the fatigue resistance of the girder, it is concluded that the deterioration of the specimens under fatigue loading most likely is due to concrete damage or reinforcing rebar rather than steel girder fatigue.

The safe fatigue stress range of the top layer rebar of the slab can be computed using Equation (4-3). The maximum strain obtained from the test for the middle rebar of the top layer is shown in Figure Figure 4-27 for the three specimens. The applied end cantilever load range was between 2 and 106 kips for specimen one. Therefore, the minimum stress corresponding to 2 kips is small and ignorable. For test specimens two and three the minimum stress was tensile and small. With this assumption the second term of the right side of Equation (4-3) vanishes. The remaining terms substituting 0.3 for h/r ratio gives

$$f_f = 21 + 8(0.3) = 23.4 \text{ksi}$$

The safe range stress of 23.4 ksi is equivalent to 806 micro-strain, assuming an elastic approach as described in Equation (3-5). The measured strain is less than this value for the three test specimens. Therefore, the reinforcing bars most likely did not participate in the fatigue damage of the entire system.

The ratio of minimum stress to the maximum stress in the concrete from the conducted tests is about zero since the minimum applied load at the end of cantilever beam was close to zero. Taking into account this assumption, the Equation (3-4) is simplified as:

$$\frac{f_{\max}}{f'_c} = 1 - 0.0685 \log N \quad (4-6)$$

The maximum concrete stresses are given in Table 4-7 based on the number of cycles of each test (Table 4-6) and Equation (4-6). The maximum induced stress from the cycling test is not obtainable directly from the test results since the strain was measured during the tests. The measured strain at the critical location, i.e. at the bottom diaphragm between the two bottom flanges, was converted to the equivalent stress using the following constitutive law (CEB, 1990):

$$f_c = \frac{0.85 f'_c (a - 206,000 \varepsilon_c) \varepsilon_c}{1 + b \varepsilon_c} \quad (4-7)$$

Where:

$$a = 6193.6 (0.85 f'_c + 1.015)^{-0.953}$$

$$b = 8074.1 (0.85 f'_c + 1.450)^{-1.085} - 850$$

$$f_c = \text{Stress in Concrete (ksi)}$$

$$\varepsilon_c = \text{Strain in Concrete (in/in)}$$

$$f'_c = \text{Specified 28 Day Concrete Crushing Stress (ksi)}$$

The stresses computed from the test results and Equation (4-7) are listed in Table 4-7. It is observed that the applied stress for the first specimen and the third specimen is below the maximum fatigue resistance of concrete. The data was not available for the second test, but it is expected that the

applied stress was more than the maximum fatigue resistance computed from Equation (4-6) for this specimen. In fact, the second specimen concrete crushed under cycling stress.

Test	N cycles	f'_c (ksi)	f_{max} (ksi)	
			Equation (3)	Test
1	2,000,000	6.26	3.56	2.15
2	2,780,000	7.14	3.98	NA [†]
3	5,515,516	5.89	3.17	2.75

† The strain was not available throughout the test due to failure of embedment gages

Table 4-7: The Maximum Fatigue Stress in the Concrete

4.8 ULTIMATE TESTS

The ultimate load test was carried out to investigate the behavior of the specimen under the ultimate load and evaluate the strength of the system. The cycling loading setup was changed for the ultimate strength test. Loading of the specimen was achieved by placing a spreader beam on the deck at each end of the specimen. Threaded rods extended from the spreader to the basement of the structures laboratory. For the ultimate load test, load was increased slowly in 10 to 25-kip increments. Load was applied incrementally until the specimen failed. The loading system for the second test is shown in Figure 4-31. The first ultimate test rig is similar to the second test. The location of application of the load was different for each test. The distance of the spreader beam center to the centerline of the pier (moment arm) in each test is given in 4-8. The reason for the difference between tests was due to using different types of hydraulic rams in each test.



Figure 4-31: Ultimate Test Setup for the Second Specimen

Test	Moment arm (ft)	
	Cycling	Ultimate
1	14	12
2	14	15
3	14	15

Table 4-8: Location of the Application of the Load with Respect to Pier Centerline

4.8.1 TEST FAULTS

In the first test at a load of 225 kips, the hydraulic pump used to load the west side of the specimen failed to apply additional load. The specimen was then unloaded and the failed pump removed. The test was restarted and at 255-kips load, the pump used to load the east side failed to increase

load. The specimen was unloaded and this pump removed. The third attempt to apply failure load was successful.

In the second test at a load of 266.6 kips, the specimen was unloaded because of a problem in the system and then reloaded.

The test setup for the third specimen ultimate load test varied slightly from the first and second specimens as shown in Figure 4-32. Two attempts were made at performing the ultimate load test on the third specimen. During the first attempt, it was found that one of the four hydraulic rams was faulty, so the test was aborted. The ram was repaired and reinstalled and the test could then be run. Due to a malfunction with the Megadac software, however, there were no data recorded until a load of about 340 kips had been reached. Data from the first attempt at running the test was used where appropriate to fill in some of the gap in the data, as the highest load applied to the system at that time was approximately 74 kips, so no permanent deformation would have occurred. At a load of approximately 380 kips, the hydraulic rams reached their maximum stroke, so the specimen was unloaded and the rams re-stroked. The rams were retracted and the spreader beam that they sat on was raised closer to the ceiling. The test was then resumed and loading of the specimen continued until a load of approximately 420 kips. The string potentiometer on the east span had retracted fully near the end of the test, so it no longer provided deflection measurements. The test was stopped for the concern of safety. The excessive deflections had caused the Dywidag rods to bend, and further loading could have caused the rods to fail.

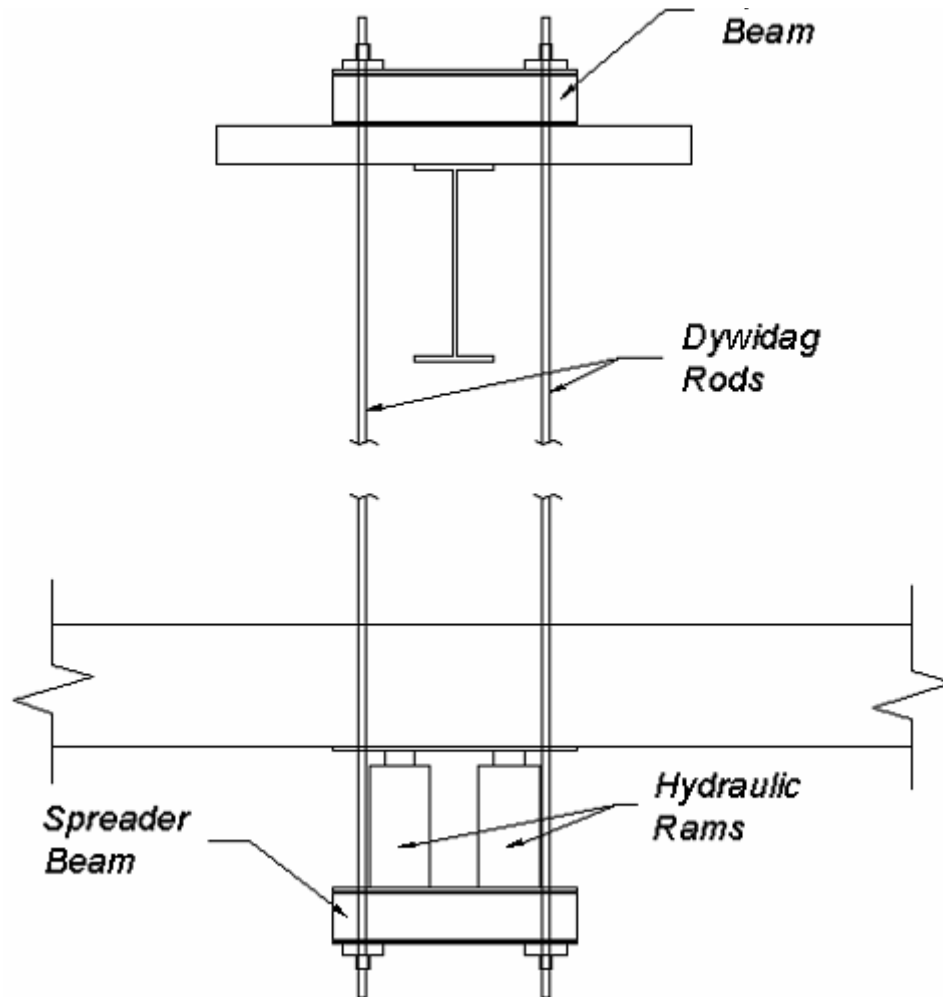


Figure 4-32: Schematic of the Loading Setup

4.8.2 TEST RESULTS

4.8.2.1 LOAD-DEFLECTION

The load-deflection plots were generated for both the west and east side cantilever in each test. Since the moment arm of test setups was different, the moment-drift curves were created from the successful load-deflection loadings. The moment-drift responses of the three specimens are seen in one combined plot in Figure 4-33. The saw tooth appearance of the curve was caused by pauses for data collection, in which relaxation of the specimen occurs due to the onset of plastic flow. The ultimate load, moment and deflection of specimens are listed in Table 4-9. The values shown in the

table refer to the maximum of the ultimate parameter from either the west or east cantilever in each test. The ratio of the ultimate moment of each test specimen to the ultimate moment capacity of the second specimen (the weakest one) is also given in Table 4-9. Notice that the moment capacities of the first and third specimens are almost equal and 1.5 times of that the second one.

For the first test, it can be shown that inelastic behavior begins near a load of 320 kips or a moment of 3840 kip-ft. Investigation into experimental results showed that the reinforcement near the girder centerline had reached yield at this load. In the second test the system response was linear up to the moment level of about 1800 kips-ft. At the moment magnitude of 3930 kips-ft the system was unloaded due to a problem in the loading system. As a result of the initial loading, the system displayed a permanent set of approximately 0.75 inches. Upon subsequent reloading, the system responded linearly until intersecting the original load-deflection curve. Despite incurred damages, the initial stiffness during reloading was nearly equal to the original stiffness. The moment deflection of the third specimen in the initial loading stages is not accurate since the manual voltage readings from the pressure cells and deflections from the pen plotters were used to create the plot, as the Megadac data was unavailable for the first portion of the test..

4.8.2.2 CRACKING

The first tensile cracking in the specimen is determined using the measured strain and comparing it with tensile cracking of concrete. The tensile strain of concrete at the failure can be estimated by using the concrete elasticity modulus. In fact, it is assumed that there is a linear strain-stress curve for concrete in tension (Park, Paulay, 1974). The tensile cracking strain of the slab concrete was then easily computed by dividing the tensile strength by the elastic modulus. The average tensile cracking strain using this approach is about 126 micro-strain (Table 4-10). The load level at

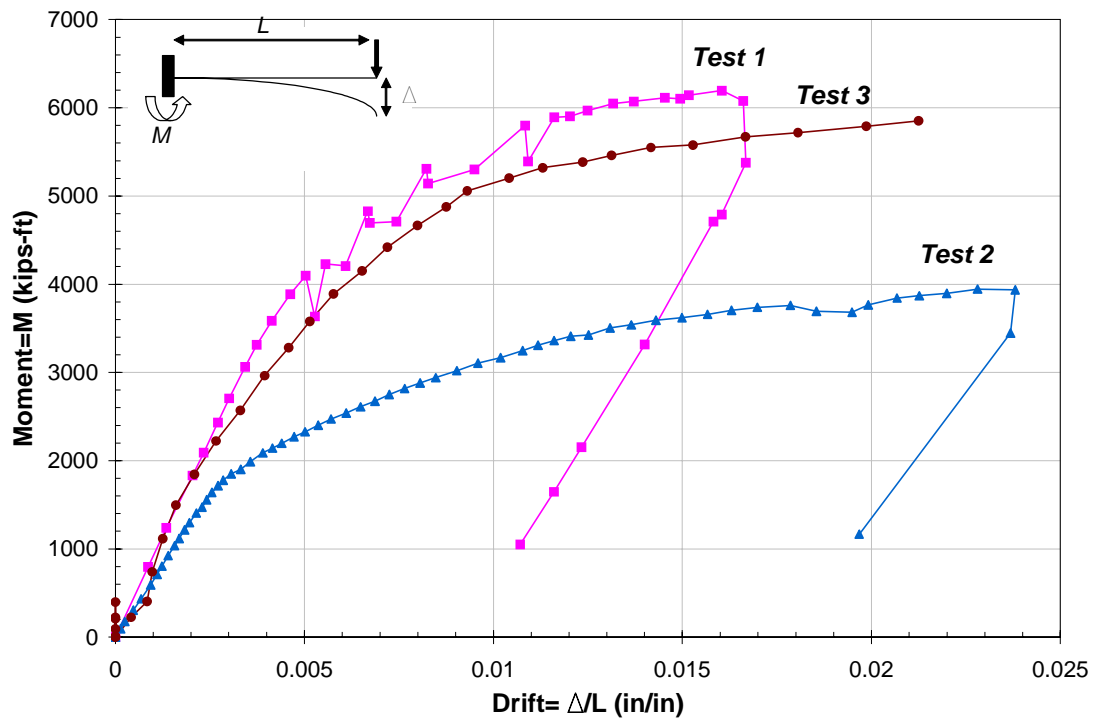


Figure 4-33: Moment-Drift Plots of the Three Experiments

Test	Displacement	Load	Moment	Moment Ratio to the 2nd test
	in	Kips	Kips-ft	
1	2.59	516	6192	1.56
2	4.12	263	3945	1
3	4.50	391	5865	1.48

Table 4-9: Ultimate Displacement, Load, and Moment of Specimens

which the tensile cracking was initiated can be evaluated using the rebar strain gage readings during the ultimate tests. The cracking load was obtained using the strain measured by strain gage welded on the middle rebar of top layer reinforcement of the deck. The cracking load is given in Table 4-10. The strain in the top layer rebar was not available for the third

test due to test error, but it was assumed to be close to cracking loads obtained from the first and second tests.

The first specimen was subjected to significant displacement after the system had passed the elastic limit. The cracking after the ultimate test on the deck around the centerline of the pier can be seen in Figure 4-34. Some of the cracks initiated during the cycling test were widened in the ultimate test. The cracks penetrated through the depth of the slab at the edge of the diaphragm. There were both transverse and longitudinal crack in the slab. A 45° crack was observed at the diaphragm lateral face (see Figure 4-34) which indicates that the crushing or cracking of the diaphragm had been reached to the outer face. This implies that the entire concrete diaphragm was participating in the resistance mechanism. It was not observed that any major crack existed around the bottom flange and the web.

From the beginning of the ultimate load test two, cracks in the concrete slab began to increase in width. Most of the cracks had formed during fatigue cycling and further increased in width during the ultimate load test. The majority of cracking occurred near the edge of the diaphragm. However, there were some large cracks over the pier centerline that were wider than those near the edge of the diaphragm. There were additional cracks through the depth of the slab. Figure 4-35 shows that these cracks propagated farther during the ultimate load test. The marked cracks formed during the cycling load test and the unmarked cracks propagated due to the ultimate load test. Figure 4-35 shows cracking of the concrete after the test concluded. The location of these cracks was under the slab at the corner area between the slab and the girder top flange.

The cracks on the concrete deck in the third specimen are seen in Figure Figure 4-36. As it was noticed in the previous tests, the major cracks are longitudinal and parallel to each other. These cracks penetrated through the depth of the slab, as seen in Figure 4-36. The 45° cracking at the face

of diaphragm is observed in this test too. The cracks were also observed at the inside face of the diaphragm initiating from the bottom flange toward the slab in approximately a 45° angle. As it was noted for the first test, the inclined cracks at the diaphragm face indicate that the failure of diaphragm concrete in these two specimens is not localized. This also implies that the end bearing plate could prevent the local crushing of concrete.

Test	Cracking Strain	Cracking Load
	Micro-strain	Kips
1	126.37	31.14
2	126.37	27.30
3	126.37	NA

Table 4-10: Cracking Strain and Corresponding Load for the Tested Specimens

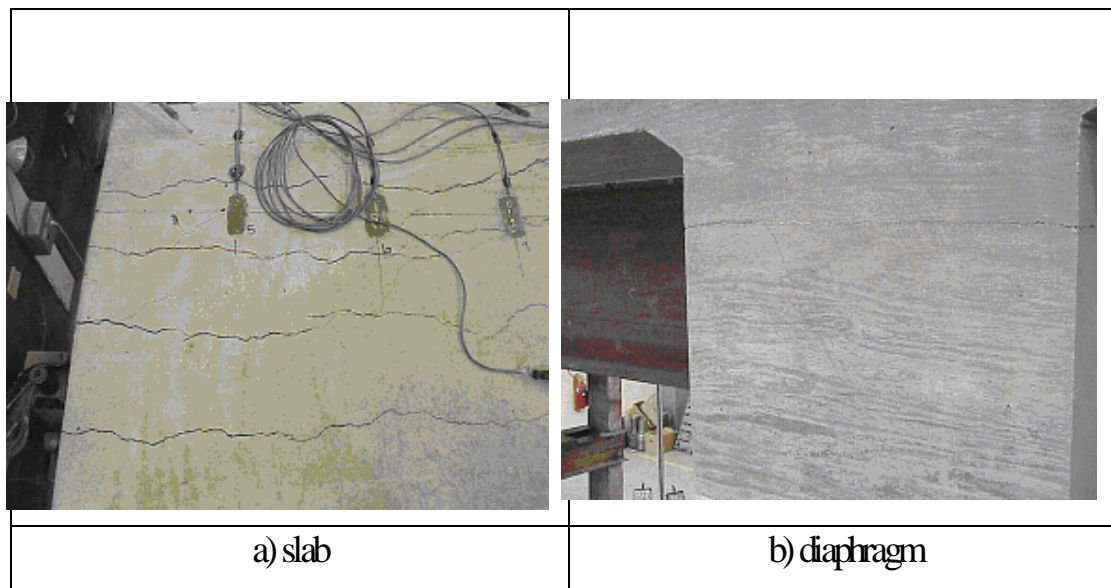


Figure 4-34: The First Test Cracking After the Ultimate Test

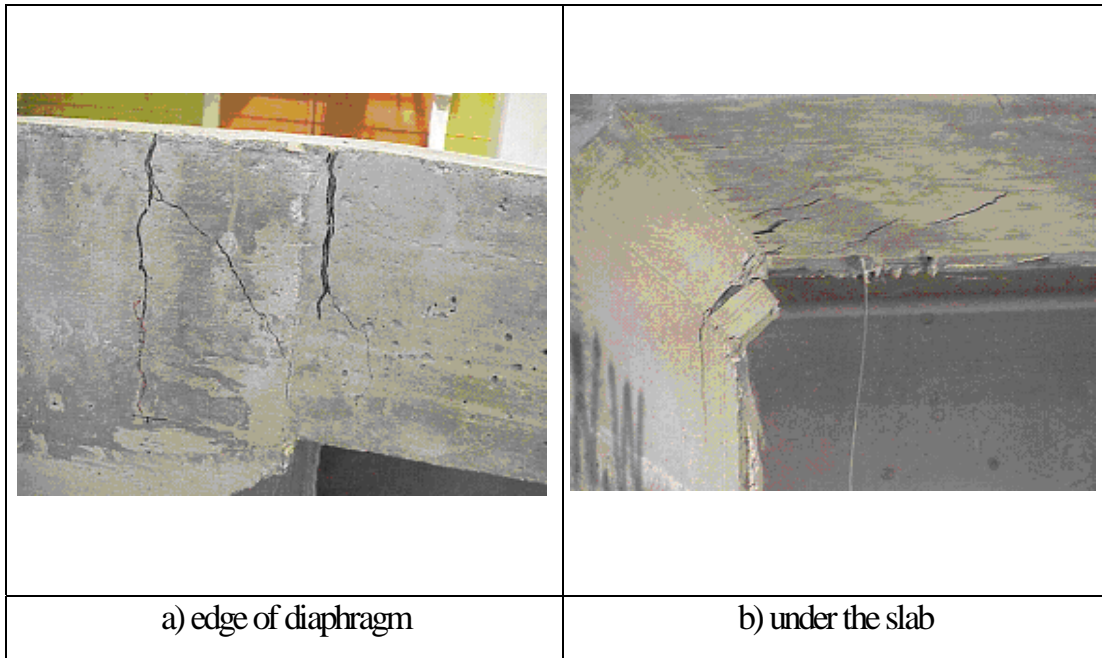


Figure 4-35: Cracks After Ultimate Test Two

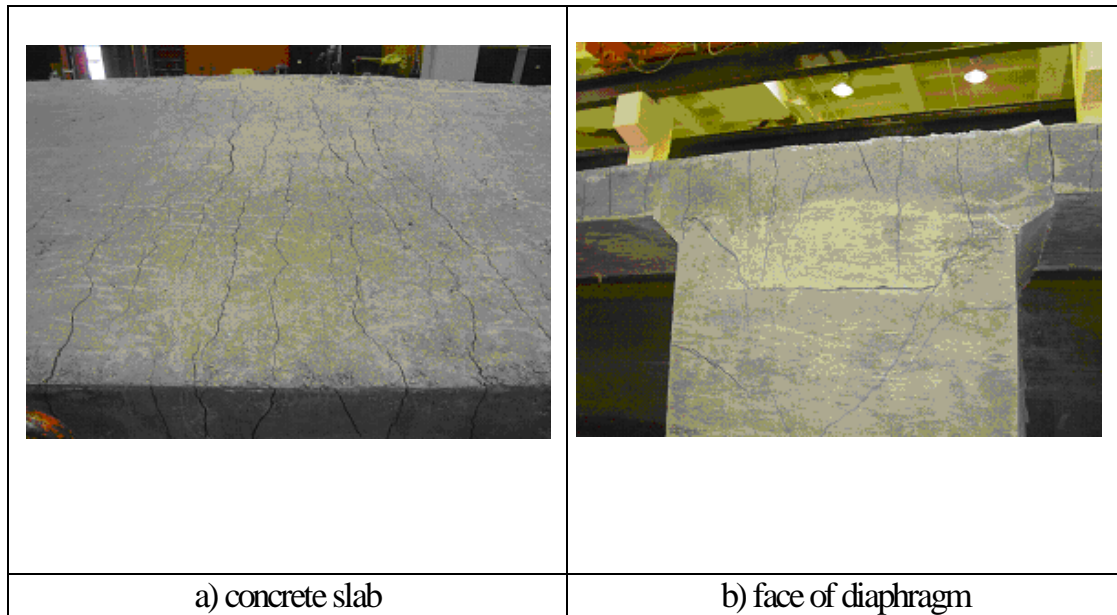


Figure 4-36: Concrete Cracking After the Third Specimen Test

4.8.2.3 YIELDING IN REBAR

Investigation into experimental results shows that the first yield in all of the specimens occurred in the top layer reinforcement near the girder centerline. In the first specimen the yielding of the top layer rebar before the bottom plate was expected since the section was designed so that the top rebar reached to yield before crushing of the bottom concrete (Lampe, 2001).

Figure 4-37 shows the moment at the pier centerline where yield started at the top layer rebar. The strain of each rebar at the centerline of the pier was measured by strain gages mounted on the bars. Based on the material test, yield strain of the rebar was determined. The applied load to the cantilever at which the measured strain passed the yield strain was identified from the test data and multiplied by the cantilever length to obtain the moment at the centerline of the pier. In the first test, all of the rebar, with a strain gage mounted on them, yielded. Based on the experimental data, only two rebar of test specimen number two yielded. In the third test, the data from only one of the strain gages attached to the top rebar outside of the diaphragm was retrievable. Since this rebar was far from the critical section (pier centerline) it is expected that most of the rebar in the third specimen yielded.

In the first test, as the middle bars yielded, load was shed to adjacent reinforcing steel as the load increased. This shedding pattern is expected for the other two tests too, though there is not enough data to prove it. According to this trend, the rebar close to the axis of the girder takes more load and reaches yield earlier than the rebar farther from the axis (see Figure 4-37). In fact, this demonstrates the shear lag phenomenon in the concrete slab and the concept of effective width. In specimen number two, the outer rebar stayed in the elastic stage when the specimen failed. In this case, the concrete in the diaphragm did not resist long enough to permit all the slab rebar to reach yield.

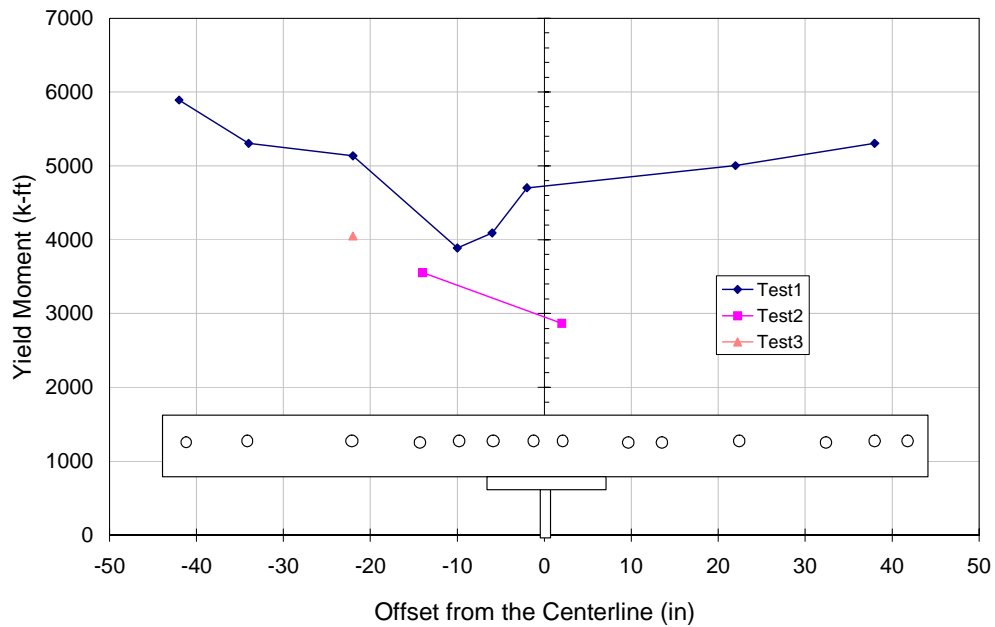


Figure 4-37: Moment at Which Yield Started in Top Layer Rebar at Pier Centerline

4.8.2.4 YIELDING IN BOTTOM FLANGE

In the first specimen, the bottom flange yielded after the onset of yielding in the top layer reinforcements. The location of the first yield was between the two girders, where bottom flange was extended to connect the beams.

In the second specimen, there was not any plate to connect the bottom flanges. The strain gages attached to the bottom flange near the pier centerline did not function properly during the ultimate test. The extrapolation of strain measured from the gages installed at the farther distance indicates that the steel girder had not reached yield at this region.

Most of the strain data obtained from the third test is erroneous. There is not a robust indication for yielding of the bottom flange in this test.

4.8.2.5 DUCTILITY OF CONNECTIONS

The ductility of the connections is defined as the displacement at collapse condition divided by the deflection of the first yield in the system. Based on this definition, the ductility ratios of the three specimens are given in Table 4-11. In this table, the first yield load of specimen three was interpolated based on the first yield load of the first specimen and the yield load obtained from the only strain gage functional in the top layer of the third specimen. Notice that the first specimen has the maximum ductility ratio and the second specimen has the minimum.

Test	First Yield Load	Yield Displacement	Ultimate Displacement	Ductility ratio
	Kips	in	in	
1	320	0.66	2.59	3.92
2	191	1.54	4.12	2.67
3	290	1.45	4.50	3.10

Table 4-11: Yield Load, Displacements, and Ductility Ratios of the Three Specimens

4.8.2.6 CRUSHING OF CONCRETE

In the first test, the strain recorded by embedment gages placed inside the diaphragm between the two girders is shown in Figure 4-38. The strain shown in the figure is from three sets of embedment gages located in three elevations measured from the bottom flange center and one set of strain gages welded on the bottom plate. In each elevation, the average strain obtained from the gages is shown in the plots. The recorded strain from embedment gages did not pass the standard failure strain of the concrete (3000 micro-strain). However, the strain measured by the strain gages welded on the bottom plate (0 inch elevation) indicates larger strain than the standard concrete strain. The embedment gages in lower elevations (1

inch and 3 inches) show a disorder in readings before reaching the ultimate load level (see Figure 4-38). It seems embedment gages reached their limit at this point and failed. The visual observation of the demolished section after the ultimate load test verifies this, since the embedment gages at these locations were distorted. The test observations such as the inclined cracks at the face of the diaphragm (see Figure 4-34) indicate that concrete at the bottom level of the diaphragm might have crushed. As shown in Figure 4-38, the bottom plate strain gages passed the 3000 micro-strain at load level of 450 kips.

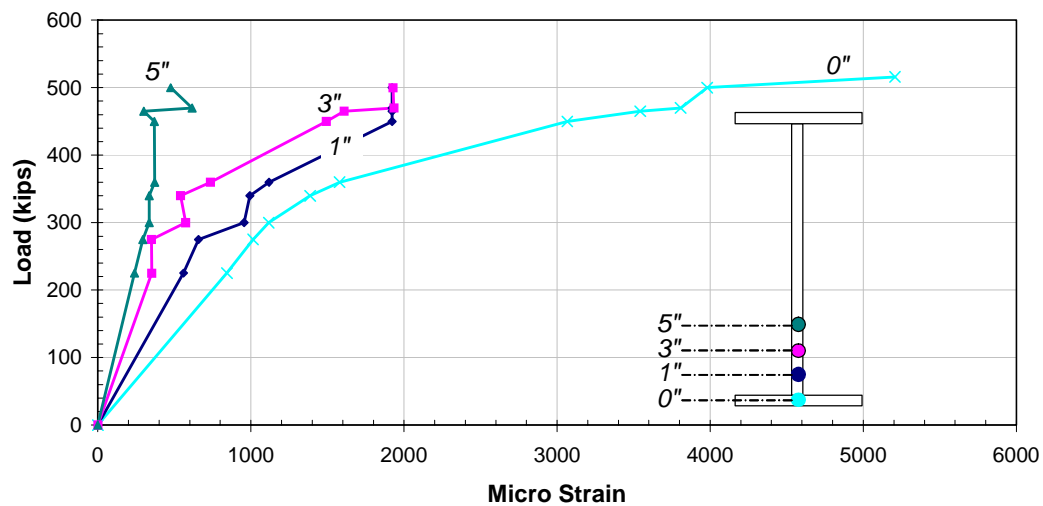


Figure 4-38: Strain in Concrete Diaphragm Between Two Girders in Test 1 at Three Elevations from Bottom Flange

In the second test, the crushing of the concrete was noticeable from the cycling test. Figure 4-39 shows the volumetric increase of the concrete between two bottom flanges under compression. By increasing the load, the bottom flanges penetrated farther into the concrete diaphragm and further crushed the concrete. The two bottom flanges moved toward each other about 3 inches (Figure 4-40). The initial distance between two girders

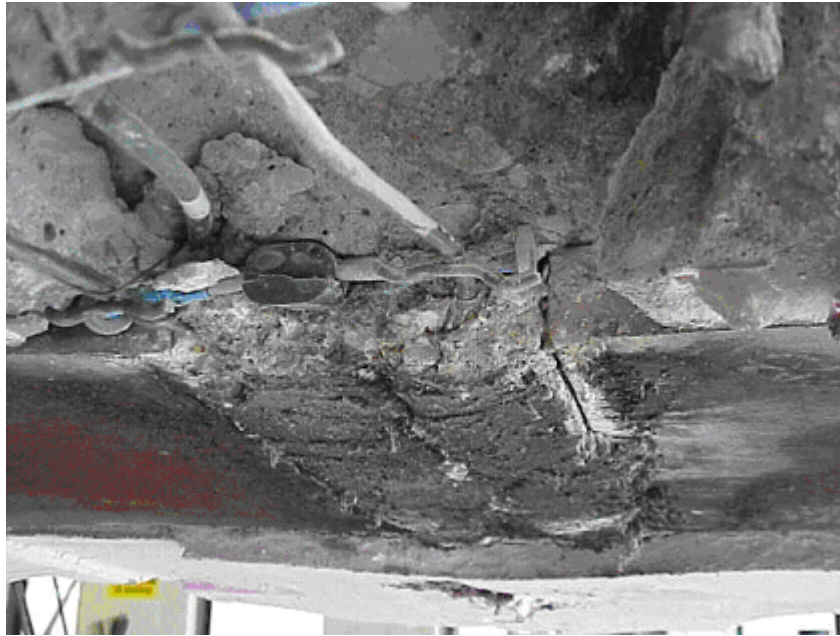


Figure 4-39: Penetration of the Bottom Flange of Specimen 2 into the Diaphragm

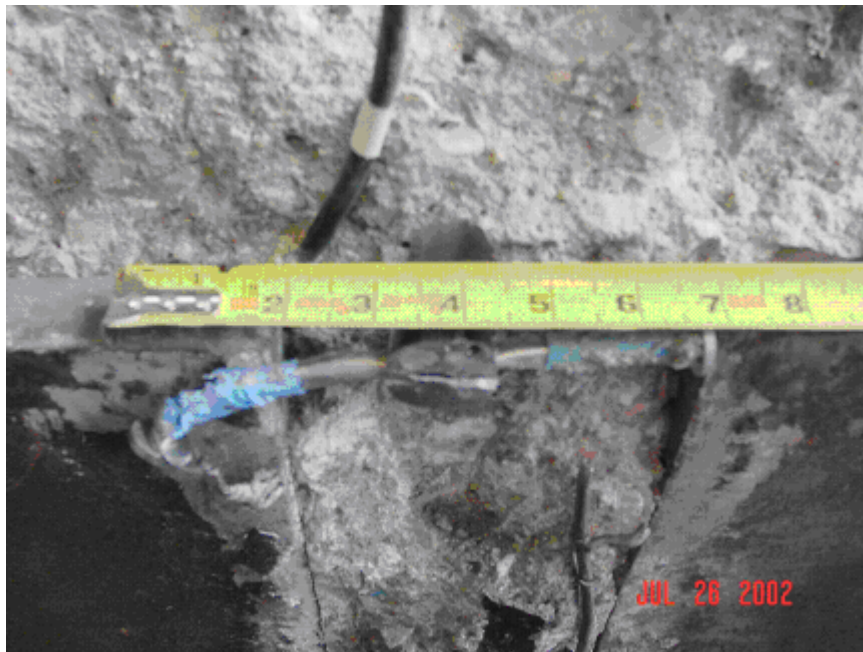


Figure 4-40: Relative Displacement of Bottom Flange After Ultimate Test Two and Deformation of an Embedment Gauge

was eight inches, therefore the true strain, ε , of concrete at bottom level of the core region between two flanges is

$$\varepsilon = \ln\left(1 + \frac{3}{8}\right) = 0.318 \frac{\text{in}}{\text{in}}$$

which is much higher than the standard 0.003 in/in concrete failure strain. The concrete between the two flanges bulges out as seen in Figure 4-39. This indicates that the concrete components (aggregates and matrix) under compression stress tend to escape laterally to a direction that there is the minimum resistance. The neoprene pad side was the softest side for the concrete to deform. The gages embedded inside the concrete diaphragm between the two girders did not work properly from the beginning of the cycling test. As it was observed after the dissection of the girder, the embedment gages in this region were largely deformed as seen in Figure 4-39. It seems the high compressive force at the bottom of diaphragm broke the gages during the tests. Some of the gages away from the girder measured relatively small strain during the ultimate test. This indicates that the concrete damage was highly localized around the interface of the bottom flange and the diaphragm. In fact, the steel girder bottom flange and part of the web acted like the edge of a knife that cut through the concrete diaphragm.

In the third specimen, the embedment gages between the two bottom flanges had the same fate as it was explained for the second test. The high compressive stress dismantled the gages during the ultimate test loading. A few gages farther from the bottom flange survived and measured the concrete strain throughout the test. The load-strain plots of two embedment gages placed at the centerline of the pier are shown in Figure 4-41. The strain in embedment gage 10 is passing the standard crushing strain of the concrete (3000 micro-strain). Therefore, the concrete in vicinity of this gage and at the lower depth might be crushed. Figure 4-42 shows the

displacement of the bottom flanges into the diaphragm. The maximum displacements of the bottoms of the girders were 0.38" for the east span and 0.33" for the west span, according to Figure 4-42. Assuming that the obtained displacements are uniformly distribute over the thickness of the concrete diaphragm, which is a conservative assumption since the steel girder had very smaller strain than the concrete, then the average strain in bottom of the diaphragm at the failure can be computed based on true strain formula as:

$$\varepsilon = \ln \left[1 + \frac{(0.40 + 0.44)}{8} \right] = 0.099 \frac{in}{in}$$

which has passed the crushing strain of the concrete i.e. 0.003 in/in. It is noted that the 0.003 in/in is the approximate failure strain of the concrete for the uniaxial stress condition, but in the conducted tests the stress state is similar to a multi-axial state as it will be discussed in Chapter 6.

4.8.2.7 STRAIN DISTRIBUTION AT THE BOTTOM OF DIAPHRAGM

The measurement of the concrete strain was difficult at the ultimate condition. The problem was more severe for the second and third test for which the embedment gages placed at the critical locations such as bottom of concrete core failed. The only strains obtained which were supposed to be more accurate were from the gages placed farther from the bottom flanges. The distribution of strain at the bottom of diaphragm concrete obtained from the few functioning embedment gages is shown in Figure 4-43 for the three tests. The only plot which gives some information about the strain distribution is the first test curve.

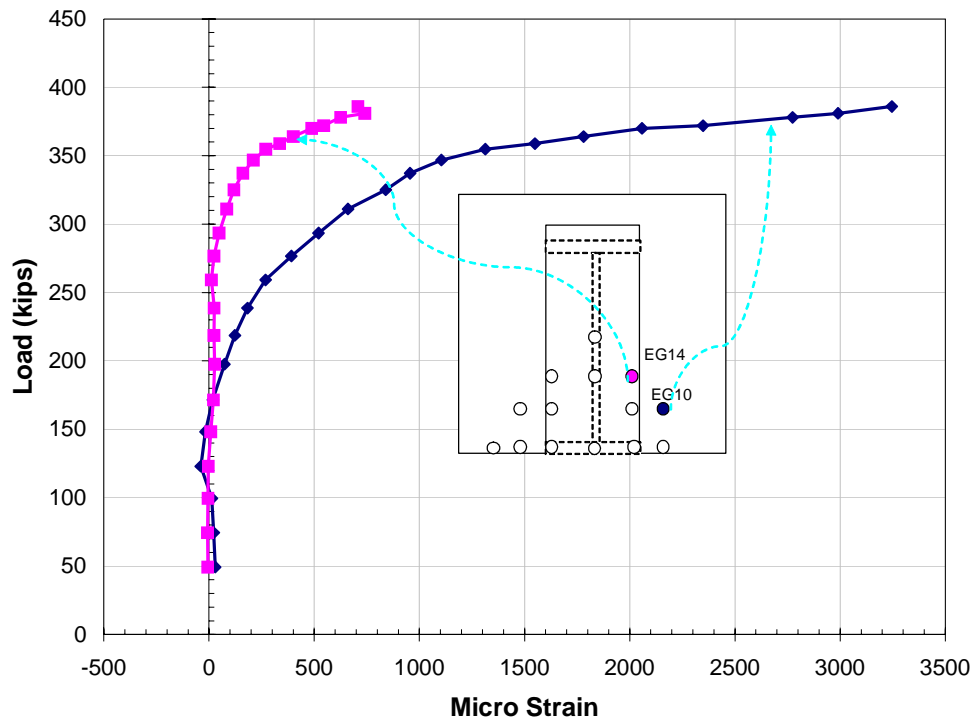


Figure 4-41: Concrete Strain at the Pier Centerline From the Third Ultimate Test

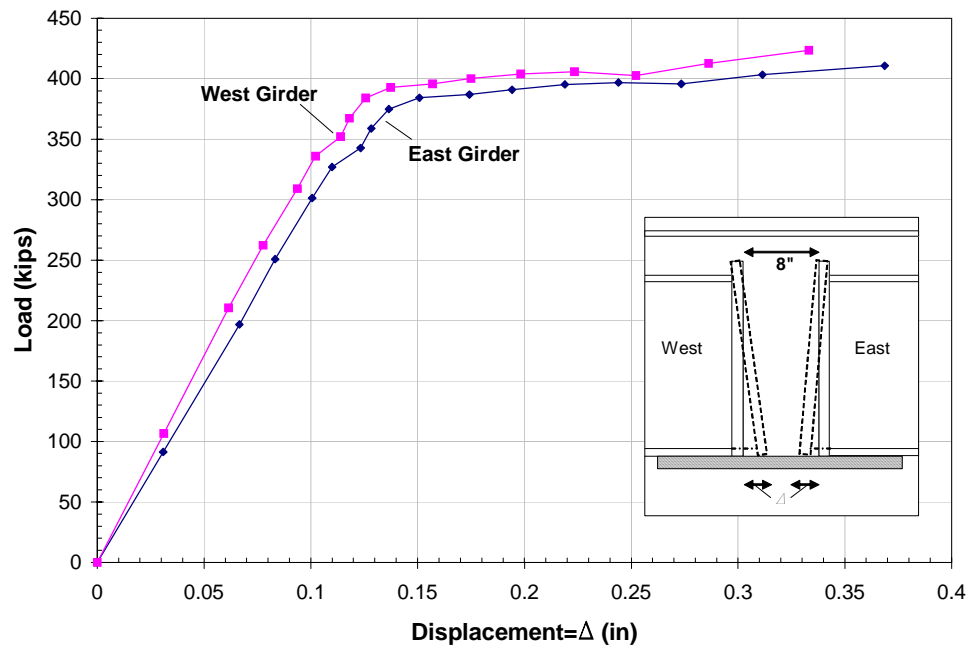


Figure 4-42: Penetration of Bottom Flanges into the Diaphragm Versus Applied Load (3rd Test)

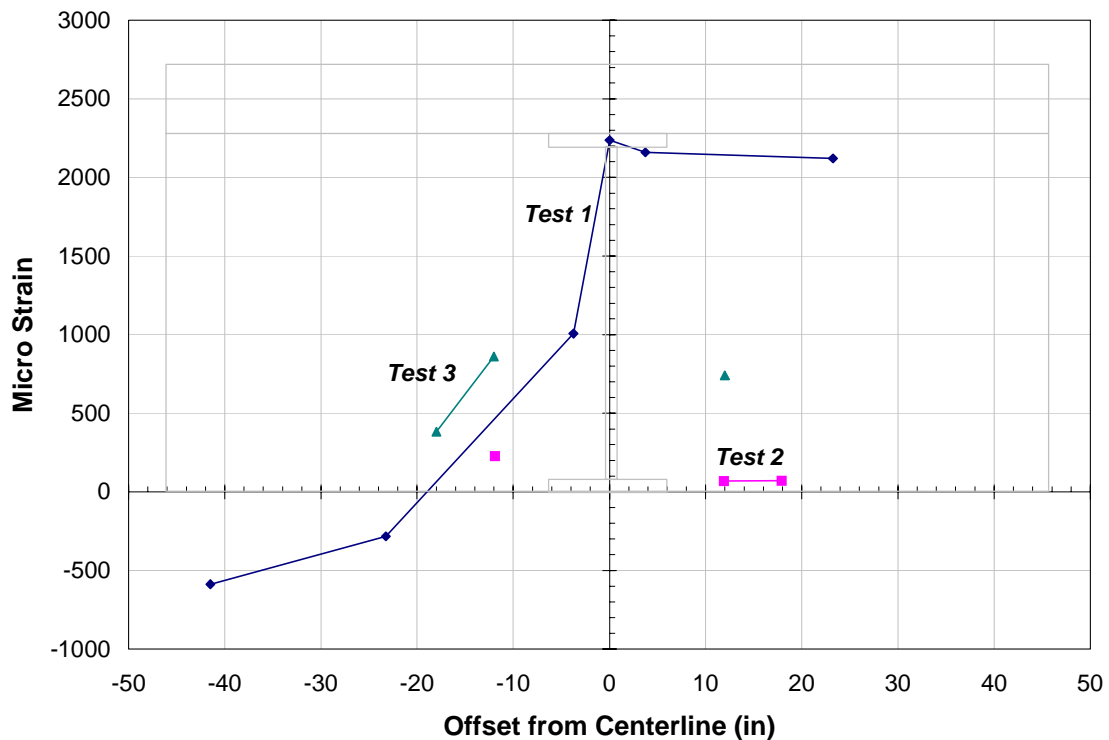


Figure 4-43: Strain Distribution at Pier Centerline Inside Concrete Diaphragm Along the Width of the Diaphragm

4.8.2.8 VERTICAL STRAIN PROFILE

The strain distribution along the depth of the section has a crucial role on determining the resistance mechanism. The strain distribution inside the concrete diaphragm is shown for the first test in Figure 4-44. Unfortunately, due to high compressive stress in this region most of the embedment gages placed inside the diaphragm of the second and third specimens failed during the ultimate tests. As it is seen in Figure 4-44, the strain distribution at the centerline of the pier inside the diaphragm is not linear. The vertical strain profile is also illustrated in Figure 4-45 from the embedment gages inside the diaphragm of the first specimen but not at the pier centerline. The strain distribution obtained from the three tests at a section outside of the diaphragm is depicted in one plot in Figure 4-46. In this case the strain profile is much closer to a linear pattern than the previous cases.

The variation of strain along the depth of the third specimen is very close to the first specimen behavior. It is noted that the applied moment at this section is almost equal for the two tests (test 1 and test 3). These plots indicate that the assumption that the plane sections remain plane can be justified for the steel girder strain profile. However, it is somewhat questionable inside the concrete diaphragm.

Most of the models developed for identification of the stress distribution of steel and concrete structures rely on the assumption that the plane section remains plane. Based on this hypothesis, the strain distribution across the depth of girder is linear. In the previous sections, it was shown that the strain distribution is not linear based on the fatigue test results. To explore the reason for the nonlinearity of strain distribution, a idealistic model of the deformation of the section over the pier under the moment is depicted in Figure 4-47. The separation of the steel girder from the concrete diaphragm at interface in the tension zone is indicated in Figure 4-47 by a gap. Based on this layout, the gages embedded in the upper part of diaphragm do not record the tensile strain. However, the bottom part of the diaphragm participates in transferring the compressive forces and thus the gages record the strain.

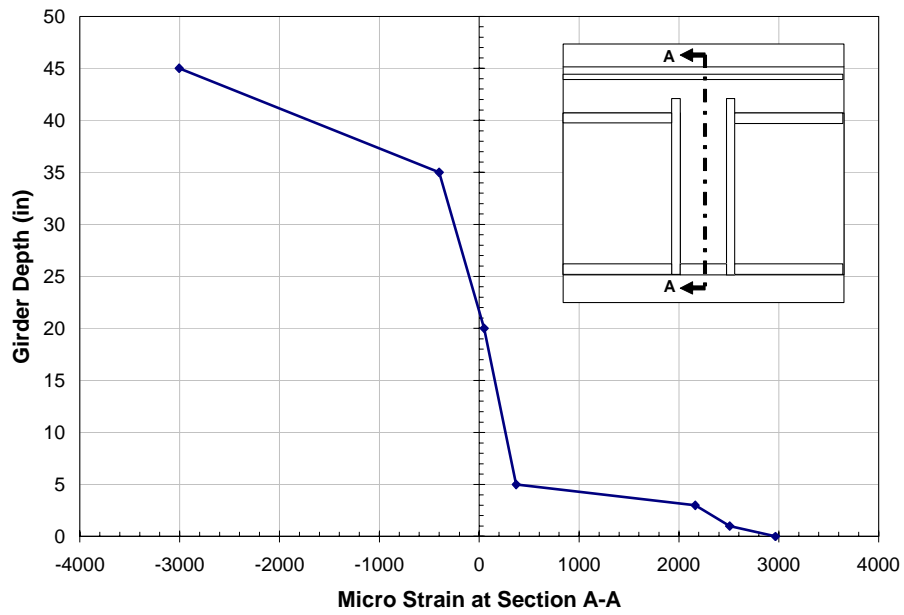


Figure 4-44: Vertical Strain Distribution of Test 1 Near Ultimate Load

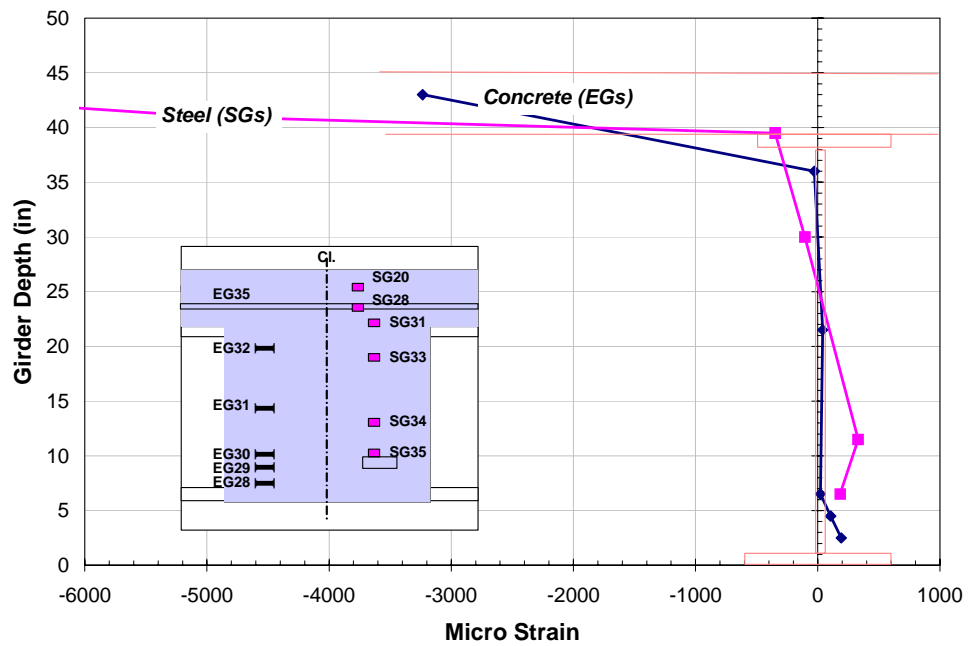


Figure 4-45: Strain Profile Inside the Concrete Diaphragm at the Ultimate Condition of the First Test

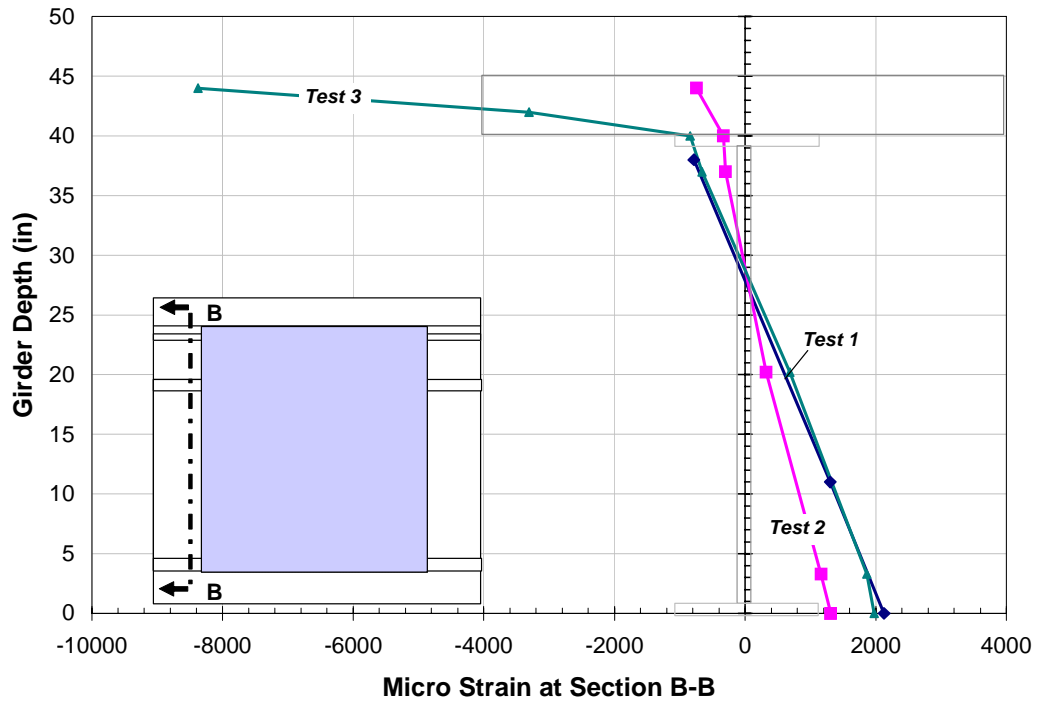


Figure 4-46: Strain Distribution Outside the Diaphragm at Near Ultimate Load

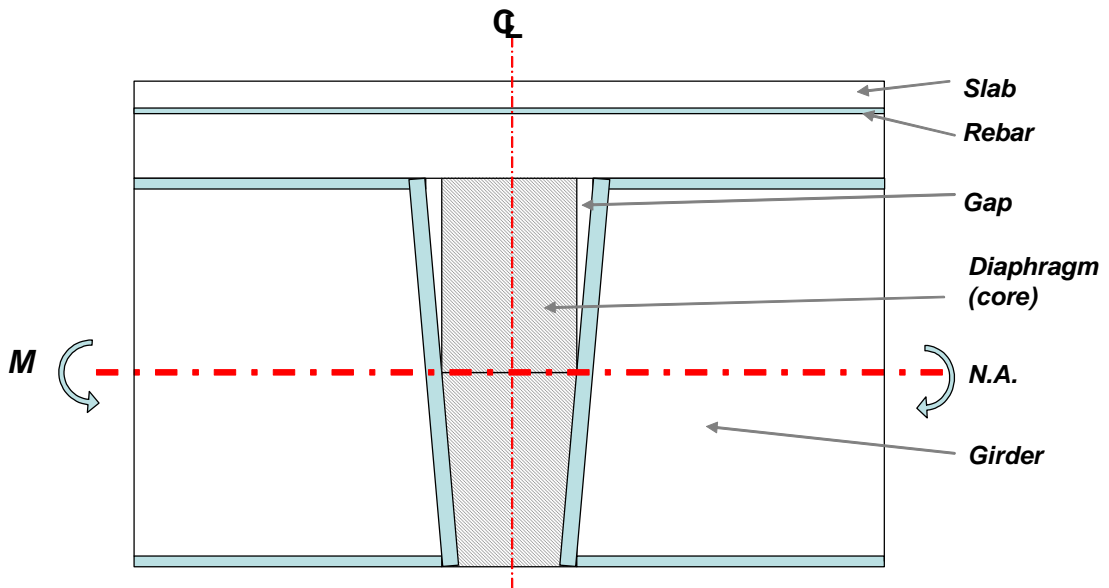


Figure 4-47: Exaggerated Deformed Shape of the Girders at the Pier Location

4.8.2.9 STRAIN AT BOTTOM FLANGE

The strain in the bottom flange (inside the core) of the first specimen passed the yield limit. The yielding was not observed in the other two tests at the bottom flange. The strain responses of the three specimens are shown in one plot in Figure 4-48. As seen in this figure, the strain jumped around the intersection of the bottom flange and the end bearing plate in the first test. The reduction of the strain inside the core diaphragm might be due to the compressive resistance of the concrete which shares part of the compressive force with the bottom flange. The contribution of the concrete also can be seen in the test three strain profile in Figure 4-48. The decrease in strain inside the diaphragm with respect to the outside of the diaphragm can be for the composite action of the concrete diaphragm and steel girder. Unfortunately, the strain gages mounted inside the diaphragm failed to record the strain during ultimate load test two.

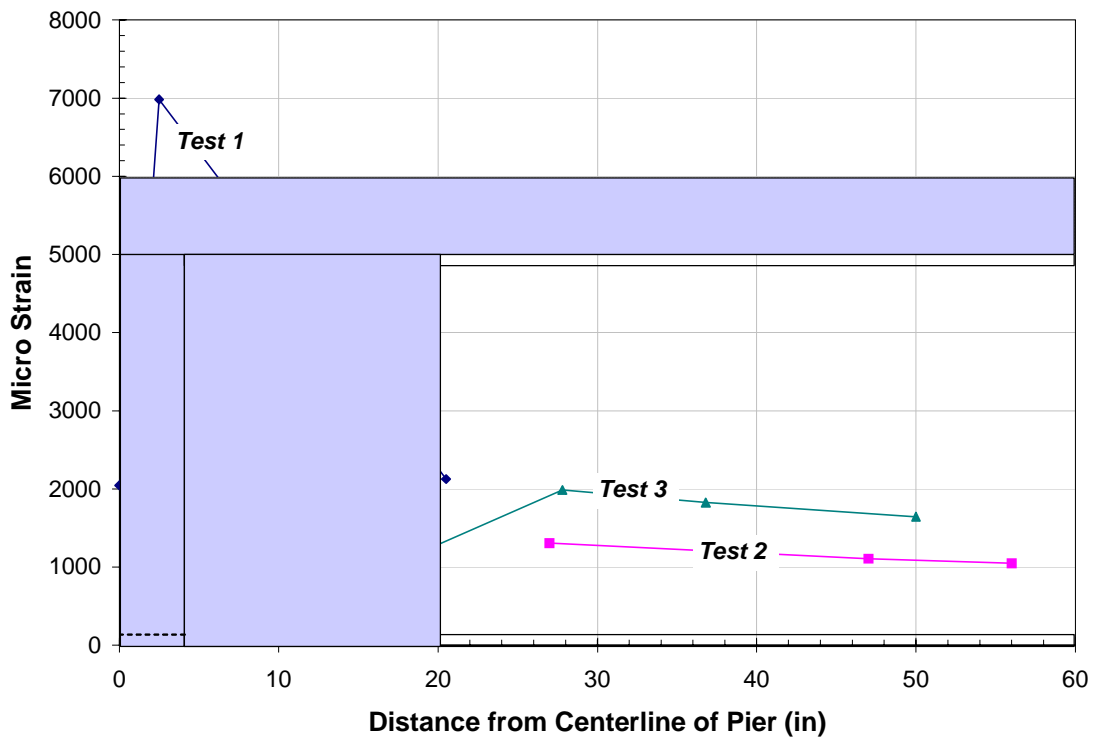


Figure 4-48: Strain Profile in the Bottom Flange Along the Longitudinal Axis of the Steel Girder

4.8.2.10 STRAIN AT TOP FLANGE

The strain profile along the girder length on the top flange is shown in Figure 4-49. The strain plots are at the ultimate condition of each test. The strain drops substantially near the edge of the top flange. Obviously, the tension at the edge of flange shall be very small because the cracked concrete attached at the tip of the flange cannot transfer the tension force. The strain also decreases outside of the diaphragm for the second and the third test as seen in Figure 4-49. The inclined cracks observed under the slab of second specimen indicate that the failure of the slab around the edge of diaphragm caused a strain release at this region.

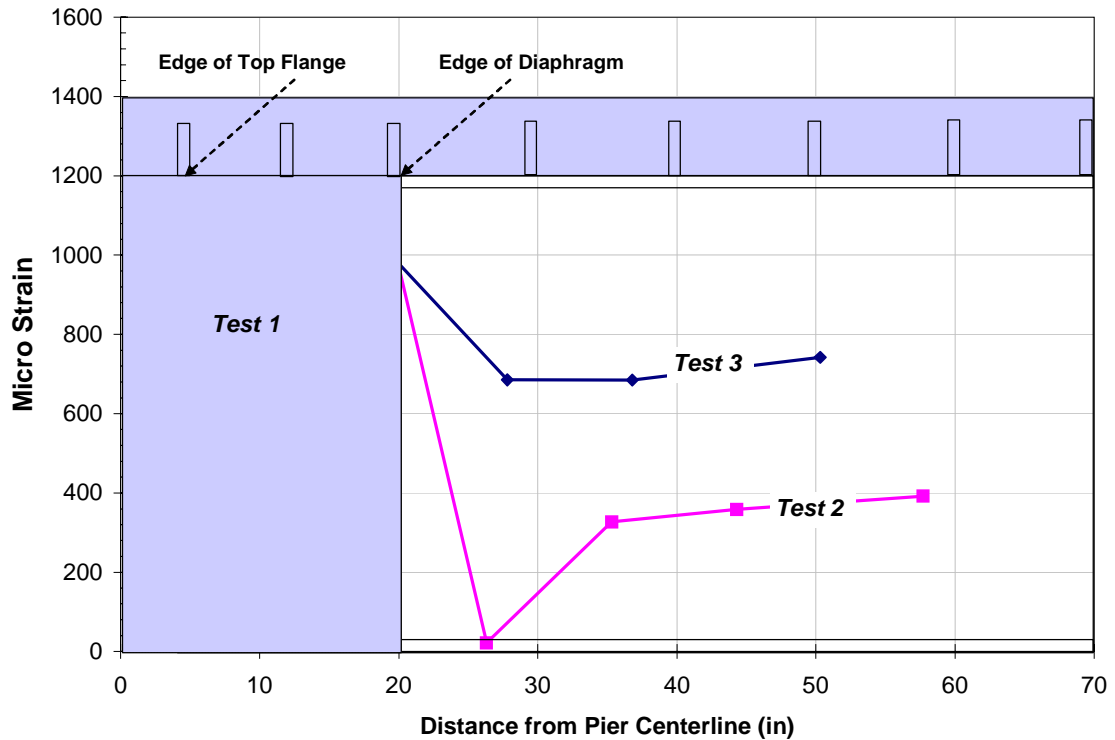


Figure 4-49: Strain Distribution on the Top Flange

4.8.2.11 BONDING OF STEEL AND CONCRETE

The bonding between the steel girder and the concrete or composite action is investigated by the test results in this section. The connectivity of the top flange and the concrete slab was assured by designing and providing an adequate number of shear studs on the top flange. The visual observation of the studs after conclusion of the ultimate tests and dissections of the specimens did not show the failure of the studs. However, the local cracking of the concrete at the intersection of the top flange and deck was observed in the second specimen after the ultimate test. These cracks might be due to the slippage of the studs inside the concrete slab or shear failure of concrete slab in the longitudinal direction. In the first test, the strain profiles of the concrete diaphragm and steel girder and rebar in the vertical direction were plotted in one plot as shown in Figure 4-45. The longitudinal position of the strain gages and embedment gages are close to each other. Although the strain recorded in the concrete gages is less than those measured by gages on the steel components, the trend of strain profile is similar. If there was a substantial slipping between top flange and slab, then one expects to see a strain distribution as illustrated in Figure Figure 4-50-a, while the recorded strain is somehow similar to Figure 4-50-b. This implies the slab and steel girder do not bend completely separate; however, there is a strain discontinuity between the steel and concrete. The actual interaction of steel and concrete is close to a complete composite action rather than non-composite behavior. It is observed that both the top layer and the bottom layer rebar in three tests are in tension which also indicates that the tested specimens had composite action at the ultimate condition. Again, the magnitude of this composite action is not known.

Bonding between deck rebar and concrete can be shown by strain comparison obtained from the gages attached on the rebar and those embedded in the adjacent concrete. There were several gages embedded in the concrete slab in the first test. The strain distribution obtained from the embedment gages inside the concrete slab and strain gages welded on the top

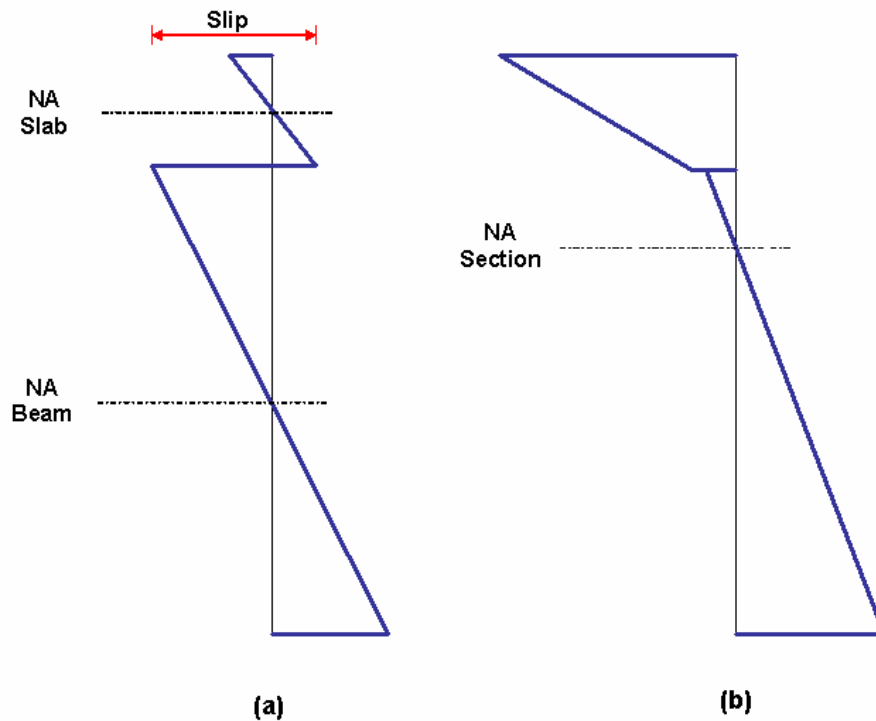


Figure 4-50: Strain Profile for (a) a Non-composite Section and (b), a Semi-Composite Section

layer rebar were plotted in Figure 4-51. The strain shown in Figure 4-51 are at the first yield load (340 kips), since the recorded strain at higher load levels are not correct for all the gages. The vertical locations of the embedment gages inside the deck were almost the same as the top layer of rebar. It is observed that in general (with two exceptions) the concrete strain is less than the strain of the reinforcement over the pier and edge of diaphragm. The vertical distribution of strain in the first test also indicates the same result, i.e. the strain recorded inside the concrete is less than that of steel girder. The strain discontinuity between concrete and steel occurs for three reasons.

1. Slippage between concrete and steel
2. Large strain gradient between concrete and adjacent steel
3. Instrumentation shortcoming

The slippage might have contributed to the strain difference in some degree, but large slippage of rebar resulted in less strain in the rebar, since the force is transferred from the steel girder to the rebar through the concrete slab. If there is large slippage of rebar, it bears less load and thus less strain. In addition, no cracking was observed corresponding to the rebar slippage in the first test. Furthermore, there is not any mechanistic reason to justify a large strain gradient between concrete and adjacent rebar. Since two adjacent rebar in the deck almost have the same strain, one expects that the embedment gage between them also have the same strain. But, as it was mentioned earlier, the difference between the strain measured in concrete and reinforcement exceeds 1200 micro-strain (see Figure 4-51). The instrumentation shortcoming can be a more reasonable explanation for this discrepancy. As shown in Figure 4-52, the concrete under tension has parallel cracks as was observed on the slab of tested specimens. The embedment gage can not bridge over all the cracks because of its short length. Therefore, the measured strain is limited to the distance between two adjacent cracks (bc in Figure 4-52). However, the steel rebar is extended over all the cracks and the strain gage attached to it can measure the deflection of a longer range of the slab.

In the first test, the transfer of the compressive stress from the steel girder to the concrete diaphragm can be shown by a strain profile inside the diaphragm as depicted in Figure 3-43. If there was not any bonding between the concrete and the steel girder, the strain distribution inside the concrete diaphragm at the location shown in Figure 3-43 would had been close to zero. But, the strain at one inch above the bottom flange inside the diaphragm (EG28 in Figure 3-43) is about 200 micro-strain. This indicates that the concrete has taken part of the compressive force, though only a small portion. The transfer of compressive force could have been done either by the shear bars passed through the girder web or the bonding of the steel girder and the concrete or both manners.

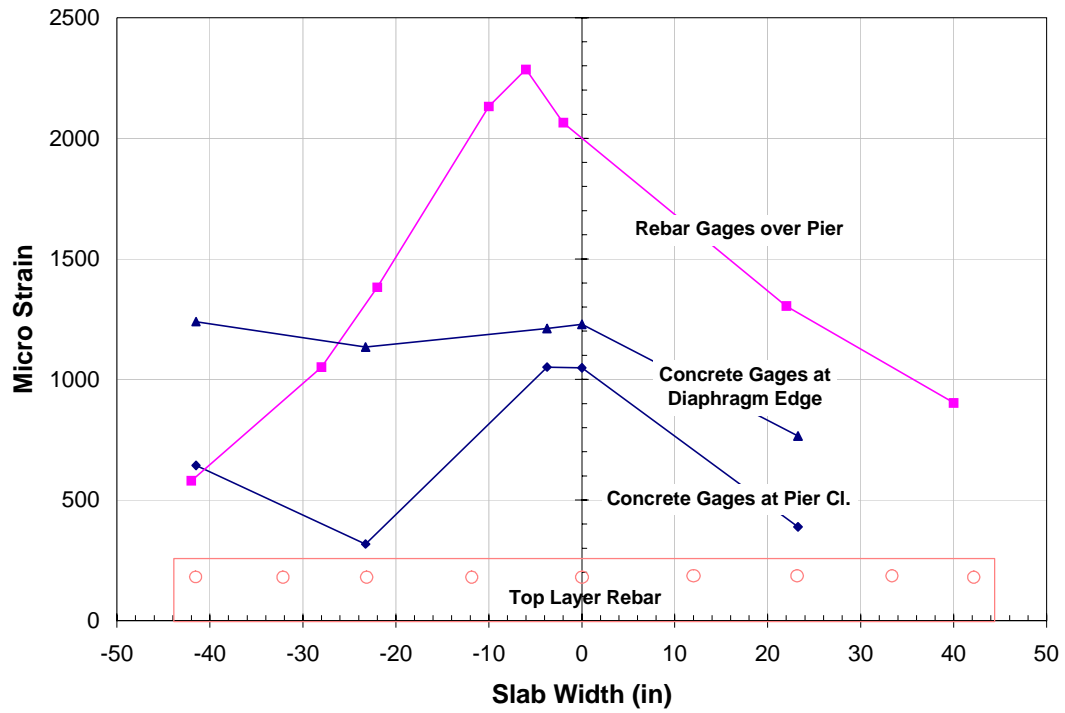


Figure 4-51: The Strain in the Slab During Ultimate Test One at a Load of 340 kips

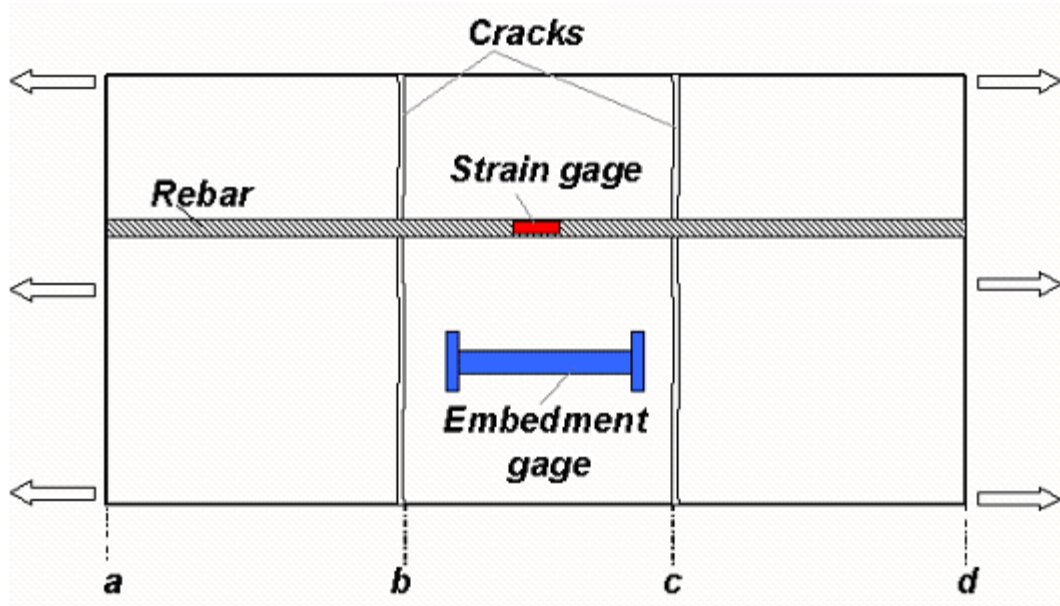


Figure 4-52: A Concrete Specimen Under Uniaxial Tension

In the second test, the penetration of the bottom flange into the diaphragm, along with the large cracks (see Figure 4-53 and Figure 4-54) indicates that the steel girder and concrete bonding failed during the second test. There is some test observations that show that slippage occurred even earlier, during the cycling test. After conclusion of the ultimate test, the dissection of the second specimen revealed that the shear reinforcements that were placed inside the diaphragm for continuity of steel and concrete failed. These reinforcements were run-through the beam web by drilling wholes in the beam web. Figure 4-55 and Figure 4-56 show the large deformations of a shear bar at the interface of the web plate and the concrete diaphragm. The mode of failure for these bars seemed to be shear failure. The strain measured by gages attached on the web around the shear bars (see Figure 4-57) indicates that the large deformation of bars or their failure could have been started after a load of 114 kip.

In the third test, one reason for continuity of the concrete diaphragm and steel girder is the inclined cracks on the face of diaphragm after the ultimate test, as shown in Figure 4-58. The crack pattern indicates that part of the diaphragm concrete resisted the compressive force; otherwise the crack should have been at the interface of the steel girder web and the concrete diaphragm. In addition, as it was described in the previous sections the longitudinal profile of strain at the bottom flange indicated that there is a contribution in compressive resistance by the concrete diaphragm, since the strain of the steel girder decreases inside the diaphragm.

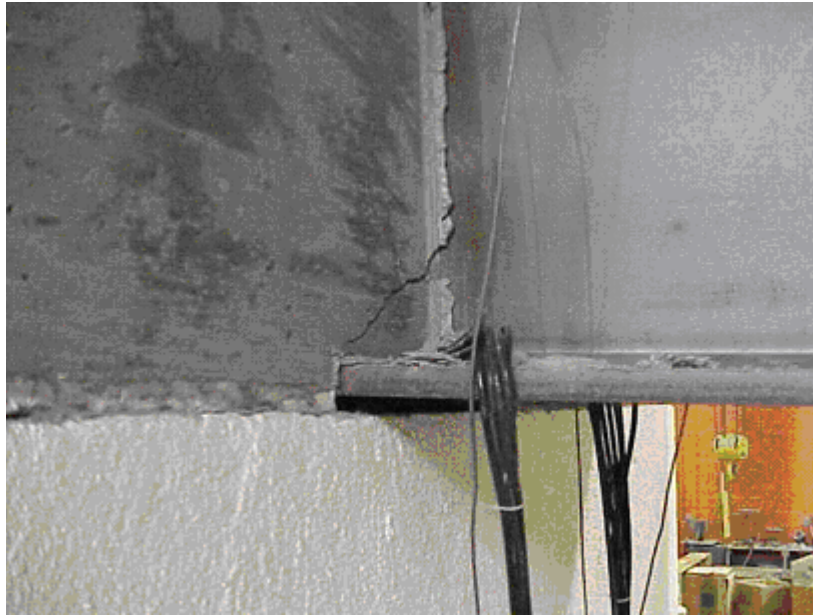


Figure 4-53: Cracking of Concrete Diaphragm Around Bottom Flange of Specimen 2

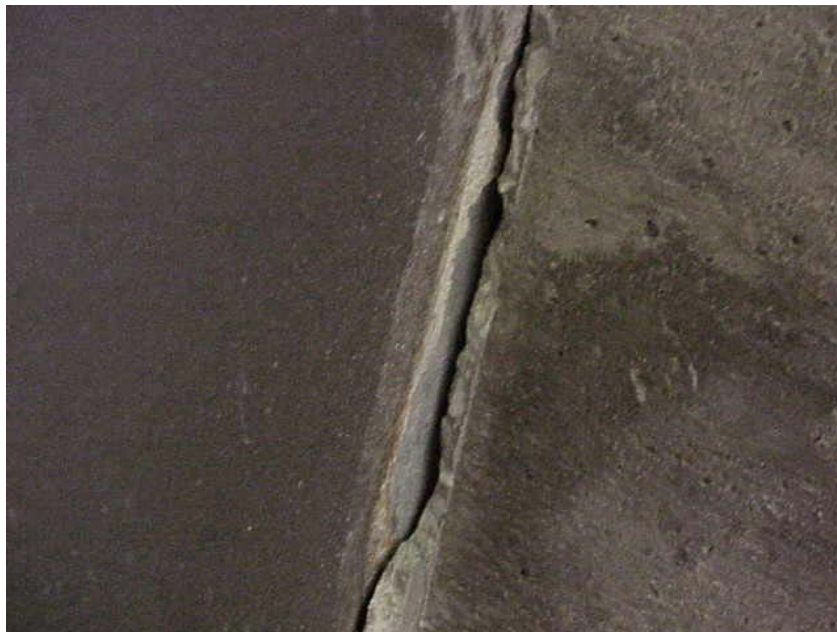


Figure 4-54: Separation of Steel Web and Concrete Diaphragm During Test 2

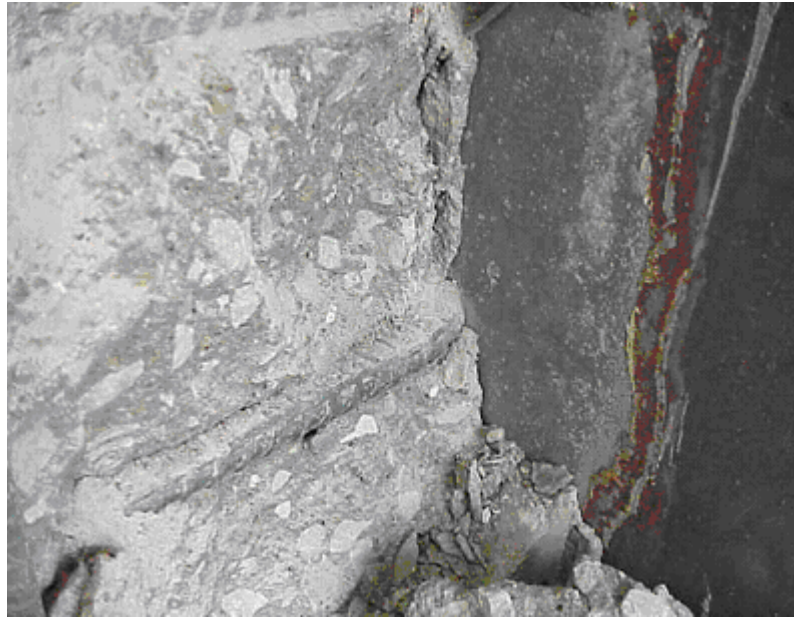


Figure 4-55: Large Deformation of Shear Bars Inside Diaphragm After Test 2

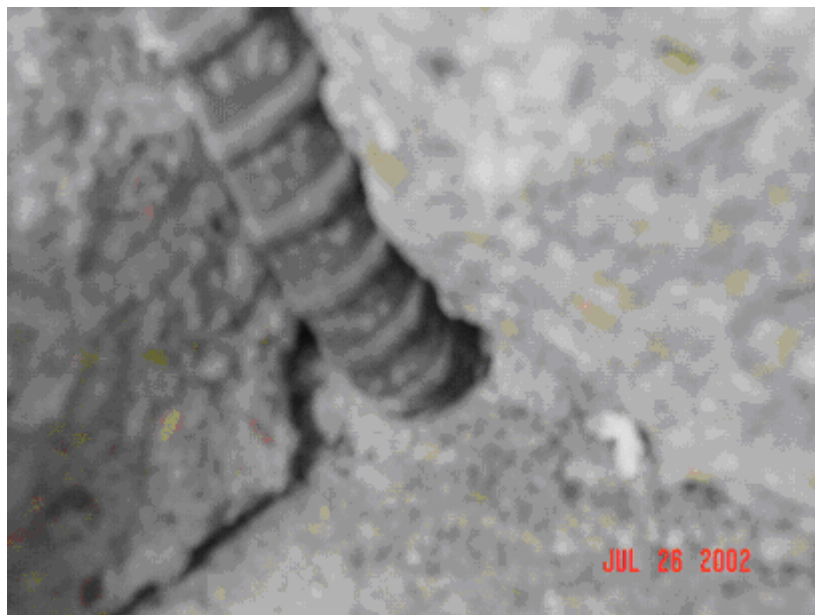


Figure 4-56: Shear Failure of Diaphragm Shear Bar After Specimen 2 Ultimate Test

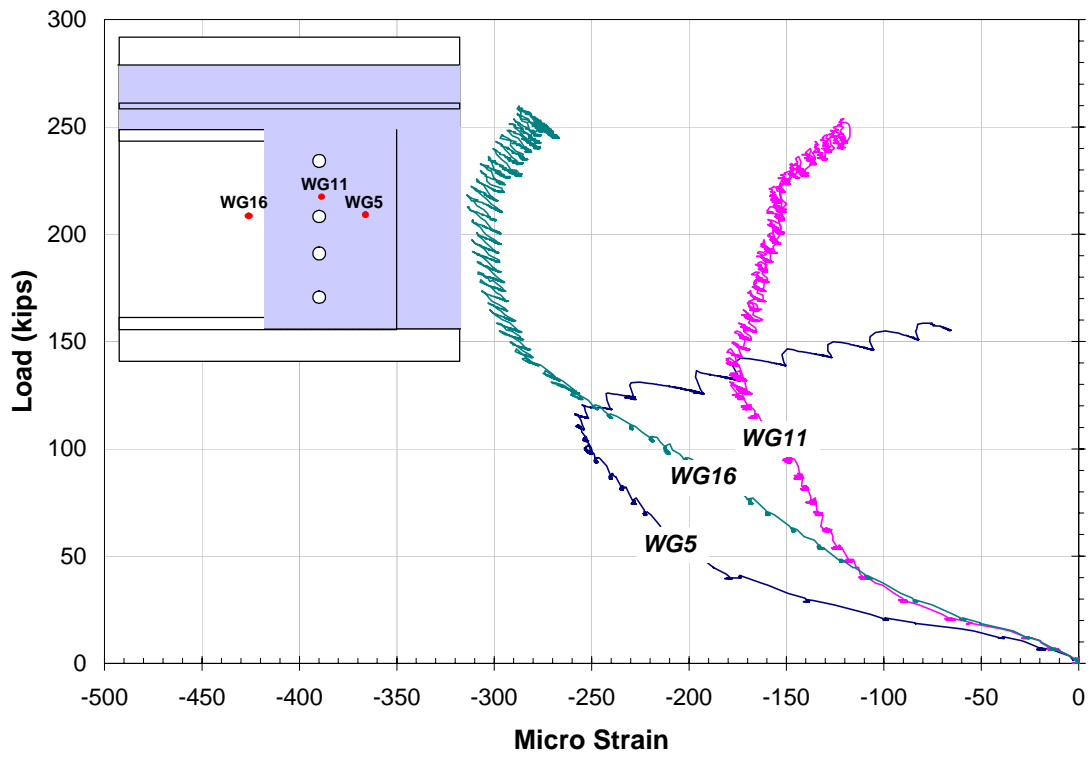


Figure 4-57: Strain of Three Points Around the Web Shear Rods

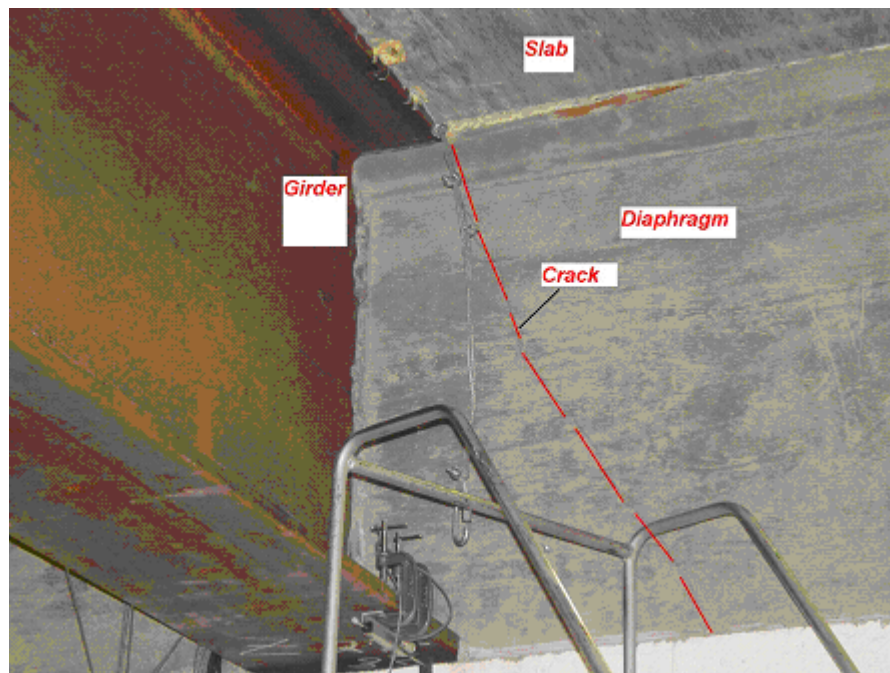


Figure 4-58: Cracking of the Diaphragm During the Third Test

4.8.3 RESISTANCE MECHANISM

4.8.3.1 TEST 1

The test results presented in the preceding sections is summarized to give a general picture of the load-resistance mechanism of the system. The first specimen behavior in ultimate loading is shown in Figure 4-59. The load-deflection curve shown in this figure is the average of the east and west girders. The saw tooth shape of the curve has been modified in this plot. The following steps identify the first specimen's structural behavior:

1. The cracks remaining from the cycling test widened and propagated on the concrete slab surface from the early stage of loading (five percent of ultimate load). These cracks originated at the diaphragm edge and centerline of the pier.
2. The yielding started at the top layer of reinforcements at 62 percent of the ultimate load capacity of the specimen. The location of the first yield was around the girder axis and centerline of the pier.
3. After the short load interval (65 percent of ultimate load) following the yielding of the top layer rebar, the bottom plate strain passed the yielding limit.
4. The concrete between the two end bearing plates at the bottom of the diaphragm experienced a strain of more than 0.003 in/in at 87 percent of ultimate load.
5. The entire top layer of rebar passed the yielding limit at 95 percent of ultimate load.
6. All of the slab rebar around the pier centerline yielded at 98 percent of the measured ultimate load.

The collapse of the first specimen might have occurred after the top layer of rebar passed its ultimate plastic strain or necking point. Otherwise, the

collapse should have been due to failure of shear rods and crushing of concrete, as was the case in the second test, but the test results do not confirm this type of failure.

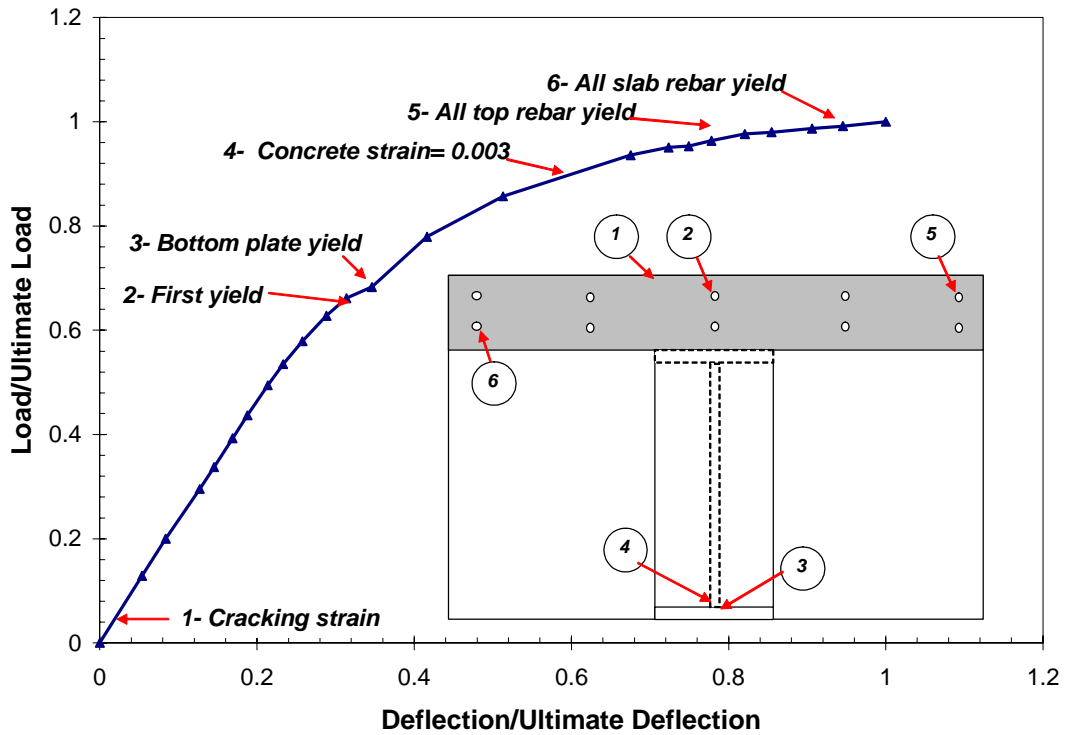


Figure 4-59: Load Resistance Stages for the First Test

4.8.3.2 TEST 2

The load-deflection response of the second specimen is shown in Figure 4-60. The deflection values in the plot are the average obtained from the readings of the east and west girders. Due to damage to the instrumentation, there were not adequate data to quantify the structural behavior of the system as it was achieved for the first specimen. However, based on the visual observations along with the recorded data, the behavior of the system might be as following:

1. The cracks formed during the cyclic loading grew from the beginning of loading, especially on the surface of the deck.
2. Local crushing of concrete occurred at the interface of the bottom flange and the concrete after cracking, but there is not enough data to locate a more exact load level.
3. The large deformation and failure of the shear rod occurred at 43 percent of ultimate load.
4. At 78 percent of the ultimate load, the first bar in the middle of the top layer of rebar at the pier centerline yielded.
5. The slab concrete around the top flange and the edge of the diaphragm failed at about 97 percent of ultimate load.

It is noted that the bonding between the steel girder and the concrete diaphragm had failed during the cycling test and so has not been shown here. The failure of the specimen occurred after failure of the concrete deck, as seen in Figure 4-35. This type of crushing can be due to the shear failure of the slab concrete shown in Figure 4-61. The large rotation of the steel girder inside the diaphragm demanded a large pull out displacement at the top flange. As a result, there would have been a relatively large concentrated tension force in the top flange. The concrete deck could not provide

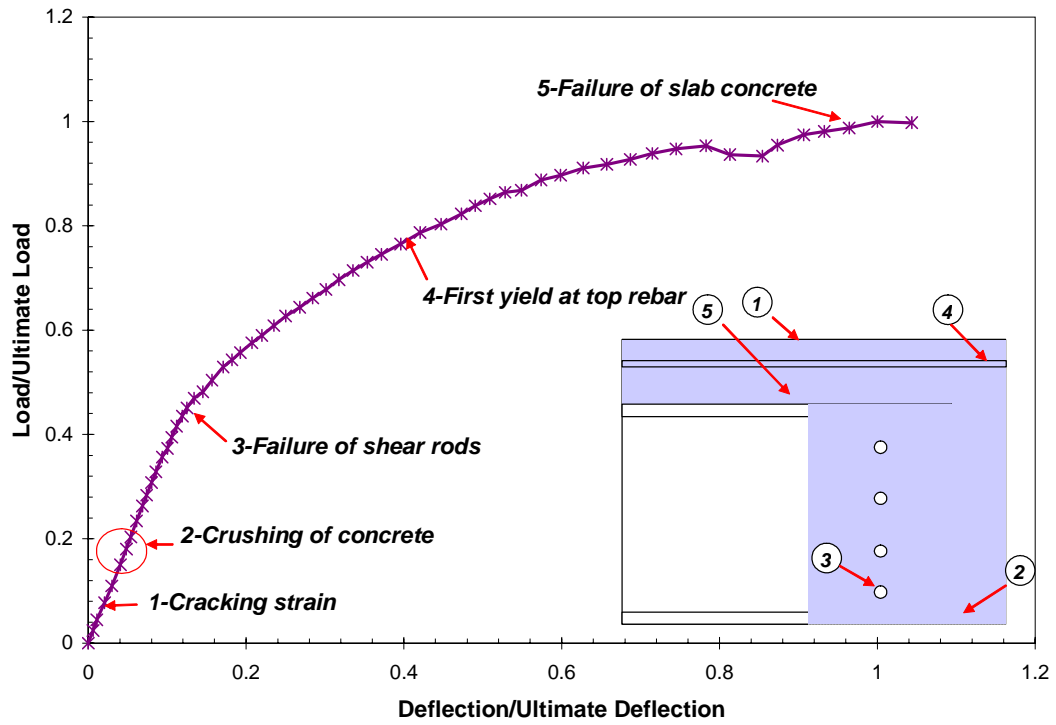


Figure 4-60: Structural Behavior During the Second Ultimate Test

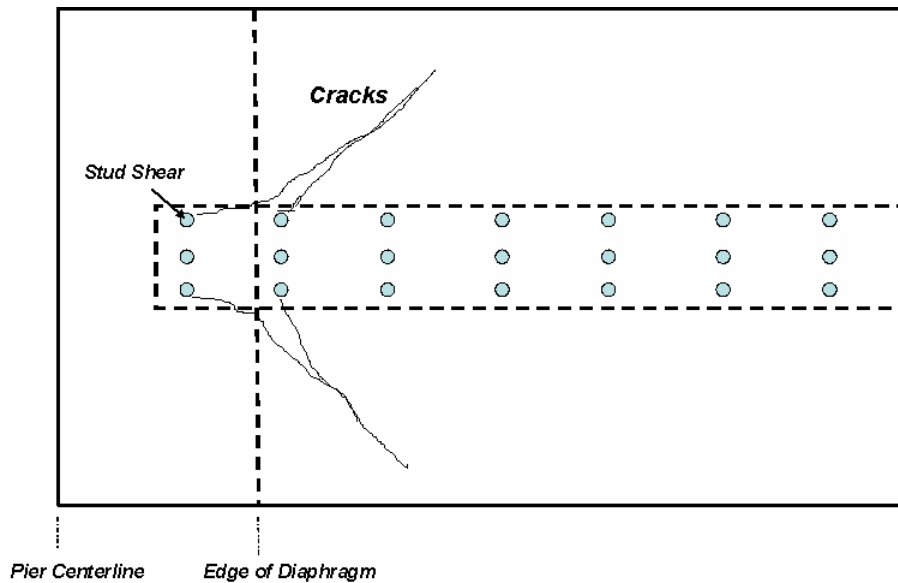


Figure 4-61: Failure of the Concrete in the Second Specimen Slab

adequate shear resistance to transfer the concentrated tension force of the top flange to the adjacent rebar.

4.8.3.3 TEST 3

The load-deflection response of the third specimen is shown in Figure 4-62. The presented plot is the average of the east and west girders' potentiometer readings. Due to error in the test procedure, this plot has been modified. The identification of the exact locations of the structural events of the test were not possible due to errors in measurements. However, test observations and results indicate that the resistance of the specimen might be as follows:

1. Concrete cracks formed during the cycling test propagated from the beginning of the ultimate test.
2. The first yield was probably initiated at about 60 percent of ultimate load.
3. All of the top layer rebar likely yielded at 80 percent of the ultimate load and caused the slope of the load-deflection plot to change around this point.
4. The failure of the specimen occurred as inclined cracks were formed throughout the concrete diaphragm.

It should be noted that not all of the above stages or their order have been verified by test results due to instrumentation errors.

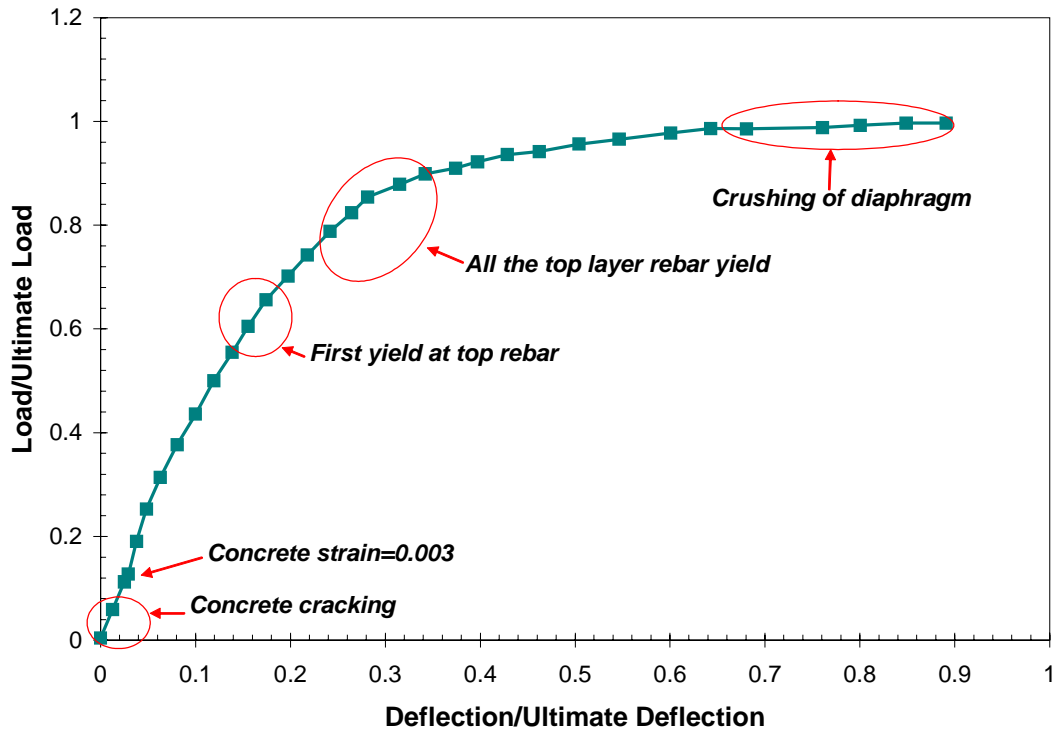


Figure 4-62: The Load-Deflection Response of the Third Specimen

4.9 SUMMARY

The test results and observations indicate that the cracking of the concrete slab around the pier region is the first damage in the specimens. The next failure can be yielding, crushing, or debonding of steel and concrete. The order of these events depends on the strength of the materials, steel ratio, and dimensions. The results of the three conducted tests give a good understanding of the resistance mechanism, but due to limitation in experimentation, a general mechanism cannot be derived. Furthermore, the numbers of tests are not adequate to quantify the ultimate capacity of the structure. To obtain more information about the behavior of system a series of finite element analysis was carried out to complement the experimental studies. The procedure and results of the numerical studies are presented in Chapter 5.

Finite Element Model Development & Verification

5

5.1 INTRODUCTION

A study was conducted using nonlinear three-dimensional finite element models of the three tests. The connections were simple for dead load and continuous for live load. The tests consisted of two cantilever I-beams sitting on a pier as described in Chapter 4.

In the first part of this chapter, the details of the developed numerical model are described. The commercial finite element software ANSYS 5.7 (1998) was used. The geometry and material properties of the models were based on the actual data obtained from the laboratory. Material and geometrical nonlinearities were included in the numerical simulations. A sen-

sitivity analysis was done for the development of the finite element models.

In the second part of this chapter, the results of the finite element analyses are compared to the actual test results to verify the accuracy of the finite element analysis. Different aspects of the specimens' behavior were investigated. The load-deflection plots obtained from the analyses are presented along with the experimental response for each test specimen. The yielding pattern and cracking behavior are illustrated to verify the numerical model. Then, the strain at the monitored locations of the test specimens are compared with the finite element results. The force transfer mechanism of each test is discussed using results from the finite element simulation results.

5.2 FINITE ELEMENT MODEL DEVELOPMENT

5.2.1 GEOMETRY OF MODELS

The geometry of the developed finite element model was obtained from Nick Lampe's Master's thesis (2001) and a drawing from Lincoln Steel Company. Since these two references did not contain all the information for building a detailed finite element model, further dimensions and details were acquired from the lab observations and measurements of the three tested specimens. It is noted that there are several differences between the dimensions of the three tests. The major differences of the specimens were discussed in Chapter 4.

The components of the finite element model are illustrated in Figures 5-1 through 5-3. The steel I-girder beam was a rolled W40X215 section for all three tests. At the end of the I-beam in Test one and Test three, an endplate was welded to the end of the I-beam in contact with the concrete. It should be pointed out that Test two did not have this plate. In Test one and Test two, two types of stiffeners were welded to the end bearing plate to

strengthen it. For Test one the stiffener was welded in a horizontal situation (shown in Figure 5-2 as a stiffener), and in Test two it was welded in a vertical position (shown in Figure 5-2 as a gusset plate). It should be mentioned that the location of the gusset plate in the real test specimen is one inch from the edge of the bottom flange, but in the finite element modeling as shown in Figure 5-2 it was placed at the edge of the flange for the sake of simplicity of modeling. In addition to these plates, one transverse stiffener was welded to the I-beam at the location of the loading beam as shown in Figure 5-2. In the tested specimens there were two transverse stiffeners in this location, but since there was no observed stress concentration during analysis, thus one of them did not include in the finite element model.

The concrete slab width and thickness were the same for the three tests, ignoring the construction tolerance. Two layers of reinforcement were modeled in the longitudinal direction in the concrete slab with equally spaced rebar. The layout of reinforcement is not exactly like tests, but the total area of rebar in each layer is the same as the tests. Transverse reinforcements were also considered by using the ANSYS smeared rebar capability. Three rows of shear studs were provided on the top flange as the physical models.

Due to symmetry in some models, only half of the specimen was modeled as shown in Figures 5-1 and 5-2. The connection of the diaphragm to the web of the I-beam was achieved by four shear bars. In addition to the shear bars, there were several transverse reinforcements in the form of stirrups in the diaphragm. The location and numbers of these rebar are not exactly as the same as tests, but the total area is the same.

The diaphragm rests on a neoprene bearing pad located on the pier as seen in Figure 5-2. The pier is not modeled, since it has little influence on the

load-deflection behavior of the specimen. The dimensions and properties of the neoprene pad were obtained from the lab data.

The comparison between test results and analysis revealed that the loading beam used to transfer the load of the rams to the specimen was important for uniform distribution of load across the slab width. For this reason, the loading beam was included in the simulations. The actual load beam consists of two I-beams attached together, but in the simulations only one I-beam with the same cross section properties of two beams was employed.

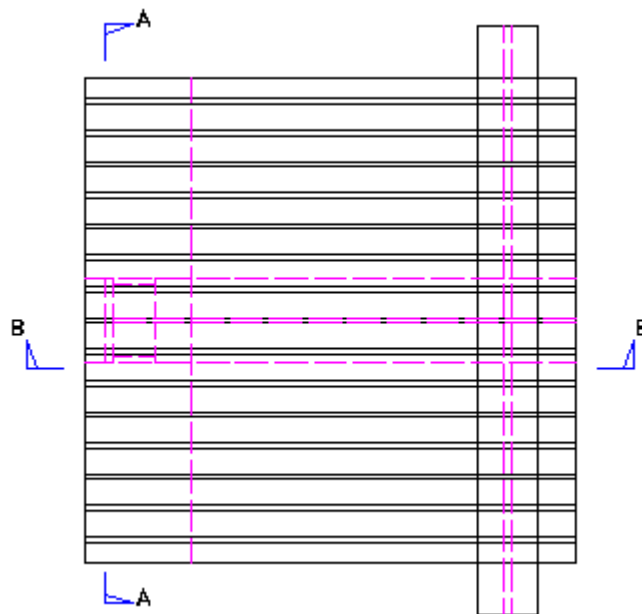


Figure 5-1: Plan View of Finite Element Model Component

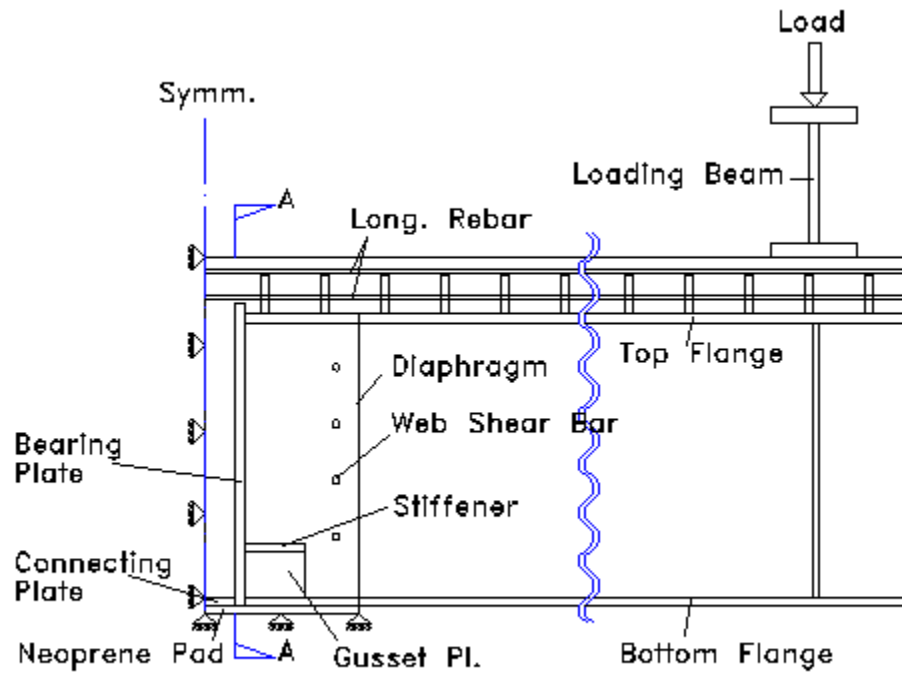


Figure 5-2: Longitudinal Section View (Sec B-B) of Finite Element Model Components

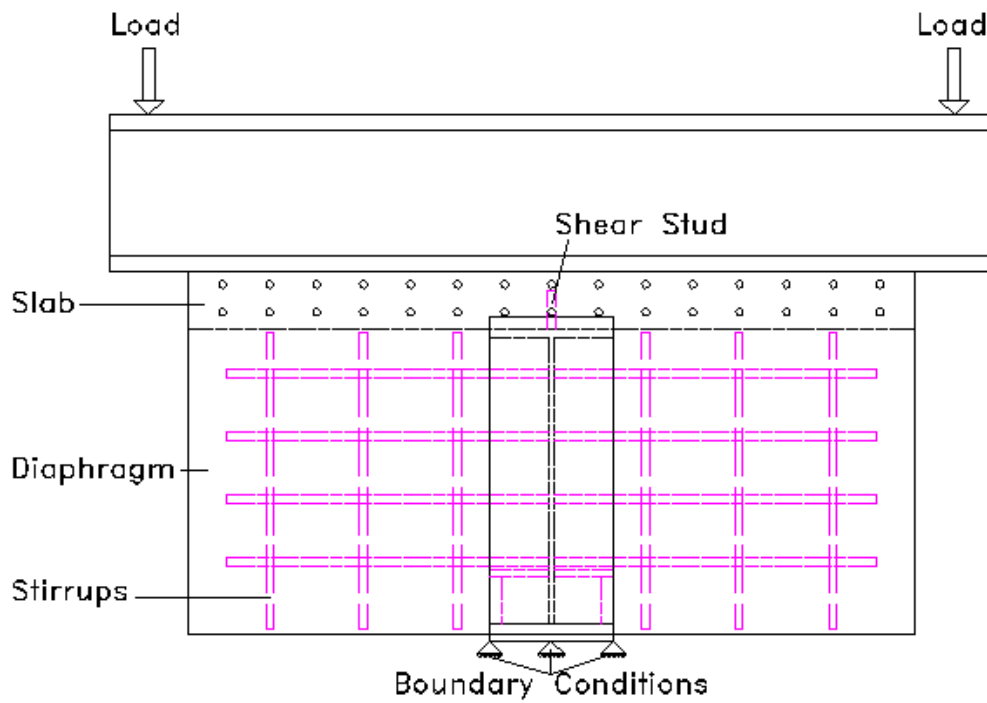


Figure 5-3: Transverse Section View (Sec A-A) of Finite Element Model Components

5.2.2 MATERIAL PROPERTIES

5.2.2.1 STEEL

The I-beam material behavior was obtained from the lab data. For experimental verification, engineering material stress-strain curves obtained from material tests of Test one were converted to true stress-strain curves and input into the finite element models (see Figure 5-4). The ANSYS 5.7 Multilinear Isotropic Hardening option was used to input the true stress strain curves. This option uses the von Mises yield criteria coupled with an isotropic work hardening assumption and allows for up to 100 different stress and strain points per curve. For derivation of the stress-strain curve, the modulus of elasticity was set to 29000 ksi. The Poisson's ratio was assumed to be 0.3 for all the steel materials.

The yield stress and tangent modulus of the stiffeners was assumed to be similar to the material properties of the I-beam since lab data was not available. This assumption was reasonable considering none of the stiffeners in the three tests yielded. For the stiffeners and connecting plate a Bilinear Isotropic Hardening option within the ANSYS program was used to model the material behavior. This option is similar to the multilinear isotropic hardening option, except that a bilinear curve is used instead of a multilinear. A value of 29000 ksi was used for the elastic portion of the material curve, 54 ksi as yield stress, and 250 ksi was used for a strain hardening modulus (Figure 5-5).

The yield strength and ultimate strength of the rebar placed inside the concrete was determined using the tensile tests. A multilinear strain-stress curve was constructed based on the rebar test of the second specimen. The average of the yield stress and the ultimate stress obtained from the bar's sample tests were considered in the analyses. The multilinear strain-stress curves input for each specimen are shown in Figure 5-6.

It was found from both tests, results and finite element analyses that only a small region of the steel beam, reinforcement and stiffeners close to the critical section developed yielding. Therefore, for saving computational time and required memory, part of the steel girder outside of the diaphragm was modeled by using a linear stress-strain material property..

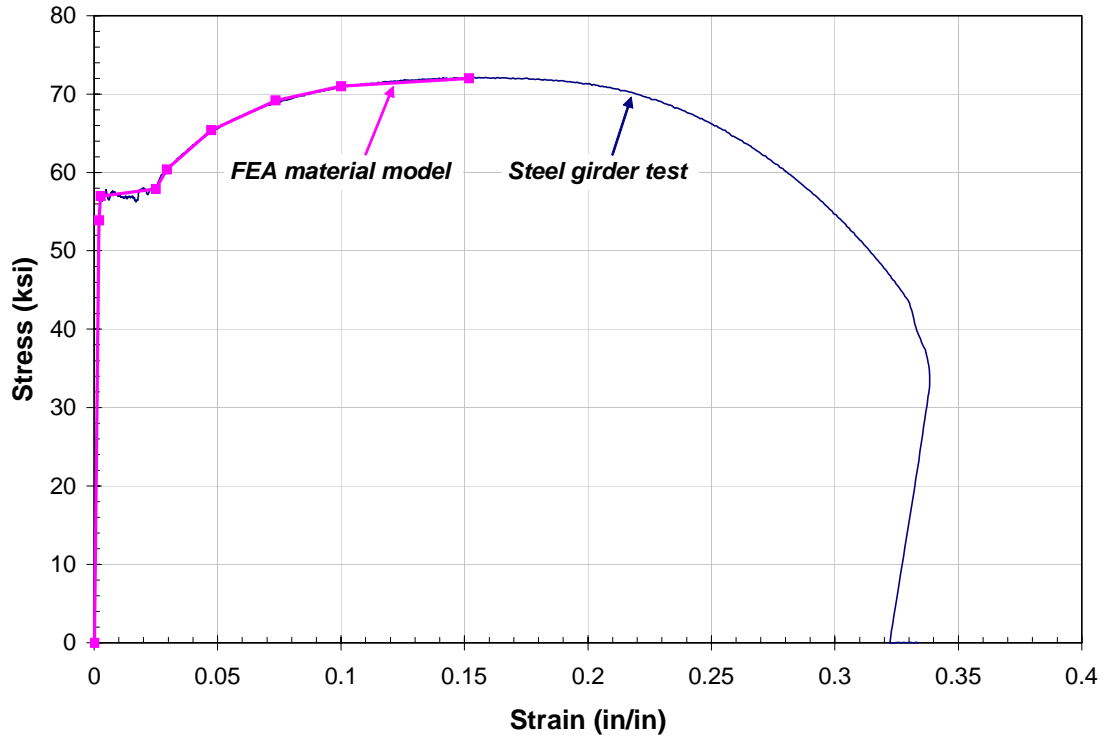


Figure 5-4: Multilinear Approximation of Steel Girder Stress-Strain Response

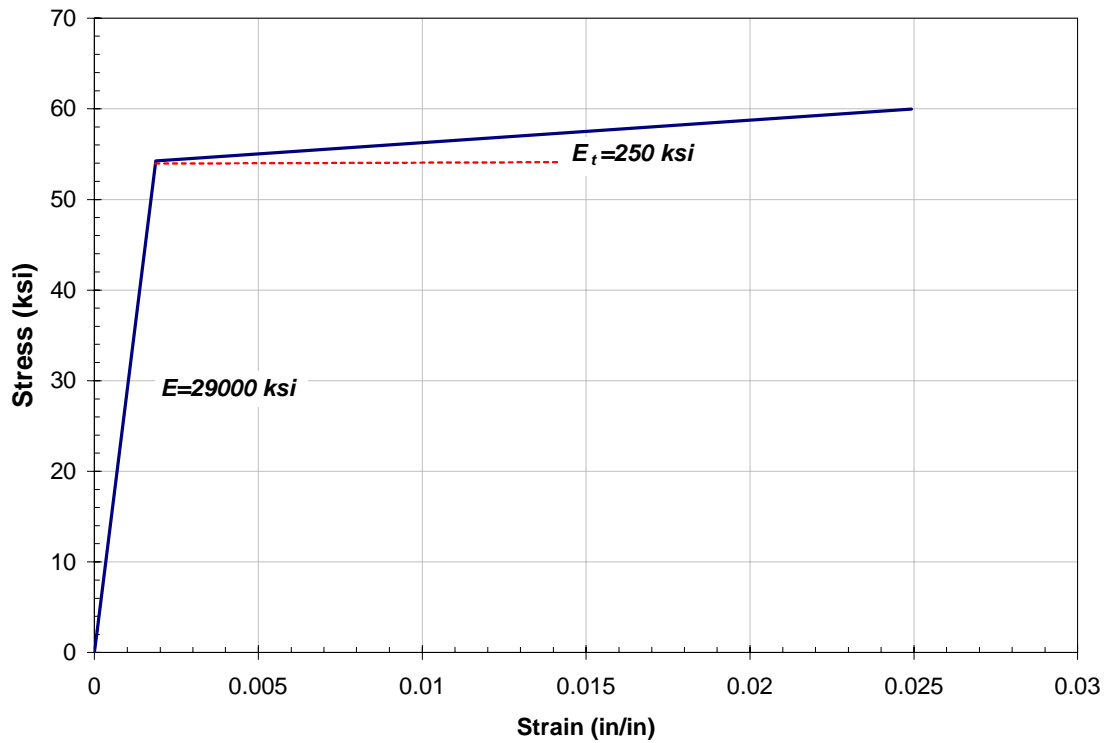


Figure 5-5: Bilinear Stress-Strain Model for Steel Girder Elements

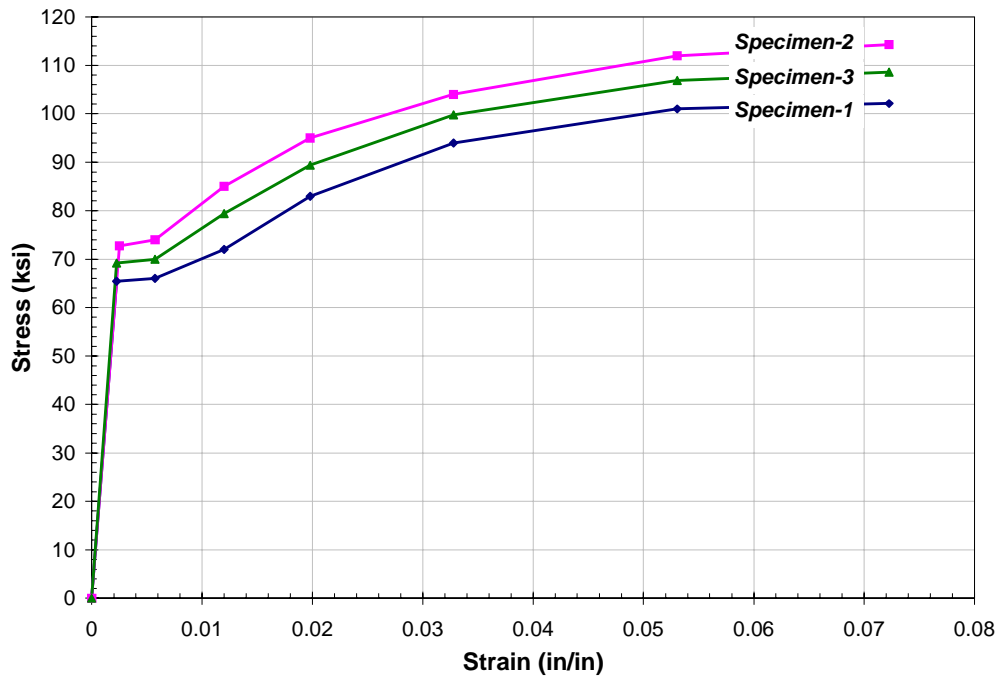


Figure 5-6: Average of rebar sample tests for the three specimens

5.2.2.2 CONCRETE

Two important characteristics of the behavior of tested specimens were cracking and crushing of concrete. The concrete model of the ANSYS program was used to simulate the nonlinear behavior of the specimen except for part of the second specimen. The numerical model of the second specimen was very unstable due to highly localized crushing of the concrete. In this case, to track the load-deflection, the concrete at the bottom of the diaphragm was modeled using a multi-linear elastic material.

ANSYS provides a three-dimensional, eight-noded solid isoparametric element, Solid65, to model the nonlinear response of brittle materials based on a constitutive model for the triaxial behavior of concrete after Williams and Warnke (1975). In this model, cracking and crushing are determined by a failure surface. Once the failure surface is reached, concrete cracks if any principal stress is tensile while crushing occurs if all principal stresses are compressive. Failure surface is a function of five parameters: ultimate uniaxial tensile strength, ultimate uniaxial compressive strength, ultimate biaxial compressive strength, ultimate compressive strength for a state of biaxial stress superimposed on hydrostatic stress state, and ultimate compressive strength for a state of uniaxial stress superimposed on hydrostatic stress state. In the foregoing analyses the ultimate uniaxial compressive strength is taken from the lab tests, and the other parameters are assigned based on ANSYS defaults or theoretical formulas.

In the material model, concrete is assumed to be an isotropic material prior to cracking. The concrete behavior is simulated through a smeared crack model rather than tracking individual cracks. Cracking is permitted in three orthogonal directions at each integration point. When a crack has been detected, the stiffness matrix of the element is adjusted so that the stiffness of the element in the direction perpendicular to the plane of crack vanishes. Furthermore, the shear transfer on this plane is reduced by introduction of a shear transfer coefficient in the modified stiffness matrix. The

shear retention model used in ANSYS can be defined for the open and closed cracks. These cracks are irrecoverable and they will remain for the rest of the analysis, but they may open or close. After cracking, the elastic modulus of the concrete element is set to zero in the direction parallel to the principal tensile stress direction.

Crushing occurs when all principal stresses are compressive and lie outside the failure surface; subsequently, the elastic modulus is set to zero in all directions (ANSYS, 1998), and the element effectively disappears.

5.2.2.2.1 Tensile Behavior

Concrete in tension was considered a linear-elastic material until the uniaxial tensile stress, f_t , at which concrete cracks. The tensile strength of concrete was calculated based on the AASHTO (2004) recommendation for the direct tensile strength, f'_t , for normal weight concrete as:

$$f'_t = 0.23\sqrt{f'_c} \quad (5-1)$$

where

$$f'_c = \text{Specified compressive strength of concrete (ksi)}$$

The modulus of elasticity, E_c , is taken from AASHTO (2004) formula for normal weight concrete:

$$E_c = 1820\sqrt{f'_c} \quad (5-2)$$

The calculated tensile strengths and elasticity moduli of test specimens are listed in Table 5-1.

Test	f'_c (ksi)		f'_t (ksi)		E (ksi)		ν	β_t
	Slab	Dia.	Slab	Dia.	Slab	Dia.		
1	4.98	6.26	0.51	0.58	4061.50	4553.64	0.2	0.2-0.5
2	5.45	7.14	0.54	0.61	4248.83	4863.18	0.2	0.2-0.5
3	7.24	5.90	0.62	0.56	4897.12	4420.76	0.2	0.2-0.5

Table 5-1: Material Properties Input in Analyses

The stress relaxation multiplier was chosen to be 0.99. The sample analysis showed that the variation of these parameters had only a slight effect on the response of the specimens. Since three specimens were tested under cycling load prior to the final test, it was observed that the concrete slab was cracked before the ultimate test. This was not considered in simulation of the ultimate tests. The concrete tensile strength does not influence the ultimate capacity of the connection, but it affects the load-deflection behavior in the early stage of loading and strain distribution inside the specimens.

5.2.2.2.2 Compressive Behavior

The stress-strain behavior of the concrete material in ANSYS was linear up to crushing or cracking stress, and then it suddenly dropped to zero stress. This causes the element under the maximum tensile or compressive stress to fail and thus the entire model. However, in the real concrete structure, the nonlinear behavior of concrete before crushing allowed the critical elements to be more ductile and transfer part of their load to adjacent elements. To have a more accurate model, the concrete in compression was considered to be a multilinear-elastic prior to crushing in the conducted analyses. In this model, the uniaxial compressive stress-strain curve is assumed to be represented by using a parabola (Paulay, 1974)

$$\frac{\sigma}{f'_c} = \frac{2\varepsilon}{\varepsilon_0} - \left(\frac{\varepsilon}{\varepsilon_0} \right)^2 \quad (5-3)$$

$$\varepsilon_0 = \frac{2f'_c}{E_c} \quad (5-4)$$

where

ε_0 = Concrete strain at peak compressive stress f'_c . The value of ε_0 is almost constant at 0.0025 for normal-strength concrete.

ε = uniaxial strain (in/in)

σ = uniaxial stress (ksi)

f'_c = specified compressive strength of concrete (ksi)

E_c = modulus of elasticity (ksi)

It is noted that the finite element material model (as shown in Figure 5-7) cannot track the softening part of the strain-stress curve. As described previously, the failure surface, S , is a function of the ultimate uniaxial tensile strength, f_t , ultimate uniaxial compressive strength, f'_c , ultimate biaxial compressive strength, f_{cb} , ultimate compressive strength for a state of biaxial stress superimposed on hydrostatic stress state, f_1 , and ultimate compressive strength for a state of uniaxial stress superimposed on hydrostatic stress state, f_2 . At least two parameters, ultimate uniaxial tensile strength and ultimate uniaxial compressive strength, should be inputted to specify the failure surface based on the ANSYS default assumptions. ANSYS assumptions are valid for the stress state while the hydrostatic

stress component is less than f'_c multiplied by the square root of three. In the foregoing analyses, the ultimate uniaxial compressive strength is taken from the lab tests, ultimate uniaxial tensile strength is taken as AASHTO modulus of rupture, and the other parameters are assigned based on ANSYS defaults as follows:

$$f_{cb} = 1.2f'_c$$

$$f_1 = 1.45f'_c$$

$$f_2 = 1.725f'_c$$

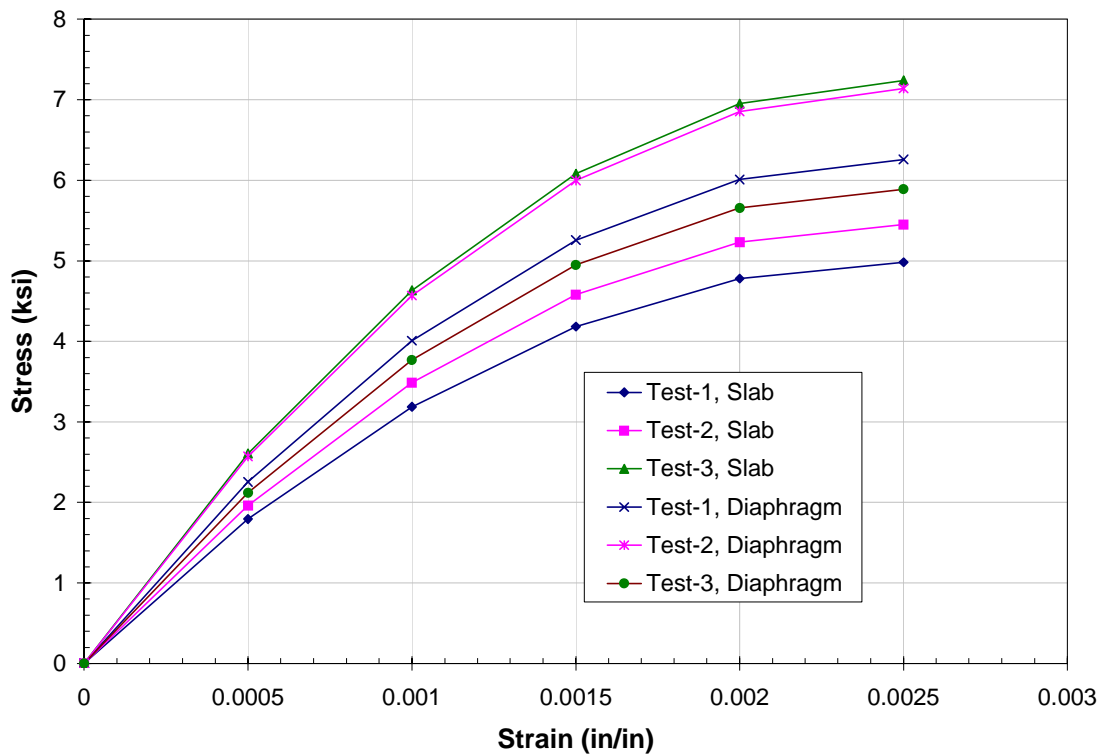


Figure 5-7: Pre-Peak Stress-Strain Plots for Concrete Material

The detail of a similar material model, three parameter model, is discussed in Appendix A of this report.

5.2.2.2.3 Shear Transfer Coefficient

The decrease of shear transfer capability across an existing crack is taken into account by introducing a coefficient. The shear transfer coefficient, t , represents conditions of the crack face. The value of t ranges from 0.0 to 1.0, with 0.0 representing a smooth crack (complete loss of shear transfer) and 1.0 representing a rough crack (no loss of shear transfer) (ANSYS, 1998). The value of t used in many studies of reinforced concrete structures, however, varied between 0.05 and 0.25 (Kachlakev et al., 2001). The choice of shear transfer coefficient is not critical if the value is selected between 0.1 and 0.5 (Chung, 2005). The shear transfer coefficient was set to 0.2 and 0.4 for the open and closed cracks, respectively. The finite element modeling of the concrete cylinder test showed that the greater shear transfer coefficient for the open crack results in compressive strength greater than the test results. The simulation indicates that very small shear transfer coefficient for the open crack caused numerical instability. The sample finite element analyses also showed that the numerical results were not very sensitive to the magnitude of the shear transfer coefficient for the closed cracks in tested specimens.

5.2.2.3 ELASTOMERIC BEARING PAD

The elastomeric bearing pad, Fiberlast, was made by Voss Engineering, Inc. Since all of the required mechanical properties of the employed bearing pad were not provided by the manufacturer manual, a compressive test was carried out in the Structural lab for more information. Based on the strain-stress curve of the material (Figure 5-8), the modulus of elasticity was taken as 7202 psi by a linear fit. It is noted that the beginning of the strain-stress response of the specimen was not linear due to the test errors and has been omitted in this plot. The Poisson's ratio is taken as 0.33 and the material is assumed to be elastic and linear in the analysis. The shear modulus is 230 ± 30 psi based on the manufacturer specification.

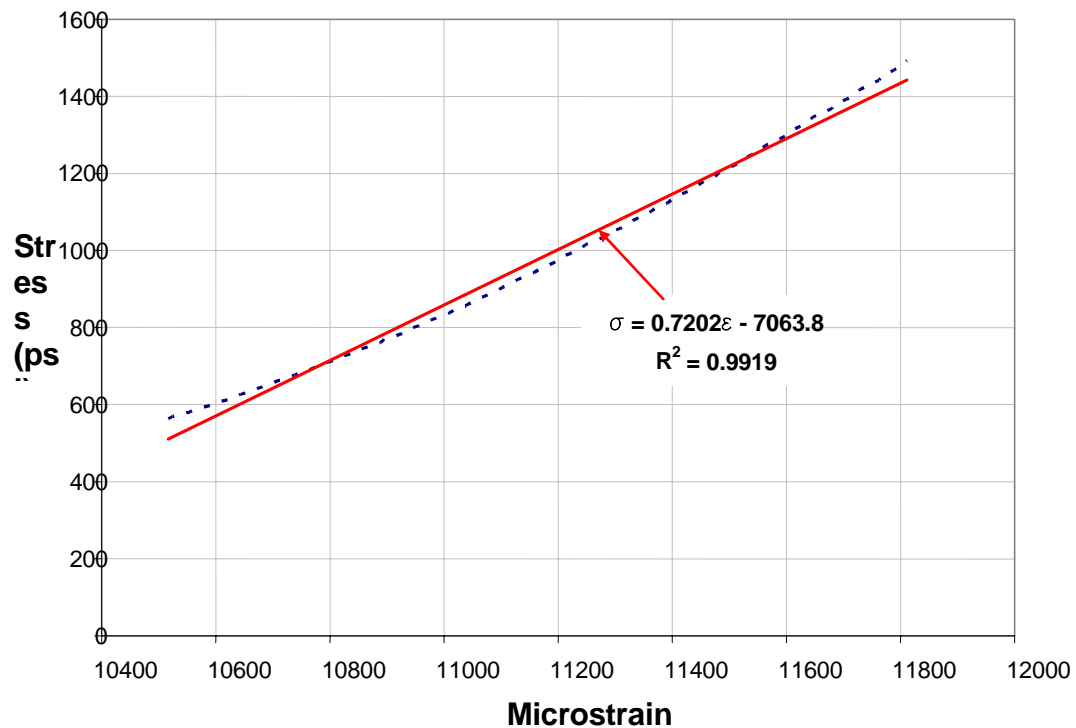


Figure 5-8: Part of Neoprene Stress-Strain Curve

5.2.3 ELEMENT TYPE

In the simulations, the rebar and stirrups inside the concrete were modeled using truss elements, embedded within the solid mesh. The shear connectors on the top flange, web shear bars, and loading beam were modeled by the beam elements. The flanges, web, and stiffeners were all modeled using 4-node shell elements. The concrete diaphragm and slab were simulated by 8-node brick elements. The element types used in modeling of test specimens are shown in Figure 5-9.

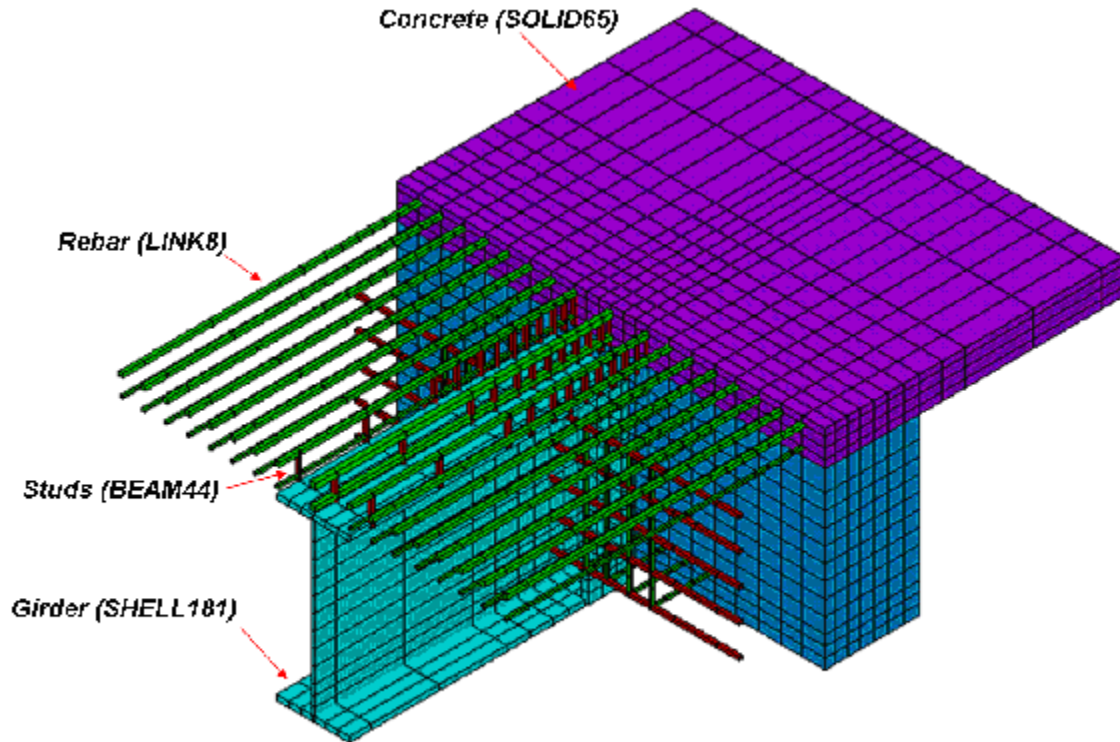


Figure 5-9: A Portion of a Finite Element Model of Specimens and Employed Element Types

5.2.3.1 LINK ELEMENT

The rebar and stirrups in the concrete (see Figure Figure 5-10) were modeled using three dimensional link elements, embedded within the solid mesh. This option was favored over the alternative smeared stiffness capability as it allowed the reinforcement to be precisely located whilst maintaining a relatively coarse mesh for the surrounding concrete medium. The LINK8 element in ANSYS has three translation degrees of freedom in each node. LINK8 has plasticity and large deformation capabilities. In this case reinforcement only can take the axial forces as a truss element. Ignoring the bending of rebar saved computation time and memory. To evaluate the accuracy of this model, more simulations were done while rebar were modeled by the beam elements. It was observed that including bending proper-

ties did not change the analysis results significantly. The cross section of each rebar was obtained by dividing of total reinforcement area from the test to the number of rebar in two layers in the slab.

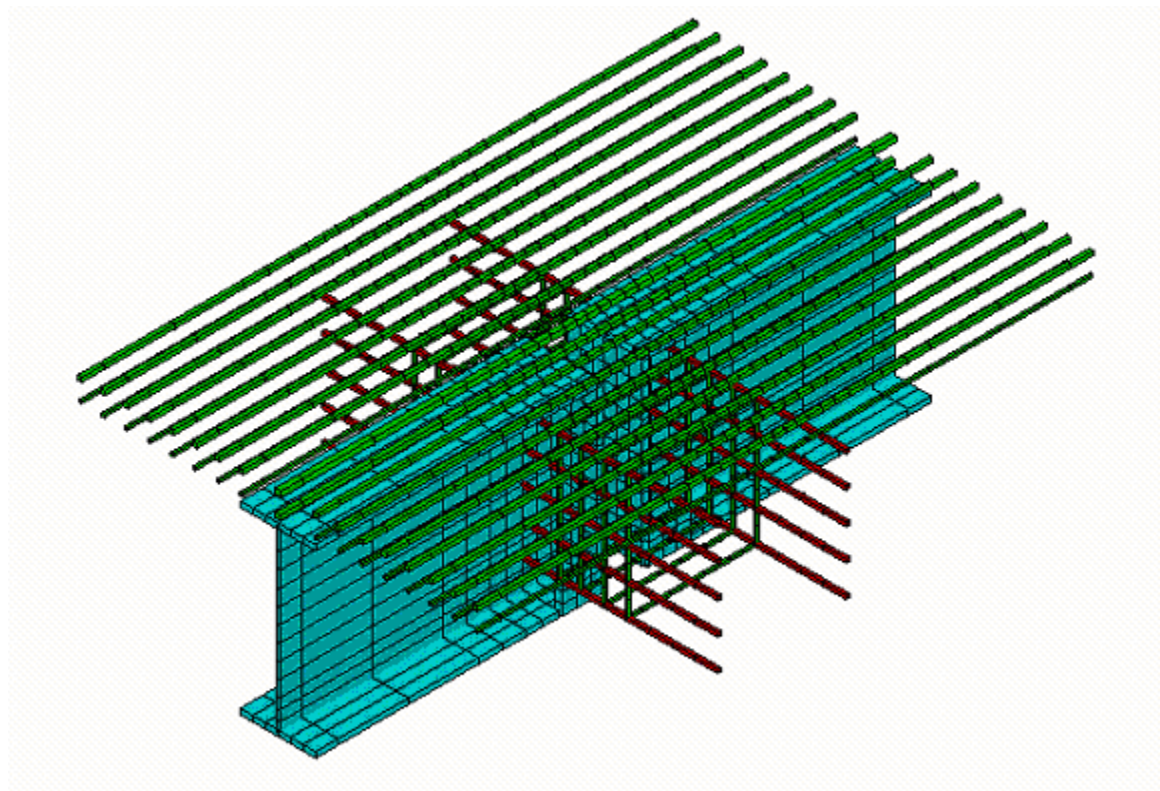


Figure 5-10: Modeling of Rebar and Stirrups with Link Elements

5.2.3.2 BEAM ELEMENT

The shear connectors on the top flange, web and loading beam were modeled by beam elements (BEAM44). BEAM44 in ANSYS is a 3-D elastic element with six degrees of freedom in each end. BEAM44 includes the bending, axial load, and torsion of the members. In some trial simulations, the slab reinforcements were created by this element to compare the results with the spar elements.

5.2.3.3 SHELL ELEMENT

The flanges, web, and stiffeners were all modeled using shell elements. SHELL181 is the name of the ANSYS element that was used. SHELL181 is

suitable for analyzing thin to moderately thick shell structures. It is a four-node element with six degrees of freedom at each node. It is well-suited for linear, large rotation, and/or large strain nonlinear applications.

5.2.3.4 SOLID ELEMENT

The concrete diaphragm and slab were simulated by 8-node brick elements (see Figure 5-11). The SOLID-65 (3-D reinforced concrete solid) of ANSYS element library was selected to model these parts. SOLID65 is suitable for the three-dimensional modeling of concrete members with or without reinforcing bars. The element is capable of modeling cracking in tension and crushing in compression. In concrete applications, the solid capability of the element was used to model the concrete while the rebar capability was sometimes used for modeling reinforcement behavior in some locations. The element is defined by eight nodes having three degrees of freedom at each node: translation in the nodal x, y, and z directions. Up to three different rebar specifications may be defined in this element type.

The elastomeric bearing pad was modeled by SOLID45. The element is a 3-D solid defined by eight nodes with three translational degrees of freedom at each node. The element has plasticity and large deformation capabilities.

5.2.4 MESHING

5.2.4.1 MESH SIZE

The detailed finite element analysis representing a realistic model required enormous elements that easily exceeded the limitation of the ANSYS program. In order to optimize the mesh refinement considering such limitation, the mesh size of different parts of the model was chosen to be variable, depending on the required accuracy. In the regions that might have yielding and crushing, the element size was finer than regions with elastic behavior throughout of the analysis. For example, mesh size at the bottom of the concrete diaphragm close to the beam bottom flange was

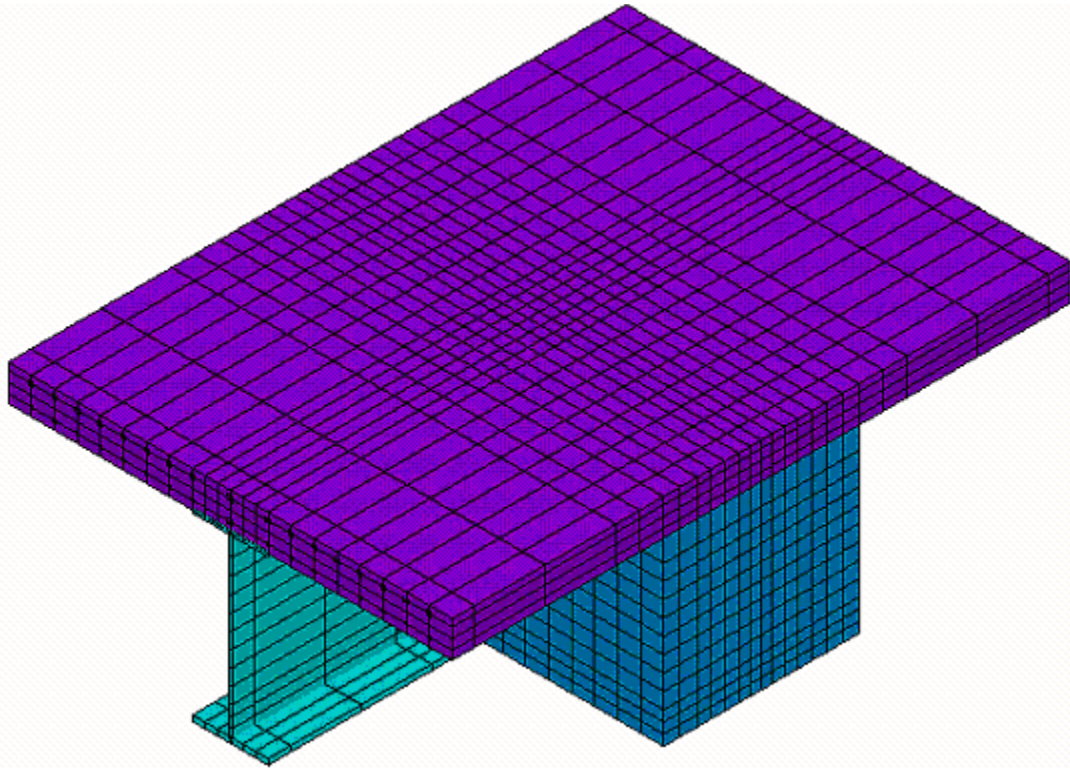


Figure 5-11: The Concrete Slab and Diaphragm Modeled by Solid Elements.

considered to be as fine as possible since crushing of concrete in this region caused instability of the analysis very fast. A mesh size was chosen to keep the aspect ratio of elements approximately close to one. All of the elements had right angles at their corners.

The meshing of a typical model is shown in Figure 5-12. The finite element mesh was selected such that the flanges, stiffeners, and gusset plate were divided into at least four elements along their width. The web was divided into at least 12 elements along its depth and 12 elements along its length. The diaphragm was meshed to have at least two elements between end bearing plate and end support. The number of elements along the diaphragm's depth was the same as the web's to maintain connectivity. The concrete slab divided along its depths into at least three solid elements due to two layers of reinforcement. The division of concrete slab along transverse direction was set to the spacing of the longitudinal rebar. The meshing of the slab along the longitudinal direction was the same as the web and

the diaphragm. The longitudinal rebar and the transverse stirrups had the same meshing pattern as that of the slab and diaphragm.

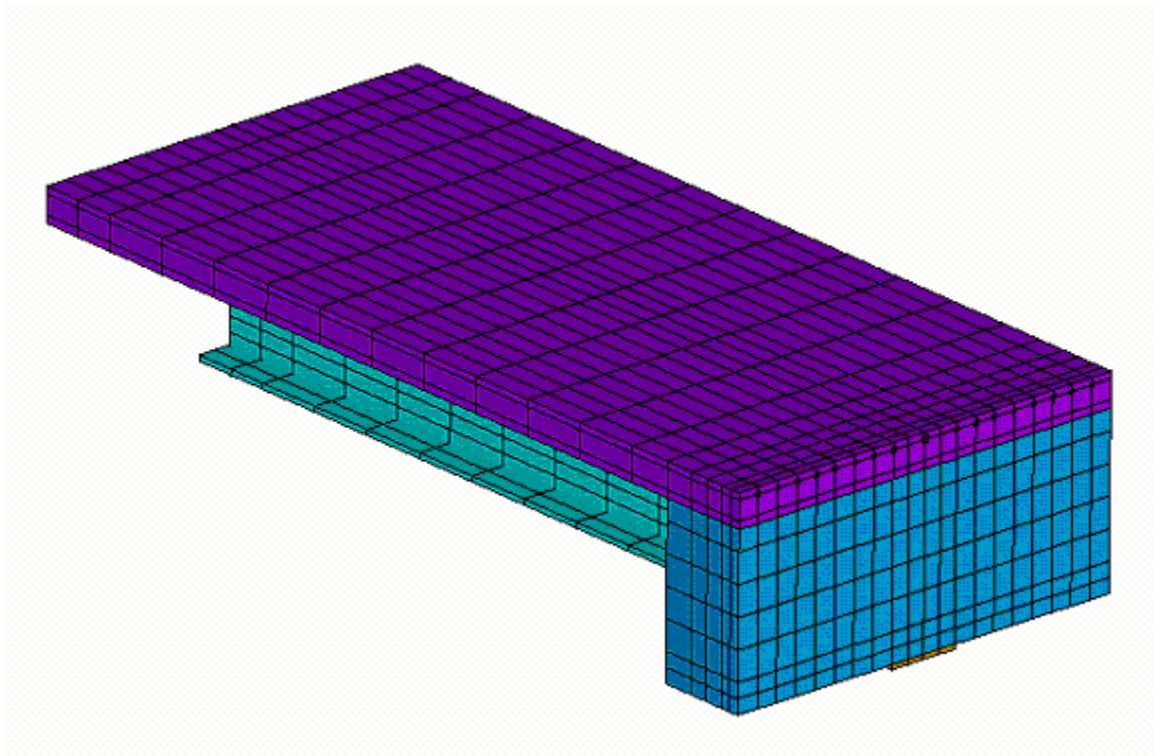


Figure 5-12: Typical Meshing of Symmetric Model

5.2.4.2 MESH SENSITIVITY

To check the numerical accuracy of the mesh, the first test was created using two different mesh sizes for each part of the model. The coarser mesh model was according to the description presented in the previous section. The finer mesh model had almost twice as many degrees of freedom as the original mesh (coarser mesh). The effect of this mesh refinement on the load-deflection behavior of the first test can be seen in Figure 5-13. The figure shows that the finer mesh produces results that are close to the original mesh. Although, the finer mesh took longer to run, for verifying experimental results the finer mesh was preferred.

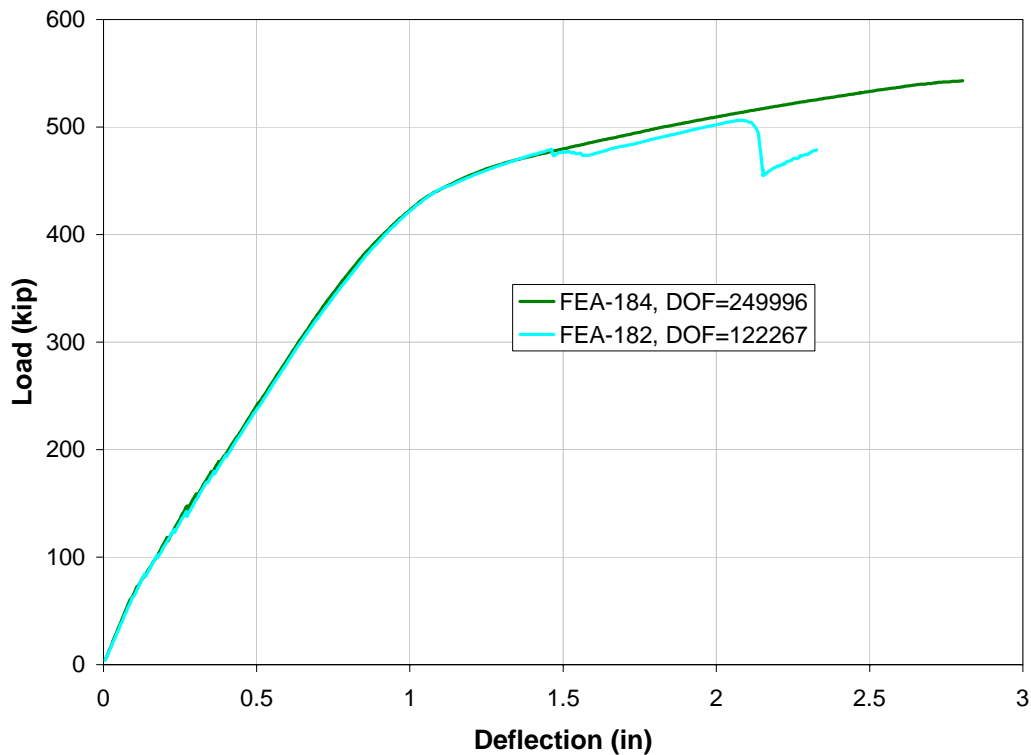


Figure 5-13: Analysis of the First Specimen with Two Mesh Sizes

For the third specimen, as seen in Figure 5-14, it was observed that downsizing the mesh would result in a smaller ultimate capacity than the actual test data. The mesh sensitivity analysis of a cube test also showed the same result. That is, larger element size exhibits higher ultimate strength and stability than a smaller size. Local stress concentration in the cube caused smaller elements to crush or crack sooner than larger elements, since the distance of Gauss points at which the stress state is calculated is greater in larger elements. In larger elements, if the stress state at a Gauss point passes the failure surface, there is a modification of the stress stiffness matrix inside the element. However, the same condition in a smaller element causes all eight Gauss points to fail. Therefore, element stiffness in the structure stiffness matrix diminishes which might lead to faster numerical instability.

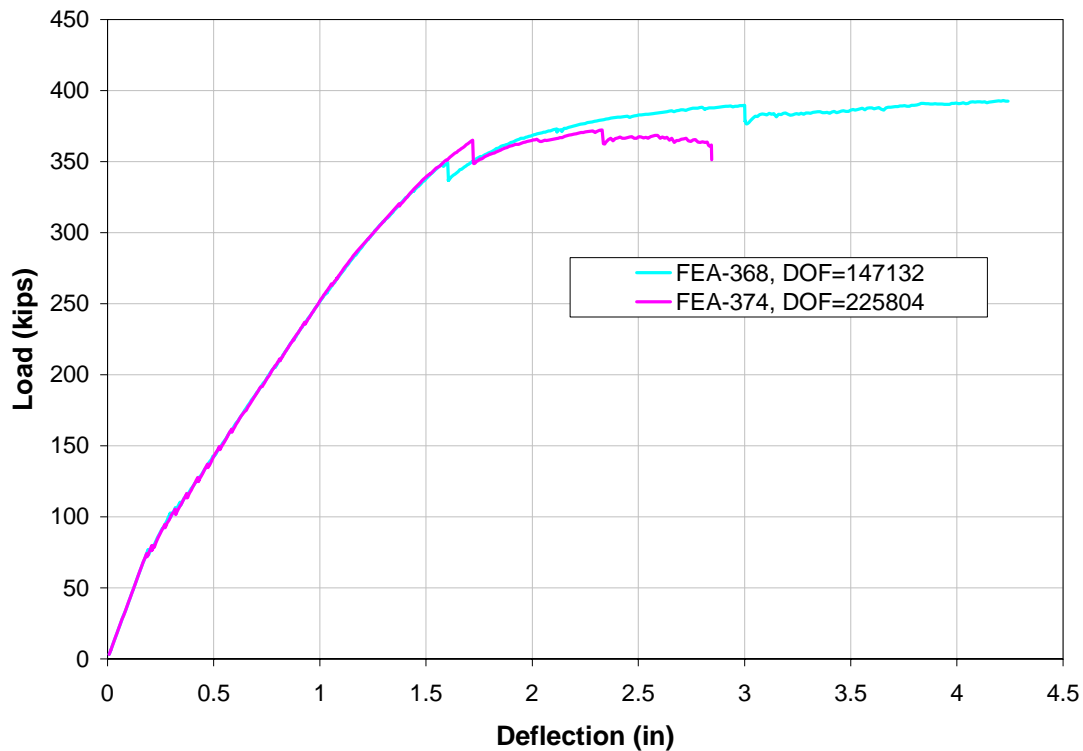


Figure 5-14: Analysis of the Third Specimen with Two Mesh Sizes

5.2.5 ELEMENT CONNECTIVITY

The shell elements were used to create the plates with zero thickness in the finite element model. Thus, there will be a slight deviation from actual physical models arising from plate to plate connections. To modify this problem, the half of each flange thickness was added to the depth of the web. The same procedure was conducted to correct the zero thickness of stiffener plates in their junctions with flanges and webs. Applying these modifications, the total depth of the section and the distance between members were as the physical specimens.

Connection of the top flange and the slab was provided by an adequate number of shear studs, so it was assumed to be fully attached. Also, in the experimental program, no slippage was observed between the concrete slab and the top flange. Two sample analyses were conducted to check the

validity of this assumption. In the first analysis, Test one was modeled by including three rows of shear studs as the physical model and in the second analysis the studs were removed and the flange was connected to the slab by their common nodes. It was observed that the difference between these two analyses was slight. However, the shear studs were modeled in the following simulations for proper shear transfer in the slab as will be explained later in this chapter.

The interface of the steel beam web and the adjacent concrete diaphragm was modeled to have slippage. However, they were connected through shear bars passing through the web and diaphragm. The analysis of Test one shows that including or ignoring the slippage between web and diaphragm does not affect the load-deflection response significantly. However, it affects the yielding, cracking and crushing pattern of the specimens. In addition, the web movement relative to the adjacent diaphragm was observed in Test two. The sample finite element analysis of Test two with and without considering slippage is shown in Figure 5-15. In this plot only the first part of the load-deflection curve is shown. It is seen that the actual behavior of the specimen is somewhere between a slipped model and a fully connected one. Also, the interface of the concrete diaphragm and the end bearing plate was assumed to be fully connected, since they were in compression in critical regions.

The elastomeric bearing pad did not have any tensile bond to the beam bottom flange in the actual physical tests. However, it was observed that the reaction of the bottom flange on the bearing pad was compressive in all tests, thus the interface can be assumed to be in contact and connected in the vertical direction. However, it was observed in Test two and Test three that the bottom flange was moving horizontally which means slippage exists between the bearing pad and the bottom flange. The horizontal relative movement between pad and beam was modeled by using roller-type boundary conditions at the bottom of bearing pad.

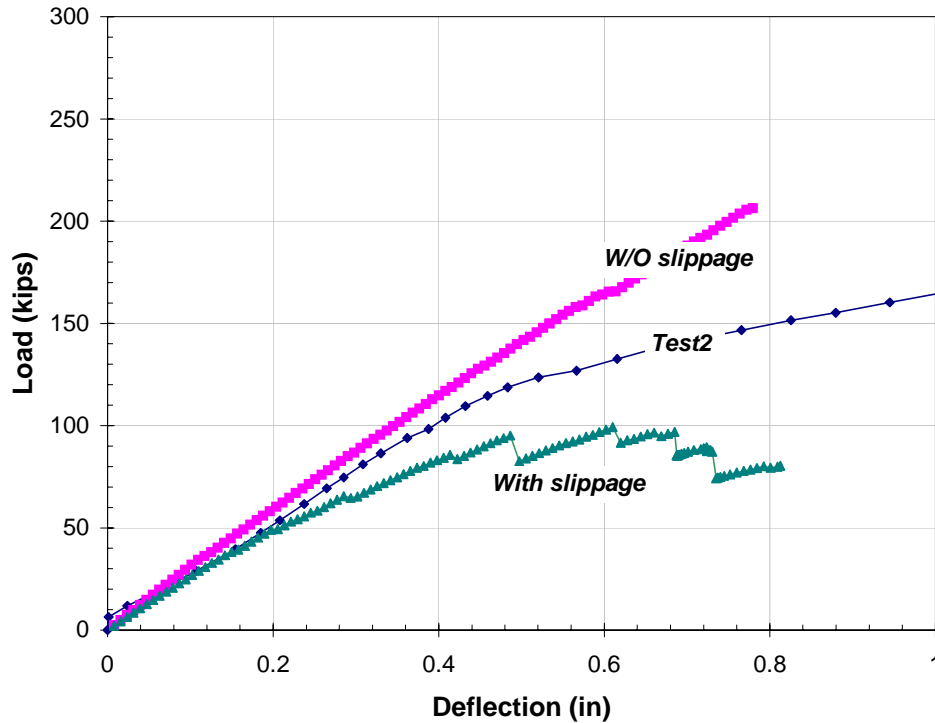


Figure 5-15: Effect of Slippage on Load-Deflection Response for Second Specimen

The steel rebar connected to the concrete slab solid element at their common nodes. The inherent assumption was the full displacement compatibility between the reinforcement and the concrete and that no bond slippage occurred.

The loading beam was resting on the concrete slab in the testing program. The loading beam was connected to the slab through several common nodes along the width of the concrete deck. This assured the distribution of the applied load across the slab more precisely to prevent the local effect of concentrated loads.

5.2.6 BOUNDARY CONDITIONS AND LOADING

In several models to save computation time, only half of the specimens were modeled due to the symmetry (see Figure 5-12). The symmetry of the tests required having fixed boundaries at the centerline of the pier. Thus, the translation of the diaphragm nodes at the end were restrained in the

three directions of x , y , and z . Another reason to restrain the diaphragm boundary in the transverse direction was crushing of the concrete. The sample analysis showed that an unrestrained diaphragm in the transverse direction would crush at a lower load level than actual test. The restraints in the three directions increased the hydrostatic stress of the solid elements and increased the radius of the failure surface. The full modeling of the specimens (Figure 5-11) indicated that even the full restraining of the nodes at the pier centerline did not resemble the actual behavior of concrete elements. For this reason, for the verification of strain results the full model (Figure 5-11) was also used in combination with the symmetric model.

The boundary conditions at the bottom of the elastomeric bearing pad were set to be as a roller, thus only vertical translations of the nodes were fixed and the other degrees of freedom were free for movement.

In the actual tests, the load was applied by two rams at the ends of the loading beam. Since hydraulic rams were under oil pressure that could not return during the loading, it was assumed that the load pattern was more displacement control than load control. Based on this assumption two equal incremental displacements were applied at the ends of the loading beam to resemble the experimentation.

5.2.7 SOLUTION STRATEGY

The analysis type was chosen to be static, since the tests were performed with a very low rate of monotonic loading. The analysis was conducted under a small deformation solution strategy for three reasons. First, it was noticed from the test results that the maximum measured strain in the steel material was well below the steel ultimate strain. Second, no out-of-plane deformation was observed in the steel beam. Third, the ANSYS manual does not recommend applying the crushing and cracking nonlinearities concurrently with the large deformation capabilities of SOLID65.

5.2.7.1 NONLINEAR ANALYSIS SOLVER

The solution method used for all analyses was the Newton-Raphson method. The type of Newton-Raphson was set to be full since the sample analyses showed it was more accurate than the modified method. The Arc Length method was used as an alternative for the Newton-Raphson technique but the solution did not converge at the cracking level of the structure. Before each solution, the Newton-Raphson method evaluates the out-of-balance load vector, which is the difference between the restoring forces (the loads corresponding to the element stresses) and the applied loads. The program then performs a linear solution, using the out-of-balance loads, and checks for convergence. If convergence criteria are not satisfied, the out-of-balance load vector is re-evaluated, the stiffness matrix is updated, and a new solution is obtained. This iterative procedure continues until the problem converges. If convergence cannot be achieved, then the program attempts to solve with a smaller load increment.

Two different solvers, Frontal Solver and Sparse Direct Solver, were used to solve the nonlinear equations. The sample analysis showed that both solvers had almost the same performance, but it was preferred to use the Frontal Solver method due to lower memory usage when compared to Sparse Direct Solver.

The force and moment tolerance were playing important roles in convergence of the nonlinear solution. If the convergence value was set to small values, the program did not converge even at early stages of loadings due to the nonlinearity caused by the concrete cracking. The convergence value was set to ANSYS default which was calculated based on SRSS (Square Root of Sum of Squares) norm and applied loads. But, for the faster convergence, the default ANSYS tolerance value was loosened one order of magnitude.

5.2.8 LOAD STEPS

The model was loaded, through applied displacement to facilitate easier convergence, in a manner consistent with the test program as it was mentioned earlier. Since the specimen experienced different phases of behavior, it was decided to apply the displacement in multiple load steps based on the test observations. The size of the displacement increment applied to the model was determined based upon the tests' load-deflection results. In each load step, a different time step was employed considering the accuracy and economy. In the first load step, steel did not yield and the only nonlinearity in the structure was the cracking of concrete in tension parts. The next load step was started from the point that concrete started crushing and a large curvature was seen in the load-deflection plot of the tests. The last load case was initiated after yielding of steel material, mainly top rebar. Based on this load scheme, appropriate time step and iteration number was selected for the nonlinear solution.

Each load step was divided into several time steps by using ANSYS Automatic Time Stepping Algorithm. The maximum size of each time step was limited to the 0.01 of each load step and minimum time step was set to 0.0001. To check the sensitivity of the step size, Test one was run with 0.01 and 0.0001 time-step size. The results from the different increment sizes were very close, however and it was concluded that the smaller 0.0001 time step size would be more accurate (see Figure 5-16).

For all the modeling cases, a sufficient number of convergence studies have been made, and the final analyses carried out using the refined model. Considering the overall length of this chapter and the importance of other material presented, the results on convergence studies are not included here.

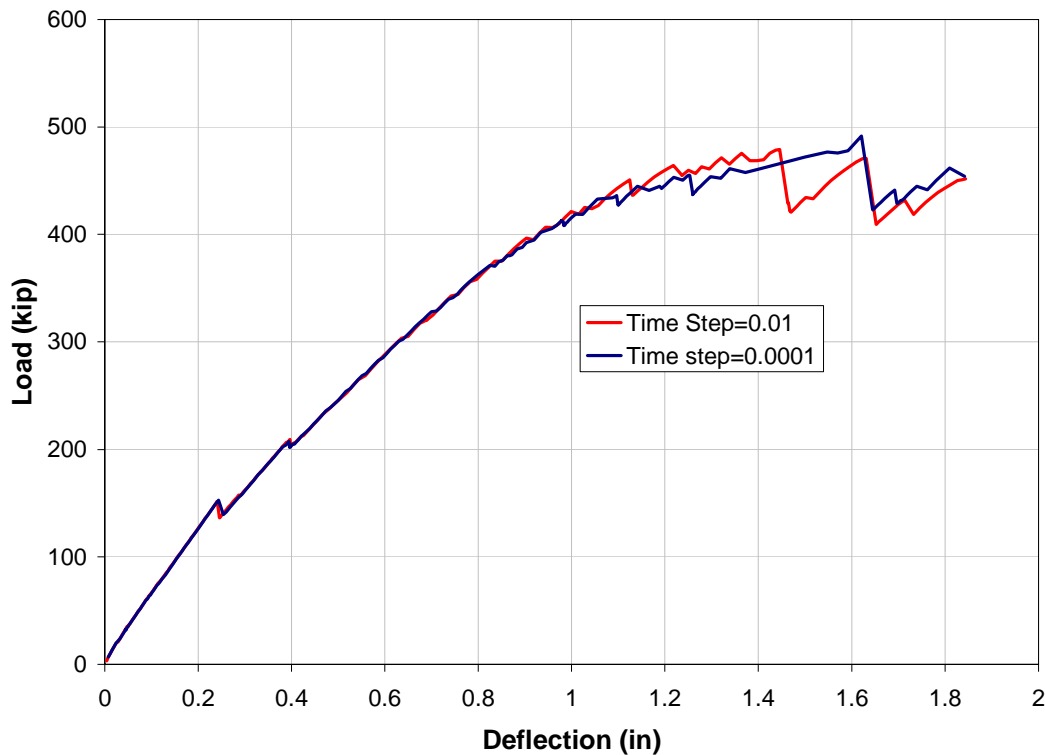


Figure 5-16: Analysis of the First Specimen with Two Time Step Sizes

5.3 EXPERIMENTAL VERIFICATION

5.3.1 FAILURE MECHANISM

The ultimate loads obtained from the finite element analysis and those of the test results have been listed in Table 5-2. The test results presented in Table 5-2 are an average of the east and the west girders. It should be noted that there was not a distinct border to define the collapse of the specimens in numerical simulations because the accuracy of the solution strategy can change the ultimate load capacity. The parameters such as mesh size, force convergence criteria, and time step in numerical analysis can change the failure capacity of a model. It was observed through many trials finite element analyses that the specimens could still resist loads after yielding of all rebar and crushing of the concrete if the force convergence criteria was large. Of course, this did not match the experimental observations. To

determine the failure capacity of the specimens in numerical analyses, the yielding of all rebar or the crushing of concrete, whichever occurred later, was considered the failure point

Specimen	Ultimate Load (kip)		Ratio	Deflection (in)		Ratio
	Test	FEA	FEA/Test	Test	FEA	FEA/Test
1(182)	516	532	1.03	2.31	2.41	1.04
2(265)	263	245	0.93	4.15	4.00	0.96
3(368)	390	372	0.95	4.05	2.84	0.70

Table 5-2: Experimental and FEA Results at the Ultimate Condition

The load deflection response of the first, second and third specimens obtained from the test program are shown in combination plots with the finite element results in Figures 5-17, 5-18, and 5-19, respectively. In the experimental program, there were two identical cantilever girders in each test specimen. The load and the deflection of each cantilever was measured independently. The responses of these cantilever beams were designated with letters E (east girder) and W (west girder) on the plots.

The finite element result was checked in linear range using hand calculation and test data. The deflection of the ends of cantilever beams was calculated from a linear theory based on the un-cracked and cracked concrete material property of the first specimen. The end deflection of the cantilever was 0.11 inches at load 100 kip using un-cracked section properties. This deflection was 0.14 if the cracked section properties were used in cal-

culations. The deflection was 0.18 inches from the finite element analysis and 0.19 inches from the Test one results at a load of 100 kip.

For all of the three specimens, it was observed that that the responses of the models were nonlinear from the initial stage of loading due to cracking of the concrete slab. The measured response of the specimen beams from ultimate tests were, initially, slightly less stiff than the finite element results. This was due to the cracks remaining in the slab from the cycling tests. It was noticed that the load-deflection of the specimens had good agreement with the finite element results during the cycling tests because the concrete was almost un-cracked. Beyond the cracking point, the almost linear response of the finite element model was consistent with the test data up to the yielding of the steel.

It can be seen in Figure 5-18, and Figure 5-19 that the load drops in some points, especially in the nonlinear range. In the displacement control solution strategy, the load resistance of the structure decreased sharply after cracking or crushing of each concrete element. In the load-control solution, this pattern was not exhibited, but there were flat slope regions.

In the first specimen, the first yielding occurred in the bottom layer of reinforcement of the slab, and after that the bottom plate that connected the two girders yielded (see Figure 5-17). In the test program, the yielding of the rebar also occurred before the yielding of bottom plate. The core concrete at the edge of the end bearing plate crushed after yielding of the bottom flange. The yielding of all rebar occurred after the local crushing of the concrete. The mode of failure predicted using the numerical model was a flexural mode of failure, consistent with the test response, due to increasing plastic strains developed in the tension reinforcement.

The numerical analysis of the second specimen was not very stable since concrete crushing occurred in the early stages of loading, as seen in Figure 5-18. In the second specimen, crushing of the concrete occurred

before yielding of the rebar. The yielding of only the top layer reinforcement of the slab caused the failure of the specimen (see Figure 5-18). The load resistant stages were almost similar to what was extracted from the experimental observations. However, the load level in each step was different.

In the third specimen, the yielding was initiated in the slab rebar and crushing occurred after the partial yielding of the slab bars. The failure occurred upon yielding of all slab reinforcements. Although the specimen showed resistance after the crushing of the concrete, the load capacity of the specimen did not exceed the load level achieved at the concrete crushing. There was a difference between experimental observation and finite element analysis. The finite element results showed that all the top layer rebar did not yield before concrete crushing, but the test observations implied that the crushing might have occurred after yielding of all reinforcements.

The general behavior of the specimens was similar to reinforced concrete beams. In the first specimen, the bottom plate was similar to compression reinforcement, which protected the concrete from premature crushing before entire yielding of the tension reinforcements. In the second specimen, the contact area between concrete and steel was very small, so the crushing of the concrete occurred before the yielding of the tensile rebar. The specimen was similar to an over-reinforced concrete beam. In the third specimen, the behavior was somewhere between specimen one and two. The crushing of the concrete in this specimen occurred after the first yielding of the reinforcement, but before the entire yielding of all the slab bars.

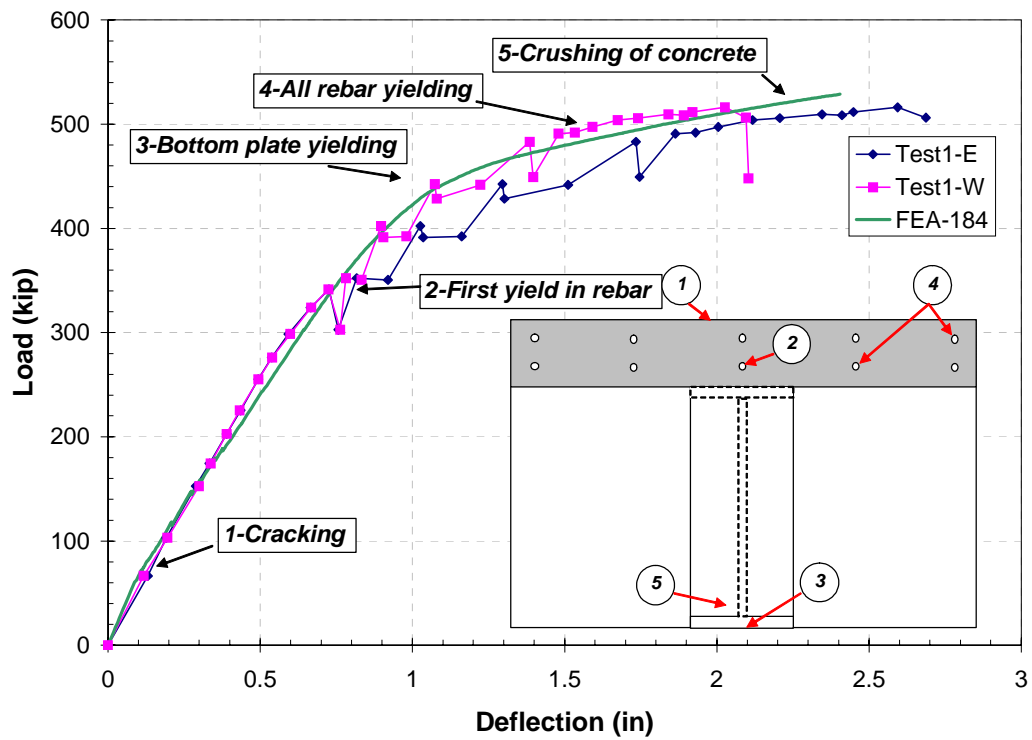


Figure 5-17: Load vs. Deflection for the First Test

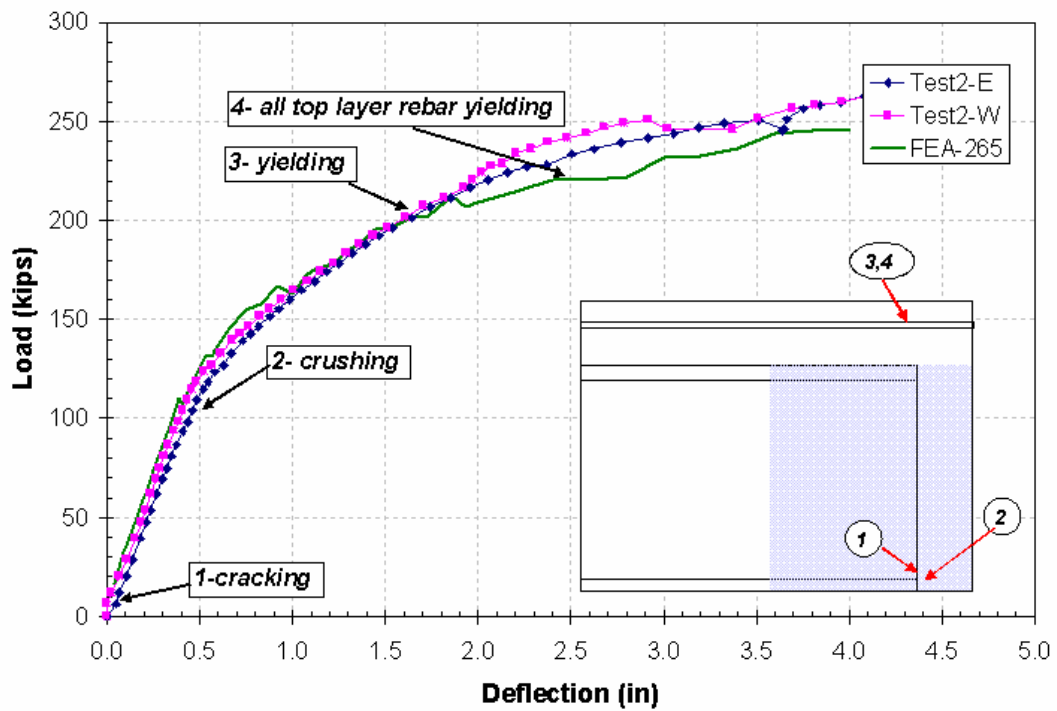


Figure 5-18: Load vs. Deflection for the Second Test

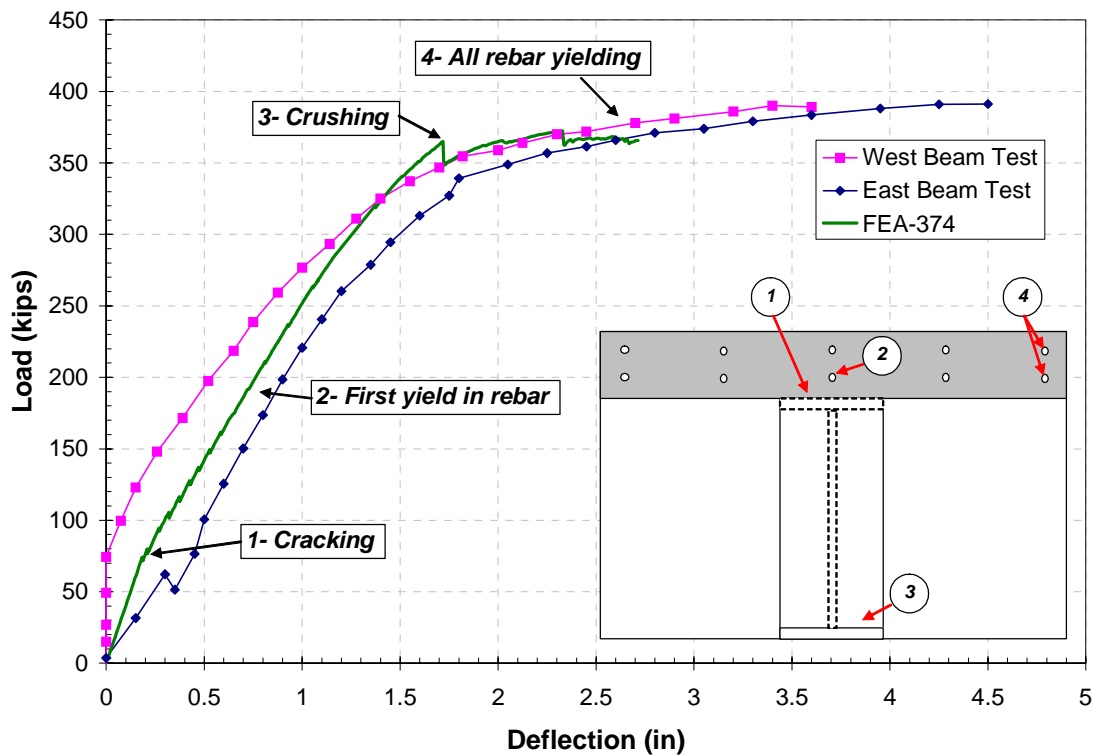


Figure 5-19: Load vs. Deflection for the Third Test

5.3.2 CRACKING BEHAVIOR

The first visible crack was reported before the cycling tests. There was not a direct indication of cracking load during the ultimate test in the experimentation records. However, the cracking maps were drawn from the cycling tests as mentioned in the Experimental chapter. If a linear strain-stress curve is adopted for the concrete in the tension region, the cracking strain is approximately 126 microstrain. The strain was calculated based on the tensile cracking strength and elasticity modulus of concrete described in the Chapter 4. Assuming that the top rebar strain was almost the same as the concrete slab strain before cracking, the results from the first test showed that the top rebar, and thus its surrounding concrete, reached the cracking strain at a load magnitude of about 30 kip.

The finite element analysis of the first specimen showed that the first cracks were formed on the concrete slab at the edge of diaphragm at a load of 53 kip as shown in Figure 5-20. The second cracks were observed at the centerline of the pier immediately after the first cracks. These cracks propagated all over the slab. It was noted that the transverse cracks were also observed on the deck underneath the loading beam from the beginning of loading, but since these cracks were far from the critical section, they did not significantly contribute in the structural behavior of the system. The tensile cracks at the bottom of the concrete core formed at a load of 188 kip. These cracks were a consequence of divergence of compression force inside the core concrete.

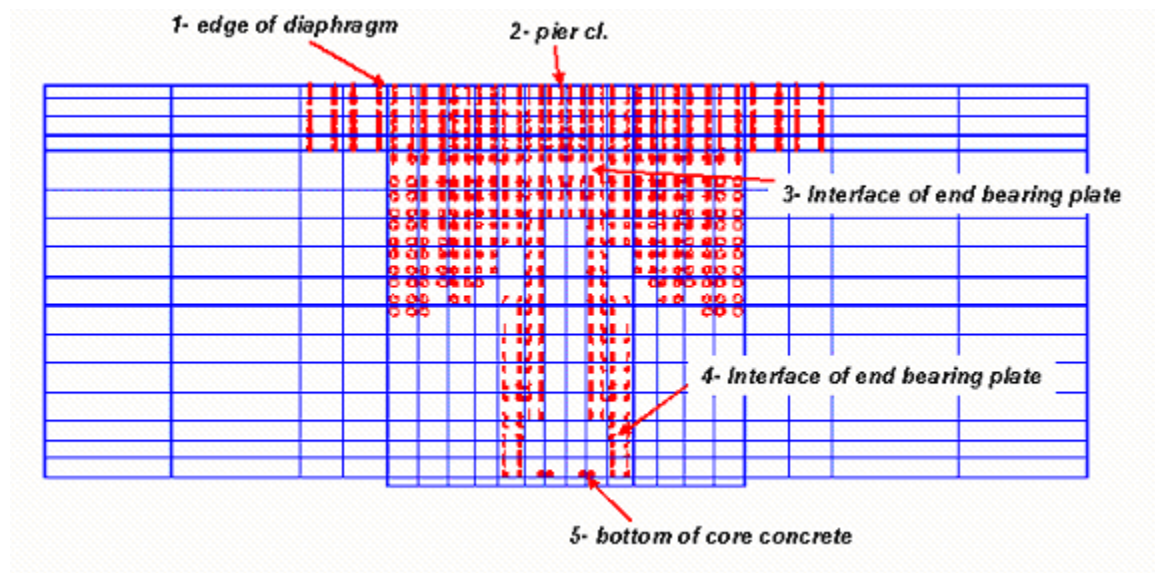


Figure 5-20: Longitudinal View of the Cracks in the First Specimen

The finite element analysis of the second specimen showed that the first cracks were formed inside the concrete diaphragm adjacent to the bottom flange from the very beginning of loading (see Figure 5-21). That was due to the movement of the bottom flange into the concrete and separation of

the steel from its surrounding concrete. The second cracks were observed in front of the web plate inside the concrete core. The planes of these cracks were parallel to the web plane and were due to the Poisson's effect. The third cracks were observed at the centerline of the pier due to direct tension in the concrete.

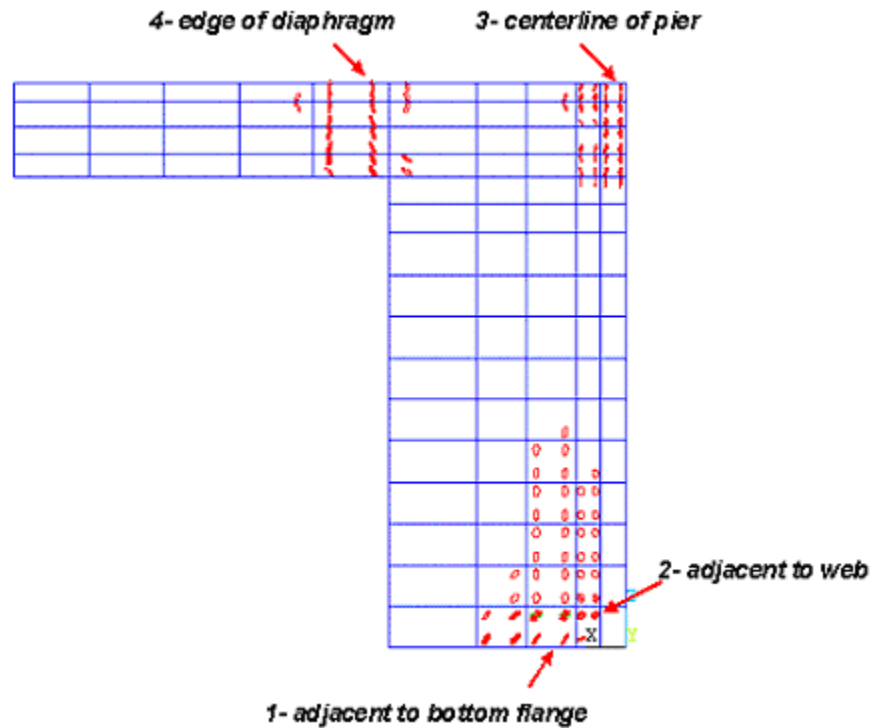


Figure 5-21: Half-Symmetric View of Diaphragm and Slab of the Second Specimen

The finite element analysis of the third specimen indicated that the first cracks were formed at the interface of top flange and the diaphragm at about 49 kip. As shown in Figure 5-22 the second cracks were observed at the bottom of the diaphragm behind the end bearing plate due to the separation of the end bearing plate and the concrete diaphragm. The next cracks were observed at the pier centerline. These cracks propagated all over the slab thereafter. The tensile cracking due to compression at the bottom of the core concrete was formed at about 110 kip (Figure 5-22).

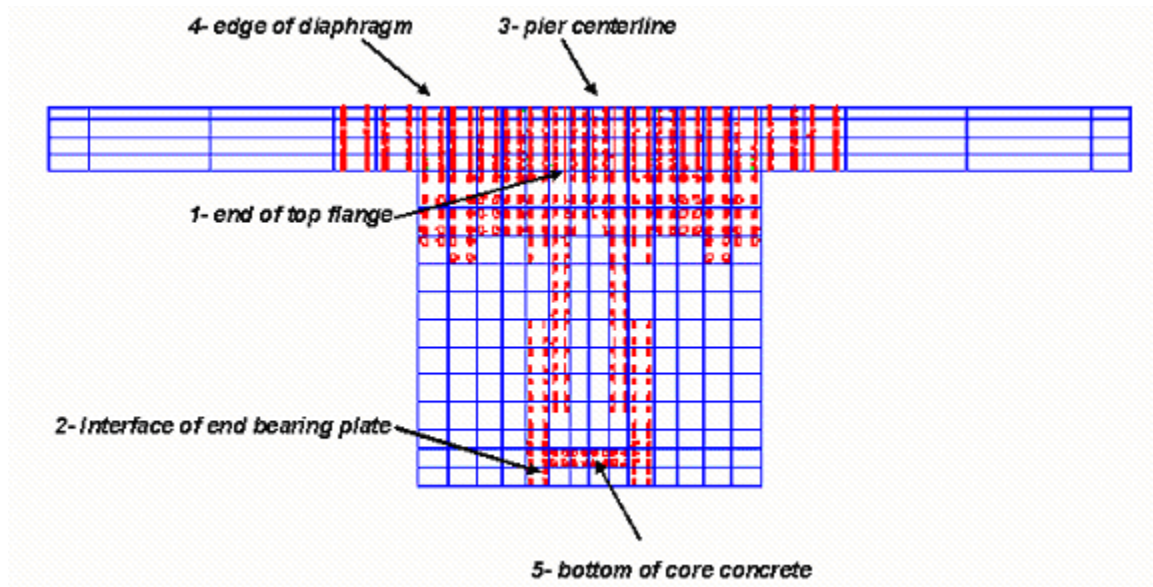


Figure 5-22: Longitudinal View of Cracks in Diaphragm and Slab of Third Specimen

5.3.3 YIELDING

In the first specimen, based on a fully cracked section at the centerline of the pier, the classical reinforced concrete theory predicted that the tensile reinforcement yielding would commence at approximately a load of 300 kip. The first yielding was recorded at the top layer reinforcement near the girder centerline at a load of 341 kip during the first test, which was consistent with the change in slope of the load deflection response of the east test beam. The numerical results indicated that first yielding onset would be at the bottom layer rebar near the girder centerline at a load of 340 kip (Figure 5-17). However, the test results showed that the first yielding occurred at the top layer reinforcement near the girder centerline at load value of 341 kip. The reason for the discrepancy was the poor shear transfer capability of concrete elements after cracking in the smeared crack

model. The first yield in the top layer rebar appeared at 346 kip, which matched the experimental results. The entire top layer rebar yielded at a load of 422 kip. All of the rebar yielded at a load of 500 kip (Figure 5-23). The distribution of the strain in the top layer rebar after the onset of yielding in this layer was compared with the test results in Figure 5-25. The bottom flange reached yield at a load of 280 kip from FEA (Figure 5-24). There was not any strain gages mounted on the bottom flange between the end bearing plate and the edge of the diaphragm to verify the finite element results. However, the bottom connecting plate yielded at a load of 346 kip in the actual test. Finite element analysis showed that the bottom connecting plate yielded at a higher load of 450 kip. Therefore, the finite element results did not track the test data. The entire slab layer reinforcements reached yield at the ultimate condition as it was observed in the experimental test.

In the second test, the first yield was observed in the top layer reinforcement of the slab at the girder centerline at about 210 kip. The numerical simulation also showed that the first yield occurred at the top layer rebar at 200 kip. The strain distributions of the top layer of rebar at the centerline of the pier obtained from the finite element analysis and test are shown in a combination plot in Figure 5-26.

The test results of the third specimen were not available to compare with the numerical data. The finite element results are shown in Figure 5-27. The sequence of yielding of the top layer reinforcement for the three specimens was shown in Figure 5-28. For the comparison purpose, the girder moment at the centerline is plotted versus the horizontal location of each bar. Notice that the first and third specimens have a similar yielding pattern.

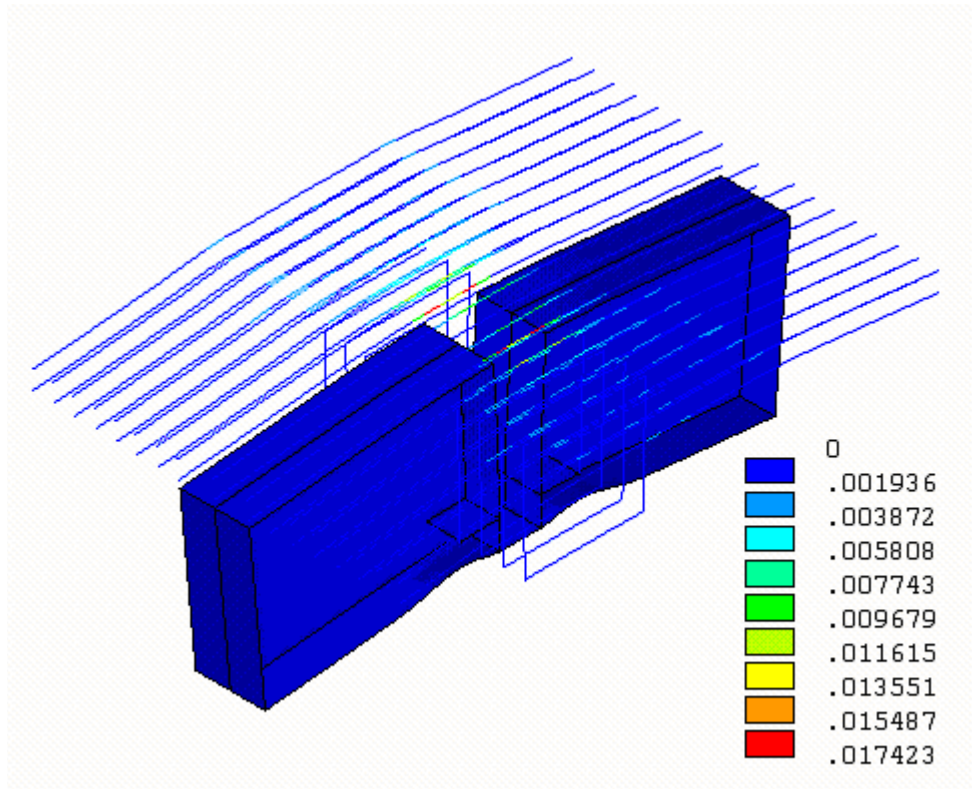


Figure 5-23: Yielding of the Slab Rebar in the First Simulation (in/in)

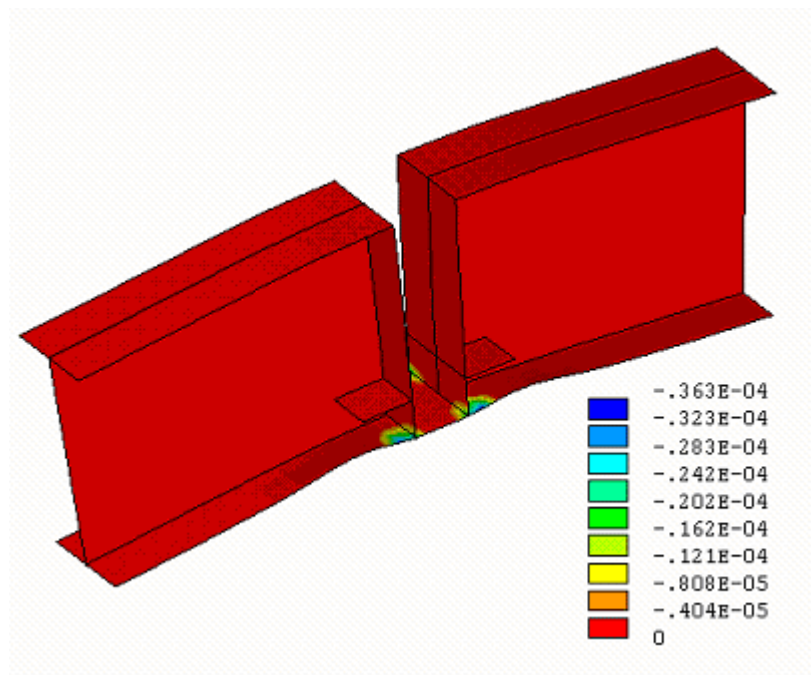


Figure 5-24: Initiation of Yielding in the Bottom Flange in the First Specimen

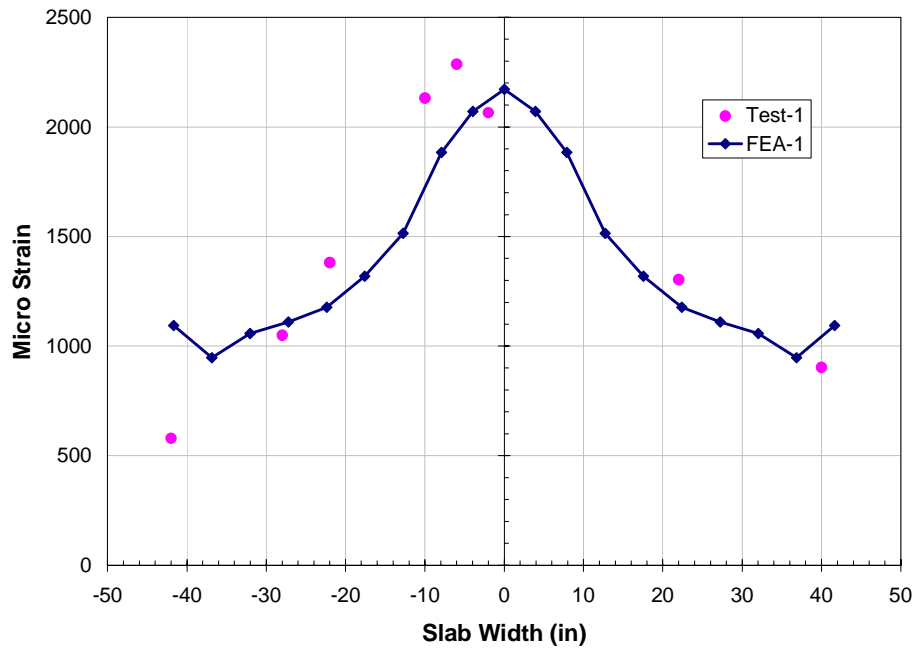


Figure 5-25: Strain Distribution in Top Layer of Rebar at First Yield at the Pier for the First Specimen

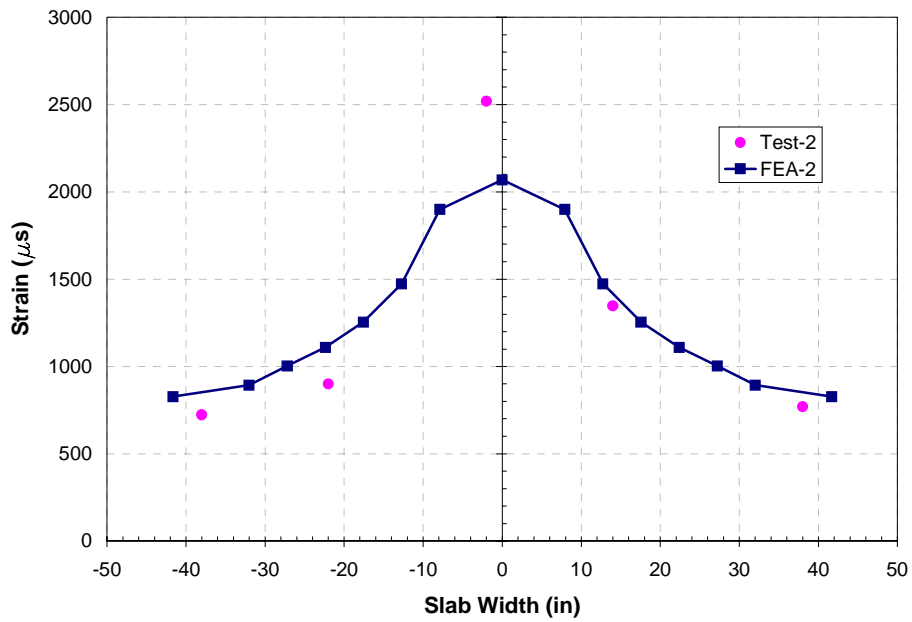


Figure 5-26: Strain Distribution in Top Layer of Rebar at First Yield at the Pier for the Second Specimen

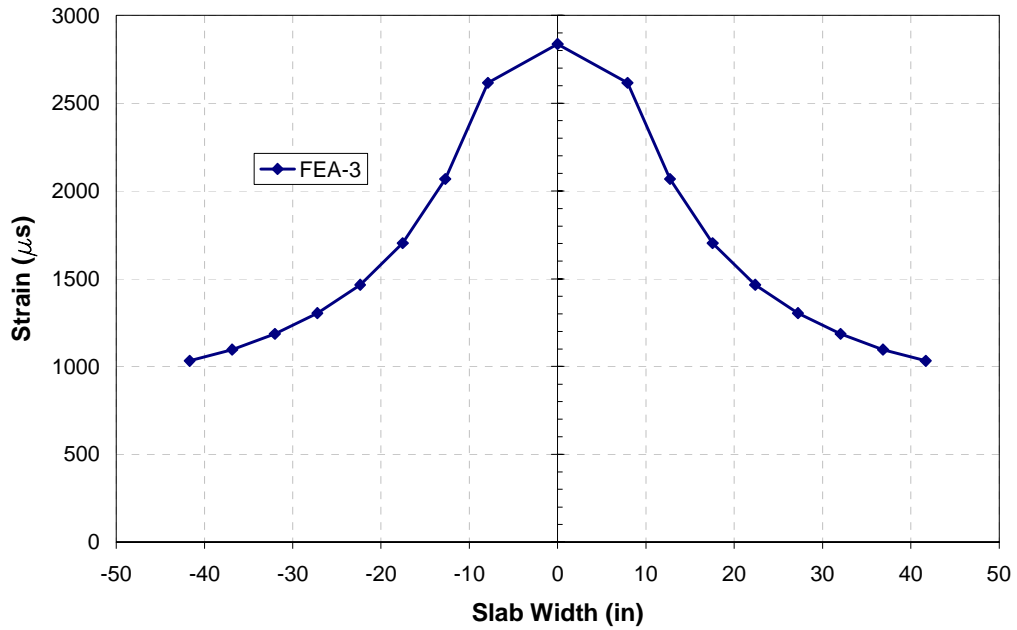


Figure 5-27: Strain Distribution in Top Layer of Rebar at First Yield at the Pier for the Third Specimen

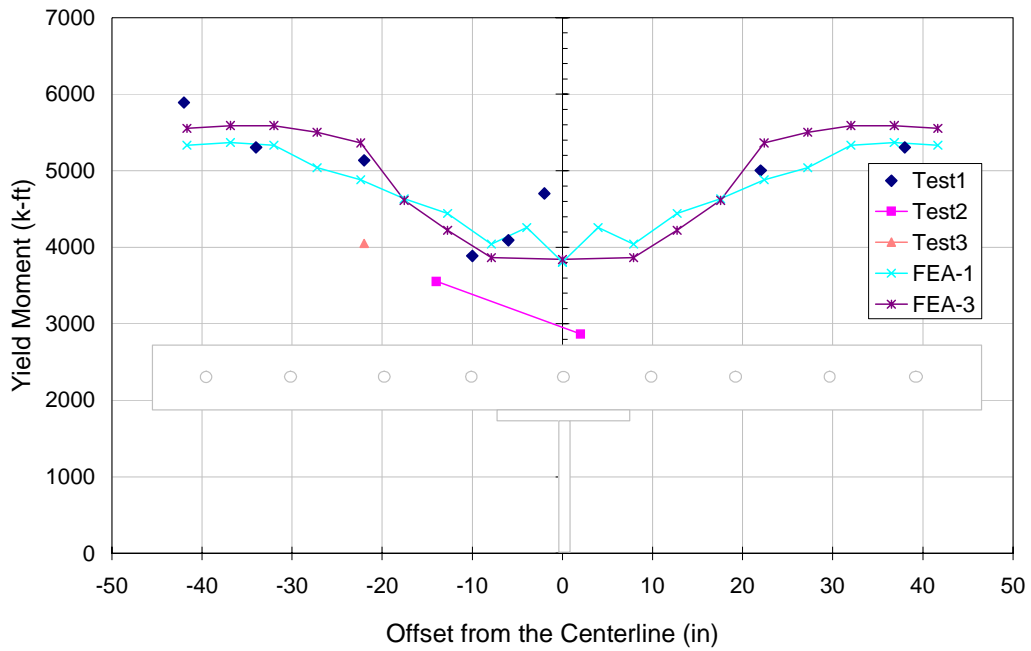


Figure 5-28: Yield Moment of Each Top-Layer Rebar in the Slab

5.3.4 CRUSHING OF CONCRETE

The crushing of the concrete is not attainable through the experimental tests because the embedment gages failed under high compressive stresses and cracks inside the core concrete were not visible. However, in the finite element analysis, the crushing could be determined based on the state of stress and defined failure surface as it was described previously.

The simulation results showed that the crushing of the concrete in the specimen, as it was expected, occurred at the interface of the end bearing pad and the concrete core in the case of the first and the third specimens or at the junction of the bottom flange and core concrete in the second specimen. In the first specimen, crushing of the core concrete occurred at a load of 470 kip (Figure 5-17). The stress contours in the longitudinal direction (x-direction) at the pier location are shown in Figure 5-29 at a load of 532 kip. The experimental observation implied that the crushing of concrete might have occurred at the ultimate load. In the second specimen, the first crushing of concrete was observed at the interface of the bottom flange and the concrete core at 108 kip. The test results indicated the concrete crushed at a load level below the one obtained from the numerical simulation. The stress contours in the x-direction in the diaphragm are seen in Figure 5-30 at the concrete crushing condition. The crushing of the core concrete occurred at a load of 365 kip for the third specimen. The concrete stress contours for the third specimen are observed in Figure 5-31 at the concrete crushing condition.

It is seen that the compression stress of the concrete can exceed the cylindrical strength of the concrete, f'_c , due to confinement effects. The concrete compression stress immediately before crushing is summarized in Table 5-3. The uniaxial compressive strength of the concrete obtained from the material testing is also shown in the same table. The over-strength of the concrete element under the multi-axial stress state compared to the uniaxial test results is listed in the table in the form of percentages. The

difference of a uniaxial strain-stress curve as a material input in the finite element analysis and behavior of a concrete element at the bottom of the diaphragm under the triaxial stress state is shown in Figure 5-32 and Figure 5-33 for the first and third tests, respectively. It was observed that the concrete stress at the ultimate condition was greater than f'_c . The strain in the third specimen was also greater than the 0.003 in/in which is usually assumed by reinforced concrete theory as a failure strain (Mattock, 1960).

Specimen	f'_c	FEA stress	Increase
	ksi	ksi	%
1	6.26	6.97	11%
2	7.14	7.72	8%
3	5.89	7.49	27%

Table 5-3: Concrete Stress Before Crushing from FEA with Uniaxial Strength

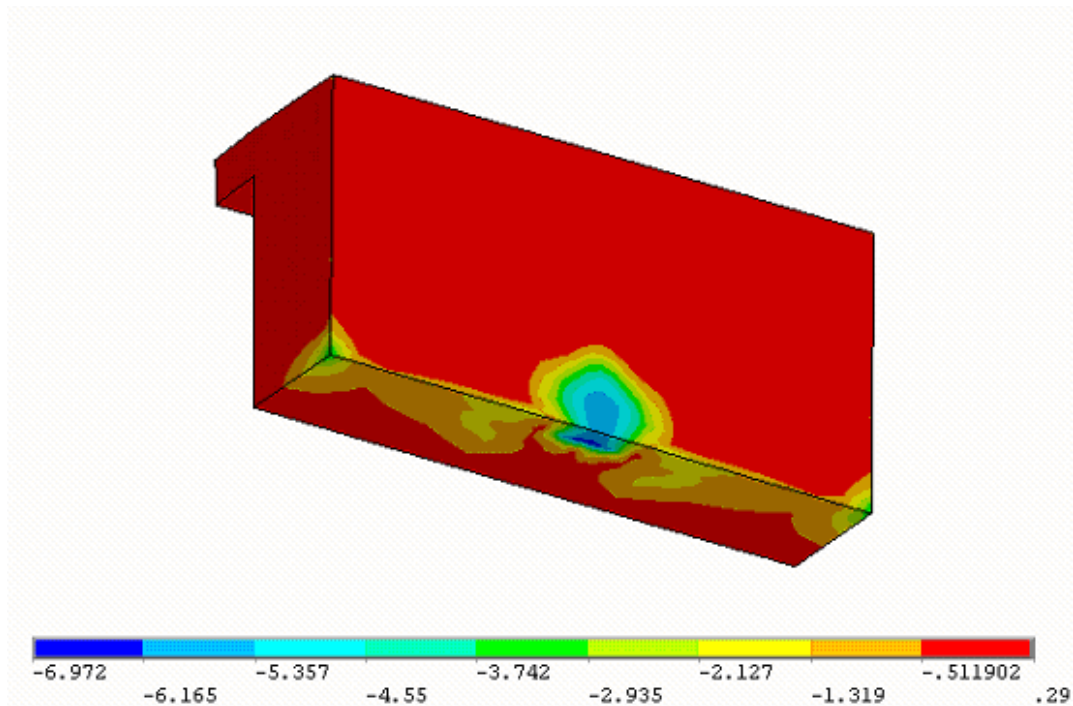


Figure 5-29: Stress (ksi) in x-dir in Concrete Diaphragm and Part of the Slab at Crushing in the First Specimen

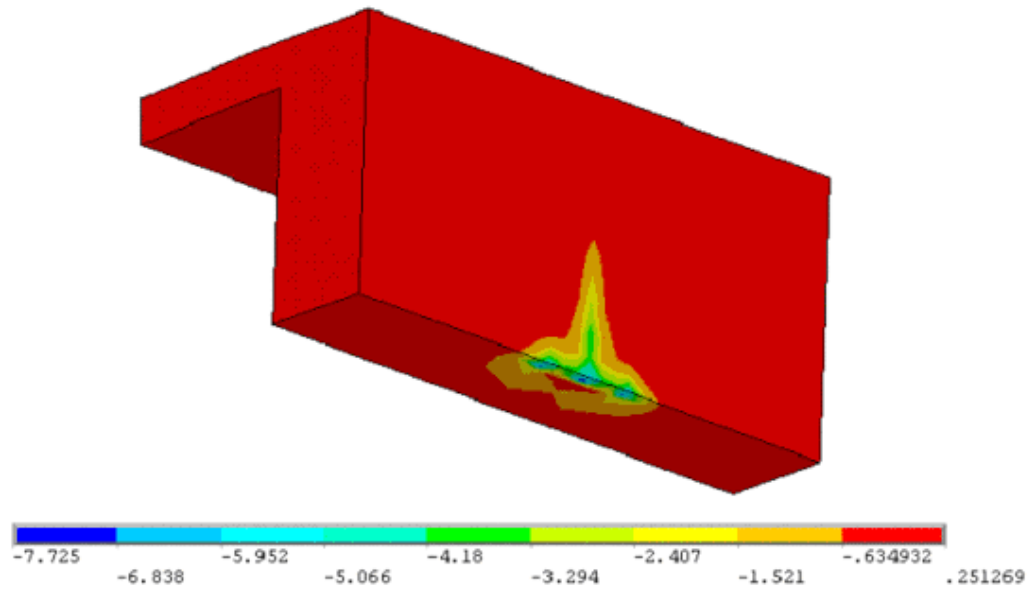


Figure 5-30: Stress (ksi) in x-dir in Concrete Diaphragm and Part of the Slab at Crushing in the Second Specimen

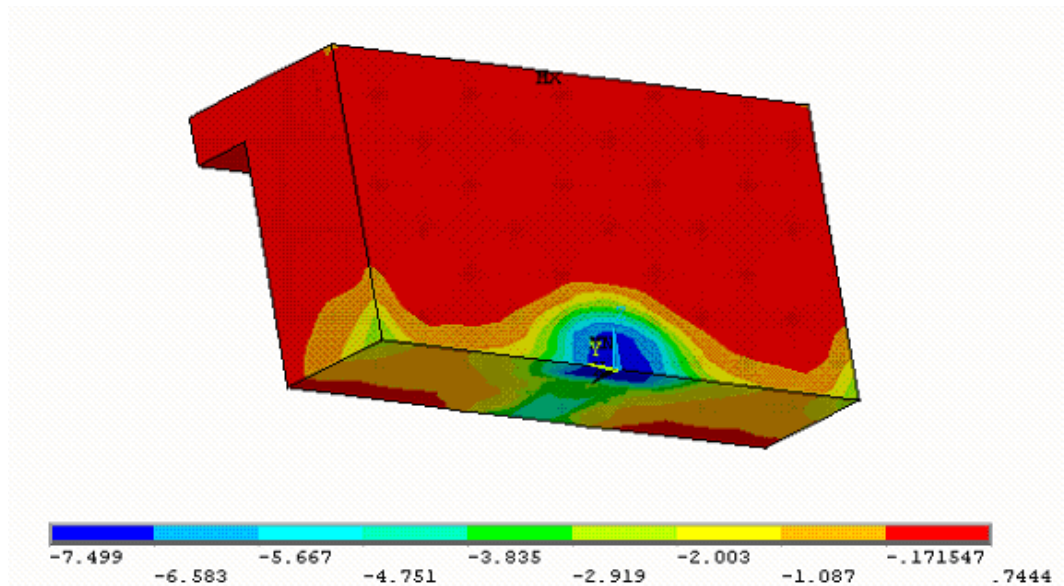


Figure 5-31: Stress (ksi) in x-dir in Concrete Diaphragm and Part of the Slab at Crushing in the Third Specimen(t=4.00, 184)

..

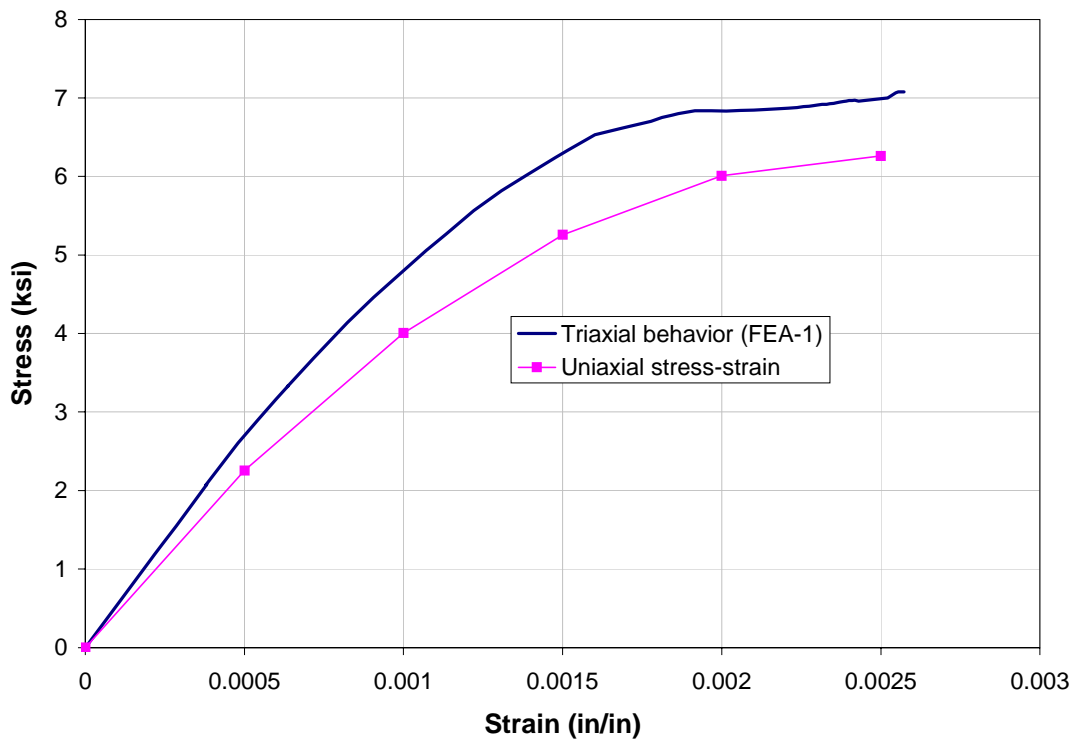


Figure 5-32: Stress-Strain Relation in Bottom of Concrete Diaphragm for the First Specimen

The stress distributions along the depth of the girder inside the concrete core for the first and the third specimen are shown in Figure 5-36 and Figure 5-37. The stress profile consists of the stress in the slab rebar and the bottom connecting plate.

5.3.5 STRAIN DISTRIBUTION

The load-strain plot of the middle rebar of the top layer of reinforcement in the slab at the pier centerline is shown in Figure 5-36 for the first test in one combined plot from the analysis and experimental results. It should be noted that the location of the strain gage mounted in the test specimen was not exactly at the centerline of the girder and the pier (SG20 in Figure 5-36). The measured strain was close to the simulations in the early stages of loading, but they diverged after yielding. The same plot can be seen in Figure 5-37 for the second specimen. Due to the test failures and numerical

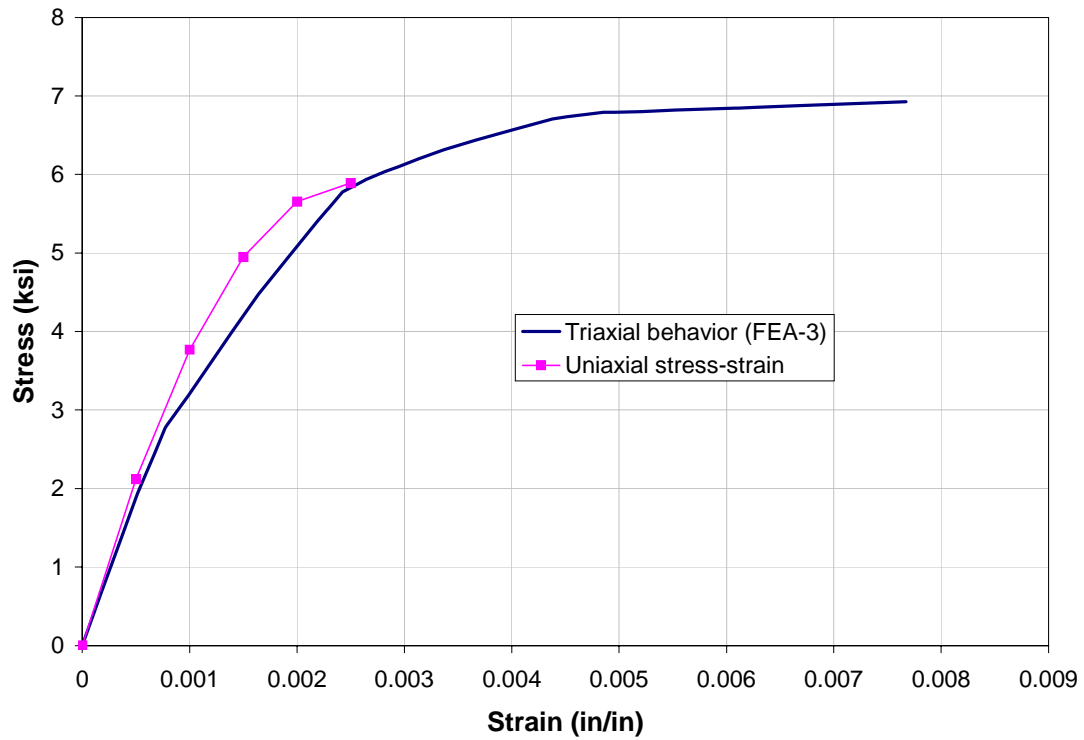


Figure 5-33: Stress-Strain Relation in Bottom of Concrete Diaphragm for the Third Specimen

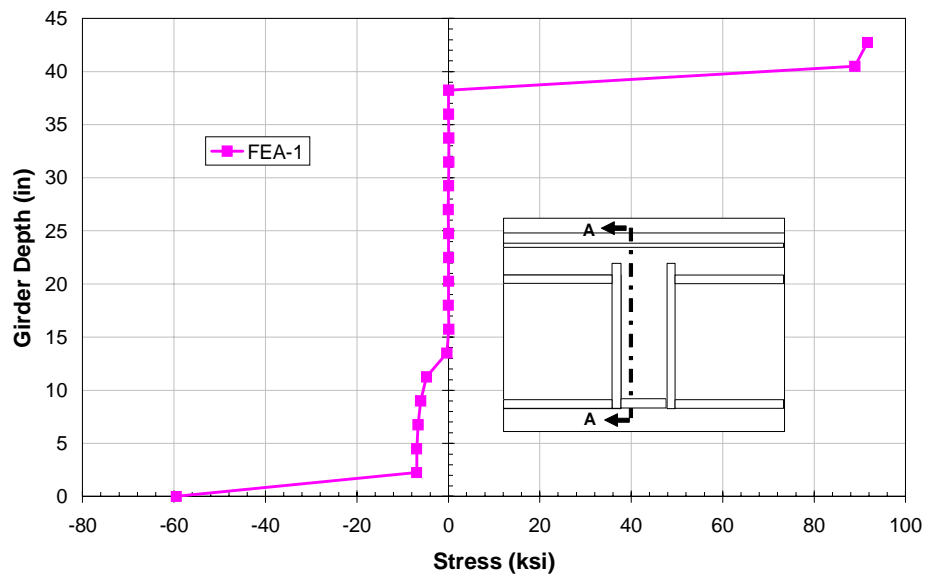


Figure 5-34: Stress Distribution in the Concrete Core for the Test one Ultimate Condition

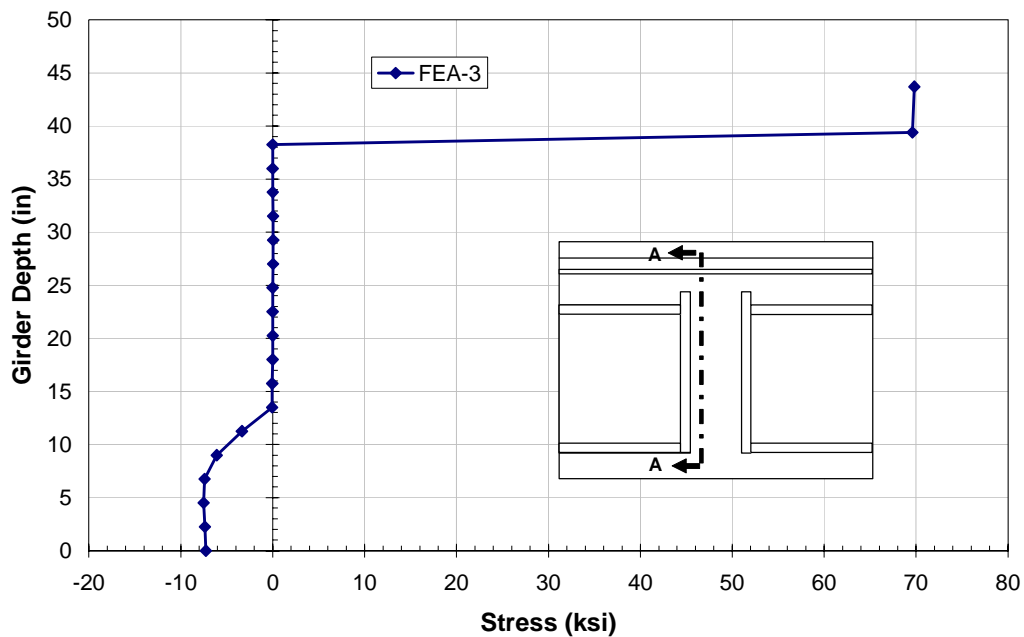


Figure 5-35: Stress Distribution in the Core Concrete in the Third Test at the Ultimate Condition

instability in this specimen, the strain readings at higher loads were erroneous.

The 3-D strain distribution of the concrete diaphragm at the centerline of the pier is shown in Figure 5-38 at a load of 360 kip for the first specimen test. At this load level, the top layer rebar started to yield in addition to the bottom connecting plate. The strain measured at higher load levels close to the ultimate load was not correct due to failure of embedment gages. The experimental data (Figure 5-38) was based on the limited readings and the surface was constructed based on the interpolation between the measured points. The finite element analysis of the first specimen results in a strain surface at the same load and location is shown in Figure 5-39. The saw-tooth shape of strain surface in the finite element plot is due to the cracking of the concrete elements. The strain of the nodes connected to the cracked elements was not increased while strain of nodes attached to the

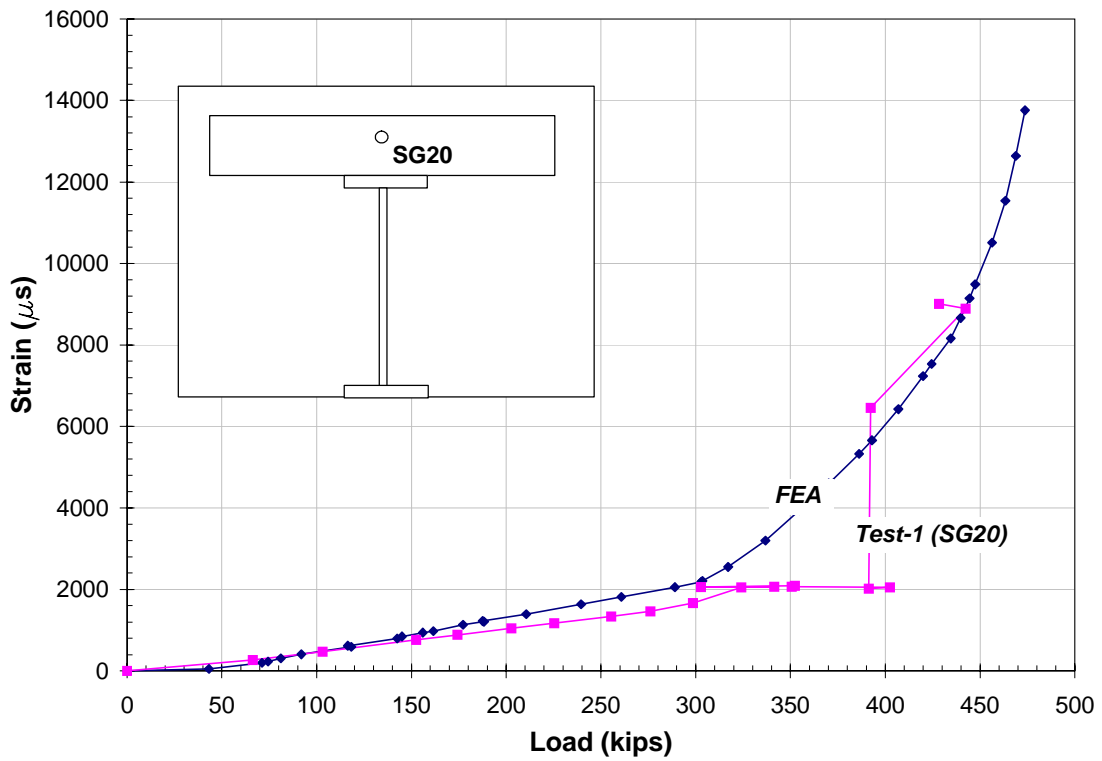


Figure 5-36: Strain History of One of the Top Layer Rebar in the First Specimen

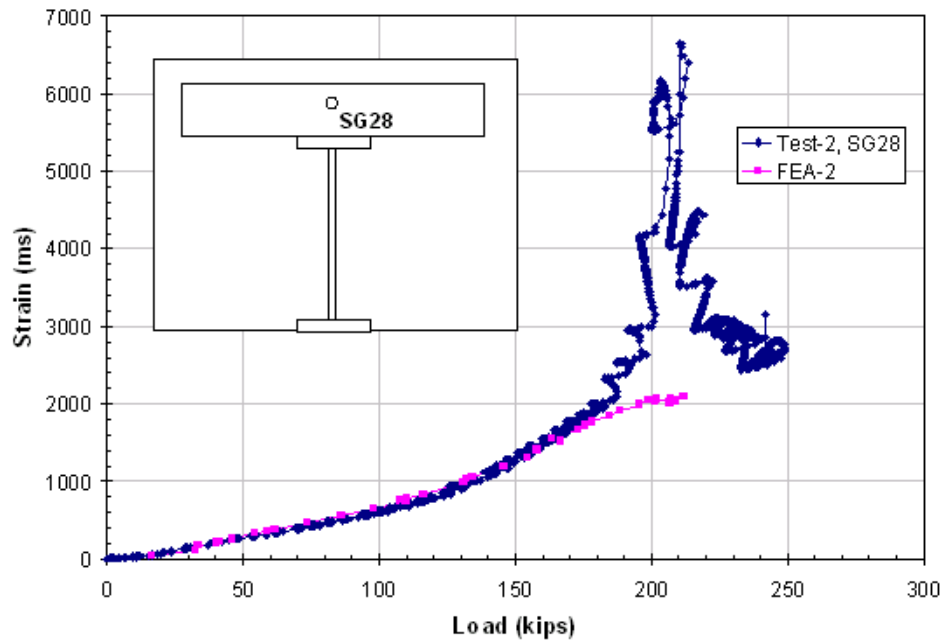


Figure 5-37: Strain History of One of the Top Layer Rebar in the Second Specimen

bars did increase. The strain surface of the third specimen before occurrence of crushing (346 kip) in the concrete is shown in Figure 5-40. The general shape of the strain surface is similar to the first specimen. It is observed that the strain is not distributed in a linear form in any direction.

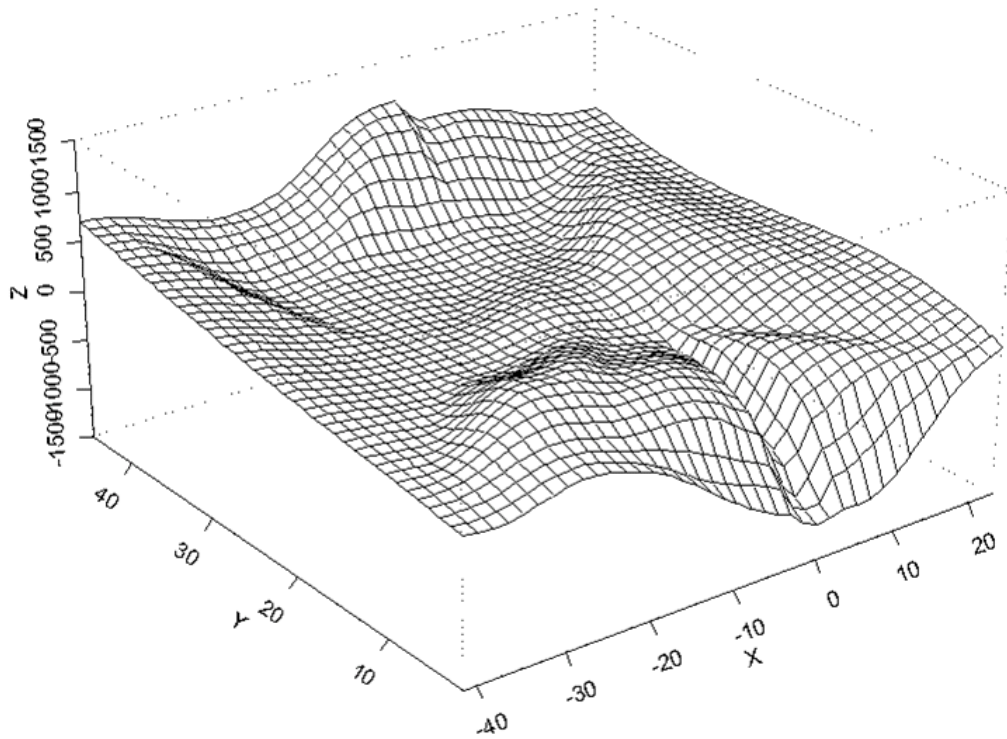


Figure 5-38: Strain Distribution in Concrete Diaphragm, Test 1 at 360 kip

The strain profiles of the girder along its depth at the centerline of the pier are shown in Figure 5-41, Figure 5-42, and Figure 5-43. These plots are at two different load levels (410 kip and 500 kip) before the failure of the first specimen. In Figure 5-42, the strain of the top rebar was obtained from extrapolation since the measured data from the gages were erroneous for the last load steps. The strain distributions obtained from finite element analysis of the first specimen at the same loads and locations are shown in the same plots. Notice that the strain at the bottom of the diaphragm obtained from the finite element analysis is less than that of the experimental results of the first specimen.

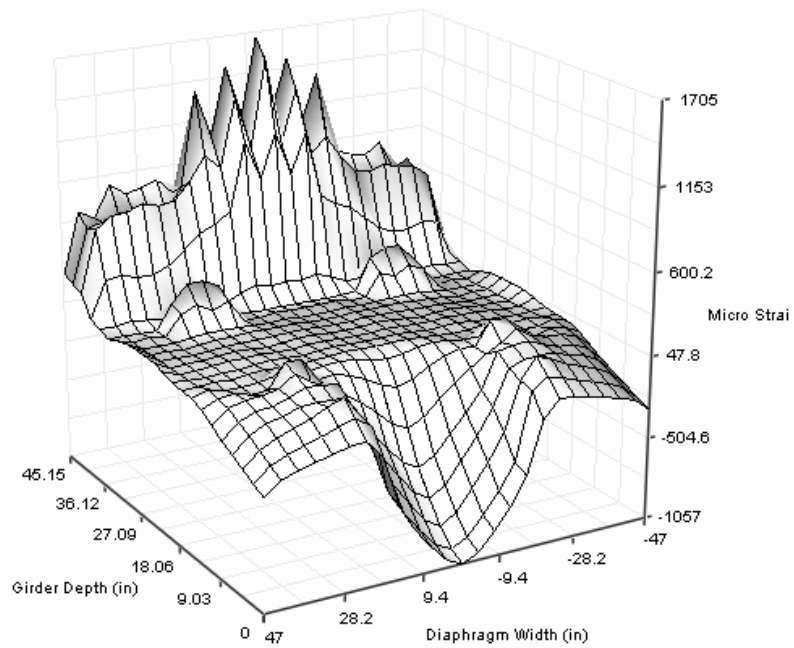


Figure 5-39: FEA Model Strain Distribution at the Pier Centerline at 360 kip, Test 1

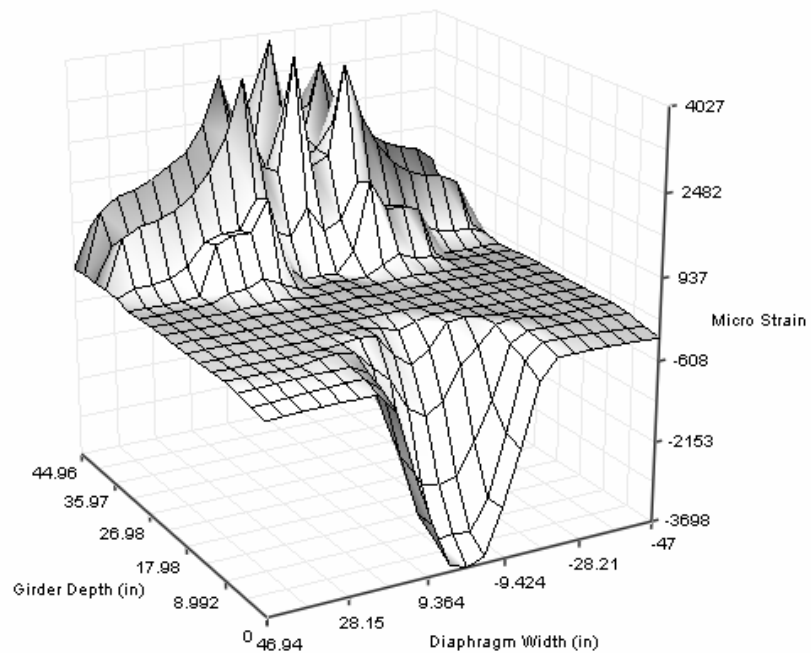


Figure 5-40: FEA Model Strain Distribution at Pier Centerline Before Crushing, Third Specimen, 346 kip

The finite element results of the third specimen before crushing of the concrete (346 kip) at the pier centerline are also plotted in Figure 5-43. It is noticed that the strain distribution is not linear across the depth of the web as it is assumed in conventional reinforced concrete theory. The separation of the end bearing plate from the concrete core in the tensile region caused the concrete elements to experience very small strain. Therefore, the vertical strain in the tension region of the concrete was almost zero. However, the strain distribution in the steel girder was almost linear outside of the diaphragm as shown in Figure 5-44 and Figure 5-45. This indicates that the plane-remain-plane hypothesis can be applied outside of the concrete diaphragm.

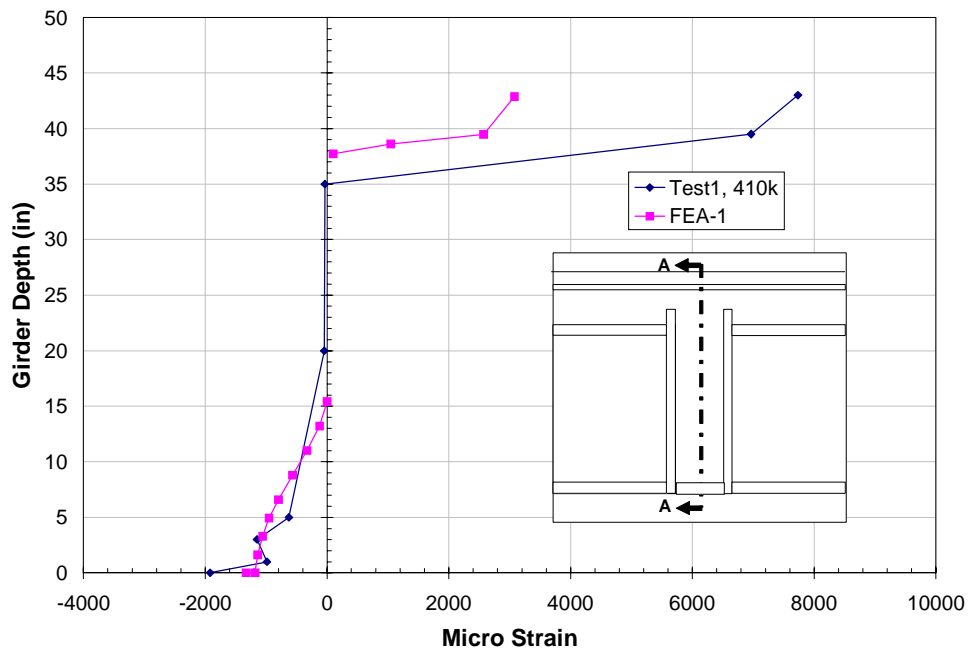


Figure 5-41: Strain Distribution of the First Specimen at the Pier Centerline 410 kip

The strain profile of the bottom flange is shown in Figure 5-46 and Figure 5-47 for the first and third tests, respectively. In all three tests, the strain of the bottom flange decreased inside the diaphragm. One reason for the reduction of the strain could be the composite action of the concrete

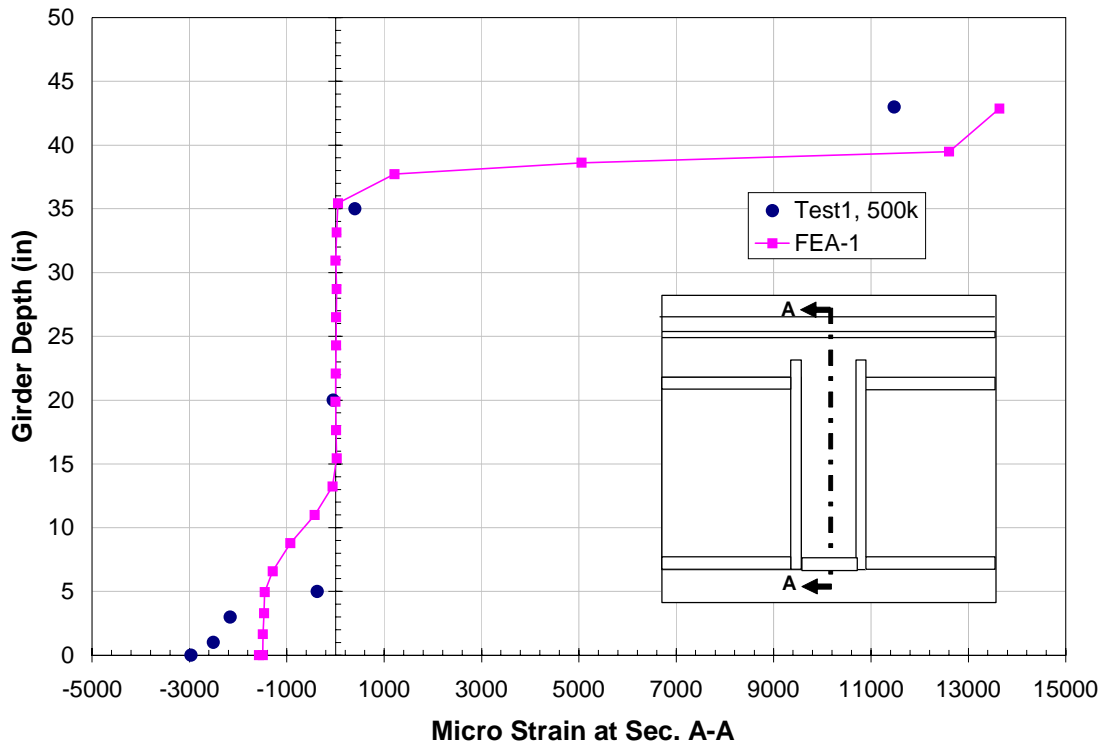


Figure 5-42: Strain Distribution of First Specimen at Pier Centerline, 500 kip

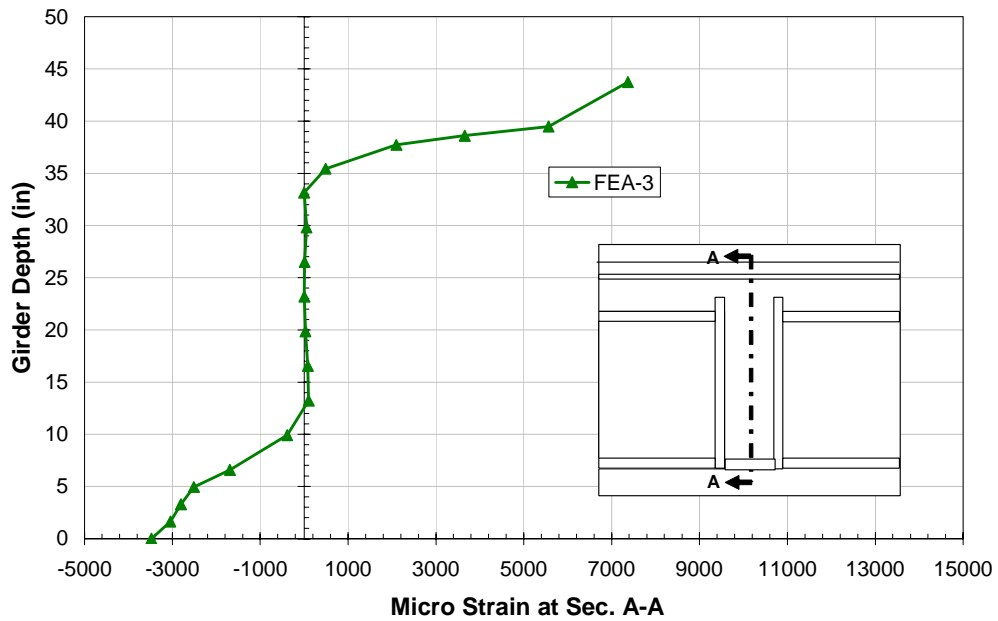


Figure 5-43: Vertical Distribution of Strain at Pier Centerline Before Concrete Crushing, Third Specimen

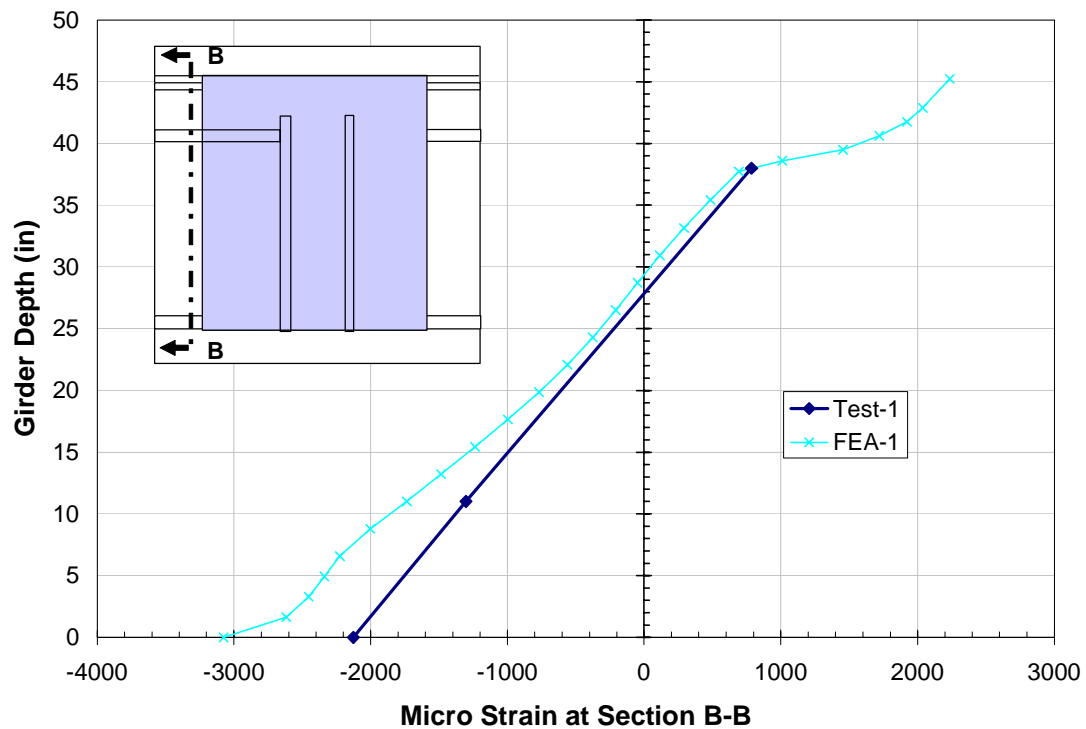


Figure 5-44: Vertical Profile of Strain Outside Diaphragm Before Collapse, First Test diaphragm and bottom flange. The other reason is the support resistance. The bearing pad slightly reduces the applied moment and thus the strain in the bottom flange.

The strain profile of the top flange is shown in Figure 5-48 and Figure 5-49 for the first and the third specimens, respectively. The strain at the edge of the top flange was zero as was expected due to the small tensile strength of the concrete. The plots indicated that the maximum strain was almost at the edge of diaphragm. This implies that the shear transferred by studs was also at its maximum at the edge of the diaphragm.

The strain distribution at the bottom of the diaphragm at the yield condition is compared with the finite element results in Figure 5-50 for the first test. The strain profiles from the test results and the simulation had the same pattern; however, the test strain had a greater magnitude at the centerline. The strain distribution at a load level before collapse of the speci-

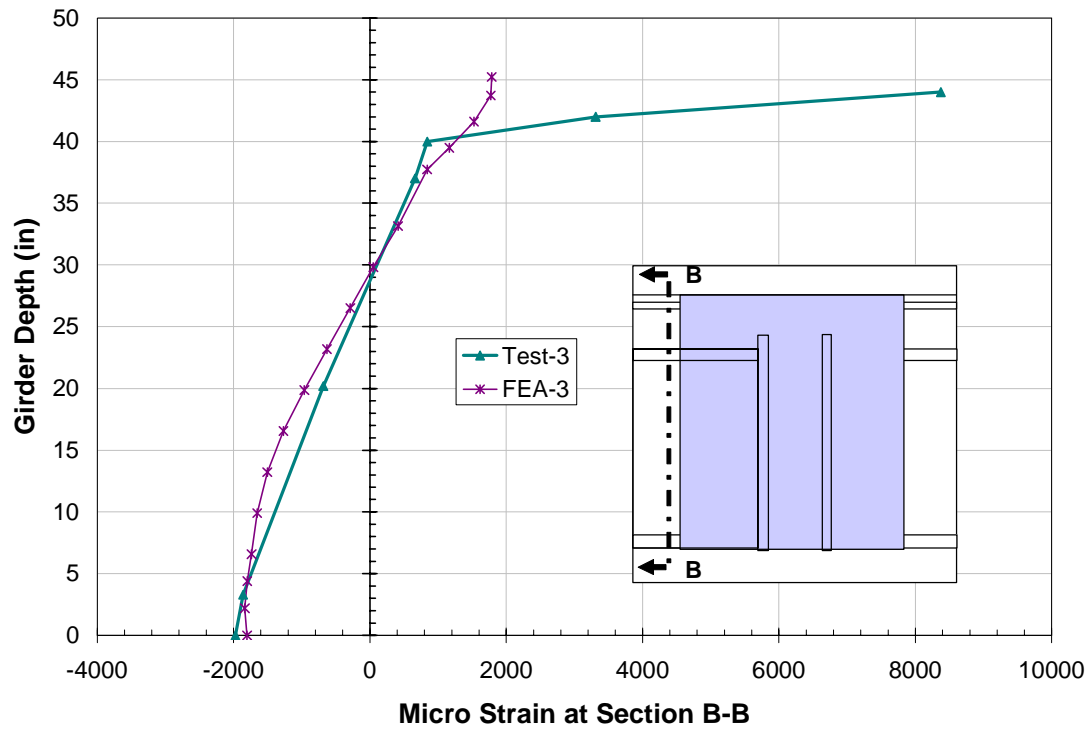


Figure 5-45: Vertical Profile of Strain Outside Diaphragm Before Collapse, Third Test

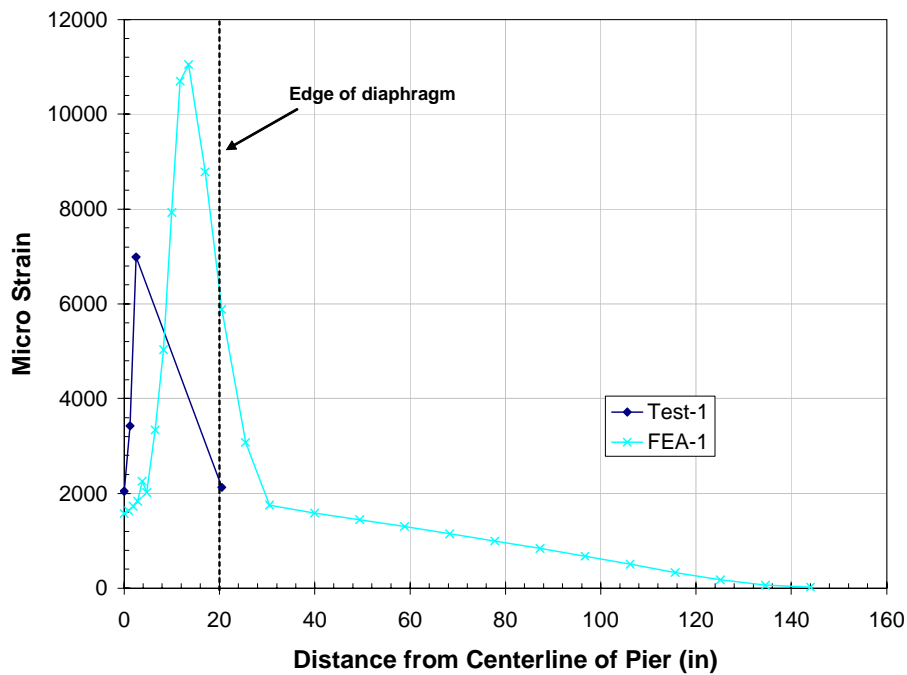


Figure 5-46: Strain Along Bottom Flange at the Ultimate Condition, First Test

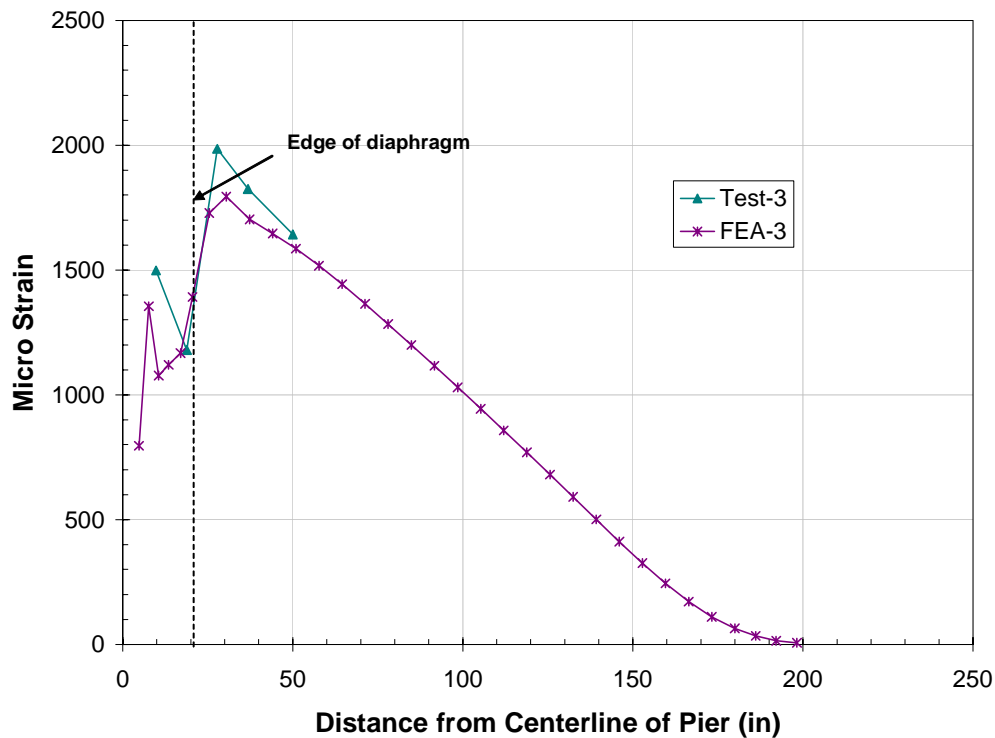


Figure 5-47: Strain Along Bottom Flange at the Ultimate Condition, Third Test

men (500 kip) is seen in Figure 5-51. The test and finite element results do not show much correlation in this case. The strain distributions at the ultimate condition at the centerline of the pier also are shown for the second and the third test in Figure 5-52 and Figure 5-53. Not many strain records were available in these tests due to the instrumentation failures. It was observed that the strain, and consequently compressive stress, in the concrete diaphragm was concentrated more within the boundaries of end bearing plates in the conducted tests. Therefore, it can be concluded that most of the concrete compressive strength was contributed by the concrete core within the end bearing plate width.

The strain distributions in the top layer rebar at the ultimate load condition are also shown in Figure 5-54, Figure 5-55, and Figure 5-56 for the three tests. The shape of the strain profile was almost similar to what was observed at the yielding condition (see Figure 5-25, Figure 5-26, and Figure

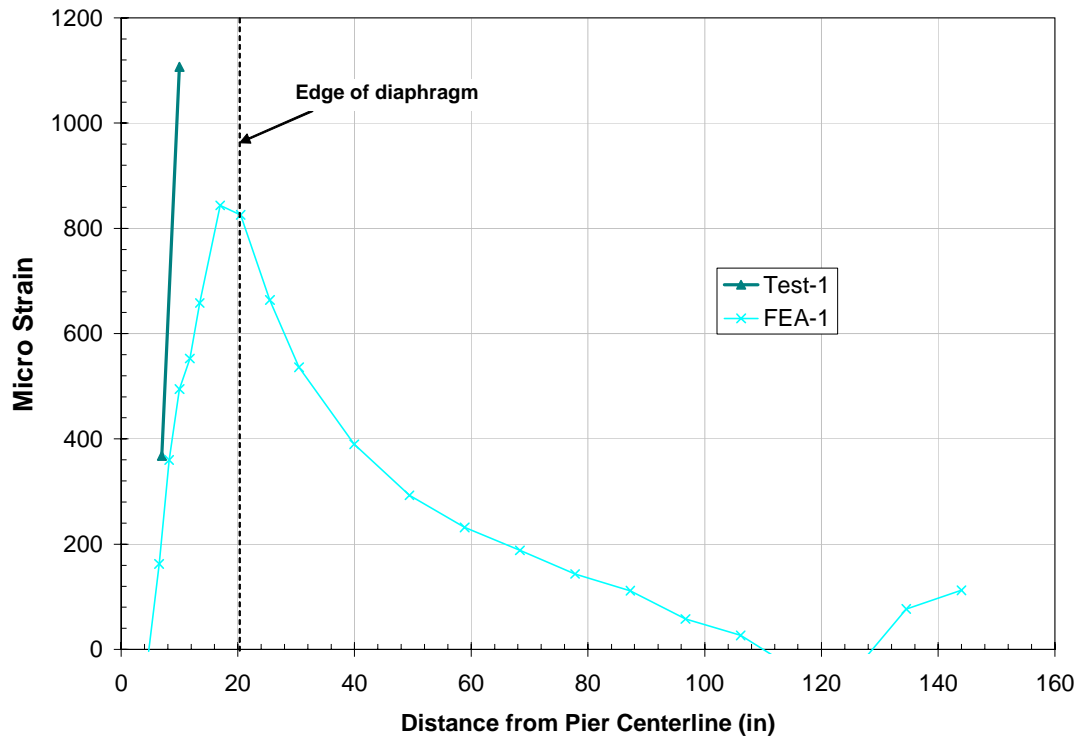


Figure 5-48: Strain Along Top Flange at the Ultimate Condition, First Test

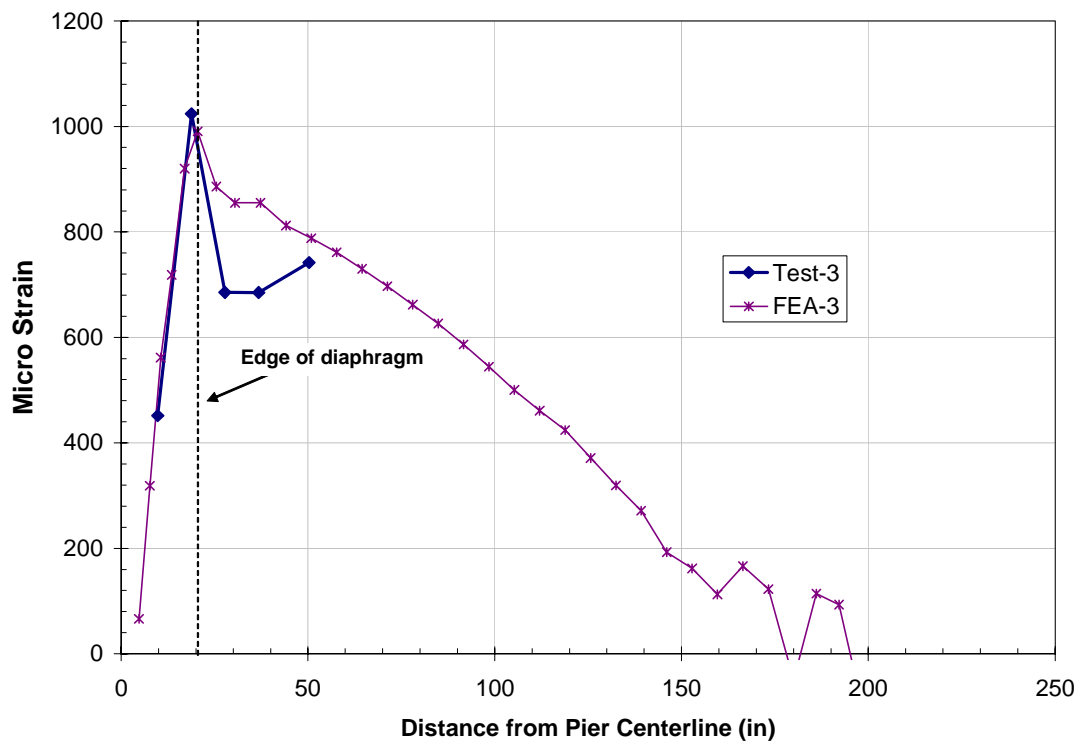


Figure 5-49: Strain Along Top Flange at the Ultimate Condition, Third Test

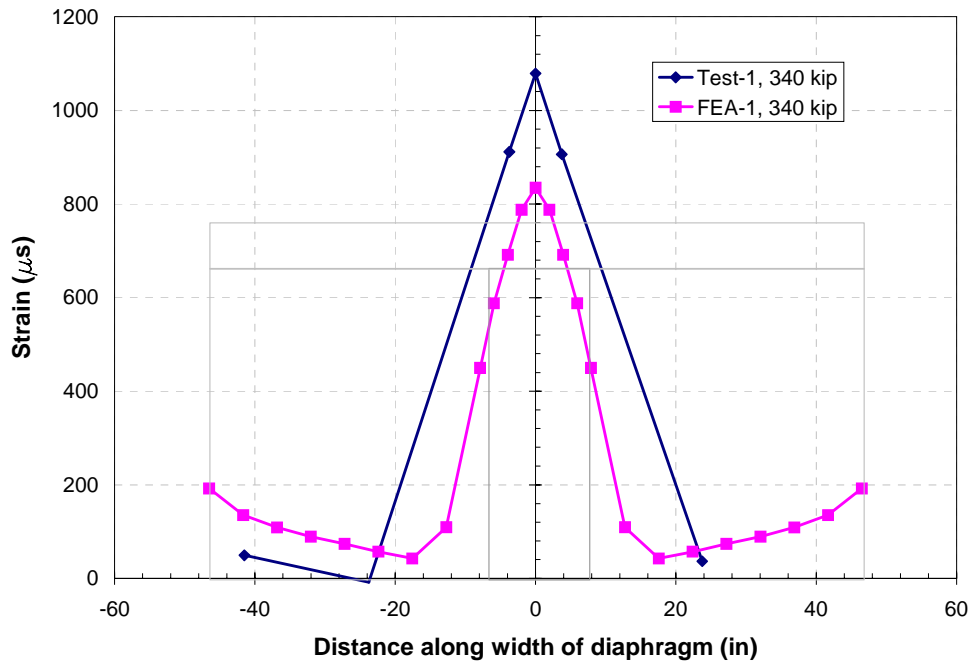


Figure 5-50: Strain Distribution in Bottom of Concrete Diaphragm at Pier Centerline, at First Yield, First Test

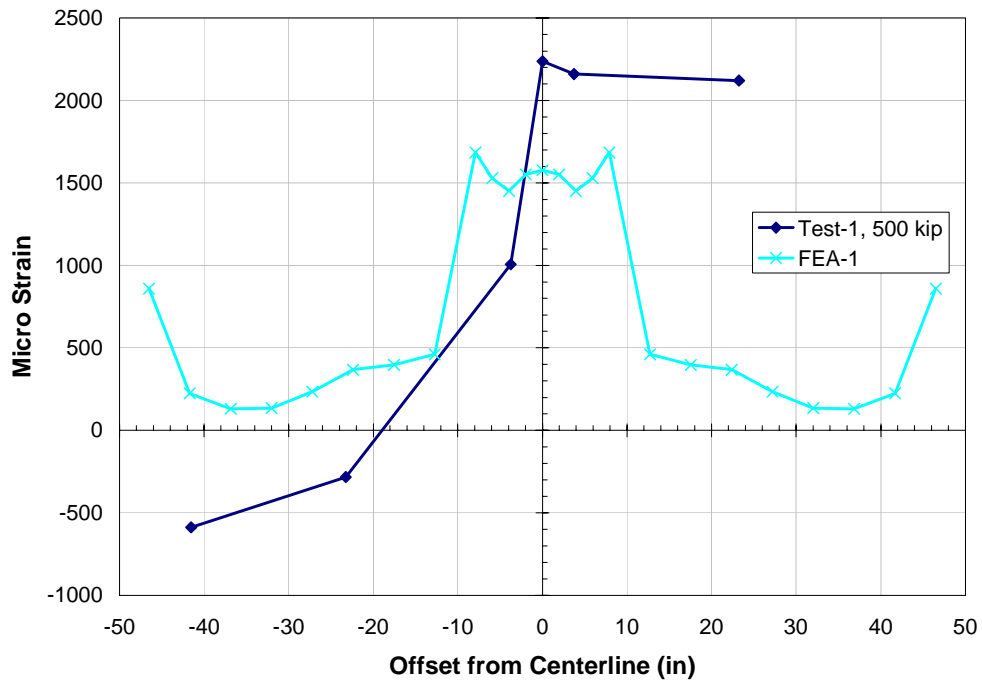


Figure 5-51: Strain Distribution at Bottom of Concrete Diaphragm at Pier Centerline, First Test at 500 kip

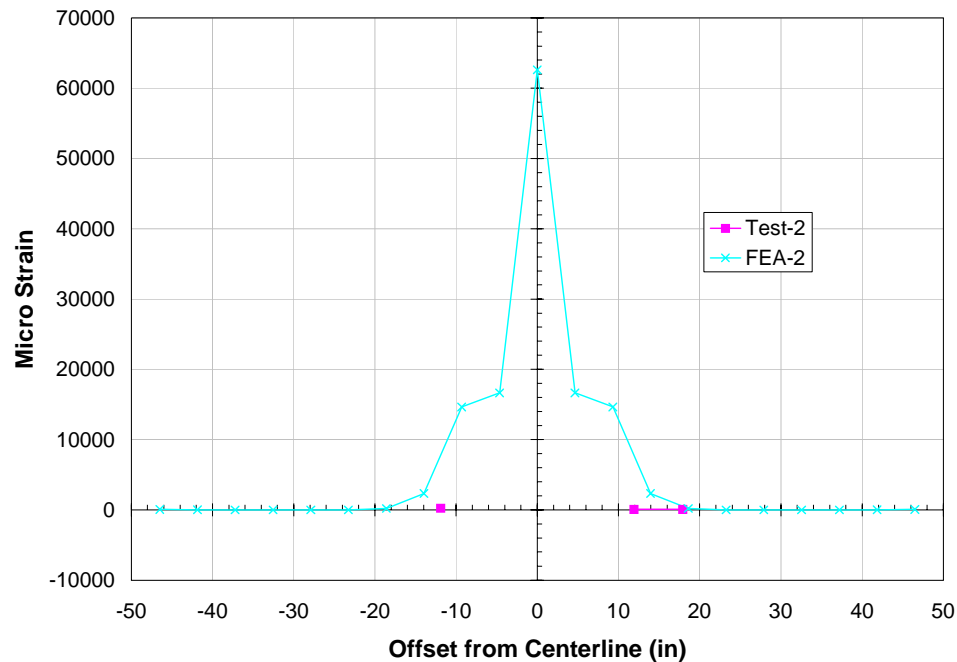


Figure 5-52: Strain Distribution at the Bottom of the Concrete Diaphragm at Pier Centerline at Ultimate Condition, Second Test

5-27). It was observed that the strain distribution was similar to a bell-shape diagram for all three tests.

The movement of the bottom flange into the concrete diaphragm was measured in the third test. The finite element prediction of this movement and the test results are shown in one plot in Figure 5-57. There is a significant difference between the linear part of the plot of the third specimen and the finite element analysis. Since there was a test failure at the beginning of the third test, the linear part was constructed based on a linear interpolation. It was observed that the movement of the bottom flange of the second specimen into the concrete diaphragm was more than twice that of the first and the third specimen. This shows the importance of end bearing plates to prevent the local crushing of the concrete and large penetration of the steel girders into the concrete diaphragm.

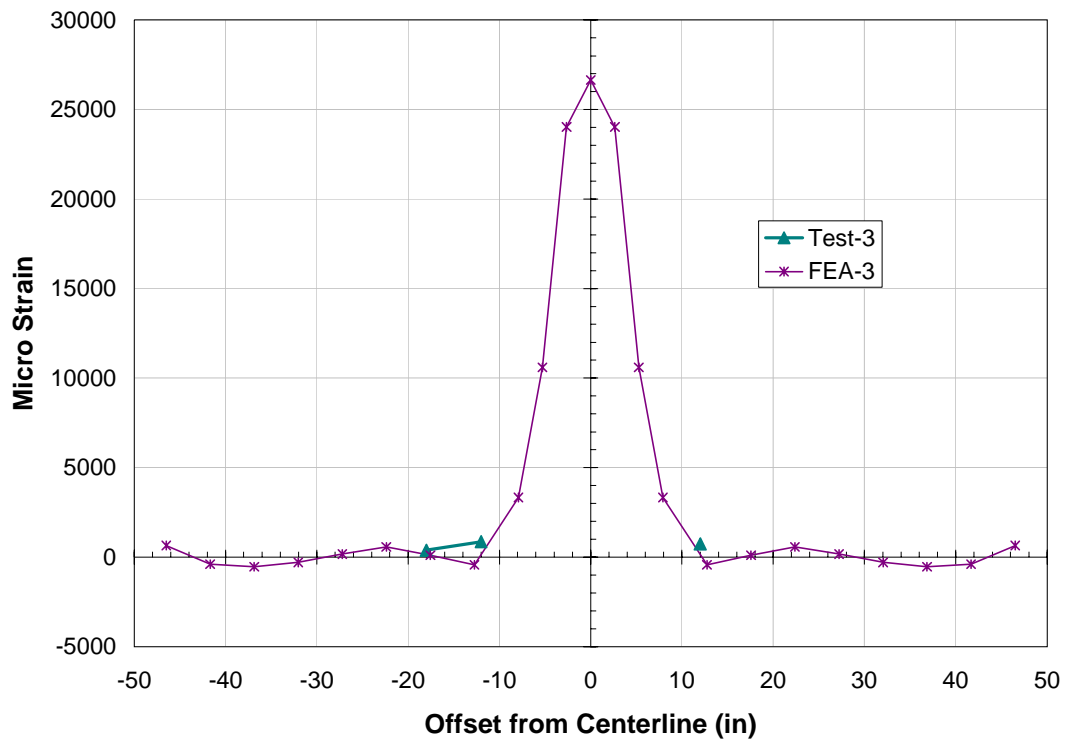


Figure 5-53: Strain Distribution at Bottom of Diaphragm at Pier Centerline, Third Test

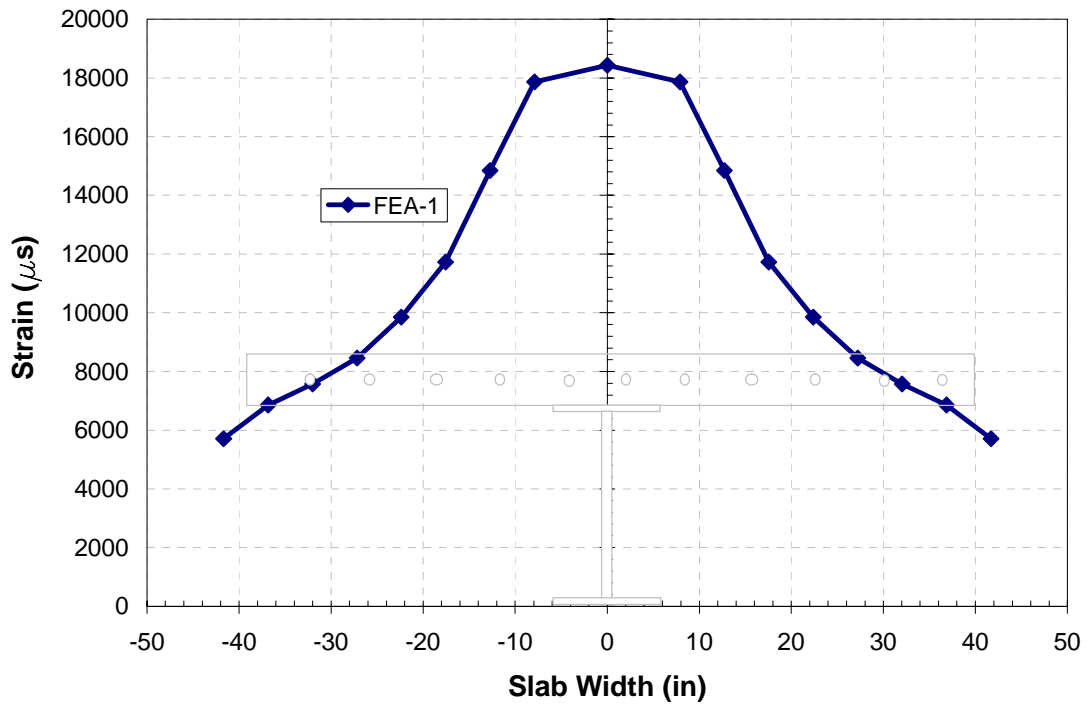


Figure 5-54: Strain Distribution in Top Layer Rebar at Ultimate Condition, First Test

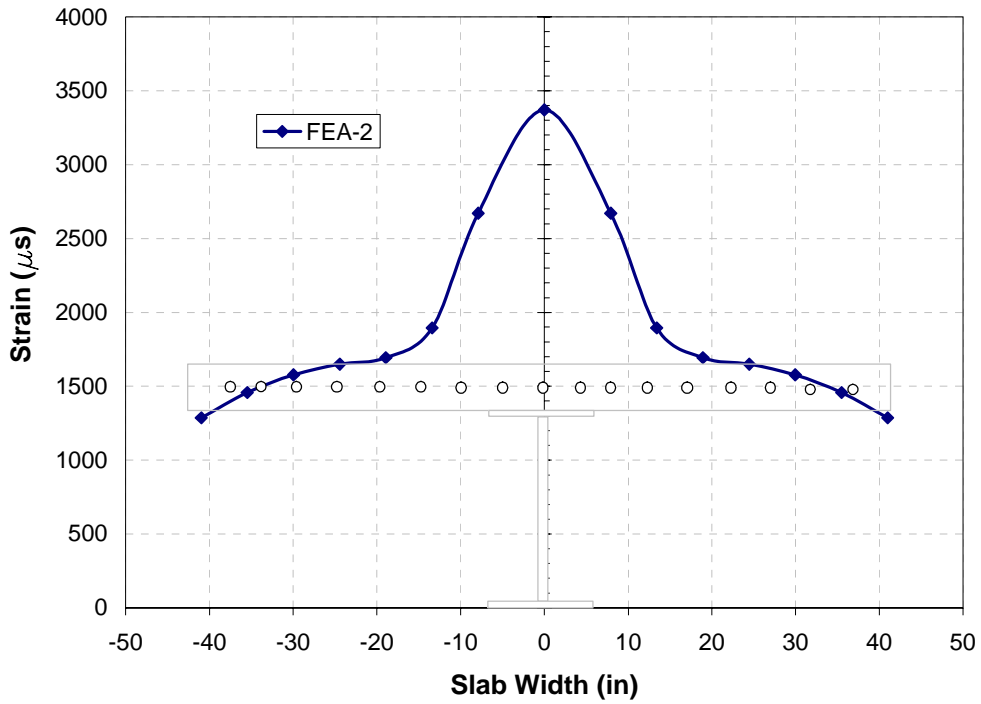


Figure 5-55: Strain Distribution in Top Layer Rebar at Ultimate Condition, Second Test

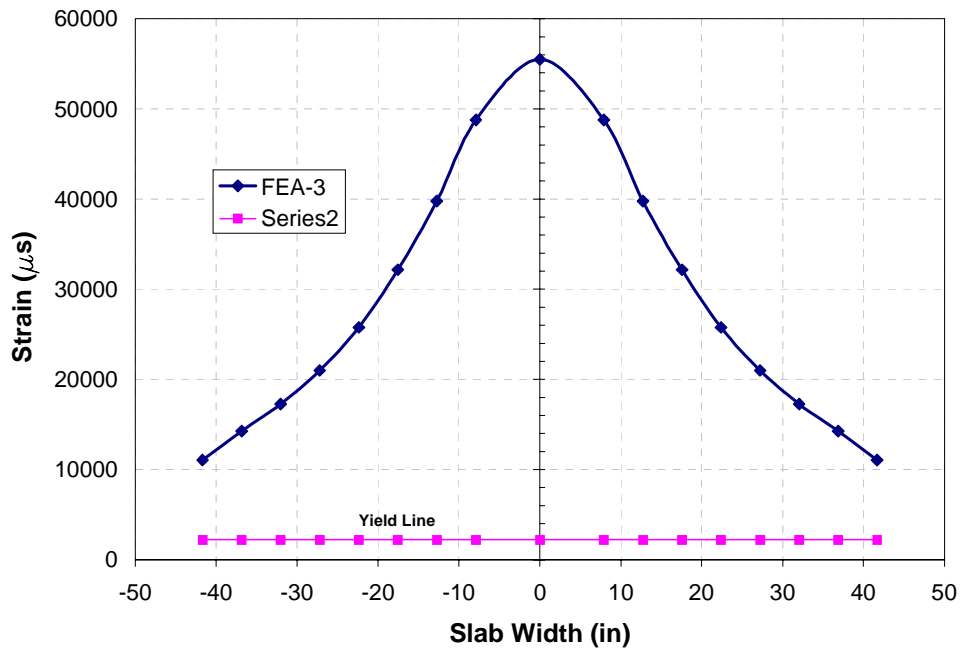


Figure 5-56: Strain Distribution in Top Layer Rebar at Ultimate Condition, Third Test

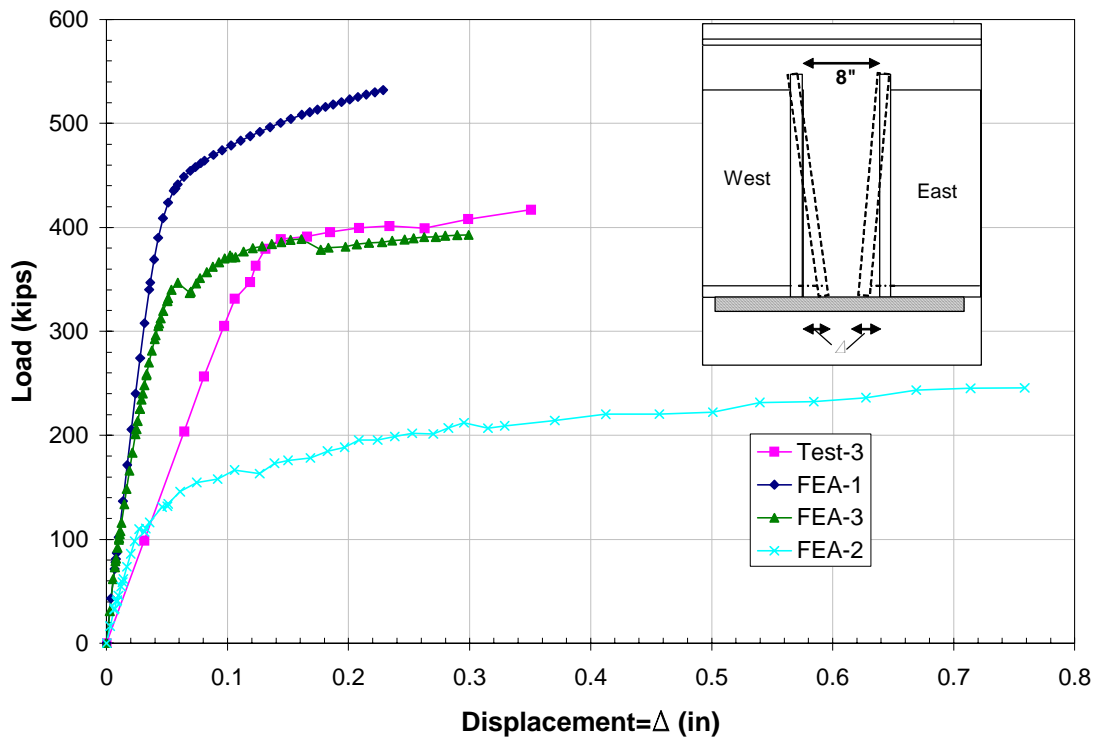


Figure 5-57: Movement of Bottom Flange into Concrete Diaphragm

5.4 CONCLUSION

The detailed simulations of three full scale tests and comparison of analysis data with that of experimental measurements were addressed. The simulation results are consistent with the experimental measurements at overall load-deflection behavior and ultimate capacity. The strain obtained from the analysis is somewhat different than that of the tests especially after yielding. The analysis of the first test is numerically more stable in comparison with the two later tests, because the bottom connecting plate prevented the premature crushing of the concrete.

In the second test simulation, there is a good agreement between load-deflection behaviors before crushing of the concrete, however the numerical approach does not capture well the test curve after the concrete crush-

ing. The stress concentration at the contact interface of the bottom flange, web and concrete diaphragm causes sudden crushing of concrete solid elements which leads to an ill-conditioned numerical solution.

The third test simulation showed better numerical stability than the second test, however, there were not enough experimental data available to validate all aspects of the model. The overall response of the third specimen is closer to the first specimen than the second specimen.

Mathematical Modeling of the Structural Behavior

6

6.1 INTRODUCTION

In this chapter, the mechanical behavior of the connection types one and three are described in the form of mathematical models. The mathematical explanation is based on the equilibrium of the forces and moments, and a deformation field based on the test and simulation observations. Since the prediction of response of the entire connection requires an extensive numerical approach, the resisting system was broken down into its components and each component behavior was studied separately. For this purpose, the key parameters in the resisting mechanism were derived from the experimental and numerical studies. Solid mechanics concepts and formulas were employed to find general formulas for the structural behavior.

6.2 MODES OF FAILURE

Based on the test results and the finite element studies, it was observed that there are three main modes of failure for the specimens.

1. All of the slab's rebar at the pier centerline yielded. Collapse is due to the excessive plastic strain of the reinforcements.
2. The concrete crushed at the bottom part of the diaphragm under compression.
3. Some of the deck rebar yielded, but crushing of the concrete caused the collapse of the specimen.

In general, if the compressive strength of the concrete is high or there is a connecting plate, as in the first specimen, the first mode of the failure is more likely to occur. The excessive plastic strain of the steel rebar causes a drop in strength of the steel due to necking effect. The ultimate strain is determined from the material testing; however, according to CEB-FIP (Park and Paulay, 1974) the maximum tensile strain in the steel at the flexural strength of the member can be limited to 0.01 in/in. The conducted material tests show that the rebar steel can sustain much higher strain than the CEB-FIP recommendation.

If the ratio of reinforcement in the slab is high, the concrete might crush before yielding of rebar as seen in the second specimen. If the concrete in the compression region of the diaphragm is weak, it might crush after yielding of some of the rebar as was observed in the third test specimen. It was observed that the general failure modes are similar to those of reinforced concrete beams. In addition to the three described failure modes, other conditions are possible. The shear failure of the concrete slab, fracture of shear studs and local buckling of the steel girder are some examples. The latter types of failure are not discussed in this study; however, the required strength for some of them is addressed based on the other works.

6.3 FORCES AND STRESSES IN THE SPECIMENS

The applied moment and shear force are resisted by the specimen at the pier centerline through their structural component. There were a total of eight resisting elements at the centerline of the pier that transferred the applied moment to the support. These components were as follows:

- slab top layer rebar,
- slab bottom layer rebar,
- top layer stirrups,
- bottom layer stirrups,
- concrete in tension,
- concrete in compression,
- bottom plate,
- bearing pad.

6.3.1 THE FIRST SPECIMEN

For the first specimen, the contribution of each component at the ultimate condition was obtained from the finite element analysis results. For this purpose, the neutral axis of the section at the ultimate load was calculated using force equilibrium at the pier centerline section. It is mentioned that the neutral axis is not in the form of a line as was discussed in Chapter 5; however, the defined notional neutral axis was assumed to be a straight line. The depth of the neutral axis was assumed to be at an elevation in which the total tensile force over this elevation was equal to the total compression force under this elevation. The depth of the neutral axis from the bottom of the bottom flange was about 13.2 inches for the first test.

The area of each resisting component was obtained from the test data and given in Table 6-1. It should be mentioned that the area of concrete in tension was calculated by multiplying the width of the diaphragm to the depth of the girder above the neutral axis. The area of the concrete in compres-

sion was assumed to be equal to the depth of neutral axis times the width of the end bearing plate. The force in each component was computed using numerical integration of nodal force of all the elements in that component (Table 6-1). The analysis results indicate that about 77 percent of the concrete compression force at the pier centerline was resisted by concrete within the end bearing plate width or the core concrete. The moment of each element was computed about the centerline of the bottom plate (Table 6-1). The summation of moments of all of the components was seven percent less than the test result. Part of this difference was due to the effect of the bearing pad on the total moment, which had not been included in the current calculations for the sake of simplicity. The average stress in each component was calculated by dividing the force by its area. The calculated stresses are listed in Table 6-1. It is observed that the average stress in rebar was more than the specified yield stress. This was due to the strain hardening of the rebar. It can also be seen that the top and bottom layer rebar have almost the same average stress.

The distance from the location of the resultant compressive force in the concrete to the centerline of the bottom plate was calculated by using the moment of each node's force (concrete elements in compression) about the bottom of the diaphragm divided by the total concrete compressive force. This distance was about 4.9 inches which was about 0.37 of the depth of the neutral axis. In the conventional reinforced concrete beam theory (ACI-318, 2004), the location of the compressive force is about 0.425 of the depth of the neutral axis for normal concrete.

The contribution of each resisting component on the total moment strength of the specimen at the pier centerline is listed in Table 6-3. It should be noticed that more than 90 percent of the total strength of the specimens at the pier centerline was provided by the slab rebar, bottom plate and concrete in compression. In another words, the tensile strength of the concrete and resistance of the stirrups can be ignored.

Resisting Component	Area	Distance from bottom plate	Force	Moment	Average Stress
	in ²	in	kip	kip-in	ksi
Top Layer Rebar	13.6	43	1036.8	44573.8	76.2
Bottom Layer Rebar	5.8	39.5	439.9	17372.1	75.8
Top Layer Stirrups	2.4	33.1	177.7	5881.8	74
Bottom Layer Stirrups	2.4	6.6	69.8	458.9	28.9
Concrete in Tension	3011.3	28.9	193.2	5582.2	0.06
Concrete in Compression	208.8	4.9	-1003.8	-4919	-4.8
Bottom Plate	18.2	0	-913.6	0	-50.3
Sum			0	68949.8	

Table 6-1: The force and stress in the resisting components of the first test at the pier centerline at the ultimate condition

6.3.2 THE THIRD SPECIMEN

For the third specimen, the contribution of each component at the ultimate condition was obtained from the same approach as described for the first specimen in the previous section. The area of each resisting component, the distance of the center of each component to the bottom fiber of diaphragm, resistance force, moment about the lowest fiber of the diaphragm, and average stress in each component is given in Table 6-2. The analysis results indicate that about 70 percent of the concrete compression force at the pier centerline was resisted by concrete within the end bearing plate width. The depth of the neutral axis from the lowest fiber of the diaphragm was about 14.8 inches.

The summation of moments of all of the components was 12 percent less than the test result. Note that the effect of the bearing pad on the total moment was not included in Table 6-2. It can be observed that the average stress in the reinforcements was more than the specified yield stress. This was due to the strain hardening of the rebar. It can also be seen that the top and bottom layer rebar have approximately the same average stress.

The moment of each resisting component about the notional neutral axis was computed and its percentage with respect to the total moment strength of the specimen at the pier centerline is given in Table 6-3. Notice that more than 90 percent of the strength was provided by the slab rebar and the concrete in compression. In addition, the computed tensile stress of the concrete was negligible.

The distance of the center of the concrete region in compression to the bottom fiber of the concrete diaphragm was about 5.6 inches which is about 0.42 of the depth of the neutral axis. In the conventional reinforced concrete beam theory (ACI-318), the location of the compressive force is 0.425 (0.85/2) of the depth of the neutral axis. The location of compressive resultant force had a good agreement with that predicted by reinforced concrete theory.

Resisting Component	Area	Distance from bottom	Force	Moment	Average Stress
	in ²	in	kip	kip-in	ksi
Top Layer Rebar	13.6	43.7	973	42520.1	72.5
Bottom Layer Rebar	5.8	39.5	423	16708.5	72.9
Top Layer Stirrups	2.4	33.1	168	5560.8	70
Bottom Layer Stirrups	2.4	6.6	-144	-950.4	-60
Concrete in Tension	3011.3	31.8	198	6296.4	0.06
Concrete in Compression	208.8	5.6	-1618	-9028.4	-7.74
Sum			0	61107	

Table 6-2: The force and stress in the resisting components of the third test at the pier centerline at the ultimate condition

Resisting element	Test 1	Test 3
Slab Rebar	60.82%	66.77%
Stirrups in tension	5.09%	5.42%
Concrete in tension	4.35%	6.03%
Stirrups in compression	0.00%	1.58%
Concrete in compression	12.37%	20.20%
Bottom plate in compression	17.37%	NA
Total	100.00%	100.00%

Table 6-3: The contribution of each resisting element in test one and three

6.4 STRAIN AND STRESS DISTRIBUTIONS

To find the flexural capacity of the connections at any section, a strain field or a deformed shape of the section is required. The test measurements of strain in the specimens indicated that strain distribution was not linear in any of the three directions of the space inside the concrete diaphragm. The strain distribution in the top rebar and the bottom of the concrete diaphragm was similar to a normal distribution, as was discussed in previous chapters. The strain distribution can be defined in three lines in order to derive a strain field on plane of a section. Based on the test observations and simulations results, the strain distributions at the pier centerline section are determined in three lines as follows:

1. along the girder depth (z axis in Figure 6-1,a)
2. along the slab rebar (Figure 6-1, c)
3. along the diaphragm width (y axis in Figure 6-1, b)

By combining the three distributions, one can construct a surface (Figure 6-2) representing the strain distribution at the pier centerline. The test and finite element analysis results are used to evaluate the accuracy of the assumptions.

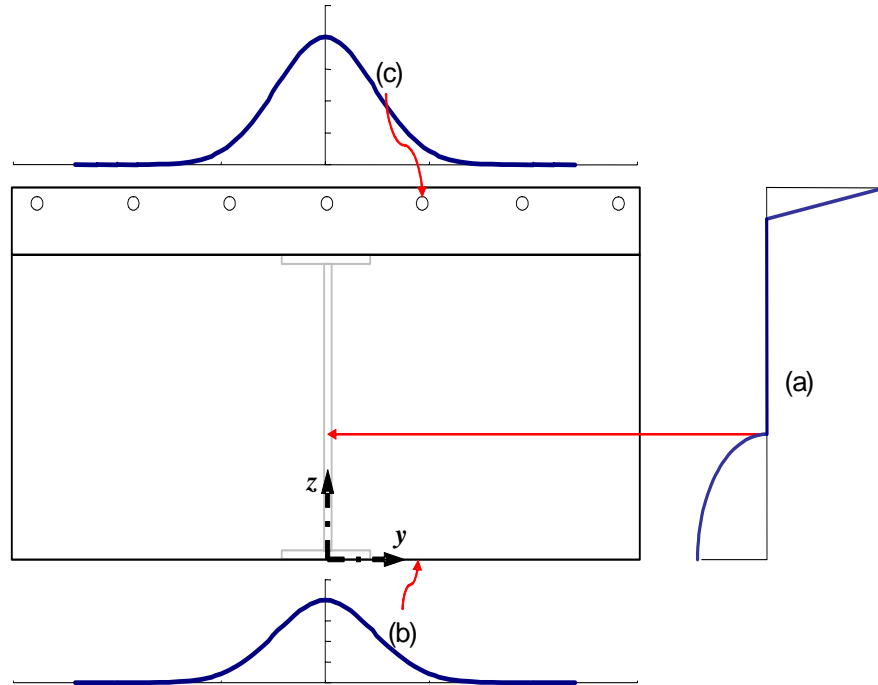


Figure 6-1: Strain distribution at the three lines at the pier centerline

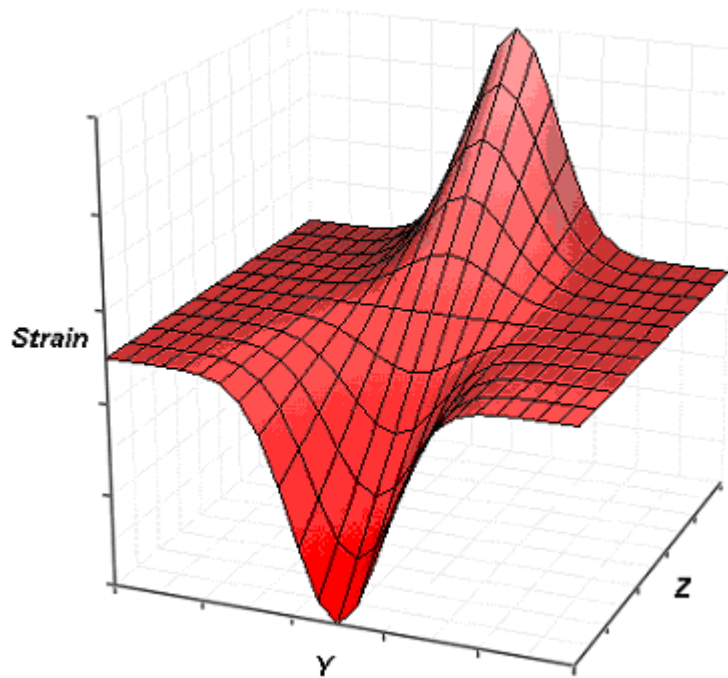


Figure 6-2: Strain surface at the pier centerline

6.4.1 VERTICAL DIRECTION

In the vertical section (z-axis), along the depth of the girder, a linear distribution assumption, i.e. the plane-stay-plane hypothesis (the Bernoulli's principle), is not valid. However, it was shown that part of this nonlinearity is due to the embedment gages readings after the cracking of the concrete. This phenomenon was also noticed in the finite element results. The profiles of the deflection of the sections inside the concrete diaphragms are shown in Figure 6-3 and Figure 6-4 for the first specimen and the third specimen, respectively. Notice that the linear assumption for the deflection does not exactly match the deflection profile. However, the concrete tension region can be omitted from these plots since the FEA (finite element analysis) results indicated that the tensile strength of the concrete was negligible. The strain distribution of the third specimen at the pier centerline excluding the tensile points is shown in Figure 6-5. It can be seen that the trend the strain follows is an almost linear distribution. The strain distribution of the first test is not linear even after removing the tensile points as shown in Figure 6-6. However, the strain distribution in sections farther from the pier centerline tends to be linear. For the following calculations a linear strain distribution along the girder depth is adopted.

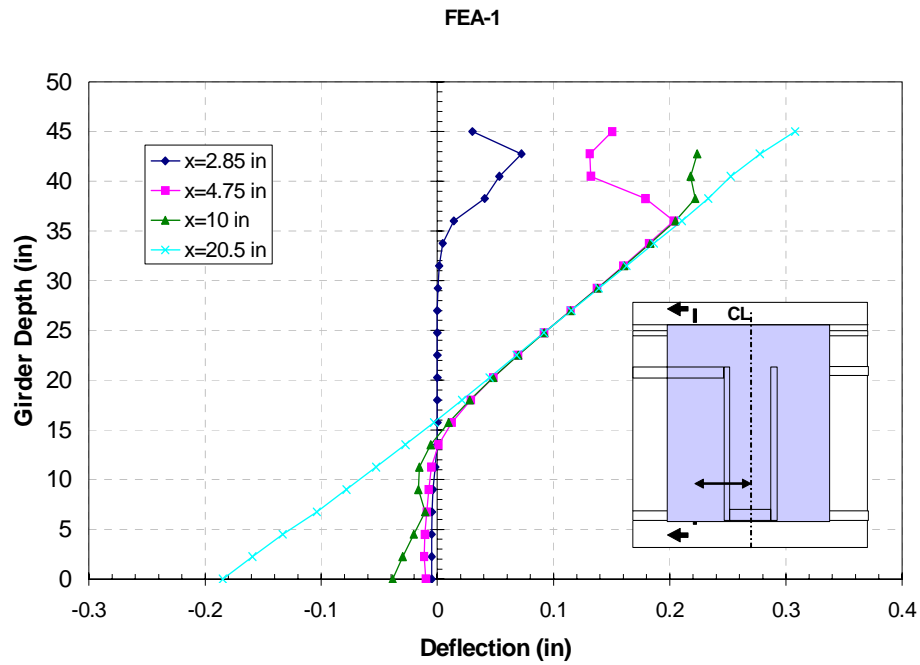


Figure 6-3: Deflection profiles (in longitudinal direction) of the first specimen at ultimate condition

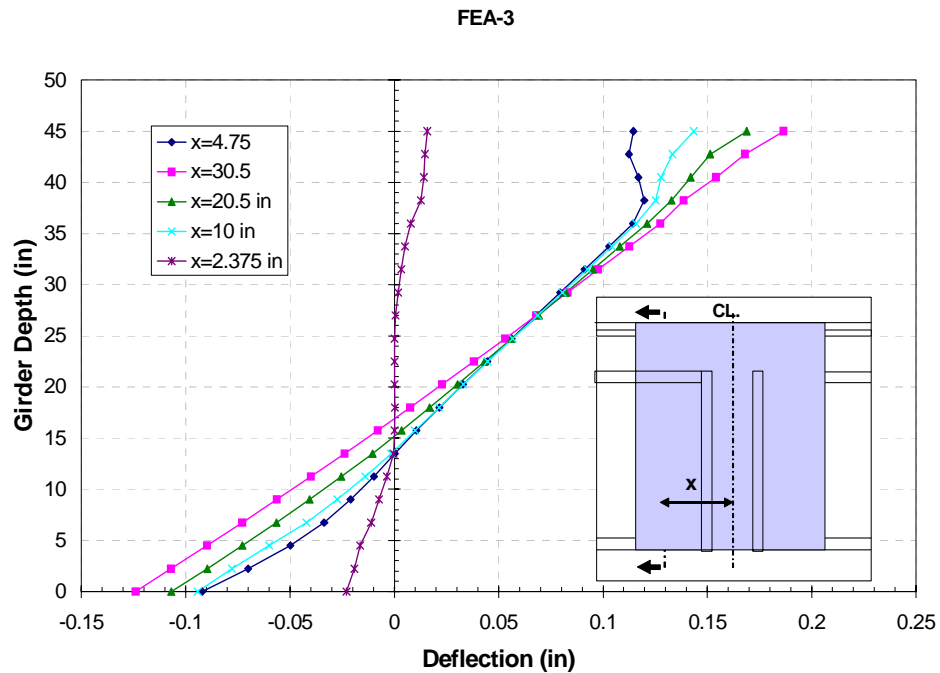


Figure 6-4: Deflection profiles (in longitudinal direction) of the third specimen at the ultimate condition

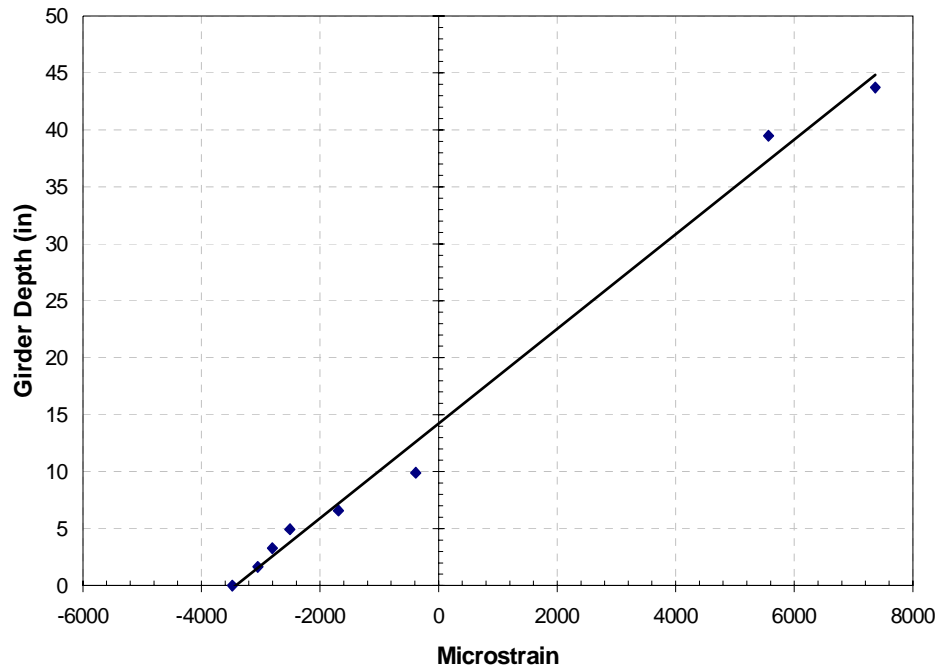


Figure 6-5: Strain profile at the pier centerline of the third specimen at a load of 350 kip

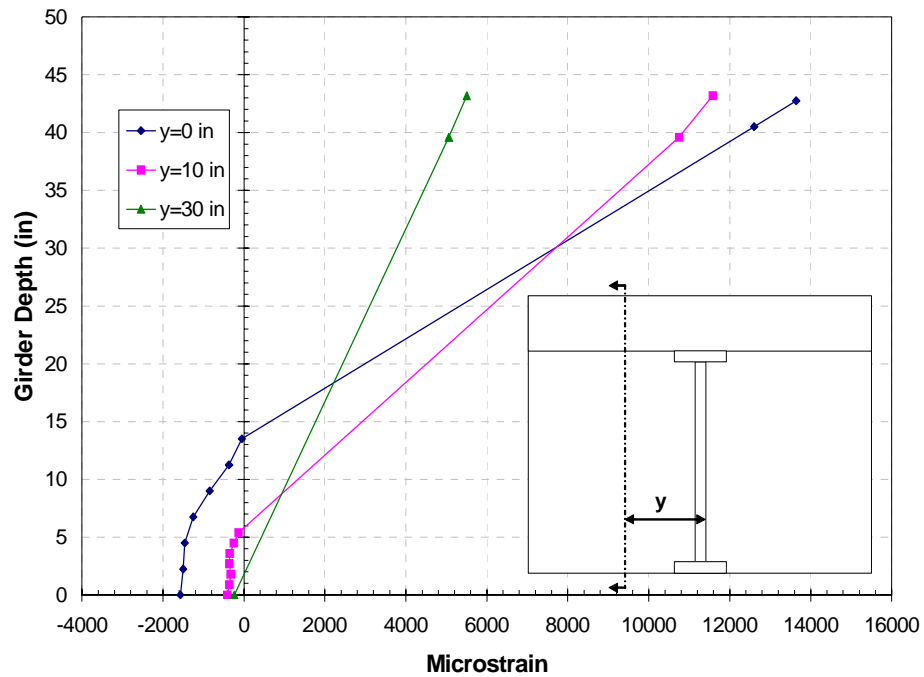


Figure 6-6: Strain profile at the pier centerline of the first specimen at different location along the width of diaphragm for load of 500 kip

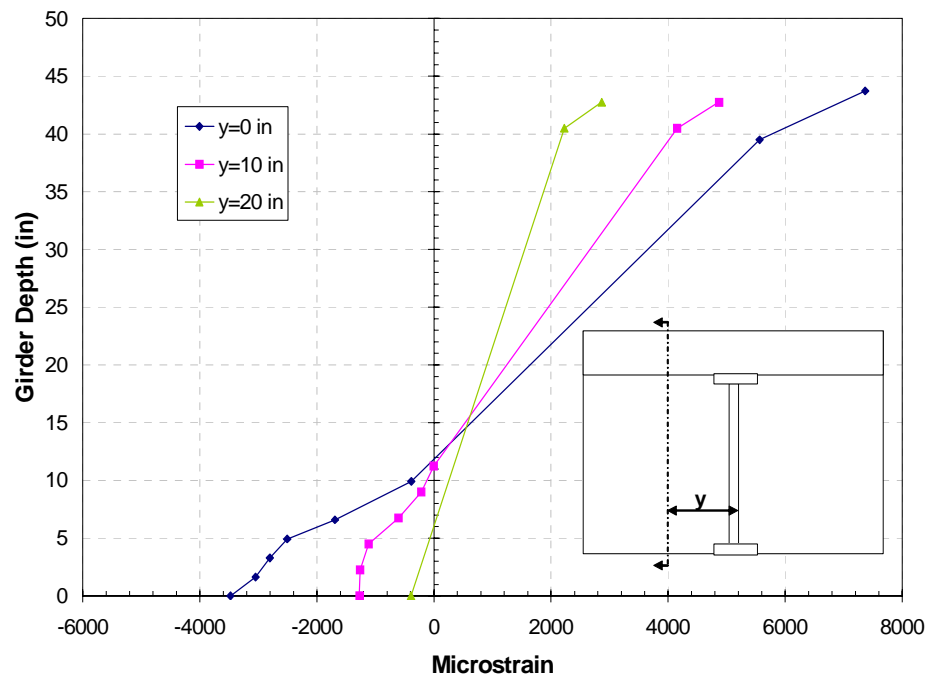


Figure 6-7: Strain profile at the pier centerline of the third specimen at different location along the width of diaphragm for load of 350 kip

6.4.2 STRESS DISTRIBUTION IN SLAB REBAR

It is evident from both test data and finite element analysis that the stress is not uniformly distributed in the slab rebar along the slab width. For a beam with a long flange, it is shown based on an elastic approach, that the stress distribution is not uniform at the top flange or slab. Timoshenko and Goodier (1970) computed the stress distribution by using a stress function that satisfies the 2-D linear elasticity differential equation along with the boundary conditions. This solution has been used as a basis for the design codes to evaluate the effective width of the slab contributing in bending resistance in the form of simple expressions. The main reason for nonlinearity of strain, and consequently stress in the slab is the shear lag phenomenon. In past works, researchers have usually tried to find the distribution based on an elastic approach or numerical methods (Ansourian, 1975). However, to calculate the capacity of a composite rein-

forced concrete slab and a girder at the ultimate condition, the elastic assumptions such as homogenous material and linearity are no longer valid. In the following section, an approach is presented to calculate the stress distribution in slab rebar at the ultimate condition when concrete is in tension.

As shown in Figure 6-7, the applied moment, M , is resisted by a couple of a tension force, T , at the slab and a compression force, C , at the bottom flange in the negative moment region of a continuous girder. In the composite section, most of the tension force should be resisted by slab rebar. The transferred tension force in the concrete slab is resisted by the tensile strength of the concrete and rebar. It was observed during the tests that the cracks formed through the depth of the concrete slab at the ultimate condition. Therefore, the tensile strength of concrete in the slab can be ignored and all the tension force can be assumed to be resisted by the reinforcement. Since the tension force is transferred through the top flange to the slab rebar, it can be assumed to be a concentrated force acting at the middle of the slab as shown in Figure 6-8.

For a simpler model, two assumptions are made:

1. The slab can be assumed to act as a continuous beam supported by rebar similar to 1-D springs.
2. The shear is transferred to the rebar through the concrete slab.

These assumptions are correct if the shear strength of the slab concrete is adequate to transfer the applied shear between the rebar and the steel girder. In addition, there should not be any slippage between the concrete and the reinforcement.

It was observed in experimental tests that parallel cracks formed throughout the slab (see Figure 6-9). The concrete slab can be assumed to consist of transverse strips between these cracks which are connected by the longitudinal rebar of the slab. Each strip can be assumed to be a concrete beam

under the tension from the rebar forces. A simple model of slab strips analogous to a beam on multiple supports is shown in Figure 6-10. It can be seen that in this simple model, the shear deformation of the concrete between two adjacent bars causes a shear lag between the two bars. Of course, concrete does not have a substantial tensile strength at the ultimate condition to transfer part of the tension force, T , to the supports, but it has the shearing resistance to distribute this force among the slab reinforcement.

To find a formula for induced force in each rebar, the system can be assumed elastic. This might not be a realistic assumption at the ultimate condition, while rebar yield and concrete cracks; however, the experimental results and finite element analysis have shown that all of the rebar in the slab usually yield in the specimens similar to the first or third specimen. Hence, it can be assumed that all of the slab rebar have the same tangent modulus, assuming a bilinear stress-strain relationship. Furthermore, the concrete is also cracked throughout the slab depth, so it has almost uniform cracked shear stiffness. Therefore, if all the rebar have the same tangent elastic modulus and the slab has uniform shear stiffness, then the entire system consisting of the steel reinforcements and the concrete slab can be treated as an elastic system, though with inelastic material properties. For instance, a transverse strip of the concrete slab is shown in Figure 6-11 as a beam resting on eight springs which resemble the rebar. Each bar has an axial deflection denoted by δ in Figure 6-11.

The half of the beam due to symmetry as shown in Figure 6-11 is considered as a cantilever (see Figure 6-12) resting on continuous springs and have only shear deformations. This beam is an example of the Winkler foundation method. The differential equation of the beam is given by

$$\frac{d\delta}{dy} = -\frac{kv}{G_c A_c} \quad (6-1)$$

where:

δ = deflection of the beam as a function of y

k = shear stress factor, which is about 1.5 for rectangular sections

v = shear force in any section of the beam

G_c = shear modulus

$A_c = t_s \Delta$

t_s = slab thickness

Δ = crack spacing according to Equation (6-17)

G_c is the shear modulus, which can be considered for the condition of closed cracked condition as 0.4 of the elastic state. This value is based on the shear modification factor used in the finite element analyses as discussed in Chapter 5. The shear force in any section of the cantilever is readily given by the following equation, based on the force equilibrium in the vertical direction:

$$v = \frac{T}{2} - \int_0^y k_r \delta dy \quad (6-2)$$

where the uniform stiffness of the slab rebar across the slab width can be defined in the following form:

$$k_r = \frac{E_s A_s}{b_s \Delta} \quad (6-3)$$

where:

E_s = tangent modulus of the slab reinforcements

A_s = total area of longitudinal steel rebar in the slab

b_s = width of the concrete slab

Substituting Equation (6-2) into differential Equation (6-1), we get

$$\frac{d\delta}{dy} = \frac{-1.5}{0.4G_c A_c} \left(\frac{T}{2} - \int_0^y k_r \delta dy \right) \quad (6-4)$$

Taking the derivative of both sides of Equation (6-4) with respect to y results in

$$\frac{d^2 \delta}{dy^2} - \frac{1.5k_r}{0.4G_c A_c} \delta = 0 \quad (6-5)$$

The general solution for this ordinary differential equation is

$$\delta = Ae^{\lambda y} + Be^{-\lambda y} \quad (6-6)$$

where:

$$\lambda = \sqrt{\frac{1.5k_r}{0.4G_c A_c}} \quad (6-7)$$

The boundary conditions for this equation are as follows:

As $y \rightarrow \infty$, $\delta = 0$

For $y = \frac{b_s}{2}$, $v = 0$

Applying these two conditions, the constant in Equation (6-6) can be found (A=0). Thus, the deflection of the beam is,

$$\delta = \frac{T\lambda}{2k_r \left(1 - e^{-\frac{\lambda b_s}{2}}\right)} e^{-\lambda y} \quad (6-8)$$

If distribution of strain is assumed to be uniform along the length of the composite girder, the strain can be approximately considered as

$$\varepsilon = \frac{\delta}{L} \quad (6-9)$$

where,

L = Length of the cantilever girder

Substituting Equation (6-8) into Equation (6-9)

$$\varepsilon = \frac{T\lambda}{2Lk_r \left(1 - e^{-\frac{\lambda b_s}{2}}\right)} e^{-\lambda y} \quad (6-10)$$

The tension force in slab can be obtained approximately from the moment at each section using the following formula:

$$T = \frac{M}{d} \quad (6-11)$$

where d is the distance between the center of the slab reinforcements and the center of the compression force in the concrete diaphragm. Shear force, V , at each section is,

$$V = \frac{M}{L} \quad (6-12)$$

Substituting Equation (6-12) into Equation (6-11) and the result into Equation (6-10) we get,

$$\varepsilon = \frac{V\lambda}{2dk_r \left(1 - e^{-\frac{\lambda b_s}{2}}\right)} e^{-\lambda y} \quad (6-13)$$

In the general force transfer mechanism of the connection, the strain consistency requires that the initial value of strain at $y=0$ be equal to the strain obtained from the section strain surface. If the initial value considered as ε_s , the Equation (6-13) is rearranged as follows:

$$\varepsilon = \varepsilon_s e^{-\lambda y} \quad (6-14)$$

In the preceding calculations, the width of the assumed beam, Δ , is taken equal to the approximate distance between transverse cracking. The crack spacing can be computed according to the following formula (Navy, 2003):

$$\Delta = \frac{A_t f_t'}{n \pi d_b \mu} \quad (6-15)$$

where:

d_b = reinforcing element diameter

μ = bonding stress between rebar and concrete according to Equation (6-16)

f_t' = concrete tensile strength in ksi, according to Equation (6-30)

$A_t = b_s t_s$

n = number of rebar

The bonding stress is defined by the following equation:

$$\mu = \frac{\sqrt{f'_c}}{1.25\pi d_b m_f} \quad (6-16)$$

$$m_f = 1.4 \text{ (modification factor according to AASHTO-LRFD (2004))}$$

$$f'_c = \text{concrete compression strength in ksi}$$

Substituting Equation (6-15) into Equation (6-16) yields the following equation:

$$\Delta = \frac{1.25(0.23)A_t m_f}{n} = \frac{0.4b_s t_s}{n} \quad (6-17)$$

6.4.2.1 COMPARING WITH THE TEST RESULTS

The material and geometry of tested specimens were selected to check the agreement of derived formulas with the test results. As an example, the third test specifications are presented in this section. The shear modulus of concrete in the longitudinal direction (x-dir) is given by:

$$G_c = \frac{E_c}{2(1+\nu)} \quad (6-18)$$

The elastic modulus for the slab concrete, E_c , and Poisson's ratio, ν , were determined in Chapter 5. Substituting E_c and ν from Table 5-1 into Equation (6-18), G_c for the third test is given as 4417 ksi. The deck thickness, t_s , for all three tests was about 7.5 inches. Substituting the third test specifications into Equation (6-17) the crack spacing, Δ , is computed to be 7.5 inches.

The tangent modulus of the steel bars was obtained from the material properties of bars as discussed in Chapter 5. In the forging calculations, it

is assumed that the tangent modulus is about five percent of the elastic modulus.

$$E_s = 0.05(29000) = 1450ksi$$

The total reinforcement area in the top and bottom layers was 19.4 in² in the third specimen. If a continuous model is used, the distributed steel over the width of the slab is used in the stiffness equation. The stiffness of each rebar is computed by substituting the input values in Equation (6-3). The resulting value is given as 40.1 ksi. The other third test data required for the calculations as follows:

$$V = 390 \text{ kip (at ultimate condition)}$$

$$A_c = \Delta t_s = 56.5 \text{ in}^2$$

$$d = 43 \text{ in}$$

$$b_s = 93 \text{ in}$$

Substituting these values into Equation (6-14) gives the strain distribution across the diaphragm width as shown in Figure 6-13 and Figure 6-14 for the first and the third tests, respectively. It is observed that there is a good agreement between the finite element strain and that predicted by Equation (6-14) at the ultimate condition. It is noted that the initial strain was selected based on the finite element model at the edge of the steel girder. The strain of the slab rebar within the top flange width is assumed to be flat due to high rigidity of the steel girder in this region. It should be noted that the origin of the y-coordinate in Equation (6-14) has been shifted as much as $b_f/2$ to the right to obtain the exponential curve from the edge of the steel top flange in which b_f is the width of the girder flange.

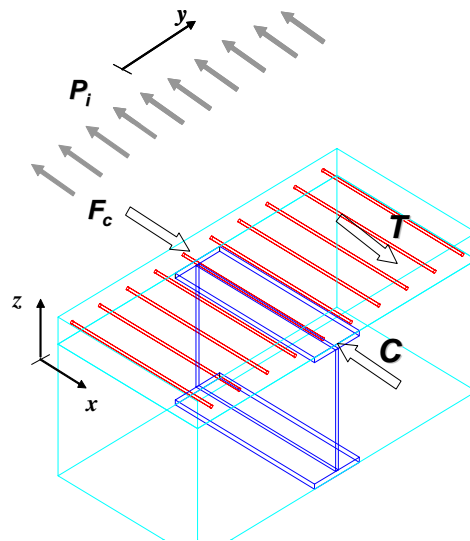


Figure 6-8: Free body diagram for a slice of the diaphragm

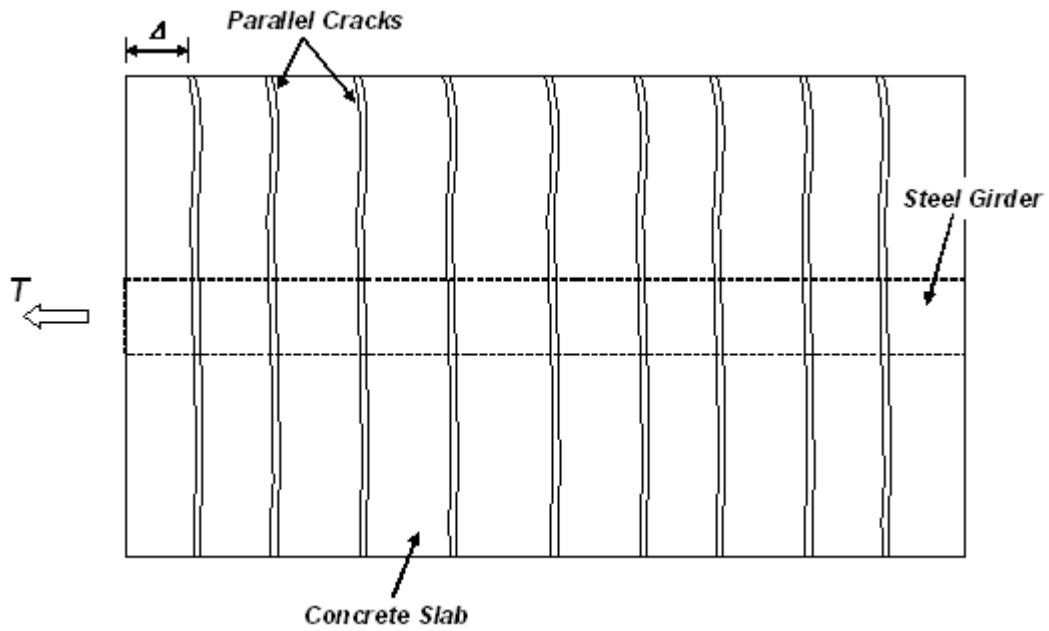


Figure 6-9: Plan view of concrete slab and parallel cracks

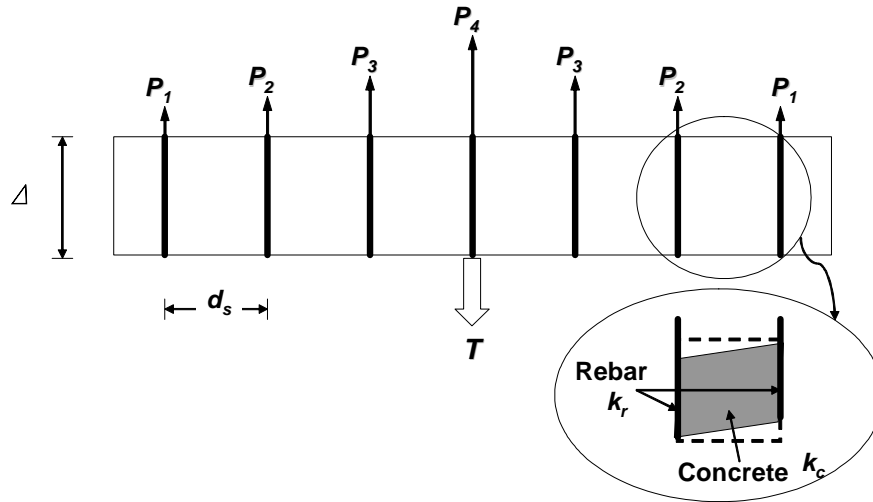


Figure 6-10: A strip of the concrete slab with the reinforcements and the applied loads

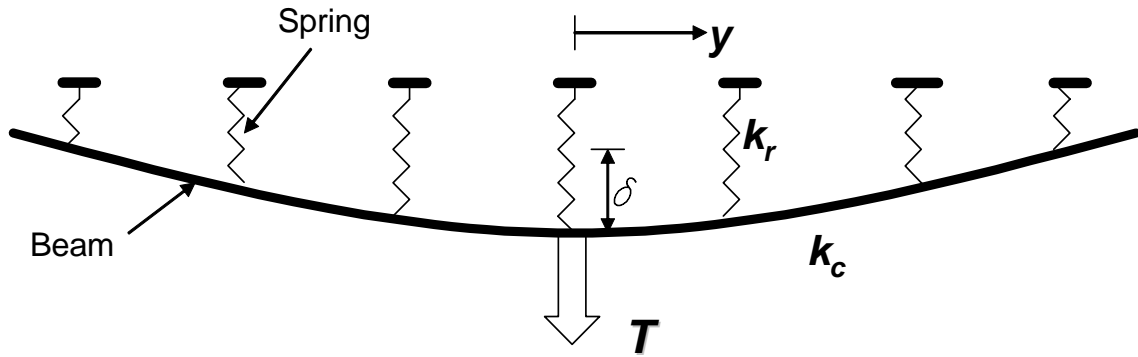


Figure 6-11: Beam-spring model for the concrete slab and the rebar

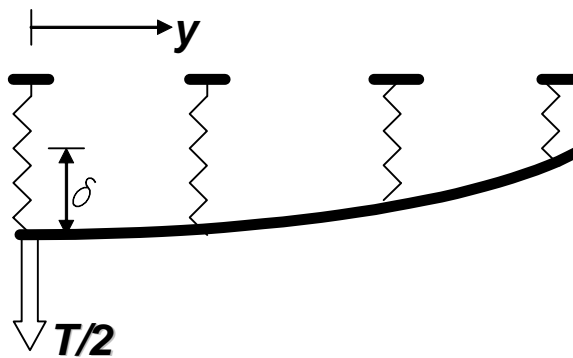


Figure 6-12: Winkler model for half of the concrete slab and the rebar

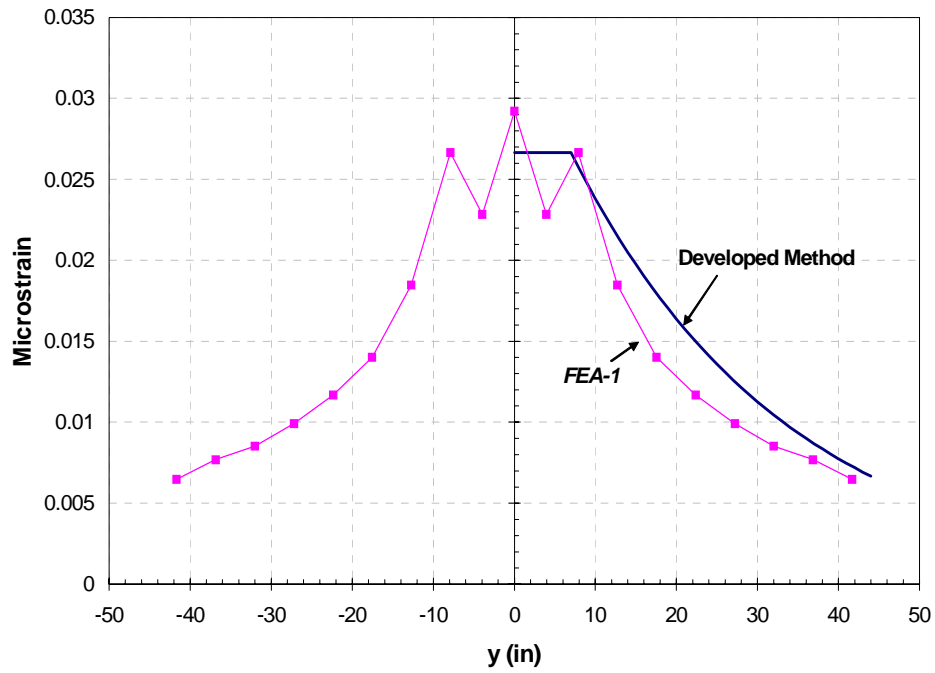


Figure 6-13: Comparison of Winkler method and FEA results for the first test at a load of 500 kips

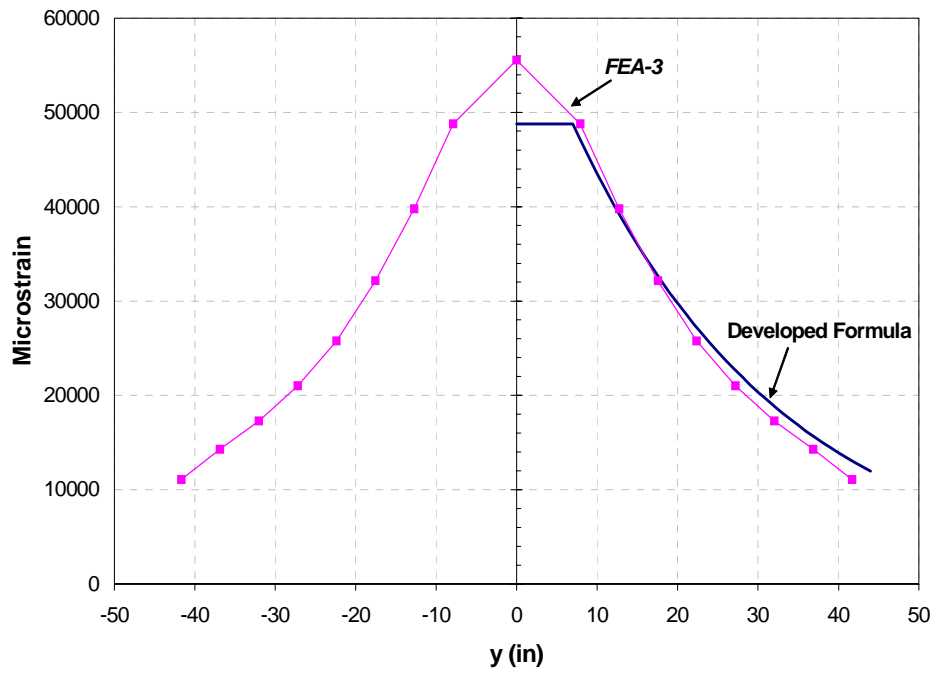


Figure 6-14: Comparison of Winkler method and FEA results for the third test at a load of 382 kips

6.5 CONCRETE BEHAVIOR

6.5.1 CONCRETE FAILURE STRAIN

The compressive resistance of the bottom part of the concrete diaphragm has a substantial contribution to the total moment capacity of the connections, especially in the second and the third type. The test results indicate that the concrete in the core region under the compressive stress exhibits very large strain at collapse. For example, in the third specimen the strain of the concrete at the bottom of the core region exceeded 0.01 in/in. This is against basic assumptions in the design of reinforced concrete beam sections, which assumes the concrete section collapses at a strain of about 0.003 in/in, according to ACI-318 (2004). It is also observed that the specimens did not collapse after crushing of the lowest fibers of the concrete core in the finite element simulations. These facts reveal that the current concrete material model used in ACI-318 (2004) for the design of reinforced concrete beams may not be capable of predicting the behavior of the proposed connections.

It was shown by experimental work in Chapter 4 that the concrete confinement enhanced its ductility at failure. The experimental works of Kupfer and Hilsdorf (1969) on biaxial behavior of concrete show that the failure strain of concrete increases in the biaxial compression-compression state. Also, it was observed that assuming a small concrete failure strain of about 0.003 in/in with a linear strain distribution across the depth the section resulted in a small steel strain in slab rebar which did not match both experimental and analytical results. In addition, some investigations show that the computed flexural strength of a reinforced concrete beam is usually relatively insensitive to the value of the assumed maximum concrete strain (Park and Paulay, 1974). Therefore, a new concrete model is proposed which is more ductile at failure.

In the present study, the model of Filippou and Kwak (1990) is used after some modifications. These modifications are introduced in order to adapt the model for the compressive behavior of concrete in tested specimens. The material follows a second degree parabola (AB in Figure 6-15) up to the maximum stress, f_c , in the biaxial state. Beyond this stress, the behavior is followed by a linear descending branch (line BC) which represents strain softening. The maximum stress is computed based on a three parameter model as described in Appendix A. The maximum strain, ε_{3m} , in the biaxial stress state is given by the following equation (Fillipou and Kwak, 1990):

$$\varepsilon_{3m} = \varepsilon_{co} \left(3 \frac{f_c}{f'_c} - 2 \right) \quad (6-19)$$

where ε_{co} is the strain corresponding to the concrete compressive strength f'_c under uniaxial stress conditions. The ratio of the maximum biaxial stress, f_c , to the uniaxial stress can be computed according to the Equation (6-31),

$$\frac{f_c}{f'_c} = \frac{0.38}{\sqrt{f'_c}} + 1 \quad (6-20)$$

The maximum uniaxial strain, ε_{co} , of the concrete can be found according to the following equation (Park and Paulay, 1974):

$$\varepsilon_{co} = \frac{2f'_c}{E_c} \quad (6-21)$$

where according to AASHTO-LRFD (2004),

$$E_c = 1820\sqrt{f'_c} \quad (6-22)$$

Combining Equations (6-19) through (6-22) gives,

$$\varepsilon_{3m} = 0.00125 + \frac{\sqrt{f'_c}}{910} \quad (6-23)$$

where f'_c is in ksi. The slope of the descending line, Z , for the uniaxial compression tests (Park and Paulay, 1974) is approximately

$$Z = \frac{0.15f'_c}{0.001} \quad (6-24)$$

Based on the finite element results, the stress in the concrete core at the lowest fiber tends to zero. However, Park and Paulay (1974) recommend the crushing stress about 20 percent of the concrete compressive strength to account for the ability of concrete to sustain very large strain. If this value is adopted for the current cases, the concrete failure strain, ϵ_c , in the biaxial stress state is readily obtained from geometry show in Figure 6-15.

$$\epsilon_c = \epsilon_{3m} + \frac{0.8f'_c}{Z} \quad (6-25)$$

substituting Equation (6-23) and (6-24) into Equation (6-25),

$$\epsilon_c = 0.00658 + \frac{\sqrt{f'_c}}{910} \quad (6-26)$$

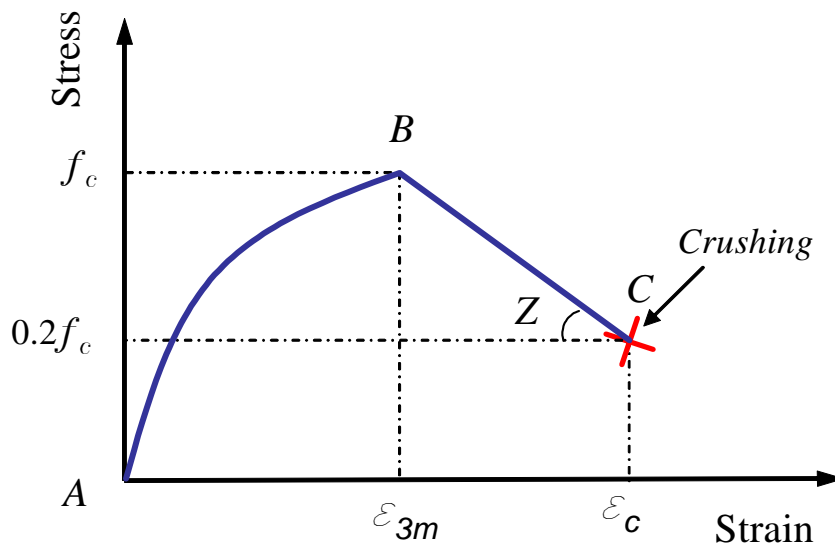


Figure 6-15: The developed concrete model in compression

6.5.2 CONCRETE STRENGTH

The crushing of the concrete between two end bearing plates (the core concrete) is a main reason for the collapse of the specimens or change in slope of the load-deflection curves. Based on the finite element results, most of the compressive force in the bottom flange of the steel girder is transferred through the core concrete. The crushing of the concrete occurs inside the core concrete between the two end bearing plates. This region is confined between the end bearing plates and the concrete diaphragm. Therefore, the stress state is similar to a multi-axial state as shown in Figure 6-16. The finite element results also confirm that the compressive stress in this region is higher than the uniaxial compressive strength of the concrete. The confinement of the core concrete by the surrounding concrete diaphragm and the end bearing plates enhances the ultimate strength and strain of the concrete. This was proven by many tests as shown in Figure 6-17. ANSYS used a five parameter concrete model to evaluate the concrete strength in the triaxial stress state as shown in Figure 6-18. A simpler model, three parameter concrete, was implemented to achieve a closed-form solution for the design purpose.

In this approach, the crushing of the concrete core under the applied compressive stresses from the end bearing plate is identified using a simple model as shown in Figure 6-19. The applied pressure, q , is resisted by the direct concrete compressive strength, f_c , plus shear resistance denoted by s in Figure 6-19,

$$qab_f = 2sat_c + f_c ab_f \quad (6-27)$$

where:

a = depth of compression stress block in core region

b_f = width of the end bearing plate which is equal to flange width in current study

t_c = thickness of concrete core

Simplification of Equation (6-27) gives,

$$q = 2s \frac{t_c}{b_f} + f_c \quad (6-28)$$

The concrete compressive strength, as discussed earlier due to the diaphragm, confinement is more than the uniaxial compressive strength, f'_c . This strength can be computed based on a three parameter biaxial state of stress as described in Appendix A or a linear approximation as discussed herein. For a linear approximation of the failure surface, the lateral stress, shown by p in Figure 6-19, is assumed to be less than 20 percent of the normal stress, which is a reasonable assumption based on the fact that concrete cracks in this direction and the cracking stress of concrete is less than 20 percent of the compressive stress. Based on a linear fit of the failure surface presented in Appendix A (Equation (A-15)), the relationship of normal stress, f_c , and lateral principal stress, p , can be described in the following formula:

$$f_c = 1.6p + f'_c \quad (6-29)$$

The finite element analysis of the tested specimens indicates that the first principal stress in the core concrete region is not more than the tensile strength of the concrete. In addition, the experimental studies done by Kupfer et. al. (1968) indicates that the biaxial tensile strength of concrete is approximately equal to its uniaxial strength. In addition, the ANSYS fail-

ure surface for the concrete as shown in Figure 6-18 does not allow tensile stress beyond the uniaxial tensile strength. Based on these reasons, the bursting pressure, p , is assumed as the tensile splitting strength of the concrete, f'_t . Therefore, the lateral stress can be taken as the tensile strength as it is discussed in Appendix B. The tensile strength is taken from the AASHTO-LRFD (1998) formula for the splitting tensile strength in ksi:

$$f'_t = 0.24\sqrt{f'_c} \quad (6-30)$$

Substituting Equation (6-30) into Equation (6-29) gives

$$f_c = 0.38\sqrt{f'_c} + f'_c \quad (6-31)$$

According to Appendix B, Equation (6-31) is valid in the following ranges:

$$0.1 \leq \frac{b_f}{b_s} \leq 0.3 \quad (6-32)$$

and

$$0.1 \leq \frac{t_c}{b_s} \leq 1.0 \quad (6-33)$$

Shear strength is computed based on the AASHTO-LRFD (1998) recommendation:

$$s = \left(0.063 + \frac{0.126}{\beta} \right) \sqrt{f'_c} \quad (6-34)$$

where β is the ratio of long side to short side of the compression rectangle through which the compressive force is transmitted and f'_c is in ksi. Substituting Equation (6-34) and (6-31) into Equation (6-28) the following relationship is derived for the concrete strength in the core region:

$$q = \frac{2t_c}{b_f} \left(0.063 + \frac{0.126}{\beta} \right) \sqrt{f'_c} + 0.38\sqrt{f'_c} + f'_c \quad (6-35)$$

The shear aspect ratio, β , is taken as the ratio of the depth of the stress block to the end bearing plate width. Therefore, Equation (6-35) is reduced to:

$$q = 0.38 \left(1 + \frac{t_c}{b_f} \right) \sqrt{f'_c} + f'_c \quad (6-36)$$

Hawkins (1968) performed 18 series of tests on concrete specimens loaded through plates that in turn were loaded with a very rigid punch. His studies aimed to investigate the connections in prestressed members. The load transfer mechanism in the core region is similar to Hawkins' eccentric plate loading tests. Equation (6-36) was verified using Hawkins' edge loading tests on the cubes. The test specimens' characteristics and results are compared with predicted strength from Equation (6-36) in Table 6-4. It can be seen for the size ratios satisfying Equation (6-32) and (6-33) conditions, the test and predicted results have good agreements.

The total compressive force resisted by the core concrete can be computed from the following formula:

$$F_q = qab_f \quad (6-37)$$

where a is computed based on the total force equilibrium of the section at ultimate condition and can be assumed as:

$$a = \beta c \quad (6-38)$$

in which c is the depth the neutral axis from the lowest fiber of the core concrete. The ratio of β is adopted from ACI-318 (2005) recommendations to evaluate the total compressive resistance of the concrete core in an equivalent rectangular stress block.

$$\beta = 0.85 - (q - 4.0)(0.05) \quad (6-39)$$

The finite element parametric studies showed that this formula was a reasonable estimate for the current cases.

Finite element analyses show that the stiffness of the end bearing plate shall be adequate to provide an almost uniform stress distribution on the core concrete. The stiffness of the end bearing plate and its supporting stiffeners can be computed based on Roberts' and Breen's (2000) limitation for the ratio of the deflection of the end bearing plate, δ , to the thickness of the plate, t_e , as:

$$\frac{\delta}{t_e} \leq 0.0008 \quad (6-40)$$

The deflection of the end bearing plate under applied compression pressure, q , can be computed using the theory of plate and shells. If half of the end bearing plate, limited by the bottom flange, web plate and stiffeners, is considered as a square plate with three simply supported edges and one free edge (Timoshenko, 1959), the maximum deflection of the plate is given by:

$$\delta = \frac{0.01qb_f^4}{16D} \quad (6-41)$$

where:

$$D = \frac{E_s t_e^3}{12(1-\nu^2)} \quad (6-42)$$

t_e = end bearing plate thickness

Substituting 0.3 for ν and 29000 ksi for the elasticity modulus in Equation (6-42) and combining Equations (6-42) and (6-41), then substituting into Equation (6-40) gives,

$$\frac{b_f}{t_e} \leq \frac{7.63}{\sqrt[4]{q}} \quad (6-43)$$

Test Series	f'_c psi	$2b$ in	$2a$ in	$2c$ in	q/f'_c Test	b_f/b_s	t_c/b_s	q ksi	q/f'_c Equation	$Eq./Test$
L	6400	1	1	6	2.42	0.17	1	15.97	2.49	1.03
L	6400	1.17	1.17	6	2.22	0.2	1	14.72	2.3	1.04
L	6850	1.42	1.42	6	2.01	0.24	1	14.11	2.06	1.03
L	6400	1.72	1.72	6	1.99	0.29	1	12.37	1.93	0.97
L	6870	2.42	2.42	6	1.75	0.4	1	11.55	1.68	0.96
L	5540	3	3	6	1.4	<u>0.5</u>	1	9.1	1.64	<u>1.17</u>
L	4370	1.72	1.72	6	1.95	0.29	1	9.3	2.13	1.09
L	6920	1.42	1.42	6	2.12	0.24	1	14.22	2.06	0.97
L	6920	2	2	6	1.77	0.33	1	12.39	1.79	1.01
L	6920	3	3	6	1.52	0.5	1	10.9	1.58	1.04
M	3840	2	2	6	1.91	0.33	1	7.92	2.06	1.08
M	3840	3	3	6	1.71	0.5	1	6.81	1.77	1.04
R	6790	1.15	2.25	6	2.2	<u>0.38</u>	1	20.4	3.01	<u>1.37</u>
R	6790	1.1	2.8	6	2.23	<u>0.47</u>	1	24.14	3.56	<u>1.59</u>
R	6400	1	3	6	2.21	<u>0.5</u>	1	27.44	4.29	<u>1.94</u>
R	6830	1	4	6	2.05	<u>0.67</u>	1	34.5	5.05	<u>2.46</u>
R	6580	1	5	6	1.71	<u>0.83</u>	1	39.55	6.01	<u>3.52</u>
R	7070	1	6	6	1.73	<u>1</u>	1	47.28	6.69	<u>3.87</u>
R	6850	2	2.85	6	1.84	0.48	1	13.56	1.98	1.08
S	4940	1.5	1	6	2.13	0.25	1	9.71	1.96	0.92
S	4940	2	1	6	1.92	0.33	1	8.31	1.68	0.88
S	4940	3	1	6	1.57	0.5	1	7.18	1.45	0.93
S	4940	2	3	6	1.71	<u>0.5</u>	1	10.83	2.19	<u>1.28</u>
S	4940	3	2	6	1.48	0.5	1	7.74	1.57	1.06

Table 6-4: Comparing Hawkins' test results with predictions of Equation (6-36)

6.5.2.1 IMPLEMENTATION OF THE DEVELOPED MODEL FOR THE THIRD SPECIMEN

The concrete strength is computed using the described method for the third specimen. The characteristics of the specimen are as follows:

The concrete width in compression (b_f) = 15.8 in

The thickness of diaphragm (t_c) = 4.00 in

The concrete compressive strength (f'_c) = 5.89 ksi

According to Equation (6-35) the maximum core concrete strength, q , is computed as:

$$q = \frac{2(4)}{(15.8)} \left(0.063 + \frac{0.126}{1.2} \right) \sqrt{5.9} + 0.38\sqrt{5.9} + 5.9$$

$$q = 7.029 \text{ksi}$$

The stress magnitude is 1.19 times the concrete compressive resistance and has a good agreement with that of the finite element analysis for the third specimen (see Table 5-3). The total compressive force resisted by the core concrete can be computed using Equation (6-37) in which a is substituted from the finite element analysis:

$$F_q = qab_f = 7.03(11.2)(15.8) = 1246 \text{kip}$$

The finite element result for this force was 1256 kip, which was very close to what was predicted.

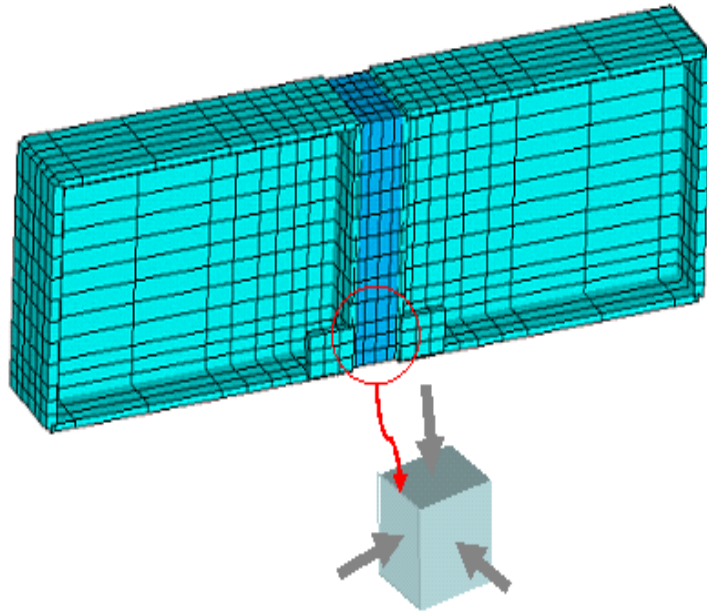


Figure 6-16: Multi-axial state of stress in the core concrete

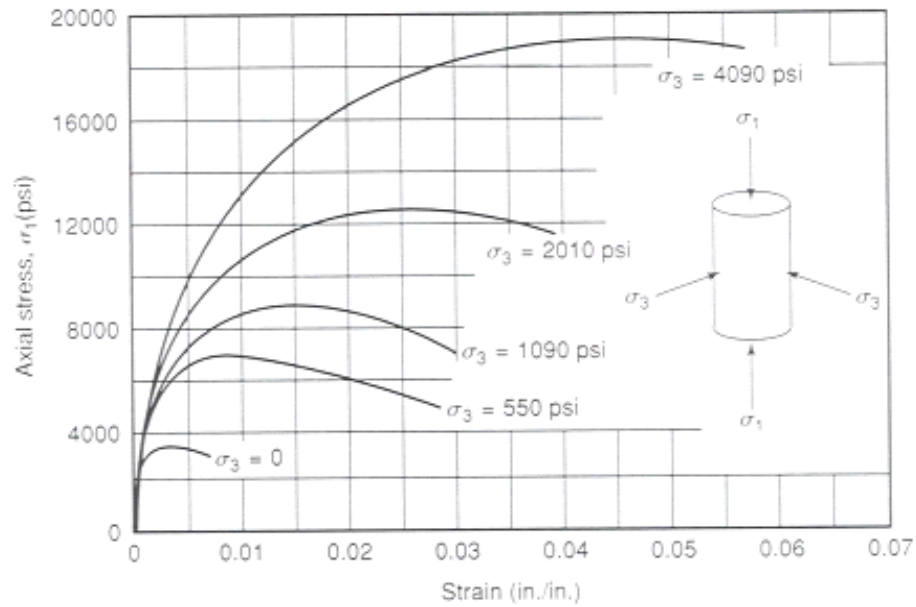


Figure 6-17: Concrete response under triaxial compression (Paulay, 1974)

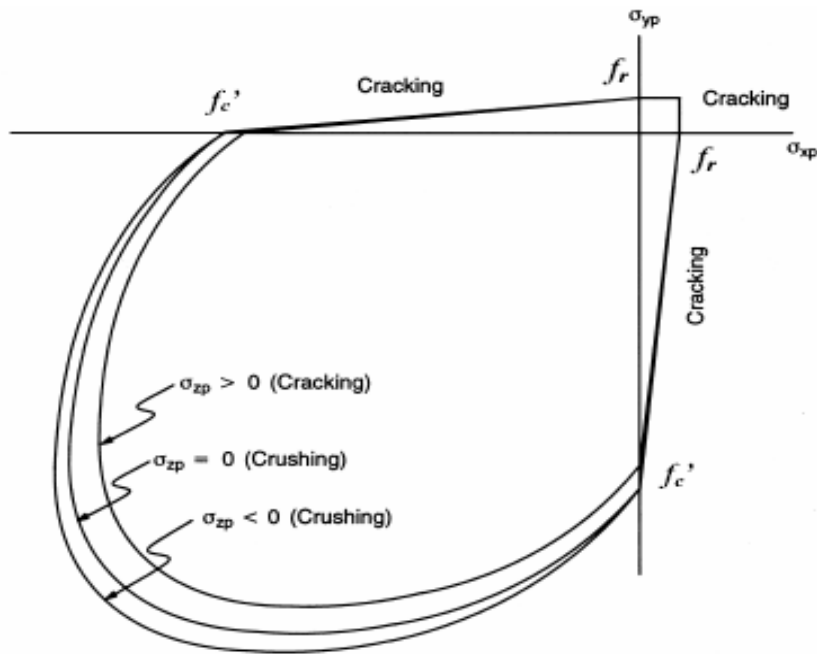


Figure 6-18: Failure surface for concrete (ANSYS)

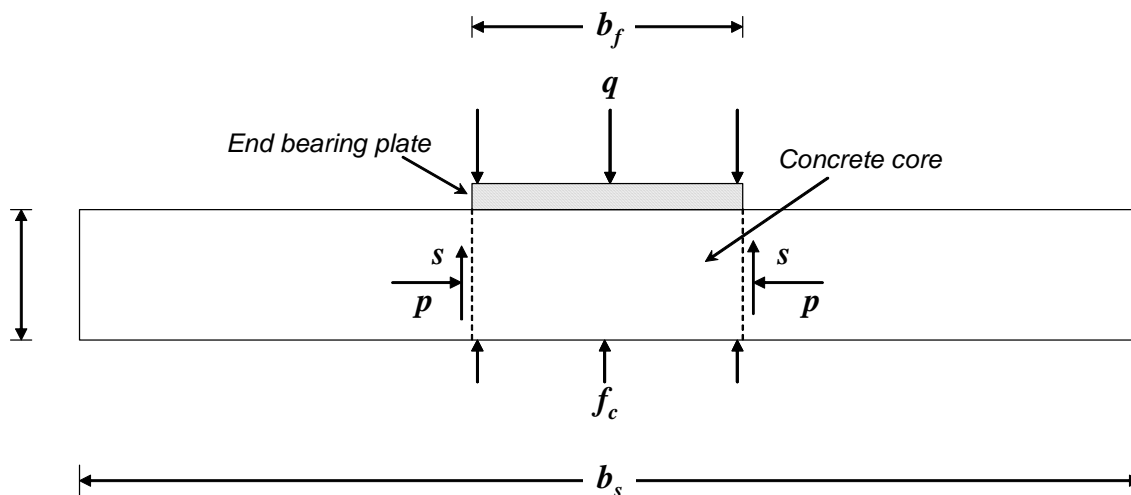


Figure 6-19: End bearing plate resting on the core concrete

6.6 OUTSIDE THE CORE CONCRETE PARTICIPATION

The core concrete between two end bearing plates usually crushes due to the applied compression force, denoted by F_q in Equation (6-37). However, the other part of the concrete diaphragm, outside the end bearing plate width, also participates in resisting the compression force. It was seen in the finite element analysis of the third specimen that about 30 percent of the compressive resistance of the concrete diaphragm at the pier centerline is provided by the concrete outside of the end bearing plate width. In some of the models, the steel girder was not connected to the concrete diaphragm; however, there was still about 20 percent compressive resistance due to the concrete outside of the core region. There were three mechanisms through which the compressive force was transferred to the concrete diaphragm outside of the core region. First, the compressive force of the end bearing plate was distributed into the concrete diaphragm similar to axial force transferred to the foundation from a column base plate. This effect was included in the previous section indirectly in calculation of the concrete compressive strength, because the shear stress, s in Equation (6-27), was transferring the compressive force to the outside of the core region. The second mechanism of transferring force was through the web

shear bars. In addition, it was observed that even if the steel girder had no bonding to the concrete diaphragm, there was a compressive resistance from the concrete diaphragm outside the core. The reason for this resistance was the strain gradient in the concrete diaphragm. In the following sections, the two latter behaviors are discussed.

6.6.1 WEB SHEAR BARS BEHAVIOR

Part of the steel girder moment in the compression region was transferred to the concrete diaphragm through the dowel action of the web shear bars. The resistance mechanism of the shear bars is similar to the shear studs. A simple form of dowel mechanism is shown in Figure 6-20. The movement of the web plate causes the slippage of the shear bar. The slippage of the shear bar induces compressive stress in the adjacent concrete. The resultant of compressive stress inside the concrete is denoted by Q in Figure 6-20. The eccentricity of concrete compression force, e , causes bending moment in shear bar. There are three modes of failure for the shear bar:

1. crushing of concrete under bearing stress
2. failure of shear bar under the flexural and shear forces
3. combination of previous two modes

In most cases the failure mode is governed by the third mode (Ohelers, 1995). The determination of the shear connector capacity analytically is complex due to the interaction of steel bars and surrounding concrete. As a result, the capacity is usually determined using empirical tests. The AASHTO formula for the nominal resistance of a shear connector is based on the experimental pushout tests done by Olgaard et. al (1971). They suggested the following statistical formula for the strength of one stud:

$$Q = 0.5A_{ss}\sqrt{f'_c E_c} < A_{ss}F_u \quad (6-44)$$

where:

A_{ss} = cross-sectional area of a stud shear connector (in²)

E_c = modulus of elasticity of the concrete (ksi)

F_u = tensile strength of a stud shear connector (ksi)

f'_c = concrete compressive strength (ksi)

In addition to this formula which gives the strength of a shear connector, the fatigue resistance of the stud shall be checked. According to AASHTO (1998) the fatigue resistance of an individual shear connector, Z_r , in kip is given by

$$Z_r = \alpha_f d_{ss}^2 \quad (6-45)$$

for which:

$$\alpha_f = 34.5 - 4.28 \log N \geq 2.75 \quad (6-46)$$

where:

d_{ss} = diameter of stud (in)

N = number of cycles

Using Equation (6-44), the ultimate strength of shear bars embedded in the test specimens can be computed. For the third test specimen, the required data and the shear bar strength are as follows:

$$A_{ss} = 0.79 \text{ in}^2 \text{ (#8 bar)}$$

$$E_c = 4420 \text{ ksi}$$

$$F_u = 65 \text{ ksi}$$

$$f'_c = 5.90 \text{ ksi}$$

$$Q = 0.5(0.79)\sqrt{5.9(4420)} < 0.79(65)$$

$$Q = 51.35 \text{ kip}$$

According to FEA, only the lowest web shear bar is prone to reach its ultimate capacity since the other bars are close to the neutral axis. Therefore, the contribution of the web shear bar in compression strength of the diaphragm is:

$$F_{ws} = 2Q = 2(51.35) = 102.7 \text{ kip}$$

The fatigue resistance of the two shear connectors according to AASHTO is obtained using the following information and Equation (6-45):

$$d_{ss} = 1 \text{ in}$$

$$N = 5,515,516 \text{ cycles (based on the third test fatigue test)}$$

$$\alpha_f = 34.5 - 4.28 \log 5515516 = 5.64$$

thus,

$$Z_r = 2(5.64)(1)^2 = 11.3 \text{ kip}$$

The minimum of the ultimate strength and fatigue resistance of the shear bars shall be added to the total diaphragm compressive resistance. In the

third test, the fatigue resistance is smaller, but it can be ignored in comparison with the compressive strength of the core concrete.

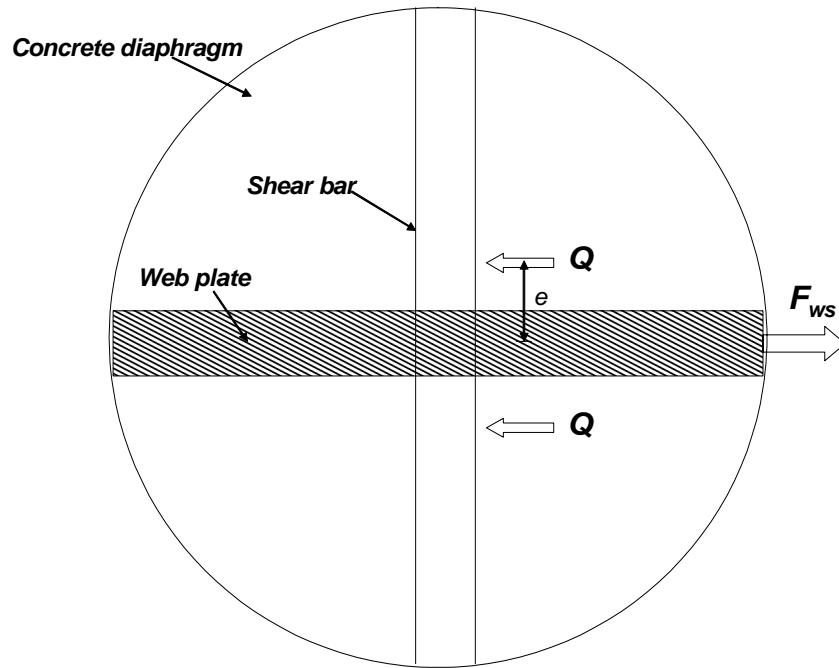


Figure 6-20: Load transfer mechanism of the web plate to the concrete through shear bars (plan view)

6.6.2 STRAIN GRADIENT

Another resistance mechanism of the concrete diaphragm outside the core concrete is the strain in this region due to the rebar tensile forces. For instance, consider a portion of the first specimen model as shown in Figure 6-21. The applied moment produces the tension forces in the slab rebar as denoted in Figure 6-21 by P_i . If a slice of concrete diaphragm with thickness ds , width Δ , and height h is separated, the free body diagram can be depicted as shown in Figure 6-22. In this model, a slice of diaphragm is assumed as a concrete beam supported by the top rebar and the diaphragm compression part. The rebar is modeled as a linear spring and the compressive part of the diaphragm as multiple supports. If full bonding of reinforcement and concrete is assumed, the strain of the slab rebar and concrete diaphragm are equal at the rebar elevation. The strain of the top

layer rebar causes a small deflection at the tip of the diaphragm slice. Part of the applied tensile force in the slab rebar is transferred to the concrete diaphragm through the bonding of the rebar and concrete. The concrete beam shown in Figure 6-22 does not resist tensile stress greater than the tensile strength of the concrete; therefore it deflects in the tension region. However, in the compression region, it is attached to the support as seen in Figure 6-22.

The strain at the tip of the beam, ε , can be obtained from the distribution defined in Equation (6-14). Thus, the deflection of the beam can be taken as

$$\delta = \Delta\varepsilon \quad (6-47)$$

The stiffness of the slice of diaphragm, k_{dc} , modeled as a beam considering both flexural and shear deformations can be computed as follows:

$$k_{dc} = \frac{1}{\frac{e^3}{3E_c I_c} + \frac{1.5e}{G_c A_c}} \quad (6-48)$$

in which beam section area, A_c , and its moment of inertia, I_c , are defined as

$$A_c = \Delta d_s$$

$$I_c = \frac{d_s \Delta^3}{12}$$

where:

d_s = width of the concrete slice

Δ = crack spacing according to Equation (6-17)

E_c = elasticity modulus of concrete

G_c = shear modulus of concrete

ε = strain of the slab rebar according to Equation (6-14)

e = the distance of the top layer rebar to the neutral axis

The induced force in the concrete diaphragm, F_{dc} , under the applied deflection is equal to:

$$F_{dc} = k_{dc} \delta \quad (6-49)$$

The transferred load to the concrete diaphragm produces almost a linear strain distribution in the diaphragm as show in Figure 6-23. The simulation results indicated that the stress of the concrete in the diaphragm outside of the end bearing plate width was well below the crushing stress. Therefore, a linear stress distribution is reasonable for the strain and stress as shown in Figure 6-23. The equilibrium of forces shown in Figure 6-23 gives

$$F_{dc} - F_t + F_{oc} = 0 \quad (6-50)$$

where F_t is the total tension and F_{oc} is the total compressive forces resisted by the concrete diaphragm slice. These forces can easily be computed based on the geometry shown in Figure 6-23 as:

$$F_t = 1/2 f_t' c_t d_s \quad (6-51)$$

$$F_{oc} = 1/2 f_t' d_s \frac{(d-e)^2}{c_t} \quad (6-52)$$

where:

f_t' = tensile strength of the concrete

c_t = the distance between the neutral axis to the maximum tensile stress depth

d = the distance between center of slab rebar to the extreme compressive fiber

The moment equilibrium of the forces about the neutral axis is given by

$$F_{dc} e - F_t \left(\frac{2c_t}{3} \right) - F_{oc} \frac{2(d-e)}{3} = 0 \quad (6-53)$$

In Equations (6-50) and (6-53), e and c_t are unknowns. Solving these two equations, e and c_t are found as functions of Δ , V , b_s , f_t' , d , t_s , E_c , and G_c . The induced compressive force in the concrete diaphragm, F_{oc} , is then easily calculated by substituting e and c_t into Equation (6-52). Summation of this load over the width of the diaphragm, except the core region, results in the contribution of the concrete diaphragm regions outside of the core concrete to the compressive strength of the concrete.

The developed method needs a numerical solution for the set of Equations (6-50) and (6-53) which might be solved by a computer program. To make a simpler approach, it was assumed that the concrete diaphragm is in an un-cracked and elastic state at the ultimate condition. The finite element simulations of the test specimens show that the contribution of concrete outside of the core region at the elastic condition is near to that of the ulti-

mate condition. The strain and stress distribution under this assumption is shown in Figure 6-24. The slab rebar strain distribution is computed according to Equation (6-14). The deflection of the beam is calculated based on the entire thickness, t_d , of the diaphragm, therefore the applied strain is given by

$$\delta = t_d \varepsilon \quad (6-54)$$

The stiffness can be written in a simpler form, assuming the eccentricity of the section, e , is almost equal to the depth of the section, d , and ignoring the bending deformation:

$$k_{dc} = \frac{0.2G_c A_c}{1.5d} \quad (6-55)$$

The induced force in the concrete diaphragm under the applied deflection, F_{dc} , is obtained according to Equation (6-49). The force equilibrium in the x-direction is similar to Equation (6-50) and gives the transferred force to the diaphragm as:

$$F_{dc} = \frac{1}{2} e f_t d_s - \frac{1}{2} (d - e) f_c d_s \quad (6-56)$$

where:

f_t = maximum tensile stress in the upper fiber of the diaphragm

f_c = maximum compression stress in the lowest fiber of the diaphragm

and the moment equilibrium about the neutral axis is given by:

$$F_{dc} e - \frac{1}{2} e f_t d_s \left(\frac{2}{3} e \right) - \frac{1}{2} (d - e) f_c d_s \left(\frac{2(d - e)}{3} \right) = 0 \quad (6-57)$$

Also, the linear stress assumption gives the following relationship between the tension and compression stresses:

$$\frac{f_t}{e} = \frac{f_c}{d - e} \quad (6-58)$$

From Equations (6-56), (6-57), and (6-58), the force eccentricity, e , the tensile stress, f_t , and the compressive stress, f_c , are computed as follows:

$$e = \frac{2}{3}d \quad (6-59)$$

$$f_t = \frac{4F_{dc}}{dd_s} \quad (6-60)$$

$$f_c = \frac{2F_{dc}}{dd_s} \quad (6-61)$$

The compression force which is resisted by the concrete outside the core region is readily obtained from the geometry shown in Figure 6-24 as follows:

$$F_{oc} = 1/2 f_t d_s \frac{(d - e)^2}{e} \quad (6-62)$$

By substituting Equations (6-59) and (6-60) into Equation (6-62), the following relationship is obtained:

$$F_{oc} = \frac{F_{dc}}{3} \quad (6-63)$$

Substituting Equation (6-56) into Equation (6-63) and considering new parameters defined in Equations (6-54) and (6-55), a single formula is given

for total compressive force resisted by the diaphragm concrete outside the core region, F_{oc} by:

$$F_{oc} = \frac{0.4G_c A_c t_d \varepsilon_s e^{-\lambda \frac{b_s}{4}}}{9d} \quad (6-64)$$

In calculations of section properties such as I_c and A_c , the entire thickness of the concrete diaphragm is used instead of the crack spacing; however, concrete shear modulus, G_c , is multiplied by 0.2 to consider these cracks. The average strain of the slab is assumed to be at the quarter of the diaphragm width using Equation (6-14). Summation of this force over the width of the concrete diaphragm outside the core region gives:

$$F_{oc} = \frac{0.4G_c t_d^2 \varepsilon_s (b_s - b_f)}{9d} e^{-\lambda \frac{b_s}{4}} \quad (6-65)$$

6.6.2.1 IMPLEMENTATION FOR THE THIRD TEST

As a numerical example of the developed method, the third test specifications were input into Equations (6-50) and (6-53) and they were solved simultaneously. The following are specimen data which were selected to represent the half of the diaphragm outside of the core region:

$$G_c = 1840 \text{ ksi}$$

$$E_s = 1450 \text{ ksi (in plastic region is about 0.05 of elastic modulus)}$$

$$f_t' = 0.5 \text{ ksi}$$

$$V = 390 \text{ kip (at ultimate condition)}$$

$$A_s = 19.4 \text{ in}^2$$

$$\Delta = 7.5 \text{ in}$$

$$t_s = 7.5 \text{ in}$$

$$t_d = 20.5 \text{ in}$$

$$A_c = 290.3 \text{ in}^2$$

$$I_c = 1375 \text{ in}^4$$

$$d = 43 \text{ in}$$

$$d_s = 5.0 \text{ in}$$

$$b_s = 93 \text{ in}$$

$$k = \frac{3}{2}$$

If the maximum strain is taken as 0.05 in/in, according to the finite element analysis, the induced load, f_{OC} , in each slice is computed using Equations (6-49) through (6-53). The variation of the compressive load versus the width of the diaphragm is shown in Figure 6-25. This load is multiplied by the ratio of diaphragm thickness to crack spacing to include the entire diaphragm thickness. The diaphragm compressive force outside of the core region obtained from the finite element analysis of the third specimen is

shown on the same plot. The developed method passes almost the average of the FEA results and has the same trend. The total compressive force resisted by the diaphragm outside of the core region is computed through summation of the loads shown on the plot of Figure 6-25 and then it is doubled to include the entire diaphragm width:

$$F_{oc} = 2 \sum f_{oc} = 425 \text{ kip}$$

The finite element analysis of the third specimen shows the compressive resistance of the concrete diaphragm outside the core region at the ultimate condition and the centerline of the diaphragm is about 455 kip. The FEA result and what was predicted by the developed method have a good agreement.

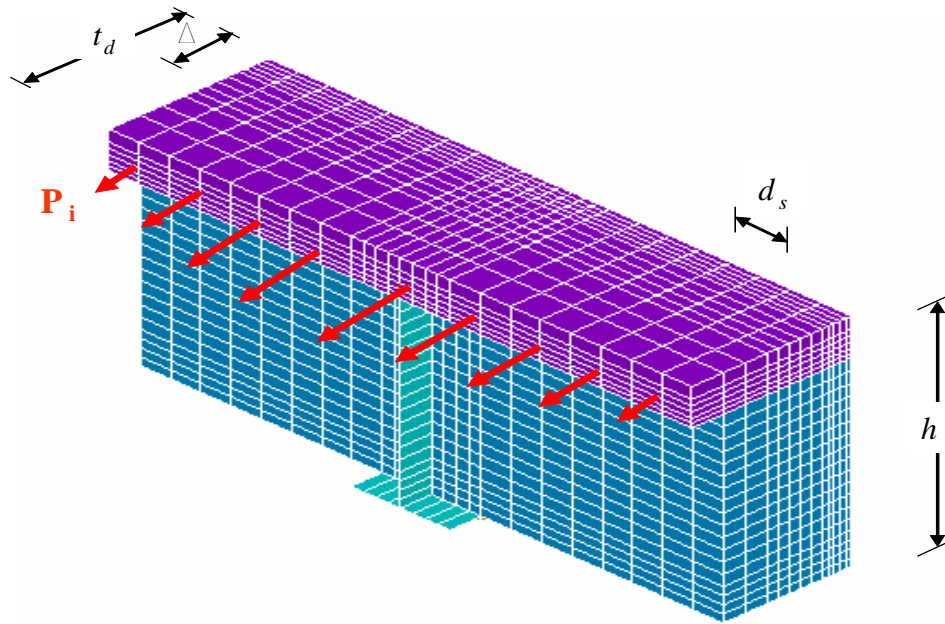


Figure 6-21: The slab concrete and the diaphragm under the rebar loads

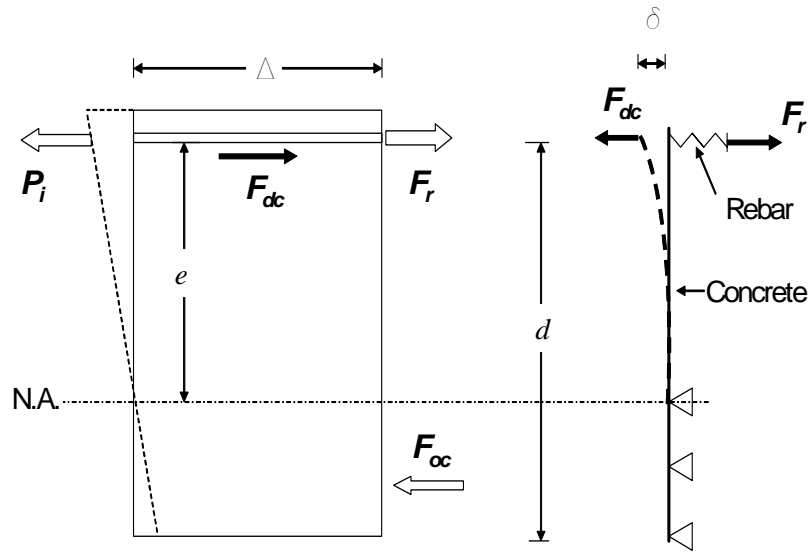


Figure 6-22: Free body diagram of a slice of the concrete diaphragm

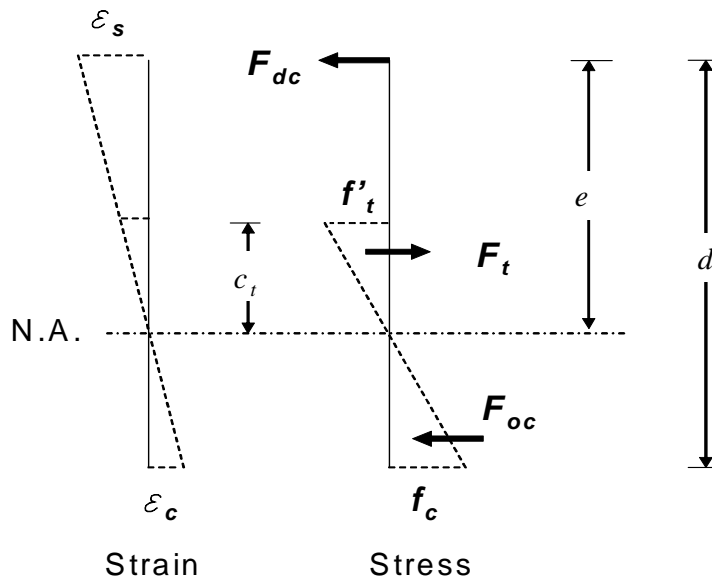


Figure 6-23: The strain and stress distribution of a slice of the diaphragm under the load transferred from the reinforcement

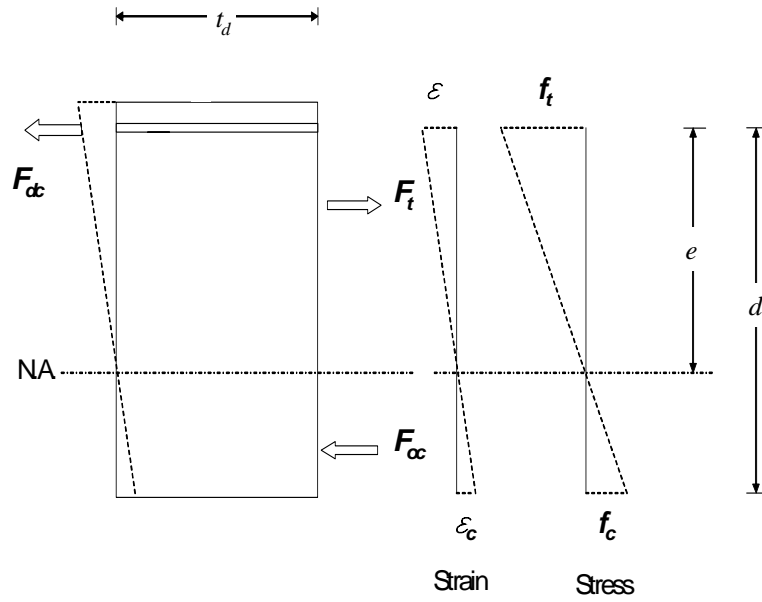


Figure 6-24: Linear stress and strain distribution inside the concrete diaphragm

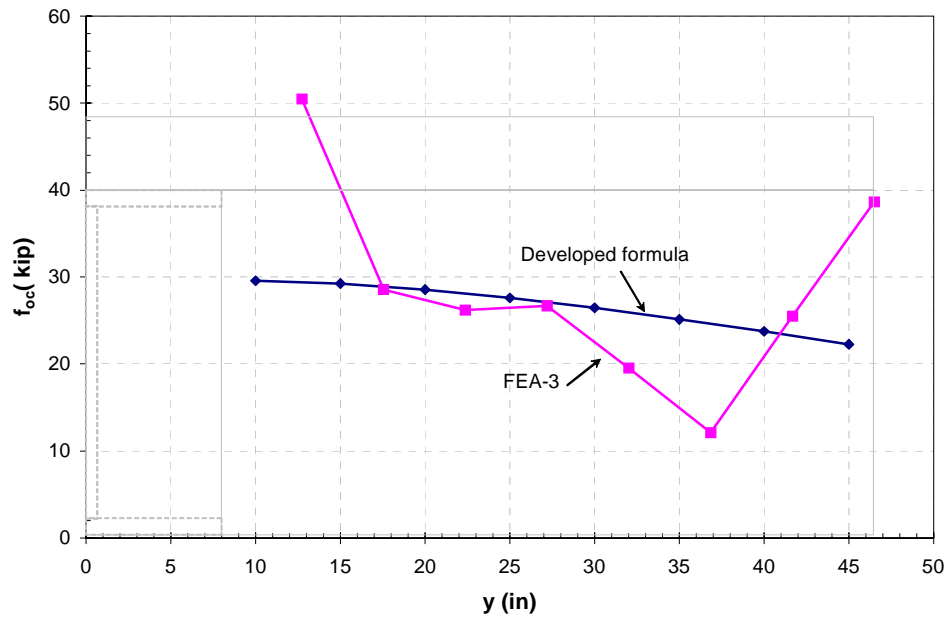


Figure 6-25: Variation of compressive force in the diaphragm along the diaphragm width

6.7 FLEXURAL CAPACITY OF THE CONNECTIONS AT THE CENTERLINE OF THE PIER

The flexural strength of the proposed connection types one, two and three could possibly be computed using a simplified approach developed from the mathematical model derived previously. The suggested framework of such a simplified design formula would likely be similar to the approach currently used to design reinforced concrete beams (Mattock, 1961). However, for each element of this framework, the equations developed previously would be employed. It is suggested that a simplified method for the design of the connections would be based on the following assumptions:

1. At ultimate strength, the concrete biaxial stress is assumed to be uniformly distributed over an equivalent compression zone bounded by the edges of the end bearing plate and a straight line located parallel to and below the neutral axis.
2. Tensile strength of the concrete is neglected in flexural calculations.
3. Strain in the concrete at each depth is assumed to be directly proportional to the distance from the neutral axis.
4. The maximum strain at an extreme edge of the concrete compression zone is computed according to Equation (6-26).
5. Stress in the reinforcing bars below yield stress for the grade of steel used may be taken as 29000 ksi times the steel strain. For strain after yield, the reinforcement stress may be considered equal to the yield stress. In another word, the strain hardening is neglected.

6.7.1 STRESS AND STRAIN DISTRIBUTIONS

For a simplified design method to be developed, certain stress and strain distributions would have to be known to find flexural capacity. According to the investigation referred to previously, the following simplified strain and stress conditions are proposed for the pier centerline section at the ultimate condition:

- A uniform strain and stress distribution over the width of the top flange (b_f in Figure 6-26) and an exponential strain distribution everywhere else (Figure 6-26). The stress distribution follows the strain distribution in the linear region which is exponential and it is uniform in yielded areas (denoted by b_e in Figure 6-26).
- A linear strain distribution is assumed in the vertical direction (z -axis) as shown in Figure 6-27. A nonlinear stress distribution for the concrete is considered in vertical direction as shown in Figure 6-27
- A uniform stress distribution is assumed for the core concrete region across the width of the end bearing plate as shown in Figure 6-28. Also, an exponential stress distribution is considered for the concrete diaphragm outside the core region as shown in Figure 6-28.

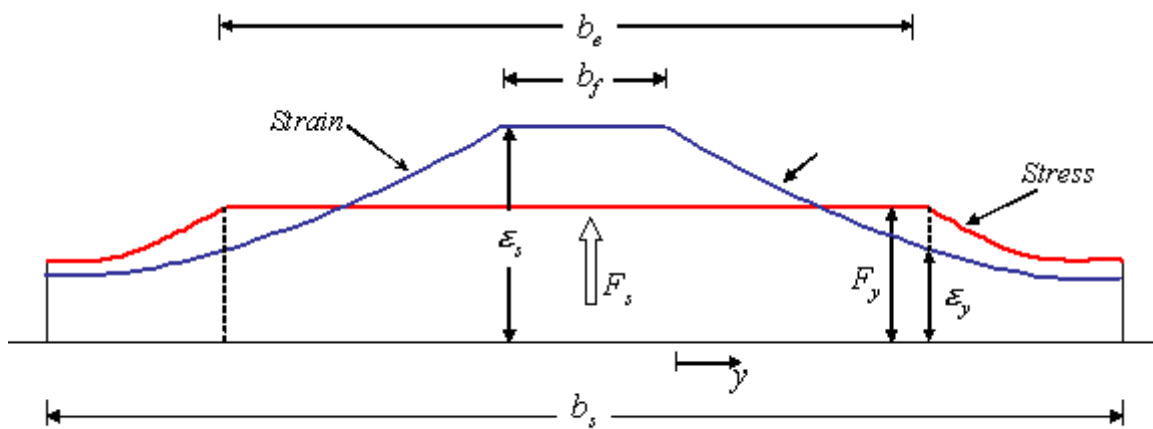


Figure 6-26: Stress and strain distribution across the width of slab in reinforcements

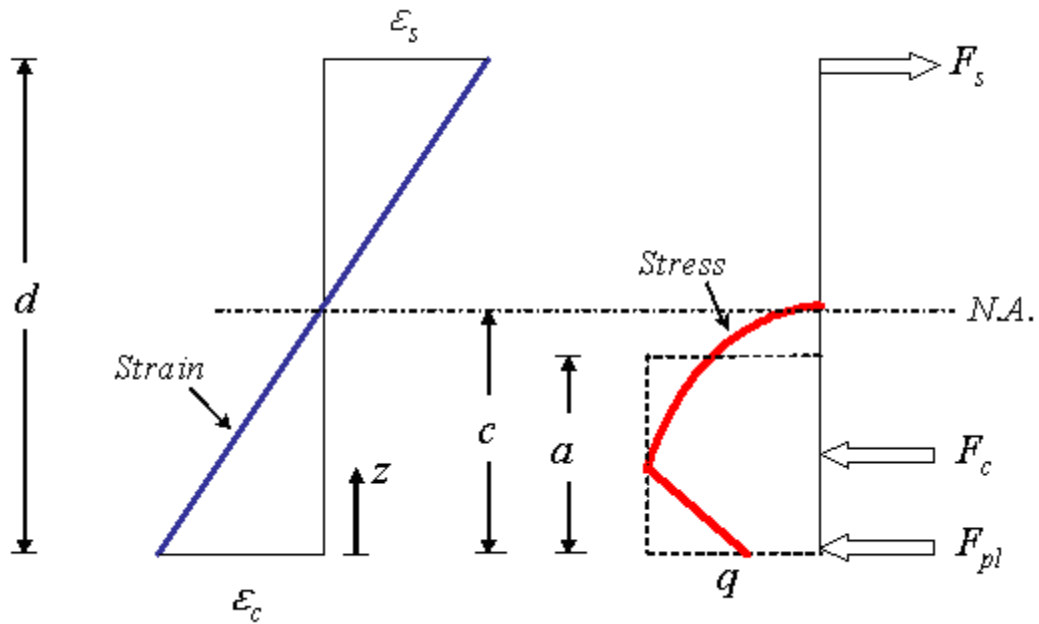


Figure 6-27: Strain, stress and force diagrams in the vertical direction at the girder axis

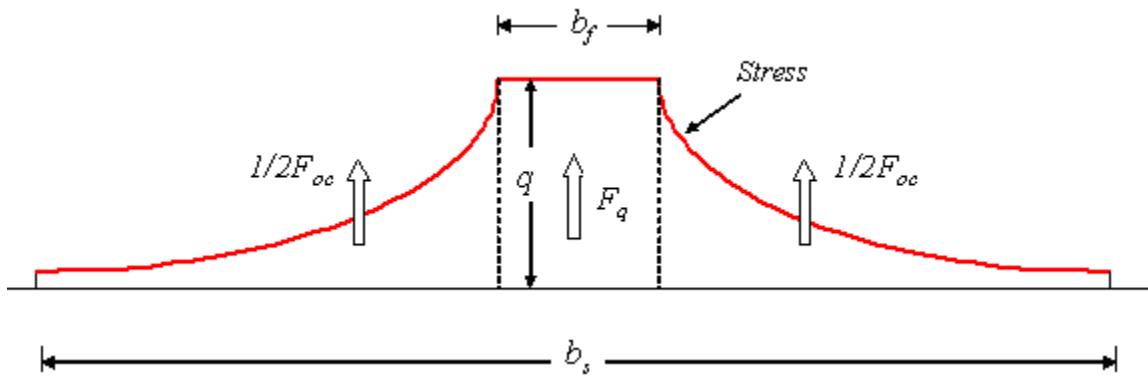


Figure 6-28: Stress distribution of the compressive concrete across the width of diaphragm

6.7.2 CONCRETE STRENGTH

Other factors needed to develop a simplified design method are material strengths. The magnitude of the compressive strength, q , of the concrete inside the core region can be obtained through Equation (6-36). It should be noted that this equation also contains the shear strength of the core region.

$$q = 0.38 \left(1 + \frac{t_c}{b_f} \right) \sqrt{f'_c} + f'_c \leq 2.25 f'_c \quad (6-66)$$

Within the following aspect ratio ranges:

$$0.1 \leq \frac{b_f}{b_s} \leq 0.3$$

and

$$0.1 \leq \frac{t_c}{b_s} \leq 1.0$$

where:

f'_c = uniaxial compressive strength of the concrete in ksi

t_c = thickness of the core concrete

b_s = width of the slab or diaphragm

b_f = width of the end bearing plate or the girder flanges

The concrete core strength has been limited to $2.25f'_c$ similar to the AASHTO-LRFD (1998) limitation for anchorage zone concrete strength with confinement. The compressive strength of the core region, F_q , is computed using an equivalent rectangular stress block as shown in Figure 6-27.

$$F_q = qab_f \quad (6-67)$$

where:

a = depth of stress block computed based on the force equilibrium

The strength of the concrete diaphragm outside the core region, F_{oc} , is obtained from the following formula:

$$F_{oc} = \frac{0.4G_c t_d^2 \varepsilon_s (b_s - b_f)}{9d} e^{-\lambda \frac{b_s}{4}} \quad (6-68)$$

where:

G_c = shear modulus of the concrete

t_d = thickness of the concrete diaphragm

ε_s = maximum strain in the slab rebar

d = the depth of center of the slab rebar from the bottom of the diaphragm

λ = a parameter which is defined according to Equation (5-7)

This load is assumed to be applied at a depth equal to the half of the stress block depth, a . By using Equations (6-67) and (6-68), one can compute the total compressive resistance, F_c , provided by the concrete diaphragm at the ultimate condition at the pier centerline as shown in Figure 6-27 and Figure 6-28.

$$F_c = F_q + F_{oc} \quad (6-69)$$

6.7.3 REINFORCEMENT STRENGTH

When all of the slab rebar are in the elastic range, a linear strain-stress relationship is adopted and the total tensile force in the deck rebar, F_s , can be computed according to the strain and stress distribution shown in Figure 6-26 as:

$$F_s = E_s \varepsilon_s A_s \frac{b_f}{b_s} + 2 \int_0^{\left(\frac{b_s-b_f}{2}\right)} E_s \varepsilon_s e^{-\lambda y} \frac{A_s}{b_s} dy \quad (6-70)$$

In Equation (6-70) the origin of the y-coordinate axis has been shifted to the edge of the flange for the sake of simplicity, as seen in Figure 6-26. Simplifying Equation (6-70) gives,

$$F_s = \rho b_f + 2 \frac{\rho}{\lambda} \left[1 - e^{-\frac{\lambda(b_s-b_f)}{2}} \right] \quad (6-71)$$

where:

$$\rho = \frac{E_s \varepsilon_s A_s}{b_s}$$

E_s = steel rebar elasticity modulus

If part of or all slab reinforcements yield, the width of the yielded area (denoted by b_e as shown in Figure 6-26) is given by,

$$b_e = \frac{-2}{\lambda} \ln \frac{\varepsilon_y}{\varepsilon_s} \quad (6-72)$$

where

ε_y = yield strain of the rebar

The total tensile force in the rebar is computed based on the following equation:

$$F_s = \frac{b_e}{b_s} A_s F_{yr} + \frac{2E_s \varepsilon_s A_s e^{\frac{\lambda b_f}{2}}}{\lambda b_s} \left(e^{\frac{-\lambda b_e}{2}} - e^{\frac{-\lambda b_s}{2}} \right) \quad (6-73)$$

where:

F_{yr} = yield strength of the slab rebar

These equations have been derived using the stress and strain distribution plotted in Figure 6-26, which is based on the Winkler foundation method described in the previous chapter.

6.7.4 CONNECTING PLATE STRENGTH

In connections similar to the first test specimen, a plate which connects two girders' bottom plates participates in transferring the compression along with the concrete. The experimental data and finite element simulations both indicate this plate yielded almost uniformly across its width. Therefore, its resistance, F_{pl} (see Figure 6-27), can be easily computed as follows:

$$F_{pl} = A_{pl} E_s \varepsilon_c \quad \text{if} \quad \varepsilon_c \leq \varepsilon_y \quad (6-74)$$

$$F_{pl} = A_{pl} F_{yp} \quad \text{if} \quad \varepsilon_c \geq \varepsilon_y \quad (6-75)$$

Where:

A_{pl} = the cross section area of the connecting plate

F_{yp} = yield strength of the plate

ε_c = concrete strain at the plate elevation

Conclusions and Recommendations

7

7.1 SUMMARY

The market analysis of bridge material in the range of short to medium span length indicated a declining trend for steel girders during the last two decades. A new construction technique was developed to enhance the competitiveness of steel girder bridges in the short to medium span length ranges. In the new method the beams were erected as simple supports under the construction loads. The continuity of girders was provided by reinforcements in deck and diaphragm after hardening of the concrete for the traffic loads. In this case the field splices were eliminated and there was no need for temporary shoring. The cost-benefit study of two bridges revealed that the cost and time of construction of superstructures decreased by employing the new technique.

In order to investigate the strength of the proposed connections, three full scale tests were planned. The design and construction of each specimen was done according to the AASHTO-LRFD provisions and practical considerations. In the first test, the bottom flanges of two adjacent girders were welded at the pier centerline and end bearing plates were welded to the ends of the girders. In the second test, the girders simply were embedded

in the concrete diaphragm. The third specimen was similar to the first specimen without connection of the bottom flanges. Extensive instrumentation was planned for each test. To consider the performance of each system under repeated loadings and fatigue phenomenon, first a cycling load test was conducted on each specimen. The ultimate load test was carried out after the cycling test for each specimen to investigate the failure mechanism of each specimen. The test results and observations indicated that the cracking of the concrete slab around the pier region was the first damage in the specimens. The next failure could be yielding in slab rebar, crushing of concrete, or debonding of steel and concrete. The order of these events depended on the strength of the materials, reinforcement ratio and aspect ratios of the specimens.

To obtain more information about the behavior of the system, a series of finite element analyses was carried out to complement the experimental studies. A detailed numerical model for the finite element analyses was developed. The geometry and material properties of the constructed models were based on the actual data obtained from the laboratory. Material and geometrical nonlinearities were included in the numerical simulations. The load-deflection response of specimens, the yielding pattern, cracking behavior, and strain distributions were compared with those obtained from experimentation to verify the numerical model. The force transfer mechanism of each test was described using the finite element simulation results. The failure modes observed in the test results were similar to what was seen from the numerical simulations.

The mechanical behaviors of the connection type one and three were described in the form of mathematical models. The mathematical explanation was based on the equilibrium of the forces and moments, and a deformation field which satisfied the boundary conditions.

The flexural strengths of the proposed connection types one, two and three were computed using a simplified approach. The framework of the simplified design formula was similar to the approach currently used to design reinforced concrete beams. The developed design equations were verified by several finite element parametric studies in the range of short to medium span bridges.

7.2 CONCLUSIONS

7.2.1 COST-BENEFIT ANALYSIS

1. The market trend of bridge construction in the United States indicates that steel bridges were less competitive in short and medium span length ranges.
2. Results of the cost comparison of the two recently-built bridges demonstrated material and girder fabrication cost savings of about seven percent over the conventional continuous girder design.
3. The required man-hours can also be reduced by the elimination of field splices. The total time of two investigated bridges could have been shortened by two to four days by using the new method over the conventional technique.

7.2.2 EXPERIMENTAL INVESTIGATION

7.2.2.1 *FATIGUE TEST*

1. The first cracks occurred on the concrete slab around the pier centerline and edge of diaphragm.
2. When the connection detail was subjected to 75 of years of simulated truck traffic, the specimens experienced about a 10 to 13 percent loss in their rigidity during the course of cyclic loading. The stiffness of the second specimen dropped suddenly at the very beginning of the fatigue loading.
3. In fatigue tests, the strain of the specimens inside the concrete diaphragm and slab rebar increased as the number of load cycles increased.

4. The deterioration of the tested specimen in the cycling loading is most likely due to damage in the concrete elements rather than the steel girder or reinforcements.

7.2.2.2 ULTIMATE TEST

1. The moment capacities of the first and third specimens were almost equal and were 1.5 times that of the second specimen.
2. The fatigue cracks propagated and widened during the ultimate test.
3. In the first test, almost all of the slab rebar yielded and, almost at the same time, the bottom flange inside the diaphragm yielded. In the second test, only rebar close to the axis of the girder yielded. The rebar also yielded in the third test, but the number of them could not be determined from the test data.
4. Ductility of the connections was the highest for the first specimen and the lowest for the second. The ductility ratio for conducted tests was varied from 2.6 to 3.9.
5. The test results implied that the concrete diaphragm under bearing of the end plate should have crushed in all three of the tests. The concrete strain at the extreme fibers of the diaphragm exceeded 0.003 in/in.
6. The strain profile was not linear along the vertical direction inside the concrete diaphragm.
7. The strain distribution in the slab rebar was similar to a bell shaped curve.
8. In specimen two and three, slippage between the concrete diaphragm and the steel girder was observed.

9. The failure of the connection detail began with yielding of the tension reinforcement in the slab close to the axis of the steel girder around the pier centerline. The crushing of the concrete occurred at the final stages of the loadings. In the first and probably the third specimen all the slab rebar had yielded before the crushing of the concrete. In the second specimen, the concrete had entirely crushed before all the rebar yielded.

7.2.3 NUMERICAL INVESTIGATION

1. The numerical analysis showed that the smeared cracking model in the finite element program (ANSYS5.7) was not capable of tracking the test observations. The discrete cracking might be simulated through smeared concrete models with a very fine mesh size which required more computational resources.
2. The crushing of the concrete in the actual test was more ductile than what was simulated by the finite element program.
3. The ultimate capacities of the specimens were predicted by the finite element analysis with an average accuracy of about three percent.
4. The first test simulation was well consistent with the experimentation for overall load-deflection behavior and ultimate capacity. The strain obtained from the analysis was somewhat different than that of the test after yielding. The analysis of the first test was numerically more stable in comparison to the two latter tests because of the connectivity of the bottom flange. In the second test simulation, there was a good agreement between load-deflection response before crushing of concrete, however the numerical approach did not capture well the test curve after crushing of the concrete. The stress concentration at the contact interface of the bottom flange,

web and concrete diaphragm caused sudden crushing of the concrete elements which lead to an ill-conditioned numerical solution. The third test simulation showed better numerical stability than the second test, however, there were not enough experimental data available to verify all aspects of the model.

5. In the first specimen, the first yielding occurred in the reinforcement of the slab. Following that the bottom plate that connected the two girders yielded. The core concrete at the interface of the end bearing plate crushed after yielding of the bottom flange. The yielding of all rebar occurred after the local crushing of the concrete.
6. In the second specimen, crushing of the concrete occurred before yielding of the rebar. The partial yielding of the top layer reinforcement of the slab caused the failure of the specimen.
7. In the third specimen, the yielding was initiated in the slab rebar and crushing occurred after the partial yielding of the slab bars. The failure occurred upon yielding of all slab reinforcements.
8. The nonlinearity in the load-deflection response of the specimens was started by cracking of the concrete. The location of initial cracks was at the diaphragm edge for the first specimen, at the interface of the bottom flange and concrete diaphragm in the second test, and the end of the top flange for the third specimen.
9. The strain distribution in the slab rebar followed the same pattern as the experimental result which was similar to a bell-shaped curve.
10. As an average for all specimens, crushing of the concrete occurred at the stress approximately 15 percent more than the uniaxial compressive strength of the concrete. In addition the concrete failure strain was higher than 0.003 in/in.

11. The strain distribution along the depth of the girder inside the concrete diaphragm was not linear.
12. The strain distribution in the concrete diaphragm along the diaphragm width was similar to the strain profile in the slab rebar.

7.2.4 MATHEMATICAL MODELING

1. It was noticed that more than 90 percent of the total strength of the specimens at the pier centerline was provided by the slab rebar, concrete in compression or the bottom plate.
2. The idealistic strain distributions at the pier centerline section could be assumed as linear along the girder depth, and exponential along the slab rebar and the diaphragm width.
3. The Winkler foundation method gave a satisfactory stress distribution in the slab rebar compared to the finite element results.
4. The strength of several concrete tests under the edge loading was predicted by a developed concrete strength formula. The accuracy of proposed equation was about one percent in comparison to the test results.
5. The contribution of the concrete diaphragm outside the end bearing plate width to total compressive resistance of the concrete was predicted for the third test with an accuracy of about seven percent.

7.3 RECOMMENDATIONS FOR FURTHER RESEARCH

The performance of connection type one and three were judged a success. The connections are inexpensive to construct, fast to perform, fatigue resistant, adequate for flexural capacity and ductile. These types of connections are suitable for short to medium span I-girder bridges with two spans; however, there are other scenarios in which the characteristics of the tested connections can be improved:

1. For highway bridges with more than two spans, the live load can cause tension at the bottom flange of the girders at the pier centerline. In this case, the first type of connection could be used; however, welding of the two bottom flanges would be vulnerable to fatigue failure. For this situation, a bolted connection at the bottom flanges is suggested.
2. The other application of the simple-made-continuous concept is in steel box girder bridges. The application of the developed formulas for the box girders can be investigated and improved. The distribution of the compression and tensile stresses in the diaphragm region for the box girder might not follow the derived distribution for the I-girders.
3. During the parametric analyses of the connections, it was noticed that the bonding of the steel girder and the concrete diaphragm could substantially improve the compressive strength of the connection. To enhance the bonding between the steel girder and the concrete diaphragm, a simple detail is suggested. In this detail the end bearing plate can be welded at the edge of diaphragm instead of the end of the steel girders. In this case, the concrete diaphragm participates in transferring the compressive force through the shear resistance. More experimental and numerical work is needed to verify this approach.

4. To enhance the strength and ductility of the concrete at the concrete core region, embedding rectangular ties in the core region is suggested.
5. The developed formulas can be rearranged in a simpler form to be used in engineering offices. For this purpose, it is suggested to use the effective width concept to replace the exponential stress distribution.
6. Using moment-curvature-analysis as another numerical tool for parametric study is recommended.

References

- [1] Dunker, K. F., and Rabbat, B. G., "Performance of Prestressed Concrete Highway Bridges in the United States - The First 40 Years," *PCI Journal*, Vol. 37, No. 3, May-June 1992, pp: 487-64.
- [2] AASHTO, *LRFD Bridge Design Specifications, Second Edition (w/1999 interims)*, American Association of State Highway Transportation Officials, Washington D.C., 1998.
- [3] Federal Highway Administration (FHWA), *Recording and Coding Guide for Structure Inventory and Appraisal of the Nation's Bridges*, Report No. FHWA-PD-96-001, December, 1995.
- [4] Barker, R. M., and Puckett, J. A., *Design of Highway Bridges*, John Wiley and Sons, Inc., 1997.
- [5] "QCONBRIDGE," Release 1.1, (1999), Washington Department of Transportation Bridges and Structures Office.
- [6] Nebraska Department of Roads, *Bridge Office Policies and Procedures Manual (BOPP)*, Bridge Divison, Nebraska Department of Roads, 1996.
- [7] Freyermuth, C. L., "Design of Continuous Highway Bridges with Precast, Prestressed Concrete Girders," *PCI Journal*, Vol. 14, No. 2, April 1969, pp. 14-39.
- [8] ACI Committee 318, *Building Code Requirements for Structural Concrete (ACI 318-95) and Commentary (ACI318R-95)*, American Concrete Institute, Farmington Hills, MI, 1995.
- [9] "SAP2000," Release 7.40, Computers and Structures, Inc., Berkeley, CA.

Failure of a Concrete Core Based on a Three Parameter Model

A

A.1 CONCRETE COMPRESSIVE STRENGTH

The strength of the concrete in a biaxial state is calculated based on a three parameter method developed by William and Warnke (1974). This model is a combination of Drucker-Prager and von Mises failure surface. In this model, cracking and crushing are determined by a failure surface. Once the failure surface is surpassed, concrete cracks if any principal stress is tensile, while crushing occurs if all principal stresses are compressive. The failure surface depends on three material parameters which will be explained in this chapter. The material behavior can be assumed to be

linear elastic until failure. The failure criterion of concrete is described in the following form:

$$\frac{F}{f'_c} - S \geq 0 \quad (\text{A-1})$$

where:

$$f'_c = \text{uniaxial crushing stress}$$

F is the average stress and defined in terms of principal stresses by:

$$F = \frac{1}{\sqrt{15}} \left[(\sigma_1 - \sigma_2)^2 + (\sigma_2 - \sigma_3)^2 + (\sigma_3 - \sigma_1)^2 \right]^{1/2} \quad (\text{A-2})$$

in which s_1 , s_2 , and s_3 are three principal stresses. S is the failure surface expressed in terms of principal stresses and three input parameters by:

$$S = r(\theta) \left[1 - \frac{\sigma_h}{z f'_c} \right] \quad (\text{A-3})$$

where s_h is hydrostatic stress, $r(\theta)$ is the elliptic trace in polar coordinates and z is a material parameter. These parameters are defined as:

$$\sigma_h = \frac{\sigma_1 + \sigma_2 + \sigma_3}{3} \quad (\text{A-4})$$

$$r(\theta) = \frac{2r_2(r_2^2 - r_1^2)\cos\theta + r_2(2r_1 - r_2) \left[4(r_2^2 - r_1^2)\cos^2\theta + 5r_1^2 - 4r_1r_2 \right]^{1/2}}{4(r_2^2 - r_1^2)\cos^2\theta + (r_2 - 2r_1)^2} \quad (\text{A-5})$$

$$z = \frac{\alpha_u \alpha_z}{\alpha_u - \alpha_z} \quad (\text{A-6})$$

where:

$$\cos \theta = \frac{2\sigma_1 - \sigma_2 - \sigma_3}{\sqrt{2}[(\sigma_1 - \sigma_2)^2 + (\sigma_2 - \sigma_3)^2 + (\sigma_3 - \sigma_1)^2]^{1/2}} \quad (\text{A-7})$$

$$\alpha_z = \frac{f'_t}{f'_c} \quad (\text{A-8})$$

$$\alpha_u = \frac{f'_{cb}}{f'_c} \quad (\text{A-9})$$

$$r_1 = \sqrt{\frac{6}{5}} \frac{\alpha_u \alpha_z}{2\alpha_u + \alpha_z} \quad (\text{A-10})$$

$$r_2 = \sqrt{\frac{6}{5}} \frac{\alpha_u \alpha_z}{3\alpha_u \alpha_z + \alpha_u - \alpha_z} \quad (\text{A-11})$$

In the described model three material parameters are required as follows:

f'_t = uniaxial tensile cracking stress

f'_{cb} = ultimate biaxial compressive strength

f'_c = uniaxial crushing stress

A.2 NUMERICAL EXAMPLE

For the practical range, uniaxial tensile strength is about 8 to 13 percent of the uniaxial compressive strength. This was investigated by a parametric study of the AASHTO-LRFD (1998) formula for the tensile strength. The biaxial compressive strength of the concrete is about 1.0 to 1.4 times the

uniaxial compressive strength of the concrete. Therefore, as an average, the following values are assigned to the material parameters:

$$\alpha_z = 0.1$$

$$\alpha_u = 1.2$$

Substituting these values into Equation (A-6), (A-10) and (A-11) gives,

$$z = 0.109$$

$$r_1 = 0.05$$

$$r_2 = 0.09$$

Substituting the above values into the three parameter formulas described in the previous section results in the failure curve shown in Figure 1 for the compression-compression quarter. An approximate formula (Equation (A-12)) for this curve was obtained using a second order parabolic fit.

$$\frac{\sigma_3}{f_c'} = 1.3 \left(\frac{\sigma_2}{f_c'} \right)^2 + 1.6 \left(\frac{\sigma_2}{f_c'} \right) - 1 \quad (\text{A-12})$$

or in a simpler form,

$$\sigma_3 = \frac{1 - 1.6\alpha - \sqrt{7.76\alpha^2 - 3.2\alpha + 1}}{2.6\alpha^2} f_c' \quad (\text{A-13})$$

where:

$$\alpha = \frac{\sigma_2}{\sigma_3}$$

Kupfer et. al. (1969) suggested the following relationship for the principal stresses at failure in biaxial stress (compression-compression quarter):

$$\sigma_3 = \frac{1 + 3.65\alpha}{(1 + \alpha)^2} f_c' \quad (\text{A-14})$$

The Equation (A-13) and Equation (A-14) have a good agreement. The linear approximation of the curve plotted in Figure 1 for small values of s_2 can be expressed as:

$$\sigma_3 = 1.6(\sigma_2) - f_c' \quad (\text{A-15})$$

in which both principal stresses have a negative sign (compressive).

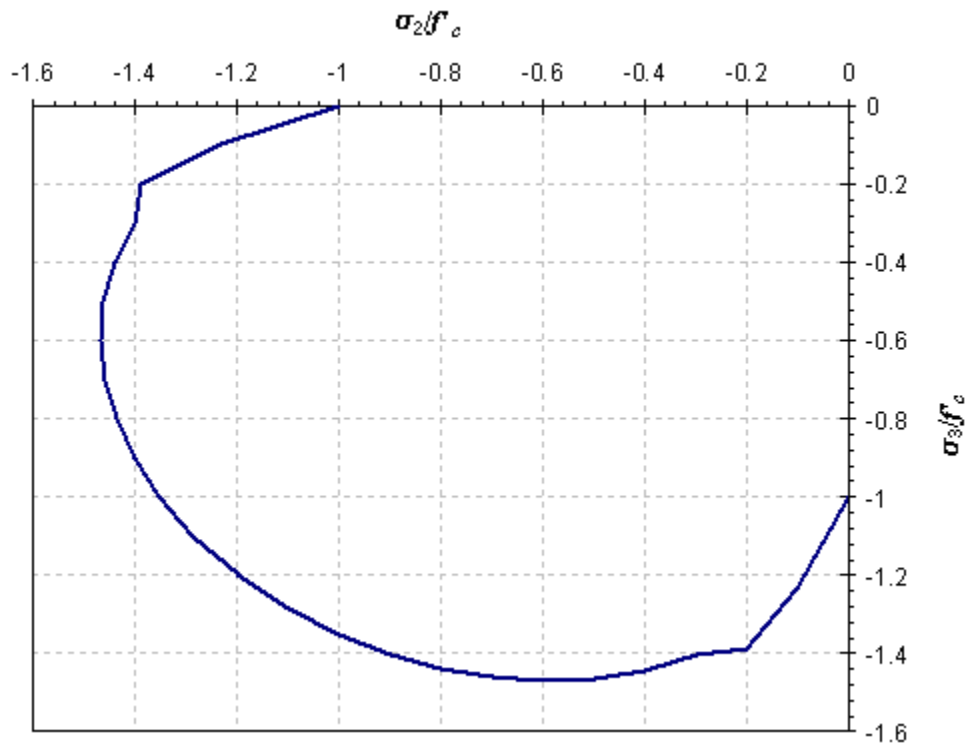


Figure A-1: Failure surface for the biaxial stress state of the concrete

Foundation Analogy

B

B.1 INTRODUCTION

The shape of the stress distribution in the concrete core is required to evaluate the strength of the concrete diaphragm. It is assumed that the concrete material behavior is linear up to the crushing or cracking point; therefore an elastic approach can be employed to investigate the stress distribution in the diaphragm prior to crushing. The finite element results show that the compression stress in the core concrete is extended beyond the end bearing plate edges across the width of the diaphragm. The test results also imply the same observation by extrapolation of strain obtained from the embedment gages close to the bottom of the diaphragm. The distribution of the compression stress due to the transferred force from the end bearing plate to the concrete core can be considered to be analogous to a steel plate resting on a concrete medium as shown in Figure 1.

B.2 STRESS DISTRIBUTION

An elastic solution for this problem has been given by Timoshenko (1951). The normal stress (x-direction) in an elastic plate under limited symmetrical loading as shown in Figure 1 is given by:

$$\sigma_x = \frac{qb_f}{b_s} + \frac{4q}{\pi} \sum_{m=1}^{\infty} \frac{\sin \frac{m\pi b_f}{b_s}}{m} \cdot \frac{\frac{m\pi t_c}{b_s} \cosh \frac{m\pi t_c}{b_s} + \sinh \frac{m\pi t_c}{b_s}}{\sinh \frac{2m\pi t_c}{b_s} + 2 \frac{m\pi t_c}{b_s}} \cdot \cos \frac{m\pi x}{b_s} \quad (\text{B-1})$$

where:

q = applied compressive uniform load on the core concrete

b_f = width of end bearing plate

b_s = width of concrete diaphragm

t_c = thickness of core concrete

The stress in the y-direction (transverse) is calculated using the following equation:

$$\sigma_y = \frac{4q}{\pi} \sum_{m=1}^{\infty} \frac{\sin \frac{m\pi b_f}{b_s}}{m} \cdot \frac{\frac{m\pi t_c}{b_s} \cosh \frac{m\pi t_c}{b_s} - \sinh \frac{m\pi t_c}{b_s}}{\sinh \frac{2m\pi t_c}{b_s} + 2 \frac{m\pi t_c}{b_s}} \cdot \cos \frac{m\pi x}{b_s} \quad (\text{B-2})$$

The stress distributions in x and y directions at the center of the core concrete for the third test specimen using the preceding formulas are shown in Figure 2 and Figure 3. The applied pressure, q , is approximately the concrete compressive strength, i.e. 6 ksi.

It can be seen that the maximum normal stress (x-dir) is about the applied pressure and its location is at the middle of the end bearing plate. This stress stretches beyond the edges of the plate into the concrete diaphragm.

However, the lateral stress (y-dir) has a maximum outside the edge of the plate and a minimum under the plate. The magnitude of the lateral stress at the edge is almost zero. The lateral stress under the plate is compressive, enhancing the concrete normal strength by providing a lateral confinement. The stress outside the plate edge is tensile causing the tensile cracking around the edges of the plate as was seen in finite element analyses.

B.3 FINITE ELEMENT MODEL

The core concrete and end bearing plates were modeled by ANSYS 5.7 to investigate the stress distribution inside the core concrete in the nonlinear state. The finite element model of the bottom slice of the concrete core and end bearing plate is shown in Figure 4. In this analysis, the plates were defined to be rigid. As shown in Figure 6, it can be observed that cracks first form around the edges of the plates, as predicted by the elastic method in the previous section. In this analysis the tensile strength of concrete was 0.5 ksi and its crushing stress was about 6 ksi. The stress contours in tensile direction are shown in Figure 5.

B.4 TIE-STRUT MODEL

Both the elastic solution and the nonlinear finite element analysis indicate that the tensile stress reaches the cracking strength of the concrete around the edge of the plate. These cracks are consequences of the divergence of the compression force at the edge of the bearing plate. A simple tie-strut model can explain the reason for this type of cracking. The bottom part of the diaphragm under the pressure from the end bearing plates is shown in Figure 7. It can be seen that the compression struts at the edge of bearing plate are inclined to spread the compressive load into the concrete core. This divergence from the right angle causes a tension force in the tie. Since in the tested specimens there is no transverse reinforcement to resist this

tension, the concrete cracks in the lateral direction. The tensile strain of point A as shown in Figure 7 shall pass the cracking strain to allow the concrete elements to crack at this point. This requires point A to move toward the right direction which compresses the lateral concrete shown as horizontal springs in Figure 7. The reactions of these springs provide the confinement to the concrete punched by the two end bearing plates. Therefore, the reactant pressure is equal to the cracking stress of the concrete at point A. This can also be seen in the elastic solution stress plot shown in Figure 3. In addition, the lateral stress obtained from the finite element analysis shown in Figure 5 indicates that the average compression stress between end bearing plates is about the cracking strength of the concrete. Therefore, the lateral stress on the edge of the core concrete can be considered approximately as the tensile strength of the concrete, f'_t , as shown in Figure 8. The elastic parametric analysis indicates this assumption is valid if:

$$0.1 \leq \frac{b_f}{b_s} \leq 0.3 \quad (\text{B-3})$$

and

$$0.1 \leq \frac{t_c}{b_s} \leq 1.0 \quad (\text{B-4})$$

The variation of stress ratio versus two size ratios, b_f/b_s and t_c/b_s , is plotted in Figure 9. The stress ratio is the lateral stress divided by the normal stress at the centerline of the core.

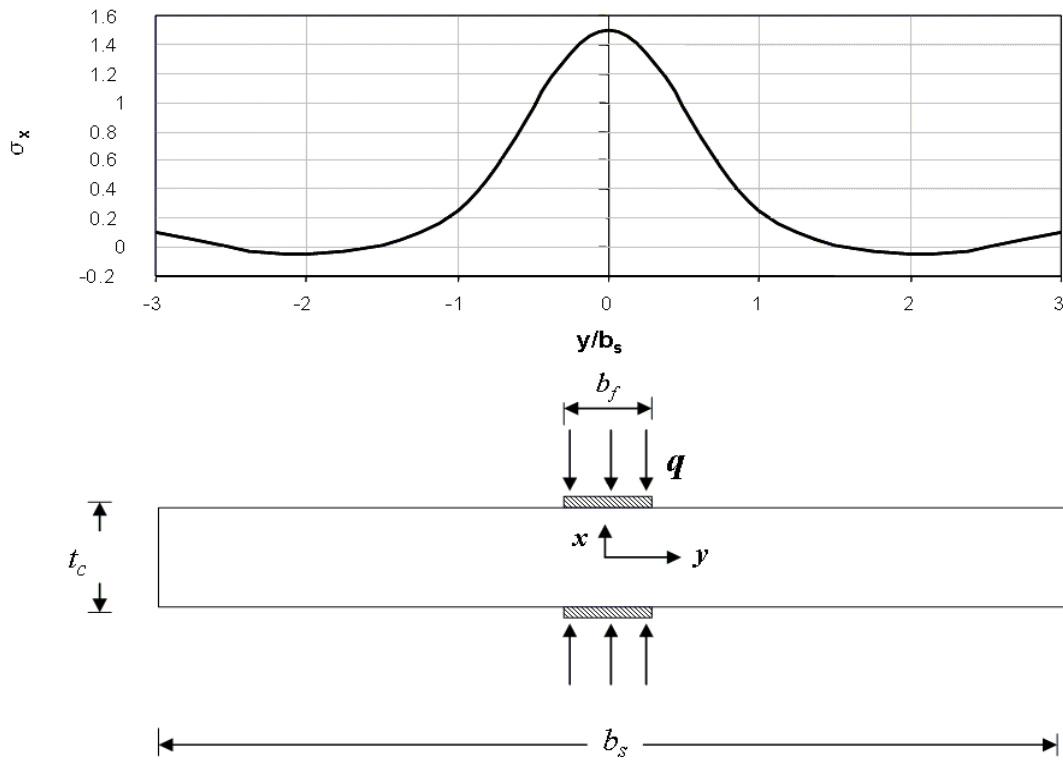


Figure B-1: A linear elastic plate under symmetrical loading and induced normal stress across the length of the plate

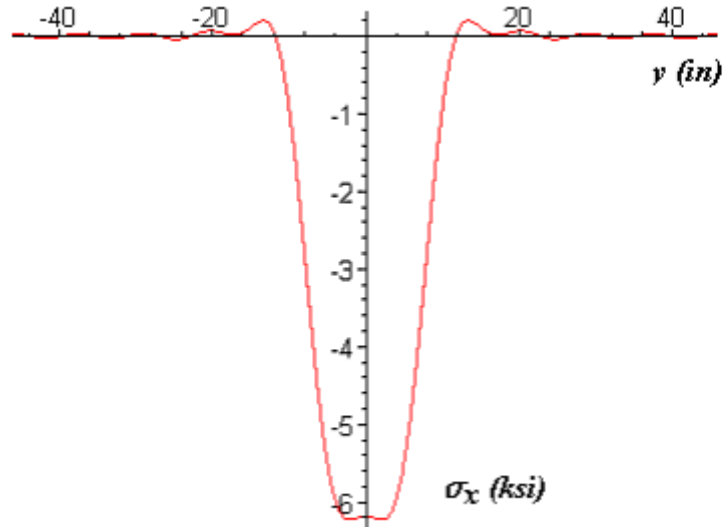


Figure B-2: Stress in the x-dir in the core concrete and diaphragm centerline for the third test under 6 ksi pressure

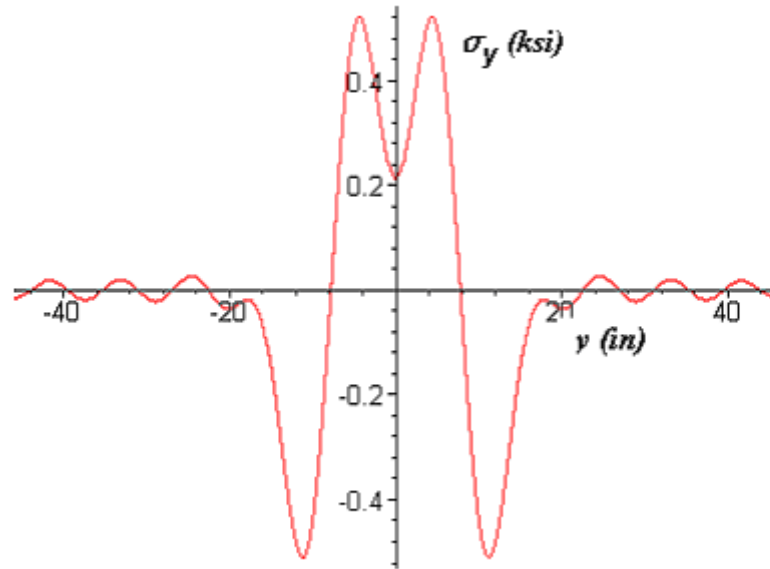


Figure B-3: Stress in the y-dir in the core concrete and diaphragm centerline for the third test under 6 ksi pressure

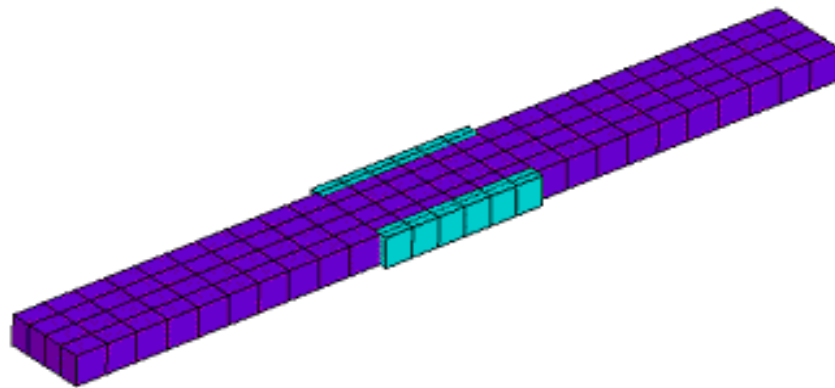


Figure B-4: Finite element model of the core concrete being pressed by two plates

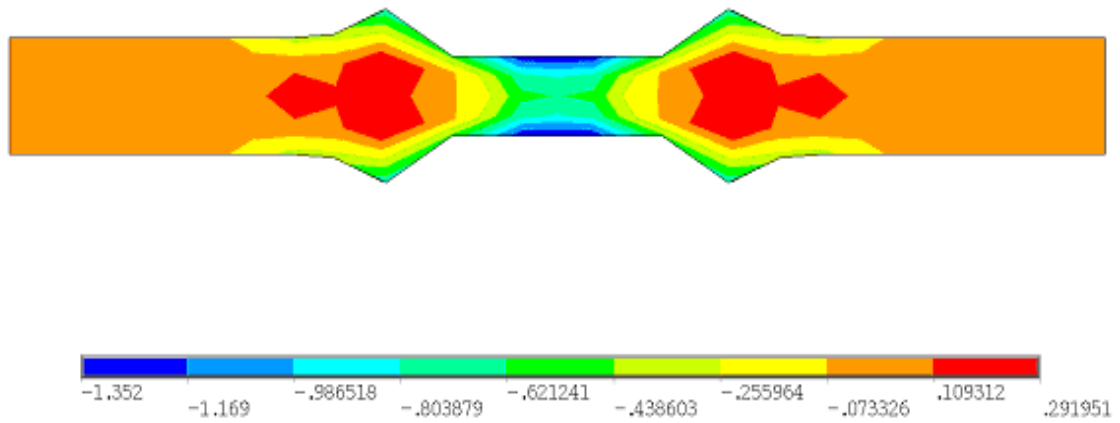


Figure B-5: Lateral stress (y-dir) contours in a deformed shape

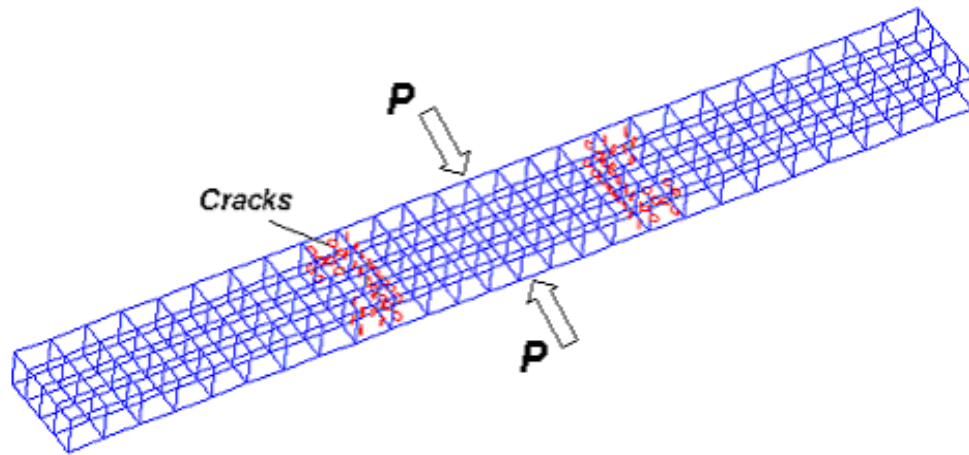


Figure B-6: Cracks formed at the edges of the plate

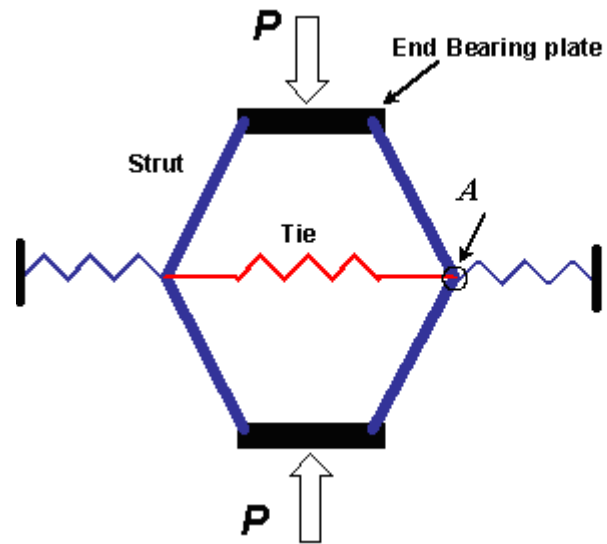


Figure B-7: A simple tie-strut model for the core concrete under compression

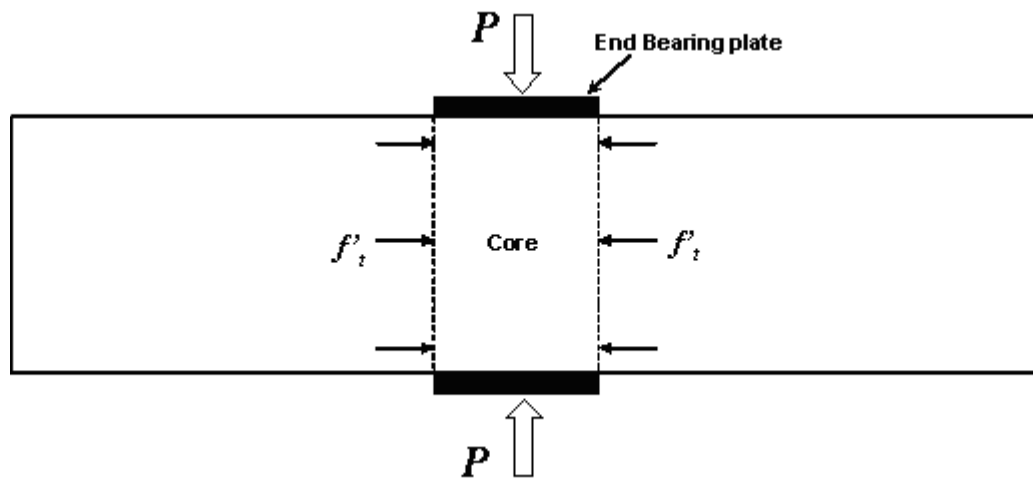


Figure B-8: An approximate estimate for the lateral pressure on the core concrete

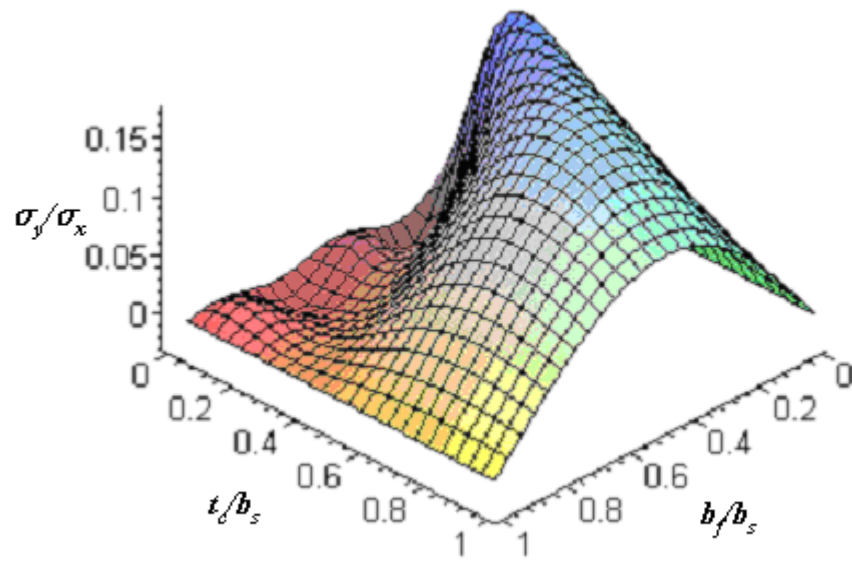


Figure B-9: The variation of stress ratio versus size ratios

Development of a Steel Bridge System - Simple for Dead Load and Continuous for Live Load

Volume 2 - Experimental Results

Atorod Azizinamini, Ph.D.
Aaron Yakel
Nick Lampe
Nazanin Mossahebi
Mark Otte

National Bridge Research Organization (NaBRO)
(<http://www.NaBRO.unl.edu>)
Department of Civil Engineering
College of Engineering and Technology

W150 Nebraska Hall
Lincoln, Nebraska 68588-0531
Telephone (402) 472-5106
FAX (402) 472-6658

Sponsored By

Nebraska Department of Roads



November, 2005

UNIVERSITY OF
Nebraska
Lincoln

Table of Contents

Table of Contents	ii
List of Figures	iv
List of Tables	viii
CHAPTER 1	
Experimental Program Description	1
1.1 PROBLEM STATEMENT	1
1.2 RESEARCH OBJECTIVES	3
1.3 REPORT CONTENT	3
CHAPTER 2	
Trial Designs	4
2.1 DESIGN CONSIDERATIONS	5
2.2 BRIDGE DESCRIPTION	5
2.3 DESIGN SUMMARY	6
2.4 MILITARY ROAD PROJECT	10
CHAPTER 3	
Common Setup and Procedures	12
3.1 GENERAL TEST DESCRIPTION	13
3.2 INSTRUMENTATION	14
3.3 CONSTRUCTION AND ERECTION	16
3.4 MATERIAL PROPERTIES	28
3.5 FATIGUE (CYCLIC LOADING)	31
3.6 ULTIMATE STRENGTH TESTING	34
CHAPTER 4	
First Specimen	36
4.1 SETUP AND PROCEDURES	36
4.1.1 CONSTRUCTION AND ERECTION	36
4.1.2 INSTRUMENTATION	38
4.1.3 MATERIAL PROPERTIES	44

4.2	SPECIMEN BEHAVIOR	45
4.2.1	NON-COMPOSITE LOADING	45
4.2.2	FATIGUE LOAD PHASE	48
4.2.3	ULTIMATE STRENGTH TESTING	59
4.3	TEST SUMMARY	65
CHAPTER 5		
	Second Specimen	66
5.1	SETUP AND PROCEDURES	66
5.1.1	CONSTRUCTION AND ERECTION	66
5.1.2	INSTRUMENTATION	68
5.1.3	MATERIAL PROPERTIES	73
5.2	SPECIMEN BEHAVIOR	74
5.2.1	FATIGUE LOAD TESTING	74
5.2.2	ULTIMATE STRENGTH TESTING	85
5.2.3	SPECIMEN DISSECTION	96
5.3	TEST SUMMARY	101
CHAPTER 6		
	Third Specimen	102
6.1	SETUP AND PROCEDURES	102
6.1.1	CONSTRUCTION AND ERECTION	102
6.1.2	INSTRUMENTATION	104
6.1.3	MATERIAL PROPERTIES	110
6.2	SPECIMEN BEHAVIOR	113
6.2.1	FATIGUE LOAD PHASE	113
6.2.2	ULTIMATE STRENGTH TESTING	124
6.3	TEST SUMMARY	132
Appendix A		
	Trial Designs	134
A.1	95' SPAN (MILITARY ROAD GEOMETRY)	135
A.2	100' SPAN (MILITARY ROAD GEOMETRY)	154
A.3	105' SPAN (MILITARY ROAD GEOMETRY)	167
A.4	90' SPAN (INITIAL DESIGN GEOMETRY)	179
A.5	90' SPAN (ROLLED SECTION DESIGN)	189
A.6	130' SPAN - 48" WEB (INITIAL DESIGN GEOMETRY)	196

List of Figures

CHAPTER 1	
Experimental Program Description	1
CHAPTER 2	
Trial Designs	4
Figure 2-1: Geometry for 90 and 130 ft Designs.....	6
Figure 2-2: Military Road Bridge Typical Cross-Section.....	11
Figure 2-3: Modified Military Road Cross-Section.....	11
CHAPTER 3	
Common Setup and Procedures	12
Figure 3-1: Conceptual Test Configuration.....	13
Figure 3-2: Data Acquisition System by Optim Electronics	15
Figure 3-3: Data Acquisition and Load Control Systems.....	15
Figure 3-4: Pier Dimensions.....	16
Figure 3-5: Pier Form Work Prior to Casting.....	17
Figure 3-6: Casting of Pier Concrete	17
Figure 3-7: Girder after Fabrication	18
Figure 3-8: Typical Placement of a Girder on the Bearing Pad.....	19
Figure 3-9: Temporary Supports	20
Figure 3-10: Diaphragm Reinforcement.....	21
Figure 3-11: Plan and Elevation of Diaphragm	22
Figure 3-12: Slab Reinforcement	23
Figure 3-13: Completed Diaphragm Forms	24
Figure 3-14: Completed Deck Forms	25
Figure 3-15: Partial Casting of Diaphragm.....	26
Figure 3-16: Completed Partial Casting of Diaphragm.....	26
Figure 3-17: Casting of Deck Slab	27
Figure 3-18: Completed Casting of Deck Slab	27
Figure 3-19: Stress-Strain Plot for Steel Girder.....	29
Figure 3-20: Yield Region showing 0.2% Offset.....	30
Figure 3-21: 220-kip MTS Actuator	33
Figure 3-22: Fatigue Loading System.....	34
Figure 3-23: Side View of Ultimate Load Test.....	35
Figure 3-24: Ultimate Load Test	35
CHAPTER 4	
First Specimen	36
Figure 4-1: Partial Penetration Weld.	37
Figure 4-2: Connection Detail of First Specimen.....	37
Figure 4-3: Plan View of Bottom Flange Gauges.....	39
Figure 4-4: Side View of Bottom Flange Gauges	39
Figure 4-5: Deck and Reinforcement Gauges.....	40
Figure 4-6: Additional Girder Instrumentation	41
Figure 4-7: Embedment Gauge Sections.....	42

Figure 4-8: Transverse Embedment Gauge Locations	43
Figure 4-9: Girder End Separation Under Simulated Dead Loads.....	46
Figure 4-10: Girder Rotation Under Simulated Dead Loads	46
Figure 4-11: Stress Rotation Relationship for SG2 and SG5	47
Figure 4-12: Stress Rotation Relationship for SG8, SG9, and SG12.....	47
Figure 4-13: Stress Rotation Relationship for SG2, SG3, and SG4.....	48
Figure 4-14: Fatigue Test Load-Deflection Graph	49
Figure 4-15: Mapping of Initial Cracks	50
Figure 4-16: Initial Crack Map for 0 Cycles	51
Figure 4-17: Crack Map after 1 Million Cycles.....	52
Figure 4-18: Crack Map after 1.5 Million Cycles.....	53
Figure 4-19: Crack Map after 2 Million Cycles.....	54
Figure 4-20: Cyclic Load Deflection Comparison.....	56
Figure 4-21: Cyclic Load Deflection Comparison.....	56
Figure 4-22: Strain Profile at Location 2	57
Figure 4-23: Strain Profile at Location 3	57
Figure 4-24: Strain Profile at Location 4	58
Figure 4-25: Horizontal Strain Distribution at Bottom of Diaphragm.....	58
Figure 4-26: Reinforcement Stress Comparison.....	59
Figure 4-27: Ultimate Capacity Test Load Deflection Curve.....	60
Figure 4-28: Horizontal Stress Distribution in Deck Reinforcement.....	61
Figure 4-29: Bottom Flange Stresses at Ultimate Capacity	62
Figure 4-30: Concrete Compressive Stress between End Bearing Plates.....	62
Figure 4-31: Moment Curvature Outside the Diaphragm.....	63
Figure 4-32: Moment Curvature at Support Centerline	64
Figure 4-33: Deck Cracking After Ultimate Loading.....	64

CHAPTER 5

Second Specimen

Figure 5-1: Connection Detail of Second Specimen.....	67
Figure 5-2: Girder Instrumentation.....	69
Figure 5-3: Slab Reinforcement Instrumentation.....	70
Figure 5-4: Diaphragm Instrumentation	71
Figure 5-5: Electrical Strain Gauges	72
Figure 5-6: Embedment Gauges	72
Figure 5-7: Deck Cracking	75
Figure 5-8: Bottom Flange Movement.....	75
Figure 5-9: Polystyrene between Pier and Diaphragm	76
Figure 5-10: Mapping of Deck Cracks.....	77
Figure 5-11: East Girder Load-Deflection Plot	78
Figure 5-12: West Girder Load-Deflection Plot	78
Figure 5-13: System Stiffness vs. No. of Cycles.....	80
Figure 5-14: East Girder Load Extremes.....	80
Figure 5-15: West Girder Load Extremes	81
Figure 5-16: Load Range vs. Number of Cycles	81
Figure 5-17: Strain Distribution Along Bottom Flange	82
Figure 5-18: Strain Distribution Just Inside Diaphragm.....	83
Figure 5-19: Strain Distribution Outside Diaphragm	85
Figure 5-20: Cracks in Slab over Pier	86

Figure 5-21:	Cracks Through the Depth of the Slab.....	87
Figure 5-22:	Gap Formed Between the Pier and the Polystyrene Insulation	88
Figure 5-23:	Girder Penetration into Diaphragm	88
Figure 5-24:	Deformed Shape of Specimen During the Ultimate Load Test.....	89
Figure 5-25:	Final Deformed Shape.....	89
Figure 5-26:	Cracking under Slab	90
Figure 5-27:	Ultimate Load Test Load-Deflection Graph.....	91
Figure 5-28:	Ultimate Load Test Moment-Deflection Graphs for Tests 1 and 2...	91
Figure 5-29:	Strain Distribution of Rebar in the Deck at Ultimate Load.....	93
Figure 5-30:	Strains in Top Layer of Reinforcement at Centerline of Pier.....	93
Figure 5-31:	Strains in Top Layer of Reinforcement at Edges of Pier.....	94
Figure 5-32:	Bottom Flange Strain Data	94
Figure 5-33:	Web Strain Distribution Out of Diaphragm.....	95
Figure 5-34:	Concrete Compressive Strain Inside Concrete Diaphragm.....	96
Figure 5-35:	Specimen After Removing the Slab	97
Figure 5-36:	Diaphragm after Demolition	98
Figure 5-37:	Gap between Diaphragm and Web	98
Figure 5-38:	Gap between Bottom Flanges	99
Figure 5-39:	Deformed Rebar	99
Figure 5-40:	Fractured Rebar.....	100

CHAPTER 6

Third Specimen..... 102

Figure 6-1:	Connection Detail for the Third Specimen.....	103
Figure 6-2:	Girder End Detail.....	103
Figure 6-3:	West Top Flange gauges	105
Figure 6-4:	East Top Flange gauges.....	105
Figure 6-5:	West Bottom Flange gauges	105
Figure 6-6:	East Bottom Flange gauges.....	106
Figure 6-7:	West Web gauges.....	106
Figure 6-8:	East Web gauges	107
Figure 6-9:	gauges in Top Layer of Reinforcement.....	107
Figure 6-10:	gauges in Bottom Layer of Reinforcement	108
Figure 6-11:	Longitudinal Location of Embedment gauges	108
Figure 6-12:	Transverse Locations of Embedment gauges.....	109
Figure 6-13:	Diaphragm Instrumentation.....	109
Figure 6-14:	Diaphragm Embedment gauges	110
Figure 6-15:	Strength Testing of Diaphragm Concrete.....	111
Figure 6-16:	Strength Testing of Deck Concrete	112
Figure 6-17:	Cracking Over the Pier and Through the Depth of the Deck.....	115
Figure 6-18:	Bottom Flange Penetration of Diaphragm	115
Figure 6-19:	Polystyrene Insulation Between the Pier and the Diaphragm	116
Figure 6-20:	East Girder Load/Deflection Curve	118
Figure 6-21:	West Girder Load/Deflection Curve.....	118
Figure 6-22:	East Girder Fatigue Loading Extremes.....	119
Figure 6-23:	West Girder Fatigue Loading Extremes	119
Figure 6-24:	Applied Fatigue Load Ranges	120
Figure 6-25:	System Stiffness vs. Number of Cycles	120
Figure 6-26:	Strain Profile Along Bottom Flange.....	122

Figure 6-27: Strain Profile Near Endplates	122
Figure 6-28: Strain Profile Near Endplates	123
Figure 6-29: Strain Profile Outside Diaphragm	124
Figure 6-30: Ultimate Test Setup	125
Figure 6-31: Ultimate Test Setup	126
Figure 6-32: Load vs. Deflection Plot for Specimen Number 3	128
Figure 6-33: Displacements of Girder Bottom Flanges Into Diaphragm	128
Figure 6-34: Embedment gauge Data at Bottom of Diaphragm	129
Figure 6-35: Embedment gauge Readings for the Second Layer of gauges	130
Figure 6-36: Embedment gauge Readings for the Third Layer of gauges	131

List of Tables

CHAPTER 1	
Experimental Program Description	1
CHAPTER 2	
Trial Designs	4
Table 2-1: Distribution Factor Summary for the 90-ft Span.....	7
Table 2-2: Distribution Factor Summary for the 130-ft Span.....	7
Table 2-3: Maximum Design Moments for the 90-ft Span	7
Table 2-4: Maximum Design Moment for the 130-ft Span.....	7
Table 2-5: 90-ft Span Design Summary.....	8
Table 2-6: Design Summary for 130 ft Span, 48 in Web.....	9
Table 2-7: Design Summary for 130 ft Span, 54 in Web.....	9
Table 2-8: Military Road Design Summary	11
CHAPTER 3	
Common Setup and Procedures	12
CHAPTER 4	
First Specimen	36
Table 4-1: Rebar Tensile Testing Results.....	44
CHAPTER 5	
Second Specimen	66
Table 5-1: Rebar Tensile Testing Results.....	73
CHAPTER 6	
Third Specimen.....	102
Table 6-1: Rebar Tensile Testing Results.....	112
References	133

Experimental Program Description

1

The following is Volume II of a two-volume report. Volume I contains a market analysis and identifies the concept of the new steel bridge system. Design procedures based on finite element analysis and recommendations for further research were also presented in Volume I. The results of the experimental program that was developed to test the design is the main focus of Volume II. A brief introduction and background of the project is provided here for reference. For more detailed information, see Volume I.

1.1 PROBLEM STATEMENT

The latter half of the twentieth century saw many changes in the design of bridges. One of the most significant changes came from the introduction of alternative materials for use in the construction of bridges. Prestressed concrete has become increasingly popular since its introduction in the

1950's (Dunker and Rabbat, 1992). The increase in the use of prestressed concrete has caused a decline in steel usage in short to medium span bridges. The diminishing competitiveness of steel bridges in the bridge market can be attributed to the following:

- A relatively lower degree of research and introduction of innovative ideas to steel bridge design and construction.
- When using bolted field splices, estimates for the average cost of material, installation and inspection of one bolt can be as high as \$20.00. In addition, ambiguity in available design provisions for the design of bolted field splices has resulted in misinterpretation of these provisions. It is not uncommon to see drastically different numbers of bolts in the web and flange splices for similar splices.
- A belief on the part of some who contend that putting more costly details in steel bridges will translate to more income. Prior to the introduction of prestressed concrete concepts to bridge applications this might have been true. The use of costly details in steel bridge construction is the primary reason for the diminishing competitiveness in the bridge market.
- Steel bridge design includes more complex procedures and provisions when compared to prestressed concrete design. This is especially true, considering the fact that there are very reliable computer programs to design complete prestressed concrete bridges.
- Construction provisions governing steel bridges are effectively developed for long span bridges; however, the majority of steel bridges constructed do not need to follow such rigorous construction provisions.
- Failure to take advantage of the fact that steel bridge superstructures are lighter than prestressed concrete alternatives. As a result, in some cases the same substructure system is used for both steel and concrete alternatives for a given bridge.
- Bearing devices at the pier locations. Though many states have stopped using pot bearings, many still use expensive details that could be simplified.

1.2 RESEARCH OBJECTIVES

The objective of this research is to develop a steel girder system that is more economical and suited for continuous span bridges.

1.3 REPORT CONTENT

This report summarizes the results from tests completed on rolled I-shaped girders representing the interior pier (negative flexure) region of a two-span bridge. The goal of this examination is to economize the use of steel in bridges commonly designed and constructed in the U.S. This report documents the details of the connection analysis and design, test setup, laboratory and field testing, and test results.

Chapter 2 contains a summary of trial designs completed within the span range determined from the market analysis. The trial designs were completed according to AASHTO LRFD Bridge Design Specifications (1998). The common setup and procedures used in testing of the different designs are summarized in Chapter 3. Chapters 4, 5 and 6 review the testing of specimens one, two and three, respectively. Each of these chapters cover test setup, instrumentation, material testing, and specimen construction specific to each sample. Each of these chapters also reviews and analyzes the data obtained from testing. Appendix A contains the calculations completed for the trial designs.

Trial Designs

2

Through the identification of the new system and the market analysis, two conclusions have been made. First, the simple support for non-composite dead loads/continuous for live loads concept exhibited definite advantages in load reduction and simplified fabrication. Second, the span range in which steel bridges have become less competitive is approximately 80 - 110 ft. Thus, a benefit-cost analysis was required to determine the economic validity of the proposed concept. To this end, a design was completed for two equal span bridges within the range of 90 - 130 ft span length. This same design was used for all three test specimens. The single characteristic of the design that was modified between each test was the detail for the connection over the pier.

2.1 DESIGN CONSIDERATIONS

The trial designs were completed in accordance with the 1998 American Association of State Highway and Transportation Officials (AASHTO,1998) Load and Resistance Factor Design Specifications (LRFD). Generation of the live load envelopes was done in part using the software package QCon-Bridge (Washington Department of Transportation,1999). Additional guidelines observed in the trial designs were taken from the Nebraska Department of Roads BOPP Manual (NDOR,1996). These guidelines include minimum width and thickness of the top flanges, and minimum web thickness. The top flanges are to be not less than 3/4-in thick and not less than 12-in wide. Minimum thickness for webs was set at 3/8-in thick. In order to facilitate the designs, optimization was done with respect to weight of the steel. The length to depth ratio (L/d) was set at approximately 28. Designs for each span length were completed for both the conventional continuous support condition and the proposed concept allowing for a representative weight comparison.

2.2 BRIDGE DESCRIPTION

The same superstructure geometry was used for both the 90-ft and 130-ft span bridges. The cast-in-place deck thickness was 8½-in with ½-in integral wearing surface. Support for the deck was provided by 4 lines of girders spaced at 10-ft center to center. Figure 2-1 shows the typical superstructure cross-section. The clear roadway dimension was 34-ft with 1½-ft wide barriers on either side. The exterior girder overhang was 3½-ft from the center of the exterior girder to the edge of deck.

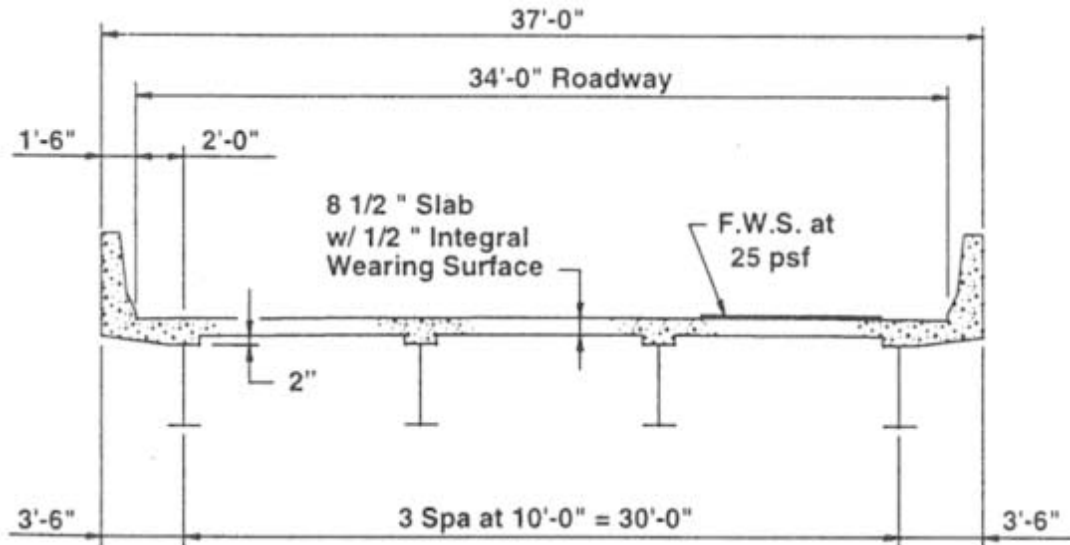


Figure 2-1: Geometry for 90 and 130 ft Designs

2.3 DESIGN SUMMARY

It was determined that the exterior girders controlled the design for flexure, and the interior girders governed shear design at the strength limit state. This was true for both the fully continuous support geometry and the proposed concept. For the proposed concept, the live load distribution factors were the same for both the positive and negative flexure regions for both the interior and exterior girders. Tables 2-1 and 2-2 contain summaries of the live load distribution factors for the 90-ft and 130-ft span bridges, respectively. The governing shear and bending moments are shown in Tables 2-3 and 2-4. Note the reduction in negative moment was due to no contribution from the non-composite dead loads for the proposed concept. AASHTO LRFD (6.10.4.4) allows an optional 10% reduction in negative moment from moment redistribution for compact sections (Federal Highway Administration, 1995). This allowance was used only for the conventional continuous design.

Design Summary

		Simple Dead Continuous Live		Continuous Dead Continuous Live	
		Positive	Negative	Positive	Negative
Exterior	Moment	0.865	0.865	0.865	0.865
	Shear	0.865	0.865	0.865	0.865
Interior	Moment	0.712	0.712	0.700	0.732
	Shear	0.965	0.965	0.966	0.966

Table 2-1: Distribution Factor Summary for the 90-ft Span

		Simple Dead Continuous Live		Continuous Dead Continuous Live	
		Positive	Negative	Positive	Negative
Exterior	Moment	0.865	0.865	0.865	0.865
	Shear	0.865	0.865	0.865	0.865
Interior	Moment	0.703	0.703	0.693	0.728
	Shear	0.965	0.965	0.966	0.966

Table 2-2: Distribution Factor Summary for the 130-ft Span

		Simple Dead Continuous Live		Continuous Dead Continuous Live	
		Positive	Negative	Positive	Negative
Moment (k-ft)	Positive	4430		4212	
	Negative	3699		5269	
Shear (kip)	Positive	287		267	
	Negative	329		348	

Table 2-3: Maximum Design Moments for the 90-ft Span

		Simple Dead Continuous Live		Continuous Dead Continuous Live	
		Positive	Negative	Positive	Negative
Moment (k-ft)	Positive	9003		7374	
	Negative	7248		11319	
Shear (kip)	Positive	347		314	
	Negative	404		437	

Table 2-4: Maximum Design Moment for the 130-ft Span

Design Summary

The 90-ft span bridge was designed as both a welded plate girder and a rolled I-shape girder. A summary of the designs is shown in Table 2-5. The values in the table are presented as ratios in the form of demand/resistance. Recall that the designs were optimized in terms of steel weight only, resulting in similar weights for the plate girder designs.

			Simple for Dead Loads		Continuous for Dead Loads		Rolled (W40x199)	
			Positive	Negative	Positive	Negative	Positive	Negative
Section Properties	Dimen- sions	Top Flng	$\frac{7}{8} \times 13\frac{1}{2}$		$\frac{3}{4} \times 14$	1×16	$1\frac{1}{16} \times 15\frac{3}{4}$	
		Web	$\frac{1}{2} \times 36$		$\frac{7}{16} \times 36$	$\frac{1}{2} \times 36$	$\frac{5}{8} \times 36\frac{9}{16}$	
		Bot Flng	$1\frac{1}{4} \times 15$		$1\frac{1}{8} \times 16$	$1\frac{1}{2} \times 16$	$1\frac{1}{16} \times 15\frac{3}{4}$	
	Weight	Area	48.6		44.25	59.5	58.4	
		Length	90		63	27	90	
		Wt (lb)	14884		9486	5466	17910	
Tot Wt		14884		14952		17910		
Service	Perm	Comp	51%	85%	49%	93%	42%	85%
	Defl	Tension	93%	78%	97%	94%	92%	64%
	LL Defl	(in)	1.297		1.276		1.246	
Strength	Flexure	Compact Section	91%	94%	97%	99%	88%	86%
	Shear		Stiffeners not Required		Stiffeners not Required		Stiffeners not Required	
	DL Defl @ Midspan	(in)	5.9		3.4		4.8	

Table 2-5: 90-ft Span Design Summary

Similar to the 90-ft span summary, Tables 2-6 and 2-7 contain the summaries for the 130-ft span designs. The first set of designs utilized a 48-in web, and the second set used a 54-in web in an attempt to decrease the dead load deflection. The 48-in and 54-in webs resulted in L/d ratios of 32.5 and 28.9, respectively.

Design Summary

				Simple for Dead Loads		Cont. for Dead Loads	
				Positive	Negative	Positive	Negative
Section Properties	Dimension	Top Flng	1 ³ / ₈ × 18	Same	3/4 × 12	2 ¹ / ₈ × 22	
		Web	7/16 × 48	Same	3/8 × 48	1/2 × 48	
		Bot Flng	1 ¹ / ₂ × 21	Same	1 ¹ / ₄ × 19 ¹ / ₂	2 ¹ / ₂ × 22	
	Weight	Area	77.25		51.375	125.75	
		Length	130		91	39	
Wt (lb)		34172		15908	16688		
	Tot Wt		34172		32596		
Service	Perm Defl	Comp	67.5%	77.6%	77.2%	76.7%	
		Tension	96.1%	67.4%	99.3%	76.8%	
	LL Defl	(in)		1.714		1.841	
Strength	Flexure	Compact Section	96.9%	Comp 99.5%	98.9%	Comp 95.5%	
				Tens 86.4%		Tens 95.4%	
	Shear		Requires Stiffeners		Requires Stiffeners		
	DL Defl @ Midspan	(in)		8.2		5.6	

Table 2-6: Design Summary for 130 ft Span, 48 in Web

				Simple for Dead Loads		Cont. for Dead Loads	
				Positive	Negative	Positive	Negative
Section Properties	Dimension	Top Flng	1 ¹ / ₄ × 16	Same	3/4 × 12	2 × 20	
		Web	7/16 × 54	Same	3/8 × 54	1/2 × 54	
		Bot Flng	1 ¹ / ₂ × 18	Same	1 ¹ / ₈ × 18	2 ¹ / ₄ × 21 ¹ / ₂	
	Weights	Area	70.625		49.5	115.375	
		Length	130		91	39	
Wt (lb)		31242		15328	15311		
	Tot Wt		31242		30639		
Service	Perm Defl	Comp	68.8%	78.0%	77.2%	76.7%	
		Tension	96.6%	67.6%	99.3%	76.8%	
	LL Defl	(in)		1.51		1.65	
Strength	Flexure	Compact Section	98.9%	Comp 100%	96.2%	Comp 94.7%	
				Tens 86.6%		Tens 95.5%	
	Shear		Requires Stiffeners		Requires Stiffeners		
	DL Defl @ Midspan	(in)		7.5		5.1	

Table 2-7: Design Summary for 130 ft Span, 54 in Web

The results of these designs were presented to the members of the advisory panel. From this meeting, the following conclusions were made:

1. The cost of the additional steel would easily be offset by the elimination of the bolted field splices.
2. The magnitude of the dead load deflection reduces the applicability of this concept to phase construction projects.

Based on the second recommendation, the decision was made to focus primarily on spans of approximately 100-ft in length and to utilize rolled beams. The Military Avenue project was selected for two reasons. First, the 95-ft spans represent a common two-span bridge constructed in Nebraska. Second, the project was recently designed and erected and would provide current cost estimates for economic comparisons between current practice and the proposed concept.

2.4 MILITARY ROAD PROJECT

The Military Road structure consisted of two 95-ft spans, and a five-girder cross-section. The girder spacing was 8'-4" and supported a 30-ft clear roadway and a pedestrian sidewalk. This superstructure geometry is shown in Figure 2-2. To simplify the design procedure, the sidewalk was removed and the number of girders reduced from five to four. This altered geometry is shown in Figure 2-3. The designs for this structure were carried out using the simple support for non-composite dead loads/continuous for composite dead and live loads concept and rolled I-shape girders. Designs for span lengths of 100-ft and 105-ft were also completed using the geometry defined in Figure 2-3. The summaries for these designs are shown in Table 2-8.

From the results in the table, increases in span length from 95-ft result in decreases in beam demand/beam capacity ratios. Thus, the designs become less optimized as the span length increases. In addition, the magnitude of the dead load deflection may warrant cambering of the girders,

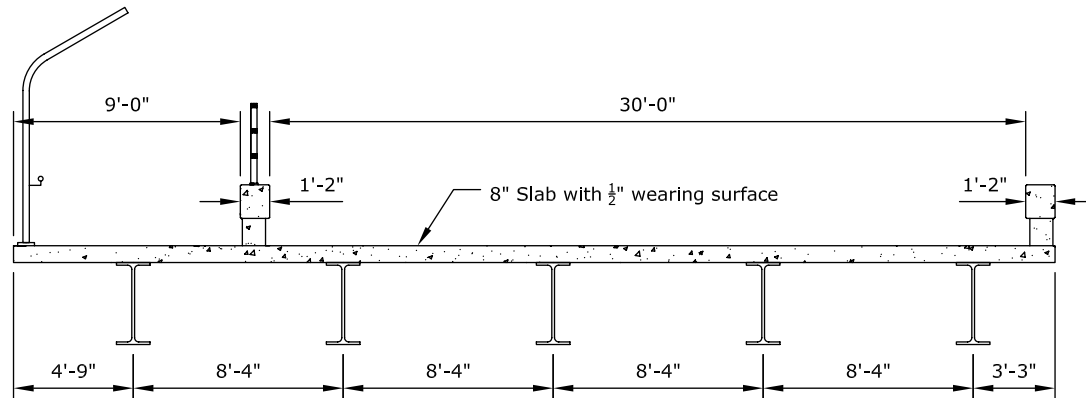


Figure 2-2: Military Road Bridge Typical Cross-Section

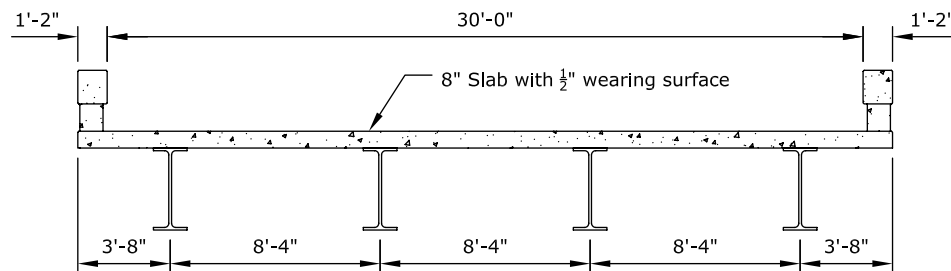


Figure 2-3: Modified Military Road Cross-Section

	Span Length (Feet)						
	95		100		105		
Section	W40×215		W40×249		W40×277		
DL Deflection (int/ext)	4.4/4.2		4.7/4.5		5.3/5.1		
LL Deflection	99.4		95.9		98.8		
Flexural Strength	Pos	92.6		88.8		88.5	
	Neg	83.0		78.2		78.3	
Permanent Deflection	Pos	96.5	48.1	91.8	48.3	92.0	50.7
	Neg	62.6	80.9	60.5	75.7	82.5	75.2

Table 2-8: Military Road Design Summary

reducing the economic benefit. The 95-ft span was selected as the model for the experimental investigation, primarily to see the cost comparison to the actual project constructed. Complete details of the design process including sample calculations can be found in Appendix A.

Common Setup and Procedures

3

Based on the analysis results and guidance from the advisory panel, the first pier connection detail was chosen for full-scale testing. An experimental investigation was carried out to check assumptions made during the design process, check validity of the FEM model, and to examine the performance of the pier connection detail under field conditions. Connection details two and three were designed based on experimental observations and analyses of the first connection detail. This chapter describes the general setup of the testing procedures and instrumentation common to all three specimens.

3.1 GENERAL TEST DESCRIPTION

The geometry of the test specimen was selected to represent an interior pier section of a two-span bridge subjected to construction and service loads. Figure 3-1 shows the conceptual test specimen geometry. The double cantilever system provides an effective means of simulating loading of the structure in the field. In this loading system, the shear/moment ratio can be accurately modeled.

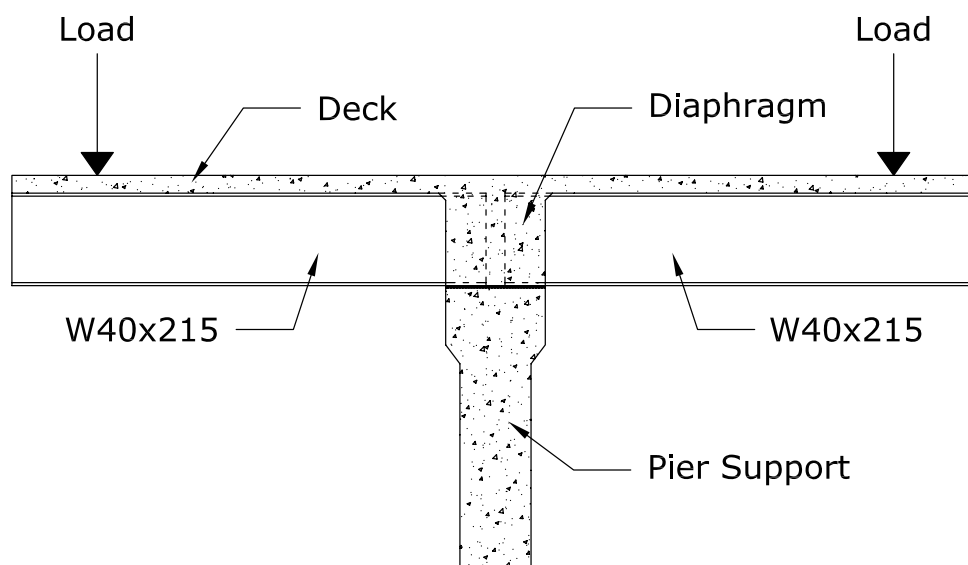


Figure 3-1: Conceptual Test Configuration

The test specimen was designed according to the AASHTO LRFD Specifications for Highway Bridges (AASHTO, 1998). The strength portion of the design, as outlined in Appendix A, is taken further to include fatigue and shear resistance. The objective was to obtain experimental data to compare with the results of the FEM analysis. In order to accurately represent the loads the structure would encounter, three load stages were identified. The load stages were:

1. Non-composite dead load (casting of wet concrete deck)
2. Cyclic fatigue loading based on a fatigue load from analysis and the detail fatigue category
3. Ultimate distributed moment based on the governing strength limit state

In order to obtain data from these load stages, several types of data collection hardware were employed.

3.2 INSTRUMENTATION

As discussed in the previous section, three main load stages were identified. Within each load stage exists a distinct load pattern warranting slight variations in instrumentation configurations. Monitoring of the specimen was done using potentiometers, bonded electrical strain gages and vibrating wire strain gauges. Collection of data was done through the use of a Megadac Data Acquisition System by Optim Electronics. This acquisition system collected data from all instruments except the vibrating wire gauges. Readings from the vibrating wire gauges were taken manually with a VS Datamate from the Slope Indicator Company. To aid in record keeping, the instruments were assigned a designation according to instrument type and location. The designations are presented within each specimen's section. The data acquisition system is shown in Figures 3-2 and 3-3.

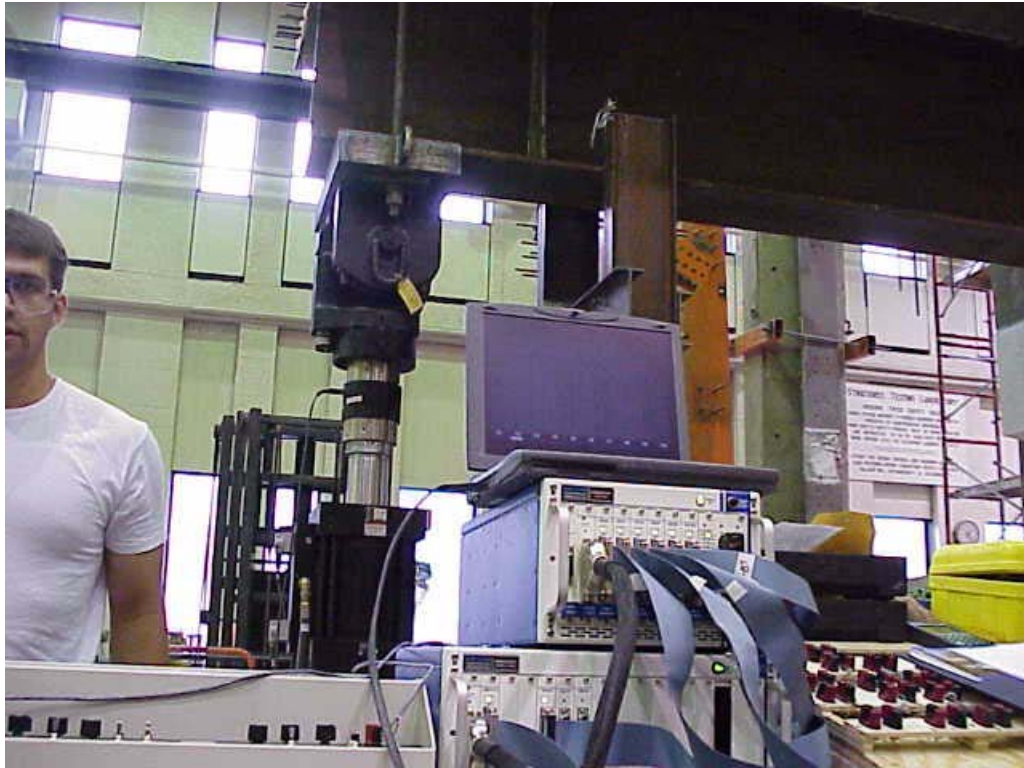


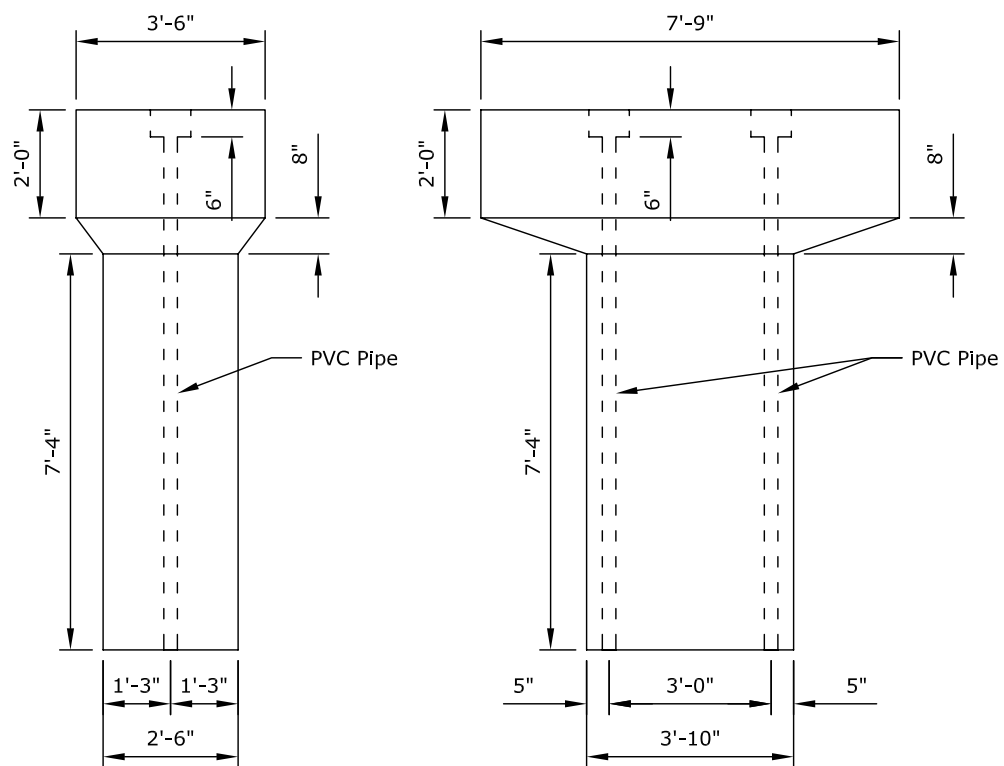
Figure 3-2: Data Acquisition System by Optim Electronics



Figure 3-3: Data Acquisition and Load Control Systems

3.3 CONSTRUCTION AND ERECTION

Construction of the test specimen was completed in the structures lab at the University of Nebraska-Lincoln (UNL). Support for the cantilever system consisted of a concrete pier similar to those used by the Nebraska Department of Roads (NDOR). The dimensions of the pier were based on the height requirements of the MTS[®] hydraulic actuators and the attachment hardware required for the fatigue test. A drawing of the pier is shown in Figure 3-4.



Pier Elevation

Figure 3-4: Pier Dimensions

After curing for seven days, the forms were removed and the pier rotated upright into position. For safety and stability reasons, the pier was post-tensioned to the lab floor at the pier centerline. Figure 3-5 shows the completed pier form-work prior to casting, and Figure 3-6 shows casting of the pier concrete.



Figure 3-5: Pier Form Work Prior to Casting



Figure 3-6: Casting of Pier Concrete

The steel girder sections were provided by local steel manufacturers. Measurements of all lengths, widths, and thicknesses of the steel girders were taken before girder placement. The length of each W40x215 girder section was 16-ft. Figure 3-7 shows a typical girder being moved into position during construction.

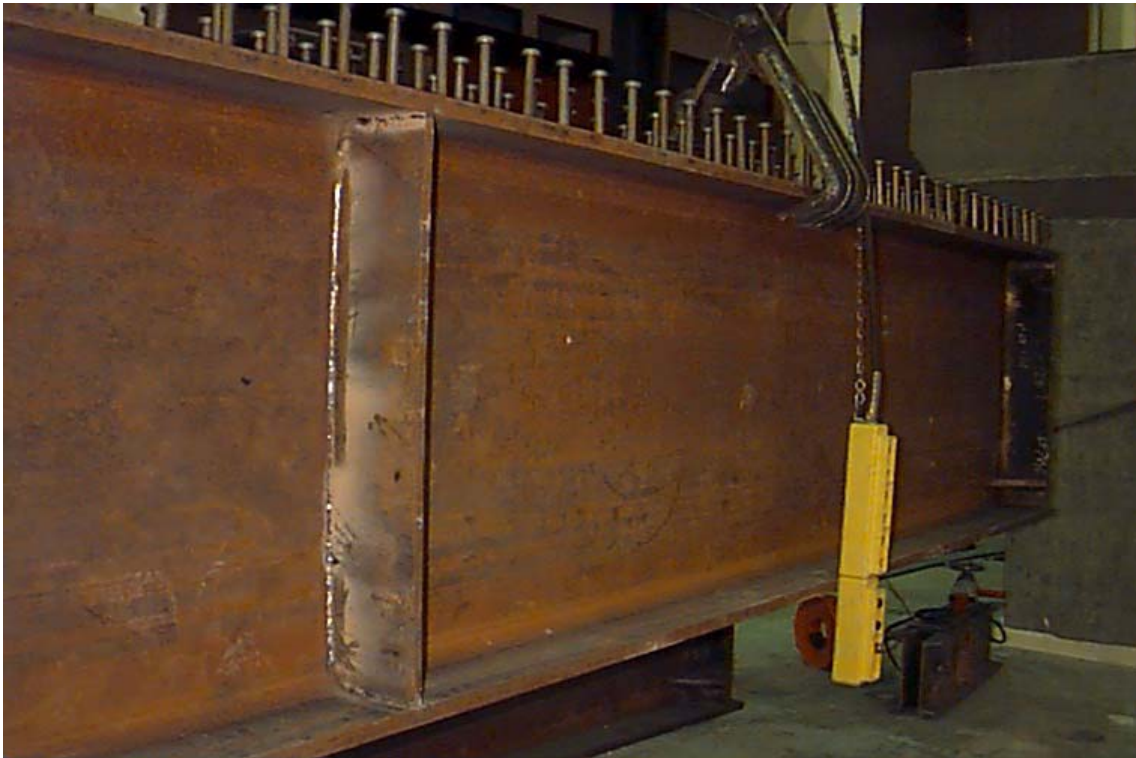


Figure 3-7: Girder after Fabrication

The elastomeric bearing pad, known commercially as "Fiberlast", was obtained from Voss Engineering. Design of this pad was completed by Voss Engineering through the use of in-house software. The pad dimensions were 15.75-in wide by 36-in long by 1-in thick. This pad was centered on the pier and permanent markings were made to insure detection of any movement in the pad during construction. Figure 3-8 shows the typical placement of a girder on the bearing pad

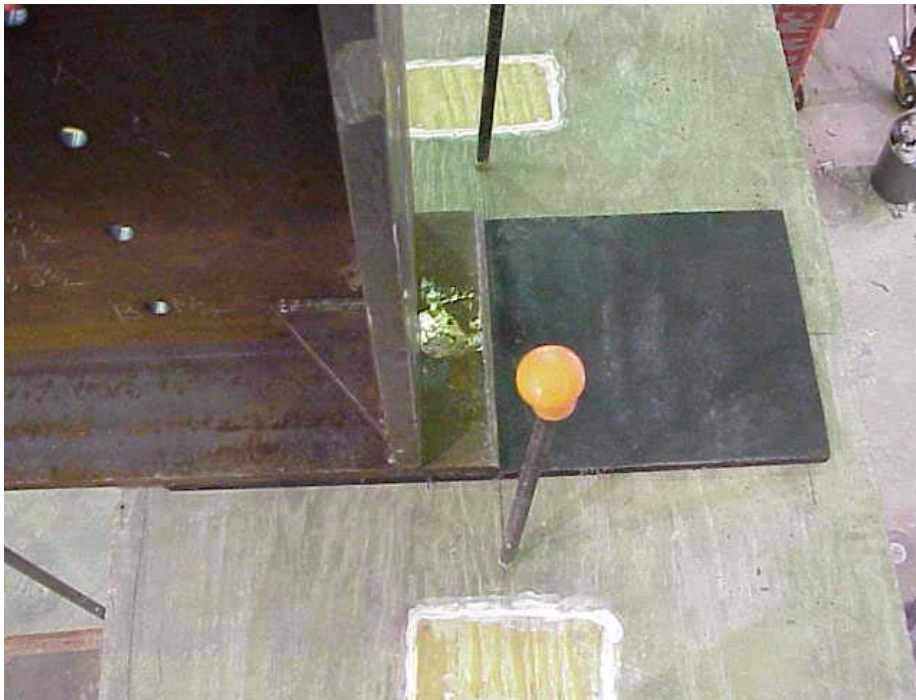


Figure 3-8: Typical Placement of a Girder on the Bearing Pad

In this double cantilever system, the test specimen is unstable until composite action is acquired; thus, temporary supports were necessary at the outer ends of each cantilever during erection and casting of the specimen. The temporary supports are shown in Figure 3-9. The hydraulic ram, also seen in Figure 3-9, was used for positioning the girder to allow deflection for simulation of non-composite dead load. During construction, cables connecting the stiffeners to the temporary supports were used to provide lateral stability.



Figure 3-9: Temporary Supports

Reinforcement for the diaphragm was similar for each specimen. Holes were drilled (preferred) or flame cut in the web for the transverse reinforcement, which consisted of five #8 bars on each face. The stirrups were #5 closed hoops spaced throughout the diaphragm. Figure 3-10 is a picture of the diaphragm reinforcement before casting. Figure 3-11 shows the plan and elevation views of the diaphragm reinforcement. A 3-in transition was formed into the diaphragm deck interface to reduce the effects of stress concentrations associated with abrupt changes in the cross-section. This is a common detail used by NDOR, which is also shown in Figure 3-11.



Figure 3-10: Diaphragm Reinforcement

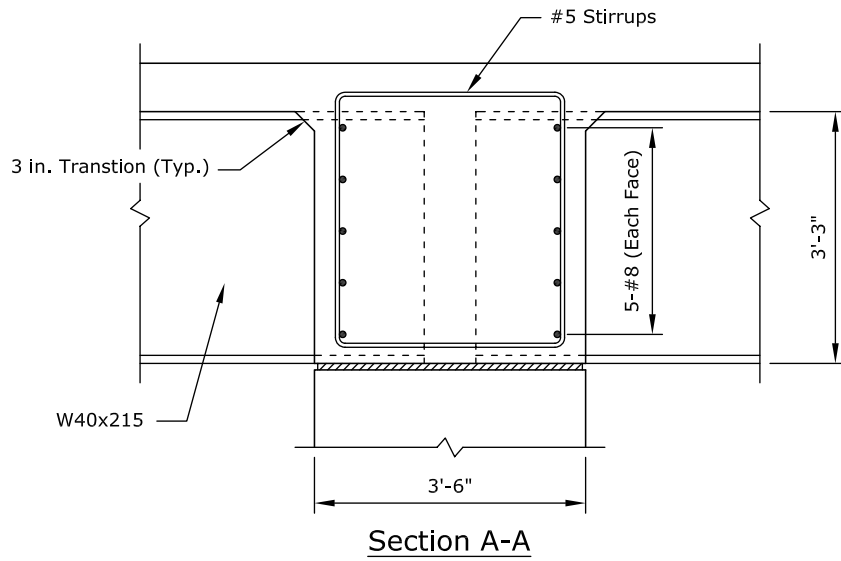
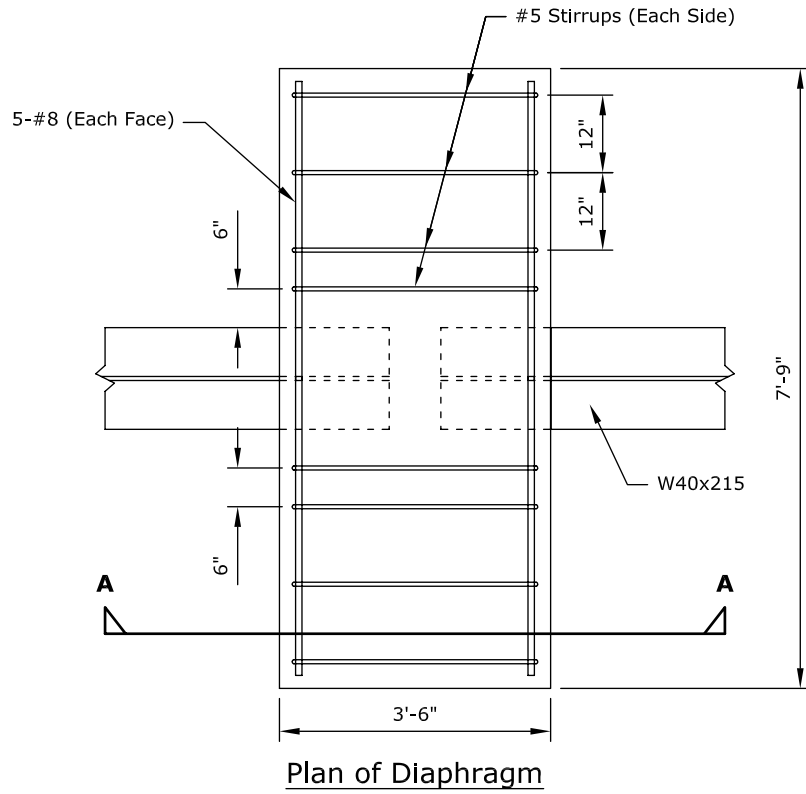
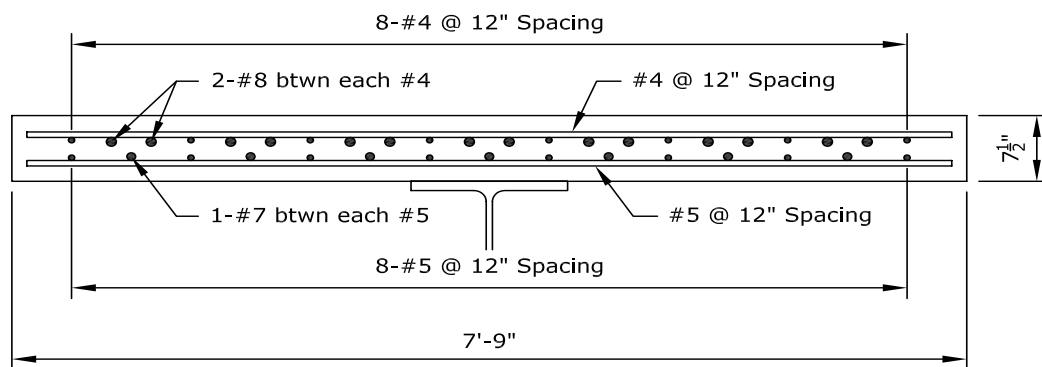


Figure 3-11: Plan and Elevation of Diaphragm

Empirical deck design was used to design the concrete slab in accordance with AASHTO LRFD Design Specifications. The longitudinal and transverse reinforcement consisted of #4 bars at 12-in spacing in the top layer and #5 bars at 12-in spacing in the bottom layer. Additional longitudinal reinforcement was designed according to reinforced concrete beam theory. The area of reinforcement required was calculated based on the assumption that the strain in the bottom concrete reached 0.003. From this assumption, the additional reinforcement required was two #8 bars centered between adjacent #4 bars in the top layer and a #7 bar centered between adjacent #5 bars in the bottom layer. This follows the typical reinforcing steel area ratio of two-thirds in the top layer and one-third in the bottom layer. The same slab reinforcement was used in each specimen to provide uniformity for comparison. Figure 3-12 shows the slab reinforcement.

Shear studs were designed according to AASHTO specifications to provide composite action between the slab and girder. The longitudinal shear stud spacing was 4.5-in along the girder with three studs spaced transversely across the top flange.



Section of Slab

Figure 3-12: Slab Reinforcement

Supports for the deck slab forms were supplied by Capital Contractors of Lincoln. These supports are similar to those used in the field. Form-work for the deck and diaphragm was added after the diaphragm reinforcement was placed. One-inch thick polystyrene was placed at the base of the diaphragm in order to prevent bonding between the pier and diaphragm concrete. Completed form-work for the diaphragm and deck is shown in Figures 3-13 and 3-14. It may be observed in some of the figures that not all of the longitudinal reinforcing was in place at the time of the partial diaphragm pour. This allowed for the most efficient use of time and labor.



Figure 3-13: Completed Diaphragm Forms



Figure 3-14: Completed Deck Forms

Casting of the slab and diaphragm was completed in two stages. The first stage consisted of casting the diaphragm to half the total depth. The second stage consisted of casting the remainder of the diaphragm and deck slab. This was done to add stability to the specimen during deck casting, which follows procedures used in the field. Figure 3-15 and 3-16 show casting of the diaphragm to partial fill. The remainder of the diaphragm and deck was cast the next day. Figure 3-17 shows the casting of the deck. The deck was then covered with burlap and plastic and moist cured, as shown in Figure 3-18. The temperature and strains were monitored during the curing phase.



Figure 3-15: Partial Casting of Diaphragm

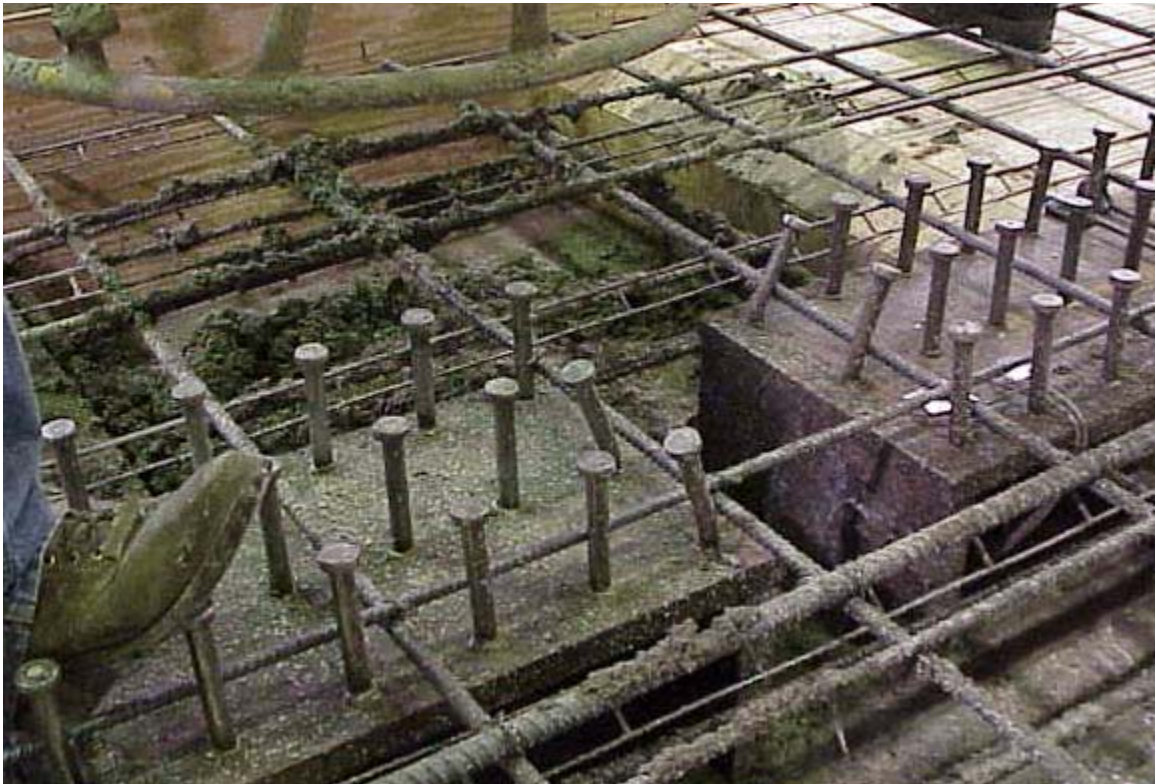


Figure 3-16: Completed Partial Casting of Diaphragm



Figure 3-17: Casting of Deck Slab



Figure 3-18: Completed Casting of Deck Slab

3.4 MATERIAL PROPERTIES

The laboratory test specimen was constructed using representative materials utilized in actual bridge construction. The deck and diaphragm were constructed with 47-BD concrete, with a specified 28-day strength of 4500 psi. The pier concrete was designed to attain a 28-day compressive strength of 5000 psi. Grade 60 reinforcing steel was used throughout the construction of each test specimen. The bridge girders were fabricated from W40 X 215 rolled I-girders conforming to ASTM A709-50W specifications. Material tests were performed to insure that the bridge components complied with specifications.

For the concrete materials, several 6-in diameter by 12-in long concrete test cylinders were made during the casting of each component. For each specimen, two concrete cylinders were tested from both the deck and diaphragm components after curing for ten days. Similar testing was completed after 28 days of curing and on the day coinciding with the ultimate strength test. Results of the concrete compressive tests are presented for each specimen within the appropriate chapters.

The pier concrete compressive strength was tested after seven days only. The compressive strength at this time was approximately 4250 psi. Pier concrete material properties were not required for data reduction. Therefore further compressive tests were not necessary.

For the steel reinforcing materials, samples of each deck reinforcing bar size were tested for mechanical properties. Each sample was tested as a full section according to ASTM A370 Specifications. Results of the tensile tests are presented for each specimen within the appropriate chapters.

For the rolled I-shaped girders, two samples were taken from the girder web and one from the tension flange. Samples were taken from regions which were subjected to low flexural stresses during the testing sequence. These samples were tested as full sections according to ASTM A370 Specifications. Figure 3-19 shows the typical results of one girder steel tensile test. Figure 3-20 shows the yield region where the 0.2% offset method was used to determine the yield strength. The average yield strength of the girder steel was determined to be 57 ksi. The stress/strain data is based on engineering strain.

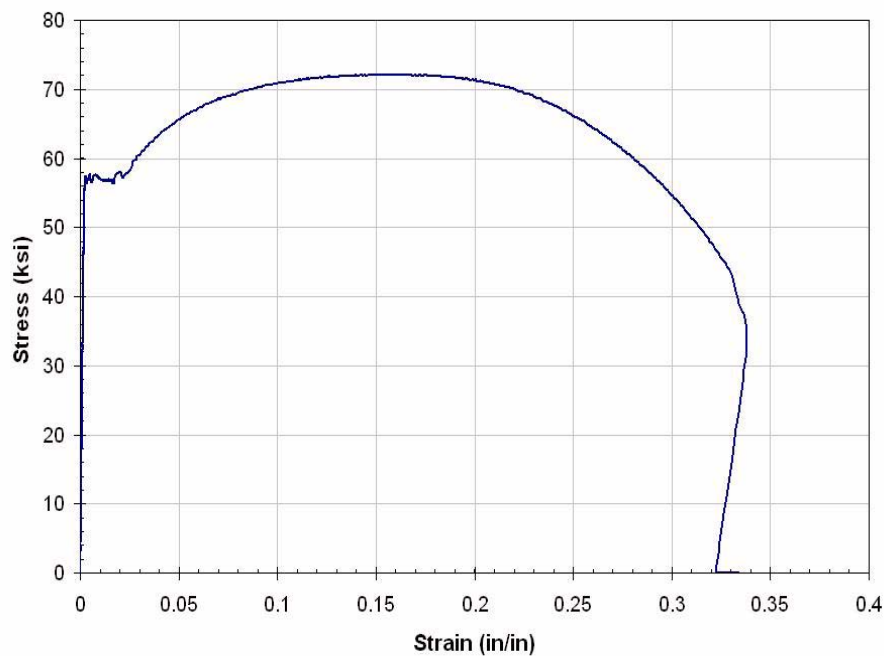


Figure 3-19: Stress-Strain Plot for Steel Girder

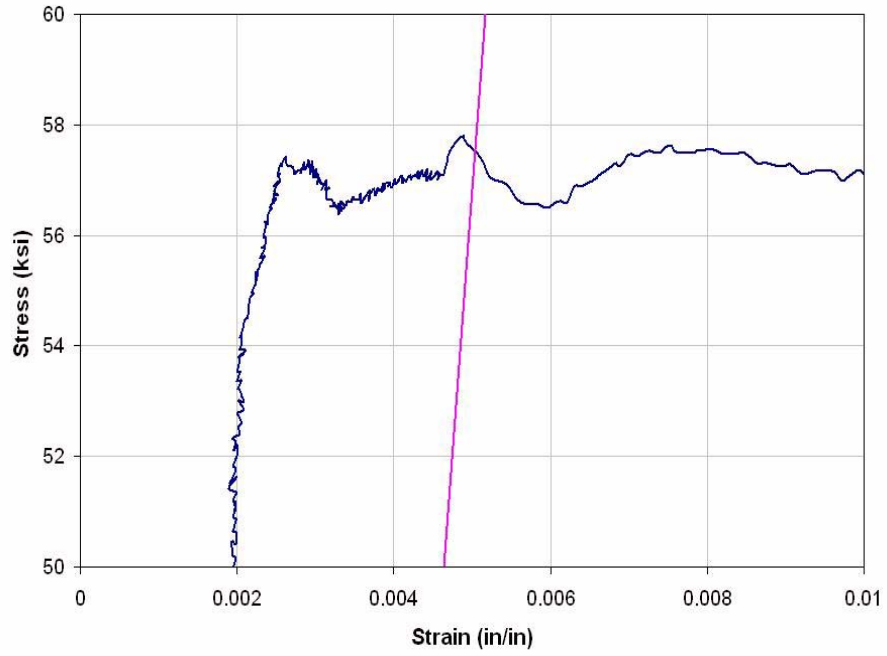


Figure 3-20: Yield Region showing 0.2% Offset

3.5 FATIGUE (CYCLIC LOADING)

Fatigue shear and moment envelopes were generated from the design live load analysis. The loads generated correspond to 135,000,000 cycles. To conserve time, the number of cycles was reduced to a target value of 2,000,000 cycles. The load required at the reduced number of cycles was based on the general S-N curve equation. The shape of a general S-N curve is defined by the following equation:

$$(\Delta F)_N = \left| \frac{A}{N} \right|^{\frac{1}{3}} \geq \frac{1}{2} (\Delta F)_{TH} \quad (3-1)$$

where

$(\Delta F)_N$ = nominal fatigue resistance (ksi)

A = constant based on the fatigue category

n = number of stress range cycles per truck passage

$(\Delta F)_{TH}$ = fatigue threshold value based on fatigue category

N = (365)(75)n(ADTT)_{SL}

(ADTT)_{SL} = single lane average daily truck traffic

For any given detail, $(\Delta F)_N$ can be related to the fatigue moment by multiplying both sides of Equation 3-1 by the section modulus, S. The result is Equation 3-2. Here S depends on the location of the detail.

$$S(\Delta F)_N = S \left| \frac{A}{N} \right|^{\frac{1}{3}} \quad (3-2)$$

For the same detail subjected to different moments, Equation 3-3 takes the following form.

$$M = S \left| \frac{A}{N} \right|^{\frac{1}{3}} \quad (3-3)$$

Moment M_1 corresponds to a number of cycles N_1 as shown in Equation 3-4. A similar expression for moment M_2 and N_2 is shown in Equation 3-5:

$$M_1 = S \left| \frac{A}{N_1} \right|^{1/3} \quad (3-4)$$

$$M_2 = S \left| \frac{A}{N_2} \right|^{1/3} \quad (3-5)$$

Dividing Equation 3-4 by Equation 3-5 yields the following results. The S and A terms cancel out and since the number of cycles will always be positive, the absolute value can be omitted. Equation 3-6 gives the relationship:

$$\frac{M_1}{M_2} = \left(\frac{N_2}{N_1} \right)^{1/3} \quad (3-6)$$

From analysis, the governing fatigue moment was found to be $M_1 = 352$ kip · ft with $N_1 = 135,000,000$ cycles. With M_1 and N_1 known and requiring that $N_2 = 2,000,000$ cycles, substituting these values into Equation 3-6 results in the following relationship:

$$\frac{352}{M_2} = \left(\frac{2,000,000}{135,000,000} \right)^{1/3} \quad (3-7)$$

Solving Equation 3-7 gives $M_2 = 1433$ kip · ft or an applied load $P = 102$ kips, located at 14 ft from the specimen centerline. In a bridge of two equal spans, at no time will the bottom flange experience tension. In order to insure this trend and that the target load would be reached, the lower bound of the cyclic load range was shifted slightly upward from zero for each specimen.

Due to the reduced strength of specimen two and three, the required load of 102 kips was reduced. To satisfy the fatigue requirement, the number of cycles was increased according to Equation 3-6.

The cyclic load was applied using 220-kip MTS actuators, as shown in Figures 3-21 and 3-22. Displacement control was used throughout the course of the fatigue investigation. The specimen was loaded slowly to peak load, and the cracks in the deck slab were mapped. The cyclic loading was continuous except for short pauses for vibrating wire gauge readings, to be taken once every 24 hours. Cracks were monitored at regular intervals of cyclic loading. Following fatigue testing, the loading system was altered for the ultimate strength test.



Figure 3-21: 220-kip MTS Actuator



Figure 3-22: Fatigue Loading System

3.6 ULTIMATE STRENGTH TESTING

The system used for fatigue loading was changed for the ultimate strength test. The MTS equipment was replaced with four 300-kip actuators. Two actuators were placed at each end of the cantilever specimen. The point of load application varied for each specimen, reducing or increasing the moment arm to accommodate the geometry of the laboratory's strong floor.

For the ultimate strength test, load was increased slowly in load stages of 10 to 25-kip increments. At the end of each load stage, both the load data and electrical instrument data was collected. The time required to collect data from the vibrating wire gauges was approximately 30 minutes. In order to conserve time, data from the vibrating wire instruments was collected after every other load step. Each specimen was loaded until failure, indicated by the inability to carry load as deflection increased. The loading system is shown in Figures 3-23 and 3-24.



Figure 3-23: Side View of Ultimate Load Test



Figure 3-24: Ultimate Load Test

First Specimen

4

This chapter outlines the experimental observations and data at various stages in the investigation of the first specimen. The construction of the first specimen concluded in June, 2000. The fatigue test was performed between July, 2000 and August, 2000 and the experiment concluded with the ultimate load test also performed in August, 2000.

4.1 SETUP AND PROCEDURES

General setup and procedures were given in Chapter 3. The following information is specific to the first specimen.

4.1.1 CONSTRUCTION AND ERECTION

For specimen one, the bottom flange of both girder sections was extended out four inches beyond the edge of the top flange and web. The flanges were then joined by a partial penetration weld as shown in Figure 4-1. Bear-

ing stiffeners were attached flush at this web edge with gusset plate stiffeners within the compression zone. This detail can be seen in Figure 4-2.



Figure 4-1: Partial Penetration Weld.

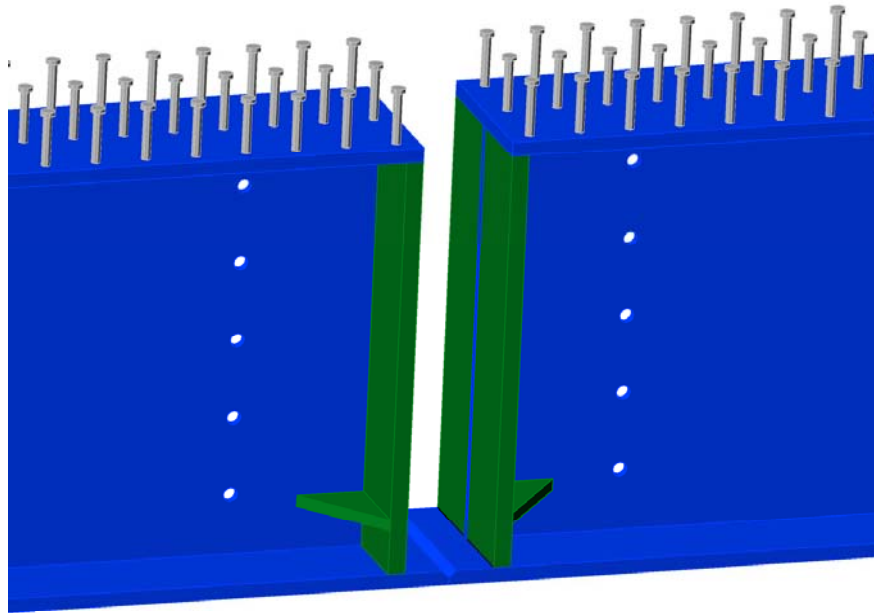


Figure 4-2: Connection Detail of First Specimen

4.1.2 INSTRUMENTATION

Three separate load stages were identified for the first specimen, each requiring slightly different instrumentation. The devices included electrical strain gauges, vibrating wire strain gauges, vibrating wire embedment gauges, and potentiometers. To aid in record keeping, instruments were assigned a designation according to location and type as follows:

SG - steel surface electrical strain gauges

EG - concrete embedment vibrating wire strain gauges

VW - steel surface vibrating wire gauges

CG - concrete surface electrical strain gauges

Pots - potentiometers (linear transducers)

Gauges SG1 through SG7 were located on the top surface of the bottom flange over the pier, as shown in the plan view of Figure 4-3. Figure 4-4 illustrates the locations of gauges SG8 through SG14 located across the thickness of the bottom flange near the diaphragm centerline.

Strain gauges attached to the deck reinforcement and the deck surface are shown in Figure 4-5. Gauges SG15 through SG30 were attached to select reinforcing bars placed within the deck slab, as illustrated in Section A-A of Figure 4-5. Gauges with a CG designation were attached to the top surface of the concrete deck slab, with gauges CG1 through CG4 located at the diaphragm centerline. As Figure 4-5 indicates, gauges CG1 through CG4 are paired with corresponding reinforcement instrumentation. Gauges CG5 through CG9 and CG10 through CG12 were located 21.5" East and West, respectively, from the diaphragm centerline. As shown in Figure 4-5, two linear transducers were located across the diaphragm edges, each with a 10" gauge length.

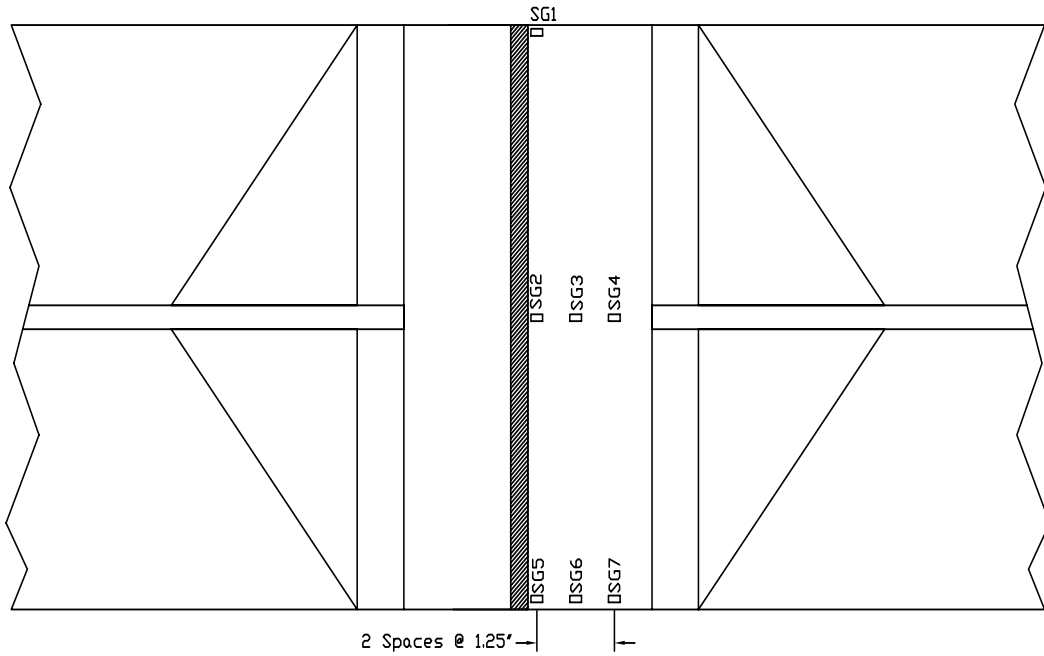


Figure 4-3: Plan View of Bottom Flange Gauges

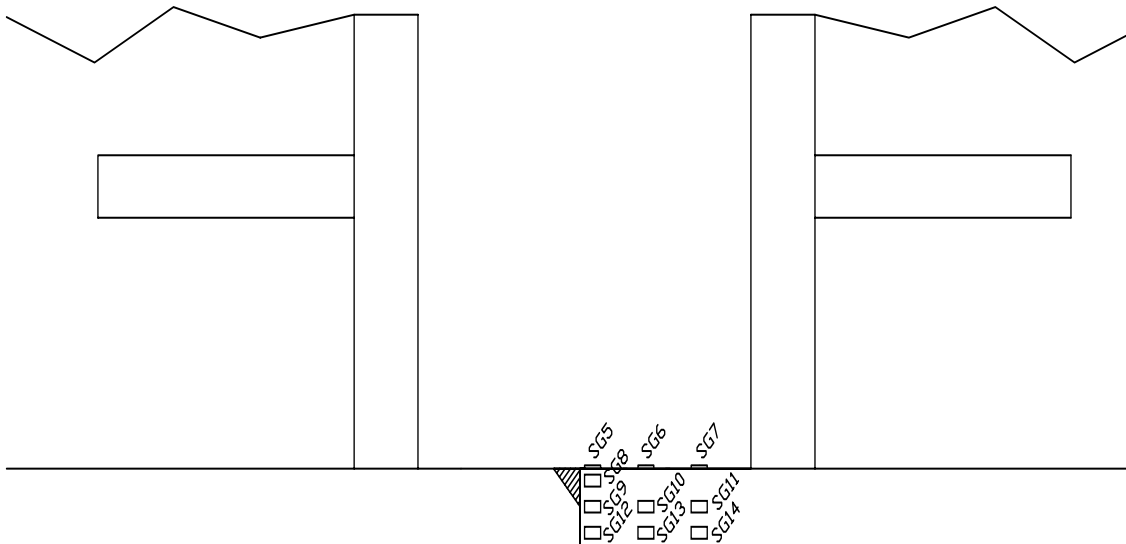


Figure 4-4: Side View of Bottom Flange Gauges

Additional instrumentation attached to the steel girders is shown in Figure 4-6. Gauges SG31 through SG37 were located within the limits of the concrete diaphragm at the locations shown in Figure 4-6. Gauges VW1, VW2, and VW5 were attached to the girder web immediately outside the diaphragm. Instrumentation of the bottom flange outside the diaphragm consisted of both VW and SG type gauges. The VW gauges were centered within the width of the flange and the SG gauges were placed at the flange width quarter points.

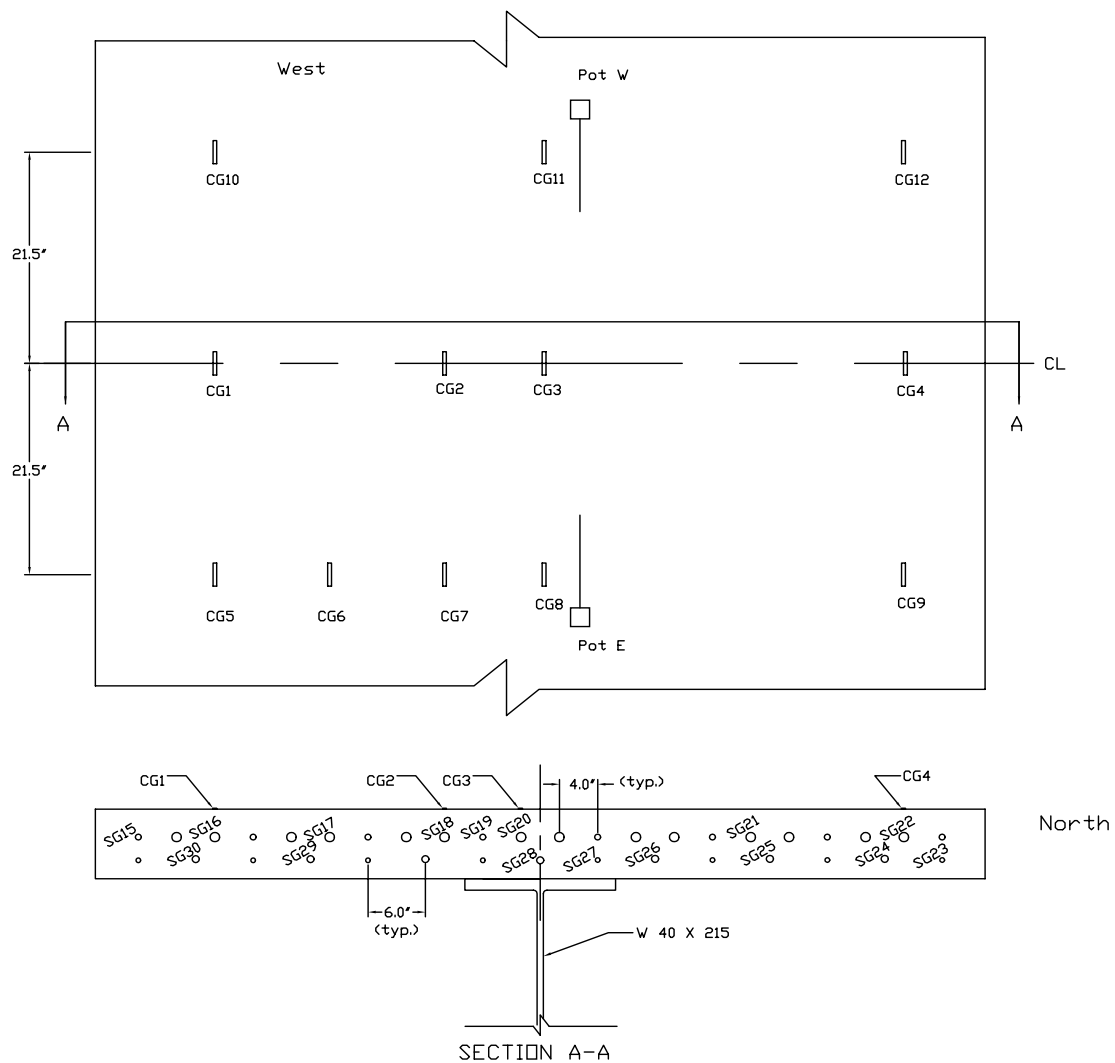


Figure 4-5: Deck and Reinforcement Gauges

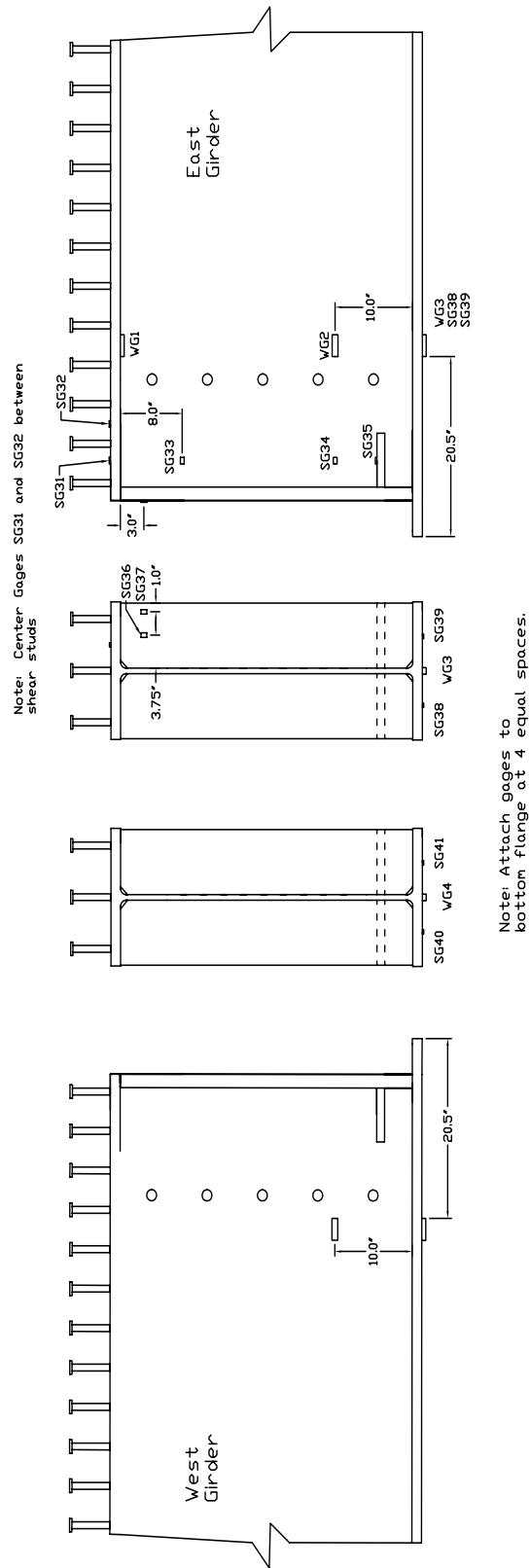


Figure 4-6: Additional Girder Instrumentation

Embedment gauges, designated EG, were used to monitor strains in the concrete diaphragm and deck at several locations. Embedment gauges were placed at sections A, B, and C shown in Figure 4-7. Section A corresponded with the specimen centerline, where EG gauges were placed both in the diaphragm and deck. Section B was located 6" from the outside edge of the diaphragm, where only EG gauges were placed in the diaphragm. Section C was at the deck/diaphragm interface, where gauges were placed only in the deck. In the transverse direction, EG gauges were grouped in vertical planes at predetermined locations. Figure 4-8a illustrates the transverse groups at section A (specimen centerline), divided into groups 1 through 5 as shown. Similarly, Figure 4-8b shows EG groupings at sections B and C.

Additional potentiometers were located at each loading point to measure deflection. The potentiometers were designated according to placement on either the east or west girder.

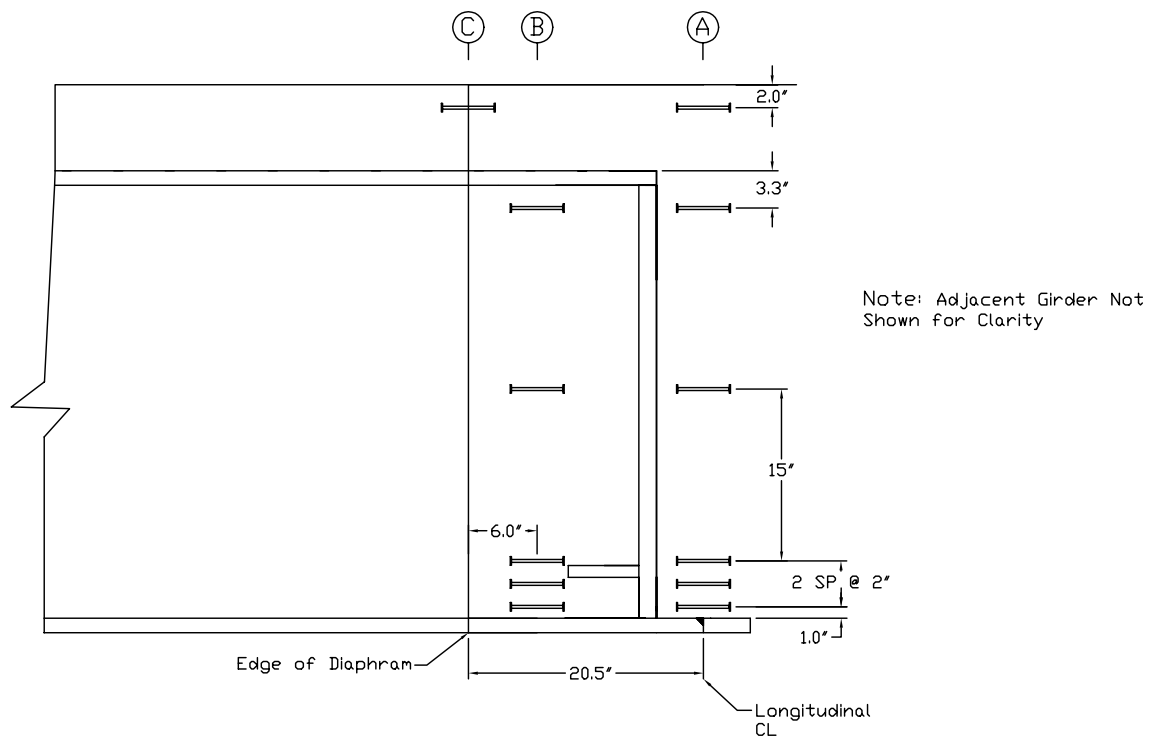
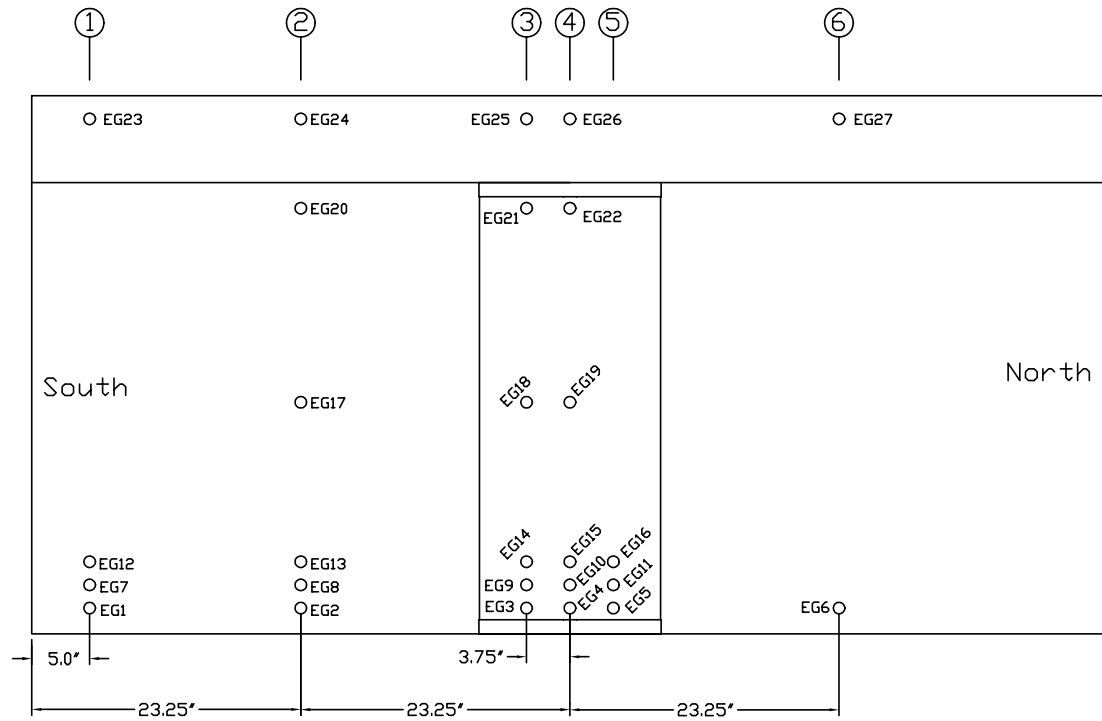
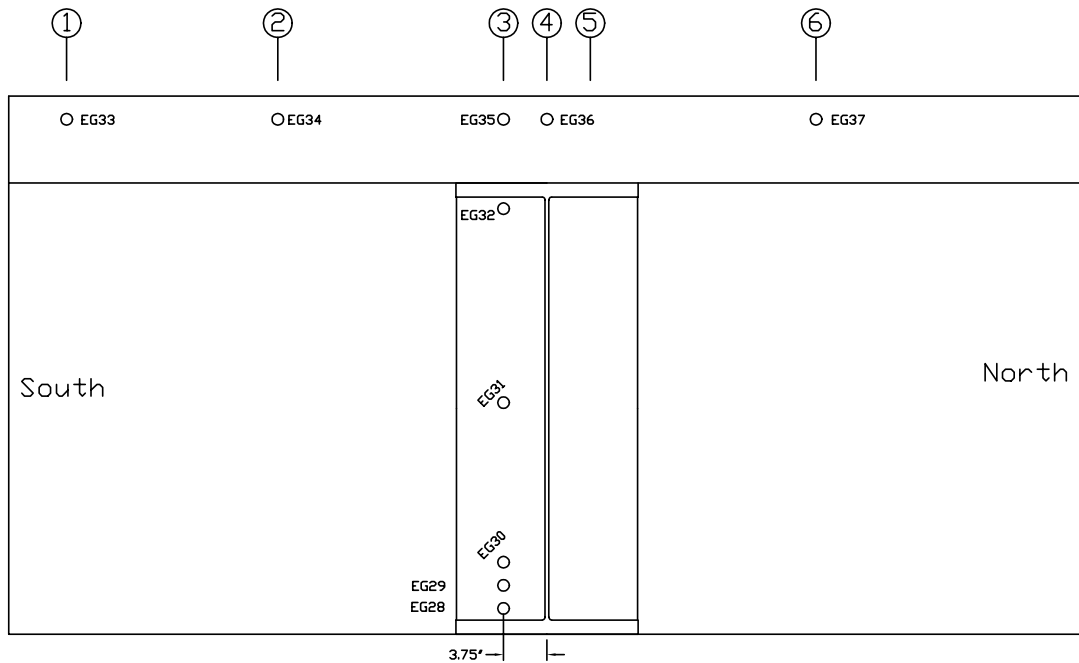


Figure 4-7: Embedment Gauge Sections



(a)



(b)

Figure 4-8: Transverse Embedment Gauge Locations

4.1.3 MATERIAL PROPERTIES

General material testing information was covered in Chapter 3. This section is concerned with the specific testing of materials for the first specimen.

Two concrete cylinders were tested from the deck and diaphragm components after curing for ten days. Similarly, four were tested after 28 days of curing. Two from each pour were tested at 49 days, which coincided with the ultimate strength test. The average 28-day compressive strength of the diaphragm and deck concrete was 5190 and 4860 psi, respectively.

Three samples of each deck reinforcing bar size were submitted to IFR Engineering for mechanical testing. Each sample was tested as a full section according to ASTM A370 Specifications. Results of the tensile tests are shown in Table 4-1. The average reinforcing bar strength was 66 ksi.

Bar	F_y (ksi)	F_u (ksi)
#4	63	101
#4	65	101
#4	65	101
#5	64	101
#5	63	101
#5	65	101
#7	70	101
#7	69	101
#7	66	101
#8	66	105
#8	65	105
#8	66	106
Avg	66	102

Table 4-1: Rebar Tensile Testing Results

4.2 SPECIMEN BEHAVIOR

The experimental investigation consisted of three distinct load stages. These were non-composite dead loads, cyclic (fatigue) loading, and ultimate strength loading.

4.2.1 NON-COMPOSITE LOADING

Simulation of non-composite dead load was produced by vertical displacement at the temporary support locations. Pressure in the hydraulic rams was released slowly until the deflection at the girder ends matched desired values. The displacement was initiated in stages, with data sets collected at each stage of displacement. Figure 4-9 shows the girder end separation relative to support displacement for the four potentiometers. A graphical representation of the girder end rotation over the support displacement interval is shown in Figure 4-10. The gap between the end bearing plates (also top flanges and webs) was set to insure that the continuous bottom flange would not reach yield when subject to the theoretical rotation. The purpose of this load stage was to monitor and record stresses generated in the flange due to the application of non-composite dead load. Gauges SG1, SG2, and SG5 were located adjacent to the flange weld at the centerline of the girders. Gauge SG1 was monitored manually as the support displacement was applied. Figure 4-11 contains a plot of stress-rotation data collected from gauges SG2 and SG5. The maximum stress at the outer-most fiber reached 47 ksi, or approximately 80% of the yield stress. Figure 4-12 shows the stress distribution across the thickness of the flange near the specimen centerline from gauges SG8, SG9, and SG12. Figure 4-13 shows the stress vs. rotation data at the girder centerline for gauges SG2, SG3, and SG4. As expected, the highest stresses remain below yield and occur at the specimen centerline.

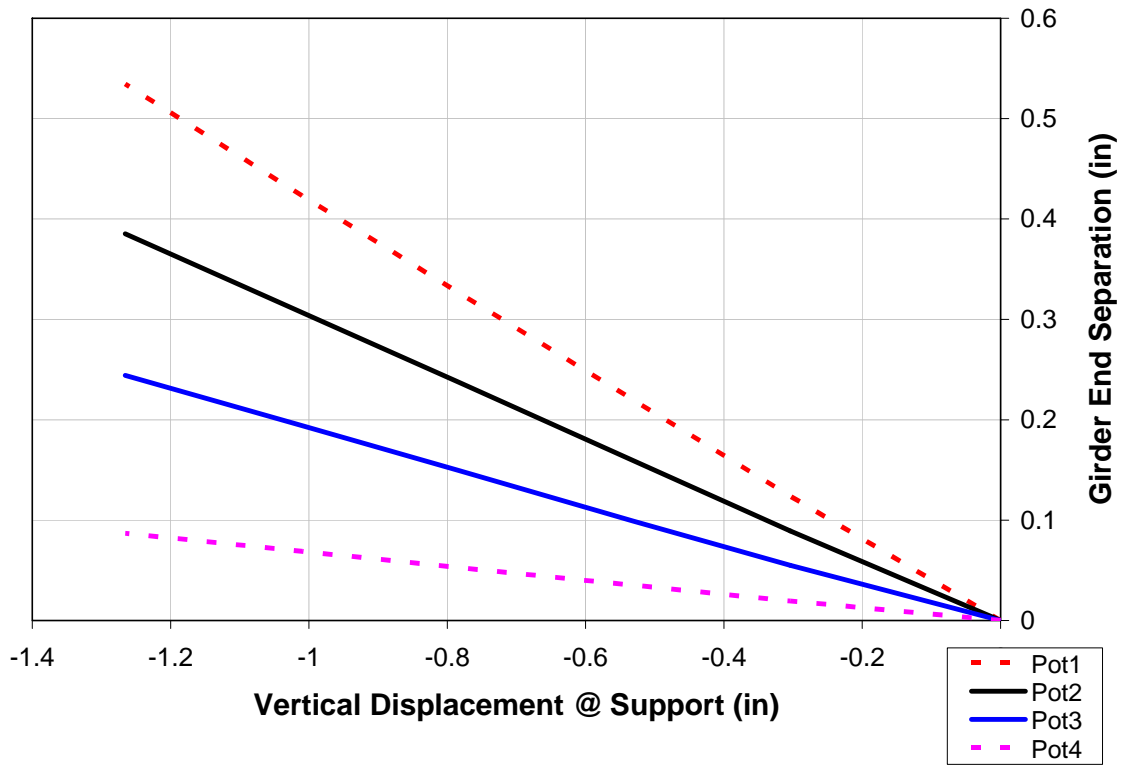


Figure 4-9: Girder End Separation Under Simulated Dead Loads

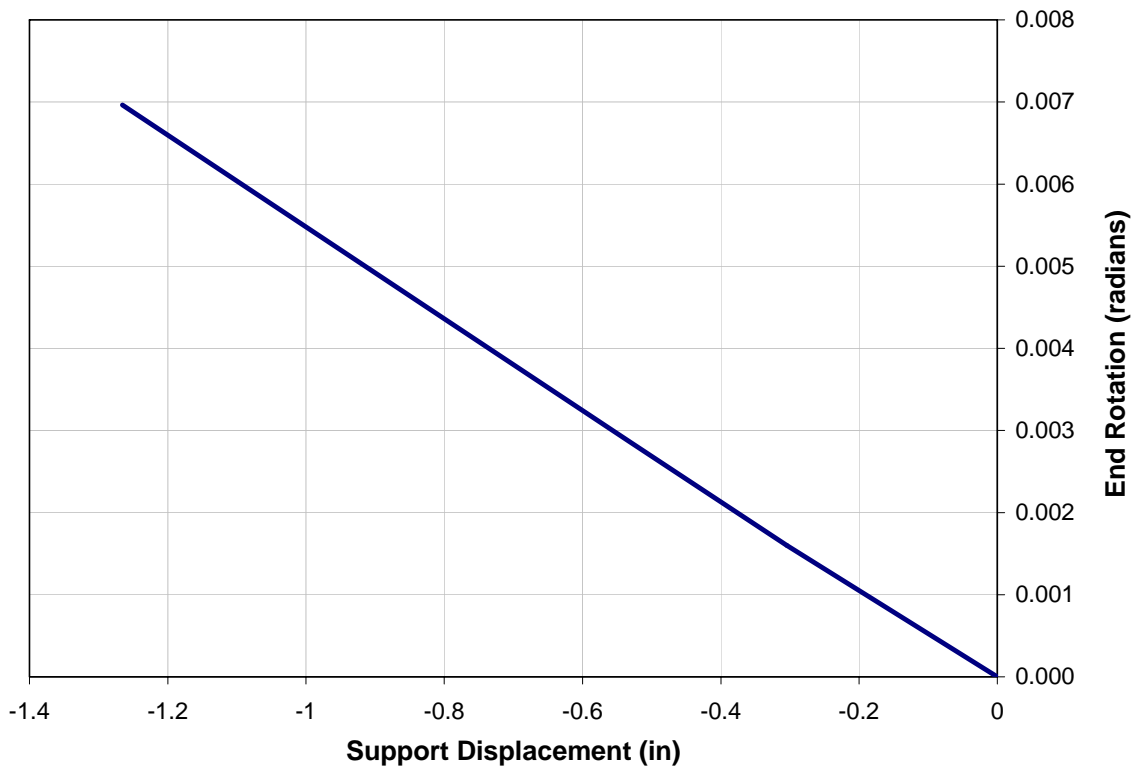


Figure 4-10: Girder Rotation Under Simulated Dead Loads

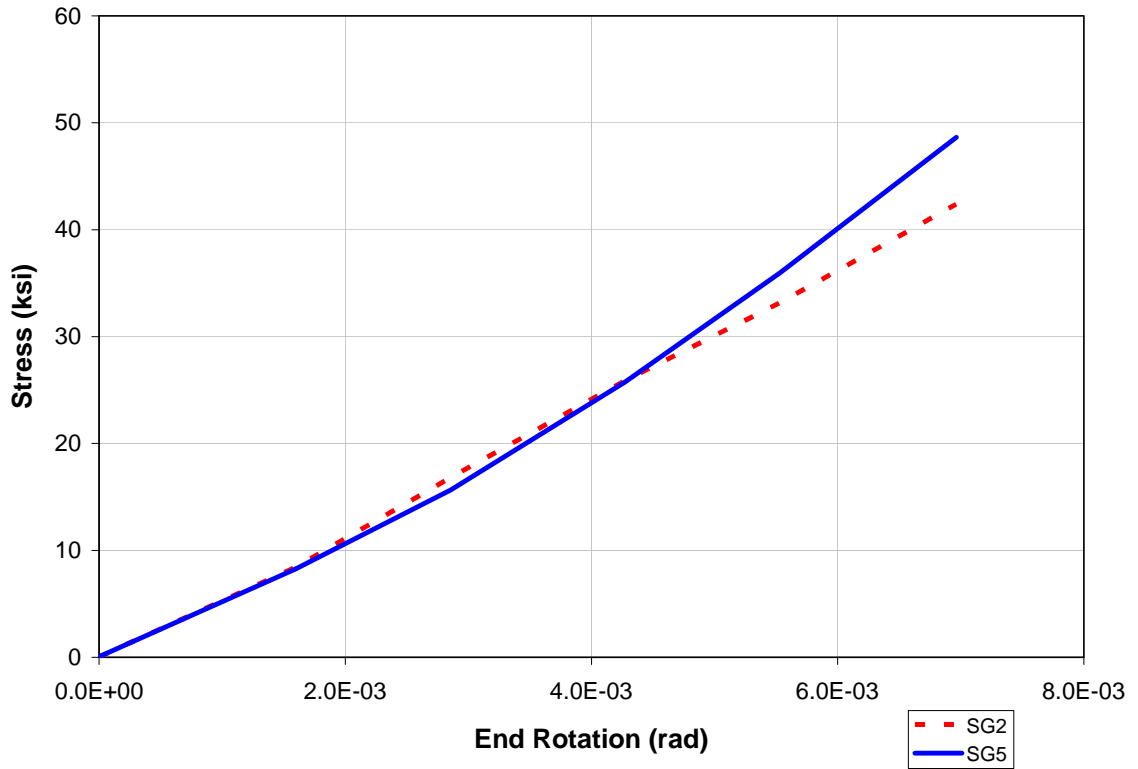


Figure 4-11: Stress Rotation Relationship for SG2 and SG5

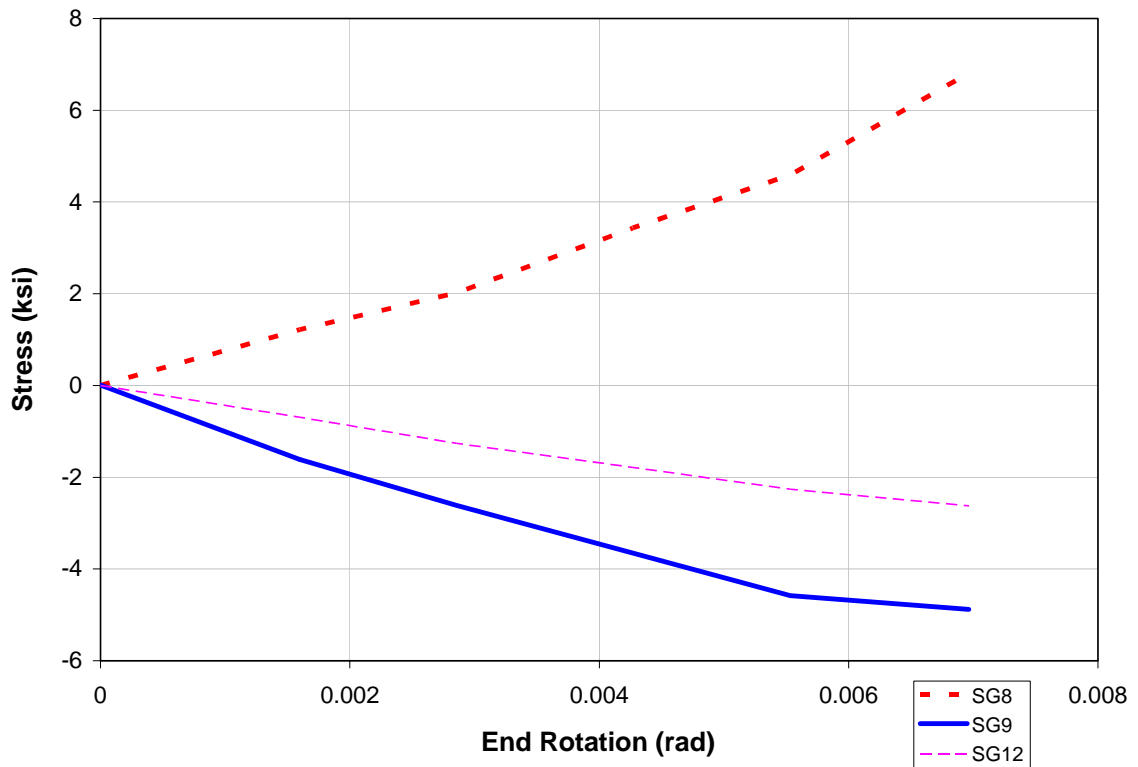


Figure 4-12: Stress Rotation Relationship for SG8, SG9, and SG12

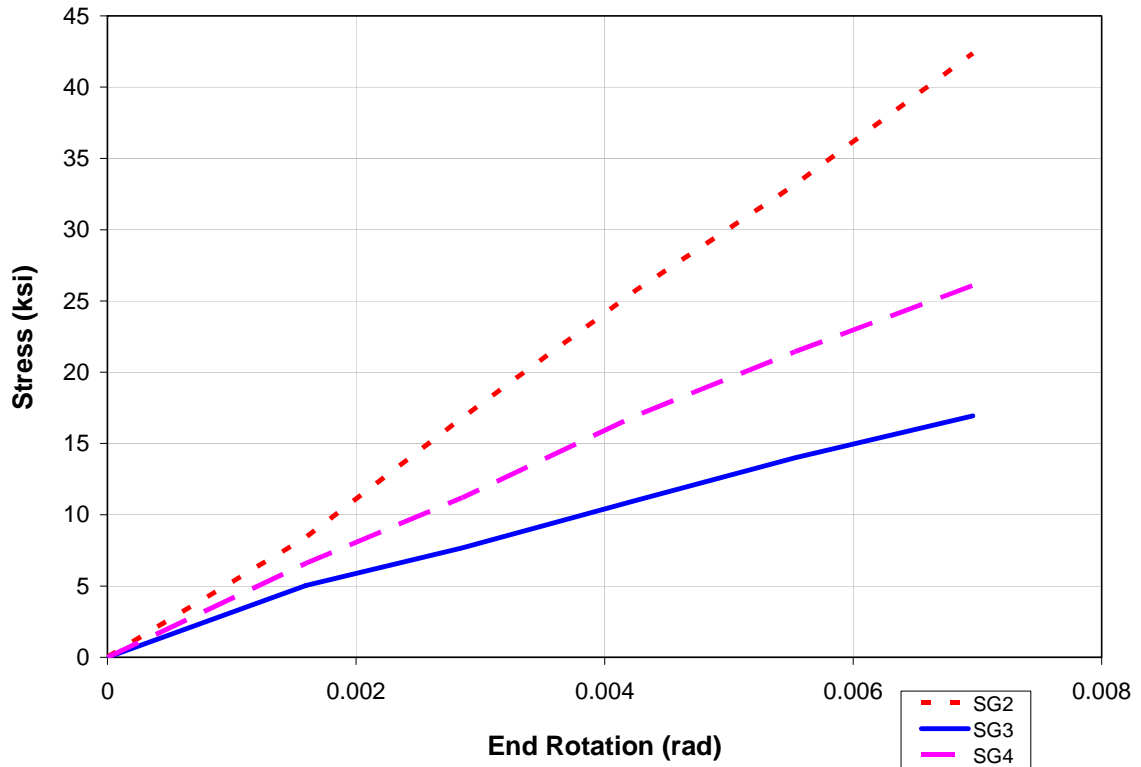


Figure 4-13: Stress Rotation Relationship for SG2, SG3, and SG4

4.2.2 FATIGUE LOAD PHASE

The cyclic load range was 2 to 106 kips to ensure that at no time did the bottom flange experience tension. The initial ramp to 106 kips was applied incrementally with pauses for the collection of data sets. A plot of the load-deflection curve is shown in Figure 4-14. The breaks in the plot are at the pauses for data collection, where deflection was held constant and the load relaxed through force redistribution in the deck reinforcement.

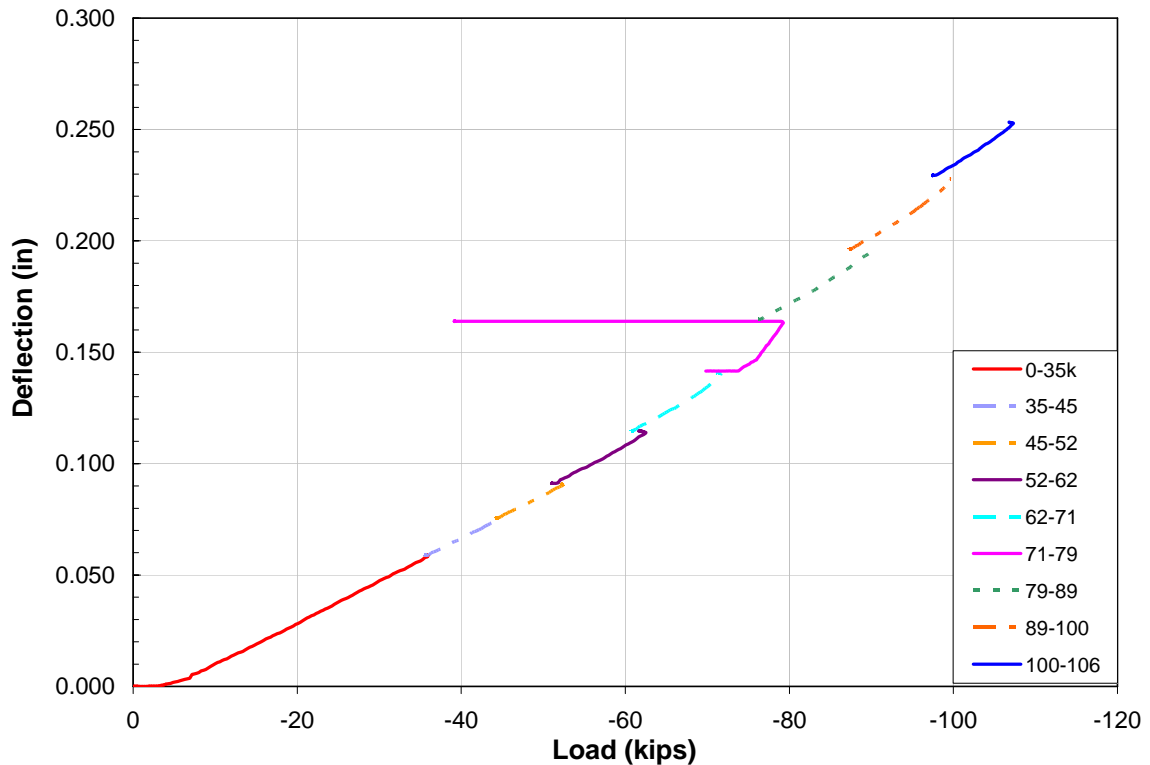


Figure 4-14: Fatigue Test Load-Deflection Graph

Several gauges attached to the surface of the concrete deck slab were lost due to the concrete cracking. The cracks on the surface of the deck slab were documented prior to application of fatigue cycles. Figure 4-15 shows mapping of the cracks at 106 kips. For location reference, the instrumentation is located directly above the diaphragm.

Figure 4-16 contains a crack map at maximum load prior to any cycling. The majority of cracking occurred near the edge of the diaphragm. At this location there was an abrupt change in rigidity. Mapping of deck cracking was done at 1 million, 1.5 million and 2 million cycles of load, shown in Figures 4-17, 4-18 and 4-19 respectively. From these maps, the largest crack widths occurred at the diaphragm edge, near the edge of the slab. Additional cracks had formed farther out from the diaphragm centerline. A comparison of the crack widths from 1 million to 1.5 million load cycles shows that there was virtually no change in crack widths over this interval. A comparison of the crack widths from 1.5 million to 2 million load cycles

show little recognizable change. There were a few additional short cracks propagating inward from the edge of the deck, but the measured widths of existing cracks were unchanged.



Figure 4-15: Mapping of Initial Cracks

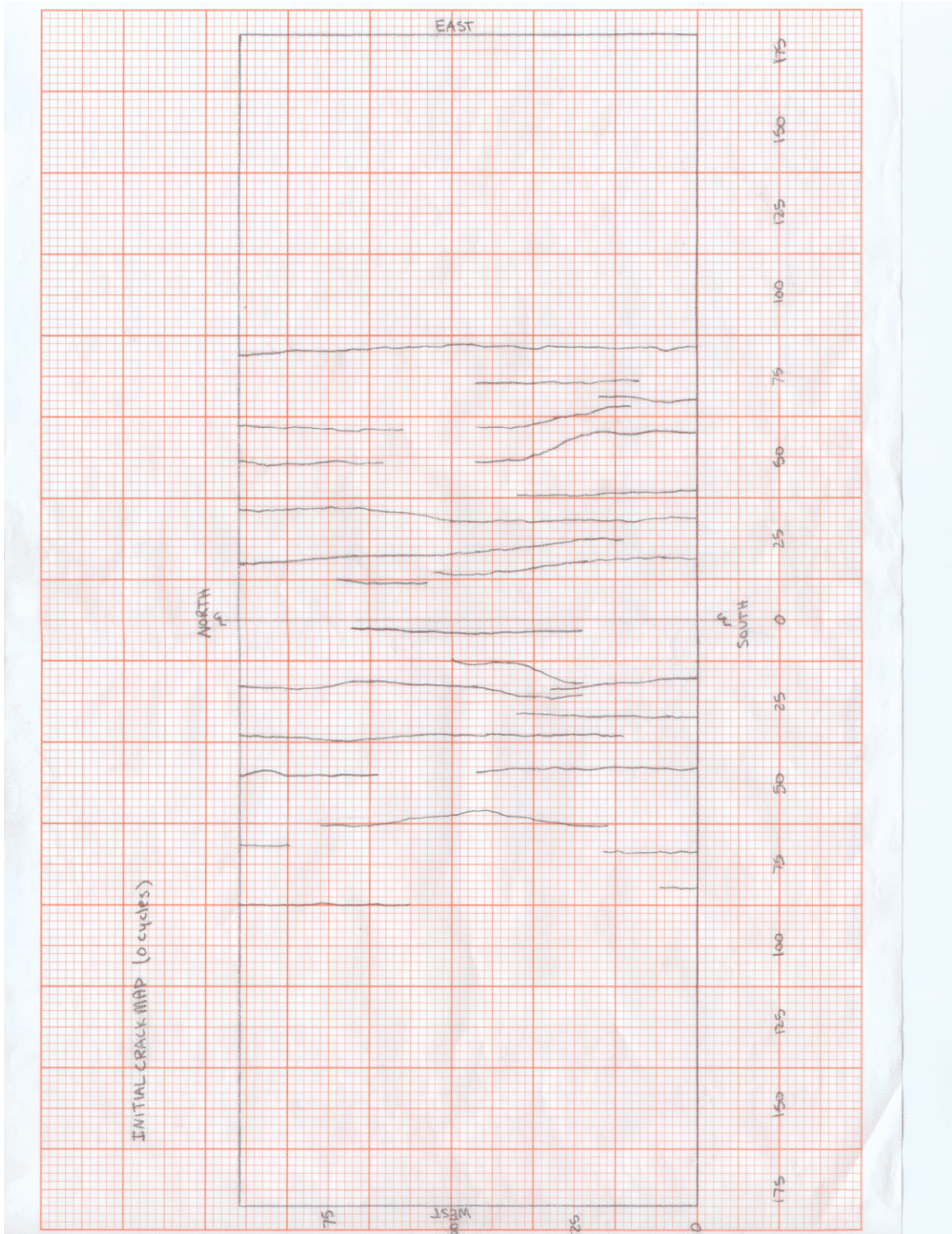


Figure 4-16: Initial Crack Map for 0 Cycles

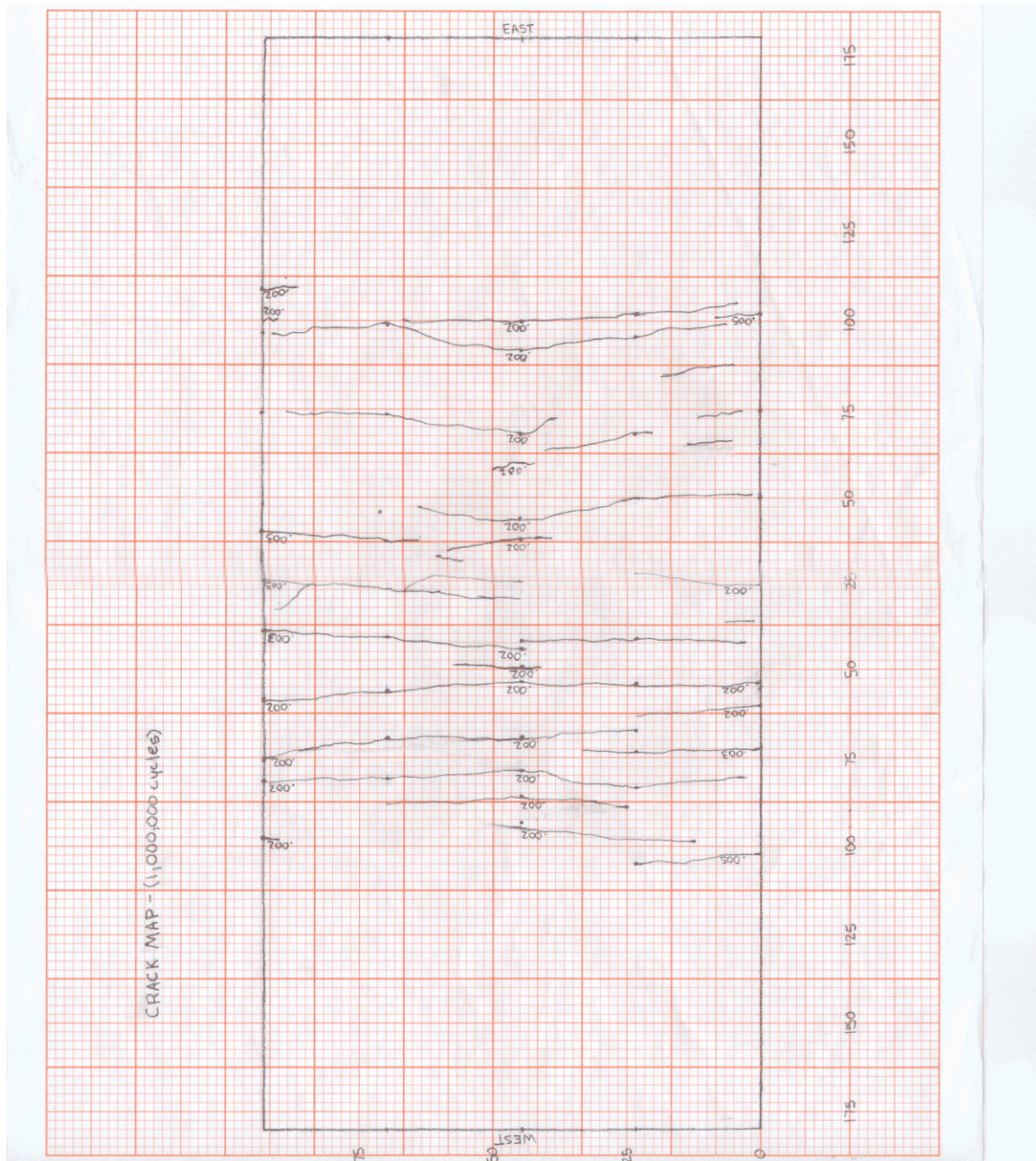


Figure 4-17: Crack Map after 1 Million Cycles.

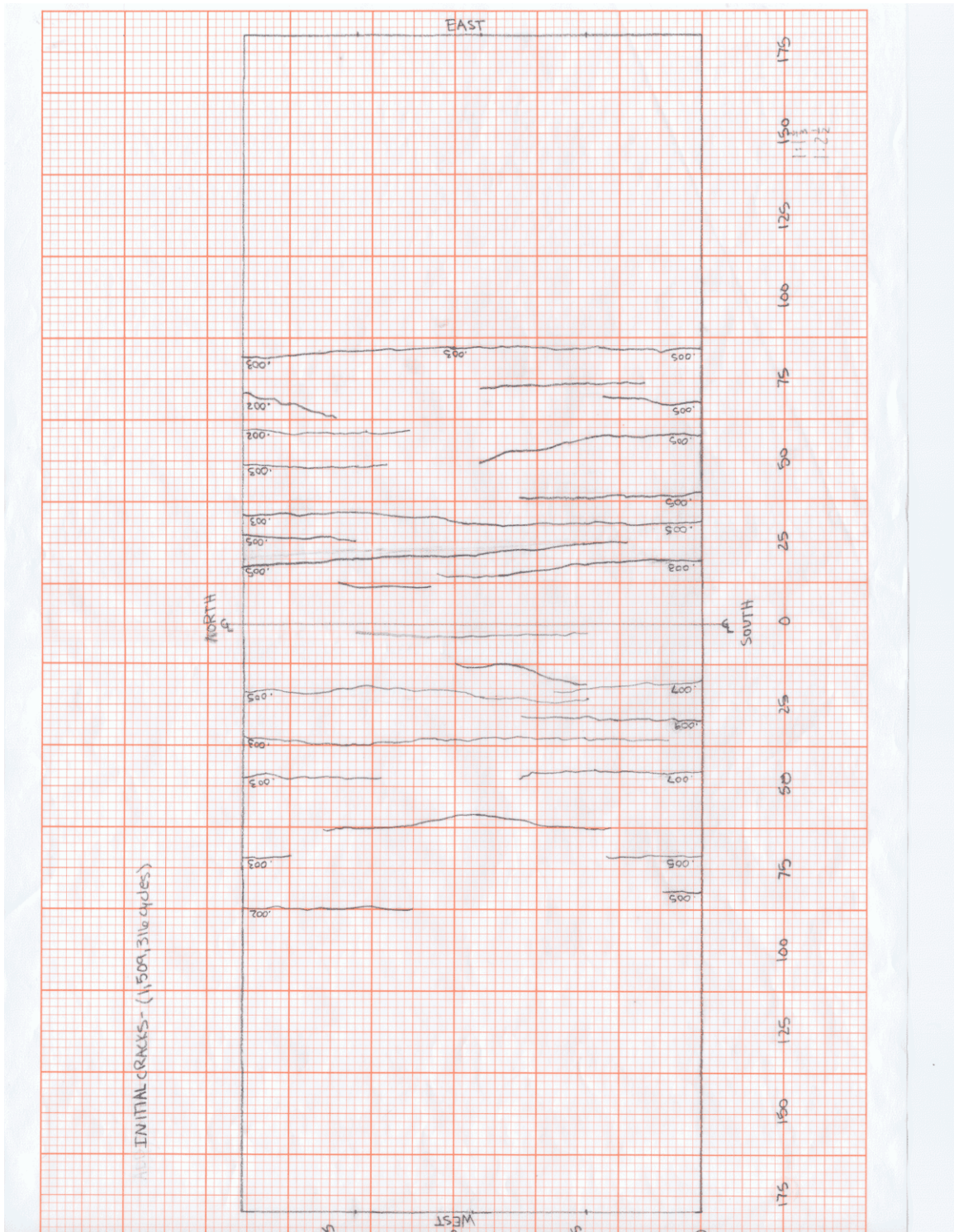


Figure 4-18: Crack Map after 1.5 Million Cycles

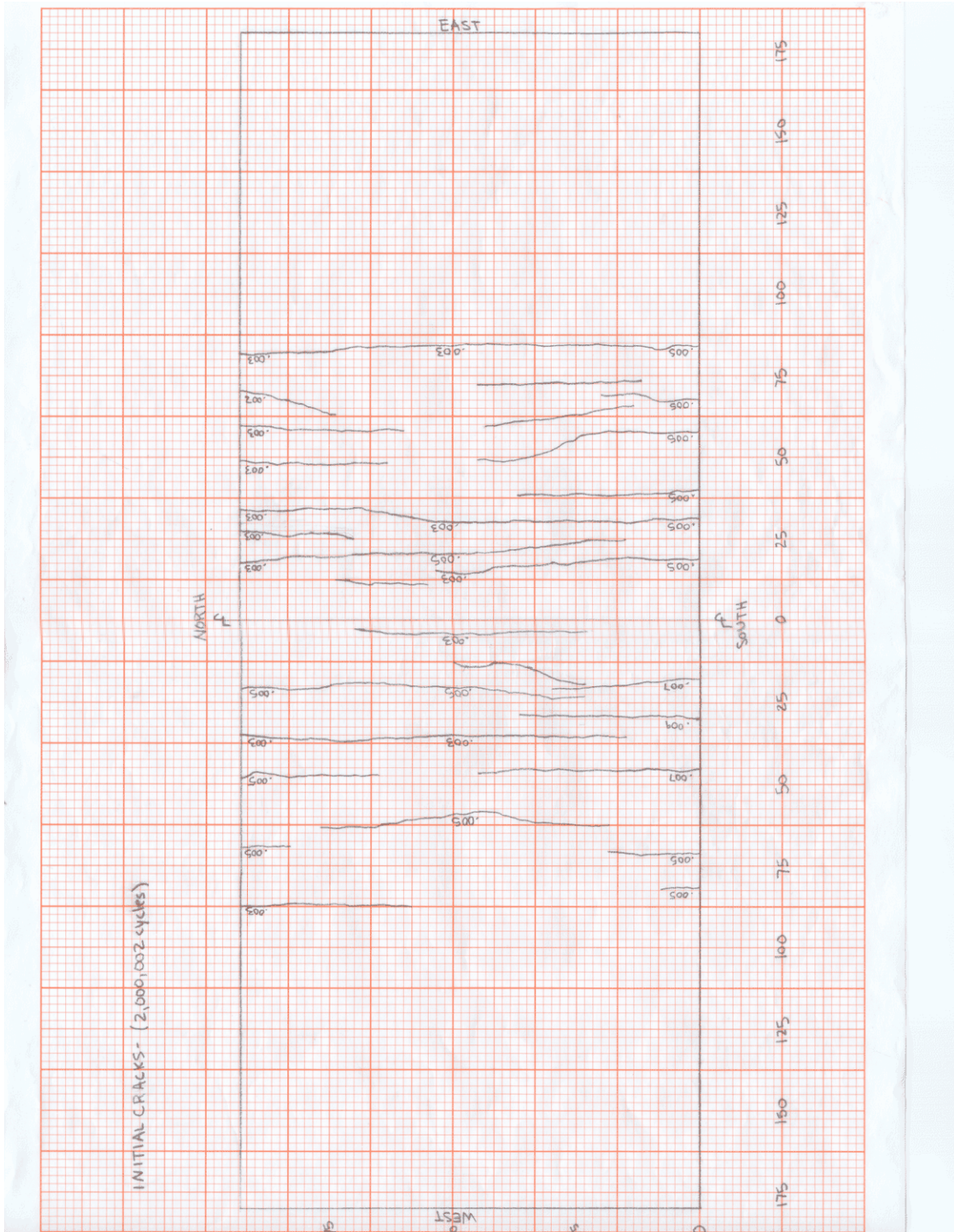


Figure 4-19: Crack Map after 2 Million Cycles

During the fatigue portion of the experimental investigation, data sets were collected once daily. The loading frequency was set at two cycles per second, which resulted in data sets being collected at every 172,800 cycles of load. The daily sets were collected at peak static load, minimum static load, and continuously over an interval of five cycles at a loading rate of $\frac{1}{2}$ -cycle per second. Load-deflection plots for the specimen during the fatigue test are shown in Figures 4-20 and 4-21. These plots were generated from data collected during the five cycles of loading. The first plot contains loops at 0, 1, and 2 million cycles, in which little change in specimen stiffness is observed over the complete interval.

The second plot contains loops at all cycle values where data was collected. The specimen did experience some reduction in stiffness. At approximately 7400 cycles, the maximum displacement was increased from 0.3083 to 0.3115 in. Referring again to Figure 4-20, the increase in displacement and the loss of specimen stiffness are evident between zero and one million cycles. The initial load-deflection plot has a greater slope than similar data at subsequent loading cycles. There was virtually no change in specimen response throughout the remaining fatigue cycles

The embedment gauge locations were specified as to provide a means for generating strain profiles across the depth of the diaphragm, these locations were labeled as Section 1 through Section 6 (Figure 4-8 contains section locations). Figure 4-22 contains the strain distribution plot for Section 2. Similarly, Figures 4-23 and 4-24 contain information for Sections 3 and 4, respectively. In each of these plots, the strain distributions exhibited only slight variations over the two million cycle interval.

A similar plot is shown in Figure 4-25, across the bottom of the diaphragm. Like the previous results have shown, some redistribution of stress occurred initially and virtually none throughout the remaining two million cycles.

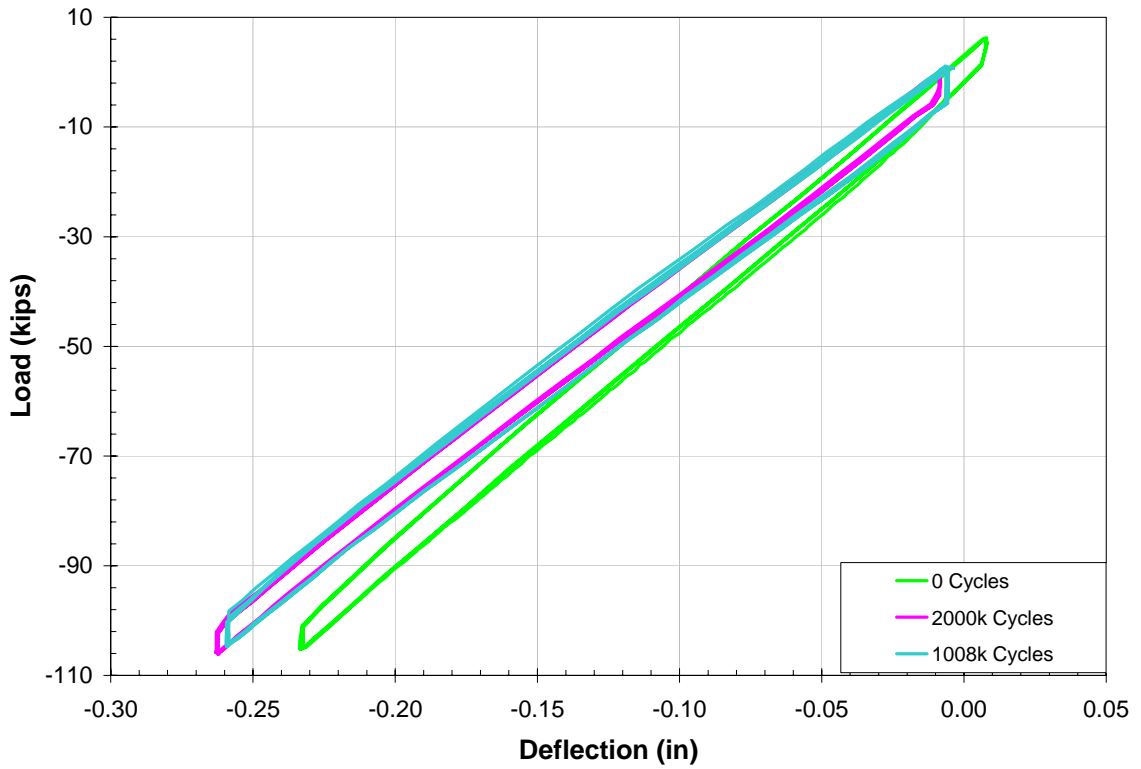


Figure 4-20: Cyclic Load Deflection Comparison

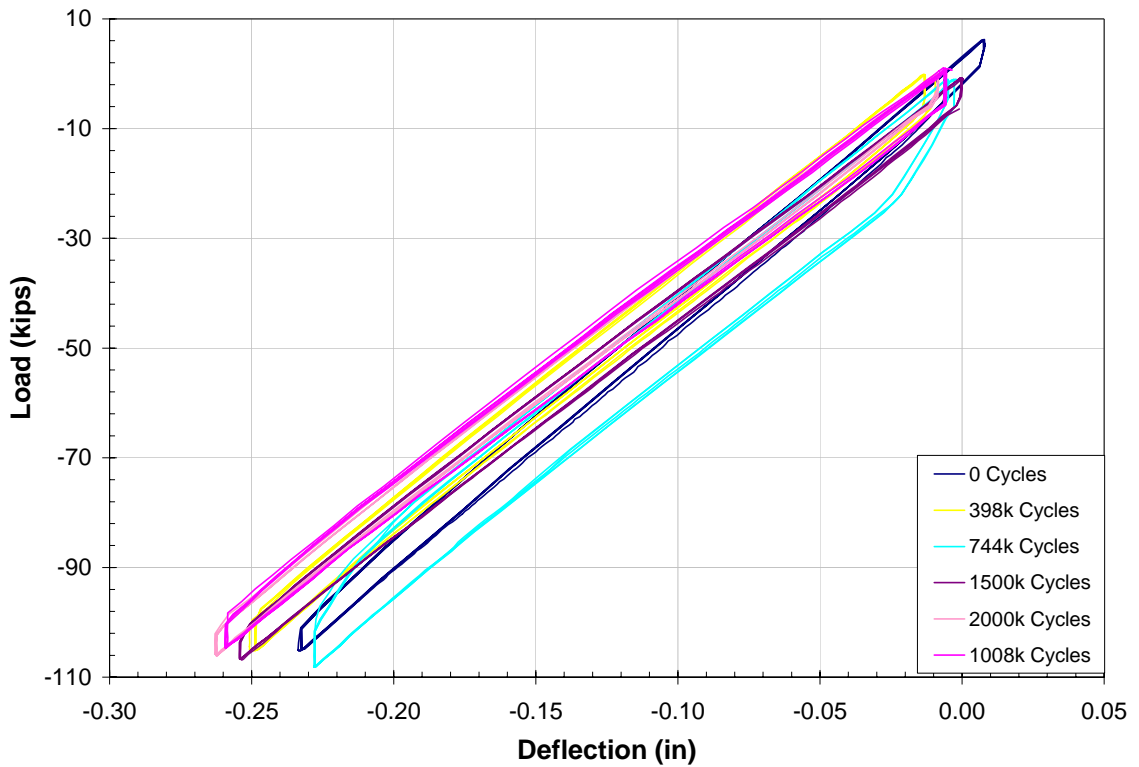


Figure 4-21: Cyclic Load Deflection Comparison

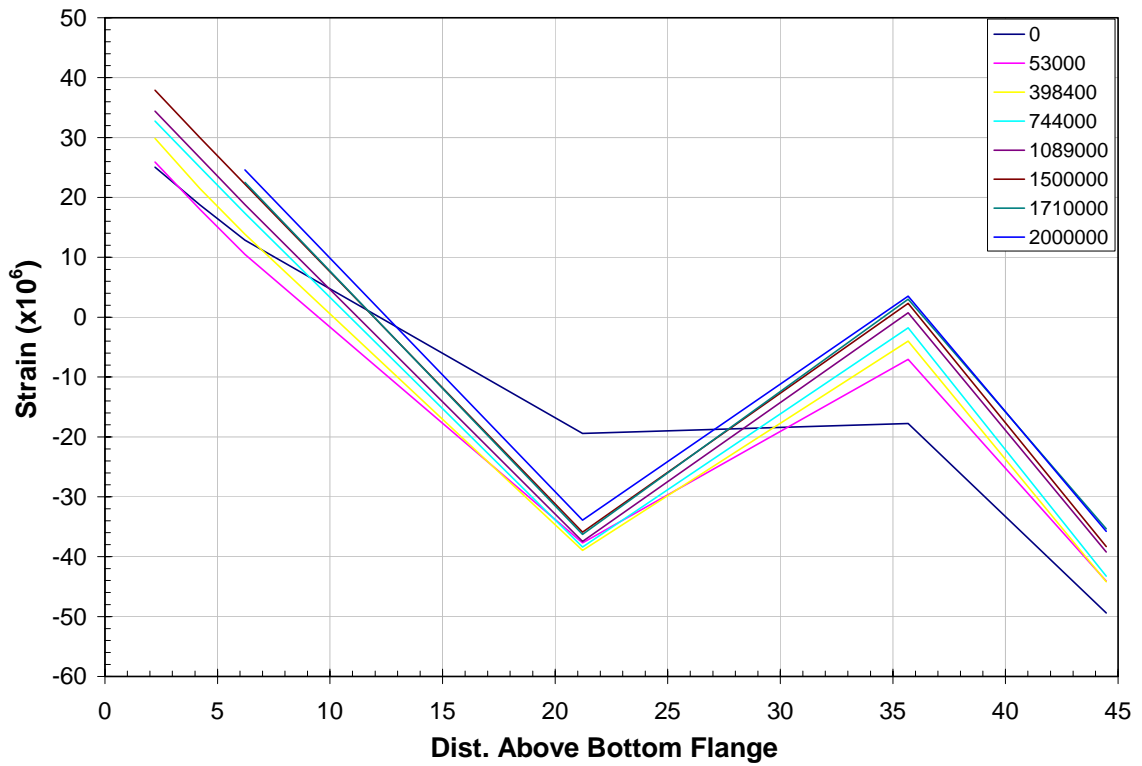


Figure 4-22: Strain Profile at Location 2

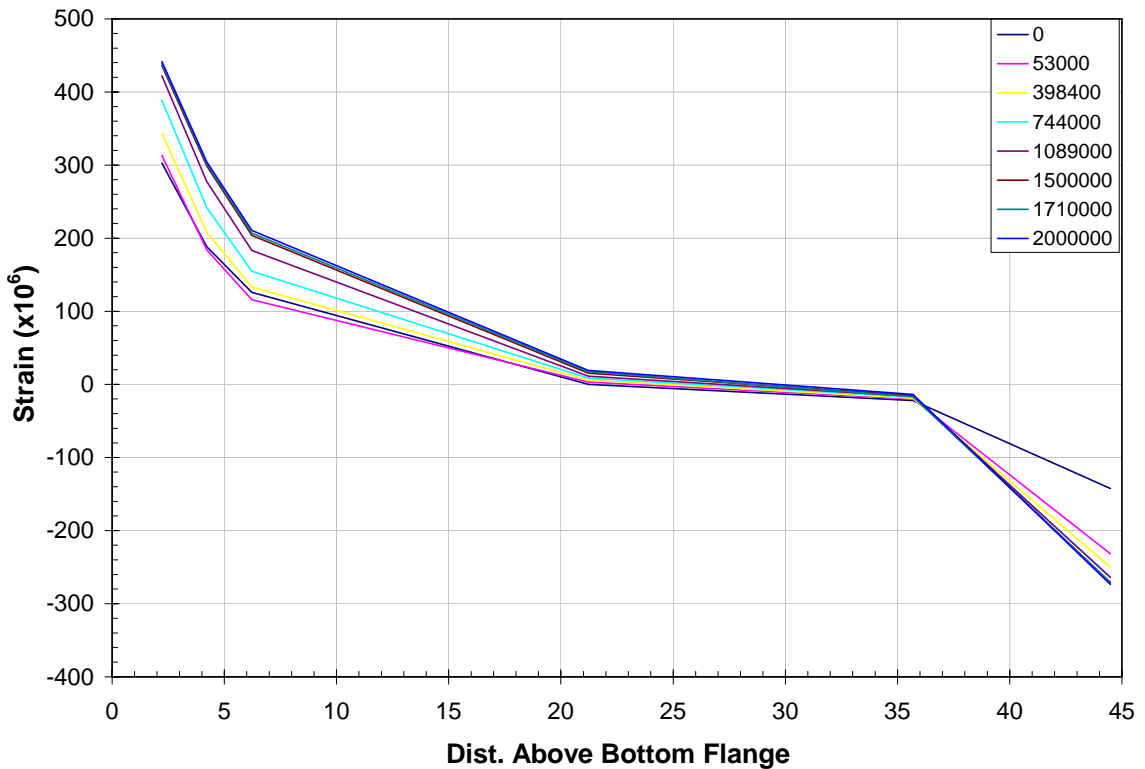


Figure 4-23: Strain Profile at Location 3

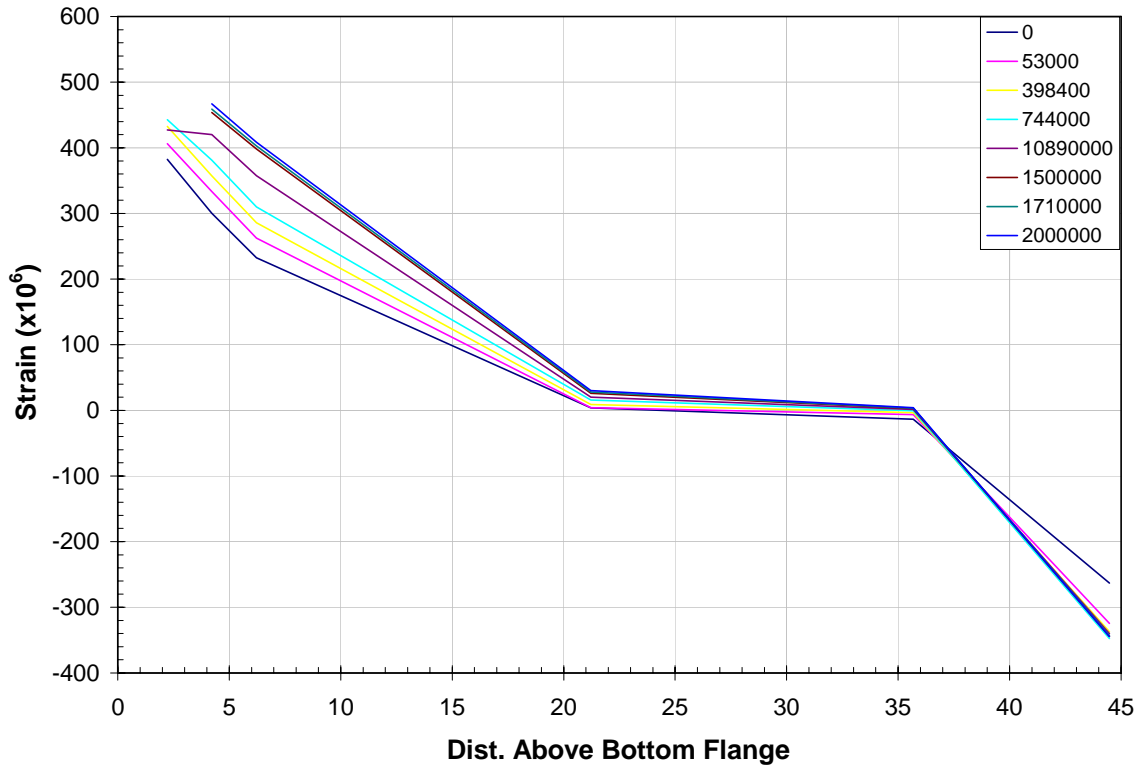


Figure 4-24: Strain Profile at Location 4

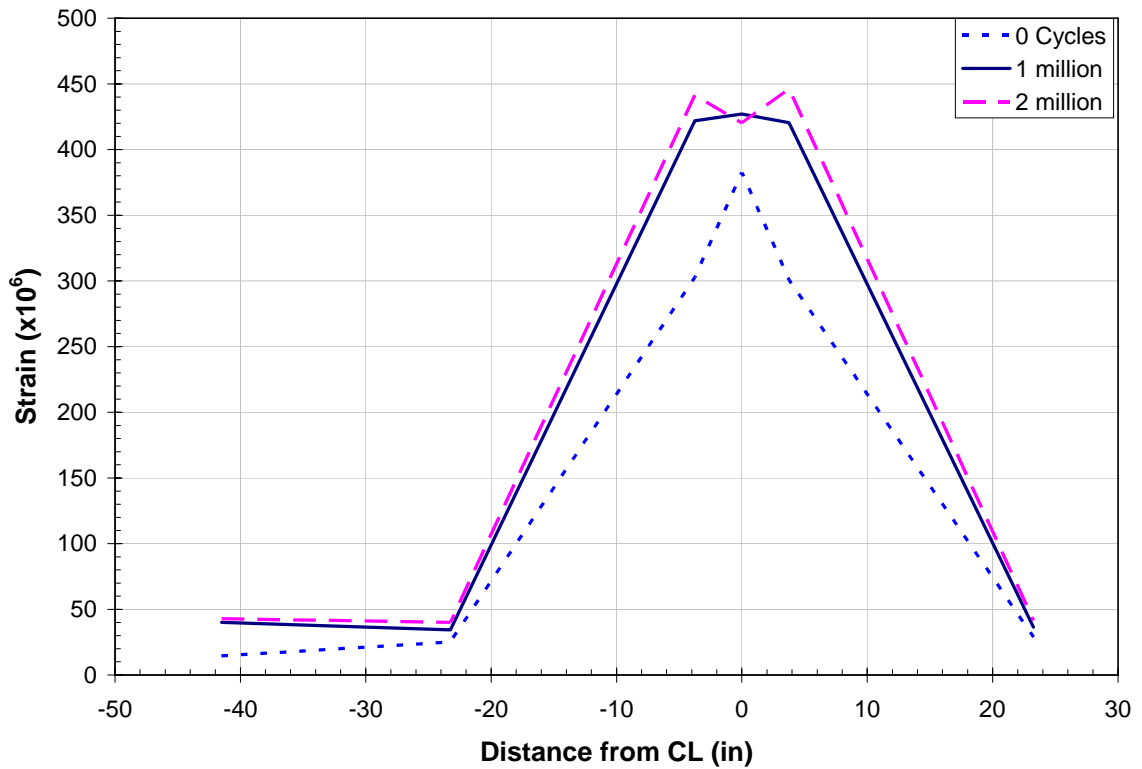


Figure 4-25: Horizontal Strain Distribution at Bottom of Diaphragm

The stress in the deck reinforcement was also monitored over the two million cycle interval. Figure 4-26 shows stress plots for four reinforcing bars in the deck; gauges SG15 and SG22 were located near the outermost edge of the effective slab and gauges SG18 and SG20 were located near the centerline. The tensile stress in the reinforcing steel varied only slightly over the two million cycles.

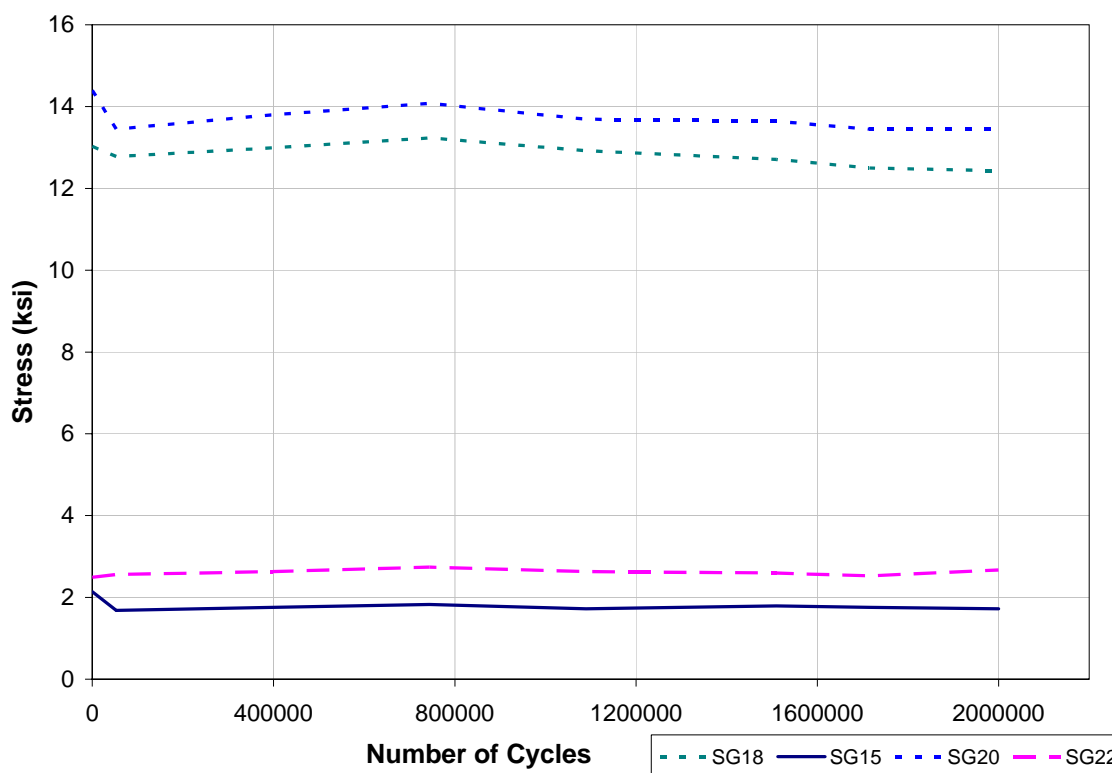


Figure 4-26: Reinforcement Stress Comparison

4.2.3 ULTIMATE STRENGTH TESTING

For the ultimate strength test, the load was applied incrementally until the specimen failed. At a load of 225 kips, the hydraulic pump used to load the west side of the specimen failed to increase load. The specimen was then unloaded and the defective pump removed. The test was restarted and at 255 kips the pump used to load the east side failed to increase load. The specimen was unloaded and this pump removed. The third attempt to

apply failure load was successful. The load deflection curve for the successful loading is shown in Figure 4-27. From this curve it can be shown that inelastic behavior begins near a load of 350 kips or a moment of 4200 $\text{kp} \cdot \text{ft}$. From strain gauge observations, the reinforcement near the girder centerline reached yield at this load. The saw tooth appearance of the curve was caused by pauses for data collection, in which relaxation of the specimen occurs due to the onset of plastic flow.

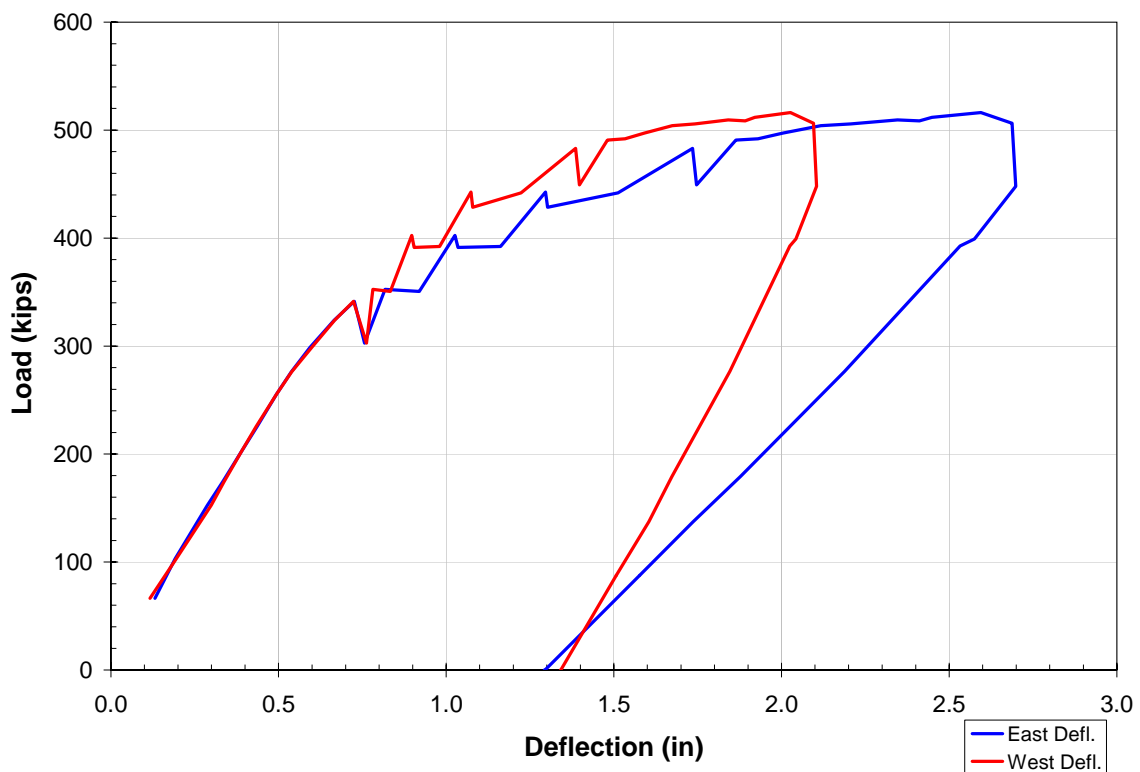


Figure 4-27: Ultimate Capacity Test Load Deflection Curve

Examining the stress in the deck reinforcement, bars located near the middle of the deck yielded first. As the load increased, the middle bars yielded and load was shed to adjacent reinforcing steel. Figure 4-28 shows the load shedding pattern from first yield to final condition. Similar trends were observed in stresses in the bottom flange, as shown in Figure 4-29. The solid line represents compressive stress outside the concrete diaphragm. Note the linear increase in stress up to stresses near 50 ksi. The dashed line indicates compressive stress near the pier centerline inside the

diaphragm. Initially the slope is flatter than the solid line indicating the concrete is resisting a significant portion of the compressive force. Compressive stress in the concrete between the end bearing plates is shown in Figure 4-30. The stress in the concrete one inch above the flange experiences a rapid increase at a load of about 275 kips. The maximum value of stress approaches 5 ksi.

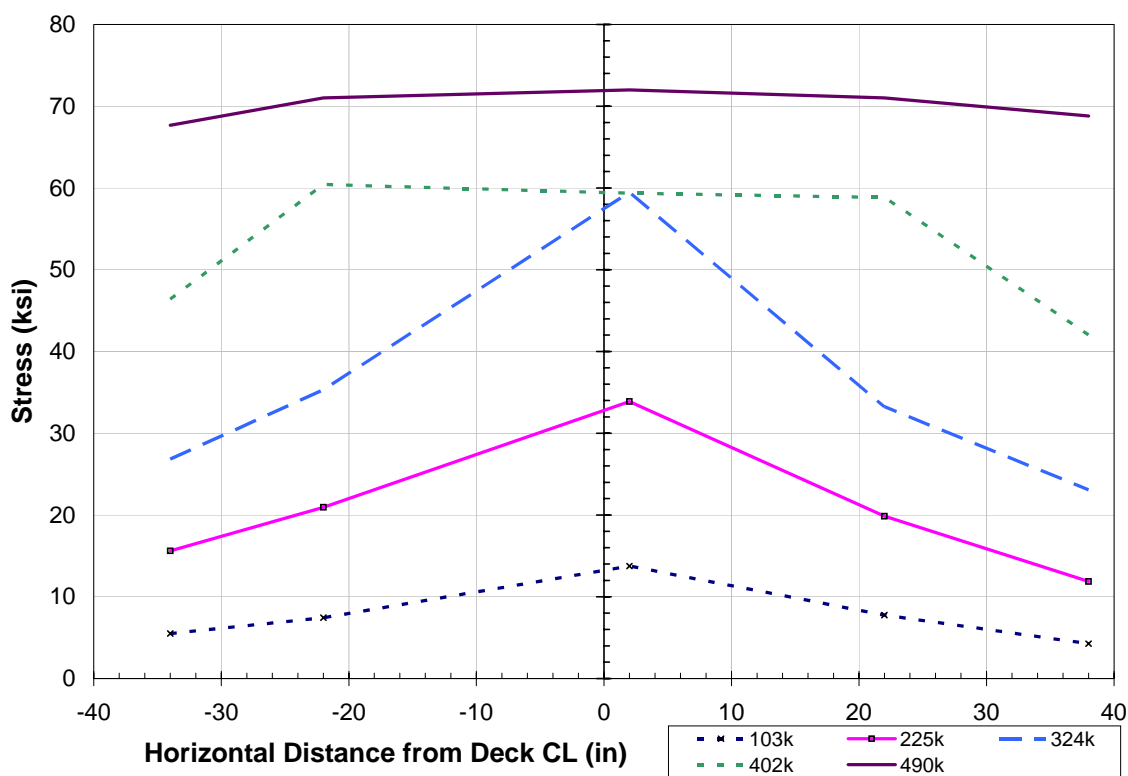


Figure 4-28: Horizontal Stress Distribution in Deck Reinforcement

Results from moment-curvature analysis are shown for the diaphragm centerline and outside the diaphragm. Using both the actual measurements and material properties obtained from the girders, a similar moment-curvature investigation was conducted at both the support centerline and outside the diaphragm. The analysis at the diaphragm edge was performed neglecting the top flange of the wide-flange section, since the limited length of embedment allows for a limited number of shear connectors required to develop the tensile capacity of the flange. Similar analysis was performed using the actual material properties for the concrete and steel

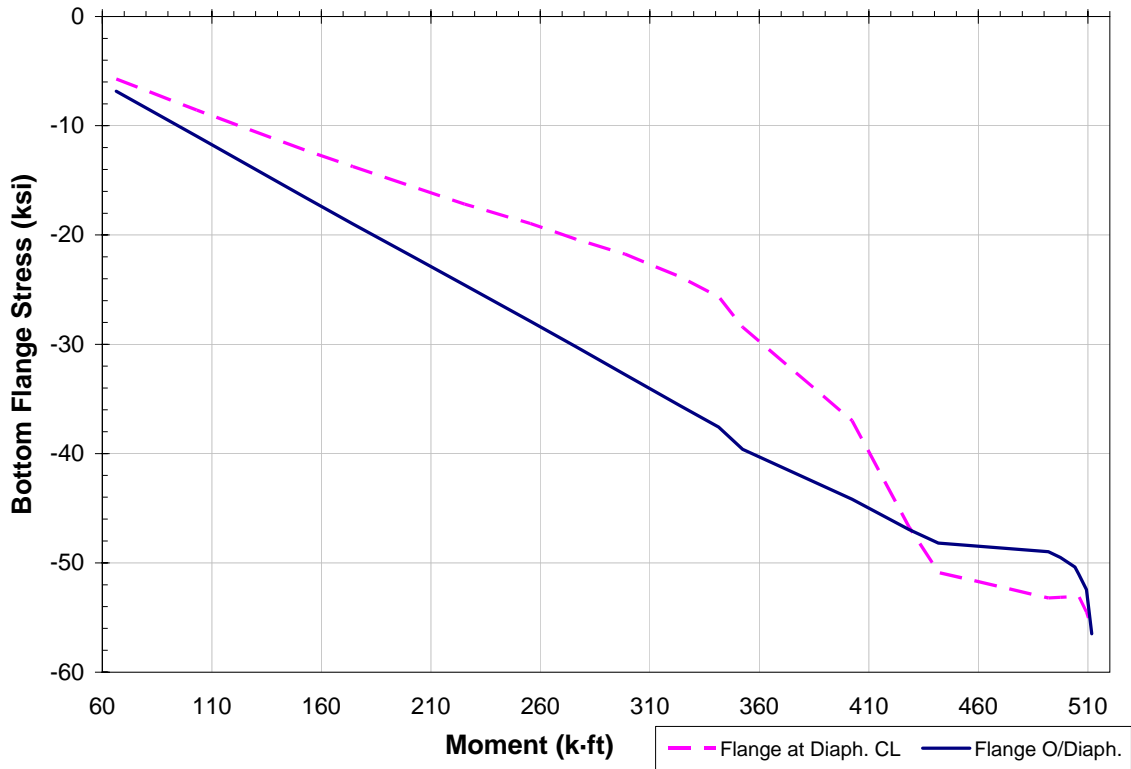


Figure 4-29: Bottom Flange Stresses at Ultimate Capacity

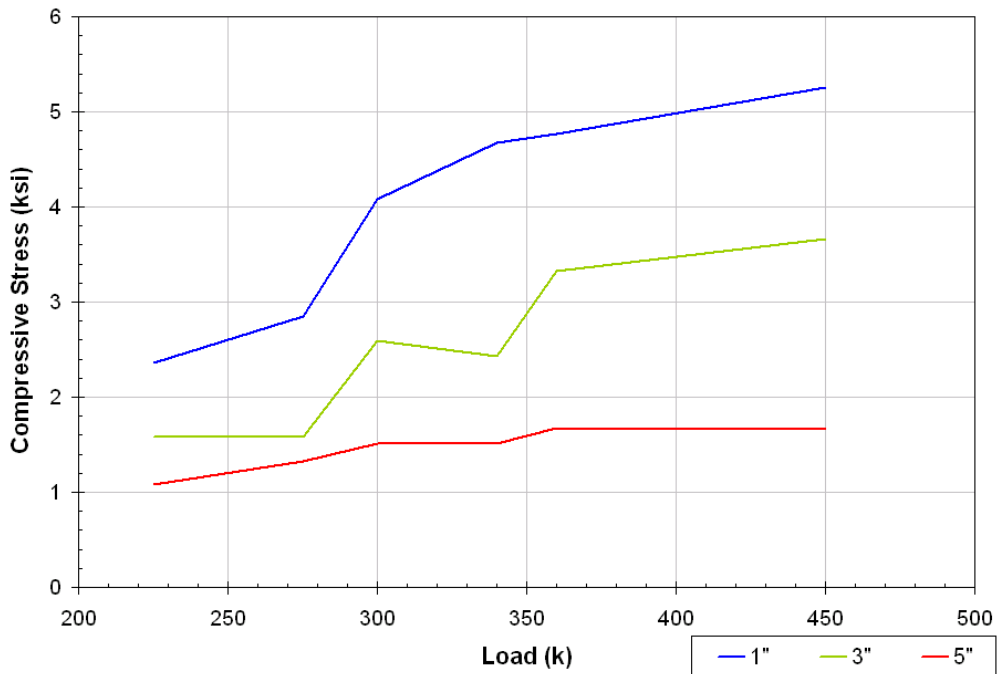


Figure 4-30: Concrete Compressive Stress between End Bearing Plates

members. The results are shown in Figures 4-31 and 4-32. As these plots illustrate, the predicted and experimental trends are similar. At the diaphragm centerline, the experimental results exceed the predicted using the actual material properties. At the diaphragm edge, the experimental results closely resemble those obtained when the top flange is neglected. The system behaved well under ultimate strength loading. The specimen was subjected to significant displacement after the system exceeded the elastic limit. Figure 4-33 shows cracking over the pier after the ultimate load test.

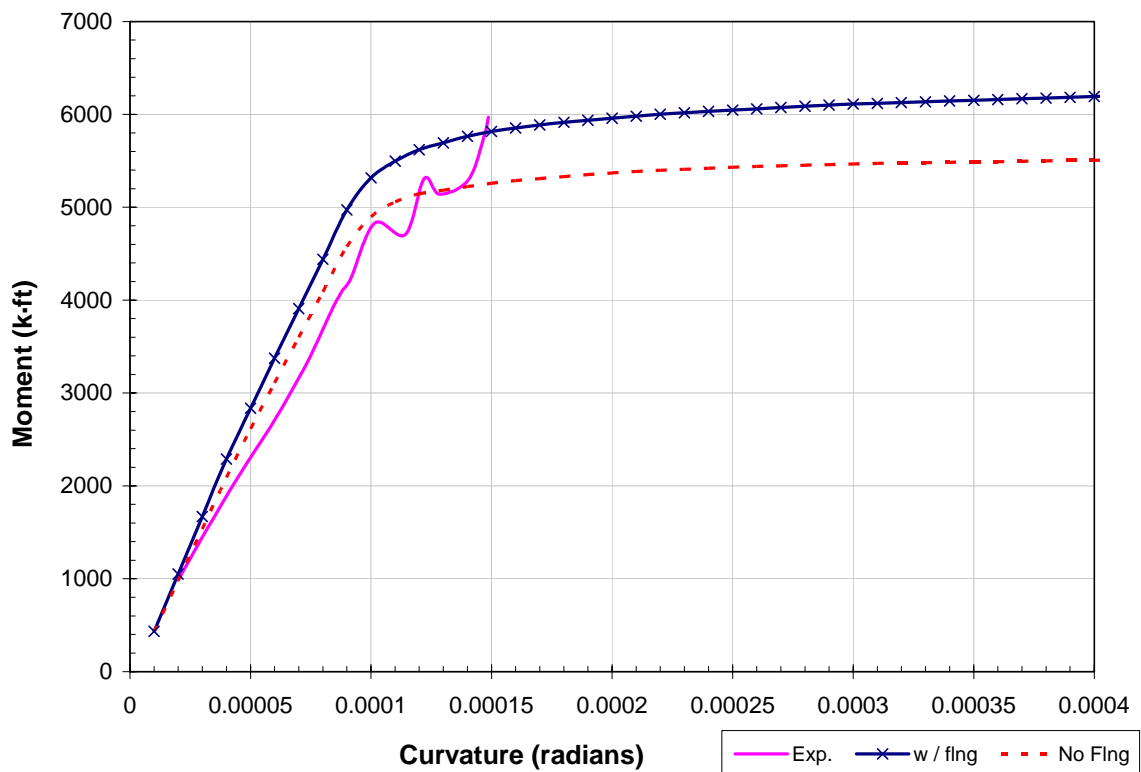


Figure 4-31: Moment Curvature Outside the Diaphragm

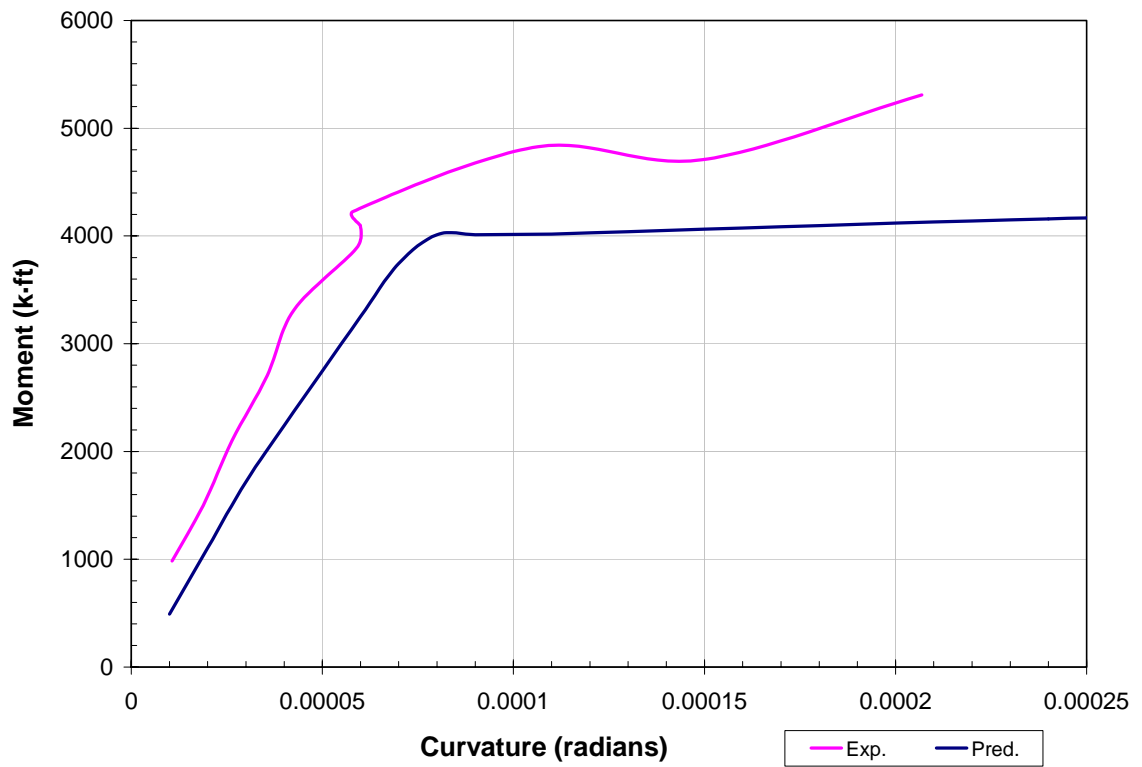


Figure 4-32: Moment Curvature at Support Centerline

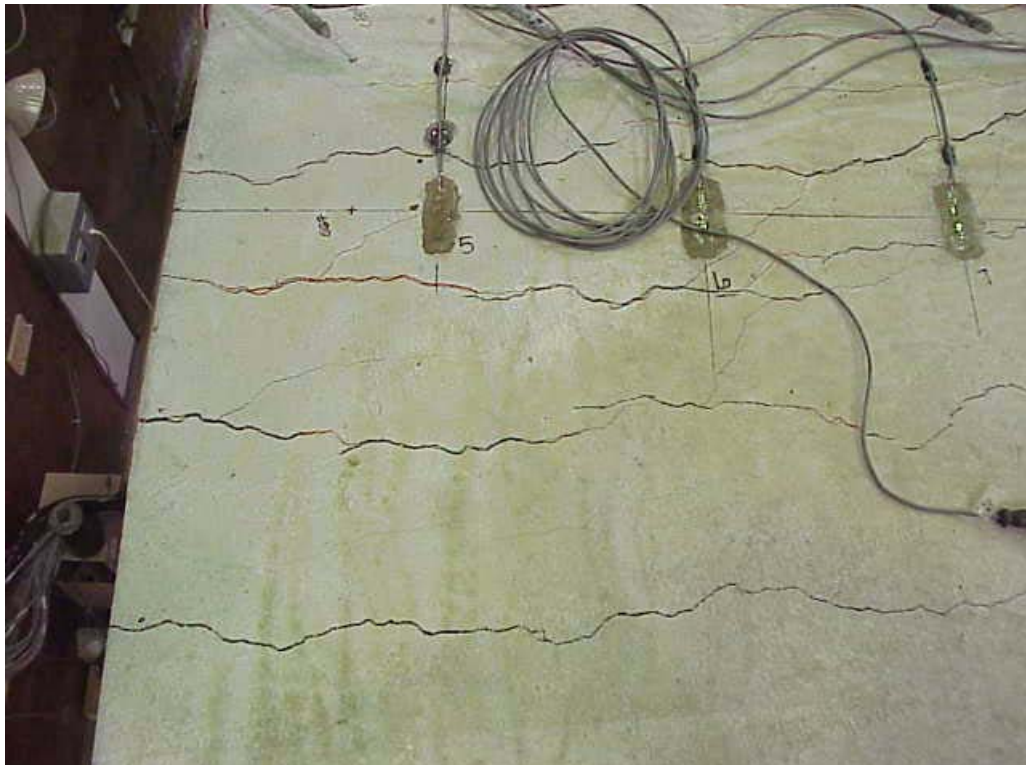


Figure 4-33: Deck Cracking After Ultimate Loading

4.3 TEST SUMMARY

This research was conducted to investigate the performance of the first connection detail of the proposed steel bridge system. From the experimental results several conclusions can be made:

1. No appreciable decrease in rigidity or increases in strains were evident in the system when subjected to heavy truck traffic over the design life of the structure. The result was an initial reduction in specimen stiffness near 7400 cycles, however, the system behavior remained virtually unchanged over the remaining load cycles.
2. From the deck reinforcement stress plot, "failure" of the specimen was ultimately caused by yielding of the deck reinforcement. This ductile mode of failure is shown in the load-deflection curve, during which the specimen was subjected to additional deflection, with only small decreases in stiffness. The plots showing stresses in the reinforcement provide insight into this mechanism, with load shedding to adjacent bars when additional moment was applied.
3. The magnitude of compressive stress in the concrete diaphragm was approximately 5 ksi. From the finite element analysis, the maximum stress in the concrete was 5.9 ksi for the case with a continuous flange and end bearing plates. Since the location of this gauge was one inch above the surface of the bottom flange, the experimental value would be larger near the flange surface.
4. The design of the test specimen was based on a Strength I limit state moment of 3911 kp-ft. From the experimental results, first yield occurred near 4200 kp-ft. A resulting over-design of approximately 7% occurred. Further, using the actual material properties results in a moment capacity of 4330 kp · ft.

Second Specimen

This chapter outlines the experimental observations and data at various stages in the investigation of the second specimen. The construction of the second specimen concluded in January, 2002. The fatigue test was performed between March, 2002 and May, 2002 and the experiment concluded with the ultimate load test performed in June, 2002.

5.1 SETUP AND PROCEDURES

General setup and procedures were reviewed in Chapter 3. Information specific to the second specimen is given below

5.1.1 CONSTRUCTION AND ERECTION

For specimen two, the bottom flanges of the girders were not connected leaving an eight-inch gap between them. No bearing stiffeners were used for this specimen. Since no damage was done to the pier during the testing

or removal of specimen one, it was used again for the second specimen. Two of the vertical rebar anchoring the turndown over the pier were cut off during removal of the previous specimen. New bars were installed in new holes using epoxy. Details of the specimen can be seen in Figure 5-1.

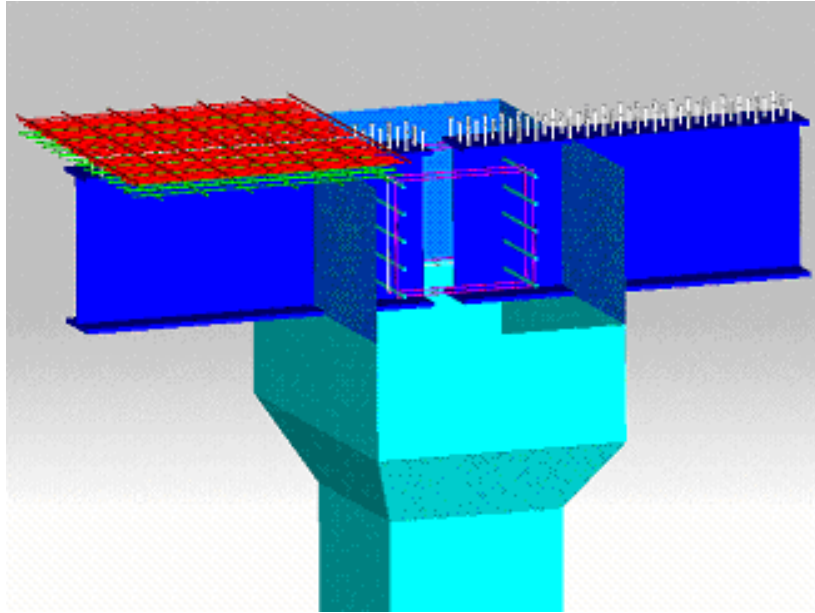


Figure 5-1: Connection Detail of Second Specimen

5.1.2 INSTRUMENTATION

Two separate load stages were identified for the second specimen, each requiring slightly different instrumentation. The devices included electrical strain gauges, vibrating wire embedment gauges, and potentiometers. To aid in record keeping, instruments were assigned a designation according to location and type as follows:

FG - steel surface electrical strain gauges located on the girder flange

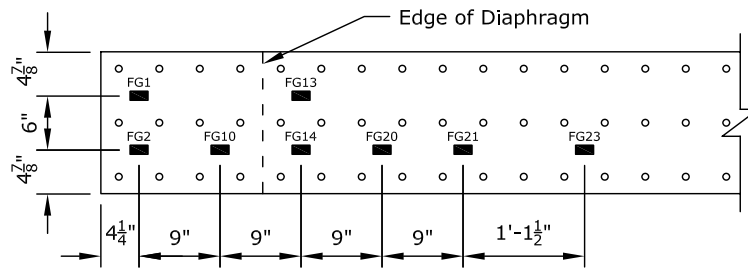
WG - steel surface electrical strain gauges located on the girder web

RG - steel surface electrical strain gauges located on the rebar

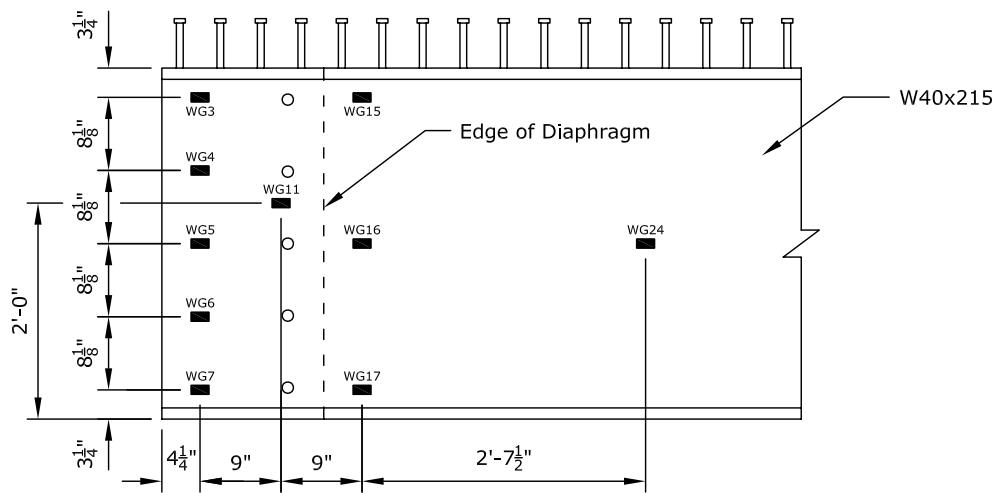
EG - concrete embedded vibrating wire strain gauges

Pots - potentiometers

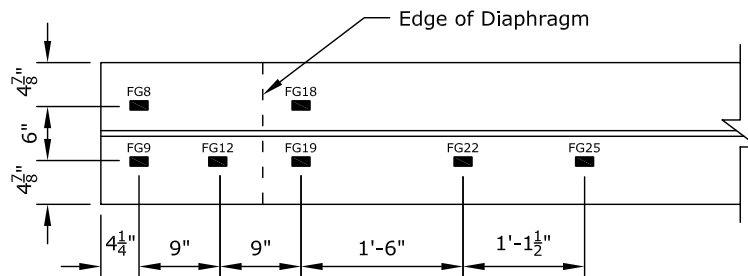
The location of girder strain gauges, (FG or WG) 1 through 25, are shown in Figure 5-2. The location of strain gauges bonded to the slab reinforcement, RG26 through RG46, are shown in Figure 5-3. The location of concrete embedment gauges, EG1 through EG13, are shown in Figure 5-4. Figures 5-5 and 5-6 show pictures of the girder strain gauges and diaphragm embedment gauges respectively. During the ultimate load test, potentiometers were located at each load point in order to measure the deflection.



Top Flange Gauges

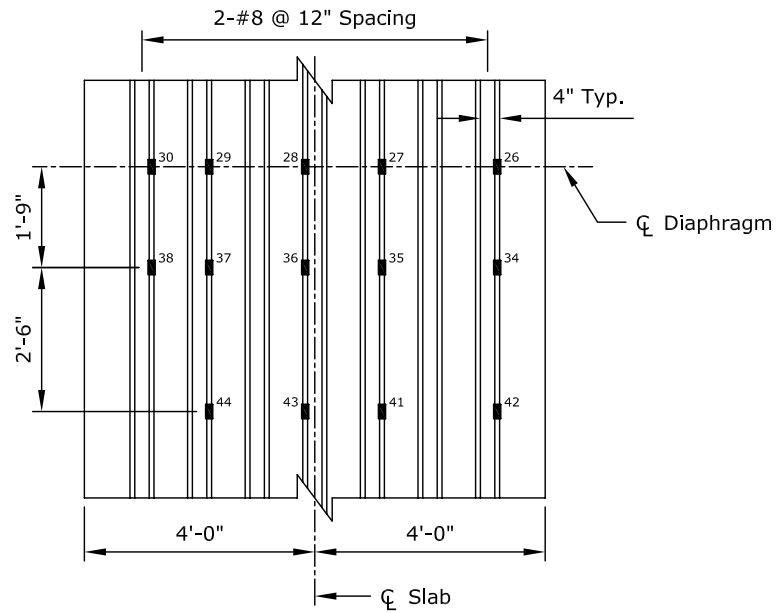


Web Gauges

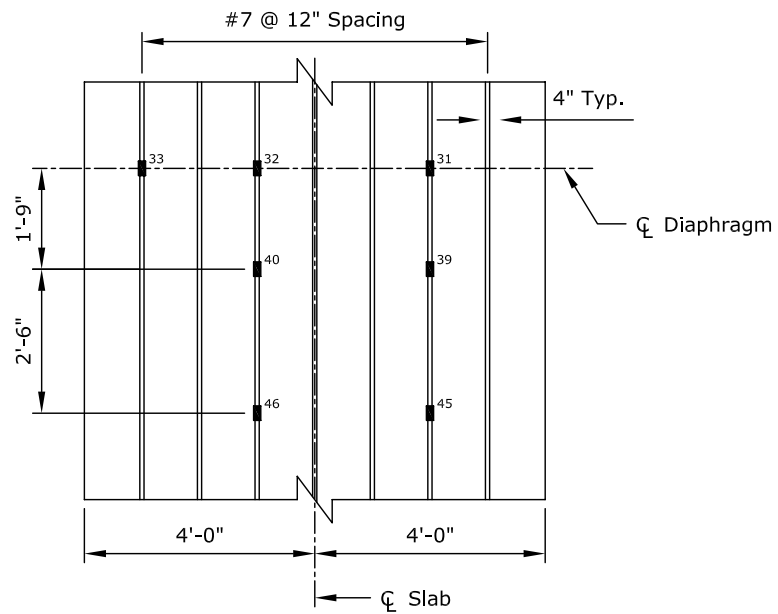


Bottom Flange Gauges

Figure 5-2: Girder Instrumentation

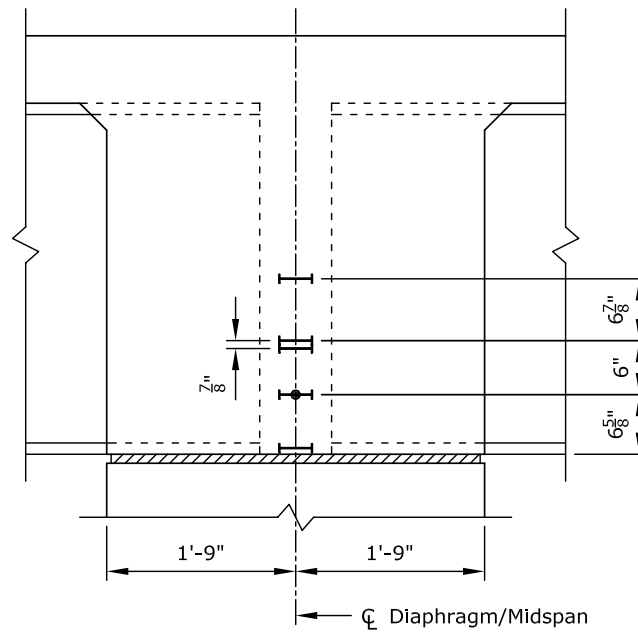


Slab Top Layer

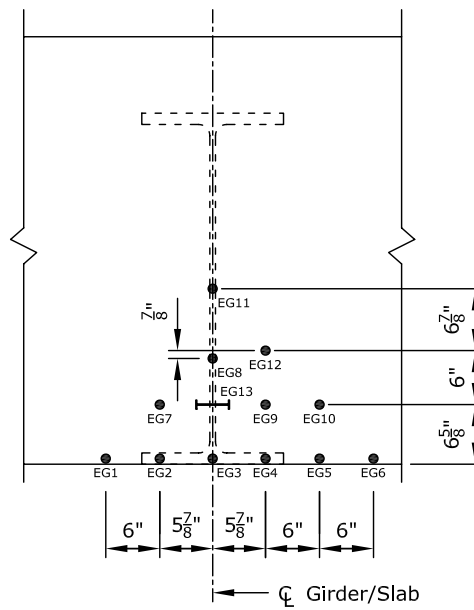


Slab Bottom Layer

Figure 5-3: Slab Reinforcement Instrumentation



Diaphragm Embedment Gauges



Midspan Section of Diaphragm

Figure 5-4: Diaphragm Instrumentation

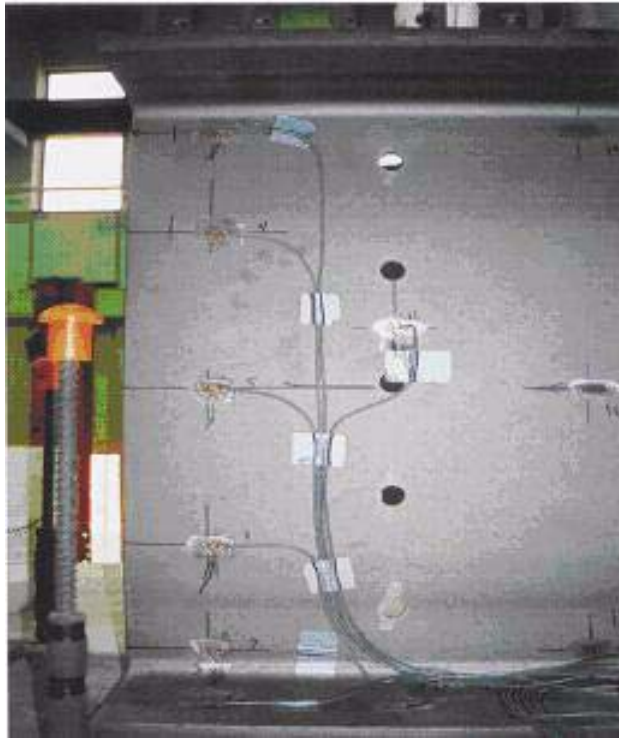


Figure 5-5: Electrical Strain Gauges

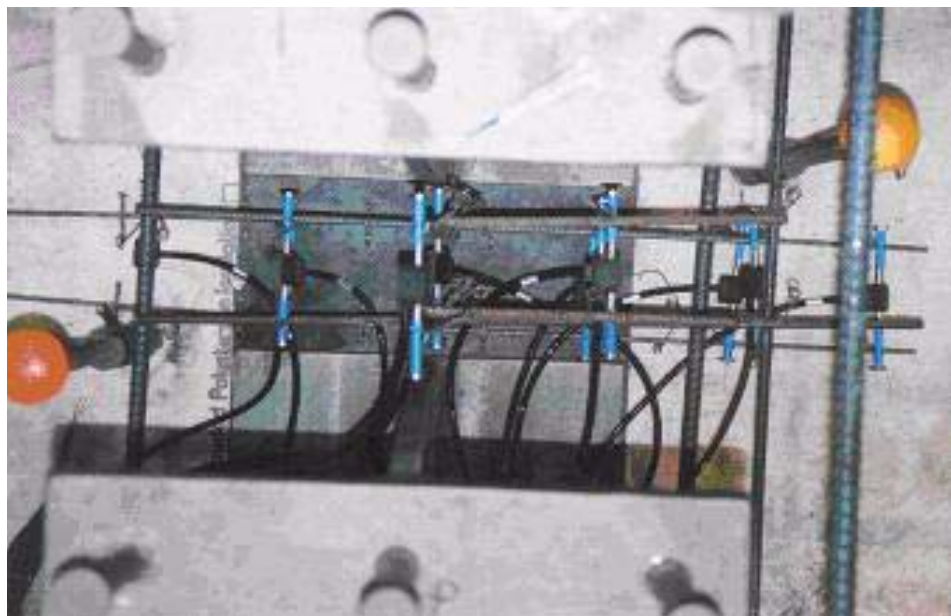


Figure 5-6: Embedment Gauges

5.1.3 MATERIAL PROPERTIES

General material testing information was covered in Chapter 3. This section is concerned with the specific testing of materials for the first specimen.

Two concrete cylinders were tested from the deck and diaphragm components after curing for ten days. Similarly, four were tested after 46 days of curing. Two from each pour were tested at 120 days, which coincided with the ultimate strength test. The average 46-day compressive strength of the diaphragm and deck concrete was 7120 and 5300 psi, respectively.

Two samples of each deck reinforcing bar size were tested as a full section according to ASTM A370 Specifications. Results of the tensile tests are shown in Table 5-1. The average reinforcing bar strength was 73 ksi.

Bar	F _y (ksi)	F _u (ksi)
#4	71	114
#4	72	115
#5	77	123
#5	76	122
#7	68	109
#7	67	110
#8	75	111
#8	75	111
Avg	73	114

Table 5-1: Rebar Tensile Testing Results

5.2 SPECIMEN BEHAVIOR

The experimental investigation consisted of two distinct load stages. These were cyclic (fatigue) loading and ultimate strength loading. Non-composite dead loading was not directly tested for the second or third specimen.

5.2.1 FATIGUE LOAD TESTING

Displacement control was used through the course of the fatigue investigation. After applying a few cycles, it became apparent that the specimen could not resist the desired end loads of 106 kips. The maximum load achieved from the applied displacement had decreased to approximately 74 kips. As a result, the number of applied loading cycles had to be increased. The maximum displacement was adjusted three times during the cycling load test. The fatigue testing was terminated after applying approximately 2,780,000 cycles due to load deterioration.

Figure 5-7 shows cracking in the deck over the pier and near the edge of the diaphragm during the fatigue test. The initial cracks were observed near the diaphragm edge. Figure 5-8 shows the bottom flange of the girder where it penetrates the diaphragm. As cycling progressed, the bottom flanges moved farther into the diaphragm. This movement was visually observed during the fatigue test.

As was described in Chapter 3, polystyrene insulation was placed between the pier and the diaphragm to allow rotation of the girders over the pier. Figure 5-9 shows that no gap formed between the pier and the foam around the edge of the pier during the cycling load test. Figure 5-10 shows mapping of the cracks during the test. The majority of the cracking occurred near the edge of the diaphragm where there was an abrupt change in rigidity.



Figure 5-7: Deck Cracking

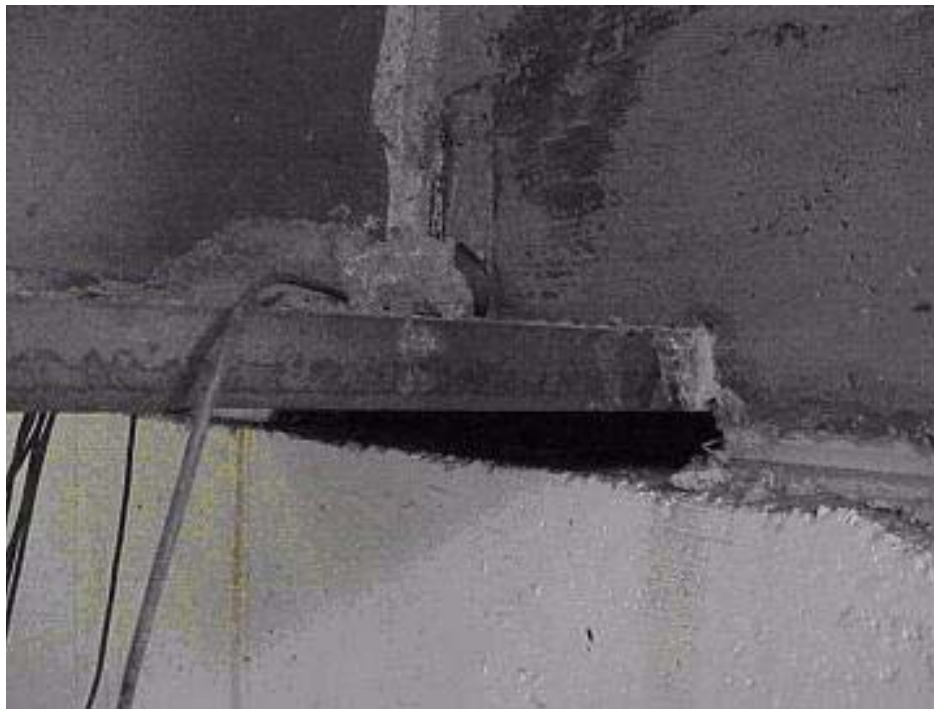


Figure 5-8: Bottom Flange Movement



Figure 5-9: Polystyrene between Pier and Diaphragm

The fatigue loading frequency was set at two cycles per second. At the beginning of the day, prior to the start of applying fatigue loads, the specimen was subjected to a similar set of fatigue loads that were done at a lower frequency (one cycle every ten seconds).

In this report, these cycles are referred to as slow cycle tests. At the start of each day, the specimen was subjected to a five slow cycle test (five cycles run at one cycle per ten seconds). At the beginning of each of these five slow cycle tests, the specimen was held at the peak end load and data was collected from all instruments, including the embedment gauges. During the application of the five slow cycles, data from all instruments except embedment gauges were collected and stored in the computer.

Load-deflection plots for the specimen during the fatigue test are shown in Figures 5-11 and 5-12. These plots were generated from data collected



Figure 5-10: Mapping of Deck Cracks

during the five slow cycles of loading at the start of each day. These plots show that as the cycles increased, the maximum load diminished. At certain points during cycling, the deflection was increased in order to bring the maximum end loads closer to the target value. These adjustments can be seen in the plots where the shifts in deflection occur.

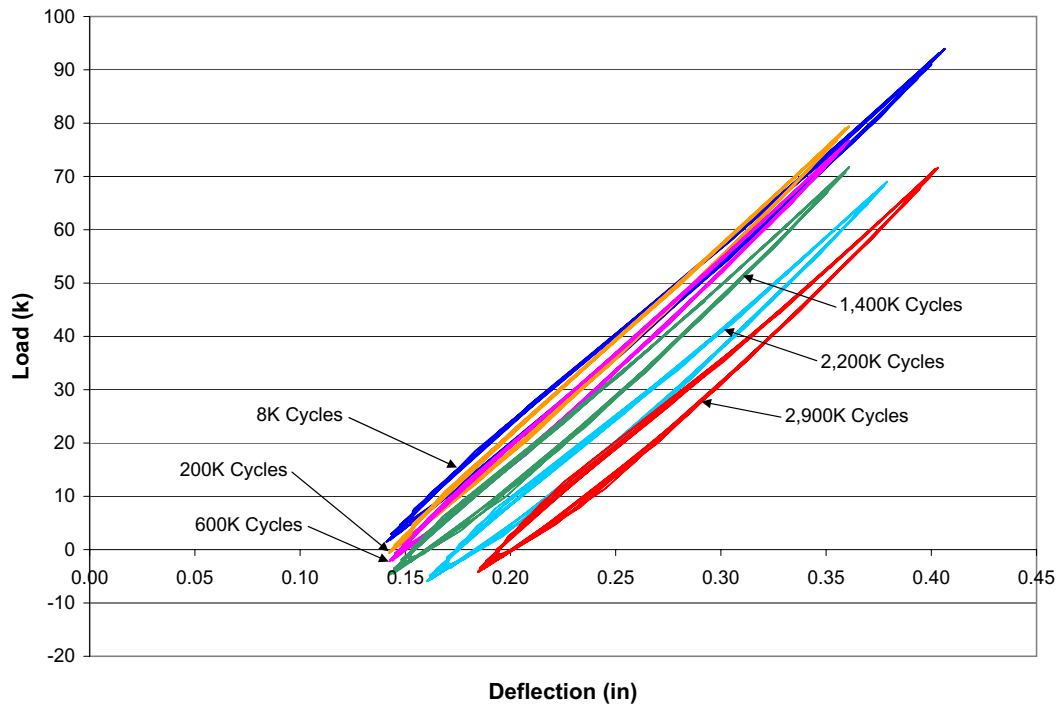


Figure 5-11: East Girder Load-Deflection Plot

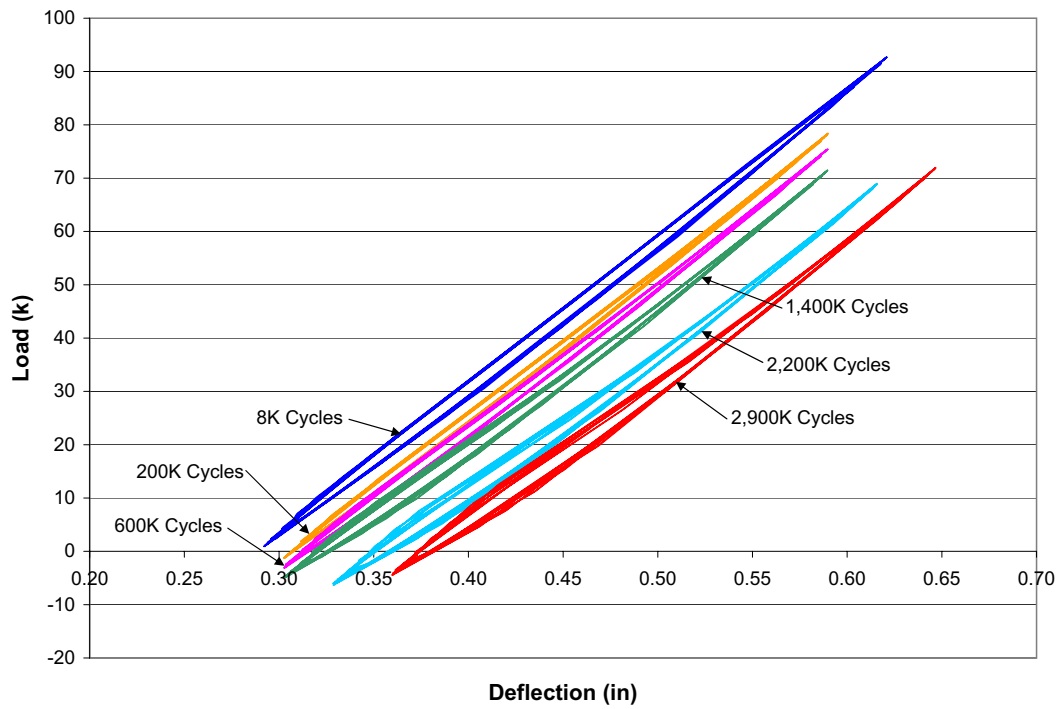


Figure 5-12: West Girder Load-Deflection Plot

From the load-deflection data shown in Figures 5-11 and 5-12, the system stiffness can be found. The system stiffness is defined by the following equation:

$$K_{ld} = \frac{(P_{\max} - P_{\min})}{(\Delta_{\max} - \Delta_{\min})} \quad (5-1)$$

where

- K_{ld} = stiffness
- P_{\max} = maximum applied load
- P_{\min} = minimum applied load
- Δ_{\max} = maximum deflection
- Δ_{\min} = minimum deflection

The stiffness for each side of the specimen at various load cycles is calculated and shown in Figure 5-13. Notice that, initially, the stiffness was very high for each side, then immediately dropped after the cycling began. The stiffness continued to diminish for each side throughout the rest of the cycling.

The applied load extremes for the East and West Girders are shown in Figures 5-14 and 5-15, respectively. The range between the minimum and maximum loads is shown in Figure 5-16. The range is determined by taking the difference between the minimum and maximum load from a particular cycle. It can be seen that the range of the applied end loads diminished during the fatigue test.

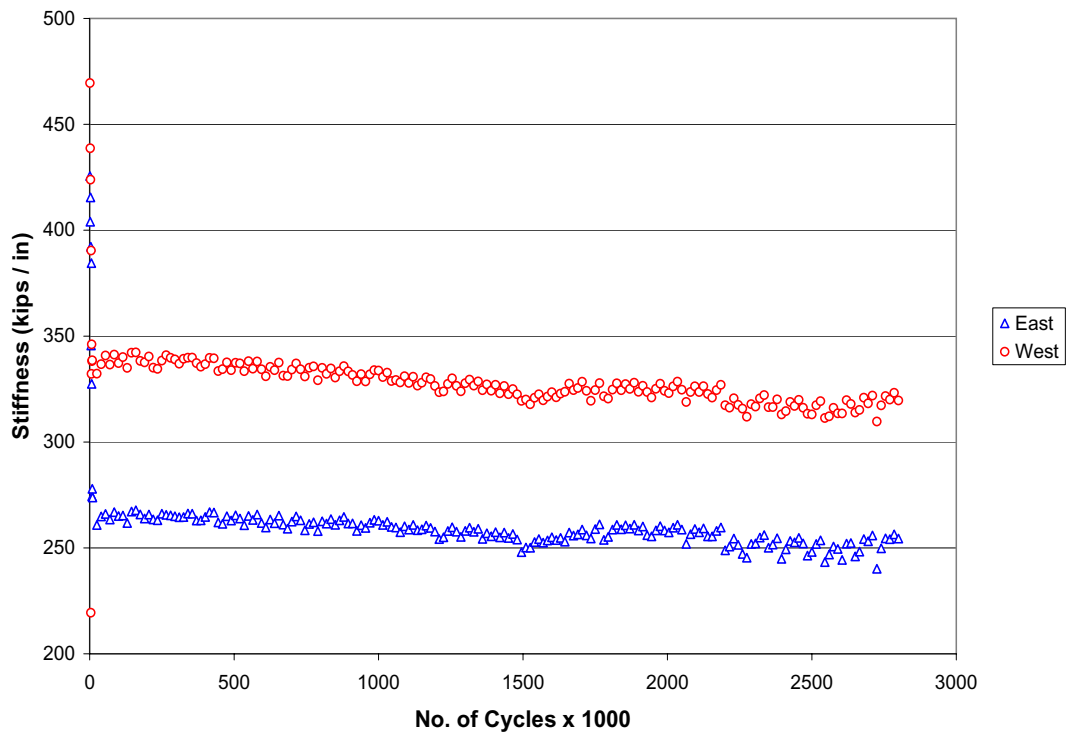


Figure 5-13: System Stiffness vs. No. of Cycles

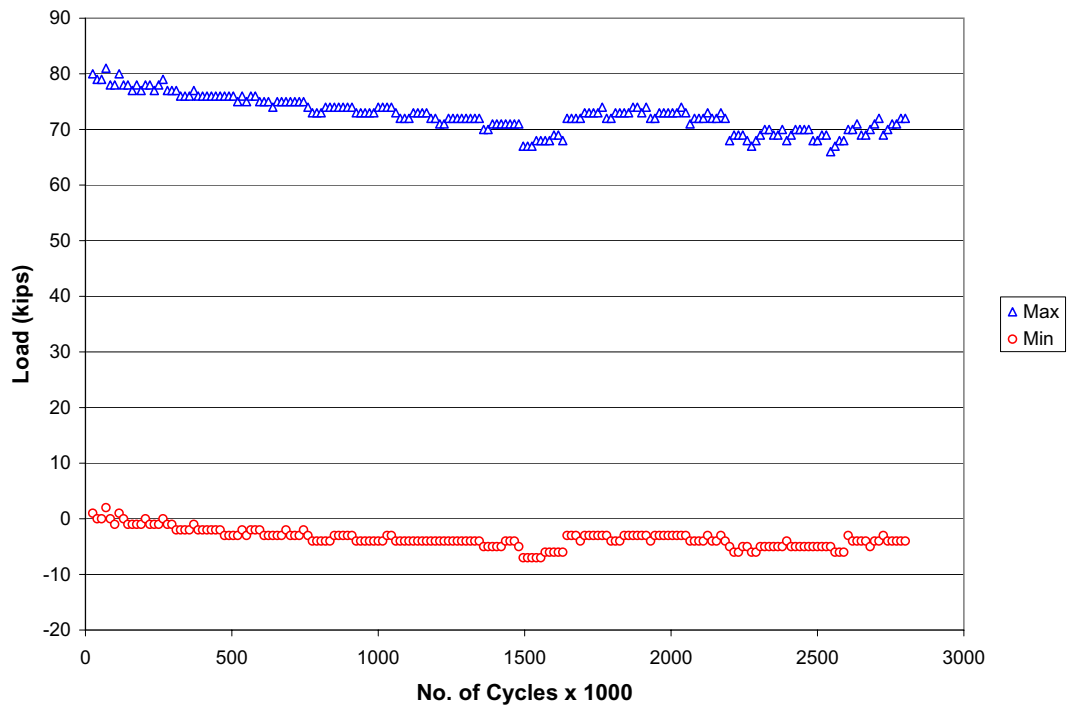


Figure 5-14: East Girder Load Extremes

Specimen Behavior

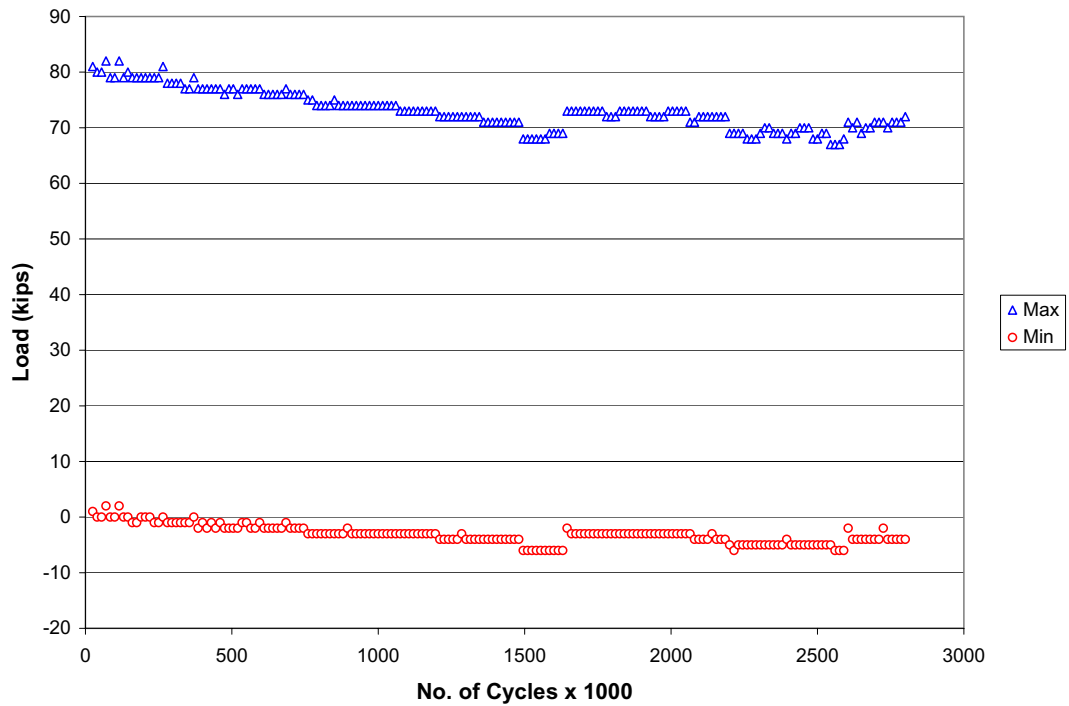


Figure 5-15: West Girder Load Extremes

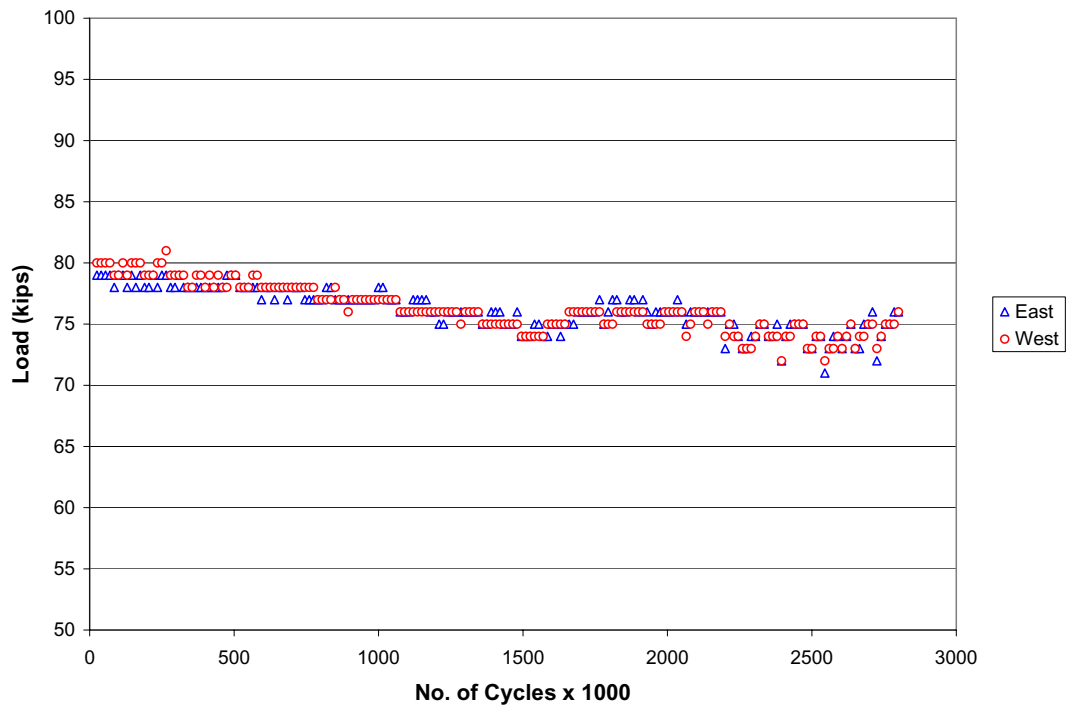


Figure 5-16: Load Range vs. Number of Cycles

The strain from gauges located along the bottom flange of the east girder is shown in Figure 5-17. The strain was taken from the fifth cycle of the five slow cycle tests. The number of cycles is noted for each set of strain values.

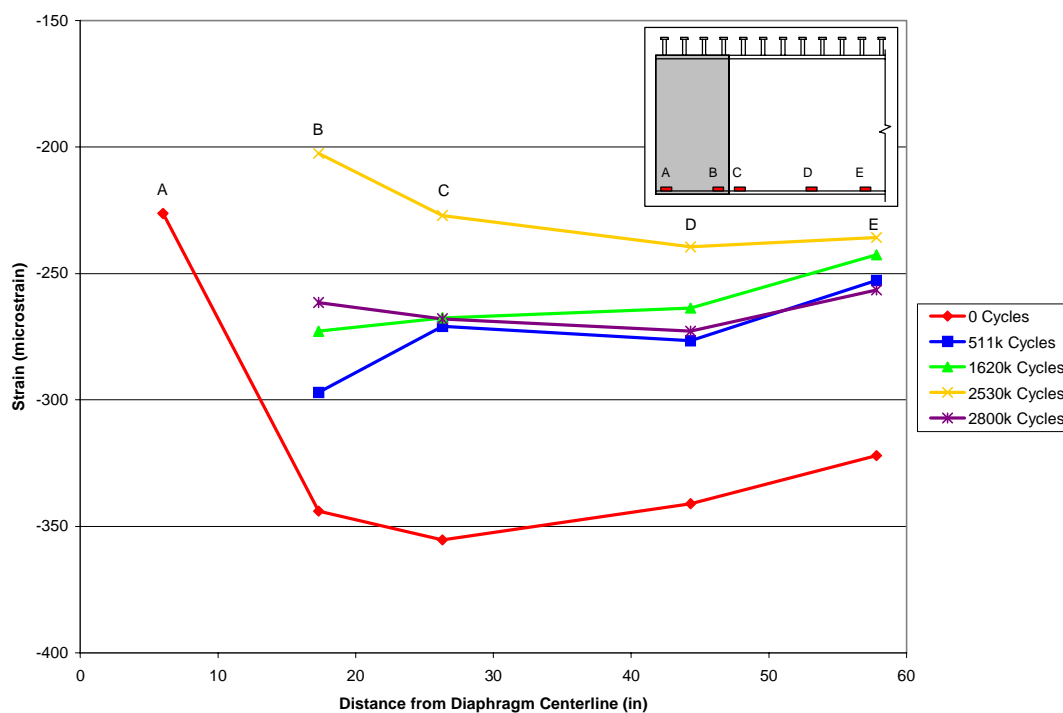


Figure 5-17: Strain Distribution Along Bottom Flange

Initially, compressive strains in the portion of the bottom flange inside the diaphragm were lower than those outside of the diaphragm. This indicates that the concrete was resisting a portion of the compressive force. From the initial cycling to 511,000 cycles, all of the compressive strains decreased. This was caused by the reduction in the applied load to the system. At 511,000 cycles, the flange compressive strains inside the diaphragm (Point B) were higher than the strains outside the diaphragm (Point C). This occurred due to slippage of the girder inside the diaphragm. Since the end load had to be reduced, some crushing of the concrete most likely occurred at this point as well. At 1,620,000 cycles, the bottom flange compressive strains inside the diaphragm decreased slightly from the previous cycle point. It is possible that as cycling continued, the height of crushed

concrete in the diaphragm between the girder ends increased. As a result, the strains in the bottom flange of the girder inside the diaphragm decreased over the course of cycling more than the strains outside of the diaphragm. The crushed concrete was unable to carry the compressive force in the bottom flanges, so the compressive force moved into the web, which transferred compression into uncrushed concrete. As the height of crushed concrete increased, the strains in the bottom flange inside the diaphragm continued to decrease. Data for 2,800,000 cycles shows higher compressive strains at each location than for 2,530,000 cycles because the applied load had been adjusted shortly before ending the cycling test.

The strain gauges located on the girder just inside of the concrete diaphragm are shown in Figure 5-18. The strain was taken from the fifth cycle of the five slow cycle tests. The number of cycles is noted for each set of strain values. .

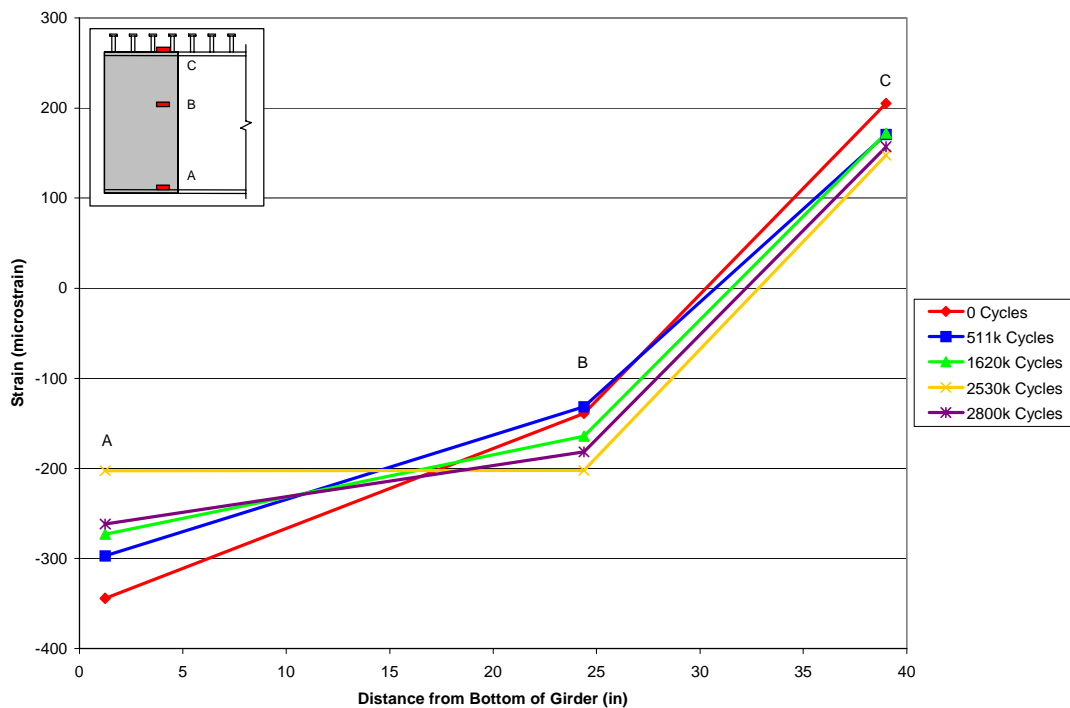


Figure 5-18: Strain Distribution Just Inside Diaphragm

At this location, compressive strain in the bottom flange (Point A) and tensile strain in the top flange (Point C) decreased as cycling progressed. Compressive strains in the web (Point B) increased over time. The decreasing compressive strain in the bottom flange and the increasing compressive strain in the web at this location indicate that more compressive force was being transferred to the web as cycling progressed. This may have been a result of the concrete crushing in the diaphragm between the flanges, as discussed previously. After 2,530,000 cycles were run, the end loads were increased, causing the increase in compressive strain in the bottom flange and a small increase in tensile strain in the top flange. The web exhibited a slight decrease in compressive strain.

The strain gauges located on the girder just outside of the concrete diaphragm are shown in Figure 5-19. The strain was taken from the fifth cycle of the five slow cycle tests. The number of cycles is noted for each set of strain values.

The decrease in the strains from 0 to 511,000 cycles was due to a decrease in the applied end loads to the specimen. Between 511,000 and 2,530,000 cycles, compressive strains in the bottom flange (Point A) and the lower part of the web (Point B) decreased. During this time, tensile strains in the upper part of the web (Point D) and the top flange (Point E) decreased as well. There was a slight increase in the compressive strain in the middle of the web (Point C). Shortly after 2,530,000 cycles were run, the end loads were increased, causing small increases in compressive strains near the bottom flange and tensile strains near the top flange, shown by the points plotted for 2,800,000 cycles.

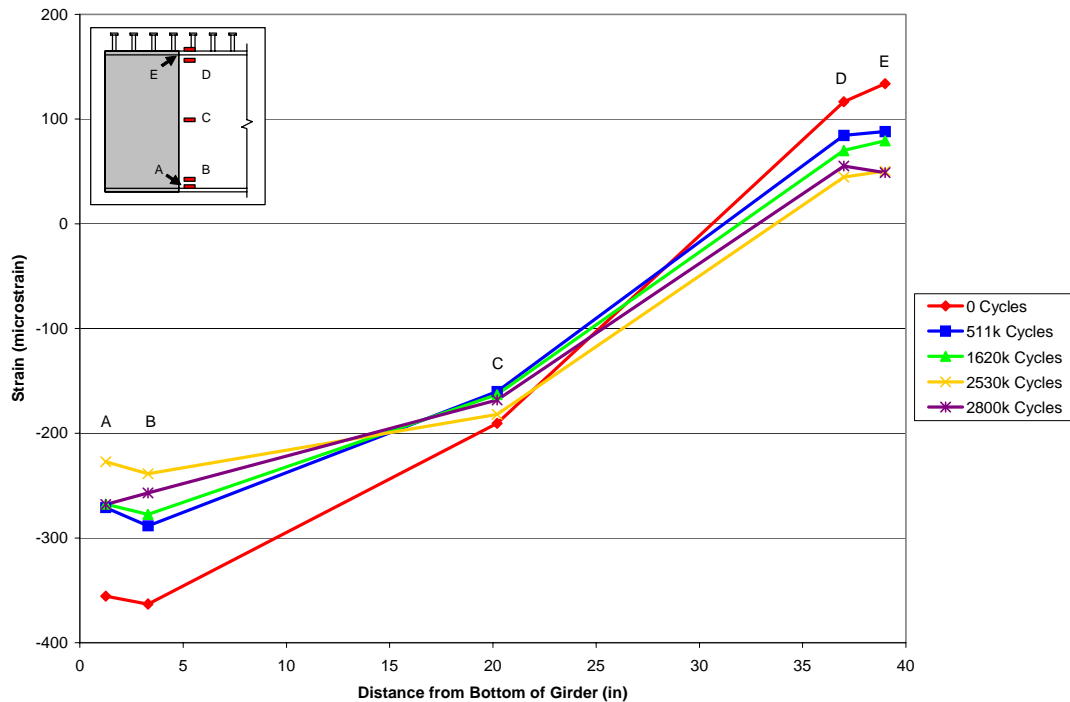


Figure 5-19: Strain Distribution Outside Diaphragm

5.2.2 ULTIMATE STRENGTH TESTING

For the ultimate load test, the end loads were increased slowly in 10 to 25 kip increments until the specimen failed. At a load of 267 kips, the specimen was unloaded because of a problem in the hydraulic system and then reloaded again.

At a load of 256 kips, a loud noise was heard from the specimen. Load continued to be applied to the specimen. At a load of 267 kips a second loud noise was heard. The load started to decrease. At a load of 255 kips, a third loud noise was heard. At this time, the specimen was unloaded.

From the beginning of the ultimate load test, cracks in the concrete slab began to increase in width. Most of the cracks had formed during fatigue loading and further increased in width during the ultimate loading. Figure 5-20 shows the cracking observed on the slab over the pier while the

specimen was being loaded. The majority of cracking occurred near the edge of the diaphragm. However, there were some large cracks over the pier centerline that were wider than those near the edge of the diaphragm.



Figure 5-20: Cracks in Slab over Pier

Additional cracks through the depth of the slab are shown in Figure 5-21. The marked cracks formed during the fatigue load test and the unmarked cracks formed from the existing cracks during the ultimate load test.

Figure 5-22 shows that during the ultimate load test, a gap was formed between the pier and the polystyrene insulation near the edge of the pier. This can be explained as the girders pried the diaphragm up off the pier as the bottom flanges were penetrating to the diaphragm.



Figure 5-21: Cracks Through the Depth of the Slab

Figure 5-23 shows crushing of the concrete around the bottom of the girder where it penetrates the diaphragm. By increasing the load, the bottom flanges moved farther into the concrete diaphragm and caused further girder rotation and crushing of the concrete. The final deformed shape of the specimen after the ultimate load test is shown in Figures 5-24 and 5-25. Figure 5-26 shows cracking under the slab at the corner area between the slab and the girder.



Figure 5-22: Gap Formed Between the Pier and the Polystyrene Insulation

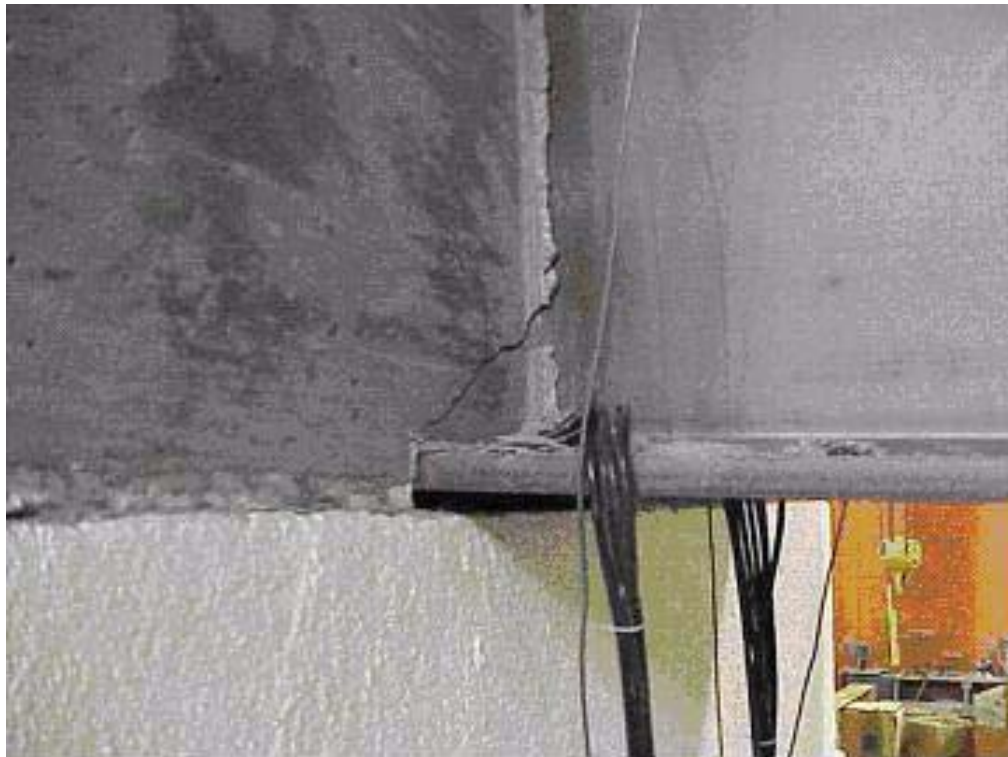


Figure 5-23: Girder Penetration into Diaphragm



Figure 5-24: Deformed Shape of Specimen During the Ultimate Load Test



Figure 5-25: Final Deformed Shape



Figure 5-26: Cracking under Slab

During the ultimate load test, data from all of the sensors was collected at the end of each load stage. The information obtained was examined in order to investigate how the loads were carried within the system.

The load-deflection curve for the ultimate load test is shown in Figure 5-27. From this curve, it can be seen that the system response was linear up to the load of about 120 kips. At the load of 262 kips, the system was unloaded because of a problem in the loading system. As a result of the initial loading, the system displayed a permanent set of approximately 0.75". Upon subsequent reloading, the system responded linearly until intersecting the original load-deflection curve. Despite accrued damages, the initial stiffness during reloading was nearly equal to the original stiffness. The ultimate load of the system in reloading was about 261 kips. Figure 5-28 shows the moment deflection data for both Tests 1 and 2. Here it can be seen that the maximum moment in Test No. 2 is approximately two-thirds of the maximum moment observed in Test No. 1.

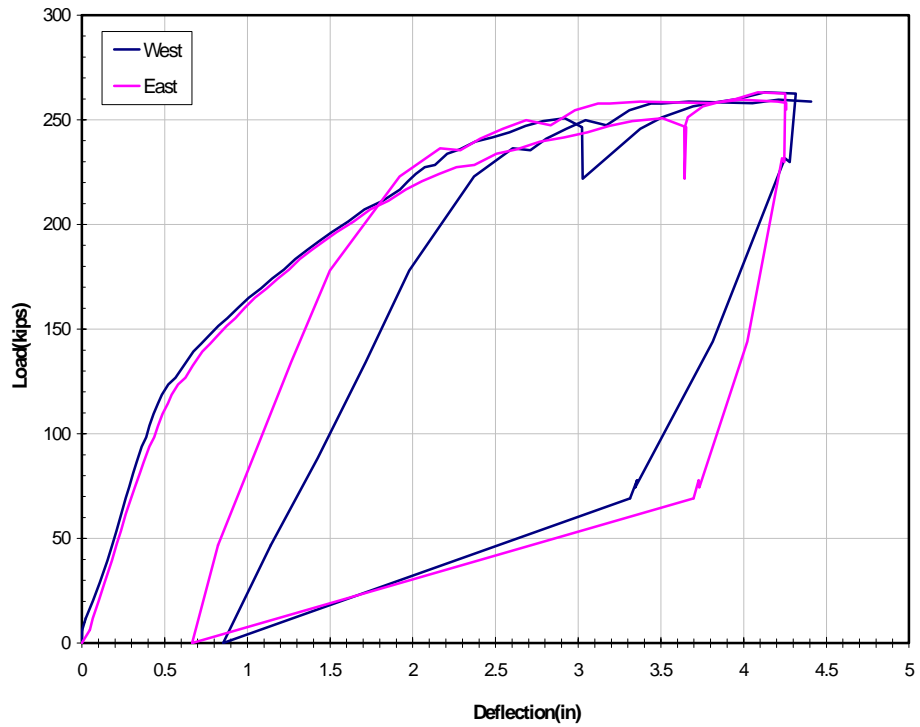


Figure 5-27: Ultimate Load Test Load-Deflection Graph

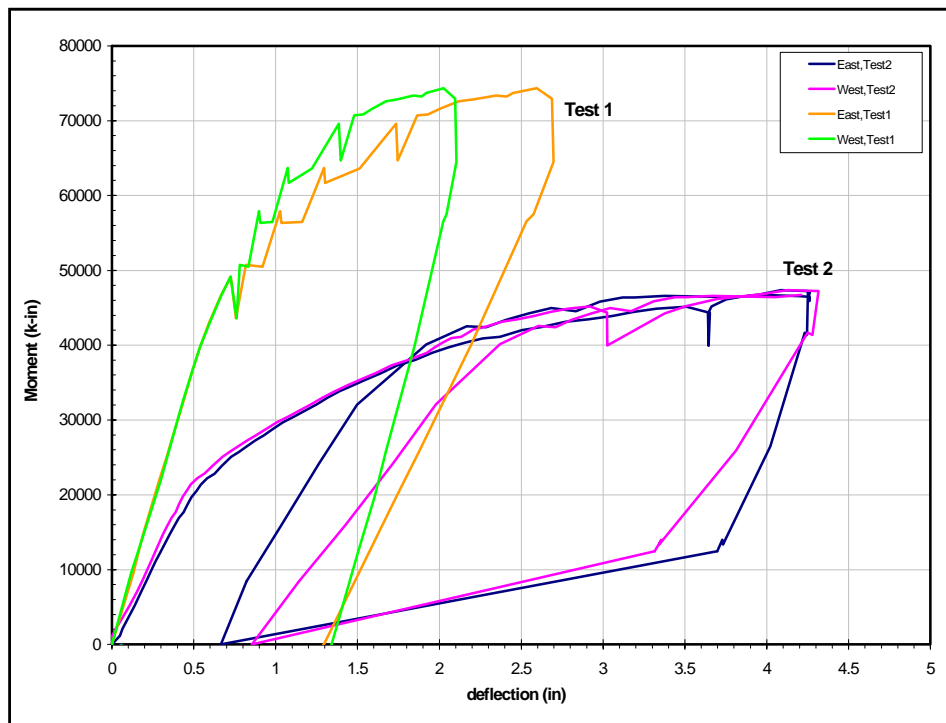


Figure 5-28: Ultimate Load Test Moment-Deflection Graphs for Tests 1 and 2

Information obtained from Test No. 1 indicates that the mode of failure of the first connection detail was due to the yielding of tension reinforcement in the slab. The connection was subjected to significant displacement after all the reinforcement had yielded without a noticeable decrease in load.

Examining the strain in the deck reinforcement shows that the bars located near the middle of the deck yielded first. As the middle bar yielded, load was shed to adjacent reinforcing steel with the increase in load. Not all bars yielded, however. Figure 5-29 shows the strain distribution of rebar in the deck at ultimate load. The upper solid line represents the yield strain of the rebar and the lower solid line shows the width of the deck. As can be seen in this figure, some rebar did not yield at ultimate load. The gray ellipse in this graph shows the area where the rebar yielded, but no data was available, as gauges had failed after yielding, prior to ultimate load. Figure 5-30 shows the strain at the centerline over the pier for the top layer of rebar. Notice that not all bars yielded from the loading. Also notice the load-shedding pattern. Figure 5-31 shows the strains of the top layer of bars at the edge of the diaphragm. Except gauge SG38, all gauges show strains less than yield strain.

Figure 5-32 shows the strains in the bottom flange for the initial loading. The dashed line represents compressive strain outside the concrete diaphragm. The solid line indicates compressive strain near the pier centerline inside the diaphragm. Note the linear increase in strain. Strain gauge 12 ceased to function at a load of 178 kips. Initially, the slope of the dashed line and the solid line are equal. The dashed line shows the maximum strain of 1186 microstrain, which indicates that the bottom flange out of the diaphragm did not yield at the ultimate load.

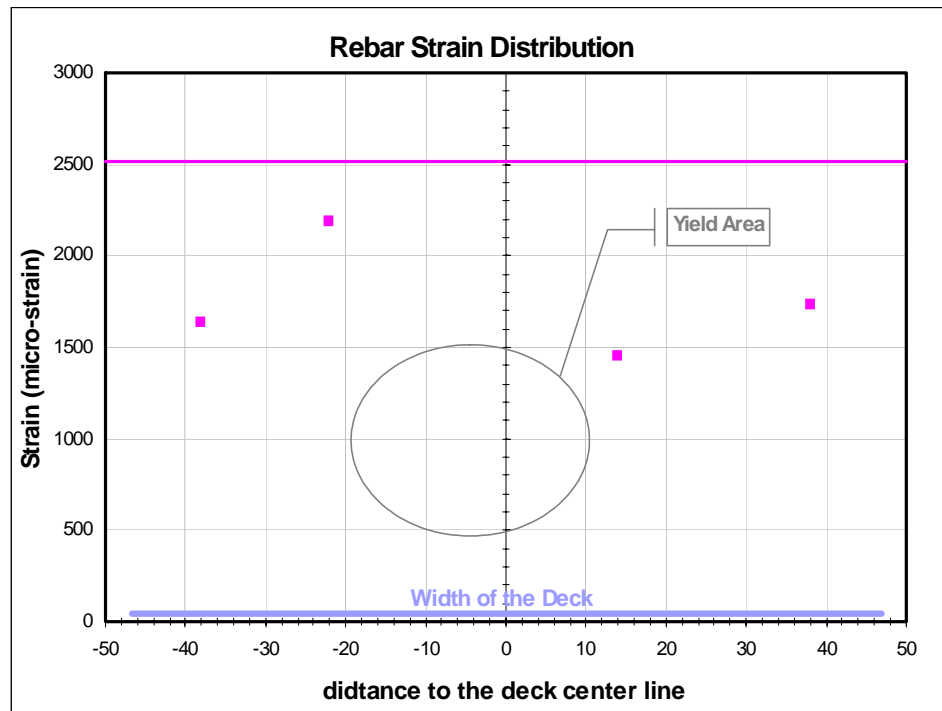


Figure 5-29: Strain Distribution of Rebar in the Deck at Ultimate Load

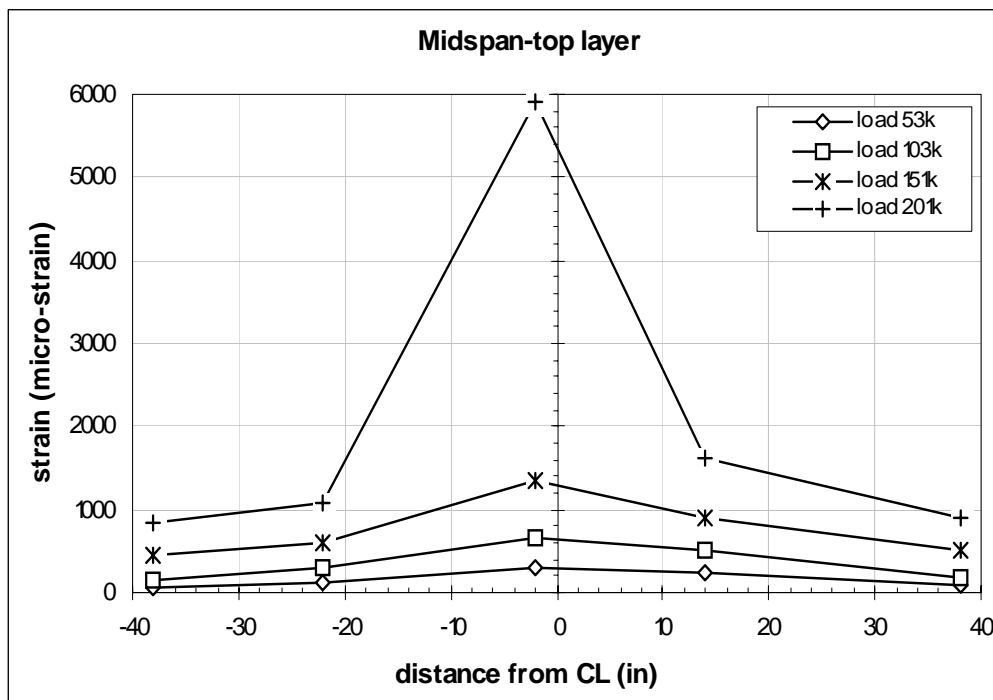


Figure 5-30: Strains in Top Layer of Reinforcement at Centerline of Pier

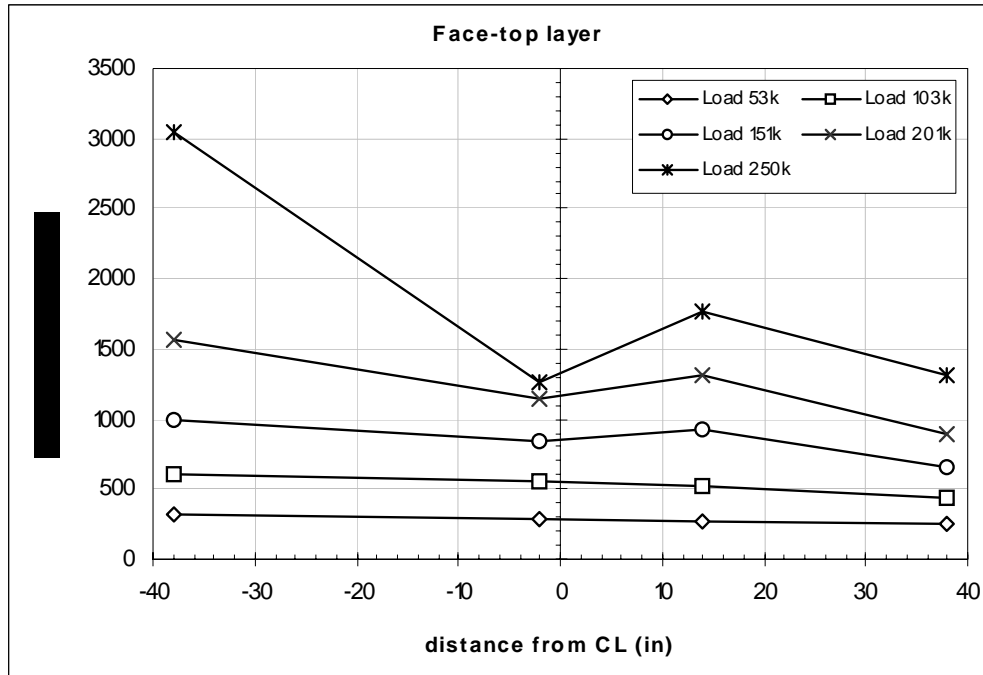


Figure 5-31: Strains in Top Layer of Reinforcement at Edges of Pier

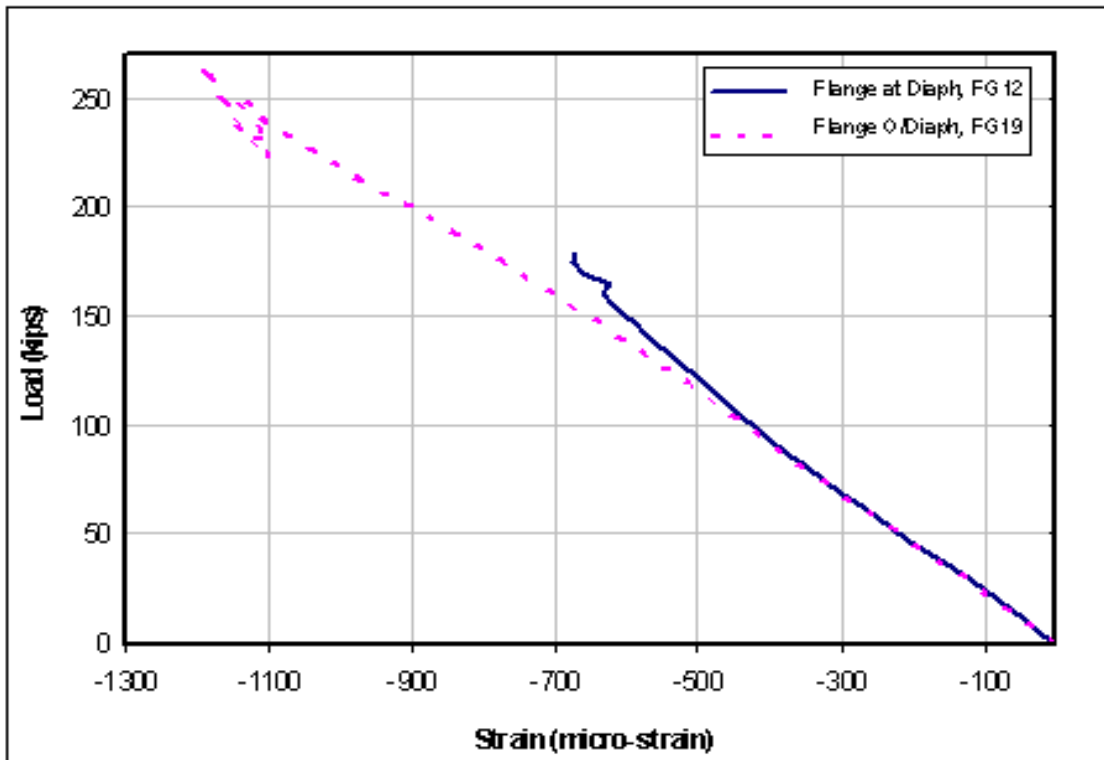


Figure 5-32: Bottom Flange Strain Data

Figure 5-33 shows the strain distribution of the web out of the diaphragm from strain gauges 15, 16 and 17. The solid line represents strain distribution at the maximum load of the first loading. The dashed line represents the strain distribution at the maximum load of the second loading. This graph indicates that strain distribution of the web outside the diaphragm is close to linear. It can be seen from this figure that strain data from gauges 17 and 16 at the bottom and middle of the web, respectively, show the same value for both loadings.

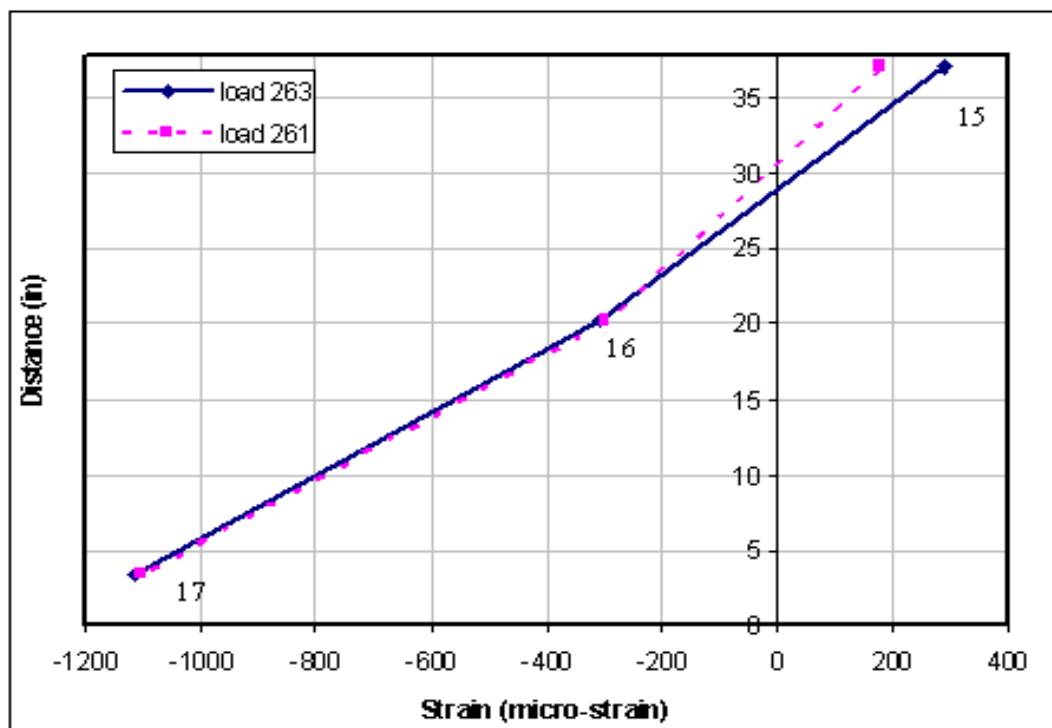


Figure 5-33: Web Strain Distribution Out of Diaphragm

Compressive strain in the bottom of the concrete diaphragm is shown in Figure 5-34. The data was collected from gauges EG5 and EG10. These two gauges were in the same horizontal location, which were 12" from the web centerline. EG10 was 6.6" above EG5. This graph shows that the maximum strain at this distance was about 130 microstrain. This indicates that the concrete outside of the bottom flanges (location of EG5 and EG 10) did not make a significant contribution to the section capacity.

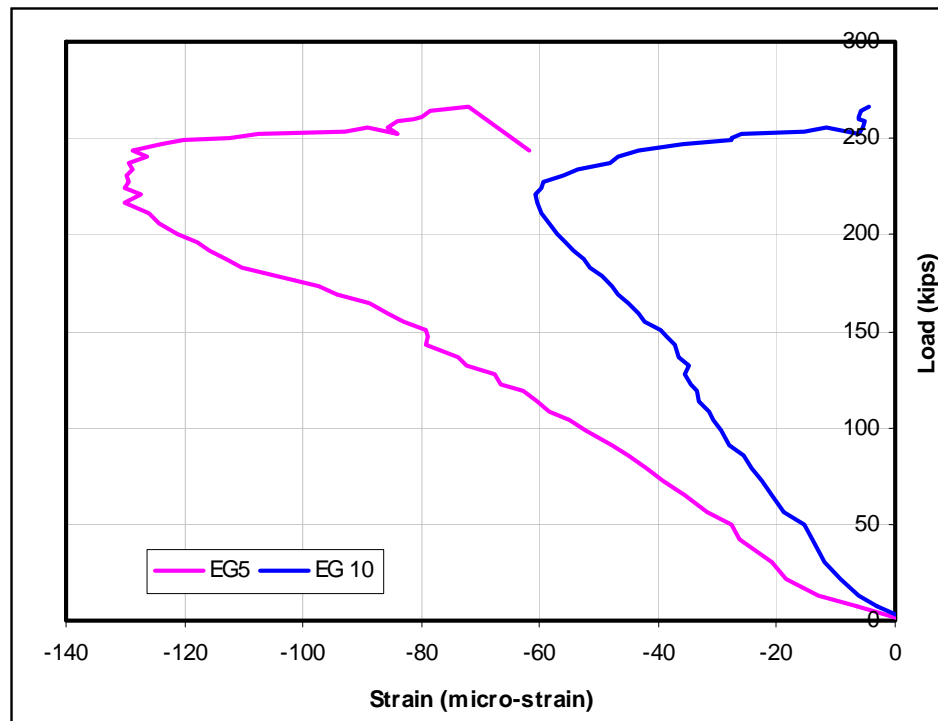


Figure 5-34: Concrete Compressive Strain Inside Concrete Diaphragm

5.2.3 SPECIMEN DISSECTION

After the ultimate load test was concluded, the specimen was dissected in order to investigate what had happened inside of the diaphragm. First, the concrete slab was removed. Figure 5-35 shows the specimen after removing the slab. Figure 5-36 shows the remains of the test specimen after removing the concrete slab and a portion of the concrete diaphragm. Figure 5-37 shows the gap between the girder web and concrete diaphragm. The gap was created by horizontal movement of the concrete diaphragm in the direction perpendicular to the girder web. Figure 5-38 shows the gap between the bottom flanges in the concrete diaphragm. It can be seen that the concrete between the bottom flanges is pushed out. During the construction of the test specimen the gap was set at 8". As a result of the bottom flanges pushing against the concrete diaphragm and crushing

of the concrete in the vicinity of the bottom flanges, the gap decreased to 5”.

As a result of the crushing of the concrete between the bottom flanges the girder ends embedded in the concrete diaphragm experienced rotation. This rotation caused large deformation in the reinforcement running perpendicular to the girder web. Fracture of these bars occurred near the girder web, where holes were drilled to allow continuous reinforcement in the diaphragm. Figure 5-39 shows the level of deformation for a bar that was near the fracture point. Figure 5-40 shows a few bars that actually fractured.



Figure 5-35: Specimen After Removing the Slab



Figure 5-36: Diaphragm after Demolition



Figure 5-37: Gap between Diaphragm and Web



Figure 5-38: Gap between Bottom Flanges



Figure 5-39: Deformed Rebar



Figure 5-40: Fractured Rebar

5.3 TEST SUMMARY

This research was conducted to investigate the performance of the second connection detail of the proposed steel bridge system. From the experimental results, some conclusions can be made:

1. Appreciable decrease in rigidity and increase in strains was evident in the system when subjected to heavy truck traffic over the design life of the structure. Reduction in the specimen stiffness occurred immediately and the desired load of 106 kips was reduced, requiring a higher number of load cycles.
2. From the diaphragm strain plot, crushing of the concrete between the bottom flanges and slippage of the girders in the diaphragm ultimately caused "failure" of the specimen. The ultimate load moment caused a large compressive force in the bottom flanges of the girders. These compressive forces need to be transferred through the diaphragm to the adjacent girder. Concrete between the girders crushed when it was subjected to the high amount of compression force. Crushing of the concrete continued by the increasing movement and rotation of the two girders. Concrete was no longer capable of transferring the load once it crushed and consequently there was no longer enough composite action between the concrete and the girders.
3. The deck reinforcement strain plot shows that the first yielding of rebar over the center of the pier occurred at a load of approximately 190 kips. As the moment was increased, load was shed to adjacent bars until failure of the specimen occurred at a load of 270 kips. Figure 5-30 shows strains in the reinforcement, providing insight into the compression failure mechanism of the specimen. Since some bars across the test specimen had not yielded at the ultimate load of 270 kips.
4. The design of the test specimen was based on a Strength I limit state moment of 3911 k-ft. From the experimental results, yield moment occurred near 1900 k-ft, which is approximately 48% of the demand moment.

Third Specimen

This chapter outlines the experimental observations and data at various stages in the investigation of the third specimen. The construction of the third specimen concluded in December, 2002. The fatigue test was performed between January, 2003 and August, 2003 and the experiment concluded with the ultimate load test performed in April, 2004.

6.1 SETUP AND PROCEDURES

General setup and procedures were reviewed in Chapter 3. Information specific to the third specimen is given below

6.1.1 CONSTRUCTION AND ERECTION

For specimen three, the bottom flanges of the girders were not connected to each other and there was an 8" gap between them. Plates were attached to the end of each girder as shown in Figures 6-1 and 6-2. Since no damage

was done to the pier during the testing or removal of specimen two, it was used again for the third specimen. Two of the vertical rebar anchoring the turnout over the pier were cut off during removal of the previous specimen. New bars were installed in new holes using epoxy..

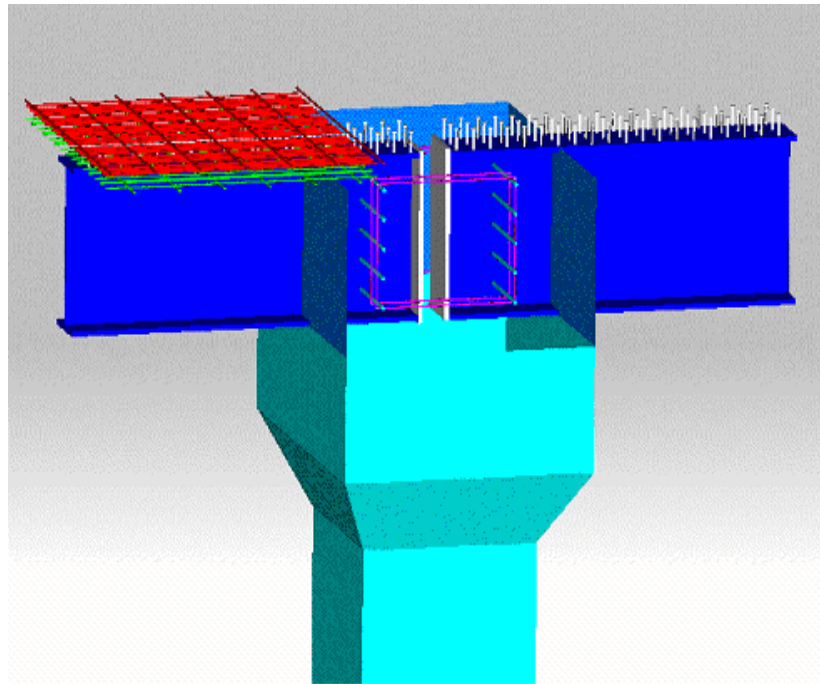


Figure 6-1: Connection Detail for the Third Specimen

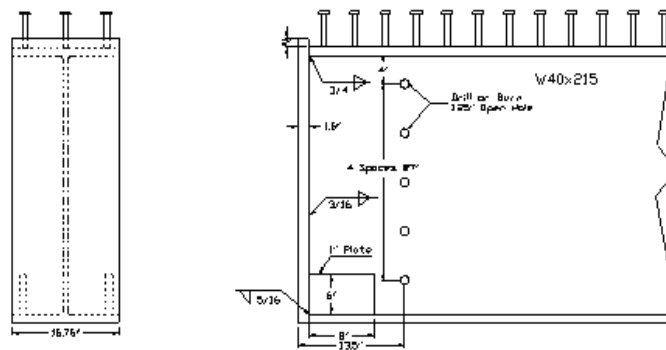


Figure 6-2: Girder End Detail

6.1.2 INSTRUMENTATION

Two separate load stages were identified for the second specimen, each requiring slightly different instrumentation. The devices included electrical strain gauges, vibrating wire embedment gauges, and potentiometers. To aid in record keeping, instruments were assigned a designation according to location and type as follows:

FG - steel surface electrical strain gauges on top or bottom flange

WG - steel surface electrical strain gauges located on the girder web

RG - steel surface electrical strain gauges located on rebar

EG - concrete embedded vibrating wire strain gauges

Pots - potentiometers

Gauges FG1 through FG41 were placed on the top surfaces of the top and bottom flanges, as shown in Figures 6-3 through 6-6. Figures 6-7 and 6-8 illustrate that gauges WG11 through WG29 were located on the webs and gusset plates. Gauges RG41 through RG55 were attached to selected reinforcing bars placed within the deck slab, as shown in Figures 6-9 and 6-10. Embedment gauges were used to monitor strains in the concrete diaphragm around the specimen centerline. Figures 6-11 and 6-12 illustrate the locations of the embedment gauges. Spring potentiometers were attached to the girders to monitor bottom flange movement into and out of the diaphragm. During the ultimate load test, string potentiometers were positioned at each load point in order to measure the deflection at that point. Figures 6-13 and 6-14 are pictures of the specimen instrumentation

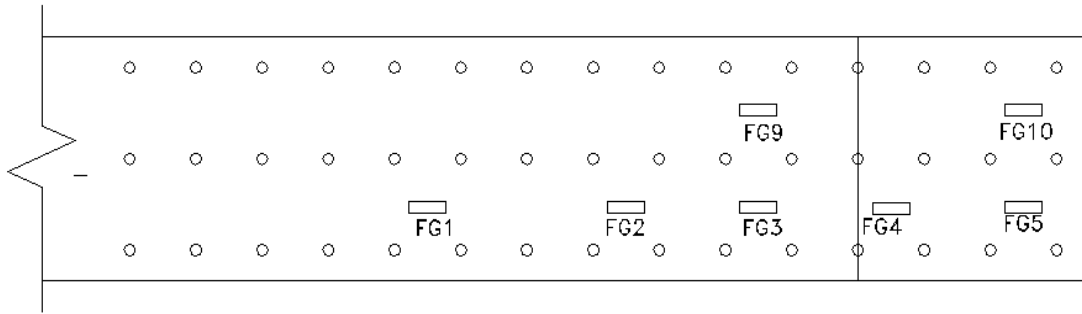


Figure 6-3: West Top Flange gauges

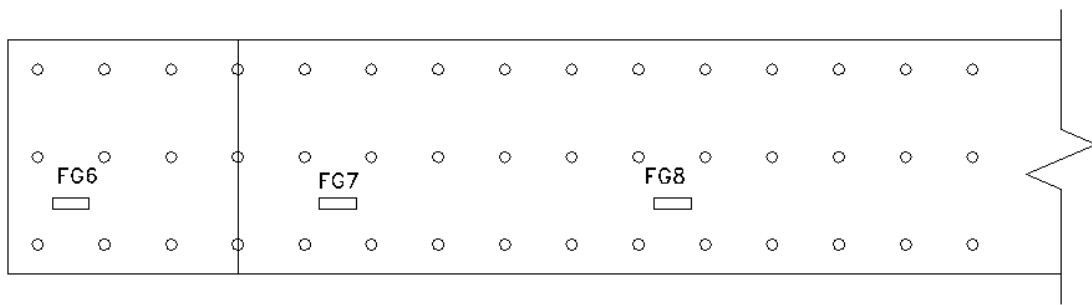


Figure 6-4: East Top Flange gauges

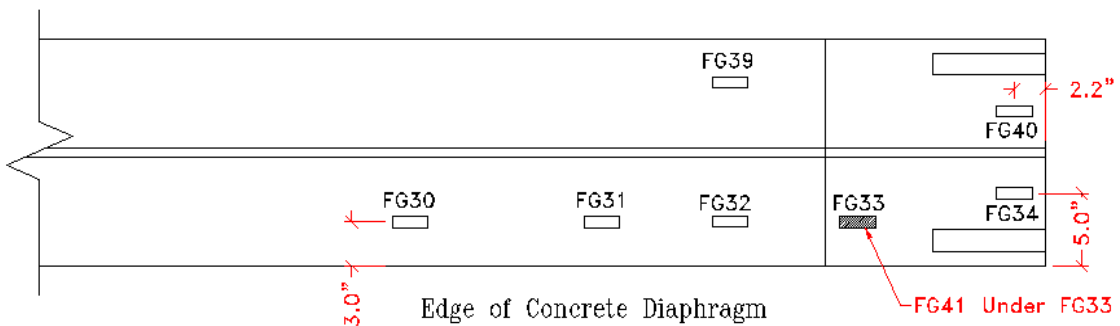


Figure 6-5: West Bottom Flange gauges

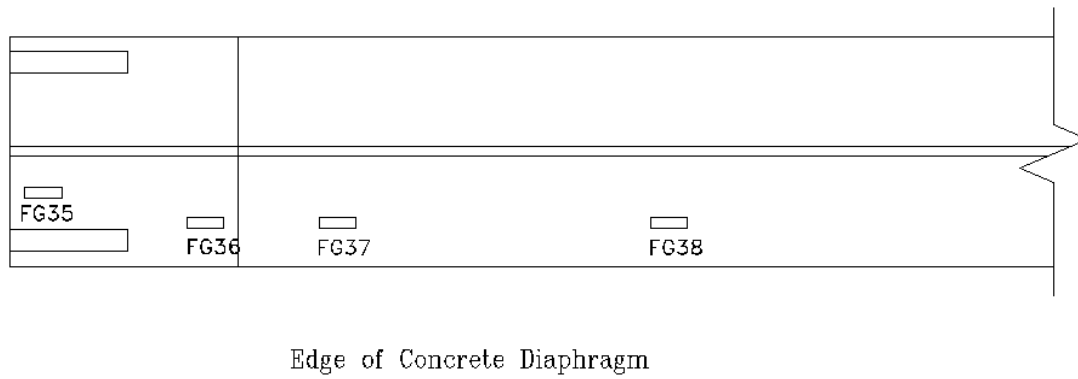


Figure 6-6: East Bottom Flange gauges

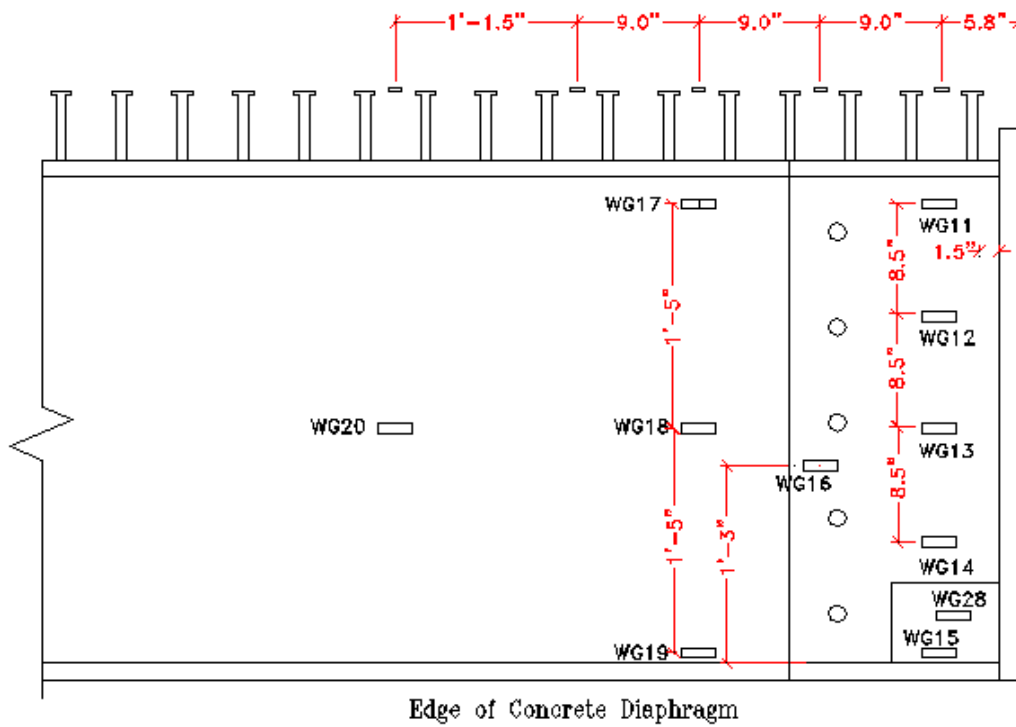


Figure 6-7: West Web gauges

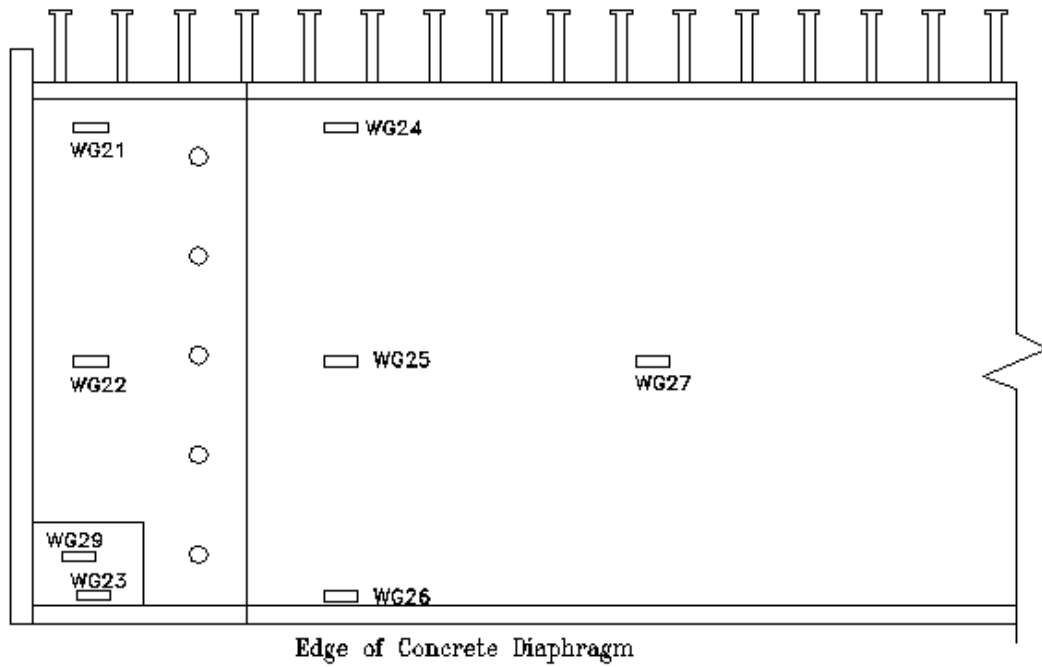


Figure 6-8: East Web gauges

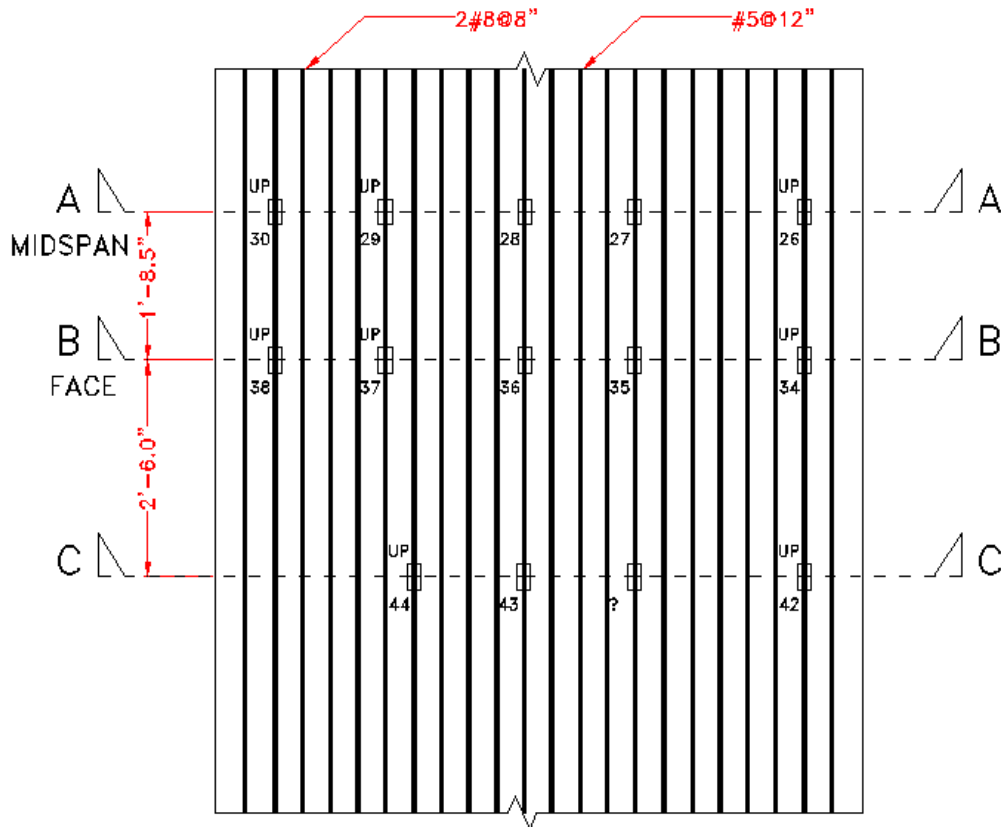


Figure 6-9: gauges in Top Layer of Reinforcement

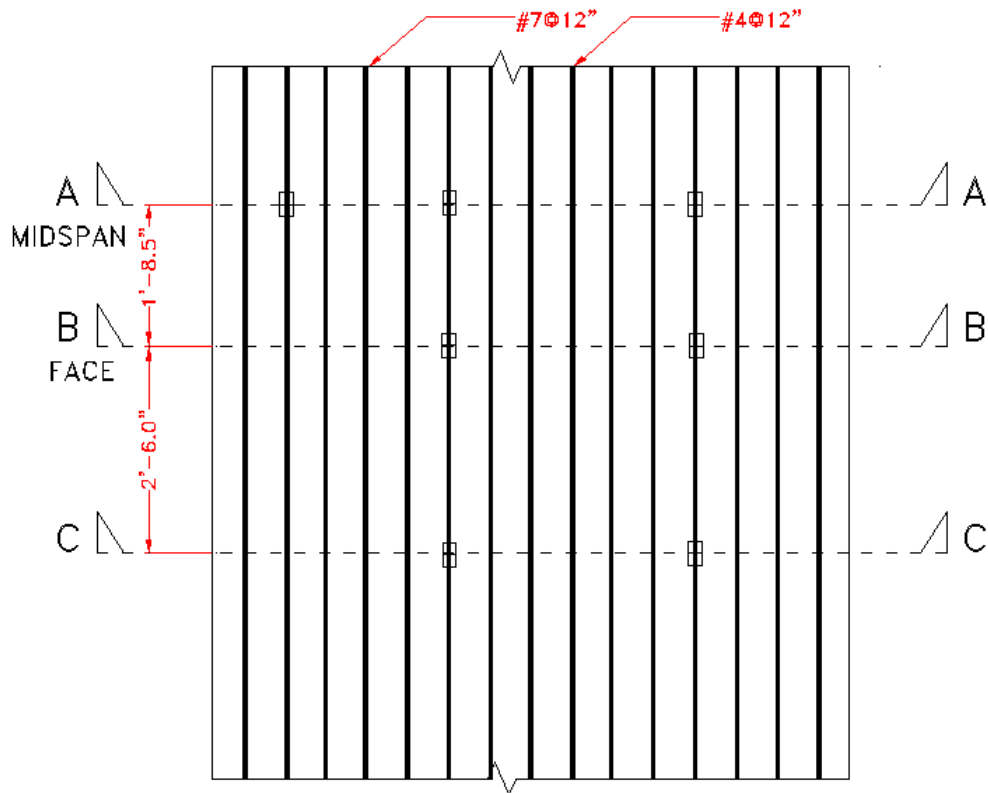


Figure 6-10: gauges in Bottom Layer of Reinforcement

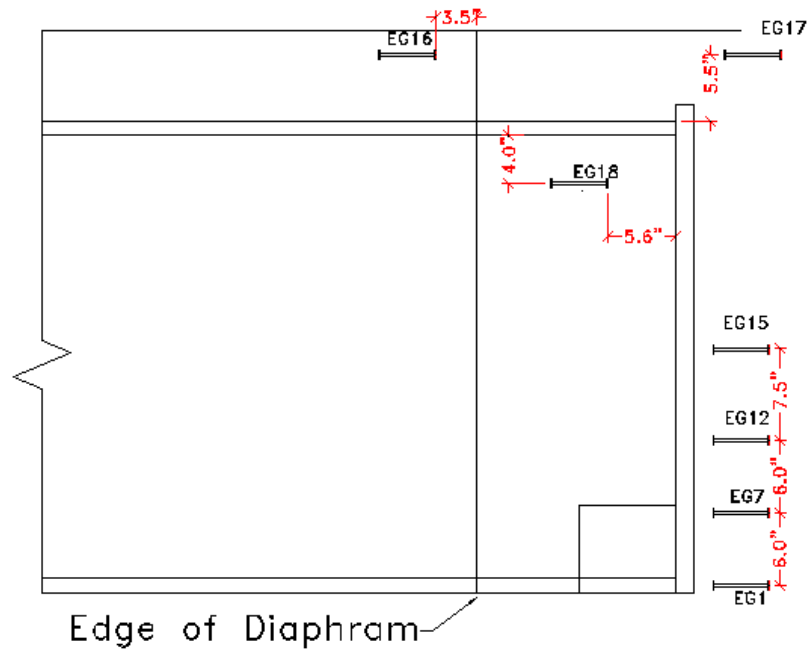


Figure 6-11: Longitudinal Location of Embedment gauges

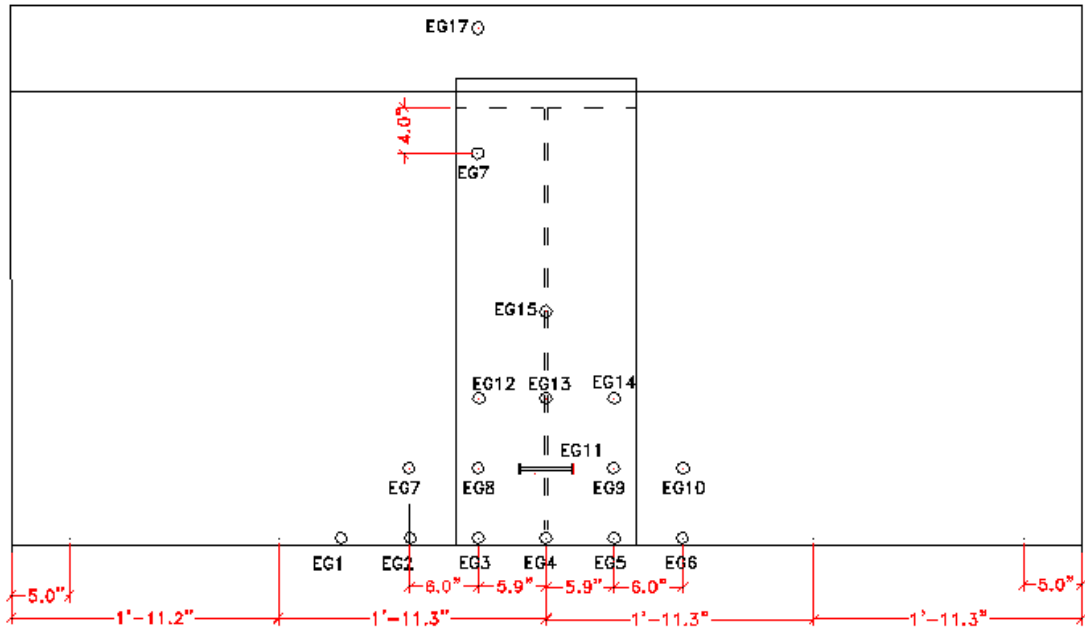


Figure 6-12: Transverse Locations of Embedment gauges

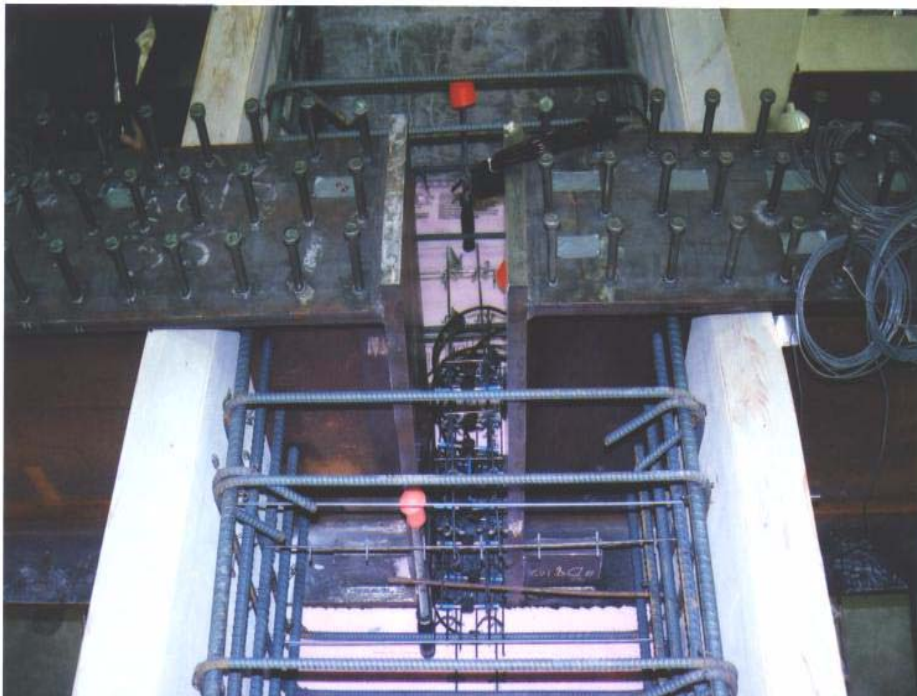


Figure 6-13: Diaphragm Instrumentation

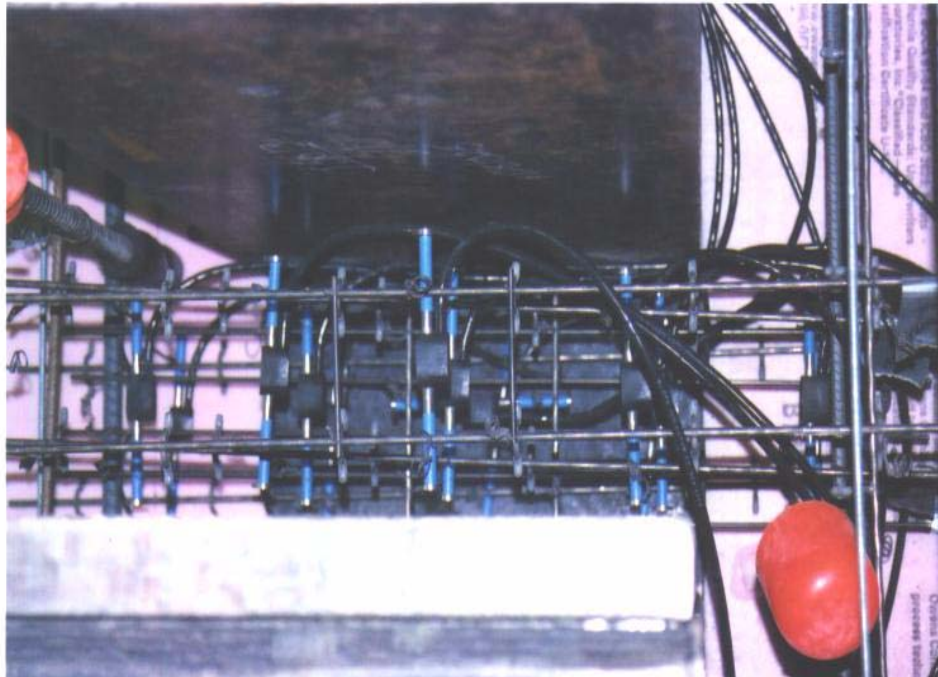


Figure 6-14: Diaphragm Embedment gauges

6.1.3 MATERIAL PROPERTIES

Several component tests were performed in order to ensure that the bridge components complied with published material specifications.

Results of the 28-day concrete compressive tests for the diaphragm concrete are shown in Figure 6-15. The 28-day compressive strengths of the two samples of diaphragm concrete were 6020 and 5780 psi. The 28-day compressive strengths of the two samples from the deck slab were 7420 and 7060 psi. Figure 6-16 shows the results of the deck concrete tests. Cylinders were also tested for the deck on the day of the first attempt at the ultimate load test. These tests yielded an average strength of 6950 psi. Cylinders for the diaphragm were tested on the day of the second attempt of the ultimate load test, averaging 4650 psi.

For the steel reinforcing materials, samples of each deck reinforcing bar size were tested in the structural lab of the University of Nebraska-Lincoln.

Results of the tensile test are shown in Table 6-1. The average reinforcing bar yield stress was approximately 70 ksi.

The bridge girders used in the third specimen came from the same stock pieces as the first specimen, therefore the girder steel was not tested again for mechanical properties.

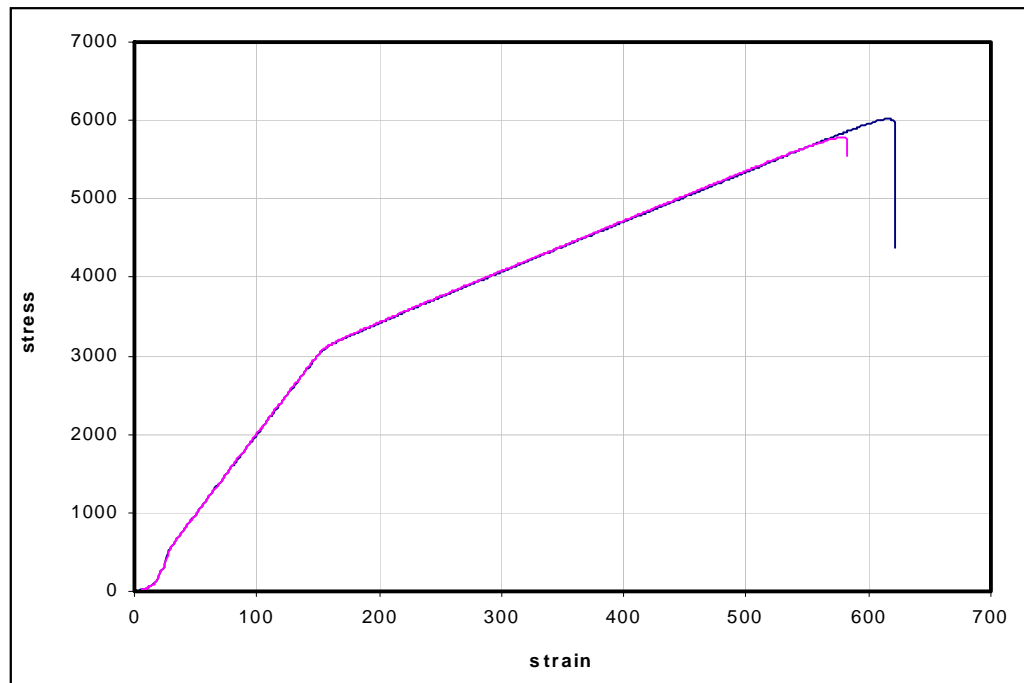


Figure 6-15: Strength Testing of Diaphragm Concrete

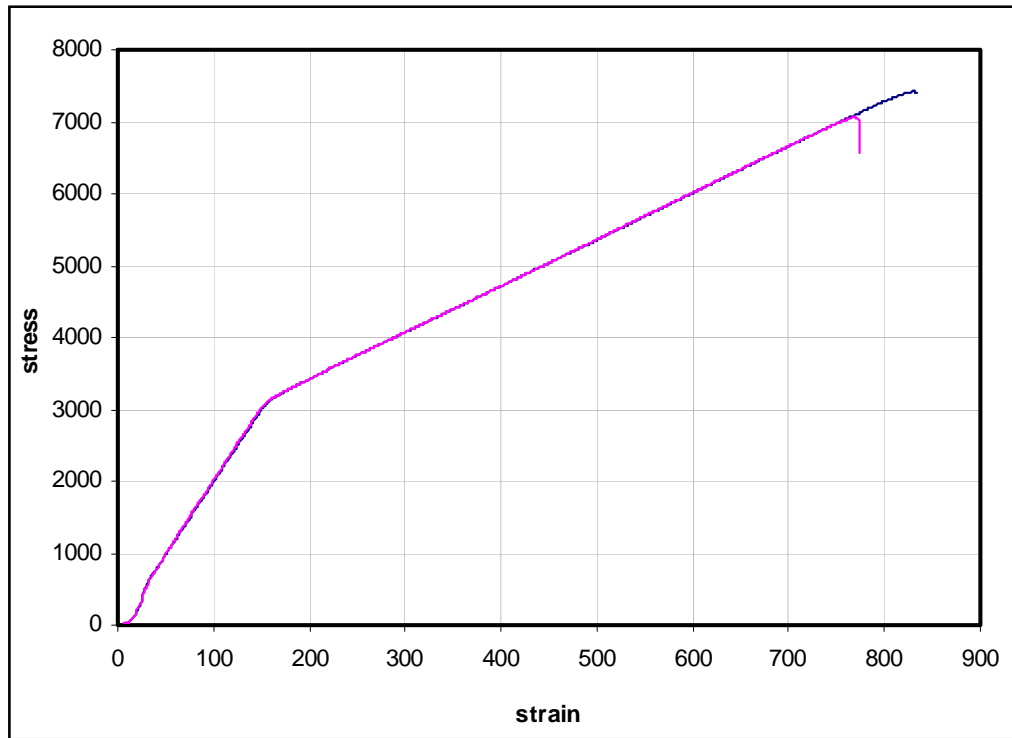


Figure 6-16: Strength Testing of Deck Concrete

	Area in ²	Yield Strength ksi	Ultimate Strength ksi
#4	0.2	70.3	113.4
#5	0.31	68.9	108.7
#7	0.6	64.3	104.6
#8	0.79	73.2	107.8

Table 6-1: Rebar Tensile Testing Results

6.2 SPECIMEN BEHAVIOR

6.2.1 FATIGUE LOAD PHASE

To begin initial cyclic loading on the third specimen, slow cycling (one cycle every ten seconds) was performed to compare calculated and actual deflections. If there was a difference, the deflection was adjusted accordingly. After applying the slow cycles, based on results from the first and second experiments, it was decided to reduce the maximum load to approximately 70 kips and increase the load steadily if the specimen did not show a significant drop in stiffness. Ten-thousand cycles were initially run and upon completion, the data was investigated prior to continuation of cycling. Based on the findings, it was decided to continue. Thirty-thousand more cycles were run, followed by data analysis, and then 40,000 more. After investigation of all data, it was determined to carry out the two million cycles. Displacement control was used through the course of the fatigue investigation. The system would then apply the desired deflection throughout the cycling test. The cycling was performed by running the test for approximately 40,000 cycles per day.

This test procedure was halted after running two million cycles in order to complete a data analysis and decide if the load should be increased. After investigation, it was decided to continue cycling the specimen by applying the increased load of 90 kips, since there was minimal deterioration of load over the course of cycling. The intent was to continue cycling until the specimen had exceeded its fatigue life. By increasing the load, fatigue life could be exceeded with fewer cycles. Once cycling continued, effort was made to run the test around the clock, stopping once per day to save data and read embedment gauges. In order to calculate the remaining number of cycles after each day of testing, a computer program was obtained to calculate the effect of each cycle on the specimen's fatigue life. The output of the program showed the percentage of the total fatigue that had been expended. Based on the percentage remaining, it could be predicted how

many more cycles were needed to exceed the total fatigue life of the specimen. The fundamental equation used in the program was derived from Equation 3-8 and is shown as Equation 6-1. Upon completion of testing, a total of 5,515,516 cycles had been run.

$$D_{accum} = \sum_{i=1}^n \left[\frac{1}{135,000,000 \left(\frac{352}{14 \cdot |P_{max,i} - P_{min,i}|} \right)^3} \right] \quad (6-1)$$

Where

D_{accum} = Fraction of fatigue life lost in specimen

n = Number of Cycles

$P_{max,i}$ = Maximum load achieved during i^{th} cycle

$P_{min,i}$ = Minimum load achieved during i^{th} cycle

Figure 6-17 shows cracking that occurred over the pier and through the depth of the deck near the edge of the diaphragm during the fatigue test. The initial cracks were observed near the diaphragm edge. Figure 6-18 shows the bottom flange of the girder where it penetrates the diaphragm. No cracking or crushing was observed during the fatigue test at this location. Figure 6-19 shows that no gap had formed between the pier and the foam around the edge of the pier during the cycling load test, similar to the previous specimen.

During the fatigue portion of the experimental investigation for the third specimen, data were collected continuously and recorded for analysis. Similar to the first two specimens, the fatigue loading frequency was set at two cycles per second.



Figure 6-17: Cracking Over the Pier and Through the Depth of the Deck



Figure 6-18: Bottom Flange Penetration of Diaphragm



Figure 6-19: Polystyrene Insulation Between the Pier and the Diaphragm

During the first two million cycles, at the beginning and the end of the day, the specimen was subjected to similar fatigue loads, but at a lower frequency (one cycle every ten seconds). These are again referred to as slow cycle tests. At the beginning and end of each day, the specimen was subjected to five slow cycles, referred to as a five slow cycle test.

During the first two million cycles, two slow cycle tests were performed each day. At the beginning of each five slow cycle test, the specimen was held at the peak end load and data were collected for all instruments, including embedment gauges.

During the application of the five slow cycles, data from all instruments except embedment gauges were collected and stored in the computer. After two million cycles, the test was run continuously, with one five slow cycle test performed at the beginning of each day.

Initially, the applied end load was 106 kips, but it was evident that it could not be continued, so the end load was reduced to approximately 70 kips. After two million cycles, the end load was increased to approximately 85 kips. This can be seen in the load-deflection plots shown in Figures 6-20 and 6-21.

The load-deflection plots were created by using five slow cycle test data from different points in cycling. Figures 6-22 and 6-23 show the maximum and minimum end loads that were applied to the system during the test. Notice that during the first two million cycles, there are two distinct lines of maximum and minimum applied loads. During this time, each day the maximum applied load would begin at approximately 70 kips, but diminish by nearly 10 kips by the end of the day's cycling. However, when cycling was started the next day, the maximum load had recovered to nearly the previous day's starting value. Once cycling began to be run continuously, this daily load shift no longer occurred. It should also be noted that the range of the applied end loads does not change from the beginning of the day to the end of the day, as seen in Figure 6-24..

Using load and deflection data, the system stiffness was found. The variation of stiffness as testing progressed can be seen in Figure 6-25. The system stiffness was defined using Equation (5-1) in Chapter 5. The plot shows stiffness values at various load cycles for each side of the system. As was the case with the second specimen, the stiffness was initially very high, but dropped soon after fatigue load was first applied. There was variability in the stiffness during the first two million cycles, but it stayed around 400,000 pounds/inch.

When the load was increased after the initial two million cycles, the stiffness dropped to about 360,000 pounds/inch and continued to decrease slightly through the rest of the testing.

Specimen Behavior

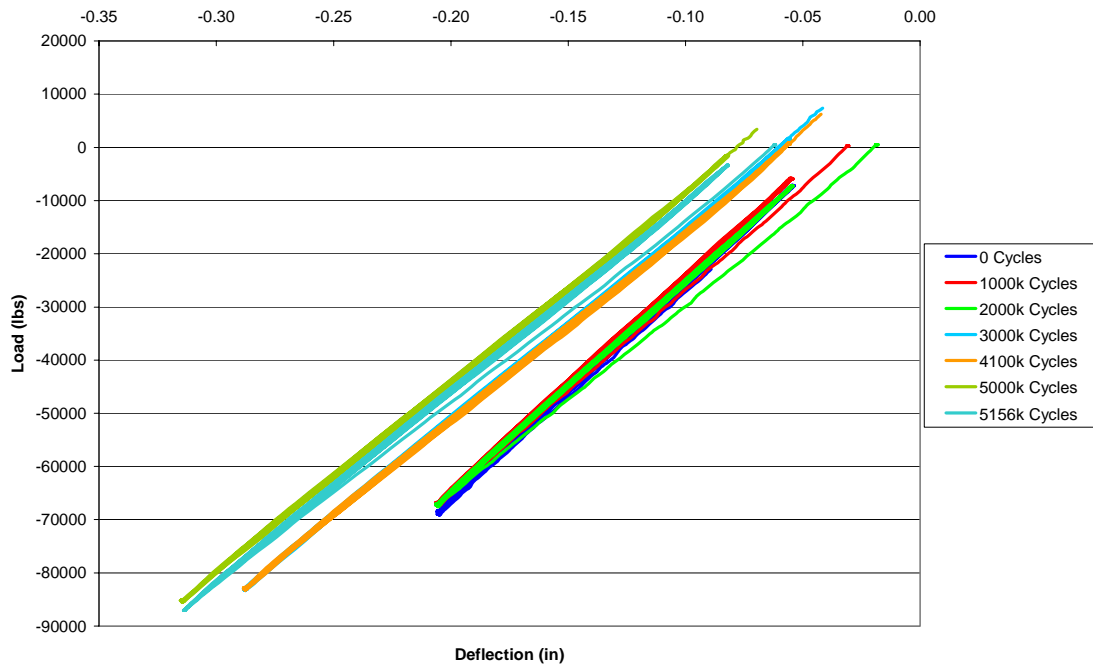


Figure 6-20: East Girder Load/Deflection Curve

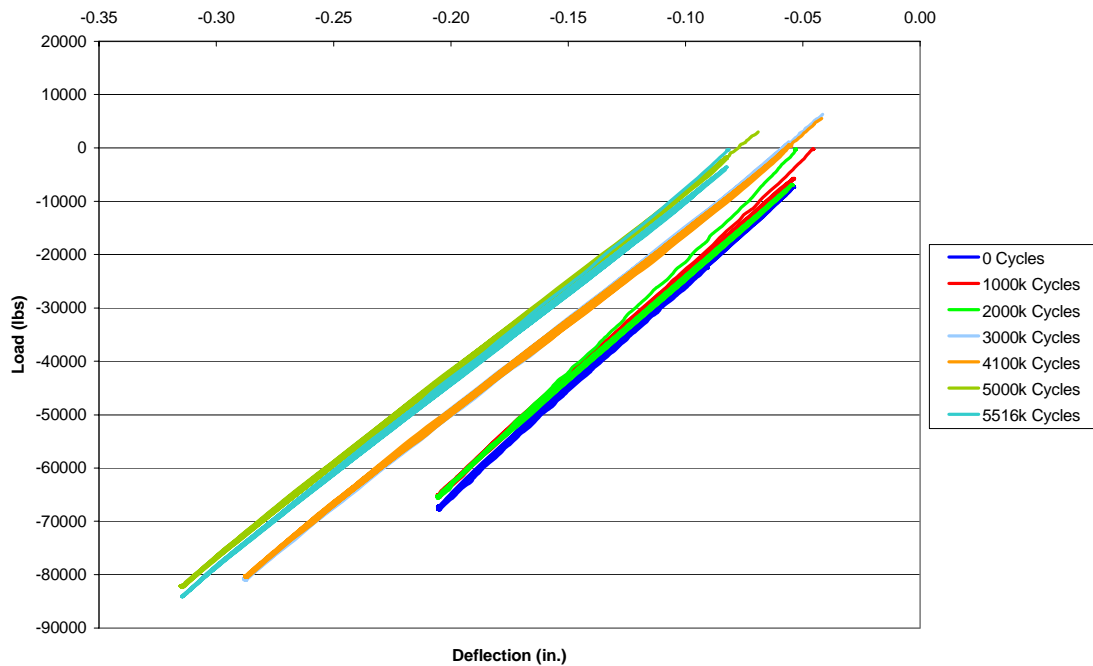


Figure 6-21: West Girder Load/Deflection Curve

Specimen Behavior

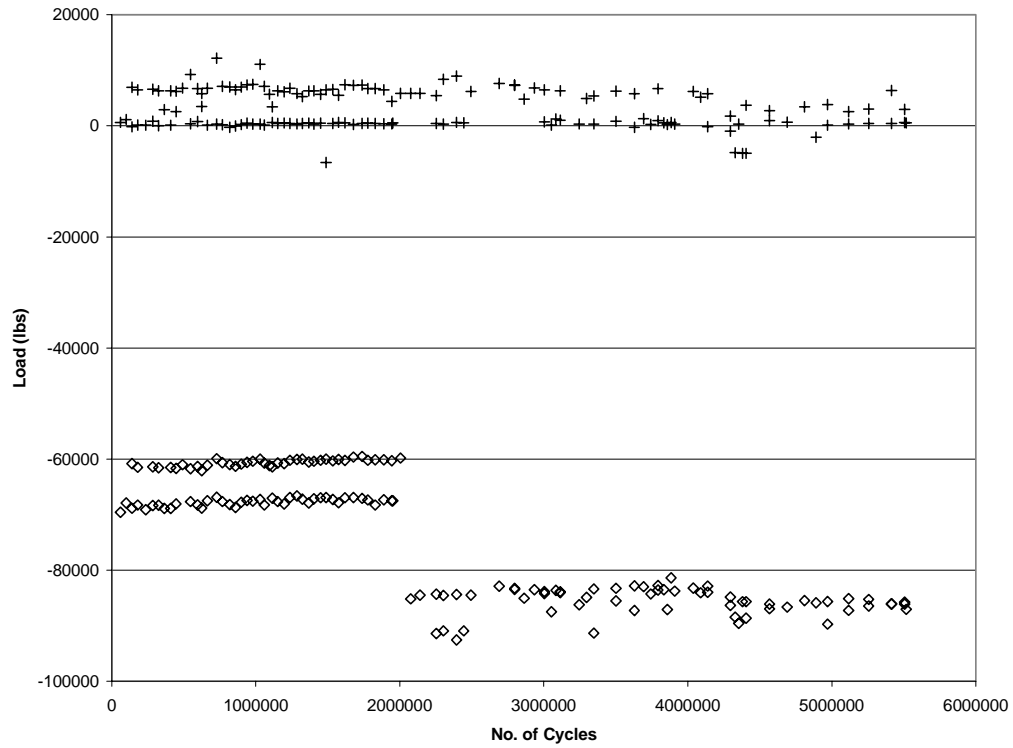


Figure 6-22: East Girder Fatigue Loading Extremes

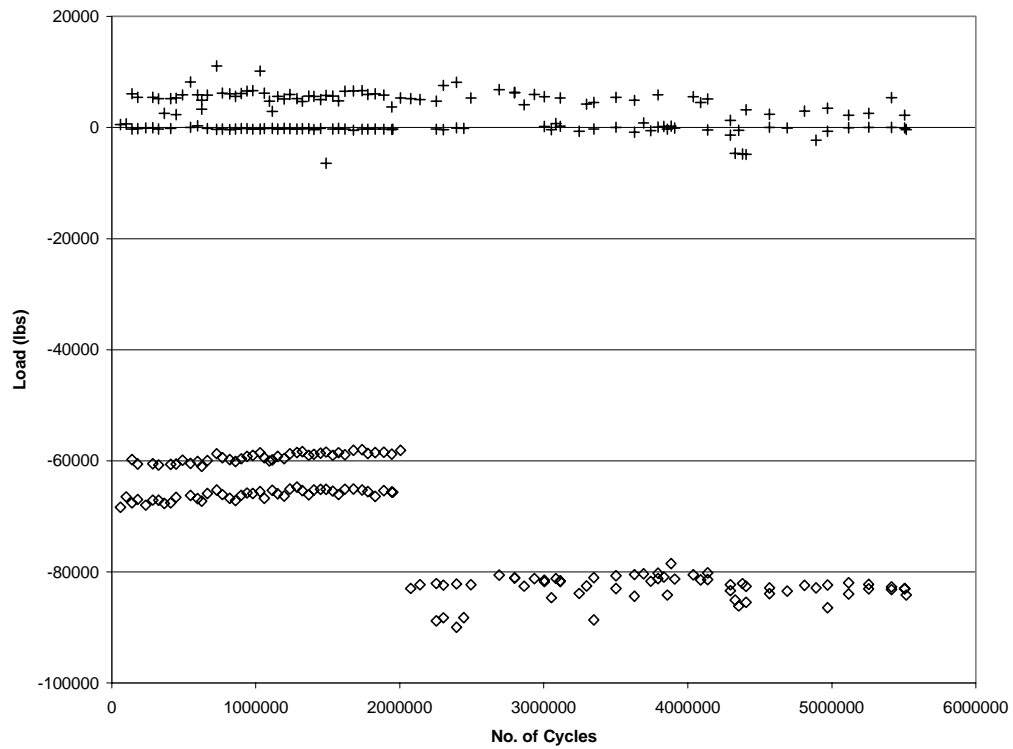


Figure 6-23: West Girder Fatigue Loading Extremes

Specimen Behavior

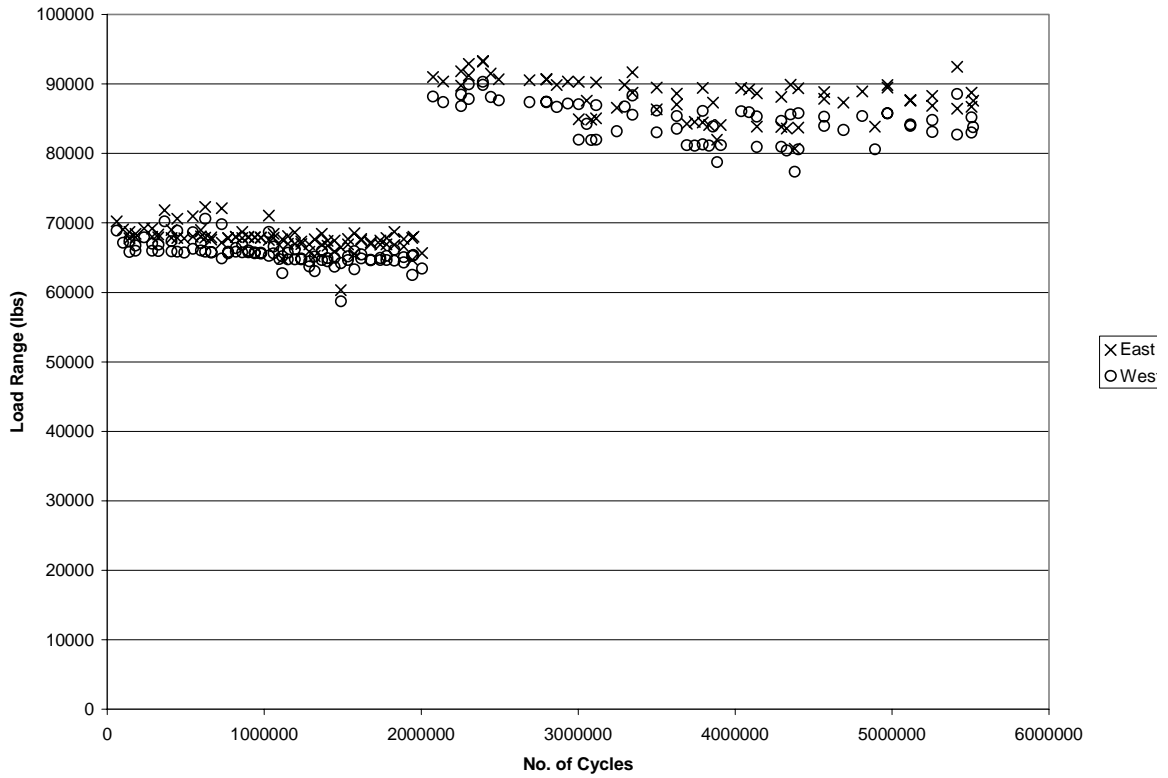


Figure 6-24: Applied Fatigue Load Ranges

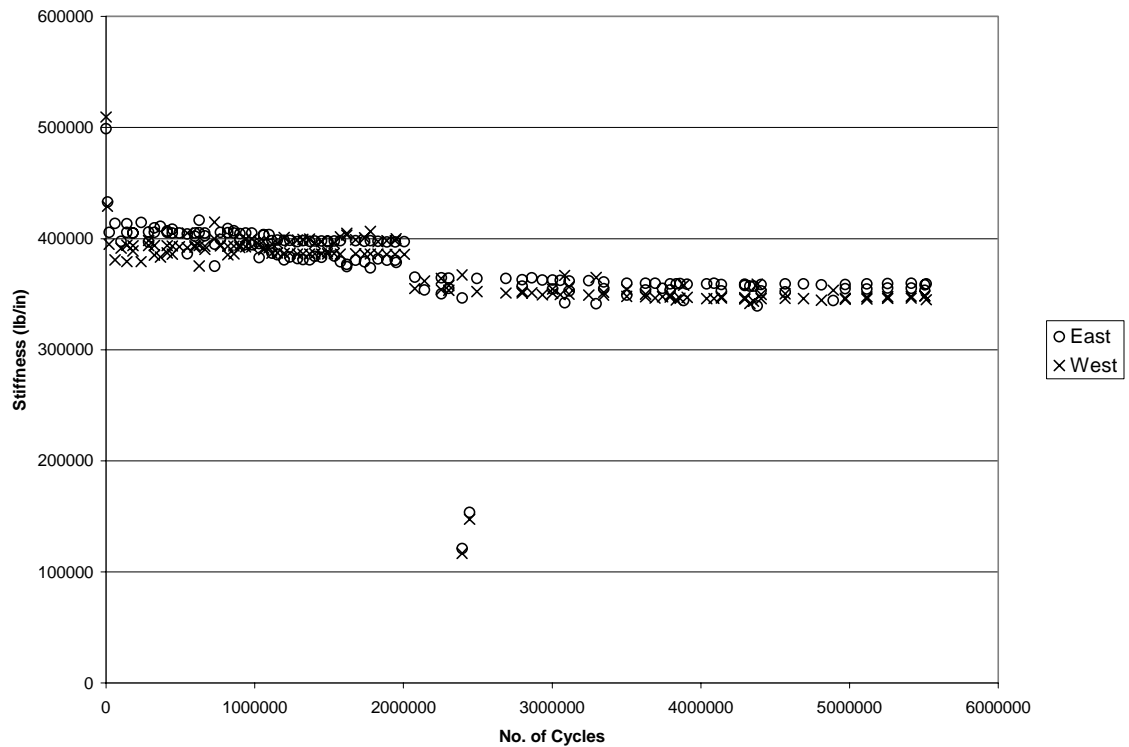


Figure 6-25: System Stiffness vs. Number of Cycles

Figure 6-26 shows strain gauge data from the bottom flanges along the length of the girders. The points shown were obtained from data recorded during the five slow cycle tests. These values are the maximum strain values for each gauge from the fifth cycle of the five slow cycle test that occurred closest to the appropriate number of cycles during the fatigue cycling test. During the first two million cycles, compressive strains in the bottom flanges varied only slightly. The exception is at location E, which is located on the bottom flange of the East girder between the web and the gusset plate. From 0 to 1,025,000 cycles, the compressive strain increased by about 50 microstrain. However, by two million cycles, the compressive strain had decreased by nearly 90 microstrain to a value of about 275 microstrain, which was less than the strain at zero cycles.

The compressive strains increased at all gauges, with the exception of location E, which decreased even more, to about 220 microstrain. Once the load was increased, compressive strains increased only very slightly during the rest of the fatigue cycling test.

Figure 6-27 shows strain gauge data from the east girder, near the centerline of the pier. The manner in which these points were obtained was explained previously. The tensile strains in the top flange and the top of the web showed little change except for when the load was increased at two million cycles, at which time the tensile strain increased. At the middle of the web, there was little change as well.

However, the compressive strain did decrease when the load was increased. Location E from Figure 6-26 is shown again here for the bottom flange as location A. As shown previously in Figure 6-26, from 0 to 1,025,000 cycles, there was an increase in compressive strain. From there, the strain decreased to below its initial value. When the load was increased, the compressive strain dropped farther. As previously mentioned, the bottom flange gauge was located between the gusset plate and the web, so in spite

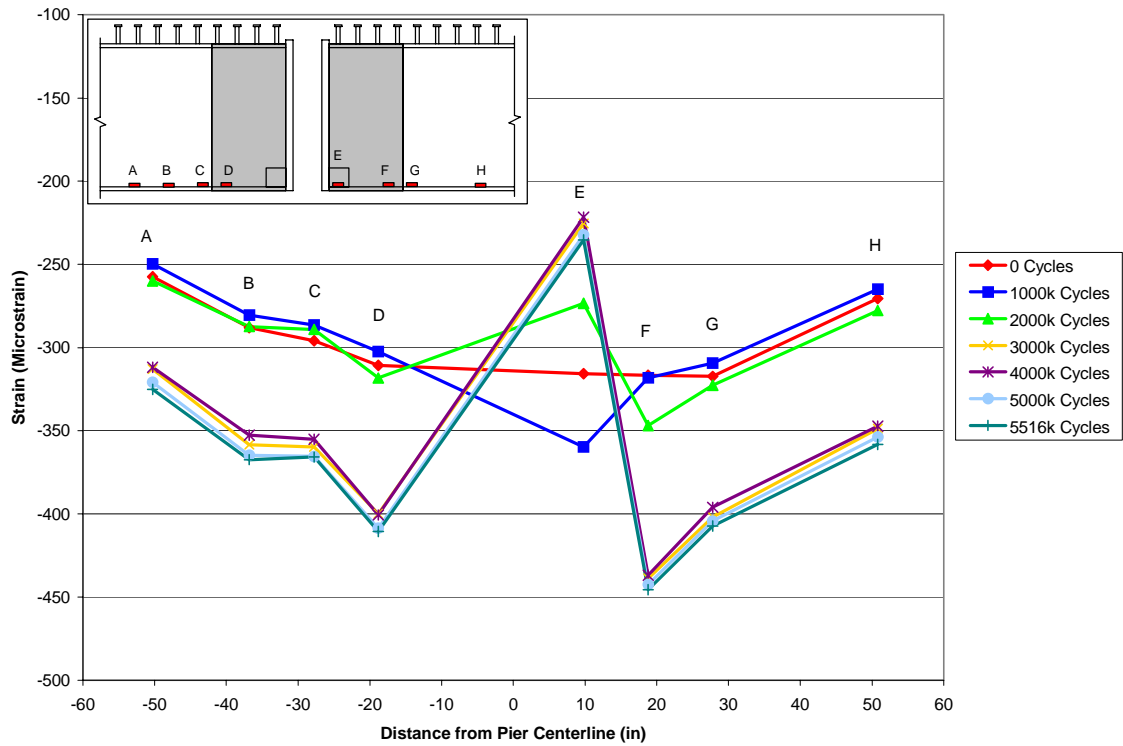


Figure 6-26: Strain Profile Along Bottom Flange

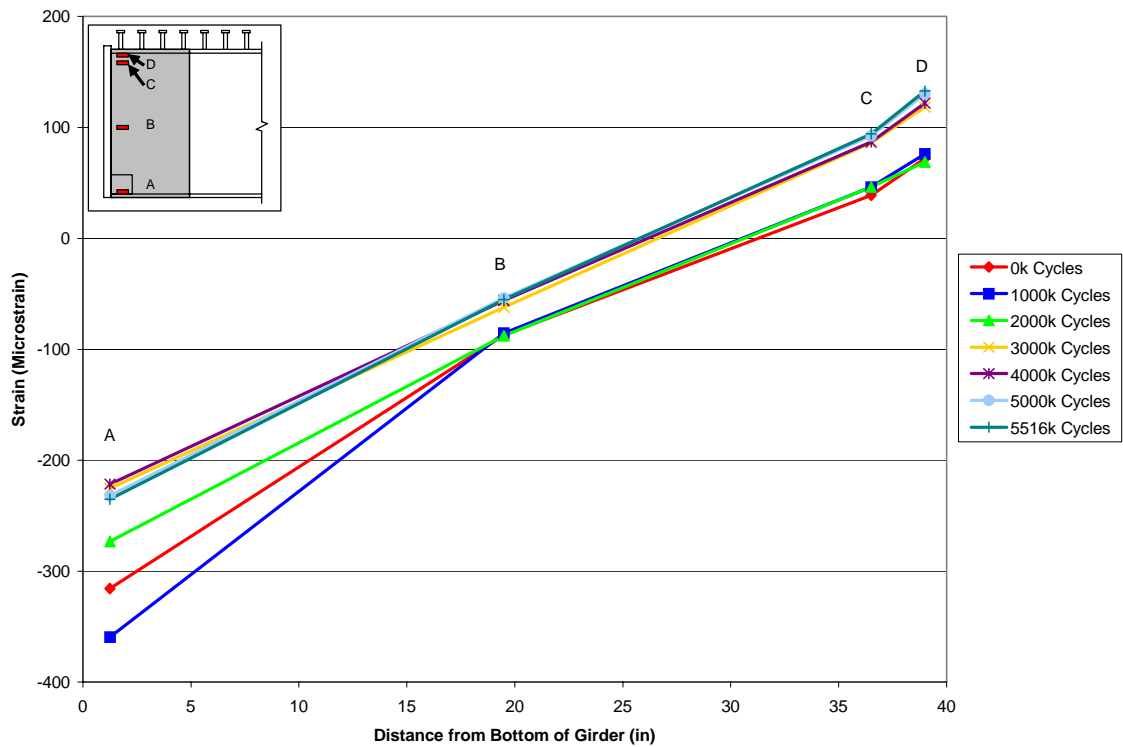


Figure 6-27: Strain Profile Near Endplates

of the fact that the compressive strains decreased at that location, it does not necessarily indicate that there was a reduction of strain across the entire flange. Unfortunately, the gauge on the gusset plate failed during cycling, so no correlation could be made with those data.

Figure 6-28 shows strain gauge data from just inside of the concrete diaphragm on the west girder. Again, there were no significant changes during the cycling, except for when the load was increased, causing tensile and compressive strains to increase. .

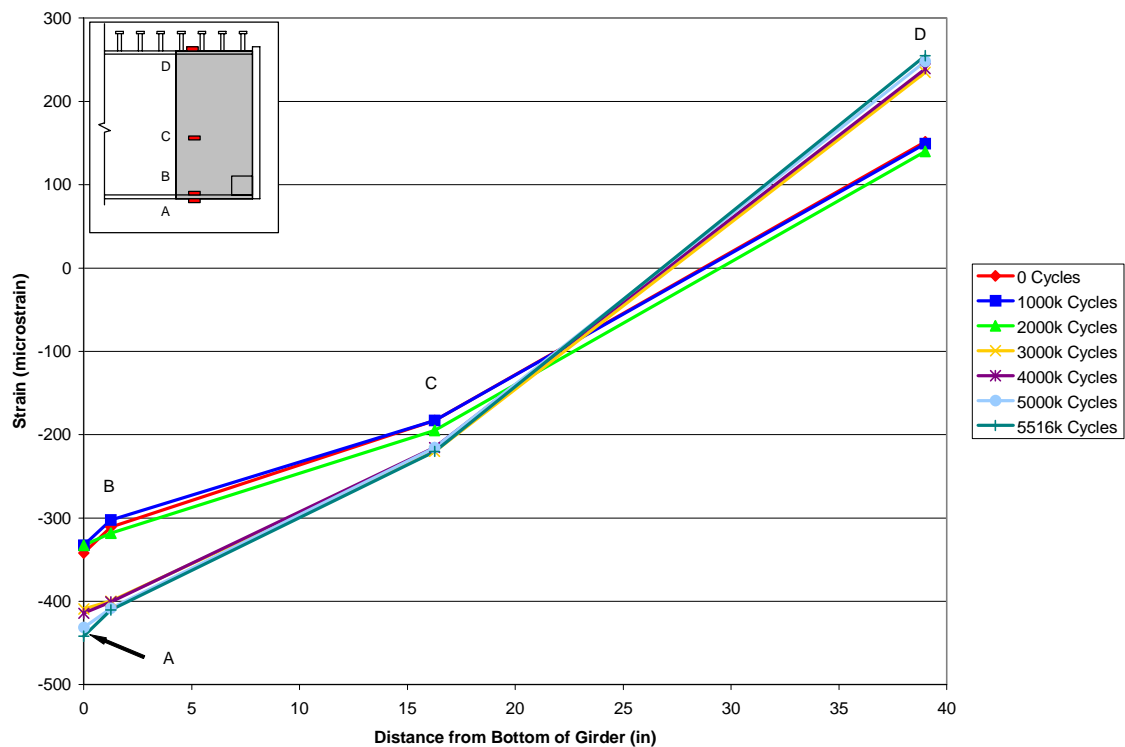


Figure 6-28: Strain Profile Near Endplates

There was a small range of variation of about 30 microstrain at the bottom of the bottom flange (location A) during the last 3,500,000 cycles. The web and flange gauges (locations C and D, respectively) showed little change as well.

Figure 6-29 shows strain gauge data from the west girder just outside of the concrete diaphragm. There was little change in tensile and compressive

strains during the first two million cycles. Compressive strains increased at locations A and B after the end load was increased, and tensile strains increased at locations D and E. There was very little change at location C, even after the change in load.

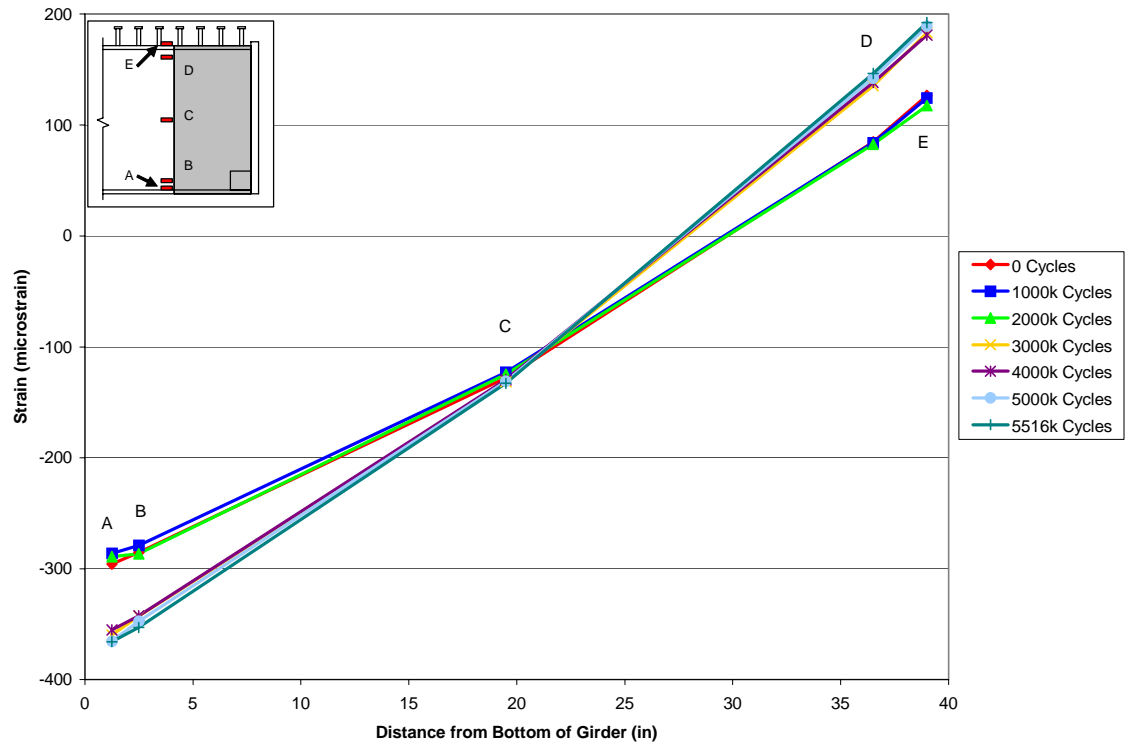


Figure 6-29: Strain Profile Outside Diaphragm

6.2.2 ULTIMATE STRENGTH TESTING

The test setup for the third specimen ultimate load test varied slightly from the first and second specimens. Hydraulic rams similar to those used in the first two tests were not available, so the setup had to be modified in order to use the different rams. The hydraulic rams were rented from F&M Mafco of Cincinnati, Ohio. Instead of a spreader beam being placed across the entire width of the deck and applying the end load outside the width of the deck, two holes were core drilled through the deck 15 feet from the cen-

terline of the pier, spaced three feet apart. The Dywidag rods were placed through the newly drilled holes, and a short spreader beam was placed between them. In the basement of the structures lab, another spreader beam was placed at the bottom end of the Dywidag rods. The hydraulic rams were placed between the ceiling and the bottom spreader bar. Therefore, the rams would apply load against the ceiling, pushing the lower spreader beam downward, and therefore applying a downward end load to the specimen. Figure 6-30 shows a drawing of the setup, and Figure 6-31 shows the setup prior to testing.

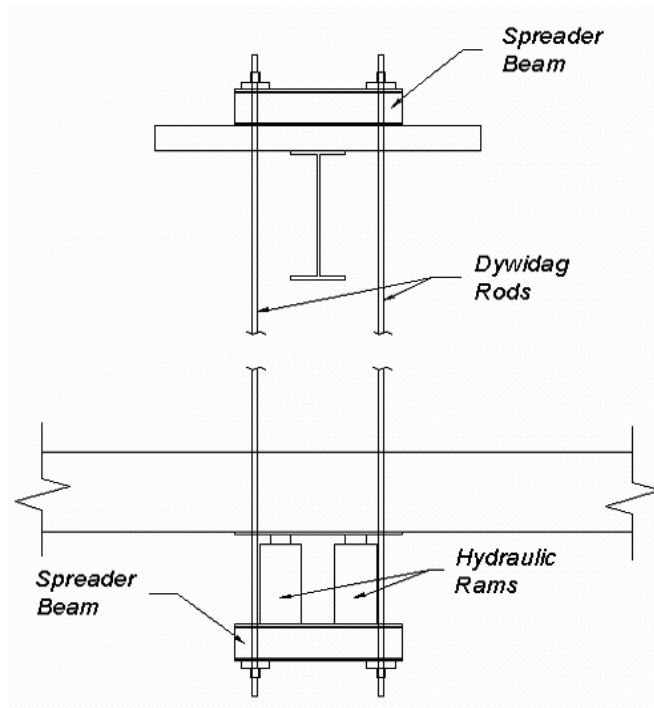


Figure 6-30: Ultimate Test Setup

Two attempts were made at performing the ultimate load test on the third specimen. During the first attempt, it was found that one of the four hydraulic rams was faulty, so the test was aborted. The ram was removed and sent for repair. When the ram was returned, it was reinstalled and the test was run.



Figure 6-31: Ultimate Test Setup

The test was performed by applying end loads in approximately 10 to 25 kip increments, referred to as load stages. At the end of each load stage, embedment gauge and pressure cell readings were recorded manually. Throughout the entire test, the Megadac was set up to record data from strain gauges, spring potentiometers, string potentiometers, pressure cells, and a load cell.

Due to a malfunction with the Megadac software, however, there were no data recorded until a load of about 340 kips had been reached. Data from the first attempt at running the test were used where appropriate to fill in some of the gap in the data. Since the highest load applied to the system at that time was approximately 74 kips, no permanent deformation would have occurred. At a load of approximately 380 kips, the hydraulic rams reached their maximum stroke, so the specimen was unloaded and the rams were re-stroked. The rams were retracted and the lower spreader beam was raised closer to the ceiling. The test was then resumed. Testing

of the specimen continued until a load of approximately 420 kips and a deflection of greater than seven inches was achieved on the east span of the specimen. The string potentiometer on the east span had retracted fully near the end of the test, and therefore no longer provided deflection measurements. The test was stopped for safety concerns. The excessive deflections had caused the Dywidag rods to bend, and further loading could have caused the rods to fail.

Figure 6-32 shows load versus deflection for the third specimen. The manual voltage readings from the pressure cells and deflections from the pen plotters were used to create Figure 6-32, since the Megadac data was unavailable for the first portion of the test, as discussed above. The graph shows that the data was linear up to approximately 300 kips, where the load began to level off for both the east and west girders. This gives a yield moment of approximately 4500 k-ft. Once the load was reapplied following re-stroking of the rams, the data was linear until it reached the original curve.

Figure 6-33 shows the displacement of the bottom flanges into the diaphragm. The maximum displacements of the bottoms of the girders were 0.58 inches for the east span and 0.51 inches for the west span. At the conclusion of the test, the permanent displacements were 0.44 inches for the east span and 0.40 inches for the west span. Since the girders were set eight inches apart during construction, the post-test distance between the flanges should have been:

$$8 - 0.44 - 0.4 = 7.16in$$

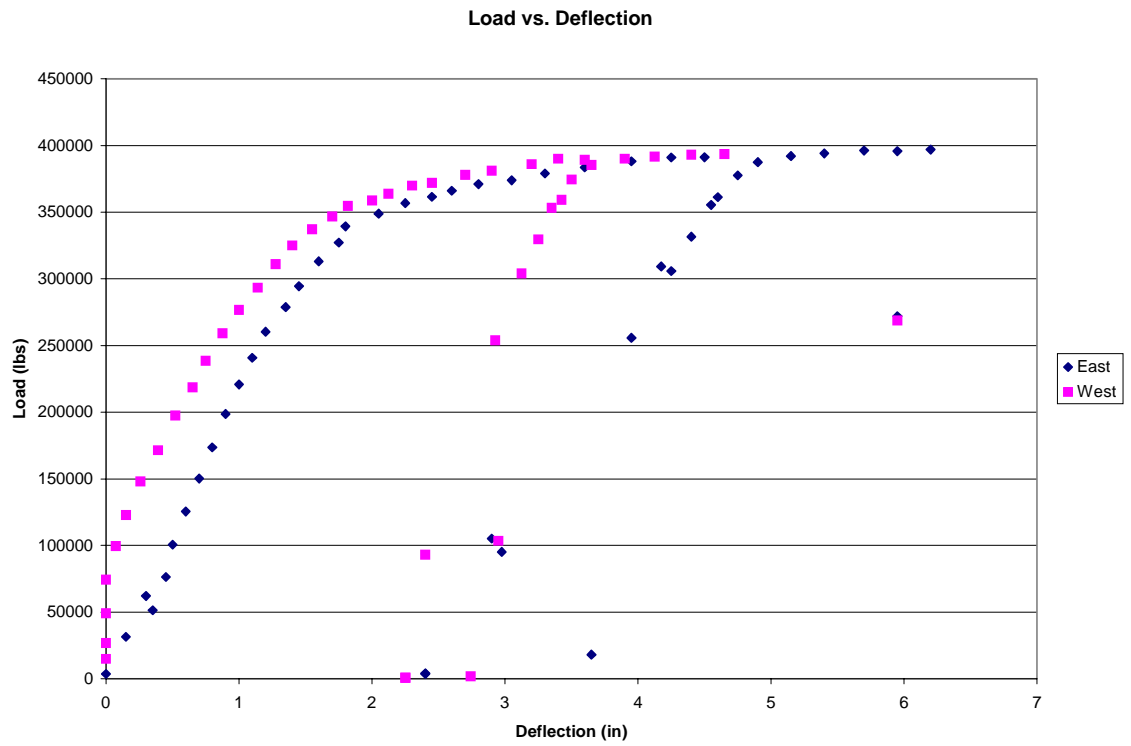


Figure 6-32: Load vs. Deflection Plot for Specimen Number 3

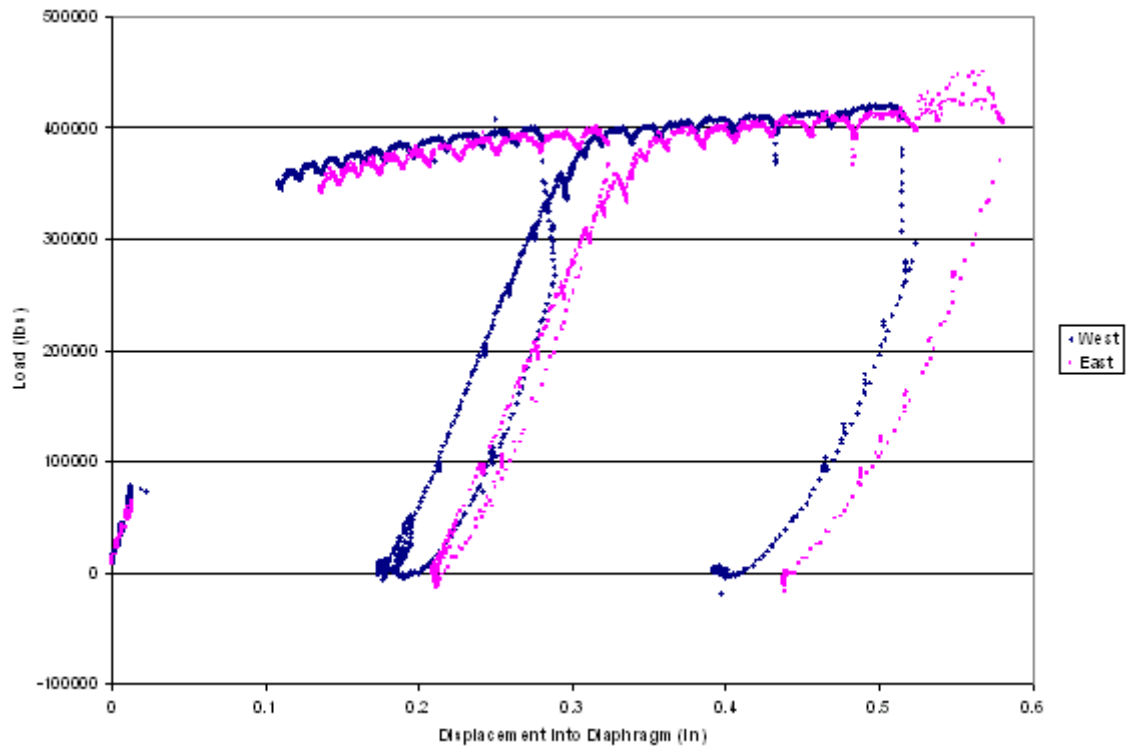


Figure 6-33: Displacements of Girder Bottom Flanges Into Diaphragm

Figure 6-34 shows embedment gauge data from outside the width of the endplates at the bottom of the diaphragm. gauges at the bottom of the diaphragm within the width of the endplates failed to read during the test. This figure shows that the compressive strains in the concrete outside the width of the endplates increased significantly as the end loads to the system were increased. This is an indication that the effective width of the compression block was wider than the width of the end plates on the ends of the girders.

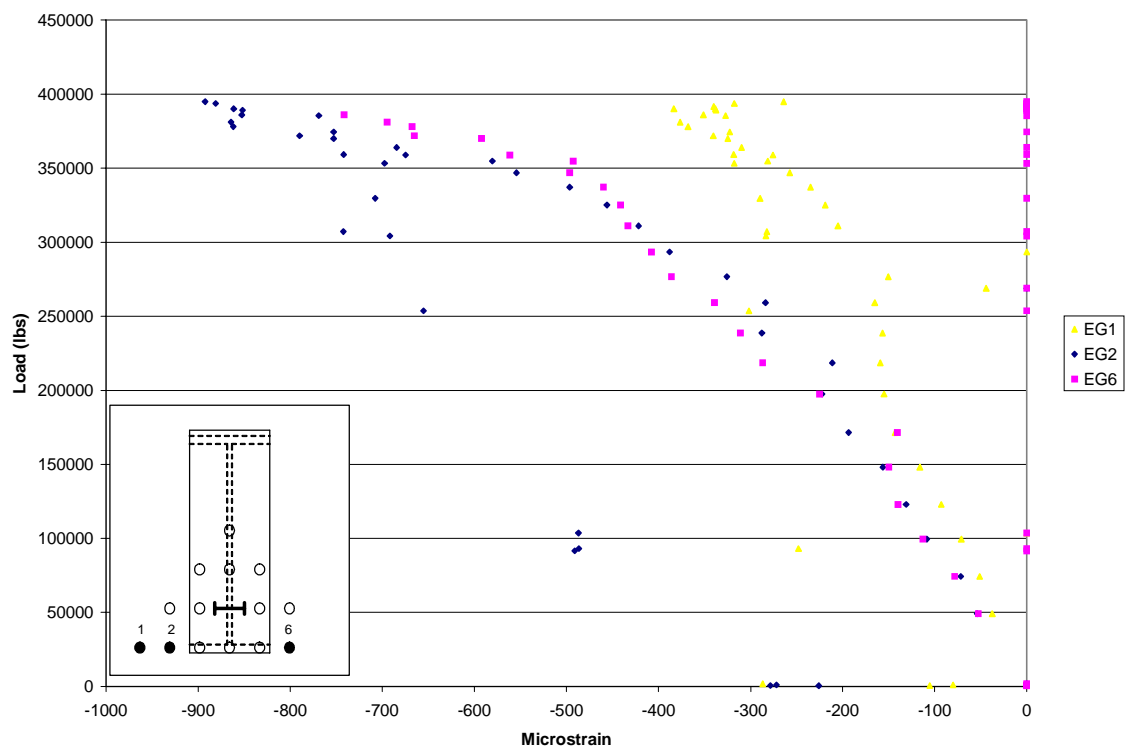


Figure 6-34: Embedment gauge Data at Bottom of Diaphragm

Figure 6-35 shows data from embedment gauges located six inches above the bottom layer of gauges. The gauges inside the width of the endplate (gauges 8 and 9) exhibit a large increase in compressive strain as the applied end load increased, but gauges 7 and 10, which lie outside the width of the end plate, show an increase in tension. However, due to the large gauge length of the embedment gauges, tensile readings are often inaccurate if a crack forms somewhere within the gauge length.

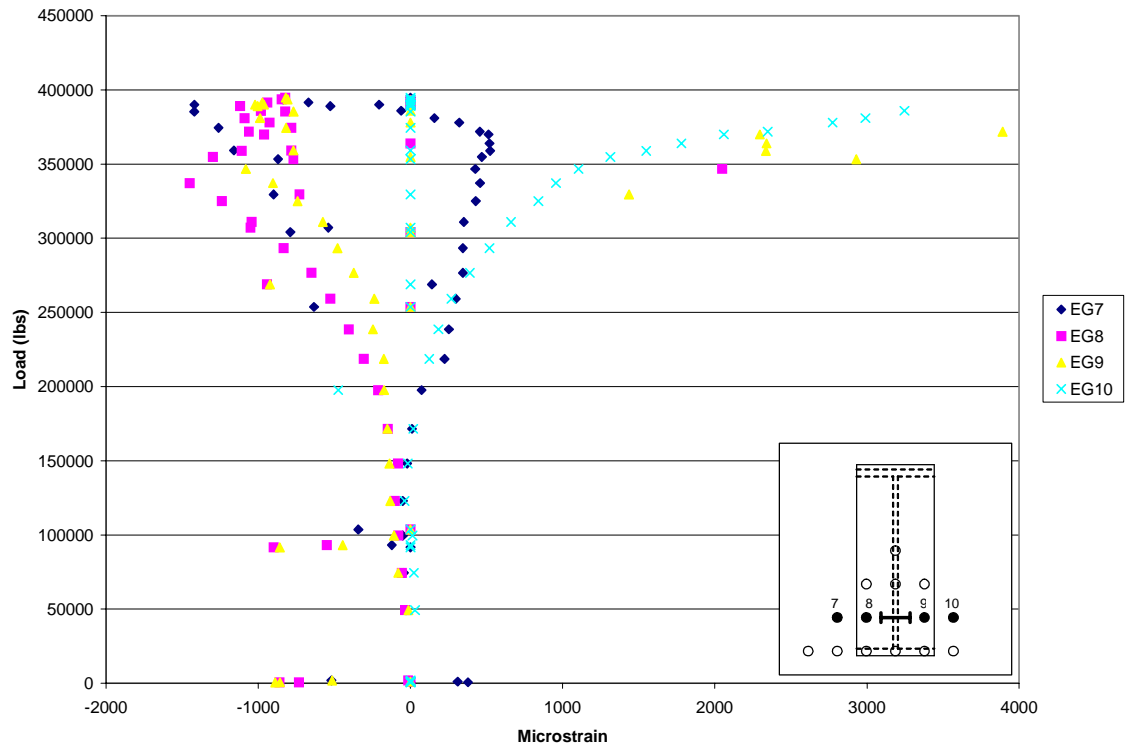


Figure 6-35: Embedment gauge Readings for the Second Layer of gauges

Figure 6-36 shows data from the three embedment gauges in the third row, which are located 12 inches from the bottom row. At this location, gauge 13, which is at the girder centerline, first shows a slight increase in compression until about 175 kips, and then begins to decrease back to nearly zero. Gauges 12 and 14 show slight tensile strains, and at about 300 kips, gauge 14 begins to show a rapid increase in tensile strain. As stated previously, however, these gauges do not accurately read tensile strains.

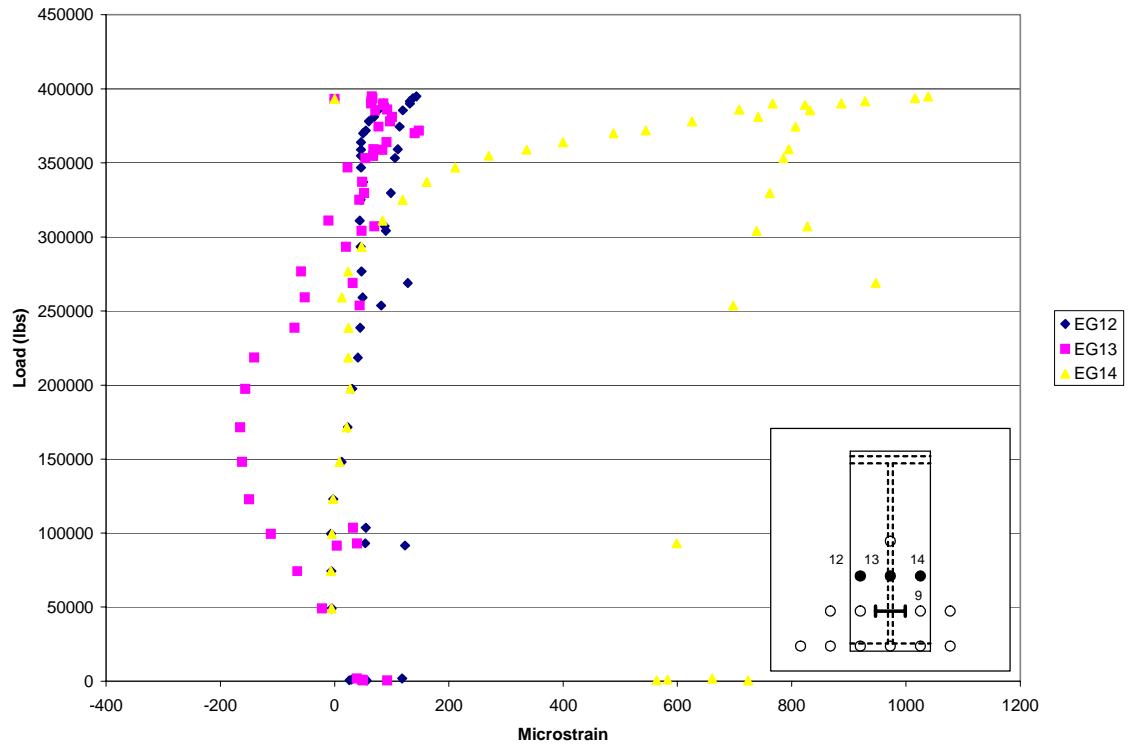


Figure 6-36: Embedment gauge Readings for the Third Layer of gauges

6.3 TEST SUMMARY

This research was conducted to investigate the performance of the third connection detail of the proposed steel bridge system. From the experimental results, several conclusions can be made:

1. Through the cycling to the end of the specimen's fatigue life, the stiffness decreased only slightly. The only major stiffness reductions occurred when load was first applied, or increased.
2. The compression block in the concrete diaphragm extends out wider than the width of the end plates attached to the girder ends.
3. The attaching of end plates to the girders resulted in less penetration into the concrete diaphragm by the bottom flanges, when compared to the second specimen on which no plates were attached.
4. The design of the test specimen was based on a Strength I limit state moment of 3911 kp-ft. From the experimental results, first yield occurred near 4500 kp-ft. A resulting over-design of approximately 15% occurred.

References

- [1] Dunker, K. F., and Rabbat, B. G., "Performance of Prestressed Concrete Highway Bridges in the United States - The First 40 Years," *PCI Journal*, Vol. 37, No. 3, May-June 1992, pp: 487-64.
- [2] AASHTO, *LRFD Bridge Design Specifications, Second Edition (w/1999 interims)*, American Association of State Highway Transportation Officials, Washington D.C., 1998.
- [3] "QCONBRIDGE," Release 1.1, (1999), Washington Department of Transportation Bridges and Structures Office.
- [4] Nebraska Department of Roads, *Bridge Office Policies and Procedures Manual (BOPP)*, Bridge Divison, Nebraska Department of Roads, 1996.
- [5] ACI Committee 318, *Building Code Requirements for Structural Concrete (ACI 318-95) and Commentary (ACI318R-95)*, American Concrete Institute, Farmington Hills, MI, 1995.

Trial Designs

A

Design calculations using the American Association of State Highway and Transportation Officials (AASHTO) Second Edition LRFD Bridge Design Specifications (1998) are presented.

A.1 95' SPAN (MILITARY ROAD GEOMETRY)

Design Assumptions

- span length = 95'
- W40 x 215 I-section girders
- number of girders = 4
- girder spacing = 8' 4"
- composite concrete slab
- slab depth = 7.5"

Calculation of Dead Loads

DC₁ Non-composite dead loads

Deck:

Interior girder, $(8''/12) \cdot (8.333') \cdot (0.15 \frac{k}{ft^3}) = 0.833 \text{ k/ft}$

Exterior girder, $(8''/12) \cdot (7.870') \cdot (0.15 \frac{k}{ft^3}) = 0.787 \text{ k/ft}$

Total DC₁

	<u>Interior Girder</u>	<u>Exterior Girder</u>
Deck	0.833	0.787
Steel	0.235	0.235
Form-work	<u>0.083</u>	<u>0.079</u>
Total DC ₁	1.151 k/ft	1.101 k/ft

DC₂ Long Term Composite Dead Load

Assume the weight per unit length of the barrier is 536 lb/ft, and all girders carry the load equally.

$$DC_2 = (0.536 * 2) / 4 = \mathbf{0.268 \text{ k/ft}}$$

DW Future Wearing Surface Load

Assume equal distribution among all girders.

$$DW = (0.025 * 30) / 4 = \mathbf{0.188 \text{ k/ft}}$$

Design Factors

Ductility η_D	1.0
Redundancy η_R	1.0
Operational Importance η_I	1.0

$$\eta = \eta_D * \eta_R * \eta_I = \mathbf{1.0}$$

Bridge is subjected to HL93 loading, the distribution factors and shear / moment envelopes are generated using QconBridge®. The shear / moment envelopes are shown on the following pages, with the distribution factors and section properties preceding.

Note: The exterior girder controls the design for flexural design and the interior controls the design for shear, as is shown in the moment and shear envelopes.

Effective Flange Width

Interior Girder:

$$\frac{1}{4} * (\text{span} * 12^{\text{in/ft}}) = \frac{1}{4} * (95' * 12^{\text{in/ft}}) = 285''$$

$$12.0 * (t_s) + (b_f/2) = 12.0 * (7.5) + (15.75/2) = \mathbf{98''} \quad (\text{controls})$$

$$\text{Spacing} = 100''$$

Exterior Girder:

$$\frac{1}{8} * (\text{span} * 12^{\text{in/ft}}) = \frac{1}{8} * (95' * 12^{\text{in/ft}}) = 143''$$

$$6.0 * (t_s) + (b_f/2) = 6.0 * (7.5) + (15.75/2) = 53''$$

$$\text{Overhang} = \mathbf{44''} \quad (\text{controls})$$

$$b_{\text{eff}} = \frac{1}{2} * \text{controlling interior} + \text{controlling exterior}$$

$$= \frac{1}{2} * 98 + 44 = \mathbf{93''} \quad (\text{governing } b_{\text{eff}})$$

Positive Flexure

Determining neutral axis (N.A.)

$$P_t = 50 * 15.75 * 1.22 = 960.75 \text{ kips}$$

$$P_c = 50 * 15.75 * 1.22 = 960.75 \text{ kips}$$

$$P_w = 50 * 36.54 * 0.65 = 1187.50 \text{ kips}$$

$$P_s = 0.85 * 4 * 93 * 7.5 = 2371.50 \text{ kips}$$

Case 1

$$P_t + P_w \geq P_c + P_s$$

$$2148.3 \not\geq 3332.25 \text{ kips}$$

N.G.

Case 2

$$P_t + P_w + P_c \geq P_s$$

$$3109.1 \geq 2371.50 \text{ kips}$$

O.K.

$$y_{bar} = \frac{t_c}{2} \left[\frac{P_w + P_t - P_s}{P_c} + 1 \right]$$

$$y_{bar} = 0.387''$$

Measured from the top of the top flange.

Plastic Moment Capacity

$$M_p = \frac{P_c}{2t_c} \left[y_{bar}^2 + (t_c - y_{bar})^2 \right] + [P_s d_s + P_w d_w + P_t d_t]$$

$$M_p = 5777 \text{ k*ft}$$

Strength Limit State

	<u>Strength I</u>	<u>Strength IV</u>
$M_{DC1} = 1192$	1490	1788
$M_{DC2} = 169$	211.3	253.5
$M_{DW} = 119$	178.5	178.5
$M_{LL+IM} = 1797$	<u>3144.8</u>	<u>N. A.</u>
	5024.5 k*ft (governs)	2220 k*ft

Ductility Requirement

$$\frac{D_p}{D'} \leq 5$$

$$D' = \beta \left(\frac{d + t_s + t_h}{7.5} \right)$$

$$D' = 0.7 * (38.98 + 7.5) / 7.5 = 4.34$$

$$D_p = 7.5 + 0.387 = 7.887$$

$$D_p / D' = 1.82 < 5$$

Section Proportional Limits

$$0.1 \leq \frac{I_{YC}}{I_Y} \leq 0.9$$

$$I_{YC} = 1/12(1.22)*(15.75)^2 = 397.2 \text{ in}^4$$

$$I_Y = 397.2 + 397.2 + 0.836 = 795.3 \text{ in}^4$$

$$I_{YC} / I_Y = 0.5$$

O.K.

Web Slenderness

$$2D_{cp} / t_w \leq 3.76 \sqrt{E / F_{yc}}$$

O.K.

(N.A. in the top flange, $D_{cp} = 0$)

Compression Flange Slenderness

$$b_f / 2t_f \leq 0.382 \sqrt{E / F_{yc}}$$

$$15.75 / 2 * 1.22 = 6.45 \leq 24.08 = \sqrt{29000 / 50}$$

O.K.

Compression Flange Bracing

O.K. (deck is braced continuously at strength limit state)

Positive Flexure Resistance

$$M_n = \frac{5M_p - 0.85M_y}{4} + \frac{0.85M_y - M_p}{4} \left(\frac{D_p}{D'} \right)$$

$$M_n = \frac{2(5820) - 0.85(4598)}{4} + \frac{0.85(4598) - 5820}{4} (1.82)$$

$$1.3 * M_y = 5977 \text{ k*ft}$$

$$M_n = 5428 \text{ k*ft}$$

$$5428 \text{ k*ft} \geq 5024.5 \text{ k*ft}$$

O.K.

Negative Flexure

Determining neutral axis (N.A.)

$$P_t = 50 * 15.75 * 1.22 = 960.75 \text{ kips}$$

$$P_c = 50 * 15.75 * 1.22 = 960.75 \text{ kips}$$

$$P_w = 50 * 36.54 * 0.65 = 1187.55 \text{ kips}$$

$$P_{rb} = 60 * 3.5 = 210 \text{ kips}$$

$$P_{rt} = 60 * 4 = 240 \text{ kips}$$

Case 1

$$P_c + P_w \geq P_t + P_{rb} + P_{rt}$$

$$2148.3 \geq 1410.75 \text{ kips} \quad \text{O.K.}$$

$$y_{bar} = \frac{D}{2} * \left[\frac{P_c - P_t - P_{rt} - P_{rb}}{P_w} + 1 \right]$$

$$y_{bar} = 11.35''$$

Measured from the bottom of the top flange.

Plastic Moment Capacity

$$M_p = \frac{P_w}{2D} \left[y_{bar}^2 + (D - y_{bar})^2 \right] + \left[P_{rt}d_{rt} + P_{rb}d_{rb} + P_t d_t + P_c d_c \right]$$

$$M_p = 4716 \text{ k*ft}$$

Strength Limit State

	<u>Strength I</u>	<u>Strength IV</u>
$M_{DC1} = 0$	0	0
$M_{DC2} = 302$	378	453
$M_{DW} = 212$	318	318
$M_{LL+IM} = 1837$	<u>3214.75</u>	<u>N. A.</u>
	3911 k*ft (governs)	771 k*ft

Section Proportional Limits

$$0.1 \leq \frac{I_{YC}}{I_Y} \leq 0.9$$

$$I_{YC} = \frac{1}{12}(1.22)(15.75)^3 = 397.2 \text{ in}^4$$

$$I_Y = 397.2 + 397.2 + .836 = 795.3 \text{ in}^4$$

$$I_{YC} / I_Y = 0.5$$

O.K.

Web Slenderness

$$\frac{2D_{cp}}{t_w} \leq 3.76 \sqrt{\frac{E}{F_{yc}}}$$

$$\frac{2 * 25.19}{0.65} = 77.51 \leq 90.55 = 3.76 \sqrt{\frac{29000}{50}}$$

$$\text{Ratio} = 0.856$$

Compression Flange Slenderness

$$\frac{b_f}{2t_f} \leq 0.382 \sqrt{\frac{E}{F_{yc}}}$$

$$\frac{15.75}{2 * 1.22} = 6.45 \leq 9.2 = \sqrt{\frac{29000}{50}}$$

$$\text{Ratio} = 0.70$$

Compression Flange Bracing

Assume adequate bracing

Negative Flexure Resistance

$$M_r = 4716 \text{ k}\cdot\text{ft}$$

$$4716 \text{ k}\cdot\text{ft} \geq 3911 \text{ k}\cdot\text{ft} \quad \text{O.K.}$$

Live Load Deflection

$$\Delta_{\text{all}} = L / 800 = 1.425''$$

$$\Delta_{\text{anl}} = 1.417'' \quad \text{O.K.}$$

Permanent Deflection

$$f_{\text{all}} = 47.5 \text{ ksi}$$

<u>Positive</u>	<u>Tension</u>	<u>Compression</u>	
M_{DC1}	$1192(12)/838.7 = 17.06$	$1192(12)/838.7 = 17.06$	
M_{DC2}	$169(12)/1015.2 = 2.00$	$169(12)/2332.4 = 0.87$	
M_{DW}	$119(12)/1015.2 = 1.41$	$119(12)/2332.4 = 0.61$	
$M_{\text{LL+IM}}$	$1797(12)^{1.3}/1103.6 = \underline{25.40}$	$1797(12)^{1.3}/6537.0 = \underline{4.29}$	
	45.86 ksi	22.83 ksi	O.K.

<u>Negative</u>	<u>Tension</u>	<u>Compression</u>	
M_{DC1}	$0^{(12)}/838.7 = 0$	$0^{(12)}/838.7 = 0$	
M_{DC2}	$302^{(12)}/1744.3 = 2.08$	$302^{(12)}/977.0 = 3.71$	
M_{DW}	$212^{(12)}/1744.3 = 1.46$	$212^{(12)}/977.0 = 2.60$	
M_{LL+IM}	$1837^{(12)1.3}/1744.3 = \underline{16.42}$	$1837^{(12)1.3}/977.0 = \underline{29.33}$	
	19.97 ksi	35.65 ksi	<u>O.K.</u>

Live Load Deflection

$$\Delta_{all} = L / 800 = 1.425''$$

$$\Delta_{anl} = 1.417''$$

O.K.

Shear Resistance

$$V_{DC1} = 52 \text{ kips} \quad * 1.25 = \quad 65 \text{ kips}$$

$$V_{DC2} = 10 \text{ kips} \quad * 1.25 = \quad 13 \text{ kips}$$

$$V_{DW} = 7 \text{ kips} \quad * 1.50 = \quad 11 \text{ kips}$$

$$V_{LL+IM} = 7 \text{ kips} \quad * 1.75 = \quad \underline{167 \text{ kips}}$$

At Strength Limit State $V_u = \mathbf{256 \text{ kips}}$

Shear Resistance V_n of Unstiffened Web

$$V_n = 0.58 * 36.54 * 0.65 * 50$$

$$= 689 \text{ kips}$$

$$V_r = 1.0 * 689 = 689 \text{ kips}$$

OK

Deck Design

Use empirical deck design, check conditions;

1. Supporting components are made of steel.
2. Deck is fully cast in place and water cured.
3. Deck has uniform thickness, except at haunches.
4. Effective length / design depth is less than 18 and greater than 6.
5. Core depth is greater than 4 inches.
6. Effective length is less than 13.5 ft.
7. Minimum slab depth is greater than 7 inches.
8. Minimum overhang is greater than 5 times the depth.
9. Deck 28 day $f'c$ is greater than or equal to 4 ksi.
10. Deck is to be composite.

From Nebraska Department of Roads Bridge Office Policies and Practice (BOPP)
Manual.

Transverse:

Top: #4 bars @ 12" spacing

Bottom: #5 bars @ 12" spacing

Longitudinal:

Minimum area of longitudinal reinforcement per inch of slab width.

$$\text{Area}_{\min} = 7.5 * 0.01 = 0.075 \text{ in}^2/\text{in}$$

$$\text{Top: } A_{\text{reinf}} = \frac{2}{3} * (0.075) = 0.05 \text{ in}^2/\text{in}$$

Use #5 bars @ 12" spacing

$$A_{\text{reinf}} = 0.31/12 * (2) = 0.052 > 0.05 \text{ in}^2/\text{in}$$

$$\text{Bottom: } A_{\text{reinf}} = \frac{1}{3} * (0.075) = 0.025 \text{ in}^2/\text{in}$$

Use #4 bars @ 12" spacing

$$A_{\text{reinf}} = 0.20/12 * (2) = 0.033 > 0.025 \text{ in}^2/\text{in}$$

Additional Reinforcement Required to Resist Strength I Design Moment.

$$M_u = 3911 \text{ k}\cdot\text{ft}$$

$$b_f = 15.75 \text{ inches}$$

$$d = 41.51 \text{ inches}$$

$$f'_c = 4.0 \text{ ksi}$$

Summing moments about the centroid of the bottom flange.

$$\Sigma M_o = 0, 0 = A_s(f_s)(d) - C_c(a/2) - M_u \quad \text{i}$$

$$\Sigma F_h = 0, 0 = A_s(f_s) - 0.85(f'_c)a(b_f) - A'_s(f'_s) \quad \text{ii}$$

Assume tension steel yields,

$$0 = A_s(2490.6) - 53.55a(a/2) - 46932$$

$$A_s(f_s) = 53.55a + 960.75$$

$$a = (60 A_s - 960.75) / 53.55$$

$$\text{Sub i - ii} \quad A_s(2490.6) = 53.55[(60 A_s - 960.75) / 53.55]^2 + 46932$$

$$A_s(2490.6) = 33.61 A_s^2 - 1076.47 A_s + 8618.49 + 46932$$

$$33.61 A_s^2 - 3567.07 A_s + 55550.49 = 0$$

$$A_s = \underline{\underline{18.96 \text{ in}^2}}$$

Check assumptions;

$$C_c - C_s = T$$

$$0.85(f'c)a(b_f) + 960.75 = 18.96(f_s)$$

$$0.85(f'c)a(b_f) = 176.85$$

$$a = 3.3 \text{ inches}$$

$$C = 3.3 / \beta = 3.885" \quad \text{OK}$$

$$f_{sa} = \frac{Z}{(d_c A)^{1/3}} \leq 0.6f_y \quad \text{Assume } Z = 130 \text{ k/in (severe exposure)}$$

$$d_c = 2 + 0.5 + 0.5 = 3"$$

$$A = 2(3) * 94 = 564 \text{ in}^2$$

$$f_{sa} = \frac{130}{11.916} = 10.9 \leq 36 = 0.6 * 60 \quad \text{OK}$$

Top Layer:

Use 2 - #8 bars between adjacent #5 bars

$$8 * 0.31 = 2.48 \text{ in}^2$$

$$14 * 0.79 = 11.06 \text{ in}^2$$

Bottom Layer:

Use 1 - #7 bar between adjacent #4 bars

$$8 * 0.2 = 1.6 \text{ in}^2$$

$$7 * 0.6 = 4.2 \text{ in}^2$$

$$A_s = 2.48 + 11.06 + 1.6 + 4.2 = 19.34 \text{ in}^2 > 18.96 \text{ in}^2 \quad \text{OK}$$

Shear Connectors

Fatigue:

$$I \text{ (steel and rebar)} = 24410 \text{ in}^4$$

pitch:

$$p = \frac{nZ_r I}{V_{sr} Q}$$

Use 5" by 3/4" diameter studs

$$n = 3, 3 \text{ per row}$$

$$Z_r = \alpha d^2 \geq 5.5d^2 / \alpha$$

$$\alpha = 34.5 - 4.28 * \text{Log}(N)$$

For $N = 2,000,000$ cycles

$$\alpha = 7.53$$

$$Z_r = 4.23 \geq 1.55$$

$$Q = 12.67 * (14.02 + (7.5 - 2)) + (6.33 * (14.02 + 2)) = 1078.4 \text{ in}^4$$

$$p = 287.2 / V_{sr}$$

Calculation of V_{sr}

$$F = M / S_{\text{bottom}}$$

$$13 = M / 977$$

$$M = 1058 \text{ k*ft (applied at 12' from centerline)}$$

$$M = V_{sr} * L$$

$$V_{sr} = 88 \text{ kips}$$

since shear is constant in the cantilever specimen

$$p = 287.2 / 88 = 3.26 \leq 4.5 = 6(.875)$$

Use 4.5" spacing

Strength:

$$Q_s = \phi_{sc} Q_n$$

$$\text{where } \phi_{sc} = 0.85$$

$$Q_n = 0.5 A_s \sqrt{f'_c E_c} \leq A_{sc} F_u$$

$$A_{sc} = 0.44 \text{ in}^2$$

$$E_c = 3605 \text{ ksi}$$

$$F_u = 60 \text{ ksi}$$

$$f'_c = 4 \text{ ksi}$$

$$Q_n = 0.5 * (0.44)(4 * (3605))^{0.5} = 26.4 \text{ kips}$$

$$A_{sc} F_u = 0.44 * (60) = 26.4 \text{ kips}$$

$$Q_r = 0.85 * (26.4) = 22.5 \text{ kips}$$

$$V_h = 19 * (60) = 1140 \text{ kips}$$

$$n = 1140 / 22.4 = 51 \text{ studs for each region}$$

$$p = (24 * 12) / (51 / 3) = 16.9" < 24"$$

O.K.

Fatigue Governs at 4.5" pitch.

Longitudinal Reinforcement

$$f_f = 21 - 0.33f_{\min} + 8\left(\frac{r}{h}\right)$$

$$f_{\min} = \frac{(302 + 212) * 12 * (14.02 + 5.5)}{24410} = 4.93 \text{ksi}$$

$$f_r = 21 - 0.33 * (4.93) + 0.8 * (0.3) = 21.77 \text{ksi}$$

$$\gamma(\Delta f) = \frac{0.75(469)(12)(14.02 + 5.5)}{24410} = 3.38 \text{ksi}$$

$$3.38 \leq 21.77 \text{ksi}$$

O.K.

Bearing Stiffeners

V_u at the interior pier section = 297 kips

If $V_u > 0.75 * \phi_b * V_n$ bearing stiffeners are required

Where $\phi_b = 1.0$

$$V_n = V_p = 0.58 * (F_{yw}) * D * (t_w)$$

$$= 0.58(50)36.54(0.65) = 689 \text{kips}$$

$$\phi_b V_n = 0.75(1.0)689 = 517$$

$$297 < 517 \text{kips}$$

Stiffeners not required

Strength Moments

Position	LL + IM				1.5	Factored		1.75(LL+IM)		Factored & Distributed Strength 1		
	DC ₁	DC ₂	DW	M+		M-	DC ₁	DC ₂	DL	M+	M-	M+
0	0	0	0	0	0	0	0	0	0	0	0	0
9.5	447	79	55	784	83	559	99	740	1372	-179	2112	561
19	795	133	93	1330	140	994	166	1299	2328	-357	3627	942
28.5	1043	163	115	1653	173	1304	204	1680	2894	-536	4574	1144
38	1192	169	119	1797	179	1490	211	1880	3145	-715	5026	1165
47.5	1242	151	106	1763	159	1553	189	1900	3086	-894	4986	1007
57	1192	109	76	1576	114	1490	136	1741	2758	-1072	4499	668
66.5	1043	42	30	1221	45	1304	53	1402	2137	-1251	3539	151
76	795	-48	-34	727	-51	994	-60	883	1272	-1690	2154	-808
85.5	447	-163	-115	265	-173	559	-204	183	463	-2048	646	-1865
95	0	-302	-212	0	-318	0	-378	-696	0	-3215	-696	-3911

Fatigue Load Combination

Position	Truck Moments (IM+1.15)		Unfactored & Distributed Fatigue Moments		Govern. Factored & Distributed Fatigue Moments		
	M+	M-	D.F.	M+	L.F.	M+	M-
0	0	0	0.709	0	0.75	0	0
9.5	521	-66	0.709	369	0.75	277	-35
19	860	-132	0.709	610	0.75	457	-70
28.5	1070	-199	0.709	759	0.75	569	-106
38	1131	-265	0.709	802	0.75	601	-141
47.5	1090	-331	0.709	773	0.75	580	-176
57	1007	-397	0.709	714	0.75	535	-211
66.5	792	-464	0.709	562	0.75	421	-247
76	469	-530	0.709	333	0.75	249	-282
85.5	185	-596	0.709	131	0.75	98	-317
95	0	-662	0.709	0	0.75	0	-352

Shear Calculations

Position	IM*(Vehicle Shears) + Lane Load										Unfactored & Distributed Shears										Total Factored Shears for Strength 1 Load Combination																																		
	Design Truck					Design Tandem					Govern. Shears					Shears					Distributed, LL + IM					1.25 DC ₁					1.25 DC ₂					1.5 DW					Factored DL					1.75*(LL + IM)					Factored & Distributed Strength Shears				
	V+	V-	V+	V-	V-	V+	V-	V+	V-	V-	V+	V-	V+	V-	V-	D.F.	V+	V-	V+	V-	V-	DC ₁	DC ₂	DW	V+	V-	V-	DC ₁	DC ₂	DW	DL	V+	V-	V+	V-	V-	V+	V-	V-																
0	112	-13	91	-10	-10	112	-13	91	-10	-10	112	-13	91	-10	-10	0.849	95	-11	11	166	91	68	13	11	95	-11	68	68	13	11	91	166	-19	258	72	72	258	72	72																
9.5	94	-13	77	-11	-11	94	-13	77	-11	-11	94	-13	77	-11	-11	0.849	80	-11	8	140	71	55	9	8	80	-11	55	55	9	8	71	140	-19	211	52	52	211	52	52																
19	78	-19	64	-20	-20	78	-19	64	-20	-20	78	-19	64	-20	-20	0.849	66	-17	5	116	51	41	5	5	66	-17	41	41	5	5	51	116	-30	166	21	21	166	21	21																
28.5	62	-31	52	-30	-30	62	-31	52	-30	-30	62	-31	52	-30	-30	0.849	53	-26	3	92	31	27	3	2	53	-26	27	27	3	2	31	92	-46	123	-15	-15	123	-15	-15																
38	48	-45	41	-40	-40	48	-45	41	-40	-40	48	-45	41	-40	-40	0.849	41	-38	-1	71	12	14	-1	-1	41	-38	14	14	-1	-1	12	71	-67	84	-55	-55	84	-55	-55																
47.5	36	-60	31	-51	-51	36	-60	31	-51	-51	36	-60	31	-51	-51	0.849	31	-51	0	53	-7	0	0	-3	31	-51	0	0	0	-3	-7	53	-89	47	-96	-96	47	-96	-96																
57	24	-74	22	-61	-61	24	-74	22	-61	-61	24	-74	22	-61	-61	0.849	20	-63	-6	36	-27	-14	-6	-6	20	-63	-14	-14	-6	-6	-27	36	-110	8	-137	-137	8	-137	-137																
66.5	15	-89	14	-72	-72	15	-89	14	-72	-72	15	-89	14	-72	-72	0.849	13	-76	-9	22	-46	-27	-9	-9	13	-76	-27	-27	-9	-9	-46	22	-132	-24	-179	-179	-24	-179	-179																
76	8	-103	8	-83	-83	8	-103	8	-83	-83	8	-103	8	-83	-83	0.849	7	-87	-8	15	-66	-41	-8	-8	8	-87	-41	-41	-8	-8	-66	15	-153	-54	-219	-219	-54	-219	-219																
85.5	3	-116	3	-93	-93	3	-116	3	-93	-93	3	-116	3	-93	-93	0.849	3	-98	-14	8	-84	-55	-14	-14	3	-98	-55	-55	-14	-14	-84	8	-172	-80	-257	-257	-80	-257	-257																
95	0	-129	0	-103	-103	0	-129	0	-103	-103	0	-129	0	-103	-103	0.849	0	-110	-17	0	-105	-68	-17	-17	0	-110	-68	-68	-17	-17	-105	0	-192	-105	-297	-297	-105	-297	-297																

Fatigue Shear Loading Combination

Position	IM*(Fatigue Truck Shears) & Lane Load		D.F.	Govern. Unfactored & Distributed Shears		L.F.	Govern. Factored & Distributed Shears	
	V+	V-		V+	V-		V+	V-
0	65	-7	0.71	46	-5	0.75	35	-4
9.5	55	-7	0.71	39	-5	0.75	29	-4
19	45	-10	0.71	32	-7	0.75	24	-5
28.5	36	-16	0.71	26	-11	0.75	19	-9
38	28	-22	0.71	20	-16	0.75	15	-12
47.5	20	-32	0.71	14	-23	0.75	11	-17
57	13	-41	0.71	9	-29	0.75	7	-22
66.5	9	-50	0.71	6	-35	0.75	5	-27
76	5	-58	0.71	4	-41	0.75	3	-31
85.5	2	-66	0.71	1	-47	0.75	1	-35
95	0	-72	0.71	0	-51	0.75	0	-38

A.2 100' SPAN (MILITARY ROAD GEOMETRY)

Design Assumptions

- span length = 100'
- W40 x 249 I-section girders
- number of girders = 4
- girder spacing = 8' 4"
- composite concrete slab
- slab depth = 7.5"

Calculation of Dead Loads

DC₁ Non-composite dead loads

Deck:

Interior girder, $(8''/12) \cdot (8.333') \cdot (0.15 \text{ k/ft}^3) = 0.833 \text{ k/ft}$

Exterior girder, $(8''/12) \cdot (7.870') \cdot (0.15 \text{ k/ft}^3) = 0.787 \text{ k/ft}$

Total DC₁

	<u>Interior Girder</u>	<u>Exterior Girder</u>
Deck	0.833	0.787
Steel	0.260	0.260
Form-work	<u>0.083</u>	<u>0.079</u>
Total DC ₁	1.176 k/ft	1.126 k/ft

DC₂ Long Term Composite Dead Load

Assume the weight per unit length of the barrier is 536 lb/ft, and all girders carry the load equally.

$$DC_2 = (0.536 * 2) / 4 = \mathbf{0.268 \text{ k/ft}}$$

DW Future Wearing Surface Load

Assume equal distribution among all girders.

$$DW = (0.025 * 30) / 4 = \mathbf{0.188 \text{ k/ft}}$$

Design Factors

Ductility η_D	1.0
Redundancy η_R	1.0
Operational Importance η_I	1.0

$$\eta = \eta_D * \eta_R * \eta_I = \mathbf{1.0}$$

Bridge is subjected to HL93 loading, the distribution factors and shear / moment envelopes are generated using QconBridge®. The shear / moment envelopes are shown on the following pages, with the distribution factors and section properties preceding.

Note: The exterior girder controls the design for flexural design and the interior controls the design for shear, as is shown in the moment and shear envelopes.

Effective Flange Width

Interior Girder:

$$\begin{aligned} \frac{1}{4} * (\text{span} * 12^{\text{in/ft}}) &= \frac{1}{4} * (100' * 12^{\text{in/ft}}) = 300'' \\ 12.0 * (t_s) + (b_f/2) &= 12.0 * (7.5) + (15.75/2) = \mathbf{98''} && \text{(controls)} \\ \text{Spacing} &= 100'' \end{aligned}$$

Exterior Girder:

$$\begin{aligned} \frac{1}{8} * (\text{span} * 12^{\text{in/ft}}) &= \frac{1}{8} * (100' * 12^{\text{in/ft}}) = 150'' \\ 6.0 * (t_s) + (b_f/2) &= 6.0 * (7.5) + (15.75/2) = 53'' \\ \text{Overhang} &= \mathbf{44''} && \text{(controls)} \end{aligned}$$

$$\begin{aligned} b_{\text{eff}} &= \frac{1}{2} * \text{controlling interior} + \text{controlling exterior} \\ &= \frac{1}{2} * 98 + 44 = \mathbf{93''} && \text{(governing } b_{\text{eff}}) \end{aligned}$$

Positive Flexure

Determining neutral axis (N.A.)

$$P_t = 50 * 15.75 * 1.42 = 1118.3 \text{ kips}$$

$$P_c = 50 * 15.75 * 1.42 = 1118.3 \text{ kips}$$

$$P_w = 50 * 36.54 * 0.75 = 1370.3 \text{ kips}$$

$$P_s = 0.85 * 4 * 93 * 7.5 = 2496.0 \text{ kips}$$

Case 1

$$P_t + P_w \geq P_c + P_s$$

$$2488.6 \not\geq 3614.3 \text{ kips}$$

N.G.

Case 2

$$P_t + P_w + P_c \geq P_s$$

$$3606.9 \geq 2496. \text{ kips}$$

O.K.

$$y_{bar} = \frac{t_c}{2} \left[\frac{P_w + P_t - P_s}{P_c} + 1 \right]$$

$$y_{bar} = 0.705''$$

Measured from the top of the top flange.

Plastic Moment Capacity

$$M_p = \frac{P_c}{2t_c} \left[y_{bar}^2 + (t_c - y_{bar})^2 \right] + [P_s d_s + P_w d_w + P_t d_t]$$

$$M_p = 6665 \text{ k*ft}$$

Strength Limit State

	<u>Strength I</u>	<u>Strength IV</u>
$M_{DC1} = 1351$	1689	2027
$M_{DC2} = 188$	235	282
$M_{DW} = 132$	198	198
$M_{LL+IM} = 1932$	<u>3381</u>	<u>N. A.</u>
	5503 k*ft (governs)	2507 k*ft

Ductility Requirement

$$\frac{D_p}{D'} \leq 5$$

$$D' = \beta \left(\frac{d + t_s + t_h}{7.5} \right)$$

$$D' = 0.7 * (39.38 + 7.5) / 7.5 = 4.375$$

$$D_p = 7.5 + 0.705 = 8.205"$$

$$D_p / D' = 1.88 < 5$$

Section Proportional Limits

$$0.1 \leq \frac{I_{YC}}{I_Y} \leq 0.9$$

$$I_{YC} = 1/12(1.42)(15.75)^3 = 462.3 \text{ in}^4$$

$$I_Y = 462.3 + 462.3 + 1.3 = 925.9 \text{ in}^4$$

$$I_{YC} / I_Y = 0.5$$

O.K.

Web Slenderness

$$2D_{cp} / t_w \leq 3.76 \sqrt{E / F_{yc}}$$

$$D_{cp} = 0 \text{ (Plastic N.A. is in slab)}$$

Compression Flange Slenderness

$$b_f / 2t_f \leq 0.382 \sqrt{E / F_{yc}}$$

$$15.75 / (2 * 1.42) = 5.55 \leq 9.2 = \sqrt{29000 / 50}$$

Compression Flange Bracing

O.K. (braced continuously at strength limit state)

Positive Flexure Resistance

$$M_n = \frac{5M_p - 0.85M_y}{4} + \frac{0.85M_y - M_p}{4} \left(\frac{D_p}{D'} \right)$$

$$M_n = \frac{2(6665) - 0.85(5307)}{4} + \frac{0.85(5307) - 6665}{4}(1.88)$$

$$1.3 * M_y = 6899 \text{ k*ft}$$

$$M_n = 6194 \text{ k*ft}$$

$$6194 \text{ k*ft} \geq 5503 \text{ k*ft}$$

O.K.

Negative Flexure

Determining neutral axis (N.A.)

$$P_t = 50 * 15.75 * 1.42 = 1118.3 \text{ kips}$$

$$P_c = 50 * 15.75 * 1.42 = 1118.3 \text{ kips}$$

$$P_w = 50 * 36.54 * 0.75 = 1370.3 \text{ kips}$$

$$P_{rb} = 60 * 3.5 = 210 \text{ kips}$$

$$P_{rt} = 60 * 4 = 240 \text{ kips}$$

Case 1

$$P_c + P_w \geq P_t + P_{rb} + P_{rt}$$

$$2488.6 \geq 1568.3 \text{ kips}$$

O.K.

$$y_{bar} = \frac{D}{2} * \left[\frac{P_c - P_t - P_{rt} - P_{rb}}{P_w} + 1 \right]$$

$$y_{bar} = 12.27''$$

Measured from the bottom of the top flange.

Plastic Moment Capacity

$$M_p = \frac{P_w}{2D} \left[y_{bar}^2 + (D - y_{bar})^2 \right] + [P_{rt}d_{rt} + P_{rb}d_{rb} + P_t d_t + P_c d_c]$$

$$M_p = 5395 \text{ k*ft}$$

Strength Limit State

	<u>Strength I</u>	<u>Strength IV</u>
$M_{DC1} = 0$	0	0
$M_{DC2} = 335$	418.75	502.5
$M_{DW} = 235$	352.5	352.5
$M_{LL+IM} = 1970$	<u>3447.5</u>	<u>N. A.</u>
	4219 k*ft (governs)	855 k*ft

Section Proportional Limits

$$0.1 \leq \frac{I_{YC}}{I_Y} \leq 0.9$$

$$I_{YC} = \frac{1}{12}(1.42)(15.75)^3 = 462.3 \text{ in}^4$$

$$I_Y = 462.3 + 462.3 + 1.3 = 925.9 \text{ in}^4$$

$$I_{YC} / I_Y = 0.5$$

O.K.

Web Slenderness

$$2D_{cp}/t_w \leq 3.76\sqrt{E/F_{yc}}$$

$$2 * 24.27 / 0.75 = 64.72 \leq 90.55 = 3.76\sqrt{29000/50}$$

Ratio = 0.71

Compression Flange Slenderness

$$b_f / 2t_f \leq 0.382\sqrt{E/F_{yc}}$$

$$15.75 / 2 * 1.42 = 5.55 \leq 9.2 = \sqrt{29000/50}$$

Ratio = 0.60

Compression Flange Bracing

Assume adequate bracing

Negative Flexure Resistance

$$M_r = 5395 \text{ k*ft}$$

$$5395 \text{ k*ft} \geq 4219 \text{ k*ft}$$

O.K.

Permanent Deflection

$$f_{all} = 47.5 \text{ ksi}$$

<u>Positive</u>	<u>Tension</u>	<u>Compression</u>	
M_{DC1}	$1351(12)/973.6 = 16.65$	$1351(12)/973.6 = 16.65$	
M_{DC2}	$188(12)/1166.8 = 1.93$	$188(12)/2450.0 = 0.92$	
M_{DW}	$132(12)/1166.8 = 1.36$	$132(12)/2450.0 = 0.65$	
M_{LL+IM}	$1932(12)1.3/1273.7 = \underline{23.66}$	$1932(12)1.3/6373 = \underline{4.29}$	
	43.61 ksi	22.95 ksi	<u>O.K.</u>

<u>Negative</u>	<u>Tension</u>	<u>Compression</u>	
M_{DC1}	$0(12)/973.6 = 0$	$0(12)/973.6 = 0$	
M_{DC2}	$335(12)/1306.8 = 3.08$	$335(12)/1045 = 3.85$	
M_{DW}	$235(12)/1306.8 = 2.16$	$235(12)/1045 = 2.70$	
M_{LL+IM}	$1970(12)1.3/1306.8 = \underline{23.52}$	$1970(12)1.3/1045 = \underline{29.41}$	
	28.75 ksi	35.95 ksi	<u>O.K.</u>

Live Load Deflection

$$\Delta_{all} = L / 800 = 1.5''$$

$$\Delta_{anl} = 1.439'' \quad \text{O.K.}$$

Shear Resistance

Positive

$$V_{DC1} = 56 \text{ kips} \quad * 1.25 = \quad 70 \text{ kips}$$

$$V_{DC2} = 10 \text{ kips} \quad * 1.25 = \quad 13 \text{ kips}$$

$$V_{DW} = 7 \text{ kips} \quad * 1.50 = \quad 11 \text{ kips}$$

$$V_{LL+IM} = 97 \text{ kips} \quad * 1.75 = \quad \underline{170 \text{ kips}}$$

$$\text{At Strength Limit State} \quad \mathbf{V_u = 263 \text{ kips}}$$

Shear Resistance V_n of Unstiffened Web

$$V_n = 0.58 * 36.54 * 0.75 * 50$$

$$= 857 \text{ kips}$$

$$V_r = 1.0 * 857 = 857 \text{ kips}$$

$$857 > 263 \text{ kips}$$

OK

Negative

$$V_{DC1} = 56 \text{ kips} \quad * 1.25 = \quad 70 \text{ kips}$$

$$V_{DC2} = 17 \text{ kips} \quad * 1.25 = \quad 21 \text{ kips}$$

$$V_{DW} = 12 \text{ kips} \quad * 1.50 = \quad 18 \text{ kips}$$

$$V_{LL+IM} = 111 \text{ kips} \quad * 1.75 = \quad \underline{194 \text{ kips}}$$

$$\text{At Strength Limit State} \quad \mathbf{V_u = 304 \text{ kips}}$$

Shear Resistance V_n of Unstiffened Web

$$V_n = 0.58 * 36.54 * 0.75 * 50$$

$$= 857 \text{ kips}$$

$$V_r = 1.0 * 857 = 857 \text{ kips}$$

$$857 > 304 \text{ kips}$$

O.K.

Strength 1 Moments																
Position	LL + IM			1.25			1.25			1.5			Factored & Distributed Strength 1			
	DC ₁	DC ₂	DW	M+	M-	DC ₁	DC ₂	DW	DC ₂	DW	DL	M+	M-	y	M+	M-
0	0	0	0	0	0	0	0	0	0	0	0	0	0	1	0	0
10	507	87	61	841	-110	633	109	92	109	92	834	1471	-192	1	2305	642
20	901	147	103	1428	-219	1126	184	155	184	155	1464	2499	-383	1	3963	1082
30	1182	181	127	1778	-328	1478	226	191	226	191	1895	3111	-575	1	5006	1320
40	1351	188	132	1932	-438	1689	235	198	235	198	2122	3381	-767	1	5503	1355
50	1408	168	118	1896	-548	1759	210	177	210	177	2146	3318	-959	1	5464	1187
60	1351	121	85	1694	-657	1689	151	128	151	128	1968	2965	-1150	1	4933	818
70	1182	47	33	1313	-767	1478	59	50	59	50	1586	2298	-1342	1	3884	244
80	901	-54	-38	783	-1039	1126	-68	-57	-68	-57	1002	1370	-1818	1	2372	-817
90	507	-181	-127	283	-1262	633	-226	-191	-226	-191	217	494	-2209	1	711	-1992
100	0	-335	-235	0	-1970	0	-419	-353	-419	-353	-771	0	-3448	1	-771	-4219

Fatigue Load Combination														
Position	Fatigue Truck Moments (IM+1.15)			Unfactored & Distributed Fatigue Moments			Govern. Factored & Distributed Fatigue Moments							
	M+	M-	D.F.	M+	M-	D.F.	M+	M-	L.F.	M+	M-	L.F.	M+	M-
0	0	0	0.709	0	0	0.709	0	0	0.75	0	0	0.75	0	0
10	557	-71	0.709	395	-50	0.709	395	-50	0.75	296	-38	0.75	296	-38
20	921	-141	0.709	653	-100	0.709	653	-100	0.75	490	-75	0.75	490	-75
30	1148	-212	0.709	814	-150	0.709	814	-150	0.75	610	-113	0.75	610	-113
40	1215	-283	0.709	861	-201	0.709	861	-201	0.75	646	-150	0.75	646	-150
50	1173	-353	0.709	832	-250	0.709	832	-250	0.75	624	-188	0.75	624	-188
60	1080	-424	0.709	766	-301	0.709	766	-301	0.75	574	-225	0.75	574	-225
70	849	-495	0.709	602	-351	0.709	602	-351	0.75	451	-263	0.75	451	-263
80	505	-565	0.709	358	-401	0.709	358	-401	0.75	269	-300	0.75	269	-300
90	197	-636	0.709	140	-451	0.709	140	-451	0.75	105	-338	0.75	105	-338
100	0	-707	0.709	0	-501	0.709	0	-501	0.75	0	-376	0.75	0	-376

Shear Calculations

IM* (Vehicle Shears) + Lane Load

Unfactored & Distributed

Position	Design Truck		Design Tandem		Govern. Shears		Shears	
	V+	V-	V+	V-	V+	V-	V+	V-
0	114	-13	92	-10	114	-13	97	-11
10	96	-13	78	-11	96	-13	82	-11
20	79	-19	65	-20	79	-20	67	-17
30	64	-32	52	-30	64	-32	54	-27
40	49	-47	41	-41	49	-47	42	-40
50	36	-61	31	-51	36	-61	31	-52
60	25	-76	22	-62	25	-76	21	-65
70	15	-90	15	-73	15	-90	13	-76
80	8	-105	8	-84	8	-105	7	-89
90	3	-118	3	-95	3	-118	3	-100
100	0	-131	0	-105	0	-131	0	-111

Total Factored Shears for Strength 1 Load Combination

Position	Distributed. LL + IM				1.25 DC ₁				1.25 DC ₂				1.5 DW				Factored DL				1.75*(LL + IM)				Factored & Distributed Strength Shears			
	DC ₁	DC ₂	DW	V+	V-	DC ₁	DC ₂	DW	V+	V-	DC ₁	DC ₂	DW	V+	V-	DL	V+	V-	V+	V-	V+	V-	V+	V-	V+	V-	V+	V-
0	59	10	7	97	-11	74	13	11	97	-11	74	13	11	169	-19	97	169	-19	169	-19	169	-19	169	-19	266	77	266	77
10	47	7	5	82	-11	59	9	8	82	-11	59	9	8	143	-19	75	143	-19	143	-19	143	-19	143	-19	218	56	218	56
20	35	5	3	67	-17	44	6	5	67	-17	44	6	5	117	-30	55	117	-30	117	-30	117	-30	117	-30	172	25	172	25
30	24	2	1	54	-27	29	3	2	54	-27	29	3	2	95	-48	33	95	-48	95	-48	95	-48	95	-48	128	-14	128	-14
40	12	-0.7	-0.5	42	-40	15	-1	-1	42	-40	15	-1	-1	73	-70	13	73	-70	73	-70	73	-70	73	-70	86	-57	86	-57
50	0	-3	-2	31	-52	0	-4	-3	31	-52	0	-4	-3	53	-91	-7	53	-91	53	-91	53	-91	53	-91	47	-97	47	-97
60	-12	-6	-4	21	-65	-15	-8	-6	21	-65	-15	-8	-6	37	-113	-28	37	-113	37	-113	37	-113	37	-113	9	-141	9	-141
70	-24	-9	-6	13	-76	-29	-11	-9	13	-76	-29	-11	-9	22	-134	-50	22	-134	22	-134	22	-134	22	-134	-27	-183	-27	-183
80	-35	-11	-8	7	-89	-44	-14	-12	7	-89	-44	-14	-12	12	-156	-70	12	-156	12	-156	12	-156	12	-156	-58	-226	-58	-226
90	-47	-14	-10	3	-100	-59	-18	-15	3	-100	-59	-18	-15	4	-175	-91	4	-175	4	-175	4	-175	4	-175	-87	-267	-87	-267
100	-59	-17	-12	0	-111	-74	-21	-18	0	-111	-74	-21	-18	0	-195	-113	0	-195	0	-195	0	-195	0	-195	-113	-307	-113	-307

A.3 105' SPAN (MILITARY ROAD GEOMETRY)

Design Assumptions

- span length = 105'
- W40 x 277 I-section girders
- number of girders = 4
- girder spacing = 8' 4"
- composite concrete slab
- slab depth = 7.5"

Calculation of Dead Loads

DC₁ Non-composite dead loads

Deck:

$$\text{Interior girder, } (8''/12) * (8.333') * (0.15 \frac{\text{k}}{\text{ft}^3}) = 0.833 \text{ k/ft}$$

$$\text{Exterior girder, } (8''/12) * (7.870') * (0.15 \frac{\text{k}}{\text{ft}^3}) = 0.787 \text{ k/ft}$$

Total DC₁

	<u>Interior Girder</u>	<u>Exterior Girder</u>
Deck	0.833	0.787
Steel	0.300	0.300
Form-work	<u>0.083</u>	<u>0.079</u>
Total DC ₁	1.216 k/ft	1.166 k/ft

DC₂ Long Term Composite Dead Load

Assume the weight per unit length of the barrier is 536 lb/ft, and all girders carry the load equally.

$$DC_2 = (0.536 * 2) / 4 = \mathbf{0.268 \text{ k/ft}}$$

DW Future Wearing Surface Load

Assume equal distribution among all girders.

$$DW = (0.025 * 30) / 4 = \mathbf{0.188 \text{ k/ft}}$$

Design Factors

Ductility η_D	1.0
Redundancy η_R	1.0
Operational Importance η_I	1.0

$$\eta = \eta_D * \eta_R * \eta_I = \mathbf{1.0}$$

Bridge is subjected to HL93 loading, the distribution factors and shear / moment envelopes are generated using QconBridge®. The shear / moment envelopes are shown on the following pages, with the distribution factors and section properties preceding.

Note: The exterior girder controls the design for flexural design and the interior controls the design for shear, as is shown in the moment and shear envelopes.

Effective Flange Width

Interior Girder:

$$\begin{aligned} \frac{1}{4} * (\text{span} * 12^{\text{in/ft}}) &= \frac{1}{4} * (105' * 12^{\text{in/ft}}) = 315'' \\ 12.0 * (t_s) + (b_f/2) &= 12.0 * (7.5) + (15.75/2) = \mathbf{98''} && \text{(controls)} \\ \text{Spacing} &= 100'' \end{aligned}$$

Exterior Girder:

$$\begin{aligned} \frac{1}{8} * (\text{span} * 12^{\text{in/ft}}) &= \frac{1}{8} * (105' * 12^{\text{in/ft}}) = 158'' \\ 6.0 * (t_s) + (b_f/2) &= 6.0 * (7.5) + (15.75/2) = 53'' \\ \text{Overhang} &= \mathbf{44''} && \text{(controls)} \end{aligned}$$

$$\begin{aligned} b_{\text{eff}} &= \frac{1}{2} * \text{controlling interior} + \text{controlling exterior} \\ &= \frac{1}{2} * 98 + 44 = \mathbf{93''} && \text{(governing } b_{\text{eff}}) \end{aligned}$$

Positive Flexure

Determining neutral axis (N.A.)

$$P_t = 50 * 15.75 * 1.575 = 1247 \text{ kips}$$

$$P_c = 50 * 15.75 * 1.575 = 1247 \text{ kips}$$

$$P_w = 50 * 36.54 * 0.83 = 1516 \text{ kips}$$

$$P_s = 0.85 * 4 * 93 * 7.5 = 2497 \text{ kips}$$

Case 1

$$P_t + P_w \geq P_c + P_s$$

$$2763 \not\geq 3744 \text{ kips}$$

N.G.

Case 2

$$P_t + P_w + P_c \geq P_s$$

$$4010 \geq 2497 \text{ kips}$$

O.K.

$$y_{bar} = \frac{t_c}{2} \left[\frac{P_w + P_t - P_s}{P_c} + 1 \right]$$

$$y_{bar} = 0.956''$$

Measured from the top of the top flange.

Plastic Moment Capacity

$$M_p = \frac{P_c}{2t_c} \left[y_{bar}^2 + (t_c - y_{bar})^2 \right] + [P_s d_s + P_w d_w + P_t d_t]$$

$$M_p = 7351 \text{ k*ft}$$

Strength Limit State

	<u>Strength I</u>	<u>Strength IV</u>
$M_{DC1} = 1543$	1929	2315
$M_{DC2} = 207$	259	311
$M_{DW} = 190$	285	285
$M_{LL+IM} = 2070$	<u>3623</u>	<u>N. A.</u>
	6095 k*ft (governs)	2910 k*ft

Ductility Requirement

$$\frac{D_p}{D'} \leq 5$$

$$D' = \beta \left(\frac{d + t_s + t_h}{7.5} \right)$$

$$D' = 0.7 * (39.69 + 7.5) / 7.5 = 4.404$$

$$D_p = 7.5 + 0.956 = 8.456"$$

$$D_p / D' = 1.92 < 5$$

Section Proportional Limits

$$0.1 \leq \frac{I_{YC}}{I_Y} \leq 0.9$$

$$I_{YC} = \frac{1}{12}(1.575)*(15.75)^3 = 512.8 \text{ in}^4$$

$$I_Y = 512.8 + 512.8 + 1.7 = 1027 \text{ in}^4$$

$$I_{YC} / I_Y = 0.5$$

O.K.

Web Slenderness

$$\frac{2D_{cp}}{t_w} \leq 3.76\sqrt{\frac{E}{F_{yc}}}$$

$$D_{cp} = 0 \text{ (Plastic N.A. is in slab)}$$

Compression Flange Slenderness

$$\frac{b_f}{2t_f} \leq 0.382\sqrt{\frac{E}{F_{yc}}}$$

$$\frac{15.75}{2*1.575} = 5.0 \leq 9.2 = \sqrt{\frac{29000}{50}}$$

Compression Flange Bracing

O.K. (braced continuously at strength limit state)

Positive Flexure Resistance

$$M_n = \frac{5M_p - 0.85M_y}{4} + \frac{0.85M_y - M_p}{4} \left(\frac{D_p}{D'} \right)$$

$$M_n = \frac{2(7351) - 0.85(5877)}{4} + \frac{0.85(5877) - 7351}{4} (1.92)$$

$$1.3 * M_y = 7640 \text{ k*ft}$$

$$M_n = 6809 \text{ k*ft}$$

$$6809 \text{ k*ft} \geq 6028 \text{ k*ft}$$

O.K.

Negative Flexure

Determining neutral axis (N.A.)

$$P_t = 50 * 15.75 * 1.575 = 1247 \text{ kips}$$

$$P_c = 50 * 15.75 * 1.575 = 1247 \text{ kips}$$

$$P_w = 50 * 36.54 * 0.83 = 1516 \text{ kips}$$

$$P_{rb} = 60 * 3.5 = 210 \text{ kips}$$

$$P_{rt} = 60 * 4 = 240 \text{ kips}$$

Case 1

$$P_c + P_w \geq P_t + P_{rb} + P_{rt}$$

$$2763 \geq 1697 \text{ kips}$$

O.K.

$$y_{bar} = \frac{D}{2} * \left[\frac{P_c - P_t - P_{rt} - P_{rb}}{P_w} + 1 \right]$$

$$y_{bar} = 12.85''$$

Measured from the bottom of the top flange.

Plastic Moment Capacity

$$M_p = \frac{P_w}{2D} \left[y_{bar}^2 + (D - y_{bar})^2 \right] + \left[P_{rt}d_{rt} + P_{rb}d_{rb} + P_t d_t + P_c d_c \right]$$

$$M_p = 5949 \text{ k*ft}$$

Strength Limit State

	<u>Strength I</u>	<u>Strength IV</u>
$M_{DC1} = 0$	0	0
$M_{DC2} = 369$	461	554
$M_{DW} = 339$	509	509
$M_{LL+IM} = 2106$	<u>3686</u>	<u>N. A.</u>
	4656 k*ft (governs)	1063 k*ft

Section Proportional Limits

$$0.1 \leq \frac{I_{YC}}{I_Y} \leq 0.9$$

$$I_{yc} = 1/12 * (1.575)*(15.75)^3 = 512.8 \text{ in}^4$$

$$I_y = 512.8 + 512.8 + 1.7 = 1028 \text{ in}^4$$

$$I_{yc} / I_y = 0.5$$

O.K.

Web Slenderness

$$2D_{cp} / t_w \leq 3.76 \sqrt{E / F_{yc}}$$

$$2 * 23.7 / 0.83 = 57.1 \leq 90.55 = 3.76 \sqrt{29000 / 50}$$

$$\text{Ratio} = 0.63$$

Compression Flange Slenderness

$$b_f / 2t_f \leq 0.382 \sqrt{E / F_{yc}}$$

$$15.75 / 2 * 1.575 = 5.0 \leq 9.2 = \sqrt{29000 / 50}$$

$$\text{Ratio} = 0.54$$

Compression Flange Bracing

Assume adequate bracing

Negative Flexure Resistance

$$M_r = 5949 \text{ k*ft}$$

$$5949 \text{ k*ft} \geq 4656 \text{ k*ft}$$

O.K.

Permanent Deflection

$$f_{all} = 47.5 \text{ ksi}$$

<u>Positive</u>	<u>Tension</u>	<u>Compression</u>	
M_{DC1}	$1543(12)/1083.1 = 17.09$	$1543(12)/1083.1 = 17.09$	
M_{DC2}	$207(12)/1288.7 = 1.93$	$207(12)/2549.9 = 0.97$	
M_{DW}	$190(12)/1288.7 = 1.77$	$190(12)/2549.9 = 0.89$	
M_{LL+IM}	$2070(12)1.3/1410.6 = \underline{22.89}$	$2070(12)1.3/6315.3 = \underline{5.11}$	
	43.68 ksi	24.06 ksi	<u>O.K.</u>

<u>Negative</u>	<u>Tension</u>	<u>Compression</u>	
M_{DC1}	$0(12)/1083.1 = 0$	$0(12)/1083.1 = 0$	
M_{DC2}	$369(12)/1156.8 = 3.13$	$369(12)/1416 = 3.83$	
M_{DW}	$339(12)/1156.8 = 2.87$	$339(12)/1416 = 3.52$	
M_{LL+IM}	$2106(12)1.3/1156.8 = \underline{23.19}$	$2106(12)1.3/1416 = \underline{28.4}$	
	29.19 ksi	35.75 ksi	<u>O.K.</u>

Live Load Deflection

$$\Delta_{all} = L / 800 = 1.575''$$

$$\Delta_{anl} = 1.556'' \quad \text{O.K.}$$

Shear Resistance

Positive

$$\begin{aligned} V_{DC1} &= 62 \text{ kips} & * 1.25 &= & 78 \text{ kips} \\ V_{DC2} &= 11 \text{ kips} & * 1.25 &= & 14 \text{ kips} \\ V_{DW} &= 10 \text{ kips} & * 1.50 &= & 15 \text{ kips} \\ V_{LL+IM} &= 99 \text{ kips} & * 1.75 &= & \underline{173 \text{ kips}} \\ \text{At Strength Limit State} & & V_u &= & \mathbf{280 \text{ kips}} \end{aligned}$$

Shear Resistance V_n of Unstiffened Web

$$\begin{aligned} V_n &= 0.58 * 36.54 * 0.83 * 50 \\ &= 955 \text{ kips} \end{aligned}$$

$$V_r = 1.0 * 955 = 955 \text{ kips}$$

$$955 > 280 \text{ kips}$$

OK

Negative

$$\begin{aligned} V_{DC1} &= 62 \text{ kips} & * 1.25 &= & 78 \text{ kips} \\ V_{DC2} &= 18 \text{ kips} & * 1.25 &= & 23 \text{ kips} \\ V_{DW} &= 16 \text{ kips} & * 1.50 &= & 24 \text{ kips} \\ V_{LL+IM} &= 113 \text{ kips} & * 1.75 &= & \underline{198 \text{ kips}} \\ \text{At Strength Limit State} & & V_u &= & \mathbf{323 \text{ kips}} \end{aligned}$$

Shear Resistance V_n of Unstiffened Web

$$\begin{aligned} V_n &= 0.58 * 36.54 * 0.83 * 50 \\ &= 955 \text{ kips} \end{aligned}$$

$$V_r = 1.0 * 955 = 955 \text{ kips}$$

$$955 > 323 \text{ kips}$$

O.K.

Strength 1 Moments

Position	LL + IM		DW	1.25		1.25 DC ₂	1.5 DW	Factored		1.75(LL+IM)		Factored & Distributed Strength 1	
	DC ₁	DC ₂		M+	M-			DC ₁	DC ₂	DL	M+	M-	y
0	0	0	0	0	0	0	0	0	0	0	0	0	0
10.5	559	96	88	898	-117	120	132	950	1571	-204	1	2521	746
21	993	163	149	1528	-234	204	224	1669	2673	-410	1	4342	1259
31.5	1303	199	183	1904	-351	249	275	2153	3331	-615	1	5484	1538
42	1490	207	190	2070	-469	259	285	2406	3622	-821	1	6028	1585
52.5	1552	185	170	2032	-585	231	255	2426	3556	-1025	1	5982	1401
63	1490	133	122	1814	-703	166	183	2211	3175	-1230	1	5386	981
73.5	1303	52	47	1407	-820	65	71	1765	2462	-1436	1	4227	329
84	993	-59	-54	839	-1113	-74	-81	1087	1468	-1948	1	2555	-861
94.5	559	-199	-183	300	-1354	-249	-275	175	526	-2369	1	701	-2194
105	0	-369	-339	0	-2106	-461	-509	-970	0	-3686	1	-970	-4656

Fatigue Load Combination

Position	Fatigue Truck Moments (IM+1.15)		Unfactored & Distributed Fatigue Moments		Govern. Factored & Distributed Fatigue Moments			
	M+	M-	D.F.	M+	M-	L.F.	M+	M-
0	0	0	0.709	0	0	0.75	0	0
10.5	629	-79	0.709	446	-56	0.75	334	-42
21	1044	-158	0.709	740	-112	0.75	555	-84
31.5	1303	-237	0.709	924	-168	0.75	693	-126
42	1383	-317	0.709	981	-225	0.75	735	-169
52.5	1339	-396	0.709	949	-281	0.75	712	-211
63	1227	-475	0.709	870	-337	0.75	652	-253
73.5	964	-555	0.709	683	-393	0.75	513	-295
84	579	-634	0.709	411	-450	0.75	308	-337
94.5	219	-713	0.709	155	-506	0.75	116	-379
105	0	-799	0.709	0	-566	0.75	0	-425

A.4 90' SPAN (INITIAL DESIGN GEOMETRY)

Design Assumptions

- span length = 90'
- I girders with approx. 36" web and $F_y = 50$ ksi
- number of girders = 4
- girder spacing = 10'
- composite concrete slab with $f'_c = 4$ ksi
- slab thickness = 8"

Designs for this geometry were completed for continuous dead and live, and simply supported for dead loads, as welded plate girders and using a rolled shape as simply supported.

Note: Optimization of the design is in terms of total steel area of the cross section, and only the strength limit state is considered in the design.

Calculation of Dead Loads

DC₁ Non-composite dead loads

Deck:

Interior girder, $(8.5"/12)*(10')*(0.15 \text{ k/ft}^3) = 1.063 \text{ k/ft}$

Exterior girder, $(8.5"/12)*(8.5')*(0.15 \text{ k/ft}^3) = 0.903 \text{ k/ft}$

Total DC₁

	<u>Interior Girder</u>	<u>Exterior Girder</u>
Deck	1.063	0.903
Concrete Haunch	0.033	0.033
Steel	0.170	0.170
Form-work	<u>0.135</u>	<u>0.079</u>
Total DC ₁	1.401 k/ft	1.185 k/ft

DC₂ Long Term Composite Dead Load

Assume the weight per unit length of the barrier is 536 lb/ft, and all girders carry the load equally.

$$DC_2 = (0.536 * 2) / 4 = \mathbf{0.268} \text{ k/ft}$$

DW Future Wearing Surface Load

Assume equal distribution among all girders.

$$DW = (0.025 * 34) / 4 = \mathbf{0.213} \text{ k/ft}$$

Design Factors

Ductility η_D	1.0
Redundancy η_R	1.0
Operational Importance η_I	1.0

$$\eta = \eta_D * \eta_R * \eta_I = \mathbf{1.0}$$

Bridge is subjected to HL93 loading, the distribution factors and shear / moment envelopes are generated using QconBridge®. The shear / moment envelopes are shown on the following pages, with the distribution factors and section properties preceding.

Note: The exterior girder controls the design for flexural design and the interior controls the design for shear, as is shown in the moment and shear envelopes.

Effective Flange Width

Interior Girder:

$$\frac{1}{4} * (\text{span} * 12^{\text{in/ft}}) = \frac{1}{4} * (90' * 12^{\text{in/ft}}) = 285''$$

$$12.0 * (t_s) + (b_f/2) = 12.0 * (8.0) + (12/2) = \mathbf{102''} \quad (\text{controls})$$

$$\text{Spacing} = 120''$$

Exterior Girder:

$$\frac{1}{8} * (\text{span} * 12^{\text{in/ft}}) = \frac{1}{8} * (90' * 12^{\text{in/ft}}) = 135''$$

$$6.0 * (t_s) + (b_f/2) = 6.0 * (8.0) + (12/2) = 54''$$

$$\text{Overhang} = 42'' \quad \text{(controls)}$$

$$b_{\text{eff}} = \frac{1}{2} * \text{controlling interior} + \text{controlling exterior}$$

$$= \frac{1}{2} * 102 + 42 = 93'' \quad \text{(governing } b_{\text{eff}})$$

Positive Flexure

Determining neutral axis (N.A.)

$$P_t = 50 * 15 * 1.25 = 843.8 \text{ kips}$$

$$P_c = 50 * 13.5 * 0.875 = 525 \text{ kips}$$

$$P_w = 50 * 36 * 0.50 = 900 \text{ kips}$$

$$P_s = 0.85 * 4 * 93 * 8 = 2543 \text{ kips}$$

Case 1

$$P_t + P_w \geq P_c + P_s$$

$$1743.8 \not\geq 3068 \text{ kips} \quad \text{N.G.}$$

Case 2

$$P_t + P_w + P_c \geq P_s$$

$$2268.8 \not\geq 2556.8 \text{ kips} \quad \text{N.G.}$$

Neutral axis lies within the slab.

$$y_{\text{bar}} = t_s \left[\frac{P_w + P_t + P_c}{P_s} \right]$$

$$y_{\text{bar}} = 7.14''$$

Measured from the top of the slab.

Plastic Moment Capacity

$$M_p = \frac{y_{bar}^2 P_s}{2t_s} + [P_c d_c + P_w d_w + P_t d_t]$$

$$M_p = 7092 \text{ k*ft}$$

Strength Limit State

	<u>Strength I</u>	<u>Strength IV</u>
$M_{DC1} = 878$	1097	1317
$M_{DC2} = 152$	190	228
$M_{DW} = 121$	182	182
$M_{LL+IM} = 1692$	<u>2961</u>	<u>N. A.</u>
	4430 k*ft (governs)	1727 k*ft

Ductility Requirement

$$\frac{D_p}{D'} \leq 5$$

$$D' = \beta \left(\frac{d + t_s + t_h}{7.5} \right)$$

$$D' = 0.7 * (38 + 8.0) / 7.5 = 4.29$$

$$D_p = 7.14$$

$$D_p / D' = 1.66 < 5$$

O.K.

Section Proportional Limits

$$0.1 \leq \frac{I_{YC}}{I_Y} \leq 0.9$$

$$I_{YC} = 1/12 (.875) * (12)^2 = 126 \text{ in}^4$$

$$I_Y = 126 + 316.4 + 0.375 = 442.8 \text{ in}^4$$

$$I_{YC} / I_Y = 0.28$$

O.K.

Web Slenderness

$$2D_{cp}/t_w \leq 3.76 \sqrt{\frac{E}{F_{yc}}}$$

Plastic neutral axis is in slab, web slenderness is satisfied.

Nominal Flexure Resistance

For $D' < D_p < 5D'$

$$M_n = \frac{5M_p - 0.85M_y}{4} + \frac{0.85M_y - M_p}{4} \left(\frac{D_p}{D'} \right)$$

$$M_y = 3886 \text{ k*ft}$$

$$M_n = 4700 \text{ k*ft}$$

$$4430 < 4700 \text{ k*ft}$$

O.K.

Shear Resistance

Each section requires stiffeners to meet the shear requirements.

Constructibility

Web Slenderness

$$2D_c/t_w \leq 6.77 \sqrt{E/f_c}$$

$$82.55 < 178.81$$

O.K.

Compression Flange Slenderness

$$\frac{b_f}{2t_f} \leq 1.38 \sqrt{\frac{E}{f_c} \sqrt{\frac{2D_c}{t_w}}}$$

$$6.86 < 12.09$$

O.K.

Compression Flange Bracing

Bracing requirements were assumed to be satisfied.

Negative Flexure Region

Plastic Moment Capacity

$$D_{cp} = \frac{D}{2A_w F_{yw}} \left(F_{yt} A_t + F_{yw} A_w + F_{yr} A_r - F_{yc} A_c \right)$$

$$D_{cp} = 20.63 \text{ in}$$

$$P_c = F_{yc} b_c t_c = 50 * 1.125 * 15 = 843.75 \text{ kips}$$

$$P_w = F_{yw} D t_w = 50 * 0.5 * 36 = 900 \text{ kips}$$

$$P_t = F_{yt} b_t t_t = 50 * 0.875 * 12 = 525 \text{ kips}$$

$$P_{rb} = F_{yrb} A_{rb} = 60 * 4 = 240 \text{ kips}$$

$$P_{rt} = F_{yrt} A_{rt} = 60 * 6 = 360 \text{ kips}$$

$$P_c + P_w \geq P_t + P_{rb} + P_{rt}$$

$$1743.8 > 1125 \text{ kips}$$

$$y_{bar} = \left(\frac{D}{2} \right) \left[\frac{P_c - P_t - P_{rt} - P_{rb}}{P_w} + 1 \right]$$

$$y_{bar} = 15.38 \text{ in}$$

Y_{bar} is measured from bottom of top flange.

$$M_p = \frac{P_w}{2D} \left[y_{bar}^2 + (D - y_{bar})^2 \right] + \left[P_{rt} d_{rt} + P_{rb} d_{rb} + P_t d_t + P_c d_c \right]$$

$$M_p = 3940 \text{ k*ft}$$

Strength Limit State

<u>Unfactored Moments</u>	<u>Strength I</u>
$M_{DC1} = 0 \text{ k*ft}$	0
$M_{DC2} = 271 \text{ k*ft}$	339
$M_{DW} = 216 \text{ k*ft}$	324
<u>$M_{LL+IM} = 1735 \text{ k*ft}$</u>	<u>3036</u>
	3699 k*ft

Web Slenderness

$$\frac{2D_c}{t_w} \leq 3.76 \sqrt{\frac{E}{F_{yc}}}$$

$$82.5 < 90.55$$

O.K.

Compression-Flange Slenderness

$$\frac{b_f}{2t_f} \leq 0.382 \sqrt{\frac{E}{F_{yc}}}$$

$$6.67 < 9.2$$

O.K.

Compression Flange Bracing

Is assumed to be adequate for these designs.

Sectional Properties

$$0.1 \leq \frac{I_{yc}}{I_y} \leq 0.9$$

$$I_{yc}/I_y = 0.71 \qquad \text{O.K.}$$

Nominal Flexure Resistance

$$M_n = 3940 \text{ k*ft}$$

$$3699 < 3940 \text{ k*ft} \qquad \text{O.K.}$$

Permanent Deflection

$$f_{all} = 47.5 \text{ ksi}$$

<u>Positive</u>	<u>Tension</u>	<u>Compression</u>	
M_{DC1}	$878(12)/_{668} = 15.77$	$878(12)/_{512} = 20.58$	
M_{DC2}	$152(12)/_{864} = 2.11$	$152(12)/_{2086} = 0.87$	
M_{DW}	$121(12)/_{864} = 1.68$	$121(12)/_{2086} = 0.70$	
M_{LL+IM}	$1692(12)^{1.3}/_{933} = \underline{28.3}$	$1692(12)^{1.3}/_{7241} = \underline{3.64}$	
	47.87ksi	25.79 ksi	<u>O.K.</u>

90' Span (Initial Design Geometry)

<u>Negative</u>	<u>Tension</u>	<u>Compression</u>	
M_{DC1}	$0^{(12)}/_{668} = 0$	$0^{(12)}/_{512} = 0$	
M_{DC2}	$271^{(12)}/_{752} = 4.32$	$271^{(12)}/_{840} = 3.87$	
M_{DW}	$216^{(12)}/_{752} = 3.44$	$216^{(12)}/_{840} = 3.09$	
M_{LL+IM}	$1735^{(12)1.3}/_{752} = \underline{35.97}$	$1735^{(12)1.3}/_{840} = \underline{32.22}$	
	43.74 ksi	39.17 ksi	<u>O.K.</u>

Intermediate stiffeners are necessary with this section to meet the shear requirements.

These designs were completed for comparison purposes only, therefore the fatigue limit state was not investigated.

The shear / moment envelopes for the controlling girder are shown on the following pages.

Strength 1 Moments															
Position	LL + IM			1.25			1.5			Factored 1.75(LL+IM)			Factored & Distributed Strength 1		
	DC ₁	DC ₂	DW	M+	M-	DC ₁	DC ₂	DW	DL	M+	M-	γ	M+	M-	
0	0	0	0	0	0	0	0	0	0	0	0	1	0	0	
9	329	71	56	740	-97	411	89	84	584	1296	-170	1	1880	415	
18	585	119	95	1255	-193	731	149	143	1023	2196	-338	1	3219	685	
27	768	147	116	1558	-290	960	184	174	1318	2726	-507	1	4044	811	
36	878	152	121	1692	-386	1097	190	182	1469	2961	-675	1	4430	794	
45	914	136	108	1660	-483	1143	170	162	1475	2905	-845	1	4380	630	
54	878	98	78	1484	-580	1097	123	117	1337	2598	-1014	1	3934	322	
63	768	38	30	1149	-676	960	48	45	1053	2010	-1182	1	3063	-130	
72	585	-43	-35	683	-908	731	-54	-53	625	1196	-1589	1	1821	-964	
81	329	-147	-116	252	-1098	411	-184	-174	54	441	-1921	1	494	-1867	
90	0	-271	-216	0	-1735	0	-339	-324	-663	0	-3037	1	-663	-3699	

Fatigue Load Combination									
Position	Truck Moments (IM+1.15)			Unfactored & Distributed			Govern. Factored & Distributed		
	M+	M-	Fatigue	D.F.	M+	M-	L.F.	M+	M-
0	0	0	0.708	0	0	0	0.75	0	0
9	485	-62	0.708	343	-44	0.708	0.75	258	-33
18	799	-123	0.708	566	-87	0.708	0.75	424	-65
27	994	-185	0.708	704	-131	0.708	0.75	528	-98
36	1048	-247	0.708	742	-175	0.708	0.75	556	-131
45	1007	-309	0.708	713	-219	0.708	0.75	535	-164
54	935	-370	0.708	662	-262	0.708	0.75	496	-196
63	736	-432	0.708	521	-306	0.708	0.75	391	-229
72	434	-494	0.708	307	-350	0.708	0.75	230	-262
81	174	-556	0.708	123	-394	0.708	0.75	92	-295
90	0	-617	0.708	0	-437	0.708	0.75	0	-328

A.5 90' SPAN (ROLLED SECTION DESIGN)

Calculation of Dead Loads

DC₁ Non-composite dead loads

Deck:

Interior girder, $(8.5''/12) * (10') * (0.15 \text{ k/ft}^3) = 1.063 \text{ k/ft}$

Exterior girder, $(8.5''/12) * (8.5') * (0.15 \text{ k/ft}^3) = 0.903 \text{ k/ft}$

Total DC₁

	<u>Interior Girder</u>	<u>Exterior Girder</u>
Deck	1.063	0.903
Concrete Haunch	0.033	0.033
Steel	0.170	0.170
Form-work	<u>0.135</u>	<u>0.079</u>
Total DC ₁	1.401 k/ft	1.185 k/ft

DC₂ Long Term Composite Dead Load

Assume the weight per unit length of the barrier is 536 lb/ft, and all girders carry the load equally.

$$DC_2 = (0.536 * 2) / 4 = \mathbf{0.268 \text{ k/ft}}$$

DW Future Wearing Surface Load

Assume equal distribution among all girders.

$$DW = (0.025 * 34) / 4 = \mathbf{0.213 \text{ k/ft}}$$

Design Factors

Ductility η_D	1.0
Redundancy η_R	1.0
Operational Importance η_I	1.0

$$\eta = \eta_D * \eta_R * \eta_I = \mathbf{1.0}$$

Bridge is subjected to HL93 loading, the distribution factors and shear / moment envelopes are generated using QconBridge®. The shear / moment envelopes are shown on the following pages, with the distribution factors and section properties preceding.

Note: The exterior girder controls the design for flexural design and the interior controls the design for shear, as is shown in the moment and shear envelopes.

Effective Flange Width

Interior Girder:

$$\frac{1}{4} * (\text{span} * 12^{\text{in/ft}}) = \frac{1}{4} * (90' * 12^{\text{in/ft}}) = 285''$$

$$12.0 * (t_s) + (b_f/2) = 12.0 * (8.0) + (15.75/2) = \mathbf{104''} \quad (\text{controls})$$

$$\text{Spacing} = 120''$$

Exterior Girder:

$$\frac{1}{8} * (\text{span} * 12^{\text{in/ft}}) = \frac{1}{8} * (90' * 12^{\text{in/ft}}) = 135''$$

$$6.0 * (t_s) + (b_f/2) = 6.0 * (8.0) + (15.75/2) = 56''$$

$$\text{Overhang} = \mathbf{42''} \quad (\text{controls})$$

$$b_{\text{eff}} = \frac{1}{2} * \text{controlling interior} + \text{controlling exterior}$$

$$= \frac{1}{2} * 104 + 42 = \mathbf{94''} \quad (\text{governing } b_{\text{eff}})$$

Positive Flexure

Determining neutral axis (N.A.)

$$P_t = 50 * 15.75 * 1.065 = 838.7 \text{ kips}$$

$$P_c = 50 * 15.75 * 1.065 = 838.7 \text{ kips}$$

$$P_w = 50 * 36.54 * 0.65 = 1187.6 \text{ kips}$$

$$P_s = 0.85 * 4 * 94 * 8 = 2556.8 \text{ kips}$$

Case 1

$$P_t + P_w \geq P_c + P_s$$

$$2026.3 \not\geq 3395.5 \text{ kips}$$

N.G.

Case 2

$$P_t + P_w + P_c \geq P_s$$

$$2865 \geq 2556.8 \text{ kips}$$

O.K.

Neutral axis lies within the top flange.

$$y_{bar} = \left(\frac{t_c}{2} \right) \left[\frac{P_w + P_t - P_s}{P_c} + 1 \right]$$

$$y_{bar} = 0.204''$$

Measured down from the top of the top flange.

Plastic Moment Capacity

$$M_p = \left(\frac{P_c}{2t_c} \right) * \left[y_{bar}^2 + (t_c - y_{bar})^2 + (P_s d_s + P_w d_w + P d_t) \right]$$

$$M_p = 5461 \text{ k*ft}$$

Strength Limit State

	<u>Strength I</u>	<u>Strength IV</u>
$M_{DC1} = 878$	1097	1317
$M_{DC2} = 152$	190	228
$M_{DW} = 121$	182	182
$M_{LL+IM} = 1692$	<u>2961</u>	<u>N. A.</u>
	4430 k*ft (governs)	1727 k*ft

Ductility Requirement

$$\frac{D_p}{D'} \leq 5$$

$$D' = \beta \left(\frac{d + t_s + t_h}{7.5} \right)$$

$$D' = 0.7 * (38.67 + 8.0) / 7.5 = 4.36$$

$$D_p = 8.19$$

$$D_p / D' = 1.88 < 5$$

O.K.

Section Proportional Limits

$$0.1 \leq \frac{I_{YC}}{I_Y} \leq 0.9$$

$$I_{YC} = 1/12(1.065)*(15.75)^2 = 347 \text{ in}^4$$

$$I_Y = 126 + 316.4 + 0.836 = 694 \text{ in}^4$$

$$I_{YC} / I_Y = 0.50$$

O.K.

Web Slenderness

$$2D_{cp} / t_w \leq 3.76 \sqrt{\frac{E}{F_{yc}}}$$

Plastic neutral axis is in top flange, web slenderness is satisfied.

Nominal Flexure Resistance

For $D' < D_p < 5D'$

$$M_n = \frac{5M_p - 0.85M_y}{4} + \frac{0.85M_y - M_p}{4} \left(\frac{D_p}{D'} \right)$$

$$M_y = 3886 \text{ k*ft}$$

$$M_n = 4700 \text{ k*ft}$$

$$5042 < 4700 \text{ k*ft}$$

O.K.

Shear Resistance

Each section requires stiffeners to meet the shear requirements.

Constructibility

Web Slenderness

$$2D_c/t_w \leq 6.77\sqrt{E/f_c}$$

$$56.22 < 216.45$$

O.K.

Compression Flange Slenderness

$$b_f/2t_f \leq 1.38\sqrt{\frac{E}{f_c}\sqrt{2D_c/t_w}}$$

$$7.39 < 16.11$$

O.K.

Compression Flange Bracing

Bracing requirements were assumed to be satisfied.

Negative Flexure Region

Plastic Moment Capacity

$$D_{cp} = \frac{D}{2A_w F_{yw}} (F_{yt} A_t + F_{yw} A_w + F_{yr} A_r - F_{yc} A_c)$$

$$D_{cp} = 25.19 \text{ in}$$

$$P_c = F_{yc} b_c t_c = 50 * 1.125 * 15 = 838.7 \text{ kips}$$

$$P_w = F_{yw} D t_w = 50 * 0.5 * 36 = 1188 \text{ kips}$$

$$P_t = F_{yt} b_t t_t = 50 * 0.875 * 12 = 838.7 \text{ kips}$$

$$P_{rb} = F_{yrb} A_{rb} = 60 * 4 = 240 \text{ kips}$$

$$P_{rt} = F_{yrt} A_{rt} = 60 * 6 = 360 \text{ kips}$$

$$P_c + P_w \geq P_t + P_{rb} + P_{rt}$$

$$2026.7 > 1438.7 \text{ kips}$$

$$y_{bar} = \left(\frac{D}{2} \right) \left[\frac{P_c - P_t - P_{rt} - P_{rb}}{P_w} + 1 \right]$$

$$y_{bar} = 11.35 \text{ in}$$

Y_{bar} is measured from bottom of top flange.

$$M_p = \frac{P_w}{2D} \left[y_{bar}^2 + (D - y_{bar})^2 \right] + \left[P_{rt}d_{rt} + P_{rb}d_{rb} + P_t d_t + P_c d_c \right]$$

$$M_p = 4320 \text{ k*ft}$$

Strength Limit State

Unfactored Moments

Strength I

$$M_{DC1} = 0 \text{ k*ft}$$

0

$$M_{DC2} = 271 \text{ k*ft}$$

339

$$M_{DW} = 216 \text{ k*ft}$$

324

$$\underline{M_{LL+IM} = 1735 \text{ k*ft}}$$

3036

3699 k*ft

Web Slenderness

$$\frac{2D_c}{t_w} \leq 3.76 \sqrt{\frac{E}{F_{yc}}}$$

$$77.5 < 90.55$$

O.K.

Compression-Flange Slenderness

$$\frac{b_f}{2t_f} \leq 0.382 \sqrt{\frac{E}{F_{yc}}}$$

$$7.39 < 9.2$$

O.K.

Compression Flange Bracing

Is assumed to be adequate for these designs.

Sectional Properties

$$0.1 \leq \frac{I_{yc}}{I_y} \leq 0.9$$

$$I_{yc}/I_y = 0.50$$

O.K.

Nominal Flexure Resistance

$$M_n = 4320 \text{ k*ft}$$

$$3699 < 4320 \text{ k*ft}$$

O.K.

This section satisfies the strength limit state for flexure.

These designs were completed for comparison purposes only, therefore the fatigue limit state was not investigated.

A.6 130' SPAN - 48" WEB (INITIAL DESIGN GEOMETRY)

Design Assumptions

- span length = 130'
- I girders with approx. 48" web and $F_y = 50$ ksi
- number of girders = 4
- girder spacing = 10'
- composite concrete slab with $f'_c = 4$ ksi
- slab thickness = 8"

This superstructure geometry was designed using the traditional continuous support and the proposed support condition.

Note: Optimization of the design is in terms of total steel area of the cross section, and only the strength limit state is considered in the design.

Continuous Dead and Live Loads

Calculation of Dead Loads

DC₁ Non-composite dead loads

Deck:

Interior girder, $(8.5"/12)*(10')*(0.15 \text{ k/ft}^3) = 1.063 \text{ k/ft}$

Exterior girder, $(8.5"/12)*(8.5')*(0.15 \text{ k/ft}^3) = 0.903 \text{ k/ft}$

Total DC ₁	<u>Interior Girder</u>	<u>Exterior Girder</u>
Deck	1.063	0.903
Concrete Haunch	0.033	0.033
Steel	0.300	0.300
Form-work	<u>0.135</u>	<u>0.079</u>
Total DC ₁	1.531 k/ft	1.315 k/ft

DC₂ Long Term Composite Dead Load

Assume the weight per unit length of the barrier is 536 lb/ft, and all girders carry the load equally.

$$DC_2 = (0.536 * 2) / 4 = \mathbf{0.268 \text{ k/ft}}$$

DW Future Wearing Surface Load

Assume equal distribution among all girders.

$$DW = (0.025 * 34) / 4 = \mathbf{0.213 \text{ k/ft}}$$

Design Factors

Ductility η_D	1.0
Redundancy η_R	1.0
Operational Importance η_I	1.0

$$\eta = \eta_D * \eta_R * \eta_I = \mathbf{1.0}$$

Bridge is subjected to HL93 loading, the distribution factors and shear / moment envelopes are generated using QconBridge®. The shear / moment envelopes are shown on the following pages, with the distribution factors and section properties preceding.

Note: The exterior girder controls the design for flexural design and the interior controls the design for shear, as is shown in the moment and shear envelopes.

Effective Flange Width

Interior Girder:

$$\frac{1}{4} * (\text{span} * 12^{\text{in/ft}}) = \frac{1}{4} * (130' * 12^{\text{in/ft}}) = 390''$$

$$12.0 * (t_s) + (b_f/2) = 12.0 * (8.0) + (14/2) = \mathbf{103''} \quad (\text{controls})$$

$$\text{Spacing} = 120''$$

Exterior Girder:

$$\frac{1}{8} * (\text{span} * 12^{\text{in/ft}}) = \frac{1}{8} * (130' * 12^{\text{in/ft}}) = 195''$$

$$6.0 * (t_s) + (b_f/2) = 6.0 * (8.0) + (14/2) = 55''$$

$$\text{Overhang} = \mathbf{42''} \quad (\text{controls})$$

$$b_{\text{eff}} = \frac{1}{2} * \text{controlling interior} + \text{controlling exterior}$$

$$= \frac{1}{2} * 103 + 42 = \mathbf{94''} \quad (\text{governing } b_{\text{eff}})$$

Positive Flexure

Determining neutral axis (N.A.)

$$P_t = 50 * 1.5 * 21 = 1575 \text{ kips}$$

$$P_c = 50 * 1.375 * 14 = 962.5 \text{ kips}$$

$$P_w = 50 * 48 * 0.375 = 900 \text{ kips}$$

$$P_s = 0.85 * 4 * 94 * 8 = 2556.8 \text{ kips}$$

Case 1

$$P_t + P_w \geq P_c + P_s$$

$$2475 \not\geq 3519 \text{ kips} \quad \text{N.G.}$$

Case 2

$$P_t + P_w + P_c \geq P_s$$

$$3437 \geq 2556.8 \text{ kips} \quad \text{O.K.}$$

Neutral axis lies within the top flange.

$$y_{bar} = \left(\frac{t_c}{2} \right) \left[\frac{P_w + P_t - P_s}{P_c} + 1 \right]$$

$$y_{bar} = 0.454''$$

Measured down from the top of the top flange.

Plastic Moment Capacity

$$M_p = \left(\frac{P_c}{2t_c} \right) * \left[y_{bar}^2 + (t_c - y_{bar})^2 + (P_s d_s + P_w d_w + P d_t) \right]$$

$$M_p = 9459 \text{ k*ft}$$

Strength Limit State

	<u>Strength I</u>	<u>Strength IV</u>
$M_{DC1} = 2780$	3475	4170
$M_{DC2} = 289$	361	434
$M_{DW} = 230$	345	345
$M_{LL+IM} = 2755$	<u>4821</u>	<u>N. A.</u>
	9003 k*ft (governs)	4949 k*ft

Ductility Requirement

$$\frac{D_p}{D'} \leq 5$$

$$D' = \beta \left(\frac{d + t_s + t_h}{7.5} \right)$$

$$D' = 0.7 * (50.875 + 8.0) / 7.5 = 5.5$$

$$D_p = 8.47$$

$$D_p / D' = 1.54 < 5$$

O.K.

Section Proportional Limits

$$0.1 \leq \frac{I_{YC}}{I_Y} \leq 0.9$$

$$I_{YC} = 1/12(1.375)*(14)^2 = 314 \text{ in}^4$$

$$I_Y = 314 + 1157 + 0.211 = 1472 \text{ in}^4$$

$$I_{YC} / I_Y = 0.21$$

O.K.

Web Slenderness

$$2D_{cp} / t_w \leq 3.76 \sqrt{\frac{E}{F_{yc}}}$$

Plastic neutral axis is in top flange, web slenderness is satisfied.

Nominal Flexure Resistance

For $D' < D_p < 5D'$

$$M_n = \frac{5M_p - 0.85M_y}{4} + \frac{0.85M_y - M_p}{4} \left(\frac{D_p}{D'} \right)$$

$$M_y = 8056 \text{ k*ft}$$

$$M_n = 9107 \text{ k*ft}$$

$$9003 < 9107 \text{ k*ft}$$

O.K.

Shear Resistance

Each section requires stiffeners to meet the shear requirements.

Constructibility

Web Slenderness

$$\frac{2D_c}{t_w} \leq 6.77 \sqrt{\frac{E}{f_c}}$$

$$151.6 < 184.5$$

O.K.

Compression Flange Slenderness

$$\frac{b_f}{2t_f} \leq 1.38 \sqrt{\frac{E}{f_c} \sqrt{\frac{2D_c}{t_w}}}$$

$$5.09 < 10.72$$

O.K.

Compression Flange Bracing

Bracing requirements were assumed to be satisfied.

Negative Flexure Region

Plastic Moment Capacity

$$D_{cp} = \frac{D}{2A_w F_{yw}} (F_{yt} A_t + F_{yw} A_w + F_{yr} A_r - F_{yc} A_c)$$

$$D_{cp} = 33.6 \text{ in}$$

$$P_c = F_{yc} b_c t_c = 50 * 2 * 22 = 2200 \text{ kips}$$

$$P_w = F_{yw} D t_w = 50 * 0.4375 * 48 = 1200 \text{ kips}$$

$$P_t = F_{yt} b_t t_t = 50 * 2 * 22 = 2200 \text{ kips}$$

$$P_{rb} = F_{yrb} A_{rb} = 60 * 3 = 180 \text{ kips}$$

$$P_{rt} = F_{yrt} A_{rt} = 60 * 5 = 300 \text{ kips}$$

$$P_c + P_w \geq P_t + P_{rb} + P_{rt}$$

$$3400 > 2680 \text{ kips}$$

O.K.

$$y_{bar} = \left(\frac{D}{2} \right) \left[\frac{P_c - P_t - P_{rt} - P_{rb}}{P_w} + 1 \right]$$

$$y_{bar} = 14.4 \text{ in}$$

Y_{bar} is measured from bottom of top flange.

$$M_p = \frac{P_w}{2D} \left[y_{bar}^2 + (D - y_{bar})^2 \right] + \left[P_{rt} d_{rt} + P_{rb} d_{rb} + P_t d_t + P_c d_c \right]$$

$$M_p = 11376 \text{ k*ft}$$

Strength Limit State

Unfactored Moments

$$M_{DC1} = 3257 \text{ k*ft}$$

$$M_{DC2} = 638 \text{ k*ft}$$

$$M_{DW} = 506 \text{ k*ft}$$

$$M_{LL+IM} = 3252 \text{ k*ft}$$

Strength I

$$4071$$

$$798$$

$$759$$

$$5692$$

$$11320 \text{ k*ft}$$

Web Slenderness

$$\frac{2D_c}{t_w} \leq 3.76 \sqrt{\frac{E}{F_{yc}}}$$

$$134.4 < 90.55$$

N.G.

$$\text{Ratio} = 1.5 > 0.75$$

Compression-Flange Slenderness

$$\frac{b_f}{2t_f} \leq 0.382 \sqrt{\frac{E}{F_{yc}}}$$

$$5.5 < 9.2$$

O.K.

$$\text{Ratio} = 0.60$$

Since web slenderness is not satisfied, the section is non compact.

Compression Flange Bracing

Is assumed to be adequate for these designs.

Sectional Properties

$$0.1 \leq \frac{I_{yc}}{I_y} \leq 0.9$$

$$I_{yc}/I_y = 0.50$$

O.K.

Nominal Flexure Resistance

$$M_n = 11376 \text{ k*ft}$$

$$11319 < 11376 \text{ k*ft}$$

O.K.

This section satisfies the strength limit state for flexure.

These designs were completed for comparison purposes only, therefore the fatigue limit state was not investigated.

Moment Summary

Position	LL + IM		1.25		1.25		1.5		Factored		1.75(LL+IM)		Factored & Dist. Strength 1		
	DC ₁	DC ₂	DW	M+	M-	DC ₁	DC ₂	DW	DL	M+	M-	M+	M-	M+	M-
0	0	0	0	0	0	0	0	0	0	0	0	0	0	0	0
13	717	140	111	1207	-181	896	175	167	1238	2112	-316	3349	-316	3349	921
26	1202	235	187	2049	-362	1503	294	281	2077	3586	-634	5663	-634	5663	1442
39	1455	285	226	2550	-543	1819	356	339	2514	4463	-951	6977	-951	6977	1563
52	1477	289	230	2755	-725	1846	361	345	2553	4821	-1269	7374	-1269	7374	1284
65	1267	248	197	2683	-906	1584	310	296	2189	4696	-1585	6885	-1585	6885	604
78	826	161	128	2365	-1086	1033	201	192	1426	4139	-1901	5564	-1901	5564	-476
91	153	30	24	1807	-1268	191	38	36	265	3162	-2219	3427	-2219	3427	-1954
104	-752	-147	-117	1059	-1727	-940	-184	-176	-1299	1853	-3023	554	-3023	554	-4322
117	-1889	-369	-294	386	-2151	-2361	-461	-441	-3264	675	-3765	-2588	-3765	-2588	-7028
130	-3257	-638	-506	0	-3252	-4071	-798	-759	-5628	0	-5692	-5628	-5692	-5628	-11319

Fatigue Load Combination

Position	Truck Moments (M+1.15)		Unfactored & Distributed Fatigue Moments		Govern. Factored & Distributed Fatigue Moments			
	M+	M-	D.F.	M+	M-	L.F.	M+	M-
0	0	0	0.708	0	0	0.75	0	0
13	766	-110	0.708	542	-78	0.75	407	-58
26	1269	-219	0.708	898	-155	0.75	674	-116
39	1578	-329	0.708	1117	-233	0.75	838	-175
52	1669	-438	0.708	1182	-310	0.75	886	-233
65	1608	-548	0.708	1138	-388	0.75	854	-291
78	1446	-658	0.708	1024	-466	0.75	768	-349
91	1120	-767	0.708	793	-543	0.75	595	-407
104	669	-877	0.708	474	-621	0.75	355	-466
117	257	-986	0.708	182	-698	0.75	136	-524
130	0	-1095	0.708	0	-775	0.75	0	-581

Shear Summary

Position	IM*(Vehicle Shears) + Lane Load									
	Design Truck		Design Tandem		Govern. Shears		Unfactored & Distributed Shears			
	V+	V-	V+	V-	V+	V-	D.F.	V+	V-	V
0	124	-16	100	-13	124	-16	0.865	107	-14	1
13	104	-17	84	-14	104	-17	0.865	90	-15	1
26	85	-24	69	-24	85	-24	0.865	74	-21	1
39	68	-39	55	-34	68	-39	0.865	59	-34	1
52	52	-54	43	-46	52	-54	0.865	45	-47	1
65	38	-70	32	-58	38	-70	0.865	33	-61	1
78	27	-86	23	-70	27	-86	0.865	23	-74	1
91	17	-101	15	-82	17	-101	0.865	15	-87	1
104	9	-117	8	-94	9	-117	0.865	8	-101	1
117	3	-132	3	-106	3	-132	0.865	3	-114	1
130	0	-146	0	-118	0	-146	0.865	0	-126	1

Total Factored Shears for Strength 1 Load Combination

Position	Distributed. LL + IM										1.75*(LL + IM)		Factored		Factored & Distributed Strength Shears	
	DC ₁		DC ₂		DW		V+		V-		V+		V-		V	
	DC ₁	DC ₂	DC ₁	DC ₂	DW	V+	V-	V+	V-	V+	V-	V+	V-	V	V+	V-
0	64	13	9	9	10	107	-14	80	16	15	111	188	-24	1	284	83
13	46	9	6	6	7	90	-15	58	11	11	79	157	-26	1	225	51
26	28	6	2	2	4	74	-21	35	8	6	49	129	-36	1	168	12
39	11	2	-1	-1	2	59	-34	14	3	3	19	103	-59	1	116	-38
52	-7	-1	-5	-5	-1	45	-47	-9	-1	-2	-12	79	-82	1	64	-89
65	-25	-8	-8	-8	-7	33	-61	-31	-6	-6	-44	58	-106	1	13	-142
78	-43	-12	-12	-12	-9	23	-74	-54	-10	-11	-74	41	-130	1	-32	-194
91	-61	-15	-15	-15	-12	15	-87	-76	-15	-14	-105	26	-153	1	-75	-245
104	-79	-19	-19	-19	-15	8	-101	-99	-19	-18	-136	14	-177	1	-116	-297
117	-96	-22	-22	-22	-18	3	-114	-120	-24	-23	-166	5	-200	1	-154	-348
130	-114	-22	-22	-22	-18	0	-126	-143	-28	-27	-197	0	-221	1	-187	-397